Gdańsk University of Technology
Faculty for Civil and Environmental Engineering

Seismic retrofitting strategies for buildings using innovative approaches

(Doctoral Thesis)

Farzin Kazemi

Supervisor:
Professor Robert Jankowski

Gdańsk, 2025

GDAŃSK UNIVERSITY OF TECHNOLOGY

The author of the doctoral dissertation: Farzin Kazemi
Scientific discipline: Civil Engineering, Geodesy and Transport

DOCTORAL DISSERTATION

Title of doctoral dissertation: Seismic retrofitting strategies for buildings using innovative approaches

Title of doctoral dissertation (in Polish): Strategie wzmacniania odporności sejsmicznej budynków z wykorzystaniem rozwiązań innowacyjnych

Supervisor

Signature

Professor dr hab. inż. Robert Jankowski

Gdańsk, year 2025

GDAŃSK UNIVERSITY OF TECHNOLOGY

STATEMENT

The author of the doctoral dissertation: Farzin Kazemi

I, the undersigned, declare that I am aware that in accordance with the provisions of Art. 27 (1) and (2) of the Act of 4th February 1994 on Copyright and Related Rights (Journal of Laws of 2021, item 1062), the university may use my doctoral dissertation entitled:
Seismic retrofitting strategies for buildings using innovative approaches
for scientific or didactic purposes.[1]

Gdańsk, 2025

signature of the PhD student

Aware of criminal liability for violations of the Act of 4th February 1994 on Copyright and Related Rights and disciplinary actions set out in the Law on Higher Education and Science (Journal of Laws 2021, item 478), as well as civil liability, I declare, that the submitted doctoral dissertation is my own work.

I declare, that the submitted doctoral dissertation is my own work performed under and in cooperation with the supervision of Professor dr hab. inż. Robert Jankowski.

This submitted doctoral dissertation has never before been the basis of an official procedure associated with the awarding of a PhD degree.

All the information contained in the above thesis which is derived from written and electronic sources is documented in a list of relevant literature in accordance with Art. 34 of the Copyright and Related Rights Act.

I confirm that this doctoral dissertation is identical to the attached electronic version.

Gdańsk, 2025

signature of the PhD student

I, the undersigned, do not agree to include an electronic version of the above doctoral dissertation in the open, institutional, digital repository of Gdańsk University of Technology.

Gdańsk, 2025

signature of the PhD student

[1] Art 27. 1. Educational institutions and entities referred to in art. 7 sec. 1 points 1, 2 and 4–8 of the Act of 20 July 2018 – Law on Higher Education and Science, may use the disseminated works in the original and in translation for the purposes of illustrating the content provided for didactic purposes or in order to conduct research activities, and to reproduce for this purpose disseminated minor works or fragments of larger works.

2. If the works are made available to the public in such a way that everyone can have access to them at the place and time selected by them, as referred to in para. 1, is allowed only for a limited group of people learning, teaching or conducting research, identified by the entities listed in paragraph 1.

GDAŃSK UNIVERSITY OF TECHNOLOGY

DESCRIPTION OF DOCTORAL DISSERTATION

The Author of the doctoral dissertation: Farzin Kazemi

Title of doctoral dissertation: Seismic retrofitting strategies for buildings using innovative approaches

Title of doctoral dissertation in Polish: Strategie wzmacniania odporności sejsmicznej budynków z wykorzystaniem rozwiązań innowacyjnych

Language of doctoral dissertation: English

Supervision: Professor Robert Jankowski

Date of doctoral defense:

Keywords of doctoral dissertation in Polish: Wzmacnianie konstrukcji na obciążenia sejsmiczne, Budynki stalowe i żelbetowe, Ocena odporności sejsmicznej, Ocena ryzyka sejsmicznego, Metody uczenia maszynowego, Graficzny interfejs użytkownika.

Keywords of doctoral dissertation in English: Seismic retrofitting, Steel and RC buildings, Seismic performance assessment, Seismic risk assessment, Machine learning methods, Graphical user interface.

Summary of doctoral dissertation in Polish: Niniejsza rozprawa doktorska przedstawia innowacyjne rozwiązania związane ze wzmacnianiem odporności sejsmicznej budynków z uwzględnieniem różnych systemów konstrukcyjnych, takich jak stalowe i żelbetowe ramy, ramy z dodatkowymi stężeniami, ściany murowane stanowiące wypełnienie oraz żelbetowe ściany nośne. Głównym celem pracy było usprawnienie procesu modelowania oraz wzmacniania budynków narażonych na oddziaływania sejsmiczne poprzez zastosowanie innowacyjnych rozwiązań pozwalających ograniczyć czas potrzebny na modernizację oraz wykorzystanie uczenia maszynowego do szacowania odpowiedzi sejsmicznej konstrukcji, poziomów zniszczenia, prawdopodobieństwa uszkodzeń oraz ryzyka sejsmicznego. W badaniach uwzględniono zarówno zewnętrzne, jak i wewnętrzne siły wywołane przez trzęsienia ziemi. Przeanalizowano oddziaływania związane ze zjawiskiem zderzeń pomiędzy sąsiadującymi ze sobą budynkami i zaproponowano współczynniki prawdopodobieństwa do ich ilościowej oceny oraz zaproponowano zastosowanie tłumików w celu ograniczenia negatywnych skutków kolizji. Oszacowano również odporność sejsmiczną ram stalowych z połączeniami sztywnymi i półsztywnymi, w których zastosowano śruby ze stopów z pamięcią kształtu. Dodatkowo przeanalizowano wpływ wypełnień w postaci ścian murowanych na zachowanie się ram stalowych poddanych wpływom sejsmicznym, z uwzględnieniem interakcji podłoże-konstrukcja. Zbadano również innowacyjną metodę wykorzystania materiałów z pamięcią kształtu w stężeniach konstrukcji w celu redukcji trwałych przemieszczeń po trzęsieniu ziemi. Zaproponowano nowy system stężający przy zastosowaniu stalowego tłumika o dwustopniowej charakterystyce odpowiedzi przeznaczony dla konstrukcji zlokalizowanych w strefach sejsmicznych o niskiej, jak i wysokiej intensywności. Uwzględniając ograniczenia dotychczasowych badań, rozwinięto zastosowanie klasycznych i zespołowych metod opartych na uczeniu maszynowym w celu zwiększenia dokładności predykcji. Metody te zastosowano do szacowania nośności granicz-

GDAŃSK UNIVERSITY OF TECHNOLOGY

-nej konstrukcji, oceny odporności sejsmicznej oraz analizy ryzyka sejsmicznego w różnych systemach konstrukcyjnych. Bazując na obiecujących wynikach dla zaproponowanych modeli opartych na uczeniu maszynowym opracowano przyjazny dla użytkownika graficzny interfejs umożliwiający doskonalenie i szersze wykorzystanie tych modeli do analizy metod wzmacniania odporności sejsmicznej konstrukcji budowlanych.

Summary of doctoral dissertation in English: This PhD thesis presents innovative approaches for retrofitting buildings equipped with various lateral force-resisting systems, such as steel moment-resisting frames (SMRFs), reinforced concrete moment-resisting frames (RC MRFs), buckling-restrained braced frames (BRBFs), infilled masonry walls (IMWs), and RC shear walls (RCSWs). The main goal was to facilitate the seismic modeling and retrofitting buildings with novel ideas to reduce the time of retrofitting and improving the seismic performance of structures, as well as to use the predictive machine learning (ML) models to evaluate seismic behavior, seismic performance levels, seismic failure probabilities, and risk assessment. The study considered both external and internal earthquake-induced forces. External forces from structural pounding between adjacent buildings were analyzed, and probability factors were proposed to quantify their effects as well as fluid viscous dampers (FVDs) were suggested to absorb the impact energies for retrofitting scheme. The research evaluated the seismic performance of SMRFs with rigid and semi-rigid joints, incorporating shape memory alloy (SMA) bolts to improve their performance. Additionally, the influence of IMWs on the seismic performance of SMRFs was examined considering soil-structure interaction (SSI) effects, which the results confirmed their influence on seismic behavior. A new concept involving SMA materials in buckling-restrained braces (BRBs) was introduced to reduce residual drifts after earthquakes. Moreover, a novel double-stage yield steel slit damper-buckling restrained brace (SSD-DYB) was experimentally developed to function effectively during both minor and major earthquakes. Recognizing the limitations of existing case-based studies, the research advanced the use of conventional and ensemble ML methods to improve predictive models. These models were developed to estimate seismic limit-state capacities, seismic performance levels, and evaluate seismic risk in various structural systems. Based on the promising results of the proposed ML models, a user-friendly graphical interface (GUI) was developed, which facilitates future enhancements and broadens the applicability of the ML models for retrofitting purposes.

Acknowledgments

I would like to express my heartfelt appreciation to my supervisor, Professor Robert Jankowski, for granting me the opportunity to pursue my doctoral studies under his guidance. His continuous academic support and invaluable advice throughout this journey have played a crucial role in shaping me into a dedicated researcher.

My sincere thanks also go to all my advisors and co-authors, with special gratitude to Professor Fabio Freddi from University College London (UCL), London, United Kingdom, Professor Antonio Formisano from University of Naples Federico II, Naples, Italy, and Professor Michalis Fragiadakis from National Technical University of Athens (NTUA), Athens, Greece, which I had the privilege of completing internships under their mentorship in 2023, 2024, and 2025, respectively, which greatly enriched my academic experience.

Most importantly, I am deeply indebted to my family, especially my late father, who devoted his ambitions to my growth. I am also especially thankful to my wife, Neda, for her unwavering encouragement, constant support, and unconditional love. Achieving this milestone would not have been possible without them by my side.

Lastly, I would like to acknowledge and thank my colleagues, friends from the countries in which I completed my internships, and everyone who, in any way, contributed to or supported me throughout this venture.

Table of Contents

Summary **1**
Streszczenie (Summary in Polish) **2**
List of Papers and Publishing policy **3**
Journal metrics and authors contribution **4**
1. Introduction **7**
2. Objectives and scope of research **12**
3. Methodology and modeling **14**
3.1. Steel structures 14
3.1.1. Modeling of structural members 14
3.1.2. Modeling of steel connections 15
3.1.3. Infill masonry walls 17
3.1.4. Soil-structure interaction 19
3.2. Buckling-restrained braced frames 20
3.2.1. Modeling of FVD devices 21
3.2.2. Modeling of SMA material 21
3.3. Development of double-stage yield steel slit damper-buckling restrained brace 21
3.4. RC structures 23
3.5. RC shear walls 24
.3.5.1 Justification of RCSW modeling 25
3.6. Machine learning methods 27
3.6.1. Data preparation 28
3.6.2. Resampling method 28
3.6.1. Feature selection methods 29
3.6.1. Hyperparameter tuning 30
3.6.2. Statistical evaluation metrics 32
3.6.3. Stacked ML models 32
4. Results and discussion **33**
4.1. Seismic probabilistic assessment of steel and RC structures including earthquake-induced pounding (Paper I) 33
4.2. Optimal retrofit strategy using FVDs between adjacent RC and SMRFs prone to earthquake-induced pounding (Paper II) 34
4.3. Enhancing seismic performance of rigid and semi-rigid connections equipped with SMA bolts incorporating SSI effects (Paper III) 35
4.4. Probabilistic assessment of SMRFs with IMWs incorporating SSI effects (Paper IV) 36

4.5. Enhancing seismic performance of steel buildings having semi-rigid connection with IMWs considering soil effects (Paper V) 37
4.6. Seismic performance evaluation of BRBFs including SMA materials (Paper VI) 38
4.7. Development and experimental validation of SSD-DYB device (Paper VII) 39
4.8. ML-based prediction of seismic limit-state capacity of SMRFs considering SSI effects (Paper VIII) 40
4.9. ML-based seismic response and performance assessment of RC buildings (Paper IX) 41
4.10. Optimization-based stacked ML method for seismic probability and risk assessment of RCSWs (Paper X) 42
5. Conclusions 44
6. Future studies 45
References 45
List of all published papers 52
List of all articles presented during conferences 55
Paper I: 57
Paper II: 100
Paper III: 127
Paper IV: 145
Paper V: 178
Paper VI: 202
Paper VII: 222
Paper VIII: 240
Paper IX: 259
Paper X: 281

Summary

This PhD thesis presents innovative approaches for retrofitting buildings equipped with various lateral force-resisting systems, such as steel moment-resisting frames (SMRFs), reinforced concrete moment-resisting frames (RC MRFs), buckling-restrained braced frames (BRBFs), infilled masonry walls (IMWs), and RC shear walls (RCSWs). The main goal was to facilitate the seismic modeling and retrofitting buildings with novel ideas to reduce the time of retrofitting and improving the seismic performance of structures, as well as to use the predictive machine learning (ML) models to evaluate seismic behavior, seismic performance levels, seismic failure probabilities, and risk assessment. The study considered both external and internal earthquake-induced forces. External forces from structural pounding between adjacent buildings were analyzed, and probability factors were proposed to quantify their effects as well as fluid viscous dampers (FVDs) were suggested to absorb the impact energies for retrofitting scheme. The research evaluated the seismic performance of SMRFs with rigid and semi-rigid joints, incorporating shape memory alloy (SMA) bolts to improve their performance. Additionally, the influence of IMWs on the seismic performance of SMRFs was examined considering soil-structure interaction (SSI) effects, which the results confirmed their influence on seismic behavior. A new concept involving SMA materials in buckling-restrained braces (BRBs) was introduced to reduce residual drifts after earthquakes. Moreover, a novel double-stage yield steel slit damper-buckling restrained brace (SSD-DYB) was experimentally developed to function effectively during both minor and major earthquakes. Recognizing the limitations of existing case-based studies, the research advanced the use of conventional and ensemble ML methods to improve predictive models. These models were developed to estimate seismic limit-state capacities, seismic performance levels, and evaluate seismic risk in various structural systems. Based on the promising results of the proposed ML models, a user-friendly graphical interface (GUI) was developed, which facilitates future enhancements and broadens the applicability of the ML models for retrofitting purposes.

Streszczenie (Summary in Polish)

Niniejsza rozprawa doktorska przedstawia innowacyjne rozwiązania związane ze wzmacnianiem odporności sejsmicznej budynków z uwzględnieniem różnych systemów konstrukcyjnych, takich jak stalowe i żelbetowe ramy, ramy z dodatkowymi stężeniami, ściany murowane stanowiące wypełnienie oraz żelbetowe ściany nośne. Głównym celem pracy było usprawnienie procesu modelowania oraz wzmacniania budynków narażonych na oddziaływania sejsmiczne poprzez zastosowanie innowacyjnych rozwiązań pozwalających ograniczyć czas potrzebny na modernizację oraz wykorzystanie uczenia maszynowego do szacowania odpowiedzi sejsmicznej konstrukcji, poziomów zniszczenia, prawdopodobieństwa uszkodzeń oraz ryzyka sejsmicznego. W badaniach uwzględniono zarówno zewnętrzne, jak i wewnętrzne siły wywołane przez trzęsienia ziemi. Przeanalizowano oddziaływania związane ze zjawiskiem zderzeń pomiędzy sąsiadującymi ze sobą budynkami i zaproponowano współczynniki prawdopodobieństwa do ich ilościowej oceny oraz zaproponowano zastosowanie tłumików w celu ograniczenia negatywnych skutków kolizji. Oszacowano również odporność sejsmiczną ram stalowych z połączeniami sztywnymi i półsztywnymi, w których zastosowano śruby ze stopów z pamięcią kształtu. Dodatkowo przeanalizowano wpływ wypełnień w postaci ścian murowanych na zachowanie się ram stalowych poddanych wpływom sejsmicznym, z uwzględnieniem interakcji podłoże-konstrukcja. Zbadano również innowacyjną metodę wykorzystania materiałów z pamięcią kształtu w stężeniach konstrukcji w celu redukcji trwałych przemieszczeń po trzęsieniu ziemi. Zaproponowano nowy system stężający przy zastosowaniu stalowego tłumika o dwustopniowej charakterystyce odpowiedzi przeznaczony dla konstrukcji zlokalizowanych w strefach sejsmicznych o niskiej, jak i wysokiej intensywności. Uwzględniając ograniczenia dotychczasowych badań, rozwinięto zastosowanie klasycznych i zespołowych metod opartych na uczeniu maszynowym w celu zwiększenia dokładności predykcji. Metody te zastosowano do szacowania nośności granicznej konstrukcji, oceny odporności sejsmicznej oraz analizy ryzyka sejsmicznego w różnych systemach konstrukcyjnych. Bazując na obiecujących wynikach dla zaproponowanych modeli opartych na uczeniu maszynowym opracowano przyjazny dla użytkownika graficzny interfejs umożliwiający doskonalenie i szersze wykorzystanie tych modeli do analizy metod wzmacniania odporności sejsmicznej konstrukcji budowlanych.

List of Papers and Publishing policy

The following published papers are used in this PhD dissertation:

I. Kazemi, F., Asgarkhani, N., Manguri, A., & Jankowski, R. (2024). Seismic probabilistic assessment of steel and reinforced concrete structures including earthquake-induced pounding. *Archives of Civil and Mechanical Engineering*, *24*(3), 178. doi.org/10.1007/s43452-024-00994-7

II. Asgarkhani, N., Kazemi, F., & Jankowski, R. (2022). Optimal retrofit strategy using viscous dampers between adjacent RC and SMRFs prone to earthquake-induced pounding. *Archives of Civil and Mechanical Engineering*, *23*(1), 7. doi.org/10.1007/s43452-022-00542-1

III. Kazemi, F., & Jankowski, R. (2023). Enhancing seismic performance of rigid and semi-rigid connections equipped with SMA bolts incorporating nonlinear soil-structure interaction. *Engineering Structures*, *274*, 114896. doi.org/10.1016/j.engstruct.2022.114896

IV. Kazemi, F., Asgarkhani, N., & Jankowski, R. (2023). Probabilistic assessment of SMRFs with infill masonry walls incorporating nonlinear soil-structure interaction. *Bulletin of Earthquake Engineering*, *21*(1), 503-534. doi.org/10.1007/s10518-022-01547-0

V. Kazemi, F., Asgarkhani, N., & Jankowski, R. (2024). Enhancing seismic performance of steel buildings having semi-rigid connection with infill masonry walls considering soil type effects. *Soil Dynamics and Earthquake Engineering*, *177*, 108396. doi.org/10.1016/j.soildyn.2023.108396

VI. Kazemi, F., & Jankowski, R. (2023). Seismic performance evaluation of steel buckling-restrained braced frames including SMA materials. *Journal of Constructional Steel Research*, *201*, 107750. doi.org/10.1016/j.jcsr.2022.107750

VII. Kazemi, F., Asgarkhani, N., Lasowicz, N., & Jankowski, R. (2024). Development and experimental validation of a novel double-stage yield steel slit damper-buckling restrained brace. *Engineering Structures*, *315*, 118427. doi.org/10.1016/j.engstruct.2024.118427

VIII. Kazemi, F., & Jankowski, R. (2023). Machine learning-based prediction of seismic limit-state capacity of steel moment-resisting frames considering soil-structure interaction. *Computers & Structures*, *274*, 106886. doi.org/10.1016/j.compstruc.2022.106886

IX. Kazemi, F., Asgarkhani, N., & Jankowski, R. (2023). Machine learning-based seismic response and performance assessment of reinforced concrete buildings. *Archives of Civil and Mechanical Engineering*, *23*(2), 94. doi.org/10.1007/s43452-023-00631-9

X. Kazemi, F., Asgarkhani, N., & Jankowski, R. (2024). Optimization-based stacked machine-learning method for seismic probability and risk assessment of reinforced concrete shear walls. *Expert Systems with Applications*, *255*, 124897. doi.org/10.1016/j.eswa.2024.124897

The author would like to acknowledge the policy of publishers and their consideration. This thesis is presented based on ten published papers (see I-X), and for the published version of the papers, following policy is considered:

- Articles from Springer are published under the CC BY 4.0 license.
- Articles from Elsevier are under copyright, but according to the publisher's policy, they can be used as part of thesis and dissertations for non-commercial purposes, provided that full attribution and recognition of the original publication are given (including DOI links to the official publications on ScienceDirect).

Journal metrics and authors contribution

The below list presents the journal metrics and the points based on the list of Polish Ministry of Science and Higher Education:

Paper	Journal	Point value (PMSHE)	Impact Factor (Web of Science)	Cite Score (Scopus)
I	Archives of Civil and Mechanical Engineering	140	4.4	7.7
II	Archives of Civil and Mechanical Engineering	140	4.4	7.7
III	Engineering Structures	140	6.4	11.2
IV	Bulletin of Earthquake Engineering	140	4.1	9.0
V	Soil Dynamics and Earthquake Engineering	100	4.6	7.9
VI	Journal of Constructional Steel Research	140	4.3	7.8
VII	Engineering Structures	140	6.4	11.2
VIII	Computers & Structures	140	4.8	7.9
IX	Archives of Civil and Mechanical Engineering	140	4.4	7.7
X	Expert Systems with Applications	200	7.5	15.0

For each paper, the PhD candidate contribution is described:

Paper I:

Farzin Kazemi (first author, corresponding author) performed analysis, conducted researches on pounding phenomena, modeled steel and reinforced concrete structures, and contributed to the study conception and design. He performed data curation, formal analysis, and validation on modeling of viscoelastic contact element. The first draft of the manuscript was written by him.

Paper II:

Farzin Kazemi (second author, corresponding author) performed analysis, conducted researches on pounding phenomena, modeled steel and reinforced concrete structures, and contributed to the study conception and design. He performed data curation, formal analysis, and validation on modeling of viscoelastic contact element. The first draft of the manuscript was written by him together with the first author.

Paper III:

Farzin Kazemi (first author, corresponding author) performed analysis, conducted researches on rigidity of steel connections, modeled steel structures with semi-rigid and rigid connections, and contributed to the study conception and soil-structure interaction effects. He

performed data curation, formal analysis, and validation on the use of shape memory alloy materials as connection bolt. The first draft of the manuscript was written by him.

Paper IV:

Farzin Kazemi (first author, corresponding author) performed analysis, conducted researches on infill masonry walls, modeled steel structures with infill masonry walls, and contributed to the study conception and soil-structure interaction effects. He performed data curation, formal analysis, and validation on modeling of infill masonry walls. The first draft of the manuscript was written by him.

Paper V:

Farzin Kazemi (first author, corresponding author) performed analysis, conducted researches on infill masonry walls, modeled steel structures with infill masonry walls and different connection rigidity, and contributed to the study conception and soil effects. He performed data curation, formal analysis, and validation on modeling of infill masonry walls together with steel connections with different rigidity. The first draft of the manuscript was written by him.

Paper VI:

Farzin Kazemi (first author, corresponding author) performed analysis, conducted researches on steel buckling-restrained braced frames, modeled steel structures implementing buckling-restrained braces and fluid viscous dampers, and contributed to the study conception and shape memory alloy material. He performed data curation, formal analysis, and validation on modeling of buckling-restrained brace, fluid viscous damper, and shape memory alloy material. The first draft of the manuscript was written by him.

Paper VII:

Farzin Kazemi (first author, corresponding author) performed analysis, conducted researches on double-stage yield buckling-restrained brace, modeled the steel frame and performed dimension analysis, and contributed to the study conception. He introduced the novel double-stage yield steel slit damper-buckling restrained brace, and conducted experimental tests. He performed data curation, formal analysis, and experimental validation on double-stage yield steel slit damper-buckling restrained brace. The first draft of the manuscript was written by him.

Paper VIII:

Farzin Kazemi (first author, corresponding author) performed analysis, conducted researches on steel frames, modeled steel structures, and contributed to the study conception and machine learning methods. He performed data curation, formal analysis, and validation on using machine learning methods for estimating seismic limit-state capacity of steel structures. The first draft of the manuscript was written by him.

Paper IX:

Farzin Kazemi (first author, corresponding author) performed analysis, conducted researches on reinforced concrete buildings, modeled reinforced concrete structures, and contributed to the study conception and machine learning methods. He performed data curation, formal analysis, and validation on using machine learning methods for estimating seismic response and performance assessment of reinforced concrete buildings. The first draft of the manuscript was written by him.

Paper X:

Farzin Kazemi (first author, corresponding author) performed analysis, conducted researches on reinforced concrete shear walls, modeled reinforced concrete shear walls, and contributed to the study conception and machine learning methods. He performed data curation, formal analysis, and validation on modeling of reinforced concrete shear wall and using machine learning methods for estimating seismic probability and risk assessment of reinforced concrete shear walls. The first draft of the manuscript was written by him.

1. Introduction

Seismic events still are the most dangerous natural disasters that may cause many deaths, casualties, and financial loss as well as a huge number of buildings with unstable conditions and safety. Meanwhile, retrofitting buildings can be a potential solution that follows the novelty of energy dissipation systems (i.e., passive, semi-active, and active systems) and uses the latest improvements in the industry. The cost of retrofitting is considered as less as 5-15% of the reconstruction of buildings regarding the selected performance level, which is very beneficial for homeowners and environmental supporters [1]. From this view, retrofitting a building is a challenging task in finding the best building performance within a cost-effective retrofitting strategy, and this may vary from building to building due to the conditions and characteristics of the structural system.

The first step in retrofitting a building is to model the real-world condition of a structure that can allow us to consider different types of retrofitting schemes, however, the placement of the building in adjacency of other structures should also be considered. Since seismic excitation considerably affects the lateral behavior of buildings by leading to structural deformations, stress concentrations, local damages of structural members, local failure of members, and potential instability, the behavior of all structural members should be precisely modeled [2, 3]. Moreover, in the general assessment of a building, two categories of external and internal forces may cause a potential structural failure, in which the external force stems from pounding force during building sway and the internal force stems from failure of structural members and redistributing the forces [4]. This external force, due to impact with adjacent structure, is not considered during the design procedure since the seismic provisions impose a formula for calculating a minimum separation gap between buildings preventing collisions. However, internal forces are considered during the design procedure, and the structural elements should be designed to resist these forces. Failing to properly design or underestimating the design spectrum can result in a weak lateral force-resisting system [5].

The external impact forces during the seismic excitations can be avoided by considering a proper separation distance between adjacent buildings. However, there are old buildings which were constructed in very close adjacency. Although the height of those structures may be limited to less than 10-story levels, the pounding phenomenon can affect them and increase local and global damages. Researchers categorized structural pounding as: floor-to-floor or floor-to-column pounding, pounding due to differences in the weight of adjacent structures, eccentric, or non-eccentric pounding, and pounding between unequal-height buildings in series [6-10]. To prevent earthquake-induced structural pounding, researchers proposed some retrofitting schemes. Implementing fluid viscous dampers (FVDs) between steel structures can be considered an optimal computational strategy to retrofit buildings, and this was improved for retrofitting damaged buildings under seismic mainshock-aftershock sequence [11, 12]. However, the placement of FVDs on the floor level of adjacent steel structures can prevent a large displacement and reduce the impact force on floor levels. The modeling approach was developed to include the seismic response of the adjacent buildings that considers the collapse effects of structures in the analysis. In addition, implementation of FVDs in between all floor levels of steel and reinforced concrete (RC) structures can be a cost-effective approach rather than using FVDs in each of the structures, and this can prevent it from being engineering application [13, 14]; therefore, it is beneficial to provide an optimal strategy for implementing FVDs based on the performance of both structures.

For internal force distribution in a lateral force-resisting system, beam-to-column connections are critical zones in both steel and RC structures, where forces are transferred between beams and columns. These connections are particularly vulnerable during

transferring loads since various deficiencies in design, detailing, and construction have highlighted potential failure modes in these regions, leading to severe consequences during earthquakes [15, 16]. The reasons behind these failures in both steel and RC structures can be noted as several common factors. First, many traditional design approaches did not fully account for the effects of cyclic loading and the associated degradation of material properties under seismic forces. Static load design codes often do not capture the dynamic behavior of connections during an earthquake, which leads to a lack of the necessary ductility and energy dissipation capacity. Second, construction quality and adherence to design detailing play a significant role in the performance of beam-to-column connections. In both steel and RC structures, small deviations from the intended design (e.g., improper welding, insufficient bolt strength, and inadequate reinforcement rebar placement) can affect the connection's behavior under seismic loads [17]. Third, in some cases, the material used in connections may lead to sudden, brittle failure modes rather than gradual yielding and plastic deformation. Brittle failures do not allow for warning signs and effective dissipation of energy, which is an essential factor during an earthquake. To prevent these failures, several strategies have been developed aimed at improving the seismic performance of beam-to-column connections [18-20]. The performance-based design approach is the most important method that explicitly considers the dynamic and cyclic nature of earthquake loading. Moreover, seismic codes provided regulations on prefabricated steel connections to ensure that they can accommodate the expected inelastic deformations. In addition to improving structural design, the use of seismic retrofit and strengthening techniques has become a critical part of ensuring the safety of existing structures. However, some studies proposed adding more bolts to critical steel connection regions [21], improving the welding, increasing the density of transverse reinforcement (e.g., hoops or stirrups) and confinement of concrete joints [22], implementing fiber-reinforced polymer wraps [23, 24], and installing energy dissipating devices to enhance the ductility of the connection [25].

Modeling of real-condition of a building has a significant influence on accurate behavior assessment; therefore, it is necessary to include all influential structural and non-structural members including infill masonry walls (IMWs), which are commonly used in steel and RC structures to partition spaces and enhance architectural functionality. While IMWs are generally considered to be non-structural elements, their interaction with the lateral force-resisting system significantly affects the overall seismic response of a building. The effects of structural IMWs on seismic performance can be both beneficial and detrimental, depending on their design, placement, and material properties. IMWs contribute to lateral stiffness, reducing overall building sway and inter-story drift during seismic excitation. In addition, properly bonded IMWs can enhance load distribution, reducing stress concentrations on primary structural elements [26, 27]. Under moderate seismic loads, IMWs can absorb and dissipate seismic energy through cracking and controlled degradation, improving the damping capacity of the structure; moreover, IMWs decrease the fundamental period of vibration, making the structure more responsive to higher-frequency ground motions [28-30]. Fig. 1 presents the damages in IMWs in steel and RC structures (Sarpol-e Zahab earthquake with M_W= 6.3, November 25, 2018, Kermanshah, Iran), in which IMWs had substantial influence on keeping the structures in life-safety performance level and prevent the total failure of structures.

On the other hand, IMWs are prone to brittle failure through diagonal shear cracking, leading to sudden strength degradation, and weak connections between IMWs and structural frames can cause out-of-plane failure, resulting in falling debris and safety hazards [31]. Partial height of IMWs for window placement can create a short column mechanism, where a column is restrained in part of its height while the remaining portion remains free, which

results in excessive shear stresses in the shorter segment, potentially leading to column shear failure (a common cause of building collapse in earthquakes). Moreover, uneven distribution of IMWs in a building can introduce torsional effects, where certain portions of the structure rotate more than others due to asymmetric stiffness. Furthermore, the absence of IMWs in lower stories (i.e., open ground floors for parking) creates a soft story mechanism, where the lower story is significantly weaker than the upper ones, increasing the collapse risk [32].

Fig. 1. Damages in steel and RC structures with IMWs (Sarpol-e Zahab earthquake with M_W= 6.3, 25 November 2018, Kermanshah, Iran).

The buckling-restrained braced frame (BRBF) is known as a structural lateral-resisting system that provides unbuckling conditions during severe ground motion excitation. In this system, a buckling-restrained brace (BRB) is usually implemented as a concentrically braced frame and consists of two main components of a steel core inside a hollow section filled with low-friction materials. This debonding material prohibits the steel core from buckling in compression conditions and allows for better and more symmetric cyclic performance [33]. The experimental studies confirm that BRBs show stable and symmetric hysteretic behavior under cyclic load and lead to a large amount of energy dissipation during earthquakes [34, 35]. Although this proper function makes them high-performance structural elements, the main drawback of BRBs is the low post-yield stiffness of their cores which can cause large residuals in story levels [37-38]. Cahís et al. [39] introduced a novel core of BRB consisting of a rectangular core shaped into two coplanar bands that can dissipate energy in acceptable promising efficiency. While the resistance of the core plays a key role in the behavior of BRB, Zheng et al. [40] investigated the BRB specimens having double restraints around the core constructed from steel tubes to prevent buckling. Reducing the weight of the BRBs can help the device to be implemented easily and this leads to the invention of all-steel BRBs [41].

Using shape memory alloys (SMAs) as a core can help the BRB device to return to its original shape before deformation and makes it a unique material that can be used for structural elements. Although several dozen types of SMAs with characteristics of

superelasticity have been used in industry, nickel-titanium (Ni-Ti) alloys are the best SMAs with a high shape recovery performance that can be suitable for structures [42]. The superelasticity effects of Ni-Ti alloys are the result of thermo-elastic transformation from the austenitic phase (high temperature) to the martensitic phase (low temperature) [43]. Eatherton et al. [44] investigated the restoring mechanism of a self-centering BRB to implement it in the building finding out that this system can limit the value of residual deformations. Ke et al. [45] proposed a performance-based methodology to enhance the seismic performance of SMRFs with SMAs. Other researchers investigated various types of SMAs for the beam-to-column connections, columns, and braces that can be used in SMRFs [46-48], and performed experimental analysis to justify using SMAs [49, 50].

Since the BRB device should reach a specific load to start the nonlinear behavior, a double-stage yield buckling restrained brace (DYB) can work in different loading steps, enabling a more gradual and controlled transition from elastic to inelastic behavior under varying load conditions [51]. Studies show that the main concern in DYB is the performance of a small segment since this segment plays a crucial role in dissipating the energy of the seismic load. Therefore, Lu et al. [52] proposed adding a frictional damper in parallel to the small segment of DYB to improve the dissipative ability. The experimental results confirmed the ability of the friction damper and improvements in the behavior of DYB. Zhang et al. [53] proposed to have two different cores for DYB, then, it would be possible to change each of them after seismic excitations. This can increase the reparability of the DYB and reduce the retrofitting cost. Yang et al. [54] proposed two parallel DYB cores to be installed in one element. This may reduce the number of DYBs in one bay just by implementing one DYB which may help to reduce the weight of the bracing system, while it can improve the seismic behavior and residual drift of the system.

Traditional approaches to retrofitting structures rely on well-established modeling and analysis techniques, such as finite element methods and empirical design guidelines, to assess structural deficiencies and optimize retrofitting strategies. These methods, while effective, often require experienced experts for modeling and extensive computational effort. However, recent advancements in machine learning (ML) algorithms are transforming this process by enabling data-driven predictions and automated analysis. It should be noted that forecasting is the bedrock of ML models and it plays a crucial role in advancing structural retrofitting analysis. ML-based models can rapidly analyze large datasets, identify patterns in structural behavior, and offer predictive models that help decision-making in retrofitting [55]. The prediction of the seismic responses can be classified as supervised learning, which uses a mathematical model for the estimation of a set of data with inputs and outputs. The accuracy of a model can be determined by comparing the predictions and outputs for the testing dataset [56]. Burton et al. [57] proposed a procedure using kernel ridge regression to estimate the collapse vulnerability. Mangalathu and Jeon [58] developed ML algorithms for estimating the shear strength of RC beam-column joints and the classification of failure modes. Worden and Green [59] used the ML algorithm to demonstrate a data-based approach for nonlinear modal analysis. Luo and Paal [60] proposed the ML-based backbone curve for the force-deformation behavior of concrete columns. Using artificial neural networks (ANNs) for predicting seismic fragility curves [61], random forest (RF) and regression trees to show the high estimation accuracy of identifying the structural safety of a four-story RC frame [62], estimating the residual capacity of damaged buildings [63], and RF algorithm for estimating structural responses for determining the seismic fragility curves of the structures [64] are another examples of the ML methods in engineering application.

Nguyen et al. [65] used the RF, ANNs, and extreme gradient boosting (XGBoost) algorithms to predict the punching shear resistance of slabs. In addition, they developed ML

algorithms to predict maximum displacements of pendulum isolation systems [66]. Noureldin et al. [67] investigated seismic qualitative and design assessment of structures based on serviceability using ML algorithms. Huang et al. [68] proposed a backpropagation neural network to predict the seismic response of structures. Yinfeng et al. [69] used the support vector machine (SVM) algorithm for predicting the nonlinear time history response of structures. Then, Lagaros and Papadrakakis [70] improved neural networks for predicting the nonlinear time history response of a three-dimensional building using six seismic excitations. De Lautour and Omenzetter [71] developed a methodology for estimating structural responses using pattern recognition of damages. Oh et al. [72] developed a neural network model for predicting the seismic response of buildings based on the correlation of records using 2700 artificial records. Luo and Paal [73] proposed a novel artificial methodology for seismic response prediction of RC structures using 272 RC column datasets. As it is obvious, ML algorithms are in the interest of many researchers so as to use them for nonlinear modal analysis [59], predicting seismic responses by achieving fragility curves [64] and predicting maximum displacements of structural systems [66].

Recent studies demonstrated that the modeling, design, and analysis of reinforced concrete shear walls (RCSWs) is complex and time-consuming modeling; however, predicting seismic responses, such as the maximum interstory drift ratio (IDR), using ML models can help in evaluating the seismic performance of RCSWs. This approach not only reduces modeling time but also provides a valuable preliminary estimation for structural assessment and decision-making. Ma et al. [74] introduced a genetic programming-based symbolic regression model to propose a backbone curve model for RCSWs considering 388 existing RCSWs for training and comparative analysis. However, Deger and Taskin [75] used the Gaussian process method to estimate the backbone curve of RCSW. Mangalathu et al. [76] ascertained the failure mode of RCSWs considering geometric layouts, material attributes, and reinforcement specifics. To achieve this, an extensive database with 393 experimental outcomes of diverse geometric configurations was compiled. The study evaluated eight ML models of Naïve Bayes, k-nearest neighbors (KNN), decision tree, RF, AdaBoost, XGBoost, LightGBM, and CatBoost to identify the most effective prediction model. Mansourdehghan et al. [77] presented a damage assessment tool utilizing visual characteristics of a damaged RCSW for recognizing the performance of damaged RCSW and estimating the maximum residual interstory drift ratio (RID) and IDR of the walls. These estimations are derived from a database consisting of 236 pictures corresponding to 72 walls. Zhang et al. [78] utilized a database comprising experimental data from 429 RCSWs sourced from existing literature. The findings demonstrated a high accuracy of 97% for estimating failure modes of RCSW, with the XGBoost and GBM algorithms proving particularly effective. Notably, factors such as cross-section area, shear-to-span aspect, and distributed reinforcement significantly affect the lateral strength of RCSWs. Chou et al. [79] introduced optimized ML methods to improve the accuracy of the formula for estimating the shear capacity of RCSWs and found out that the XGBoost algorithm with an accuracy of 97.8% had the best prediction value. Recently, RCSWs have been explored by many researchers for the targets of structural design [80], cost optimization, and evaluation of performance [81]. For example, Le Nguyen et al. [82] focused the analysis on finding the lateral stiffness of RCSWs.

Although a number of different strategies of building retrofitting were applied in the past, the recent advances in structural modeling, advanced material models, and the development of ML algorithms allow us to consider new technologies in earthquake engineering. Therefore, this PhD thesis investigates the novel retrofitting strategies intended to increase the seismic behavior of structures under seismic excitations. In this PhD thesis, both categories of external and internal forces are considered and their effects on structural behavior are investigated;

moreover, novel retrofitting procedures are considered for improving the performance level of buildings. To reduce the computational time and avoid complex modeling, ML-based predictive tools are proposed to be used in the seismic assessment of buildings with acceptable accuracy.

2. Objectives and scope of research

This PhD thesis aims to investigate novel retrofitting strategies of steel and RC structures intended to reduce the computational modeling procedure by introducing modification factors, prediction of seismic response, seismic performance level, seismic failure, and risk assessment using predictive models developed on ML algorithms. For this purpose, different structural systems of steel and RC structures, buckling-restrained braced frames (BRBFs), and RCSWs were considered. As a general assessment of adjacent buildings, the pounding phenomenon and its effects on lateral steel and RC structures were investigated in the first step (**Paper I)**. Then, a procedure of implementing a fluid viscous damper (FVD) was introduced to decrease the pounding effects and improve the performance of two colliding buildings (**Paper II)**. The seismic performance of rigid and semi-rigid connections of steel structures was investigated in **Paper III** by enhancing their performance by implementing shape memory alloy (SMA) bolts. Due to the high importance of IMWs, probabilistic assessment of steel structure including IMWs and nonlinear soil-structure interaction (SSI) was considered in **Paper IV**, followed by the investigation of seismic performance of steel buildings having a semi-rigid connection with IMWs **(Paper V)**. A novel approach to using SMA materials in buckling-restrained braces (BRBs) was considered in **Paper VI**, and the experimental study on the development of novel double-stage yield steel slit damper-buckling restrained brace (SSD-DYB) was presented in **Paper VII**. Finally, general predictive models based on ML methods were developed to predict the seismic limit-state capacity of steel structures considering SSI effects **(Paper VIII)**, seismic response and performance assessment of RC buildings **(Paper IX)**, and seismic probability and risk assessment of RCSWs **(Paper X)**.

The main purpose of **Paper I** concerns the seismic performance and fragility curve assessment of adjacent RC and steel moment-resisting frames (SMRFs) including earthquake-induced collisions. Three separation distances (SDs) were considered between adjacent RC and SMRFs. Linear viscoelastic contact elements were used to model collisions. The collapse state analyses were performed in numerical models with the possibility of considering the collapsed state of one of the structures during analysis using Tcl programming code equipped with the capability to account for damages during the analysis. The executed program allowed for accurate analysis of a model under nonlinear conditions, employing innovative methods to incorporate damages and monitor structural responses throughout the analysis. The probability factors (PFs) were proposed to modify the failure probability of adjacent buildings to avoid complex modeling and computational analysis.

The goal of the study in **Paper II** is to investigate the implementation of linear and nonlinear fluid viscous dampers (i.e., LVDs and NVDs) at the floor levels of adjacent steel and RC buildings. Optimal placement of LVDs and NVDs between steel and RC frames prone to earthquake-induced pounding was investigated to find the best seismic limit-state capacity and implementation cost. Therefore, the seismic performance levels of both adjacent structures were analyzed, while implementing LVDs and NVDs. Then, the modification factors were proposed to reduce the computational cost and avoid the complex modeling of the pounding phenomenon.

Since the connections of steel structures are more vulnerable to failure as compared to RC joints, the goal of the study in **Paper III** is to explore the seismic performance levels of SMRFs with different connections' rigidity assuming regular steel bolts. Different soil types and SSI effects were considered to investigate their influence on the seismic performance of semi-rigid connections and evaluate the vulnerability of semi-rigid connections in the case of seismic excitations. Since the rigidity reduction can significantly affect the seismic performance and limit-state capacity of SMRFs, shape memory alloy (SMA) bolts with similar diameters, as compared to regular steel bolts, were replaced in models to investigate their effects on the seismic response of SMRFs.

Paper IV provides investigations on seismic performance and limit-state capacity of the structures including IMWs with three types of implementations due to different assignments of openings in buildings. The research aims to investigate the effects of different placements of IMWs, and the nonlinearity effects of SSI on the seismic response of SMRFs. Due to different collapse states for IMWs and SMRFs, a Tcl programming algorithm was developed to control demand limitations during incremental dynamic analysis (IDA). The effects of IMWs on the seismic responses considering SSI effects assuming four soil types were studied. To determine the seismic vulnerability of SMRFs, seismic limit state capacities and seismic fragility curves were plotted and the influence of assumed parameters were investigated.

Paper V aims to investigate the effects of IMWs and the type of structural connections on the behavior of SMRFs by considering the rigidity of connections, soil type effects, and the placement of IMWs. In addition, this paper estimates the structural behavior and improvements in the performance of SMRFs subjected to three types of ground motion subsets. For brevity, the outcomes were included in the graphical user interface (GUI) intended to be a valuable tool for evaluating the potential structural vulnerabilities and making informed decisions related to seismic hazard mitigation and structural design improvements.

In **Paper VI**, the ability of LVDs and SMAs to increase the energy dissipation in buildings exposed to earthquakes was investigated. A comprehensive study was performed to improve the seismic limit-state capacity of BRBFs using these energy dissipation devices. The main purpose of the paper is to minimize residual drift of story levels by implementing LVDs and SMAs and propose prediction factors to estimate the seismic performance level of the improved lateral-resisting system. Moreover, to easily access the results of this study, a tool was developed to estimate the improvements for the purpose of reducing the time of complex modeling and analysis.

In **Paper VII**, the idea of using a novel double-stage yield steel slit damper-buckling restrained brace (SSD-DYB) is proposed and experimentally tested to use both the ability of steel slit damper (SSD) and DYB in one device. Different shapes of SSD-DYB were considered in the study to find out the effects of the number of strips, strip shape, and the width of a large segment of a device. To determine the hysteretic behavior and load-carrying mechanism of specimens, all specimens were subjected to cyclic load. Moreover, the failure mechanism of each SSD-DYB was determined and described in detail. Nine geometric configurations of steel SSD-DYB cores were optimized and introduced.

Since computational cost and analytical efforts to obtain performance levels of a structure are complicated, the aim of **Paper VIII** is to improve the process by proposing ML algorithms as a possible solution that learns to predict a wider range of damage states using a group of datasets. Therefore, ML algorithms were introduced for seismic vulnerability assessment of structures. In addition, this paper aims to explore ML algorithms to predict the seismic limit state capacity of SMRFs founded on different soil types assuming SSI effects.

An ML-based tool was proposed for the primary prediction of the seismic limit state capacity of new and already existing structures.

Paper IX develops a powerful ML-based tool with employs innovative data sampling and hyperparameter optimization methods to estimate the seismic response and seismic limit-state capacities of RC buildings. The paper investigates a wide range of data points containing 165 RC frames with different lengths and the number of bays that were numerically determined to prepare a training dataset of ML algorithms. Then, the GUI was introduced to plot the predicted ML-based median of the IDA curve while mitigating the need for complex modeling and analyses.

Finally, to fulfill the shortcomings of previous studies, the purpose of **Paper X** is to investigate the optimization-based stacked ML models to estimate the median of IDA curves that can provide the performance levels of the RCSWs structures having different input features founded on different soil types. Furthermore, the proposed ML models, which are automated in hyperparameter selection by optimization methods, were used to predict the seismic failure probability (i.e., fragility) curves that are beneficial for seismic risk assessment. The research includes a wide range of RCSWs having different span lengths, floor levels, and soil types, and was validated on a general RCSW to present its capability and reliability. After validation of the proposed ML models on the general RCSW, a user-friendly tool was developed to use the results of this research for a predictive model based on the provided database, so as to allow the database to be updated in the future by increasing numerical analysis.

3. Methodology and modeling

Different structural systems and modeling approaches were used to include the most popular lateral force-resisting systems. The modeling strategy included a symmetric structural plan with a symmetric distribution of lateral force-resisting systems at outer frames, which leads to considering the outer frame as the main system connected to interior columns using the so-called “leaning column”. Structures with different types of systems were assumed to be located in California and were modeled based on different assumptions. This section aims to provide a general view of the structural systems, engineering assumptions, and modeling methodologies employed in papers.

3.1. Steel structures

3.1.1. Modeling of structural members

Accurate modeling of buildings plays a crucial role in the total assessment of structural responses to ensure that simulations and predictions are as close as possible to real-world building performance. In steel structures, detailed modeling must capture the material’s behavior, including the transition from elastic to plastic responses, deterioration effects, and the development of plastic hinges that are critical for energy dissipation during seismic events. It is equally important to account for local buckling phenomena in slender members and the semi-rigid nature of connections (e.g., bolted, or welded joints), which may not behave as idealized pinned or fixed connections (as discussed in detail in **Paper III** and **Paper V**). Even minor discrepancies in representing these characteristics can lead to significant errors in estimating load capacity and the overall dynamic response of the structure.

The modified Ibarra-Medina-Krawinkler deterioration model (IMK hinge model) is a sophisticated modeling concept designed to capture the nonlinear and cyclic behavior of structural components under seismic loading [83, 84]. It is characterized by a backbone curve that represents the monotonic force-deformation relationship of the element and incorporates strength and stiffness deterioration through distinct parameters presented for programming the IMK hinge model in the OpenSees program. These parameters include the effective yield strength, post-yield hardening (i.e., softening in the negative direction) ratios, capping strengths, residual strength, and critical rotations such as yield, post-capping, and ultimate rotations [13, 14]. In practice, the IMK hinge model is implemented as a concentrated plastic hinge, often modeled via zero-length in both ends of an elastic element, which is integrated into the overall structural model to localize inelastic deformations at regions where high bending demands occur (i.e., end of elements). The hinge's behavior is updated dynamically based on the dissipated energy during cyclic loading, allowing it to simulate asymmetric deterioration under positive and negative loading directions. Calibrated against an extensive experimental dataset, the IMK hinge model offers a more realistic representation of the gradual degradation processes and the associated hysteretic response, hence, improving the accuracy of collapse assessments and performance-based seismic design [85, 86]. In the fiber model, after the material's yield, the force-displacement curve is continued at a constant value, exhibiting a bilinear behavior. Consequently, the fiber element is incapable of modeling degradation because its response remains constant even after yielding. In contrast, the IMK hinge model displays a descending slope after yielding, meaning that its curve does not remain constant in the degradation region. This difference in behavior can highly affect the seismic collapse assessment of structures and the IMK hinge model can improve the accuracy of modeling.

It should be noted that research studies provided in this PhD thesis employed different modeling approaches for steel structures using both fiber element (**Paper VI**) and IMK hinge model (**Paper I**, **Paper II**, **Paper III**, **Paper IV**, **Paper V**, and **Paper VIII**). However, due to different conditions of structures and modeling complexity, the fiber model was only considered for columns (**Paper VI**) while the IMK hinge model was devoted to the modeling of beams and columns. In addition, due to the importance of the P-delta effect, it was considered in all structural models.

3.1.2. Modeling of steel connections

Two types of connections of the top and seat angles with double web-angle (used in **Paper III**) and bolted unstiffened endplate (BUEP) connections (used in **Paper V**) were considered, which both are in the boundary of semi-rigid connections according to Fig. 2 (the description is included in **Paper III**). Moreover, Fig. 3 illustrates the geometric configuration of both types of semi-rigid connections. The placement of bolts and distances are presented in Table 4 in **Paper III** and Table 3 in **Paper V**.

It is confirmed that the moment-rotation behavior of the semi-rigid connection is related to the connection details, such as properties of the beam and column, placement of bolts, the end-plate thickness, and the bolts' diameter. To define the rigidity of the connections, the moment-rotation curve of the rigid connection should be calculated based on the plastic bending capacity of the beam. Then, it is possible to calculate the moment-rotation curve of a rigid connection based on the formula introduced by Sherbourne and Bahaari [87] as well as by Bahaari and Sherbourne [88]. It should be noted that the initial stiffness and strength of this curve are associated with a fully rigid connection; therefore, it is possible to achieve

relative rigidities of 80%, 70%, and 60% (for **Paper III**) and 90%, 80%, 70%, 60%, and 50% (for **Paper V**) concerning the initial stiffness and strength of fully rigid connections.

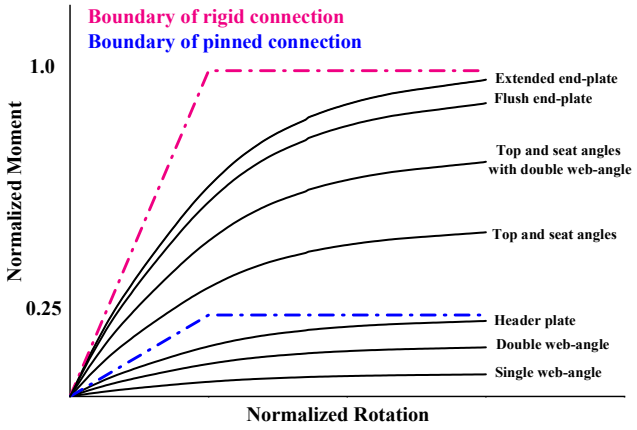

Fig. 2. Comparison of the moment-rotation curve for different types of connections (**Paper III**).

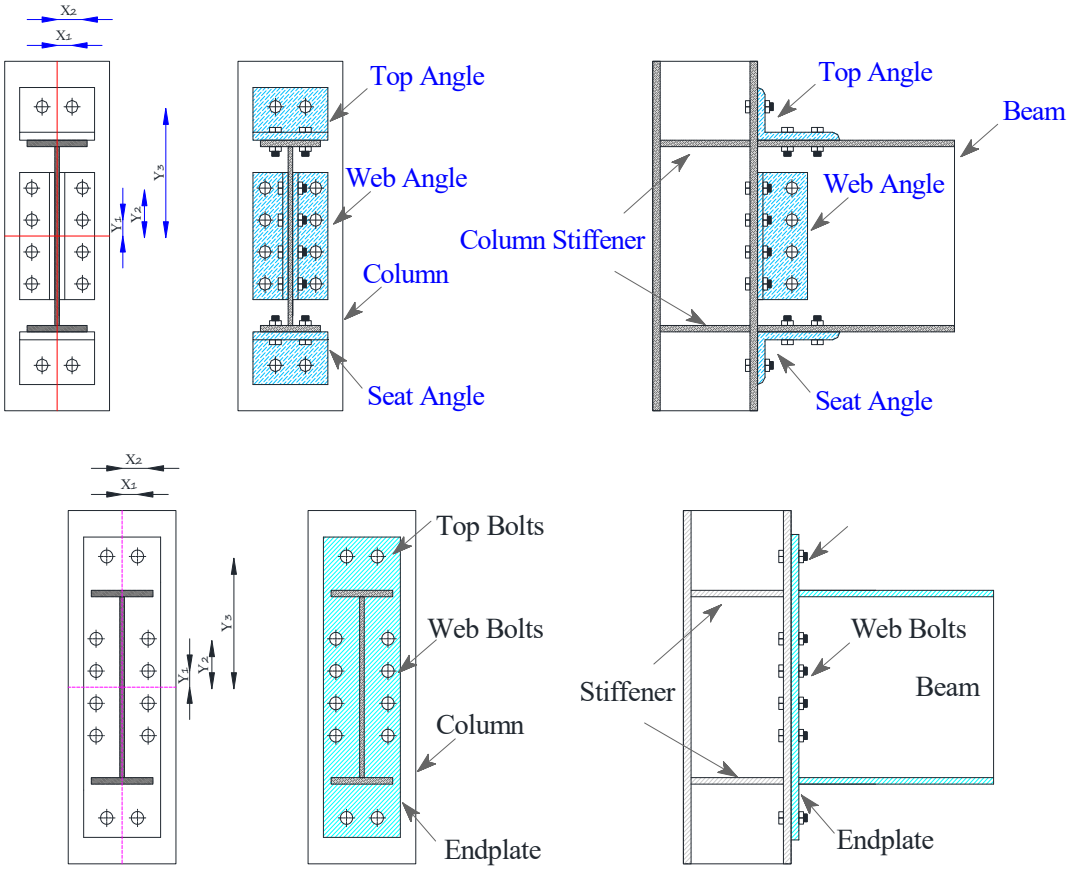

Fig. 3. General configurations of top and seat angles with double web-angle and BUEP beam-to-column connections (**Paper III** and **Paper V**).

Having the initial stiffness and strength corresponding to rigidities, the thickness of angles and the bolt diameter were calculated based on the equation proposed in [87, 88]. Then, by introducing a connection spring according to the moment-rotation backbone curve of a semi-rigid connection, the panel zone of the joint region of beam-to-column intersect was modified as presented in Fig. 4. To model fully rigid connection, it is expected that the rigid

connection can transfer all the moments from the beams into the columns; therefore, the rigid element was used instead of connection spring in the numerical models.

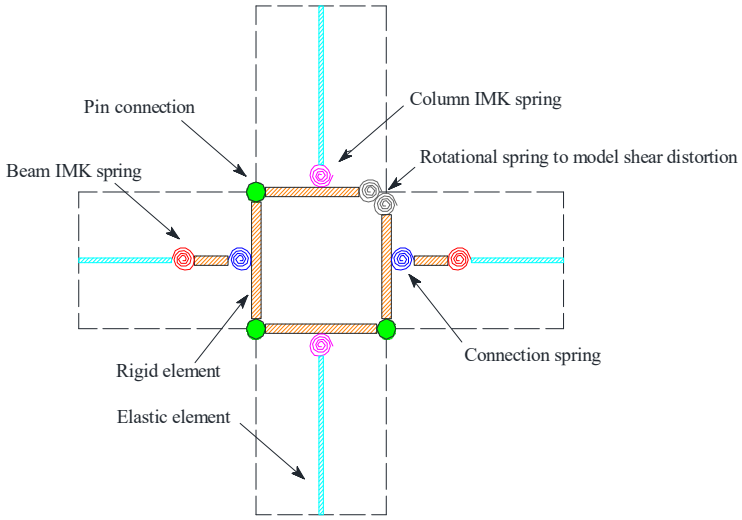

Fig. 4. Configuration of internal joints with panel zone and semi-rigid connection (**Paper III**).

3.1.3. Infill masonry walls

Several numerical models have been proposed over the past few decades to describe IMWs' effects on the lateral behavior of buildings, as well as experimental studies have been conducted for lateral behavior evaluations (e.g., see [89, 93]). The modeling approach proposed by Rodrigues et al. [94] was used for simulating the nonlinear response of IMWs in **Paper IV** and **Paper V**. Fig. 5 demonstrates the IMW modeling approach in OpenSees and the panel zone model.

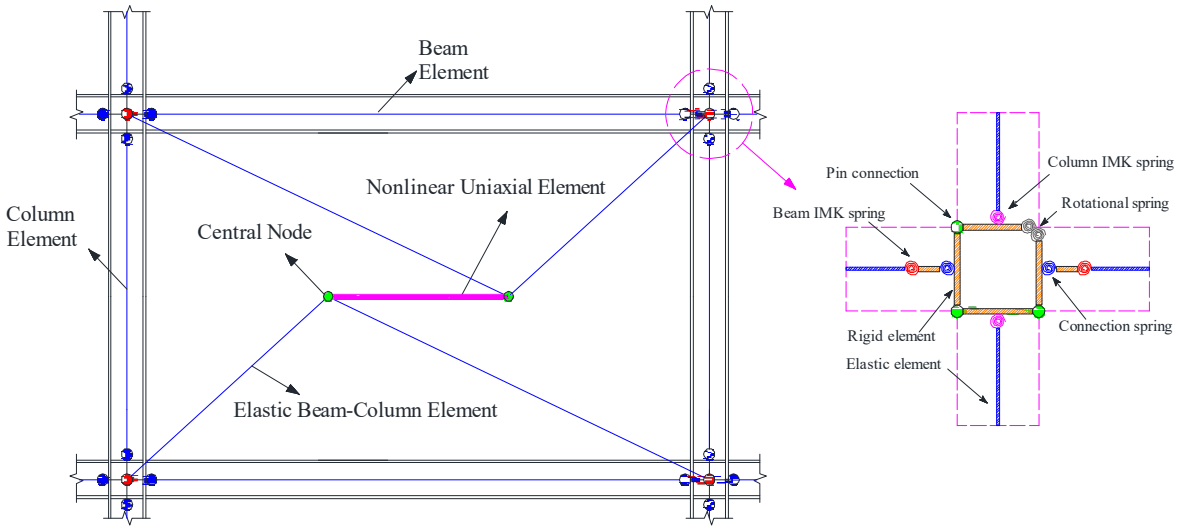

Fig. 5. Schematic view of modeling of IMW and panel zone with and semi-rigid connection in OpenSees (**Paper V**).

For defining the material of the IMW, the experimental test conducted by Kakalestis and Karayannis [95] was used as a validating test (i.e., *Test S-full infill*). Moreover, the IMW

modeling was verified with an experimental test to find out the capability of the considered modeling approach (Fig. 6). In this model, the weak material was selected with compressive strength of mortar and brick equal to 1.53 and 3.10 MPa, respectively, and a thickness of 60 mm (see **Paper IV** and **Paper V**). Then, the cyclic analysis was performed to compare the shear-displacement relation of both experimental and numerical models.

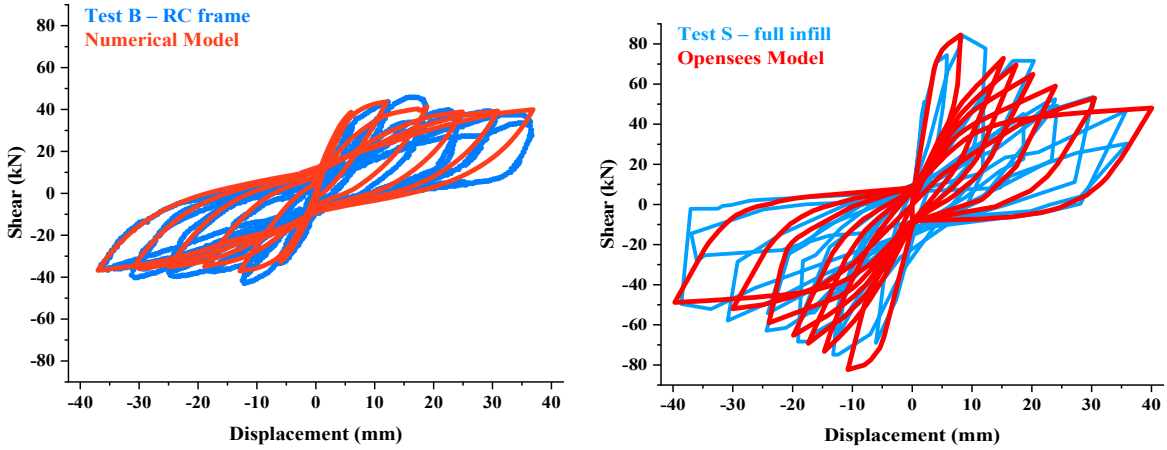

Fig. 6. Verifying the pushover curve of IMW modeled in OpenSees with experimental results of Test B-RC frame and Test S-full infill (**Paper V**).

It is recommended that the uniaxial nonlinear element be characterized by a multi-linear hysteresis curve that is defined in OpenSees as *uniaxial Material Pinching4* [96]. The influence of IMWs on structural behavior was investigated by Furtado et al. [97, 98]. According to their findings, cracks in IMW can be observed between 0.075% and 0.12% drift (d_c). According to the elasticity modulus of IMW, E_m, the d_c = 0.1%, and cracking force, F_c = 0.57 MPa were determined. For IMW with brick-and-mortar properties, the cracking strength divided into maximum strength (F_c/F_{cr}) can be adopted as equal to 0.55 based on experimental results and seismic code recommendations. By defining the *uniaxial Material Pinching4* in OpenSees, the pinching effect is presented in Fig. 7. To evaluate the influence of IMWs, three configuration types were assumed that stem from using IMWs with and without openings as presented in Fig. 8 (**Paper V**).

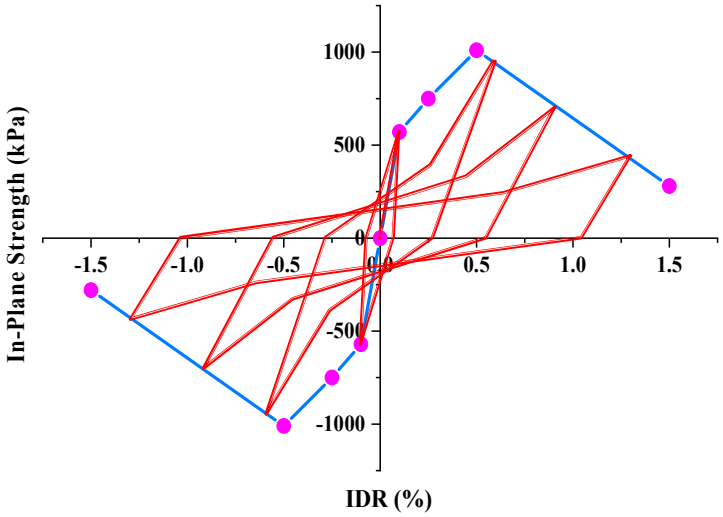

Fig. 7. Backbone curve and pinching effect of uniaxial material considered for modeling of IMW in OpenSees (**Paper V**).

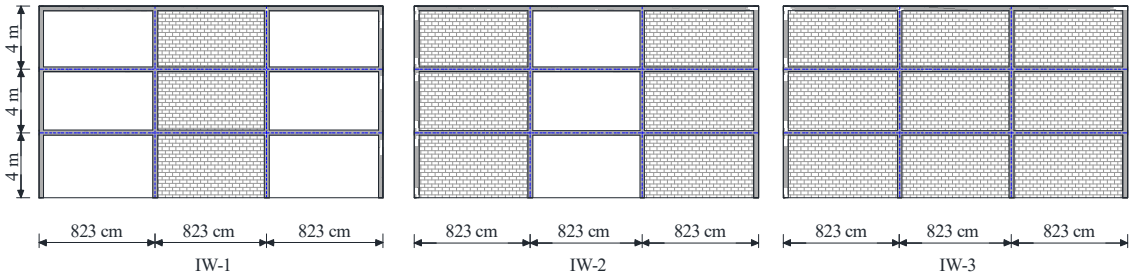

Fig. 8. Three configuration types of IMWs assumed for the 3-story SMRF and other models (**Paper V**).

3.1.4. Soil-structure interaction

Although many improvements have been undertaken to model buildings with a high amount of accuracy, it is hard to consider the effects of SSI in the designing process. Therefore, designers used some simplified procedures proposed by seismic codes to consider the SSI effects. The beam on nonlinear Winkler foundation (BNWF) model, which can be widely used for modeling shallow foundations, retaining walls, and piles, has degrading hysteretic behavior with the ability to define rules [99]. This model employs a series of nonlinear springs and dashpots in parallel to the model soil beneath the foundation [100]. To define the BNWF model parameters, the foundation of SMRFs was designed according to the soil parameters using SAFE 2016 software (**Paper III**, **Paper IV,** and **Paper VIII**). Fig. 9 presents the BNWF model and implementation of the springs and dashpots. The kind of springs used in this model plays a crucial role in soil responses. Therefore, three types of springs, known as the q-z spring, p-x spring, and t-x spring, were used to capture the vertical and rotational resistance, and the sliding and passive resistance of the foundation, respectively. Normalized load-displacement curves of these springs are plotted in Fig. 10. The BNWF model was modeled in OpenSees using material models of *QzSimple* for q-z spring, *PxSimple* for p-x spring, and *TxSimple* for t-x spring [99-102]. It is noteworthy that the material parameters of soils were calculated according to soil parameters and assigned to the models; therefore, for each soil, q-z spring, p-x spring, and t-x spring have different behaviors that can consider the SSI effects.

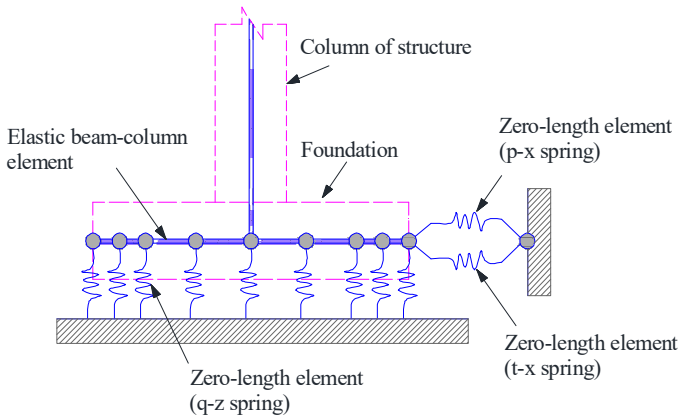

Fig. 9. BNWF model and implementation of the springs and dashpots (**Paper III**, **Paper IV**, and **Paper VIII**).

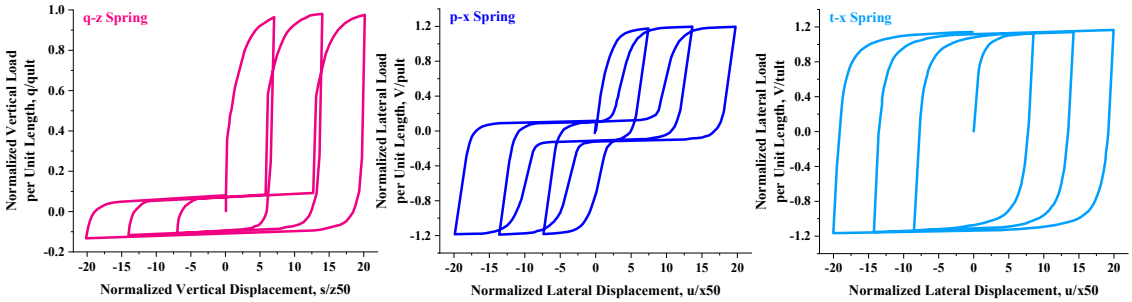

Fig. 10. Normalized load-displacement curves of the nonlinear springs (**Paper III**, **Paper IV**, and **Paper VIII**).

3.2. Buckling-restrained braced frames

To design the BRBFs, the procedures introduced in Section F-4 of ANSI/AISC 341-16 [103] and the performance-based design approach were used in **Paper VI** considering the target drift of 1.75%, which leads to the structural ductility from 3.94 to 6.25 [104]. It should be noted that beam-to-column connections as well as brace connections were assumed as pinned ones (see Fig. 11), and the yielding mechanism was limited to the braces; then, the maximum force demand on beams and columns was determined based on the expected yield of BRBs in tension and compression. In addition, for beams and columns, the yield stress of 379.2 MPa, and for the BRB core, the yield stress of 289.6 MPa was assumed. It was also assumed that the length of the BRB core is equal to 0.7 times the work point-to-work point brace length. Moreover, considering the kinematic and isotropic hardenings of material is crucial to modeling the behavior of BRB devices. Therefore, *Steel02* material with parameters of R_0=20.0, CR_1=0.925, and CR_2=0.15 were selected to obtain the kinematic hardening, and the *Hardening* material was assumed for isotropic hardening. Both materials were combined with *Parallel* material in OpenSees. In addition, the stress-strain hardening ratio of 0.003 was selected for BRB cores to model the tension-compression behavior of the BRB [36-38]. The hysteretic behavior of the BRB used for the first floor of the 6-story BRBF was verified (see Fig. 5 in **Paper VI**).

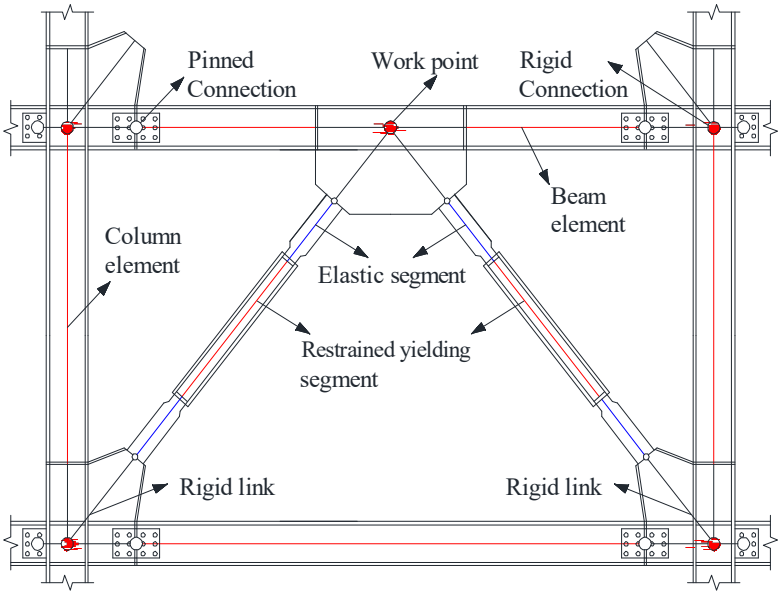

Fig. 11. Schematic illustration of the modeling approach of BRBF in OpenSees (**Paper VI**).

3.2.1. Modeling of FVD devices

FVD is a kind of energy dissipation device that transforms kinetic energy into heat energy to dissipate the seismic energy due to earthquakes. Following Pollini et al. [105], a dashpot in series with two springs was considered to model the FVD. The dashpot has the damping property of FVD, the first spring accounts for the stiffness of the supporting brace, and the second spring is the stiffness of the FVD. The general relation for FVD was presented in equations (1) to (3) in **Paper VI**. Landi et al. [107, 108] proposed a methodology to calculate the supplemental damping ratio, ξ_{FVD}, provided by FVDs based on a comparison of the demand and capacity spectrums derived from the base shear-roof displacement curve (pushover curve). Hence, the effective damping of a structure ξ_{eff}, can be determined by equation (2) in **Paper VI**, and in the first mode of vibration, the supplemental viscous damping ratio, ξ_{FVD}, can be achieved by equation (3) in **Paper VI**.

3.2.2. Modeling of SMA material

In **Paper III** and **Paper VI**, Ni-Ti SMA (Ni=49.3% and Ti=50.4%) is used that was manufactured in accordance with the standard specification for wrought Ni-Ti SMA for medical devices and surgical implants (F2063) issued by ASTM [110]. In this alloy, the percentage of the weight of nickel, carbon, hydrogen, oxygen, and nitrogen are 56.01%, 0.009%, 0.0006%, 0.024%, and 0.003%, respectively. The main crystal phases of SMAs are called austenite and martensite [111]. The changes between these phases occur due to internal forces or temperature. According to the stress-strain hysteresis curve (see Fig. 7 in **Paper III** and **Paper VI**), E_{SMA} is a modulus of elasticity for the austenite phase, R_S is the second slope of the loading phase, F_{MS} is martensite to austenite starting stress, F_{MF} is austenite to martensite finishing stress, F_{AS} is martensite to austenite starting stress, F_{AF} is martensite to austenite finishing stress, and d_L is the strain at which the transformation to martensite is completed [110-113]. The flag-shaped loop of the graph shows the superelastic loading-unloading that dissipates energy with no residual strains. The SMA model was developed based on six parameters to describe both positive and negative loading directions and a factor of $R_{esidual}$ equal to 0.00721 was considered for modeling the residual strain into the hysteresis curve [44].

In **Paper VI**, the SMA mechanical properties are defined based on the results by Eatherton et al. [44]. According to Fig. 7 in **Paper III** and **Paper VI**, the values of E_{SMA}=76530 MPa, $R_S = 0.033E_{SMA}$, F_{MS}=308 MPa, F_{AS}=221 MPa, F_{AF}=124 MPa, and d_L=0.0412m/m were considered. Similarly, it is assumed that SMA braces are buckling-restrained and can undergo compressive force without buckling. It should be noted that the SMA braces should be entered into the nonlinear behavior to dissipate the energy, while the nonlinearity should not extend to beams and columns due to the assumption of limiting the yielding mechanism to the braces. Therefore, the axial strength of both the SMA brace and BRB should be equal.

3.3. Development of double-stage yield steel slit damper-buckling restrained brace

The advanced structural SSD-DYB element is proposed in **Paper VII**. It can be implemented in seismic-resistant building design. It combines the features of a BRB with an SSD and provides a two-stage yield performance that can work as a fuse in the structure and reduce the risk of main structural damage. The SSD-DYB offers two distinct stages of energy dissipation and deformation capacity, which can help to control and enhance the seismic

behavior of a building. Fig. 12 illustrates the ideal hysteretic behavior of SSD-DYB. In the first stage, the SSD component starts yielding and absorbing the energy (i.e., the green shadow in Fig. 12), allowing for further deformation of the brace while still providing resistance to lateral forces. This yielding is intended to prevent abrupt and excessive displacements during a large seismic event, increasing the structure's resilience. The amount of dissipated energy can be controlled by the number, size, and shape of the strips. In the second stage, the large segment behaves like a traditional BRB. It remains relatively stiff until reaching its specified yield strength. During this stage, the brace provides significant lateral stiffness to the structure, helping to limit lateral drift and displacement. The secondary yielding stage is characterized by the brace undergoing plastic deformation while maintaining its load-carrying capacity (i.e., the orange shadow in Fig. 12). The core size in the large segment can control the capacity of this part.

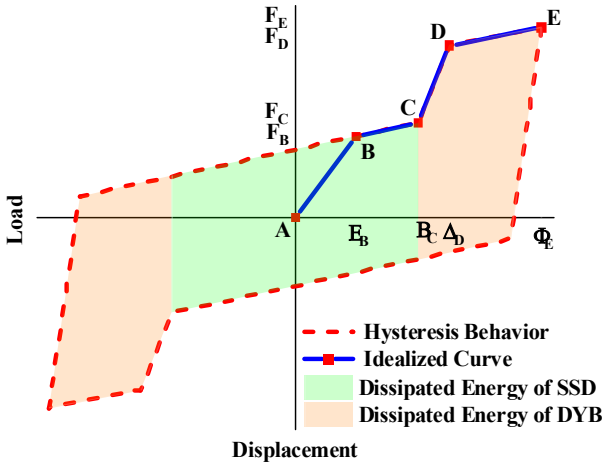

Fig. 12. Ideal hysteresis behavior of SSD-DYB (**Paper VII**).

For the purposes of experimental study, a single-span steel frame, as presented in Fig. 13, was designed with a bay length of 6 m, and height of 3 m, in which, the inverted chevron SSD-DYBs with a length of 3.5 m could be placed. Then, the SSD-DYB was rescaled to 1/5 times its real size to be investigated in the experiment test. The as-built U-shape case was used to protect each core of SSD-DYB from buckling and fulfill the need for the dissipative device. The core plates, as depicted in Fig. 13, adhere to a width of 90 mm and a length of 700 mm, which corresponds to the construction of the main cores of the SSD-DYBs. To prepare the dissipative device, the SSD-DYB core was considered inside of the as-built U-shape (see Fig. 13). The small holes equal to 19.5 mm were considered to have movements of ±6.5 mm, and the large holes equal to 39.5 mm were considered to have movements of ±16.5 mm. These holes control the first and second stages of the SSD-DYB performance. It should be mentioned that the length of the holes for each segment was calculated based on the capacity of SSD and DYB. Fig. 14 illustrates the test setup using the universal testing machine (Zwick/Roell Z400) with the ability to have both cyclic and tensile tests up to 400 kN loading force, which was used during the test.

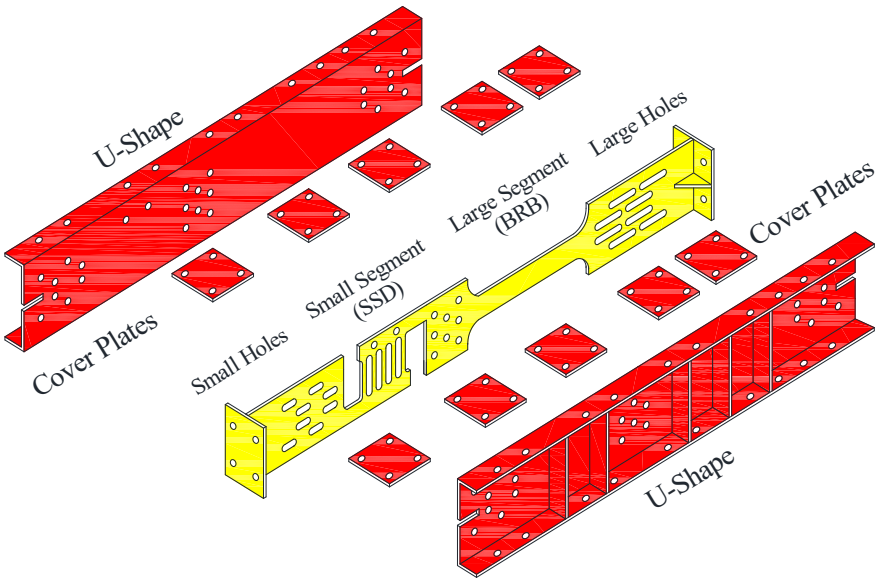

Fig. 13. 3D view and placement of the core in the as-built U-shape case (**Paper VII**).

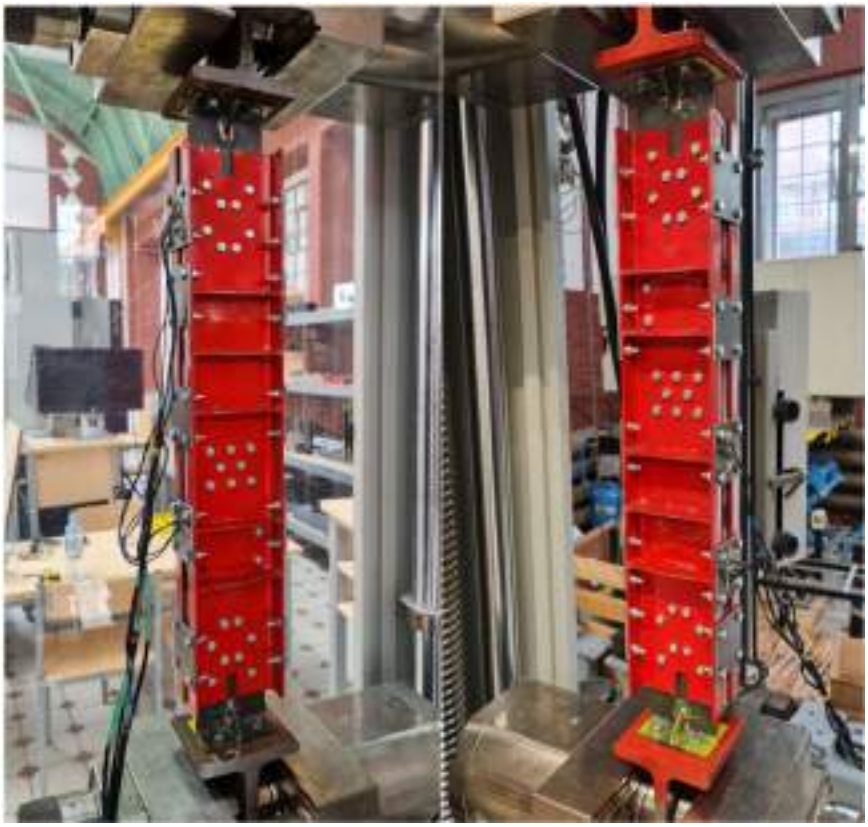

Fig. 14. Test setup of SSD-DYB on the universal testing machine (**Paper VII**).

3.4. RC structures

RC structures require a comprehensive modeling approach that encompasses the nonlinear behavior of concrete material in both confined and unconfined conditions, especially its tendency to crack under tension. In addition, the critical interaction between the concrete matrix and reinforcing rebars, including bond-slip effects that influence load redistribution and ductility, should be considered. In **Paper IX**, 2-, to 12-story RC buildings

having three-bay length types (i.e., 5 m, 6.1 m, and 7.6 m) with the symmetric plan were considered. All buildings were modeled in ETABS software based on soil type D, acceleration parameters of SD_1=0.6g and SDs=1.0g for the high-seismic construction site, and design parameters of R=8, C_d=5.5, and Ω=3 in accordance with ASCE 7-16 [114]. It is noteworthy that the acceleration parameters of the construction site were achieved based on the USGS website [115]. In addition, a floor dead load of 8.4 kN/m^2 and a floor live load of 2.4 kN/m^2 were applied to all floor levels of buildings. To design structural elements, the concrete compressive strength of 34.5 MPa was used [2]. Details of structural elements of RC frames assuming the bay length of 6.1 m were presented in Figures 5-7 (**Paper IX**). To perform collapse analysis, all buildings were modeled as two-dimensional RC frames in OpenSees assuming a leaning column for those gravity columns not included in models to consider the P-delta effects. In addition, the two-dimensional frames were modeled and verified with their corresponding buildings considering the modeling procedures used by Haselton [85]. A plastic hinge model for simulating seismic collapse was used as developed by Ibarra et al. [84] and Altoontash [86]. It should be noted that for considering the real condition of RC buildings, all panel zones were modeled, and concentrate plastic hinge models were used in the ends of structural elements with the possibility of achieving seismic collapse (for more detail on modeling see [85]). To train the ML algorithms, 165 RC MRFs were assumed to have one-, two-, three-, four-, and five-bays, and 2- to 12-story elevations with bay lengths of 5 m, 6.1 m, and 7.6 m. To assess IDR in different intensity measures, and seismic limit-state curves of all 165 RC MRFs, IDAs were performed based on the spectral acceleration in the period of the structure, $S_a(T_1)$, as intensity measure, and IDR as engineering demand parameter, considering near-fault pulse-like and no-pulse records introduced by FEMA-P695 [116]. To perform IDAs, an algorithm was developed to implement the hunt and fill method using both OpenSees and MATLAB software to reduce the time of analysis. It is worth mentioning that the programming code was developed in MATLAB to control the entire analysis procedure; and in addition, to post-process the results of the analysis.

3.5. RC shear walls

The *nDMaterial FSAM* (fixed-strut-angle-model) is a constitutive model developed by Kolozvari et al. [117] to simulate the RC panel element's behavior under cyclic load. The model assumes that strain in both reinforcement bars and concrete is the same, implying a strong bond between them. While reinforcing steel bars experience uniaxial stresses along their length, concrete behavior is described using stress-strain relationships in multiple directions, determined by concrete cracking. Despite primarily representing uniaxial behavior, the FSAM model also includes effects like biaxial damage and compression softening. To transfer shear stress alongside crack, it employs a friction-based elasto-plastic shear-aggregate interlock model and a linear elastic model for dowel action on the reinforcing steel bars. Although designed for use with the shear-flexure interaction (SFI) model for RCSW, the FSAM model can be applied in various contexts. Therefore, in **Paper X**, the *nDMaterial FSAM* was utilized assuming a friction coefficient of 1.0, and dowel action stiffness of 0.005. The parameters that define the cyclic degradation behavior of the reinforcing bars were adjusted to R_0=20, a_1=18.5, and a_2=0.15 (see Table 3 in [117]). Since these models could not perfectly comply with the experimental evaluations, the shear-flexure interaction multiple-vertical-line-element model (SFI-MVLEM) can be used to capture the axial/flexural and shear interaction of the RCSW. To use this model, Kolozvari et al. [117, 118] developed the *SFI_MVLEM* command in OpenSees to incorporate the 2D RC panels modeled with *nDMaterial FSAM*. Fig. 15 illustrates the SFI-MVLEM element used for modeling of RC shear wall in OpenSees in **Paper X**.

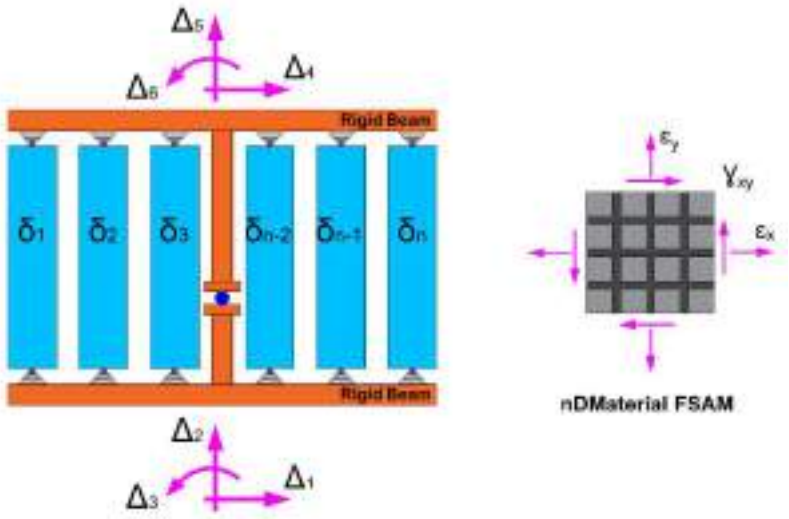

Fig. 15. SFI-MVLEM element used for modeling of RCSW in OpenSees (**Paper IX**).

3.5.1. Justification of RCSW modeling

To justify the RCSW modeling approach, the RW-A15-P10-S78 specimen investigated by Kolozvari et al. [118] was selected. Details of reinforcing and dimensions of the specimen RW-A15-P10-S78 are illustrated in Fig. 16. The specimen has two boundaries at the corners shown by the green dashed line, and the web boundary between them. Therefore, the compressive strength for confined and unconfined concrete was assumed as 72.2 MPa and 55.8 MPa, following the initial tangent modulus of 41051 MPa and 37252 MPa, respectively. In addition, the tensile strength of 2.31 MPa and the initial tangent modulus of 37252 MPa were considered. The consideration of confinement effects in the modeling approach was addressed in [117]. Distinct concrete strengths were observed between confined and unconfined sections, necessitating different modeling approaches in OpenSees. Furthermore, Kolozvari et al. [117] conducted experimental tests to ascertain the concrete strength in various sections of shear walls, including the middle and corners. This methodology of incorporating different concrete strengths aligns with the rationale of accounting for confinement effects. Moreover, the concrete strength must meet the demands of high-rise buildings. Five RC panels were modeled, in which, two outer RC panels represent the confined boundary. In addition, six SFI-MVLEM were considered along the RCSW model, which had a height of 182.9 cm and an aspect ratio of 1.5. The reinforcement ratio of 6.06 and 0.73 was used for the boundary and web of RCSW, respectively, and C=0.4 was used to consider the center of relative rotation. The RCSW model was prepared in OpenSees and displacement-controlled cyclic analysis was conducted assuming the loading protocol having drift ratios of 0.5%, 0.75%, 1.0%, 1.5%, and 2.0%. Different results of specimen RW-A15-P10-S78 were compared with the numerical model of RCSW in OpenSees, and are plotted in Fig. 17. The numerical model has acceptable accuracy to capture the different responses of RCSW and could be used for modeling of RCSWs investigated in **Paper X**.

Since the building has a regular plan, half of the building was modeled in OpenSees for performing IDAs. The structural details of the RCSWs were presented in Fig. A-1, and Tables A-1 to A-3 in **Paper X**. For each RCSW, six RC panels were modeled, in which, two outer RC panels represent the confined boundary and four RC panels were used for the web boundary. It is assumed that the confined and unconfined concrete had a compressive strength of 72.2 MPa and 55.8 MPa, respectively. However, to control the behavior of the

reinforcement bar, the parameters of R_0=20, a_1=18.5, and a_2=0.15 were adjusted for *Steel02* material [119]. Since the gravity columns can affect the results of nonlinear analysis, all gravity columns were modelled as leaning columns as presented in Fig. 18 to include the P-delta effects.

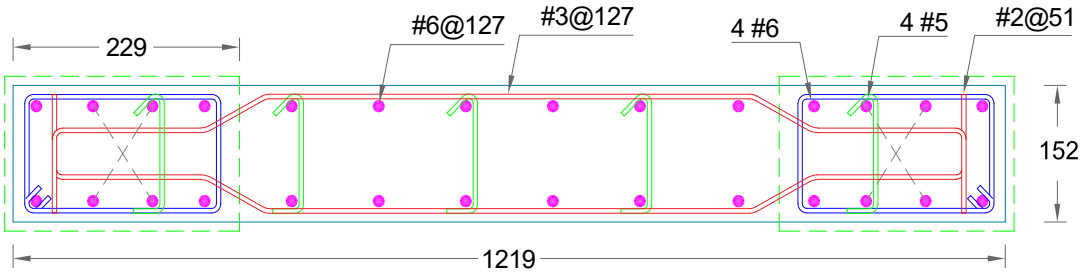

Fig. 16. Cross-section view of the RW-A15-P10-S78 specimen used for verifying modelling of RCSW (**Paper X**).

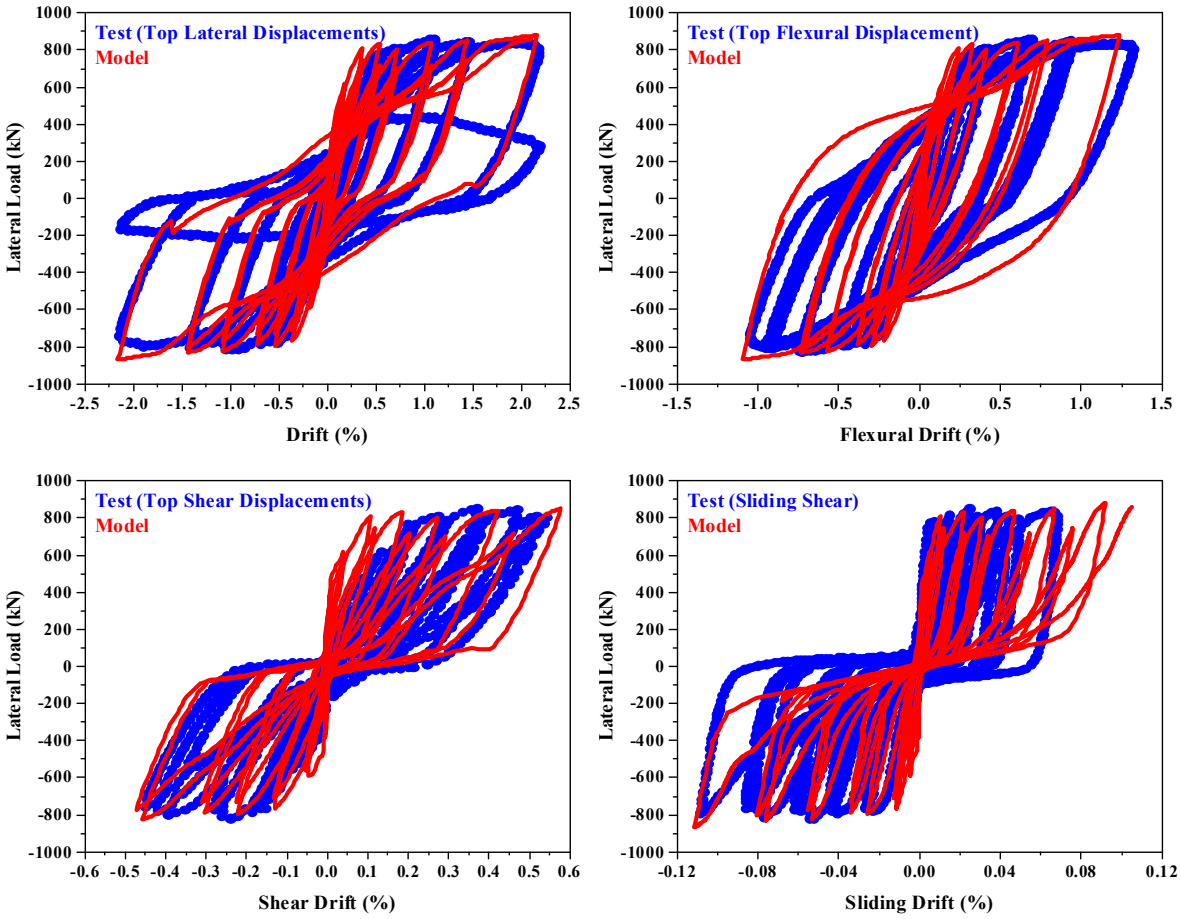

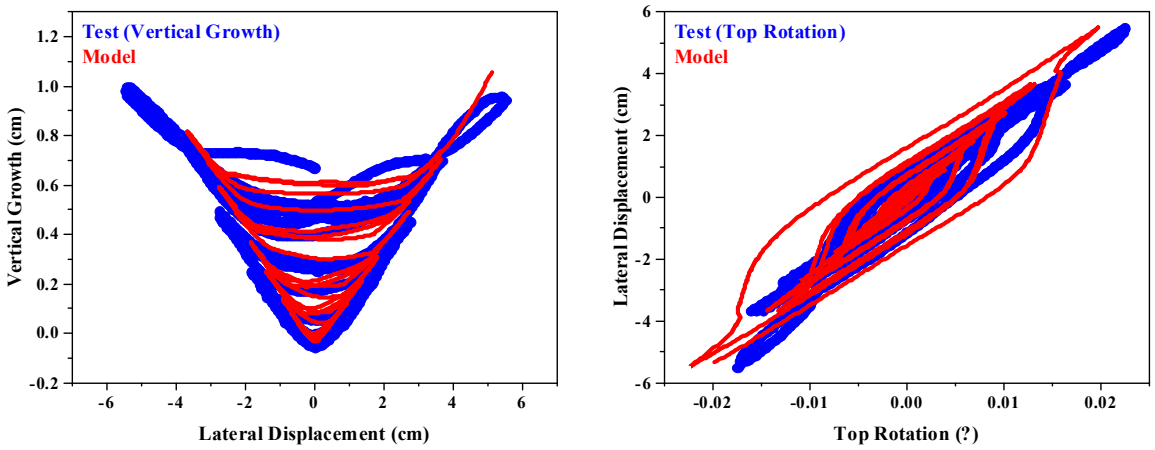

Fig. 17. Comparing the results of the test (RW-A15-P10-S78) and the numerical model of RCSW (**Paper X**).

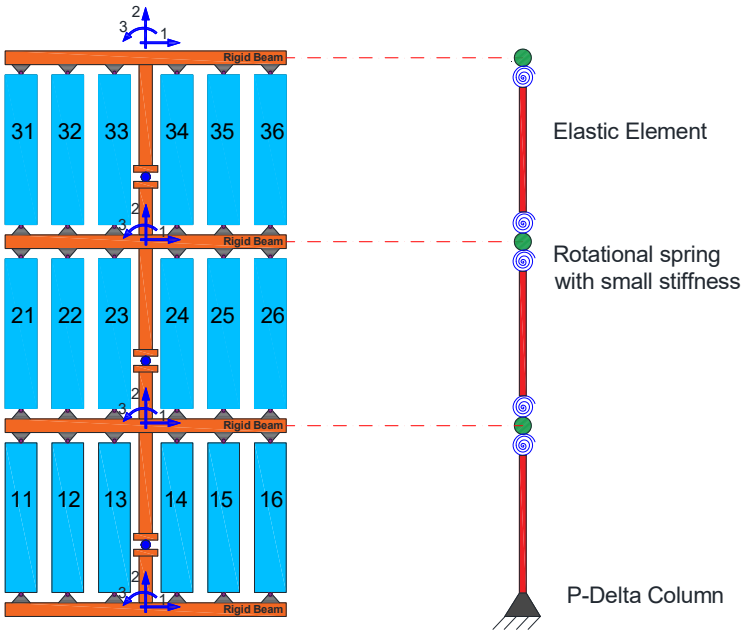

Fig. 18. Modeling of RCSW in OpenSees (**Paper X**).

3.6. Machine learning methods

Introducing ML algorithms for the purpose of estimating the seismic response of structures was performed in this PhD thesis to use innovative approaches for reducing the complexity of modeling, computational time, implementation cost, and numerical analysis. Fig. 19 illustrates the formal steps of preparing an ML-based prediction model. According to this procedure, the ML model preparation and hyperparameter optimization play a crucial role in the capability, reliability, and generalizability of the proposed ML models. Different types of ML methods were used to improve the predictive models for fulfilling the purpose of the PhD thesis, and the novel ML models were proposed for estimating the seismic limit-state capacities of SMRFs (**Paper VIII**), seismic response and performance assessment of RC structures (**Paper IX**), and seismic limit-state capacity, seismic failure probability and risk assessment of RCSWs (**Paper X**).

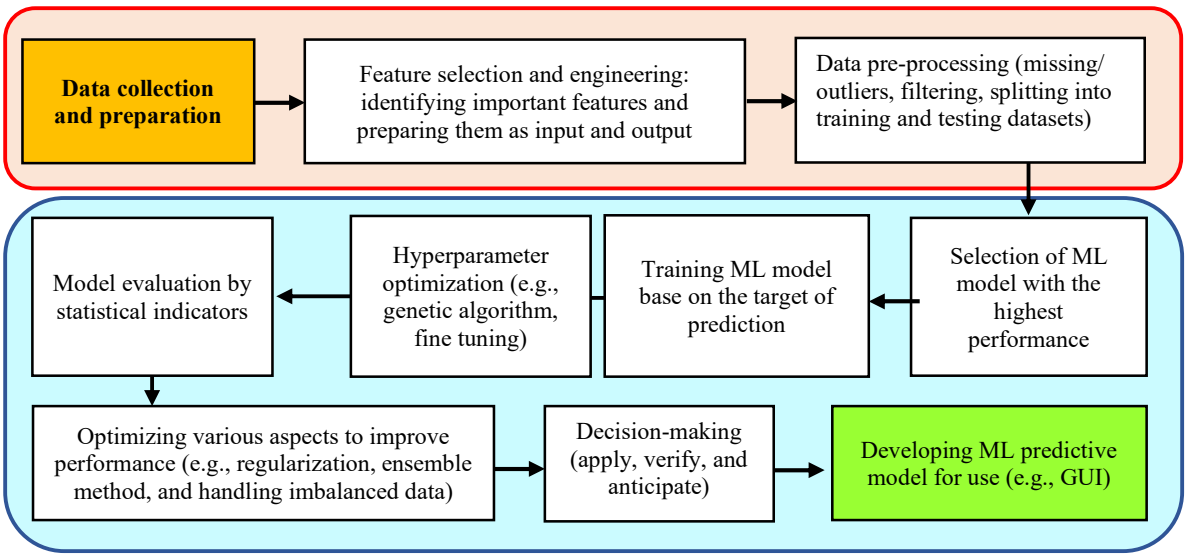

Fig. 19. Formal steps of preparing an ML-based prediction model.

3.6.1. Data preparation

According to the modeling of structures, the deformation-based index of IDR was selected as a limit threshold for the definition of seismic limit-state capacity. During IDAs, the structural response (i.e., IDR) was evaluated for a range of ground motion intensity levels (i.e., $S_a(T_1)$), and in each intensity level, the structural response was compared to a predefined threshold (i.e., collapse limit) to check whether the structure passed that threshold or not. According to the developed programming code in Tcl and MATLAB for conducting IDAs, as the intensity measure was increasing incrementally, the structural response was assessed at each step, and damage states were assigned based on the calculated values of the demands. Collapse cases occur when the structural response exceeds critical thresholds associated with failure. In accordance with FEMA 356 [120], performance levels of SMRFs in states of immediate occupancy (IO), life safety (LS), and collapse prevention (CP) were considered to correspond to IDR of 0.7%, 2.5%, and 5.0%, respectively, and for RC structures, values of 1.0%, 2.0%, and 4.0% were selected, respectively.

By capturing seismic responses of SMRFs (**Paper VIII**), RC structures (**Paper IX**), and RCSWs (**Paper X**) at floor levels, IDA curves could be plotted, and using the median of the IDA curve, the seismic performance levels of structures could be determined. It should be noted that the hunt-and-fill method was employed to reduce the computational effort and improve the accuracy of capturing the collapsed capacity. To perform IDAs, the far-field, near-field pulse-like, and near-field no-pulse records extracted from FEMA P695 [116] were used. The results of IDAs were collected for all considered structures and were prepared for training ML algorithms.

3.6.2. Resampling method

Resampling methods are essential for creating new datasets from existing samples for pre-evaluating the capability of the ML models in categories of parametric and nonparametric methods. Nonparametric techniques, like bootstrapping and permutation testing, do not depend on assumptions about the underlying data distribution, making them ideal for unknown or un-assumed distributions. Bootstrapping involves repeated random sampling with

replacement from the original sample, creating new samples to estimate statistical variability. However, permutation testing shuffles data labels to compute statistics, generating null distributions for hypothesis testing and population inferences. Since there are different methods of resampling, parametric resampling methods such as cross-validation (CV) as presented in Fig. 20, were used to better train the ML models. CV includes various techniques like *k*-fold, repeated *k*-fold, leave-one-out, random permutation, and group *k*-fold CVs. The *k*-fold CV partitions data into training and testing sets, fitting a model to the training set, and evaluating its performance on the test set iteratively. The *k*-fold technique splits data into equal folds, training the model on *k*-1 folds and evaluating the remaining fold iteratively. Repeated *k*-fold CV repeats the process *r* times for more reliable performance estimation. The leave-one-out method uses each sample for validation and others for training, providing an unbiased performance estimate. Random permutation CV shuffles and splits data for multiple performance score iterations. Group *k*-fold ensures the correlated groups remain together, preventing model evaluation on training data [121, 122].

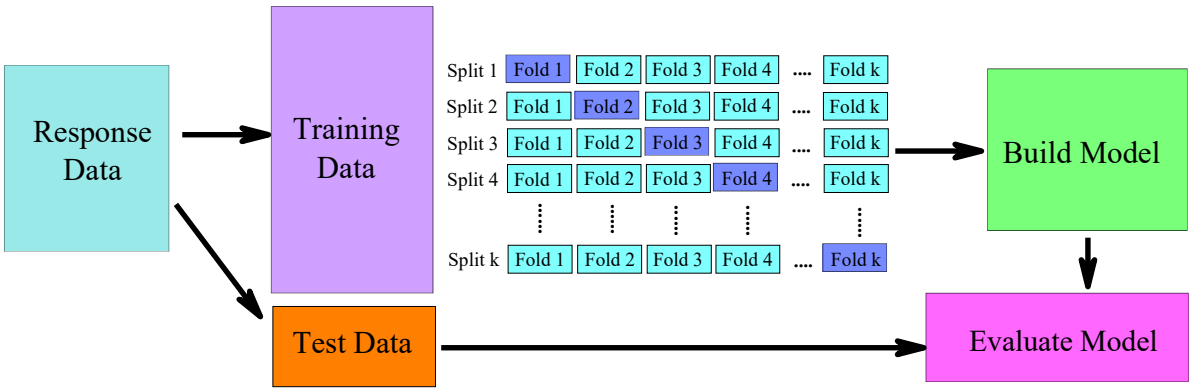

Fig. 20. Architecture of *k*-fold cross-validation (**Paper IX**).

3.6.1. Feature selection methods

Feature selection methods, crucial for identifying important features in a dataset, fall into three categories wrapper, embedded, and filter techniques (see Fig. 21). Embedded methods, like most minor absolute shrinkage and selection operator (LASSO) regression and ridge regression, can embed a penalty term to minimize coefficients of less relevant features that effectively zeroing them out. Conversely, wrapper methods, like recursive feature elimination and forward/backward selection, can train models on feature subsets and validate model performance as the criterion for selection, which is a computationally intense but precise approach. In contrast, filter methods, such as correlation-based and mutual information-based selections, can employ statistical measures to score each feature and pick the most relevant ones for a given algorithm. Using these three feature selection methods can widely empower the ability of the ML models and provide them with a tool for regulating the fluctuations of predictions.

Relative importance achieved by trial and error in one ML model is considered a reliable feature selection method since the importance of each feature can be compared (**Paper IX**). However, novel approaches of Heatmap presentation and partial dependence plots (PDPs) demonstrate the most significant input features for predictive modeling and propose neglecting those less important features to empower the predictive model. Features that have a

strong correlation with the target variable can be prioritized for model training. The PDP is an analytical tool used to assess and illustrate the effects of individual features on the prediction target within an ML model. It aids in discerning whether these effects are positive or negative concerning the model's predictive performance. PDPs are instrumental for isolating the influence of a single feature while keeping other variables constant, allowing for a comprehensive examination of how changes in the feature affect the model's predictions [123]. When exploring the PDP of a feature, it becomes evident whether increasing or decreasing values of that feature positively or negatively affect the prediction target (**Paper X**).

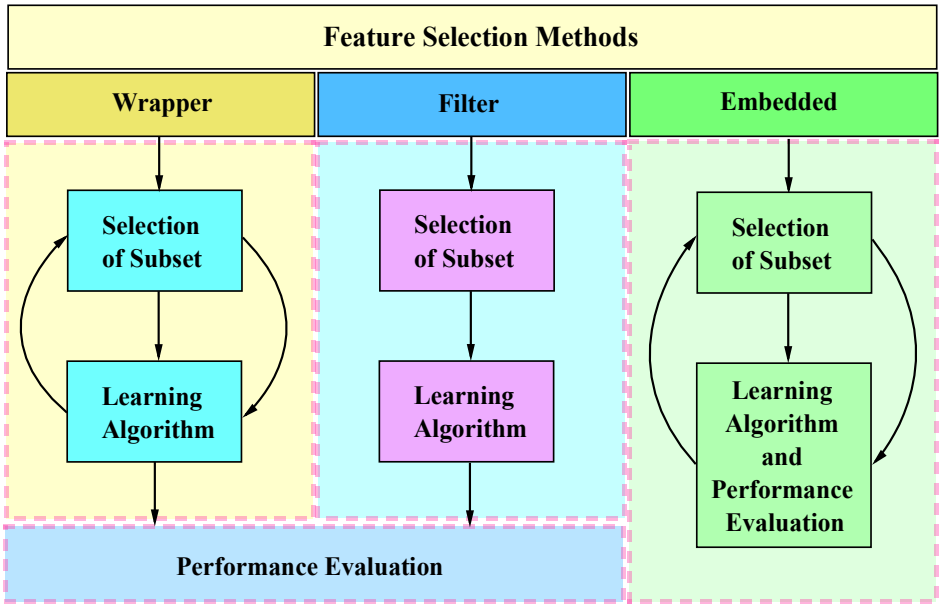

Fig. 21. Illustration of feature selection methods [23].

3.6.1. Hyperparameter tuning

Hyperparameter tuning in ML involves techniques like grid search, random search, halving search, and fine-tuning. Grid search assesses the best hyperparameter combination from predefined sets by training the model on all possible combinations as an effective yet computationally intensive method [124]. In random search, sets of hyperparameters are randomly chosen and trained to find the best set, which is suitable for high-dimensional spaces and more efficient than grid search. Halving search trains numerous candidate models on subsets of data with various hyperparameters, discarding the worst models and refining the better ones iteratively, which is ideal for large datasets and models [125]. Hyperparameter fine-tuning optimizes ML model parameters like learning rates, network layers, regularization strength, and kernel types to enhance performance on specific tasks or datasets. Fig. 22 presents the illustration of hyperparameter optimization methodology. Achieving this involves exhaustive experimentation with different hyperparameter combinations, demanding careful selection of tuned hyperparameters and search algorithms to ensure efficient and effective fine-tuning [126, 127]. The hyperparameter fine-tuning method was used in **Paper VIII**, **Paper IX**, and **Paper X** as the main method for improving the performance of ML models.

In **Paper X**, hyperparameters were fine-tuned using an optimization method combined with the tree-based pipeline optimization tool (TPOT) as a Python-based automated ML (AutoML) framework, specifically prepared from auto-sklearn (presented in Fig. 23). The

utilization of TPOT enhances the efficacy in optimizing ML pipelines, therefore, conventional ML models were improved with this hyperparameter optimization tool.

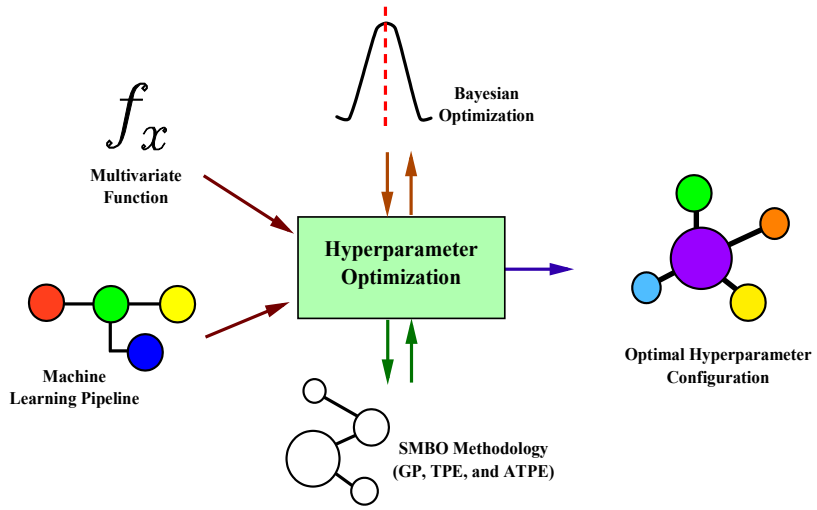

Fig. 22. Illustration of hyperparameter optimization methodology [23].

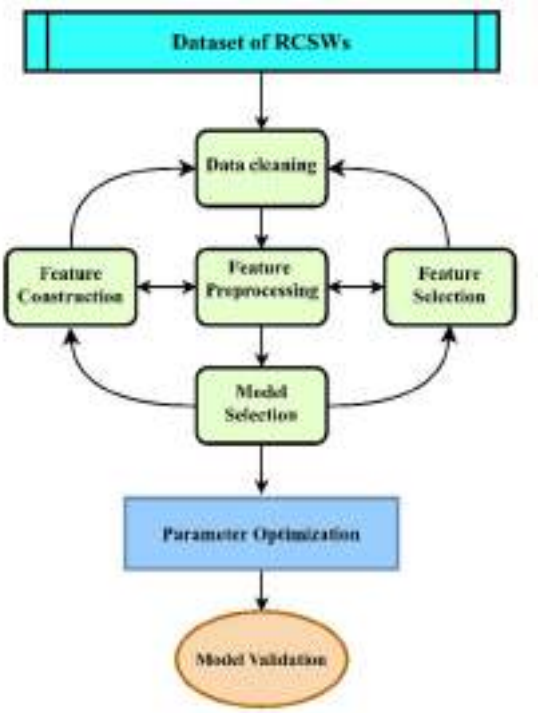

Fig. 23. Illustration of automated TPOT (**Paper X**).

Since the optimized hyperparameters can improve the performance of ML models, optimization methods of Bayesian optimization (BO), genetic algorithm (GA), particle swarm optimization (PSO), and gradient-based optimization (GBO) were used to find the best hyperparameters of stacked ML models (**Paper X**). For this purpose, those ML methods that can be regulated by hyperparameters were selected and the value of each hyperparameter was assumed as the target of optimization. This procedure is time-consuming; therefore, a small part of the dataset has been randomly selected to reduce the time of analysis and improve the efficiency of the algorithms. This can lead to finding the best hyperparameters in a small part of the dataset and doing the main analysis on the whole dataset only by the optimized hyperparameters, which can decrease the total time of execution, as compared to conventional

methods of fine-tuning. By using a multi-agent system, where each agent represents an optimization method (i.e., BO, GA, PSO, and GBO), they can communicate and share information, such as best-performing hyperparameters or exploration results (**Paper X**).

3.6.2. Statistical evaluation metrics

Statistical error indicators, often referred to as performance metrics or evaluation measures, play a crucial role in the assessment of ML models. These indicators provide quantitative insights into how well a model is performing and help data scientists and researchers make decisions about model selection, optimization, and overall effectiveness. Some of the most used statistical indicators are illustrated in Table 2 in **Paper X**. By quantifying performance, data scientists can assess which model performs better in terms of accuracy, reliability, the spread of errors, and other relevant metrics. Statistical error indicators offer a systematic and numerical evaluation of a model's performance. They provide a clear objective measure of how well the model is making predictions based on the input data. In addition, error indicators help identify overfitting (i.e., where a model is complex and fits train data but performs poorly on new datasets) and underfitting (i.e., where a model is simple and fails to capture underlying patterns) (**Paper X**).

3.6.3. Stacked ML models

A stacked ML model is a sophisticated ensemble learning method designed to improve predictive accuracy by combining multiple ML algorithms. The procedure begins with the selection of a diverse array of base learners, including ANNs, RF, ETR, BR, GBM, XGBoost, LightGBM, and CatBoost [128, 129], to ensure comprehensive data analysis. Each base learner is individually trained on the training dataset to generate initial predictions. To prevent overfitting, out-of-fold predictions are employed by partitioning the training data into *k*-folds, training each model on *k*-1 folds, and making predictions on the remaining fold. These out-of-fold predictions, combined with those on the validation set, create meta-features. A meta-learner, usually a simpler model like linear regression, is then trained on these meta-features to determine the optimal combination of the base learners' predictions. This meta-learner synthesizes the results, producing a final prediction that integrates the strengths of all individual models while minimizing their weaknesses. Through this meticulous process of combining and weighting the outputs of various algorithms, the stacked ML model achieves superior accuracy and robustness, as compared to any single ML model. Therefore, sub-models integrated into stacked ML models undergo optimization to enhance results and reduce computation time. Fig. 24 illustrates the stacked MLs used and the optimal selection of the sub-models.

To assess the effectiveness of models, an initial step is involved in the selection of optimal hyperparameters for ML models. Subsequently, these ML models are integrated into the ensemble model using respective best hyperparameters to evaluate their performance within the combined model. Recognizing that utilizing all sub-models in a singular model does not meet the objective of reducing computation time, a systematic procedure is implemented to select the optimal combination of sub-models within a stacked ML model. The process of pre-processing and combining one to six sub-models for a stacked ML model using error indicators involves several steps to improve the predictive power and robustness of the model. It is common to experiment with different combinations of sub-models, error weighting schemes, and combination methods to find the optimal ensemble configuration. In

Paper X, different combinations were selected and finally, five stacked ML models were chosen. Stacked-ML-1 includes submodels of BR, XGBoost, and GBM, and Stacked-ML-2 includes submodels of ETR, RF, and BR. Stacked-ML-3 includes submodels of ETR, RF, CatBoost, XGBoost, and GBM. Stacked-ML-4 includes submodels of LightGBM, XGBoost, and GBM, and Stacked-ML-5 includes submodels of RF, XGBoost, and GBM. It is noteworthy that these models were chosen from different combinations of models according to the results of pre-processing. In addition, the alone ML models were assumed to compare their performance with Stacked ML models (**Paper X**).

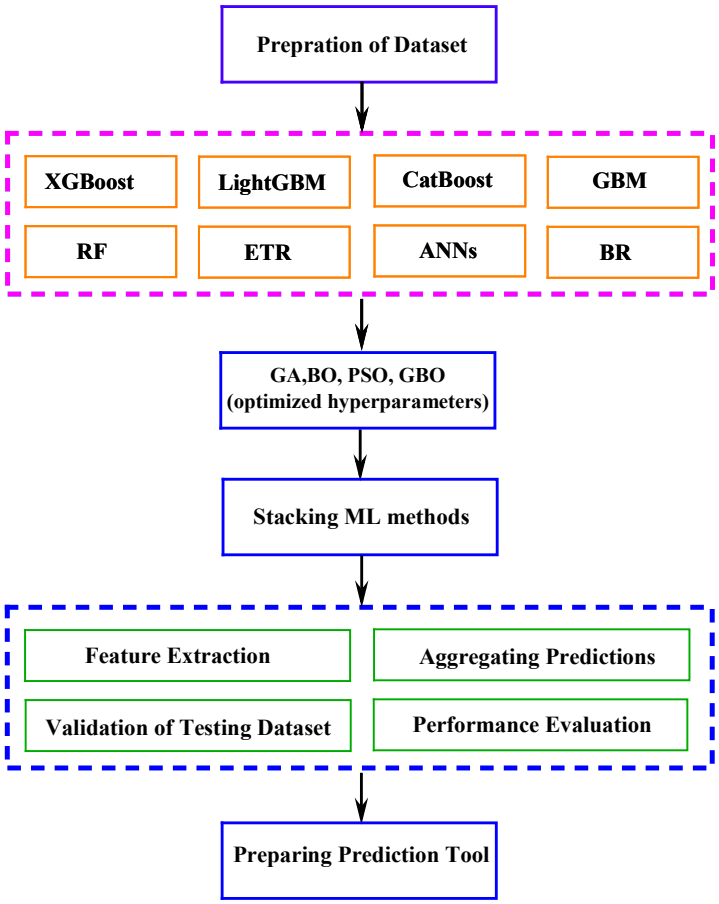

Fig. 24. Architecture of Stacked ML model and the optimal selection of the sub-models (**Paper X**).

4. Results and discussion

4.1. Seismic probabilistic assessment of steel and RC structures including earthquake-induced pounding (Paper I)

The evaluation of the limit state probability of steel structures in collision with RC structures was conducted in **Paper I**, which included near-filed pulse-like and no-pulse records introduced by FEMA-P695 [55] given SDs of 0.0, $0.5SD_{min}$, and $1.0SD_{min}$. Assuming the real condition of buildings and continuing the analysis even after the collapse of one of the buildings was the novelty of the study. According to the developed analytical model, it was possible to perform IDAs for adjacent colliding structures with different fundamental periods (e.g., $T_{1,1}$ and $T_{1,2}$) assuming the effects of collapsed structures as they happen in real conditions. The median of IDA curves and fragilities of selected structures were determined

and probability factors were proposed to estimate the limit state probability of considered colliding structures.

The findings validate that the $S_a(T_1)$ values for RC structures, across various drift thresholds, including the near-filed pulse-like record subset, are lower as compared to the near-filed no-pulse record subset. Consequently, it is evident that the near-filed pulse-like record subset has the potential to heighten the vulnerability of adjacent structures. Similar outcomes were observed for 3-story steel structures, while the $S_a(T_1)$ values of 5-story and 9-story steel structures exhibited distinct trends across different drift thresholds. It is evident that structural collisions can exert external forces on the contact level of adjacent structures. These external forces may lead to sudden changes in the moment and rotation curves as compared to the isolated condition of the structure. Examination of these external forces for 9-story steel structures colliding with 3-story RC structures, assuming an *SD* of 0.0, revealed that the maximum moment values of column and beam hinges increased by 37.96% and 13.22%, respectively. Additionally, the maximum rotation values of column and beam hinges increased by 31.25% and 29.62%, respectively.

The analysis results indicate that structural pounding can considerably affect performance levels. For instance, in 3-story and 5-story steel structures in collision with 5-story RC structures, the total collapse performance decreased by 4.22% and 4.17%, respectively, while the total collapse performance was improved by 26.14% in 9-story steel structures in the near-filed pulse-like record subset under the assumption of $1.0SD_{min}$. To apply the findings of **Paper I**, the seismic probability factors were proposed to estimate the probability of capacity levels in various performance states such as IO, LS, CP, and total collapse, assuming 0.0 and $1.0SD_{min}$, including both near-filed pulse-like and near-filed no-pulse record subsets. These proposed seismic probability factors can significantly streamline the analysis process and reduce the modeling efforts required by designers to account for collision phenomena. Furthermore, these probability factors can be widely adopted for retrofitting existing buildings by considering the additional capacity that collisions might provide. In addition, for $0.5SD_{min}$, the probability factors can be approximated through linear interpolation.

4.2. Optimal retrofit strategy using FVDs between adjacent RC and SMRFs prone to earthquake-induced pounding (Paper II)

The effects of adding FVDs between adjacent structures were carried out in **Paper II** and proper modification factors for retrofitting purposes were determined assuming three *SDs* of 0.0, $0.5D_{min}$, and $1.0D_{min}$. The results of the study indicate that by installing dampers on every floor, energy dissipation is distributed throughout the entire height of the building, directly targeting inter-story drifts and providing enhanced control over localized deformations during seismic events. This approach not only improves the overall dynamic response of the structure but also mitigates the risk of progressive collapse by ensuring that each level contributes to absorbing and dissipating external impact force due to seismic energy. Therefore, coupling adjacent structures with LVDs or NVDs can be beneficial in terms of sharing loads and moderating global movements; however, the individual floor responses can be addressed by a proper force-resisting system. The comprehensive floor-level implementation of LVDs or NVDs on all adjacent structures can be more expensive, while the proposed approach of implementing FVDs in floor levels of adjacent structures can reduce the cost of retrofitting and justifies its consideration in engineering applications.

The results confirm that pounding between adjacent structures can cause an increase in the maximum values of the moment-rotation curves of beams and columns (e.g. beam and column of the 3-story SMRF colliding with 5-story RC structure experienced an increase by

16% and 29.1%, respectively). The placement of LVDs between structures can be effective in reducing the values of the moment-rotation curves for beams and columns by 48% and 31.25%, respectively. Comparing the results of using NVDs and LVDs, LVDs attain better performance levels, as compared to the NVDs, for three different record subsets and SDs. The results confirm that implementing LVDs between adjacent structures plays a crucial role in increasing the performance levels of RC structures. For example, in the condition of 3St-3RC-4, the median of IDAs for the 3-story RC structure increased by 32.48%. Although RC structures achieved higher performance levels, the alternative conditions were caused by the reduction in the median of IDAs of the 3-story SMRF. Therefore, it is suggested to consider both structures' performance levels in the retrofitting approach and choose the best model according to the required performance levels.

Modification factors were proposed to approximately predict the median of IDAs of the structures after retrofitting, which can be easily applied to the structures with the same structural elements to help designers approximately calculate the performance levels of the colliding structures when using LVDs between the structures without involving analytical difficulties. Comparing pounding between structures with similar heights (i.e., the 3-, and 5-story) shows that adding FVDs can significantly decrease the seismic failure probability of RC structures, while it can increase the seismic failure probability of SMRFs. The results confirm that implementing FVDs can increase the failure probability of shorter structures (i.e., the 3-, and 5-story SMRFs), while the failure probability of taller structures remains unchanged. Comparing pounding between taller SMRF and shorter RC structures shows that implementing the FVD at the top of the shorter RC structure prevents the failure of the taller SMRF; then, as a result, the failure probability is reduced.

4.3. Enhancing seismic performance of rigid and semi-rigid connections equipped with SMA bolts incorporating SSI effects (Paper III)

Paper III focused on the seismic limit-state capacities of the rigid and semi-rigid connections of the 3-, 5-, 7-, and 9-story SMRFs considering SSI effects. It seems that there is different rigidity between the designed connection and the real one, which can be considered a problematic issue due to the importance of connections in the seismic performance of SMRFs. Therefore, to improve the seismic limit-state capacities of the semi-rigid connections, SMA bolts were used to control the engineering demands and increase the performance levels.

Comparison between the results for the 3-, 5-, 7-, and 9-story SMRFs show that assuming semi-rigid connections significantly decreases the values of the median of IDA curves and the rigidity of 60% has the lowest values of the median of IDA for all soil types, while rigid connection achieved higher values of the median of IDAs. For instance, assuming the rigidity of 80%, 70%, and 60% for the 3-story SMRF founded on soil type E can decrease the $S_a(T_1)$ values of the performance level of LS by 29.18%, 34.02%, and 40.19%, respectively. Considering the SSI effects can considerably decrease the $S_a(T_1)$ values of the median of IDA curves for all soil types. For example, for the 3-story SMRF founded on soil type D with the SSI effects, considering the rigidity of 80%, 70%, and 60% decreased the $S_a(T_1)$ values of the performance level of LS by 23.54%, 28.17%, and 32.67%, respectively.

Seismic fragility curves were compared to investigate the seismic probability of exceeding an assumed damage state of SMRFs. Assuming the semi-rigid connection can significantly reduce the seismic collapse probability. For example, the seismic probability of collapse of the 5-story SMRF in the rigidity of 60% for the performance level of IO, LS, CP, and total collapse experienced a reduction of 25%, 23.92%, 18.98%, and 17.70%, respectively, as compared to the rigid connection. Assuming the SSI effect in the modeling

process allows us to simulate the real condition of the building. In addition, the results show that the SSI effects can significantly decrease the seismic collapse probability; thus, it is recommended to consider the SSI effects in the seismic vulnerability assessment of SMRFs.

The superelastic behavior of SMA materials can widely help designers compensate for the gap between the design process and construction conditions. Proposed SMA bolts for semi-rigid connections can improve the seismic limit-state performance levels of SMRFs under severe earthquakes. Moreover, SMA bolts can be replaced in semi-rigid connections of existing buildings for retrofitting purposes. For brevity, implementing SMA bolts in the 7-story SMRF founded on soil type B with 80%, 70%, and 60% rigidity significantly increased the performance level of total collapse by 23.72%, 27.10%, and 30.97%, respectively. In addition, using SMA bolts for the 80%, 70%, and 60% rigidity of connections in the 7-story SMRF founded on soil type B increased the seismic collapse probability of 50% in the performance levels of total collapse by 31.76%, 36%, and 62.66%, respectively.

4.4. Probabilistic assessment of SMRFs with IMWs incorporating SSI effects (Paper IV)

Paper IV evaluated the seismic performance levels of 3-, 5-, 7-, and 9-story SMRFs founded on four soil types assuming four cases of IMWs placement prone to far-field subset of earthquakes used by FEMA-P695 [63]. The results of the study show that different placements of IMWs can significantly increase the seismic limit-state capacities of SMRFs with and without considering SSI effects. In addition, IMWs can play a crucial role in improving the seismic performances as well as the seismic collapse probability, which may be suggested for retrofitting purposes.

The $S_a(T_1)$ values in the median of IDA for the SMRFs increased by adding IMWs (i.e., Case B, Case C, and Case D) into the bare frame (i.e., Case A). Therefore, the results confirm that the placement of IMWs in all floor levels increased the lateral resisting strength and this can cause an increase in the seismic performance levels. For soil type B, the $S_a(T_1)$ values in the performance level of total collapse for the 5-story SMRF assuming IMWs placement of Case B, Case C, and Case D, increased by 41.42%, 29.28%, and 20.18%, respectively. The results also show that considering the SSI effects significantly decreases the $S_a(T_1)$ values in all performance levels compared to neglecting the SSI effects. For example, assuming SSI effects in the soil type E, the $S_a(T_1)$ values in the performance level of CP for the 5-story SMRF with IMWs placement of Case B, Case C, and Case D decreased by 37.41% (from 0.751 to 0.470), 29.55% (from 0.758 to 0.534), 24.27% (from 0.828 to 0.627), and 17.44% (from 0.854 to 0.705), respectively. Comparing the seismic probability of collapse for the performance levels of IO and LS shows that $S_a(T_1)$ values corresponding to the seismic collapse probability of 50% for the placement of IMWs in all floor levels (i.e., Case D) are higher than those for the bare frame (i.e., Case A). For brevity, the results of the 3-story SMRF founded on soil type B show that assuming Case D could increase the seismic collapse probability of the performance levels of IO and LS by 60% and 41.07%, respectively. Assuming SSI effects had a reduction influence on the seismic failure probability. Thus, this is important to model SSI and assume its significant influence on the seismic responses. In soil type B and the seismic performance level of LS, assuming SSI effects can decrease the collapse probability of the 5-story SMRF by 10.49% (from 0.305 to 0.273) and 14.52% (from 0.420 to 0.359), for Case A and Case D, respectively.

4.5. Enhancing seismic performance of steel buildings having semi-rigid connection with IMWs considering soil effects (Paper V)

Paper V investigated steel-damaged buildings due to constructional defects on the rigidity of connections, and then, a retrofitting strategy for improving their performance levels was proposed. To include all the possibilities of combinations of rigidity conditions, implementing IMWs, and effects of soil types, 384 SMRFs were modeled having 3-, 5-, 7-, and 9-story floor levels and two types of analysis of nonlinear dynamic analysis (i.e., under design-based earthquakes (DBE) and maximum considered earthquake (MCE)) and IDAs were performed subjected to three types of ground motion subsets. The comprehensive study included 3456 performance curves, therefore, to better use the results, the GUI was introduced with the ability for plotting different performance curves based on the nonlinear dynamic analysis and IDAs. As a method to improve the behavior of the building, the use of the sidewalls of the building in retrofitting models was suggested.

The connections of the structural elements had different rigidities, as compared to the designed assumption. In other words, they had less rigidity than the assumed rigid connection in the design process and this could reduce the capability of the structure in lateral loads. Due to damage to buildings during earthquakes, it was observed that the connections had a great influence on meeting the performance of the building. Constructional defects might not be considered in the design process; hence, considering the rigid beam-to-column connection would be an ideal assumption and did not follow reality. One effective method to enhance seismic performance is to use all the available capacities of the structural members which can significantly save on retrofitting costs. Therefore, manufacturing defects, including problems in the behavior of connecting structural elements (i.e., semi-rigid), should also be considered.

According to the results, under DBE and MCE levels of nearfield no-pulse records, assuming 50% rigidity of connections for the 9-story SMRF founded on soil B can increase the median of IDR by 81.05% and 83.71%, respectively; however, the median of RID increased by 2.12 and 3.03 times compared to SMRF with the rigid connection. Results also show that implementing IMWs can considerably reduce the distributed values of the median of IDR and RID in all SMRFs under DBE and MCE levels. For example, assuming the IW-3 condition in the 5-story SMRF, the median of IDR was decreased by 12.72% and 18.67%, and the median of RID was reduced by 32.1% and 21.77% under DBE and MCE levels, respectively. Implementing IMWs in a building, which had defects in its connections, can improve performance levels. For instance, implementing IW-1 and IW-3 conditions in the 3-story SMRF with 50% rigidity can reduce IDR by 16.47% and 32.26% under the DBE level, respectively. In addition, implementing IW-3 in the SMRFs with 90% rigidity can decrease the median of IDR of the 3-, 5-, 7-, and 9-story SMRFs by 3.71%, 19.55%, 16.03%, and 11.63%, respectively, and the median of RID by 47.80%, 36.32%, 44.08%, and 55.09%, respectively, under DBE level.

Tcl programming code was developed to include different collapse states of the structural members and IMWs to accurately model the real condition of SMRFs. Therefore, the results took the collapsed IMWs into consideration for plotting the IDA curve. Compared to the bare 3-story SMRF, it can be observed that adding IMWs can increase the collapse performance level by 2.04%, 5.74%, and 12.48%, for the conditions of IW-1, IW-2, and IW-3, respectively. Whereas, the rigidity of connections can decrease $S_a(T_1)$ values in the collapse performance level by 2.86%, 5.35%, 9.31%, 16.56%, and 34.65%, respectively. The proposed retrofitting strategy using IMWs can considerably improve $S_a(T_1)$ values in all performance levels. Implementing the IW-3 condition in the 3-story SMRF can improve the values of $S_a(T_1)$ by 15.04%, 13.49%, 11.07%, 14.29%, and 35.11%, for rigidities of 90%, 80%, 70%,

60%, and 50%, respectively, and the $S_a(T_1)$ values of 5-story SMRF were increased by 21.09%, 27.93%, 25.09%, 23.52%, and 23.46%, for rigidities of 90%, 80%, 70%, 60%, and 50%, respectively. Fig. 25 presents the proposed GUI to provide a convenient method for predicting the seismic limit-state performance levels of steel MRFs with different levels of rigidity in connections, different soil types, different effects from implementing IMWs, and the effects of records.

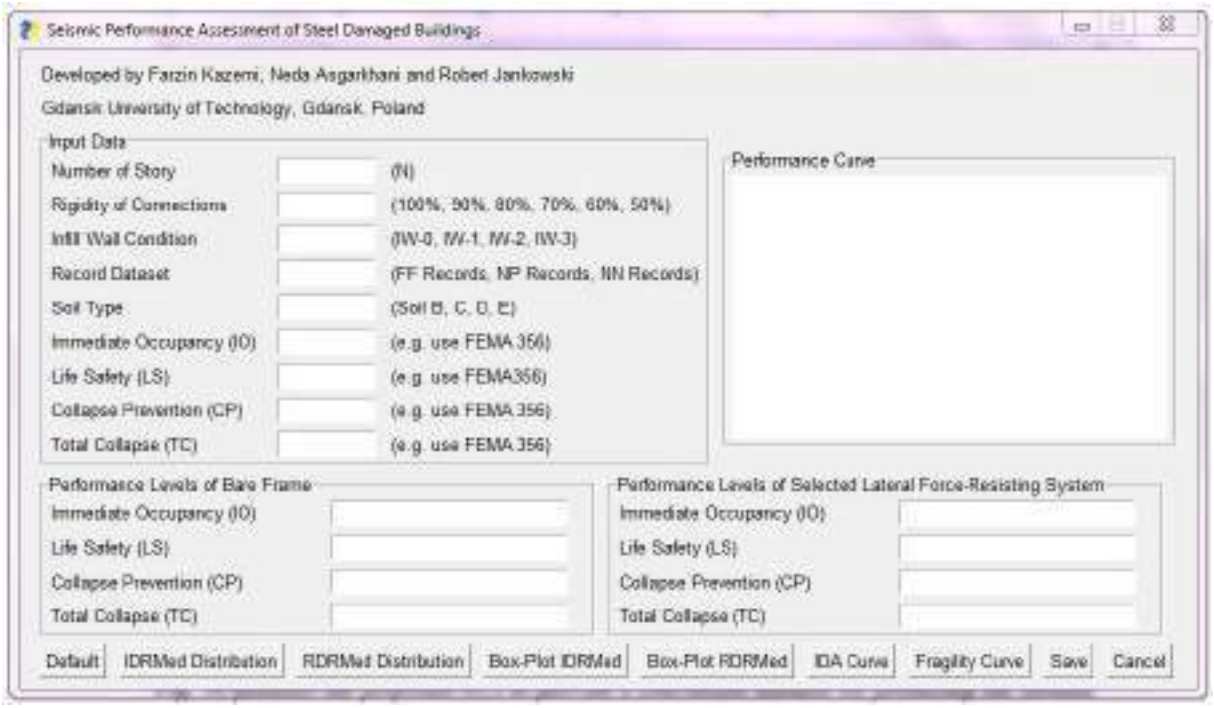

Fig. 25. Proposed GUI for predicting the seismic limit-state performance levels of steel MRFs with different conditions of rigidity, IMWs, soil types, and records (**Paper V**).

4.6. Seismic performance evaluation of BRBFs including SMA materials (Paper VI)

Paper VI focused on the seismic performance levels of BRBFs prone to large RIDs after severe earthquakes. The effects of implementing different energy dissipation devices, such as FVDs and SMAs, were investigated assuming two engineering demand parameters of IDR and RID, and proper lateral resisting systems were proposed to control assumed demands and increase the performance levels.

According to the results, the 2-story-BRB-VD had the lowest amount of maximum moment with 253.67 kNm, while the 2-story-BRB-SMA had the highest amount of maximum moment with 346.48 kNm. In addition, implemented FVDs can significantly reduce the maximum moment and rotation values of the 2-story-BRB, while these values increase by implementing SMAs in the 2-story-BRB. Moreover, considering both FVDs and SMAs implemented in the BRBFs had better performance. For example, implementing FVDs and SMAs decreased the maximum moment and rotation values of the 2-story BRBF by 11.74% and 28.57%, respectively. Replacing the steel core of BRBs with SMA material can significantly affect the seismic performance levels of 4-story, 6-story, and 8-story BRBFs assuming IDR demand. In addition, SMA material can significantly affect the seismic performance levels of 2-story, 4-story, 6-story, and 8-story BRBFs assuming RID demand. Implementing both SMAs and FVDs (e.g., the 4-story-SMA-VD) can significantly affect the

performance levels of BRBFs assuming both IDR and RID demands are subjected to near-field record subsets. This system had the highest $S_a(T_1)$ values among all considered BRBFs and can increase the performance levels more effectively than using only one of the FVDs or SMAs. Therefore, it is suggested to implement both of them in the BRBFs.

Comparing the seismic fragility curves of BRBFs based on the performance levels of IO, LS, CP, and TC, in IDR demand shows that implementing both SMAs and VDs significantly increases the seismic collapse probability corresponding to the performance levels of IO, LS, CP, and TC. For example, in the performance levels of IO, LS, CP, and TC based on the IDR, the $S_a(T_1)$ values corresponding to the seismic collapse probability of 50% for the 2-story-SMA-VD were 1.14, 2.01, 1.48, and 3,87 times of the 2-story-BRB. Moreover, implementing on both SMAs and FVDs had impressive results for controlling the RID of BRBFs. Comparing the seismic performance level of LS based on RID shows that the seismic collapse probability of 50% for the 2-story-BRB, the 4-story-BRB, the 6-story-BRB, and the 8-story-BRB can be increased by a factor of 4.36, 9.68, 6.62, and 7.66, respectively, due to using both SMAs and FVDs. The estimation factors (EFs) were calculated to estimate the seismic performance levels of structures. Using EFs can help engineers estimate the improvements of selected lateral-resisting systems compared to BRB structures. In addition, as presented in Fig. 26, the user-friendly GUI was developed to provide information for estimating the seismic performance of user-defined thresholds. It is noteworthy that GUI facilitated the design and retrofitting process as well as lateral-resisting system selection.

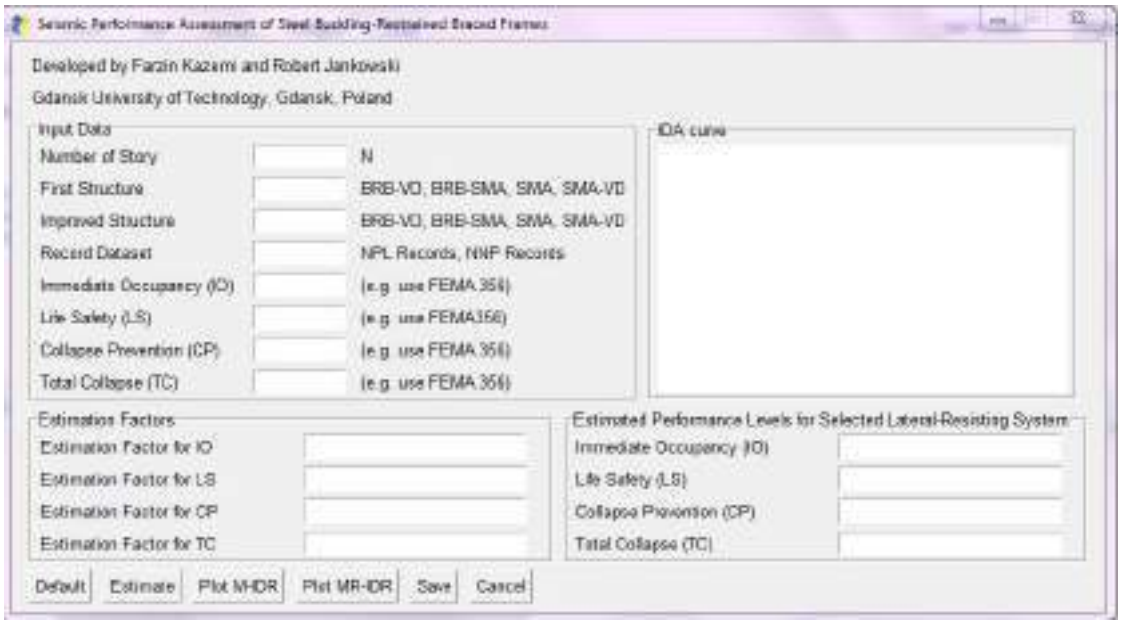

Fig. 26. Schematic view of GUI for estimating the performance levels of lateral resisting system (**Paper VI**).

4.7. Development and experimental validation of SSD-DYB device (Paper VII)

Paper VII was focused on the development and experimental validation of a novel SSD-DYB device designed for seismic resistance of structures having bracing systems. For this purpose, a single-span steel frame was designed, and based on the real size of the bracing system, a 1/5-scaled SSD-DYB was constructed. The main idea behind the proposed device was to use the energy dissipating capacity of SSD in the small segment of DYB so as to prepare the device to present a good performance in lower seismic intensity levels. At the same time, the large segment of SSD-DYB can resist higher loads to control the stability of

the structure. It is noteworthy that due to the formulation of each segment, engineers can select and design these elements to meet the performance objectives of buildings.

Experimental results reveal that the number of strips and shape of SSD can increase the maximum load of the hysteresis curve and this can help designers to adjust the size, shape, and number of strips to define different types of SSD-DYBs according to the target performance. For instance, increasing one strip to SSD-DYB-1 and SSD-DYB-2 can increase the dissipated energy by 33.48% and 12.2%, respectively. In addition, assuming the SSD-DYB-1 as a reference, the specimens of SSD-DYB-2, SSD-DYB-3, and SSD-DYB-4 increased the dissipated energy by 23.33%, 9.32%, and 11.22%, respectively. It is important to define small and large slotted holes based on the load-carrying capacity of each segment to use the maximum capacity of the device. As expected, by increasing the width of the large segment from 20 mm to 30 mm (i.e., SSD-DYB-5 to SSD-DYB-1), the maximum capacity load was increased from 18.68 kN to 27.06 kN (i.e., by 44.86%). In the total assessment of the proposed device, by changing the shape of the SSD segment, the energy dissipated by SSD-DYB-2 was increased to 1955.16 J, which is 29.18% higher than for SSD-DYB-1.

The experimental results confirm that using a safety factor of 1.5 times of total capacity of the device can guarantee the failure resistance of connections. In addition, assuming the width of the large segment is equal to 38% of the total width of the device can effectively protect against the failure of connections. According to the results, the SSD-DYB can resist more deformation, as compared to the DYB having a symmetric hysteresis curve since this device exhibits damping behavior in the small segment. In addition, it can be adjusted for the expected capacity from each part of the device, while there will be no sudden rupture and buckling in the response of SSD-DYB. The proposed optimized SSD-DYB has more compatibility with the design process and can be effectively used as an energy-dissipating device since the drawbacks of the other cores were confirmed. Optimized placement of stiffeners as well as top and bottom plates confirm the workability of the U-shape during the tests, which shows the ability of the device to replace the cores after seismic events. It should be noted that the U-shape could be the same during the experiments since there was no failure in its ability to control and transmit the external loads.

4.8. ML-based prediction of seismic limit-state capacity of SMRFs considering SSI effects (Paper VIII)

Since there is no practical method available for predicting the median of the IDA curve of steel structures, **Paper VIII** proposed an ML-based estimation method for predicting the median of the IDA curve of steel structures. Although a complex modeling process with high computational cost should be conducted to achieve the seismic limit-state capacities of structures, a database was used for estimating the median of the IDA curve of different structures other than those in the database. This allowed us to obtain the results for a range of structures without involving complex modeling and analysis.

The results of the analysis show that using only one ML algorithm for predicting the M-IDA curve is not possibly efficient for all steel structures, thus, it is suggested to try some of the ML algorithms to find the best fitting curve. For this purpose, numerical analyses were carried out to prepare datasets for training and testing the ML algorithms. Due to the unpredictable nature of seismic excitations, all algorithms were compared to find the best one with the highest accuracy of prediction by comparing the results of metrics, such as R^2, MSE, RMSE, RMSRE, and MAE, and execution time. To better illustrate the results, score markers were used for the prediction of training and testing datasets. The results of the comparison show that the ETReg, GBM, BReg, AdaBoost, and RF algorithms have the highest prediction

accuracy in the training dataset, while the ANNs, NuSVR, XGBoost, VReg, and SVM algorithms are the best prediction models in the testing dataset. In addition, the ANNs, NuSVR, and XGBoost algorithms had higher computing time among other algorithms. Tables 9 and 10 in **Paper VIII** illustrate the best ML algorithms for predicting the seismic limit-state capacities of SMRFs regarding three record subsets, excluding, and including SSI effects, respectively. In addition, the user-friendly GUI was developed to predict $S_a(T_1)$ for the seismic limit-state performance levels of SMRFs as presented in Fig. 27.

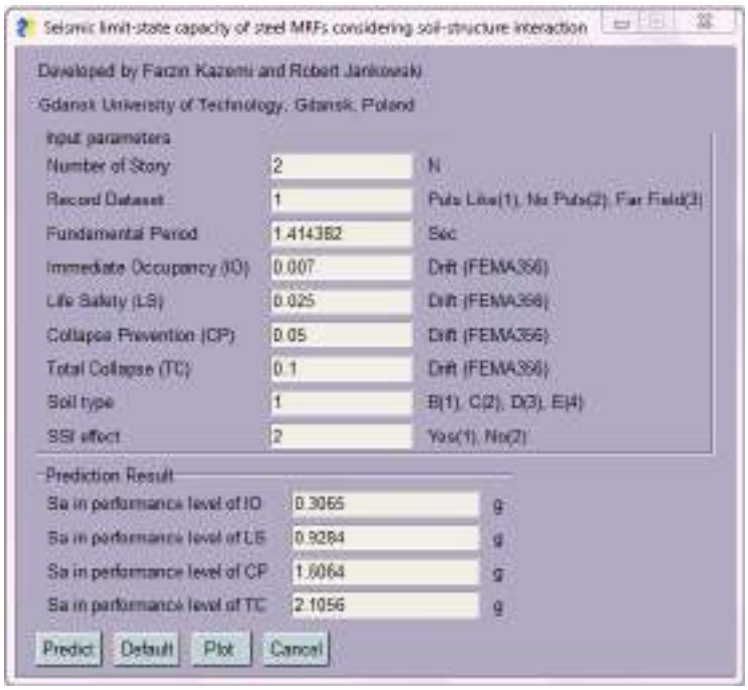

Fig. 27. Graphical user interface for prediction of the seismic limit-state capacities of SMRFs considering SSI effects (**Paper VIII**).

4.9. ML-based seismic response and performance assessment of RC buildings (Paper IX)

Since complex modeling and analysis should be performed to determine seismic responses and seismic performance levels of RC structures, **Paper IX** proposed ML-based prediction models to estimate the IDR and $S_a(T_1)$ for the median of the IDA curve of the RC MRFs. While the most of analyses are time-consuming and need to be done by high-speed computer systems, the proposed ML method can improve the estimations and consider the unpredictable nature of seismic events as a factor that affects seismic performance achievement.

The results of the study show that assuming IDR as the target of prediction, eight algorithms of PLSReg, SReg, VReg, LReg, GReg, MLPReg, SVM, and LSVR have lower R^2 values (i.e., less than 65%) and cannot be used as prediction models. On the other hand, eight algorithms of KNR, PLSReg, SReg, LReg, GReg, MLPReg, SVM, and LSVR have lower R^2 values (i.e., less than 77%) for predicting $S_a(T_1)$ as a target. In addition, ML algorithms have precise prediction values located exactly in the x=y line, assuming an allowable IDR of lower than 4.0%, which shows the ability of the proposed methods to estimate IDR in all RC MRFs. Considering the curve plotting ability that improved in ML methods based on the allowable performance levels (i.e., IDR values of 1.0%, 2.0%, and 4.0%), three algorithms of the XGBoost, ANNs, and NuSVR can predict the seismic performance levels of the 5-story RC

frame using the predicted median of IDA curves. Therefore, they can be considered as proposed prediction models for any type of RC frame.

Four RC buildings were assumed to check the reliability of prediction models. In Case A, the BReg, ETReg, ERTReg, and ANNs algorithms predicted the IDR with the accuracy of 95.7%, 93.19%, 90.27%, and 90%, respectively, and in Case B, the accuracy of 92.78%, 90.31%, 87.85%, and 90.1%, respectively, were achieved by prediction models. In Case C, the ANNs and BReg algorithms with an accuracy of 92.9% and 89.76%, respectively, in Case D, the BReg, ETReg, and ANNs algorithms with an accuracy of 92.5%, 89.93%, and 87.32%, respectively, can be considered as the best models of prediction. As presented in Fig. 28, GUI was proposed for preliminary estimation of the seismic performance levels of RC frames based on the main important features that can be introduced as input parameters. In addition, the GUI can be able to plot the predicted median of the IDA curve regarding both seismic events and facilitate the seismic vulnerability assessment of RC buildings.

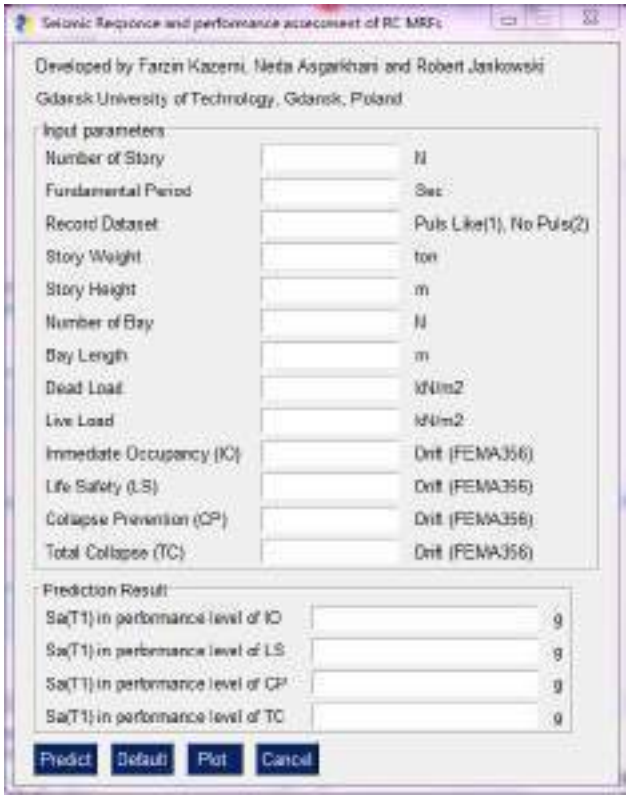

Fig. 28. GUI introduced for predicting the seismic limit-state capacity of RC MRFs (**Paper IX**).

4.10. Optimization-based stacked ML method for seismic probability and risk assessment of RCSWs (Paper X)

Paper X was focused on seismic risk assessment of RCSWs and provided an optimization-based ML prediction tool for seismic probability and risk assessment of RCSWs. The fast track of seismic risk assessment of RCSWs can help decision-makers provide a risk plan for a city and provide information on the current performance levels of buildings and the retrofitting cost. Therefore, to provide a wide range of databases, the 4-, to 15-story RCSWs having different bay lengths and four constructional soil types were investigated.

Improved ML models with resampling and pipeline methods showed significant improvements (by approximately 43.8%) in the curve-fitting ability. For instance, the

accuracy of estimating the median of IDA curves of RCSWs improved up to 99.1%. In addition, optimization-based Stacked ML models were the best-fitted curves with an accuracy of 99.4% for estimating the fragility curve in life-safety performance level. The higher accuracy of the proposed optimization-based Stacked ML models can guarantee the result of seismic risk assessment. To validate the proposed optimization-based Stacked ML models, a 5-story RCSW was modeled and analyzed to be used as a test dataset for the proposed ML models. The results confirm that Stacked ML models have curve-fitting ability and can estimate the median of IDA and seismic probability curves of a general building. According to the results, for NPL records, the Stacked ML-4, Stacked ML-5, and Stacked ML-3 with accuracies of 99.9%, 99.2%, and 98.5% are the best prediction methods, respectively, and for NNP records, the Stacked ML-4, and Stacked ML-5 with accuracies of 99.7% and 98.8% are the best prediction models. Furthermore, the proposed Stacked ML models have lower values of error indicators that confirm their ability to estimate fragility curves with higher reliability.

The proposed optimization-based Stacked ML models have a good estimation of $\lambda_{Life\text{-}safety}$ that can be used by decision-makers. The $\lambda_{Life\text{-}safety}$ for the actual curve of NPL and NNP records were determined as equal to 0.256% and 0.233%, respectively. However, the values of 0.268% and 0.215% were achieved by the proposed Stacked ML-4 for the NPL and NNP records, respectively. Moreover, Stacked ML-5 had predicted values of 0.23% and 0.192% for the NPL and NNP records, respectively. The differences between the values were in the acceptable range since the ML models can reduce the modeling time and analysis complexity while the seismic risk assessment can be performed in a couple of seconds for a wide range of buildings.

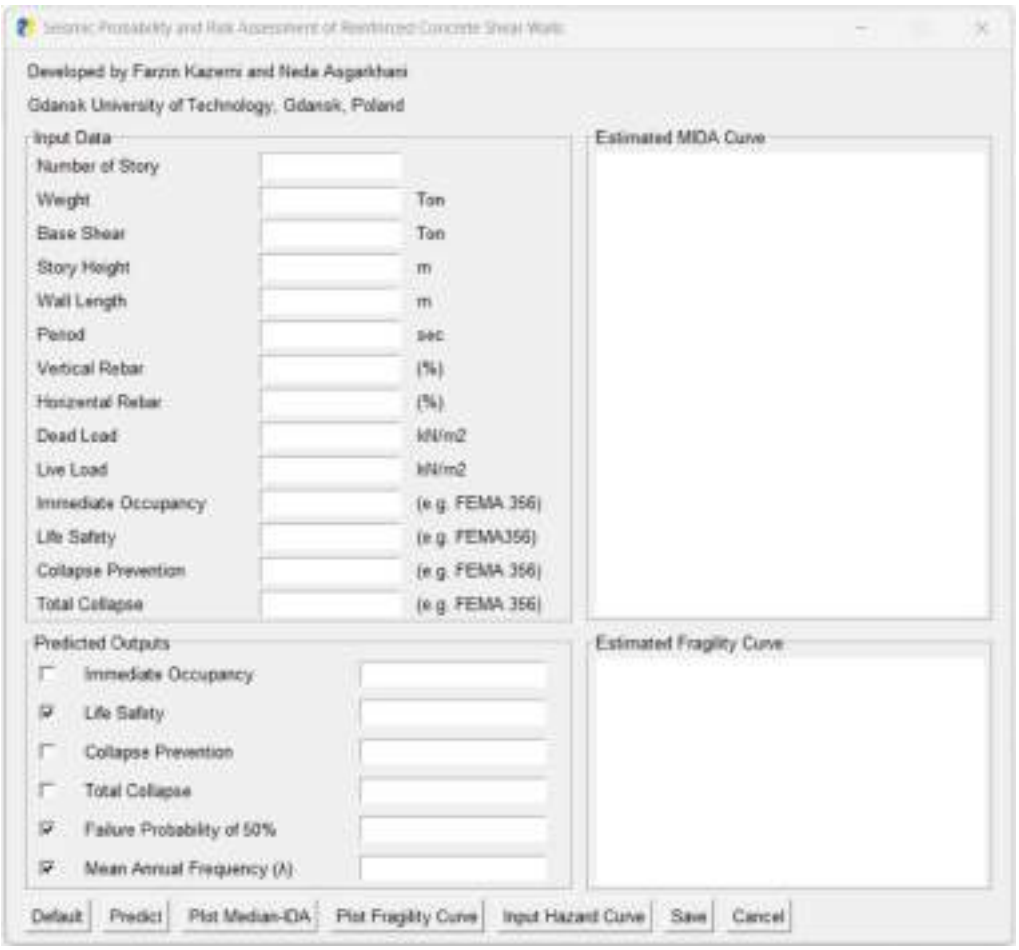

Fig. 29. GUI-based seismic risk assessment tool for RCSWs (**Paper X**).

As presented in Fig. 29, a GUI was provided that can be easily filled by the user in order to conduct a seismic risk assessment of RCSWs. The GUI can provide information for structural designers ranging from seismic performance levels of RCSWs, predicted median of IDA and seismic failure probability curves in different predefined performance thresholds, and finally, calculating mean annual frequency for assumed performance level and defined seismic hazard curve.

5. Conclusions

This PhD thesis investigated novel methods for retrofitting buildings having different lateral force-resisting systems including SMRFs, RC MRFs, BRBFs, IMWs, and RCSWs to reduce the computational modeling procedure and improve the accuracy of seismic assessments. The following main conclusions were derived from this PhD thesis:

External force due to impact force of adjacent structure during pounding phenomenon was investigated and modification factors were proposed to consider their effects on seismic design. In addition, for the existing adjacent structures, the impact force can be dissipated using FVDs implemented in floor levels, which can significantly improve the performance levels of adjacent structures.

Considering the most vulnerable parts of SMRFs (i.e., beam-to-column connections), the effects of rigid and semi-rigid connections of steel structures were investigated and SMA bolts were introduced to enhance their performance levels. The results confirm that changing the regular bolts with the SMA ones can considerably improve the performance of structures.

Considering the IMWs in outer frames showed considerable influence on the seismic behavior of structures. As a retrofitting strategy, IMWs can be used to improve the performance levels of structures by altering the fundamental period and adding extra stiffness to the frame. Therefore, probabilistic assessment of steel structures including IMWs and SSI were considered, focusing on proper modeling approach and their influence on seismic assessments. Due to the highest importance of connections rigidity and IMWs, a combination of their effects was investigated and both effects were simultaneously modeled. Considering the SSI effects improved the modeling and provided a better understanding of seismic behavior.

BRBF is a mostly important lateral force-resisting system, however, due to weakness of residual strength, it may require additional considerations for certain applications. A novel approach to using SMA material in BRB devices was investigated to improve their residual strength and recentering capacity. In addition, a novel SSD-DYB was experimentally developed and tested to propose a suitable device for both lower-, and higher-intensity seismic excitations. The device includes two segments in a core for different purposes of dissipating energies and can be replaced after earthquakes. The results confirm its behavior allowing us to use the proposed optimal design of SSD-DYB for practical implementation.

Although the results of the case study structures are reasonably accurate, they may not be directly applicable to some other scenarios. To overcome such a shortcoming, predictive models based on conventional and ensemble-based ML methods were developed. The proposed ML methods are novel in earthquake engineering and can be used to predict the seismic limit-state capacity of steel structures considering SSI effects, seismic response and performance assessment of RC buildings, and seismic probability and risk assessment of RC shear walls. It is noteworthy that the user-friendly GUI was developed for those ML models based on the provided database.

6. Future studies

Different aspects can be explored in future studies, as presented below:

- Since the pounding models only include low-, to mid-rise adjacent structures, it is suggested to include more pounding cases having floor-to-column collisions, different floor weights, mainshock-aftershock records, and using rubber damper between those colliding structures.
- Since the novel modeling of connections was introduced in this PhD thesis, it has paved the way for innovative connection designs that can tolerate higher levels of deformation and provide greater energy dissipation. The integration of smart monitoring systems, which can detect early signs of distress in connections during an earthquake, can be investigated for preventing connection failures by allowing for timely repairs and retrofits.
- To prevent premature cracking and improve IMWs contribution to lateral resistance, ensuring adequate connections between IMWs and frames while maintaining sufficient gaps to prevent unintended interaction, implementing lightweight, flexible masonry or composite panels to improve ductility and reduce seismic mass, and avoiding weak floor level can be a possible strategy for using the potential of IMWs. Therefore, future studies can be devoted to these investigations and their influence on the seismic performance of structures.
- Since SSI effects could considerably affect the response of structures, it is suggested to include novel modeling of soil–foundation–structure interaction effects considering different soils and structural systems.
- Using SMA materials in the BRB core is an innovative approach to overcome the strain-hardening effect on residual drift. However, future studies on the SMA material implementation on DYB cores and how they behave under seismic loading would be interesting.
- SSD-DYB presents a promising performance in lower seismic loads so it is suitable for retrofitting sensitive structures. It is recommended to improve its behavior with different types of materials (i.e., SMA material) and shapes. In addition, investigating its behavior under seismic loading would be suggested.
- Using ML methods to propose predictive models can significantly help structural engineers to estimate seismic performance. Future studies should look deeper into the potential of these methods in different aspects of civil engineering.

References

[1] Vitiello, U., Asprone, D., Di Ludovico, M., & Prota, A. (2017). Life-cycle cost optimization of the seismic retrofit of existing RC structures. *Bulletin of Earthquake Engineering*, 15, 2245-2271.

[2] Mohebi, B., Yazdanpanah, O., Kazemi, F., & Formisano, A. (2021). Seismic damage diagnosis in adjacent steel and RC MRFs considering pounding effects through improved wavelet-based damage-sensitive feature. *Journal of Building Engineering*, 33, 101847.

[3] Yazdanpanah, O., Mohebi, B., Kazemi, F., Mansouri, I., & Jankowski, R. (2022). Development of fragility curves in adjacent steel moment-resisting frames considering pounding effects through improved wavelet-based refined damage-sensitive feature. *Mechanical Systems and Signal Processing*, 173, 109038.

[4] Kazemi, F., Mohebi, B., & Yakhchalian, M. (2020). Predicting the seismic collapse capacity of adjacent structures prone to pounding. *Canadian Journal of Civil Engineering*, 47(6), 663-677.

[5] Qiu, C., Cheng, L., & Du, X. (2024). Seismic analysis and design of a resilient steel frame with multiple lateral force–resisting systems. *Journal of Structural Engineering*, 150(7), 04024064.

[6] Leibovich, E., Rutenberg, A., & Yankelevsky, D. Z. (1996). On eccentric seismic pounding of symmetric buildings. *Earthquake Engineering & Structural Dynamics*, 25(3), 219-233.

[7] Jankowski, R. (2005). Non-linear viscoelastic modelling of earthquake-induced structural pounding. *Earthquake Engineering & Structural Dynamics*, 34(6), 595-611.
[8] Jankowski, R. (2010). Experimental study on earthquake-induced pounding between structural elements made of different building materials. *Earthquake Engineering & Structural Dynamics*, 39(3), 343-354.
[9] Polycarpou, P. C., Papaloizou, L., & Komodromos, P. (2014). An efficient methodology for simulating earthquake-induced 3D pounding of buildings. *Earthquake Engineering & Structural Dynamics*, 43(7), 985-1003.
[10] Skrekas, P., Sextos, A., & Giaralis, A. (2014). Influence of bi-directional seismic pounding on the inelastic demand distribution of three adjacent multi-storey R/C buildings. *Earthquakes and Structures*, 6(1), 71-87.
[11] Kazemi, F., Asgarkhani, N., Manguri, A., & Jankowski, R. (2022). Investigating an optimal computational strategy to retrofit buildings with implementing viscous dampers. In *International Conference on Computational Science* (pp. 184-191).
[12] Kazemi, F., Asgarkhani, N., Manguri, A., Lasowicz, N., & Jankowski, R. (2023). Introducing a computational method to retrofit damaged buildings under seismic mainshock-aftershock sequence. In *International Conference on Computational Science* (pp. 180-187).
[13] Kazemi, F., Mohebi, B., & Jankowski, R. (2021). Predicting the seismic collapse capacity of adjacent SMRFs retrofitted with fluid viscous dampers in pounding condition. *Mechanical Systems and Signal Processing*, 161, 107939.
[14] Kazemi, F., Miari, M., & Jankowski, R. (2021). Investigating the effects of structural pounding on the seismic performance of adjacent RC and steel MRFs. *Bulletin of Earthquake Engineering*, 19(1), 317-343.
[15] Foraboschi, P. (2016). Versatility of steel in correcting construction deficiencies and in seismic retrofitting of RC buildings. *Journal of Building Engineering*, 8, 107-122.
[16] Zhang, G., Xu, L. H., & Li, Z. X. (2021). Development and seismic retrofit of an innovative modular steel structure connection using symmetrical self-centering haunch braces. *Engineering Structures*, 229, 111671.
[17] Kashyzadeh, K. R., Ghorbani, S., & Kasimovich, A. A. M. (2025). Common causes of failures in the industrial bolt and nut connections. *Engineering Failure Analysis*, 109431.
[18] Shafaei, J., Hosseini, A., & Marefat, M. S. (2014). Seismic retrofit of external RC beam–column joints by joint enlargement using prestressed steel angles. *Engineering Structures*, 81, 265-288 .
[19] Rigi, A., JavidSharifi, B., Hadianfard, M. A., & Yang, T. Y. (2021). Study of the seismic behavior of rigid and semi-rigid steel moment-resisting frames. *Journal of Constructional Steel Research*, 186, 106910 .
[20] Fang, C., Yam, M. C., Lam, A. C., & Xie, L. (2014). Cyclic performance of extended end-plate connections equipped with shape memory alloy bolts. *Journal of Constructional Steel Research*, 94, 122-136.
[21] Prinz, G. S., Nussbaumer, A., Borges, L., & Khadka, S. (2014). Experimental testing and simulation of bolted beam-column connections having thick extended endplates and multiple bolts per row. *Engineering Structures*, 59, 434-447.
[22] Ong, C. B., Chin, C. L., Ma, C. K., Tan, J. Y., Awang, A. Z., & Omar, W. (2022). Seismic retrofit of reinforced concrete beam-column joints using various confinement techniques: A review. *Structures*, 42, 221–243.
[23] Kazemi, F., Asgarkhani, N., Shafighfard, T., Jankowski, R., & Yoo, D. Y. (2025). Machine-Learning Methods for Estimating Performance of Structural Concrete Members Reinforced with Fiber-Reinforced Polymers. *Archives of Computational Methods in Engineering*, 32(1), 571-603.
[24] Hadi, M. N., & Tran, T. M. (2014). Retrofitting nonseismically detailed exterior beam–column joints using concrete covers together with CFRP jacket. *Construction and Building Materials*, 63, 161-173.
[25] Oh, S. H., Kim, Y. J., & Ryu, H. S. (2009). Seismic performance of steel structures with slit dampers. *Engineering Structures*, 31(9), 1997-2008.
[26] Preti, M., Bettini, N., & Plizzari, G. (2012). Infill walls with sliding joints to limit infill-frame seismic interaction: large-scale experimental test. *Journal of Earthquake Engineering*, 16(1), 125-141.
[27] Brodsky, A., & Yankelevsky, D. Z. (2017). Resistance of reinforced concrete frames with masonry infill walls to in-plane gravity loading due to loss of a supporting column. *Engineering Structures*, 140, 134-150
[28] Nicoletti, V., Arezzo, D., Carbonari, S., & Gara, F. (2020). Expeditious methodology for the estimation of infill masonry wall stiffness through in-situ dynamic tests. *Construction and Building Materials*, 262, 120807.

[29] Carpine, R., Ientile, S., Vacca, N., Boscato, G., Rospars, C., Cecchi, A., & Argoul, P. (2021). Modal identification in the case of complex modes–Use of the wavelet analysis applied to the after-shock responses of a masonry wall during shear compression tests. *Mechanical Systems and Signal Processing*, 160, 107753.

[30] Fardis, M. N., Bousias, S. N., Franchioni, G., & Panagiotakos, T. B. (1999). Seismic response and design of RC structures with plan-eccentric masonry infills. *Earthquake Engineering & Structural Dynamics*, 28(2), 173-191.

[31] Mazza, F., & Donnici, A. (2021). In-plane and out-of-plane seismic damage of masonry infills in existing rc structures: the case study of De Gasperi-Battaglia school in Norcia. *Bulletin of Earthquake Engineering*, 19(1), 345-376.

[32] Pujol, S., & Fick, D. (2010). The test of a full-scale three-story RC structure with masonry infill walls. *Engineering Structures*, 32(10), 3112-3121.

[33] Hosseinzadeh, S., & Mohebi, B. (2016). Seismic evaluation of all-steel buckling restrained braces using finite element analysis. *Journal of Constructional Steel Research*, 119, 76-84.

[34] Della Corte, G., D'Aniello, M., & Landolfo, R. (2015). Field testing of all-steel buckling-restrained braces applied to a damaged reinforced concrete building. *Journal of Structural Engineering*, *141*(1), D4014004.

[35] Fahnestock, L. A., Ricles, J. M., & Sause, R. (2007). Experimental evaluation of a large-scale buckling-restrained braced frame. *Journal of Structural Engineering*, 133(9), 1205-1214.

[36] Asgarkhani, N., Yakhchalian, M., & Mohebi, B. (2020). Evaluation of approximate methods for estimating residual drift demands in BRBFs. *Engineering Structures*, 224, 110849.

[37] Yakhchalian, M., Asgarkhani, N., & Yakhchalian, M. (2020). Evaluation of deflection amplification factor for steel buckling restrained braced frames. *Journal of Building Engineering*, 30, 101228.

[38] Yakhchalian, M., Yakhchalian, M., & Asgarkhani, N. (2021). An advanced intensity measure for residual drift assessment of steel BRB frames. *Bulletin of Earthquake Engineering*, 19(4), 1931-1955.

[39] Cahís Carola, F. X., Catalán Artigas, A., Benavent-Climent, A., & Trias Mansilla, D. (2023). A new Coplanar Dual Core Buckling-Restrained Brace. *Journal of Building Engineering*, 70, 106286.

[40] Zheng, S. Y., Yuan, B., Wei, M. S., Liu, X. L., Liu, X. F., Zhou, G. Y., ... & Shi, H. W. (2023). Experimental & numerical investigation of all-steel assembled cruciform buckling-restrained braces. *Journal of Constructional Steel Research*, 207, 107981.

[41] Shi, Q. X., Wang, F., Wang, P., & Chen, K. (2018). Experimental and numerical study of the seismic performance of an all-steel assembled Q195 low-yield buckling-restrained brace. *Engineering Structures*, 176, 481-499.

[42] DesRoches, R., Taftali, B., & Ellingwood, B. R. (2010). Seismic performance assessment of steel frames with shape memory alloy connections. Part I—analysis and seismic demands. *Journal of Earthquake Engineering*, 14(4), 471-486.

[43] Wilde, K., Gardoni, P., & Fujino, Y. (2000). Base isolation system with shape memory alloy device for elevated highway bridges. *Engineering structures*, 22(3), 222-229.

[44] Eatherton, M. R., Fahnestock, L. A., & Miller, D. J. (2014). Computational study of self-centering buckling-restrained braced frame seismic performance. *Earthquake Engineering & Structural Dynamics*, 43(13), 1897-1914.

[45] Ke, K., Zhou, X., Zhu, M., Yam, M. C., Wang, Y., & Zhang, H. (2022). Seismic evaluation of industrial steel moment resisting frames with shape memory alloys using performance-spectra-based method. *Journal of Building Engineering*, 48, 103950.

[46] Kim, H. J., & Christopoulos, C. (2009). Numerical models and ductile ultimate deformation response of post-tensioned self-centering moment connections. *Earthquake Engineering & Structural Dynamics*, 38(1), 1-21.

[47] Elettore, E., Freddi, F., Latour, M., & Rizzano, G. (2021). Design and analysis of a seismic resilient steel moment resisting frame equipped with damage-free self-centering column bases. *Journal of Constructional Steel Research*, 179, 106543.

[48] Xie, Q., Zhou, Z., & Meng, S. P. (2020). Experimental investigation of the hysteretic performance of self-centering buckling-restrained braces with friction fuses. *Engineering Structures*, 203, 109865.

[49] Lin, Y. C., Sause, R., & Ricles, J. M. (2013). Seismic performance of steel self-centering, moment-resisting frame: hybrid simulations under design basis earthquake. *Journal of Structural Engineering*, 139(11), 1823-1832.

[50] Wang, W., Fang, C., & Liu, J. (2016). Large size superelastic SMA bars: Heat treatment strategy, mechanical property and seismic application. *Smart Materials and Structures*, 25(7), 075001.

[51] Sun, J., Pan, P., & Wang, H. (2018). Development and experimental validation of an assembled steel double-stage yield buckling restrained brace. *Journal of Constructional Steel Research*, 145, 330-340.

[52] Lu, Y., Liu, Y., Wang, Y., Liu, J., & Huang, X. (2023). Development of a novel buckling-restrained damper with additional friction energy dissipation: Component tests and structural verification. *Engineering Structures*, 274, 115188.
[53] Zhang, A. L., Wang, H. W., Jiang, Z. Q., Guo, K., & Niu, Z. Y. (2022, January). Numerical simulation analysis of double yield points assembled buckling-restrained brace with replaceable inner core. In *Structures* (Vol. 35, pp. 1278-1294).
[54] Yang, C., Xie, L., An, N., Li, A., Liu, Q., & Wang, X. (2023). Development of a novel parallel double-stage yielding buckling restrained brace: Theoretical, experimental, and numerical investigations. *Journal of Building Engineering*, 68, 106089.
[55] Hastie, T., Tibshirani, R., Friedman, J. H., & Friedman, J. H. (2009). The elements of statistical learning: data mining, inference, and prediction (Vol. 2, pp. 1-758).
[56] Dollar, P., Tu, Z., & Belongie, S. (2006, June). Supervised learning of edges and object boundaries. In *2006 IEEE Computer Society Conference on Computer Vision and Pattern Recognition (CVPR'06)* (Vol. 2, pp. 1964-1971). IEEE.
[57] Burton, H. V., Sreekumar, S., Sharma, M., & Sun, H. (2017). Estimating aftershock collapse vulnerability using mainshock intensity, structural response, and physical damage indicators. *Structural Safety*, 68, 85-96.
[58] Mangalathu, S., & Jeon, J. S. (2018). Classification of failure mode and prediction of shear strength for reinforced concrete beam-column joints using machine learning techniques. *Engineering Structures*, 160, 85-94.
[59] Worden, K., & Green, P. L. (2017). A machine learning approach to nonlinear modal analysis. *Mechanical Systems and Signal Processing*, 84, 34-53.
[60] Luo, H., & Paal, S. G. (2018). Machine learning–based backbone curve model of reinforced concrete columns subjected to cyclic loading reversals. *Journal of Computing in Civil Engineering*, 32(5), 04018042.
[61] Wang, Z., Pedroni, N., Zentner, I., & Zio, E. (2018). Seismic fragility analysis with artificial neural networks: Application to nuclear power plant equipment. *Engineering Structures*, 162, 213-225.
[62] Zhang, Y., Burton, H. V., Sun, H., & Shokrabadi, M. (2018). A machine learning framework for assessing post-earthquake structural safety. *Structural Safety*, 72, 1-16.
[63] Zhang, Y., & Burton, H. V. (2019). Pattern recognition approach to assess the residual structural capacity of damaged tall buildings. *Structural Safety*, 78, 12-22.
[64] Kiani, J., Camp, C., & Pezeshk, S. (2019). On the application of machine learning techniques to derive seismic fragility curves. *Computers & Structures*, 218, 108-122.
[65] Nguyen, H. D., Truong, G. T., & Shin, M. (2021). Development of extreme gradient boosting model for prediction of punching shear resistance of r/c interior slabs. *Engineering Structures*, 235, 112067.
[66] Nguyen, N. V., Nguyen, H. D., & Dao, N. D. (2022). Machine learning models for predicting maximum displacement of triple pendulum isolation systems. *Structures*, 36, 404-415.
[67] Noureldin, M., Ali, A., Sim, S., & Kim, J. (2022). A machine learning procedure for seismic qualitative assessment and design of structures considering safety and serviceability. *Journal of Building Engineering*, 50, 104190.
[68] Huang, C. S., Hung, S. L., Wen, C. M., & Tu, T. T. (2003). A neural network approach for structural identification and diagnosis of a building from seismic response data. *Earthquake Engineering & Structural Dynamics*, 32(2), 187-206.
[69] Yinfeng, D., Yingmin, L., Ming, L., & Mingkui, X. (2008). Nonlinear structural response prediction based on support vector machines. *Journal of Sound and Vibration*, 311(3-5), 886-897.
[70] Lagaros, N. D., & Papadrakakis, M. (2012). Neural network based prediction schemes of the non-linear seismic response of 3D buildings. *Advances in Engineering Software*, 44(1), 92-115.
[71] De Lautour, O. R., & Omenzetter, P. (2010). Damage classification and estimation in experimental structures using time series analysis and pattern recognition. *Mechanical Systems and Signal Processing*, 24(5), 1556-1569.
[72] Oh, B. K., Glisic, B., Park, S. W., & Park, H. S. (2020). Neural network-based seismic response prediction model for building structures using artificial earthquakes. *Journal of Sound and Vibration*, 468, 115109.
[73] Luo, H., & Paal, S. G. (2022). Artificial intelligence-enhanced seismic response prediction of reinforced concrete frames. *Advanced Engineering Informatics*, 52, 101568.
[74] Ma, G., Wang, Y., & Hwang, H. J. (2023). Genetic programming-based backbone curve model of reinforced concrete walls. *Engineering Structures*, 283, 115824.

[75] Deger, Z. T., & Taskin, G. (2022). A novel GPR-based prediction model for cyclic backbone curves of reinforced concrete shear walls. *Engineering Structures*, 255, 113874.
[76] Mangalathu, S., Jang, H., Hwang, S. H., & Jeon, J. S. (2020). Data-driven machine-learning-based seismic failure mode identification of reinforced concrete shear walls. *Engineering Structures*, 208, 110331.
[77] Mansourdehghan, S., Dolatshahi, K. M., & Asjodi, A. H. (2022). Data-driven damage assessment of reinforced concrete shear walls using visual features of damage. *Journal of Building Engineering*, 53, 104509.
[78] Zhang, H., Cheng, X., Li, Y., & Du, X. (2022). Prediction of failure modes, strength, and deformation capacity of RC shear walls through machine learning. *Journal of Building Engineering*, 50, 104145.
[79] Chou, J. S., Liu, C. Y., Prayogo, H., Khasani, R. R., Gho, D., & Lalitan, G. G. (2022). Predicting nominal shear capacity of reinforced concrete wall in building by metaheuristics-optimized machine learning. *Journal of Building Engineering*, 61, 105046.
[80] Liao, W., Huang, Y., Zheng, Z., & Lu, X. (2022). Intelligent generative structural design method for shear wall building based on "fused-text-image-to-image" generative adversarial networks. *Expert Systems with Applications*, 210, 118530.
[81] Modirzadeh, M., Tesfamariam, S., & Milani, A. S. (2012). Performance based earthquake evaluation of reinforced concrete buildings using design of experiments. *Expert Systems with Applications*, 39(3), 2919-2926.
[82] Le Nguyen, K., Trinh, H. T., Banihashemi, S., & Pham, T. M. (2023). Machine learning approaches for lateral strength estimation in squat shear walls: A comparative study and practical implications. *Expert Systems with Applications*, 239, 1-19.
[83] Lignos, D. G., Krawinkler, H. Deterioration modeling of steel components in support of collapse prediction of steel moment frames under earthquake loading. *Journal of Structural Engineering*, 2010, 137(11), 1291-1302.
[84] Ibarra, L. F., Medina, R. A., Krawinkler, H. Hysteretic models that incorporate strength and stiffness deterioration. *Earthquake Engineering & Structural Dynamics*, 2005, 34(12), 1489-1511.
[85] Haselton CB. Assessing seismic collapse safety of modern reinforced concrete moment frame buildings (Doctoral dissertation, Stanford University), 2006.
[86] Altoontash, A. Simulation and damage models for performance assessment of reinforced concrete beam-column joints (Doctoral dissertation, Stanford University), 2004.
[87] Sherbourne, A. N., & Bahaari, M. R. (1997). Finite element prediction of end plate bolted connection behavior. I: Parametric study. *Journal of Structural Engineering*, 123(2), 157-164.
[88] Bahaari, M. R., & Sherbourne, A. N. (1997). Finite element prediction of end plate bolted connection behavior. II: Analytic formulation. *Journal of Structural Engineering*, 123(2), 165-175.
[89] Buonopane, S. G., & White, R. N. (1999). Pseudodynamic testing of masonry infilled reinforced concrete frame. *Journal of Structural Engineering*, 125(6), 578-589.
[90] Tasnimi, A. A., & Mohebkhah, A. (2011). Investigation on the behavior of brick-infilled steel frames with openings, experimental and analytical approaches. *Engineering Structures*, 33(3), 968-980.
[91] Smyrou, E., Blandon, C., Antoniou, S., Pinho, R., & Crisafulli, F. (2011). Implementation and verification of a masonry panel model for nonlinear dynamic analysis of infilled RC frames. *Bulletin of Earthquake Engineering*, 9(5), 1519-1534.
[92] El-Dakhakhni, W. W., Elgaaly, M., & Hamid, A. A. (2003). Three-strut model for concrete masonry-infilled steel frames. *Journal of Structural Engineering*, 129(2), 177-185.
[93] Crisafulli, F. J., & Carr, A. J. (2007). Proposed macro-model for the analysis of infilled frame structures. *Bulletin of the New Zealand Society for Earthquake Engineering*, 40(2), 69-77.
[94] Rodrigues, H., Varum, H., & Costa, A. (2010). Simplified macro-model for infill masonry panels. *Journal of Earthquake Engineering*, 14(3), 390-416
[95] Kakaletsis, D. J., & Karayannis, C. G. (2008). Influence of masonry strength and openings on infilled R/C frames under cycling loading. *Journal of Earthquake Engineering*, 12(2), 197-221.
[96] Furtado, A., Rodrigues, H., & Arêde, A. (2015). Modelling of masonry infill walls participation in the seismic behaviour of RC buildings using OpenSees. *International Journal of Advanced Structural Engineering (IJASE)*, 7(2), 117-127.
[97] Furtado, A., Rodrigues, H., & Arêde, A. (2018). Calibration of a simplified macro-model for infilled frames with openings. *Advances in Structural Engineering*, 21(2), 157-170.
[98] Furtado, A., Rodrigues, H., & Arêde, A. (2021). Effect of the infill panels in the floor response spectra of an 8-storey RC building. In *Structures* (Vol. 34, pp. 2476-2498).
[99] Harden, C. W., & Hutchinson, T. C. (2009). Beam-on-nonlinear-Winkler-foundation modeling of shallow, rocking-dominated footings. *Earthquake Spectra*, 25(2), 277-300.
[100] Rajeev, P., & Tesfamariam, S. (2012). Seismic fragilities of non-ductile reinforced concrete frames with consideration of soil structure interaction. *Soil Dynamics and Earthquake Engineering*, 40, 78-86.

[101] Raychowdhury, P., & Hutchinson, T. C. (2009). Performance evaluation of a nonlinear Winkler-based shallow foundation model using centrifuge test results. *Earthquake Engineering & Structural Dynamics*, 38(5), 679-698.
[102] Raychowdhury, P. (2011). Seismic response of low-rise steel moment-resisting frame (SMRF) buildings incorporating nonlinear soil–structure interaction (SSI). *Engineering Structures*, 33(3), 958-967.
[103] AISC 341-16. (2016). seismic provisions for structural steel buildings. Chicago, IL: *American Institute of Steel Construction*.
[104] Sahoo, D. R., & Chao, S. H. (2010). Performance-based plastic design method for buckling-restrained braced frames. *Engineering Structures*, 32(9), 2950-2958.
[105] Pollini, N., Lavan, O., & Amir, O. (2017). Minimum-cost optimization of nonlinear fluid viscous dampers and their supporting members for seismic retrofitting. *Earthquake Engineering & Structural Dynamics*, 46(12), 1941-1961.
[106] Patel, C. C., & Jangid, R. S. (2010). Seismic response of dynamically similar adjacent structures connected with viscous dampers. The IES Journal Part A: *Civil and Structural Engineering*, 3(1), 1-13.
[107] Landi, L., Lucchi, S., & Diotallevi, P. P. (2014). A procedure for the direct determination of the required supplemental damping for the seismic retrofit with viscous dampers. *Engineering Structures*, 71, 137-149.
[108] Landi, L., Conti, F., &Diotallevi, P. P. (2015). Effectiveness of different distributions of viscous damping coefficients for the seismic retrofit of regular and irregular RC frames. *Engineering Structures*, 100, 79-93.
[109] Seo, C. Y., Karavasilis, T. L., Ricles, J. M., & Sause, R. (2014). Seismic performance and probabilistic collapse resistance assessment of steel moment resisting frames with fluid viscous dampers. *Earthquake Engineering & Structural Dynamics*, 43(14), 2135-2154.
[110] Nicholson, D. E., Benafan, O., Bigelow, G. S., Sczerzenie, F., Forbes, D., Van Doren, B., Mabe, J.H., Demblon, A., & Karaman, I. (2022). An overview of ASTM standard test methods for shape memory alloy actuation materials. *SMST2022. ASM International*, 59-60.
[111] Xu, X., Cheng, G., & Zheng, J. (2018). Tests on Pretrained Superelastic NiTi Shape Memory Alloy Rods: Towards Application in Self-Centering Link Beams. *Advances in Civil Engineering*, 2018.
[112] Fang, C., Yam, M. C., Chan, T. M., Wang, W., Yang, X., & Lin, X. (2018). A study of hybrid self-centring connections equipped with shape memory alloy washers and bolts. *Engineering Structures*, 164, 155-168
[113] Beiraghi, H., & Zhou, H. (2020). Dual-steel frame consisting of moment-resisting frame and shape memory alloy braces subjected to near-field earthquakes. *The Structural Design of Tall and Special Buildings*, 29(14), e1784.
[114] ASCE 7-16. (2017). Minimum design loads and associated criteria for buildings and other structures. Reston, VA: *American Society of Civil Engineers*.
[115] United States Geological Survey, https://www.usgs.gov/programs/earthquake-hazards/hazards.
[116] Federal Emergency Management Agency (FEMA P695). (2009). Quantification of building seismic performance factors. *Federal Emergency Management Agency*.
[117] Kolozvari K., Orakcal K., &Wallace J.W. (2015). Modeling of cyclic shear-flexure interaction in reinforced concrete structural walls. i: theory. ASCE, *Journal of Structural Engineering*, 141(5): 04014135.
[118] Kolozvari K., Tran T., Orakcal K., & Wallace J.W. (2015). Modeling of cyclic shear-flexure interaction in reinforced concrete structural walls. ii: experimental validation, ASCE, *Journal of Structural Engineering*, 141(5): 04014136.
[119] Kolozvari, K., Orakcal, K., & Wallace, J. W. (2018). New opensees models for simulating nonlinear flexural and coupled shear-flexural behavior of RC walls and columns. *Computers & Structures*, 196, 246-262.
[120] FEMA-356. (2000). Prestandard and commentary for the seismic rehabilitation of buildings. *Federal Emergency Management Agency*.
[121] Kazemi, F., Shafighfard, T., & Yoo, D. Y. (2024). Data-driven modeling of mechanical properties of fiber-reinforced concrete: a critical review. *Archives of Computational Methods in Engineering*, 31(4), 2049-2078.
[122] Kazemi, F., Shafighfard, T., Jankowski, R., & Yoo, D. Y. (2024). Active learning on stacked machine learning techniques for predicting compressive strength of alkali-activated ultra-high-performance concrete. *Archives of Civil and Mechanical Engineering*, 25(1), 24.
[123] Asgarkhani, N., Kazemi, F., Jakubczyk-Gałczyńska, A., Mohebi, B., & Jankowski, R. (2024). Seismic response and performance prediction of steel buckling-restrained braced frames using machine-learning methods. *Engineering Applications of Artificial Intelligence*, 128, 10738

[124] Kazemi, F., Asgarkhani, N., & Jankowski, R. (2023). Predicting seismic response of SMRFs founded on different soil types using machine learning techniques. *Engineering Structures*, 274, 114953.
[125] Asgarkhani, N., Kazemi, F., & Jankowski, R. (2023). Machine learning-based prediction of residual drift and seismic risk assessment of steel moment-resisting frames considering soil-structure interaction. *Computers & Structures*, 289, 107181.
[126] Kazemi, F., Asgarkhani, N., & Jankowski, R. (2023). Machine learning-based seismic fragility and seismic vulnerability assessment of reinforced concrete structures. *Soil Dynamics and Earthquake Engineering*, 166, 107761.
[127] Kazemi, F., Çiftçioğlu, A. Ö., Shafighfard, T., Asgarkhani, N., & Jankowski, R. (2025). RAGN-R: A multi-subject ensemble machine-learning method for estimating mechanical properties of advanced structural materials. *Computers & Structures*, 308, 107657.
[128] Shafighfard, T., Kazemi, F., Asgarkhani, N., & Yoo, D. Y. (2024). Machine-learning methods for estimating compressive strength of high-performance alkali-activated concrete. *Engineering Applications of Artificial Intelligence*, 136, 109053.
[129] Çiftçioğlu, A. Ö., Kazemi, F., & Shafighfard, T. (2025). Grey wolf optimizer integrated within boosting algorithm: Application in mechanical properties prediction of ultra high-performance concrete including carbon nanotubes. *Applied Materials Today*, 42, 102601.

List of all published papers

1. Kazemi, F., & Jankowski, R. (2023). Enhancing seismic performance of rigid and semi-rigid connections equipped with SMA bolts incorporating nonlinear soil-structure interaction. *Engineering Structures*, 274, 114896.
2. Kazemi, F., & Jankowski, R. (2023). Machine learning-based prediction of seismic limit-state capacity of steel moment-resisting frames considering soil-structure interaction. *Computers & Structures*, 274, 106886.
3. Kazemi, F., & Jankowski, R. (2023). Seismic performance evaluation of steel buckling-restrained braced frames including SMA materials. *Journal of Constructional Steel Research*, 201, 107750.
4. Kazemi, F., Asgarkhani, N., & Jankowski, R. (2023). Machine learning-based seismic fragility and seismic vulnerability assessment of reinforced concrete structures. *Soil Dynamics and Earthquake Engineering*, 166, 107761.
5. Kazemi, F., Asgarkhani, N., & Jankowski, R. (2023). Machine learning-based seismic response and performance assessment of reinforced concrete buildings. *Archives of Civil and Mechanical Engineering*, 23(2), 94.
6. Kazemi, F., Asgarkhani, N., & Jankowski, R. (2023). Predicting seismic response of SMRFs founded on different soil types using machine learning techniques. *Engineering Structures*, 274, 114953.
7. Kazemi, F., Asgarkhani, N., & Jankowski, R. (2023). Probabilistic assessment of SMRFs with infill masonry walls incorporating nonlinear soil-structure interaction. *Bulletin of Earthquake Engineering*, 21(1), 503-534.
8. Kazemi, F., Asgarkhani, N., & Jankowski, R. (2024). Enhancing seismic performance of steel buildings having semi-rigid connection with infill masonry walls considering soil type effects. *Soil Dynamics and Earthquake Engineering*, 177, 108396.
9. Kazemi, F., Asgarkhani, N., & Jankowski, R. (2024). Optimization-based stacked machine-learning method for seismic probability and risk assessment of reinforced concrete shear walls. *Expert Systems with Applications*, 255, 124897.
10. Kazemi, F., Asgarkhani, N., Lasowicz, N., & Jankowski, R. (2024). Development and experimental validation of a novel double-stage yield steel slit damper-buckling restrained brace. *Engineering Structures*, 315, 118427.
11. Kazemi, F., Asgarkhani, N., Manguri, A., & Jankowski, R. (2024). Seismic probabilistic assessment of steel and reinforced concrete structures including earthquake-induced pounding. *Archives of Civil and Mechanical Engineering*, 24(3), 178.
12. Kazemi, F., Asgarkhani, N., Shafighfard, T., Jankowski, R., & Yoo, D. Y. (2025). Machine-learning methods for estimating performance of structural concrete members reinforced with fiber-reinforced polymers. *Archives of Computational Methods in Engineering*, 32(1), 571-603.
13. Kazemi, F., Çiftçioğlu, A. Ö., Shafighfard, T., Asgarkhani, N., & Jankowski, R. (2025). RAGN-R: A multi-subject ensemble machine-learning method for estimating mechanical properties of advanced structural materials. *Computers & Structures*, 308, 107657.
14. Kazemi, F., Mohebi, B., & Jankowski, R. (2021). Predicting the seismic collapse capacity of adjacent SMRFs retrofitted with fluid viscous dampers in pounding condition. *Mechanical Systems and Signal Processing*, 161, 107939.
15. Kazemi, F., Miari, M., & Jankowski, R. (2021). Investigating the effects of structural pounding on the seismic performance of adjacent RC and steel MRFs. *Bulletin of Earthquake Engineering*, 19(1), 317-343.

16. Kazemi, F., Shafighfard, T., & Yoo, D. Y. (2024). Data-driven modeling of mechanical properties of fiber-reinforced concrete: a critical review. *Archives of Computational Methods in Engineering*, 31(4), 2049-2078.
17. Kazemi, F., Shafighfard, T., Jankowski, R., & Yoo, D. Y. (2024). Active learning on stacked machine learning techniques for predicting compressive strength of alkali-activated ultra-high-performance concrete. *Archives of Civil and Mechanical Engineering*, 25(1), 24.
18. Kazemi, F., Asgarkhani, N., Ghanbari-Ghazijahani, T., & Jankowski, R. (2025). Ensemble machine learning models for estimating mechanical curves of concrete-timber-filled steel tubes. *Engineering Applications of Artificial Intelligence*, *156*, 111234.
19. Kazemi, F., Mohebi, B., & Yakhchalian, M. (2018). Evaluation of the P-delta effect on collapse capacity of adjacent structures subjected to far-field ground motions. *Civil Engineering Journal*, 4(5), 1066-1073.
20. Kazemi, F., Mohebi, B., & Yakhchalian, M. (2020). Predicting the seismic collapse capacity of adjacent structures prone to pounding. *Canadian Journal of Civil Engineering*, 47(6), 663-677.
21. Kazemi, F., Mohebi, B., Asgarkhani, N., & Yousefi, A. (2023). Advanced scalar-valued intensity measures for residual drift prediction of SMRFs with fluid viscous dampers. *International Journal of Structural Integrity*, 12, 20-25.
22. Asgarkhani, N., Kazemi, F., & Jankowski, R. (2022). Optimal retrofit strategy using viscous dampers between adjacent RC and SMRFs prone to earthquake-induced pounding. *Archives of Civil and Mechanical Engineering*, 23(1), 7.
23. Asgarkhani, N., Kazemi, F., & Jankowski, R. (2023). Machine learning-based prediction of residual drift and seismic risk assessment of steel moment-resisting frames considering soil-structure interaction. *Computers & Structures*, 289, 107181.
24. Asgarkhani, N., Kazemi, F., Jakubczyk-Gałczyńska, A., Mohebi, B., & Jankowski, R. (2024). Seismic response and performance prediction of steel buckling-restrained braced frames using machine-learning methods. *Engineering Applications of Artificial Intelligence*, 128, 107388.
25. Çiftçioğlu, A. Ö., Kazemi, F., & Shafighfard, T. (2025). Grey wolf optimizer integrated within boosting algorithm: Application in mechanical properties prediction of ultra high-performance concrete including carbon nanotubes. *Applied Materials Today*, 42, 102601.
26. Dehestani, A., Kazemi, F., Abdi, R., & Nitka, M. (2022). Prediction of fracture toughness in fibre-reinforced concrete, mortar, and rocks using various machine learning techniques. *Engineering Fracture Mechanics*, 276, 108914.
27. Manguri, A., Saeed, N., Kazemi, F., Szczepanski, M., & Jankowski, R. (2023). Optimum number of actuators to minimize the cross-sectional area of prestressable cable and truss structures. *Structures*, 47, 2501-2514.
28. Moaf, F. O., Kazemi, F., Abdelgader, H. S., & Kurpińska, M. (2023). Machine learning-based prediction of preplaced aggregate concrete characteristics. *Engineering Applications of Artificial Intelligence*, 123, 106387.
29. Mohebi, B., Asadi, N., & Kazemi, F. (2019). Effects of using gusset plate stiffeners on the seismic performance of concentrically braced frame. *International Journal of Civil and Environmental Engineering*, 13(12), 723-729.
30. Mohebi, B., Kazemi, F., Asgarkhani, N., Ghasemnezhadsani, P., & Mohebi, A. (2022). Performance of vector-valued intensity measures for estimating residual drift of steel MRFs with viscous dampers. *International Journal of Structural and Civil Engineering Research*, 11, 79-83.

31. Mohebi, B., Sartipi, M., & Kazemi, F. (2023). Enhancing seismic performance of buckling-restrained brace frames equipped with innovative bracing systems. *Archives of Civil and Mechanical Engineering*, 23(4), 243.
32. Mohebi, B., Yazdanpanah, O., Kazemi, F., & Formisano, A. (2021). Seismic damage diagnosis in adjacent steel and RC MRFs considering pounding effects through improved wavelet-based damage-sensitive feature. *Journal of Building Engineering*, 33, 101847.
33. Shafighfard, T., Kazemi, F., Asgarkhani, N., & Yoo, D. Y. (2024). Machine-learning methods for estimating compressive strength of high-performance alkali-activated concrete. *Engineering Applications of Artificial Intelligence*, 136, 109053.
34. Shafighfard, T., Kazemi, F., Bagherzadeh, F., Mieloszyk, M., & Yoo, D. Y. (2024). Chained machine learning model for predicting load capacity and ductility of steel fiber–reinforced concrete beams. *Computer-Aided Civil and Infrastructure Engineering*, 39(23), 3573-3594.
35. Yazdanpanah, O., Mohebi, B., Kazemi, F., Mansouri, I., & Jankowski, R. (2022). Development of fragility curves in adjacent steel moment-resisting frames considering pounding effects through improved wavelet-based refined damage-sensitive feature. *Mechanical Systems and Signal Processing*, 173, 109038.

List of all articles presented during conferences

1. Kazemi, F., Asgarkhani, N., Migda W., & Jankowski R., (2025). Optimizing performance of corrugated steel plate shear wall using machine learning-based design procedure. In *10th International Conference on Computational Methods in Structural Dynamics and Earthquake Engineering (COMPDYN)*, 15-18 June, 2025, Rhodes Island, Greece.
2. Asgarkhani, N., Kazemi, F., Migda W., Deniziak P., & Jankowski R., (2025). A machine learning approach for optimal retrofitting of steel structures with buckling-restrained braces. In *10th International Conference on Computational Methods in Structural Dynamics and Earthquake Engineering (COMPDYN)*, 15-18 June, 2025, Rhodes Island, Greece.
3. Lasowicz N., Asgarkhani, N., & Kazemi, F., (2025). A lead rubber bearing device equipped with optimal shape and rubber material. In *10th International Conference on Computational Methods in Structural Dynamics and Earthquake Engineering (COMPDYN)*, 15-18 June, 2025, Rhodes Island, Greece.
4. Kazemi F., Asgarkhani N., & Jankowski R. (2024). Machine Learning-Based Crack Detection of Infill Walls for Retrofitting Damaged Buildings. In *18th World Conference on Earthquake Engineering (WCEE)*, 30 June to 5 July, 2024, Milan, Italy.
5. Kazemi F., Asgarkhani N., Lasowicz N., & Jankowski R. (2024). Machine Learning-Based Seismic Response and Performance Assessment of Reinforced Concrete Frames. In *18th World Conference on Earthquake Engineering (WCEE)*, 30 June to 5 July, 2024, Milan, Italy.
6. Kazemi F., Asgarkhani N., Manguri A., Jakubczyk-Gałczyńska A., Lasowicz N., & Jankowski R. (2024). Improving Computational Ability of Machine-Learning Algorithms with Feature Selection Methods. In *18th World Conference on Earthquake Engineering (WCEE)*, 30 June to 5 July, 2024, Milan, Italy.
7. Mohebi B., Kazemi F., Asgarkhani N., & Lasowicz N. (2024). Predicting Interstory Drift Distribution of RC Structures Using Machine-Learning Methods. In *18th World Conference on Earthquake Engineering (WCEE)*, 30 June to 5 July, 2024, Milan, Italy.
8. Asgarkhani, N., Kazemi, F., & Jankowski, R. (2024). Active learning on ensemble machine-learning model to retrofit buildings under seismic mainshock-aftershock sequence. In *24th International Conference on Computational Science* (pp. 470-478), 2-4 July 2024, Málaga, Spain.
9. Kazemi, F., Asgarkhani, N., Manguri, A., & Jankowski, R. (2024). Seismic performance assessment of steel structures considering soil effects. *Eurasian Journal of Science and Engineering*, 10(1), 113-122, presented in *9th International Engineering Conference (IEC'2026) under theme of "Towards Engineering Innovations and Sustainability"*, 15-16 February, 2023, Erbil, Iraq.
10. Asgarkhani, N., Kazemi, F., Manguri, A., & Jankowski, R. (2024). Reducing the seismic failure potential of reinforced concrete frames. *Eurasian Journal of Science and Engineering*, 10(1), 123-131, presented in *9th International Engineering Conference (IEC'2026) under theme of "Towards Engineering Innovations and Sustainability"*, 15-16 February, 2023, Erbil, Iraq.
11. Manguri, A., Saeed, N., Kazemi, F., Asgarkhani, N., & Jankowski, R. (2024). The Effect of Minimum Actuation Limit in Shape Control of a Single-Layer Dome Frame. *Eurasian Journal of Science and Engineering*, 10(1), 77-88, presented in *9th International Engineering Conference (IEC'2026) under theme of "Towards Engineering Innovations and Sustainability"*, 15-16 February, 2023, Erbil, Iraq.
12. Kazemi, F., Asgarkhani, N., Manguri, A., Lasowicz, N., & Jankowski, R. (2023). Introducing a computational method to retrofit damaged buildings under seismic

mainshock-aftershock sequence. In *23th International Conference on Computational Science* (pp. 180-187), 3-5 July, 2023, Prague, Czech Republic.
13. Kazemi, F., Mohebi, B., & Asgarkhani, N. (2023). Estimating seismic behavior of buckling-restrained braced frames using machine learning algorithms. In *International Conference on Nonlinear Dynamics and Applications* (pp. 477-486), 18-21 June, 2023, Rome, Italy.
14. Manguri, A., Saeed, N., Kazemi, F., Asgarkhani, N., Szczepanski, M., & Jankowski, R. (2023). Computational bar size optimization of single layer dome structures considering axial stress and shape disturbance. In *12th International Conference on Mathematical Modeling in Physical Sciences* (pp. 173-185), 28-31 August, 2023, Belgrade, Serbia.
15. Mohebi, B., Kazemi, F., & Asgarkhani, N. (2023). Retrofitting damaged buildings under seismic mainshock-aftershock sequence. In *9th International Conference on Computational Methods in Structural Dynamics and Earthquake Engineering (COMPDYN)* (Vol. 21523), 12-14 June, 2023, Athens, Greece.
16. Mohebi, B., Kazemi, F., & Yousefi, A. (2022). Enhancing seismic performance of semi-rigid connection using shape memory alloy bolts considering nonlinear soil–structure interaction. In *2nd Eurasian Conference on OpenSees* (pp. 248-256), 7-8 July, 2022, Turin, Italy.
17. Kazemi, F., Asgarkhani, N., Manguri, A., & Jankowski, R. (2022). Investigating an optimal computational strategy to retrofit buildings with implementing viscous dampers. In *22th International Conference on Computational Science* (pp. 184-191), 21-23 June, 2022, London, United Kingdom.
18. Mohebi, B., Kazemi, F., & Yousefi, A. (2022). Seismic response analysis of knee-braced steel frames using Ni-Ti Shape Memory Alloys (SMAs). In *2nd Eurasian Conference on OpenSees* (pp. 248-256), 7-8 July, 2022, Turin, Italy.
19. Kazemi, F., Mohebi, B., & Yakhchalian, M. (2018). Enhancing the seismic performance of adjacent pounding structures using viscous dampers. In *The 16th European Conference on Earthquake Engineering (16ECEE)* (pp. 18-21), June 18-21, 2018, Thessaloniki, Greece.
20. Mohebi, B., Kazemi, F., & Yakhchalian, M. (2018). Investigating the P-Delta effects on the seismic collapse capacity of adjacent structures. In *16th European Conference on Earthquake Engineering (16ECEE)* (pp. 18-21), June 18-21, 2018, Thessaloniki, Greece.

Paper I:

Kazemi, F., Asgarkhani, N., Manguri, A., & Jankowski, R. (2024). Seismic probabilistic assessment of steel and reinforced concrete structures including earthquake-induced pounding. Archives of Civil and Mechanical Engineering, 24(3), 178. doi.org/10.1007/s43452-024-00994-7

Archives of Civil and Mechanical Engineering (2024) 24:178
https://doi.org/10.1007/s43452-024-00994-7

ORIGINAL ARTICLE

Seismic probabilistic assessment of steel and reinforced concrete structures including earthquake-induced pounding

F. Kazemi[1,2] · N. Asgarkhani[1,2] · A. Manguri[1,3] · R. Jankowski[1]

Received: 25 January 2024 / Revised: 12 April 2024 / Accepted: 5 June 2024 / Published online: 14 June 2024
© The Author(s) 2024

Abstract
Recent earthquakes demonstrate that prioritizing the retrofitting of buildings should be of the utmost importance for enhancing the seismic resilience and structural integrity of urban structures. To have a realistic results of the pounding effects in modeling process of retrofitting buildings, the present research provides seismic Probability Factors (PFs), which can be used for estimating collision effects without engaging in intricate and time-intensive analysis. To include the low-, to mid-rise buildings, the 3-Story, 5-Story, and 9-Story adjacent steel and Reinforced Concrete (RC) moment-resisting frames were modeled in OpenSees software capable to take into account the structure in a state of collapse during the analysis, which can provide the real condition of buildings under seismic excitations. Results of analysis confirmed that the impact force can considerably affect the moment–rotation curve of beams and columns, in which, it can affect the structural response of structures during earthquakes. Therefore, seismic PFs proposed to examine the possibility of changes in the performance levels and fragility assessments. Moreover, proposed PFs can be used as coefficient factors to facilitate the retrofitting process of buildings and improve the environmental effects.

Keywords Probability factor · Structural pounding · Seismic probabilistic assessment · Seismic performance level · Seismic retrofitting · Seismic fragility assessment

1 Introduction

During decades, the knowledge of engineers about the response and designing process significantly increased, and structures with strong capabilities against severe earthquakes were constructed. Meanwhile, during the design process, the existence of adjacent structures was neglected. Seismic codes prescribed some formula to define minimum Separation Distance (SD_{min}) and should be considered during construction, while in many cities, SD_{min} between newly constructed adjacent buildings was neglected. Favvata [1] investigated the SD_{min} for adjacent pounding structures, and showed that the SD_{min} depends on the seismic limit state and level of seismic hazard. In addition, to fulfill the shortcomings, some formulas have been proposed for evaluating SD [2]. Kazemi et al. [3] showed that colliding can impose unexpected force in the level of the impact that significantly affects the response of adjacent structures (see Figs. 4–6). Although this impact force cannot be considered during the design process, it may result in extensive local damages or even total collapse of the structural members (see [4, 5]). To prevent this extensive damages, Sołtysik et al. [6] proposed polymer elements that can be implemented between adjacent structures to reduce the impact force. In addition, Kazemi et al. [7] enhanced the seismic performance of neighboring structures through the utilization of viscous dampers. Kandemir-Mazanoglu and Mazanoglu [8] proposed an optimal placement of viscous dampers in the inter-floor spaces of the adjoining pounding structures. Proposed approaches had good improvements in seismic limit states of adjacent structures. Karayannis and Favvata [9] investigated different level Reinforced Concrete (RC) structures, in which structural collision occurs when one structure impacts the

✉ F. Kazemi
farzin.kazemi@pg.edu.pl

[1] Faculty of Civil and Environmental Engineering, Gdańsk University of Technology, ul. Narutowicza 11/12, 80-233 Gdansk, Poland

[2] Department of Structures for Engineering and Architecture, School of Polytechnic and Basic Sciences, University of Naples "Federico II", Naples, Italy

[3] Civil Engineering Department, University of Raparin, Rania, Kurdistan Region, Iraq

columns of another. This type of collision can cause local damages or even destruction of columns in the impact area [10]. In addition, some characteristics of the constructed buildings such as irregular plans and lateral-load resisting systems (with and without assuming infill masonry walls) can alter the behavior of buildings [11] and may lead to torsional movements (see [12]), which is an important reason for local damages in buildings. Jankowski [13] investigated the structural response of two adjacent structures assuming different materials implemented on the shaking table. The steel structure witnessed the highest displacement response against concrete and ceramic material. In addition, the influence of materials on the dynamic properties was investigated by Favvata et al. [14]. Their results confirm that flexural and ductility demands in columns were affected by their location of them at the top of the structure.

For accurate seismic risk evaluation of adjacent colliding structures, seismic vulnerability assessment is a vital process. Although seismic risk assessment demands a precise estimation of the seismic hazard, outcomes of the vulnerability evaluation can be used for retrofitting structures and determining damages. Kazemi et al. [15] explored seismic collapse capacity and fragility curves of the adjacent pounding structures with different heights and floor weights. Zain et al. [16] proposed a framework for seismic fragility curve assessments of RC structures that reduces the computational efforts. Mohamed and Romão [17] investigated the seismic vulnerability assessment of RC structures that were not originally designed to withstand lateral forces considering the pounding phenomenon, assuming different conditions of collision such as floor-to-floor and floor-to-column. Tubaldi et al. [18] discussed the two major issues [i.e., appropriate Intensity Measure (IM) and selecting a regression model to explain the relation between Engineering Demand Parameter (EDP) and IM] in defining a probabilistic seismic demand model for collision risk assessment. While it mentions improvements in sufficiency obtained using certain IMs, it does not provide concrete data or analysis to substantiate these claims. However, a design methodology for determining the critical SD between adjacent buildings to prevent seismic collision including performing parametric analyses and developing efficient algorithms based on linear structural models have been done by Barbato and Tubaldi [19]. Ruggieri et al. [20] used a sample made by 90 masonry churches in Piemonte, Italy, as case study for a statistical basis seismic vulnerability analysis subjected to the Valle Scrivia earthquake. Seismic damage diagnosis plays a key role for vulnerability assessment of the structures.

Vulnerability evaluations can be projected as seismic fragilities, which can be sorted into four terms of empirical, analytical, hybrid, and judgmental. Surveys from previous seismic events as the major source of vulnerability evaluation can be employed for seismic performance assessment of colliding buildings in terms of empirical process, while judgmental process relies on the opinions of the expert. Ruggieri et al. [21] proposed a visual assessment process to evaluate the seismic risk of a school in Italy using a judgmental process. A hybrid process is a combination of two judgmental and empirical evaluations. Although these processes can be easily used by researchers, the precision of the outcomes is strongly contingent upon on expert judgment and the quality of previous seismic events. Therefore, using the analytical process to fragility curve assessment of the colliding structures applying nonlinear simulations is considered to be the most reliable process [11, 22–25]. It is worth mention that the nonlinear model should contain as possible as the actual condition of structures in collision. Kazemi et al. [26] investigated *P*-delta effect on seismic limit state capacities of adjacent frames and showed that the *P*-delta effect plays a crucial role in the seismic capacity level assessment. In addition, they developed a computational strategy to consider the effects of collapsed structure on the seismic response of the adjacent structure during the analysis, which is a real condition of damaged structures during severe earthquakes. Moreover, they proposed some retrofitting strategy to improve seismic performance of steel and RC structures [27, 28].

Recently, some studies have been carried out for seismic fragility curve assessment of structures. Miano et al. [29] evaluated seismic fragilities of the RC infilled buildings stock with a parallel plane frames assuming base differential displacement. They showed that the geometrical features had a crucial effect on the vulnerability measures. Wang and Sun [30] proposed self-centering columns with low-bond high-strength reinforcement to investigate the reparability of RC buildings. The seismic fragility curves of the residual story showed that using the self-centering columns significantly mitigated the residual deformation of damage states. Yazdanpanah et al. [31] introduced a novel methodology for assessing seismic fragilities in colliding adjacent structures, utilizing an enhanced wavelet-based refined feature. Their approach showed more efficient results to estimate seismic fragility curves based on Morlet and complex Morlet (*cmorfb-fc*) wavelets. Flenga and Favvata [31] proposed a method involving optimal SD and minimum collision risk to discuss the limitations of existing methods for assessing the risk associated with this phenomenon. They introduced probabilistic method to enhance the response prediction, and a novel methodology based on fragility analysis has been introduced to assess SD_{min} across various limit states. This approach considers localized demands, including shear, on structural members, as well as scenarios involving both floor-to-floor and floor-to-column collision. However, Flenga and Favvata [32] integrated the localized inelastic demands of a multi-story RC structure into the probabilistic

assessment of seismic collision risk. One strength of the investigation is its recognition of the limited consideration given to local EDPs in probabilistic assessment. A novel approach has been developed for determining the optimal SD and assessing the acceptable risk of structural pounding in multi-story RC structures. Their findings suggest that the performance characteristics of the columns within the RC structure play a critical role as demand parameters in the probabilistic evaluation of collision risk. Moreover, they developed a risk-targeted decision model for verifying the seismic performance of a multi-story RC structure against collision, and assumed the lack of consideration for performance objectives, aseismic code-compliant design, and local inelastic demands of structural members. A novel decision framework, aimed at targeting risk, has been introduced to validate the seismic performance of RC structures concerning structural pounding [33]. Considering the impact effects and variations in geometric properties and material, Sinha and Rao [34] investigated displacement-based fragility for floor-to-floor and floor-to-column collision within an eight-story non-ductile RC frame adjacent to a three-story rigid RC frame with varying story levels. They emphasize the importance of accurately estimating structural integrity with respect to collision to prevent catastrophic failures. However, using machine-learning methods can be a useful preliminary tool for estimating performance levels and fragility curves of steel and RC buildings [35, 36].

The main purpose of this study is seismic performance and fragility curve assessment of adjacent RC and steel moment-resisting frames including the earthquake-induced collisions. Therefore, adjacent RC colliding with steel structures considering three SDs according to the seismic codes have been considered having a typical plan and connected with linear viscoelastic contact elements to assume collision phenomenon. The collapse state analyses were performed in numerical models of steel and RC structures with the possibility of destruction of one of the structures. To accurately simulate the real condition of steel and RC structures exposed to pounding, the structures were modeled in MATLAB [37] and OpenSees [38], a software application incorporating a crafted Tcl programming code, equipped with the capability to account for damages during the analysis. The executed program can accurately analyze a model under nonlinear conditions, employing innovative methods to incorporate damages and monitor structural responses throughout the analysis. This approach proves valuable in creating precise models that closely resemble the real conditions of buildings susceptible to earthquake-induced pounding. In addition, the developed Tcl algorithm possesses the capability to control engineering demands to capture the results of structural response of both structures to reduce the analysis time. Having a precise modeling approach for collision and considering the collapsed structure effects on the existing structure make this research a reliable investigation so far. Moreover, this study determines proper Probability Factors (PFs) for existing buildings or newly constructed ones to estimate the influence of collision phenomenon on the seismic performance and fragility curves based on the analytical process. Using PFs reduces the time of collision analysis and provides designers a preliminary estimation on how the collision would affect the structural performances.

2 Modeling methods

2.1 Modeling of structures

In this study, structures with 3-Story, 5-Story, and 9-Story steel and RC structures were investigated. Figure 1 shows the structural plan assumed for adjacent structures. To model

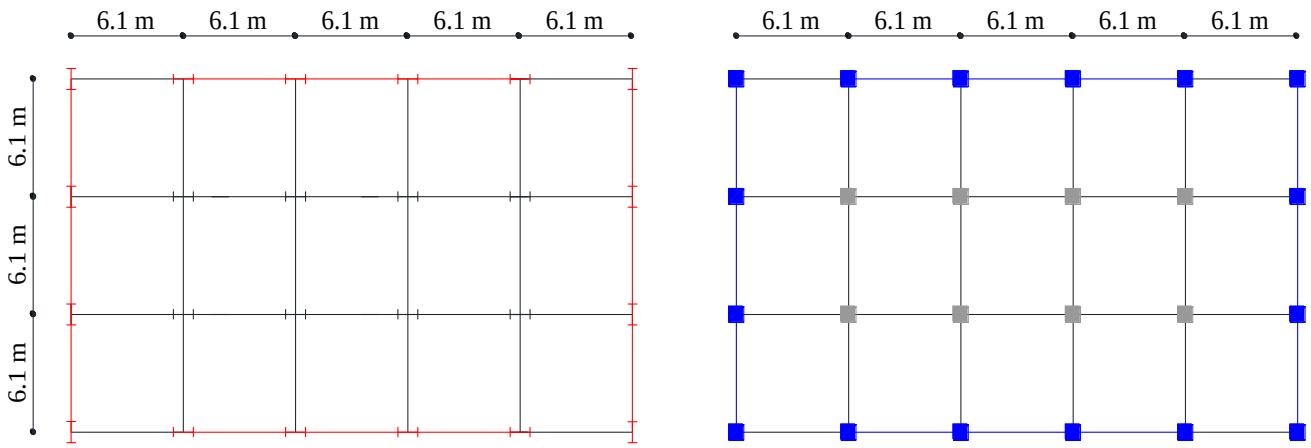

Fig. 1 Structural plan of the considered steel and RC structures

these structures, soil class *D* with seismic parameters of $SD_S = 1.0$ g and $SD_1 = 0.6$ g were assumed. In this study, for both steel and RC structures, $R = 8$, $\Omega = 3$, and $C_d = 5.5$, were selected according to ASCE/SEI 7–16 [39]. Moreover, live and dead loads of 2.39 kN/m^2 and 8.379 kN/m^2, respectively, were applied to all floor levels. All structures were modeled in ETABS 2016 based on ASCE 7–16 [39], AISC 360-16 [40], AISC 341-16 [41], and ACI 318-14 [42] provisions. Steel yield strength and concrete compressive strength equal to 345 MPa and 34.5 MPa were used, respectively. Figure 2 presents structural elements and geometry of the selected structures. To model two-dimensional steel and RC structures in OpenSees [38], all columns except those in the MRFs (see the red line for steel and blue line for RC in Fig. 1) were modeled as leaning column to consider *P*-Delta effects and connected to the main resisting frame with axially rigid links [43–45].

In the case of steel structures, two nonlinear springs located at the ends of beams and columns were employed to account for the modified Ibarra–Krawinkler model [26–28, 46] for assuming deteriorating moment–rotation hysteresis. To capture the deterioration modes of RC, an element model with the capability of considering deterioration modes (i.e., monotonic and cyclic) was used [47–49]. Tables 1 and 2 present design documentation of the structural elements of RC. *h* and *b* are the height and width of section, *s* is spacing of transverse reinforcement, ρ_{tot} is longitudinal reinforcement ratio, ρ' is longitudinal reinforcement ratio in compression, and ρ_{sh} is transverse reinforcement ratio near end of column (close spacing region).

It worth mentioning that the structures have symmetric plan in both directions and regular weight distribution. Therefore, it is only possible that they collide in X-direction due to assumptions and there is no torsion impact during pounding. Due to these assumptions, it can be possible to model two-dimensional steel and RC structures with pounding effects [26–28, 46].

2.2 2.2. Impact element model

Seismic codes prescribed minimum SD regarding experimental and analytical models. In this study, SD prescribed by ASCE/SEI 7–16 [39] was used. According to this, Eq. (1) shows SD_{min} that can be calculated as follows:

$$SD_{min} = \sqrt{\left(\frac{C_d.\delta_M}{I}\right)_1^2 + \left(\frac{C_d.\delta_M}{I}\right)_2^2}, \quad (1)$$

where δ_M is maximum inelastic deformation, and *I* is importance factor. To calculate δ_M, base shear-roof displacement curves (pushover curve) based on the first mode lateral-load distribution for both categories of structures were obtained. In this research, the distance between two adjacent structures was selected as 0.0, 0.5, and 1.0 times of SD_{min}. Table 3

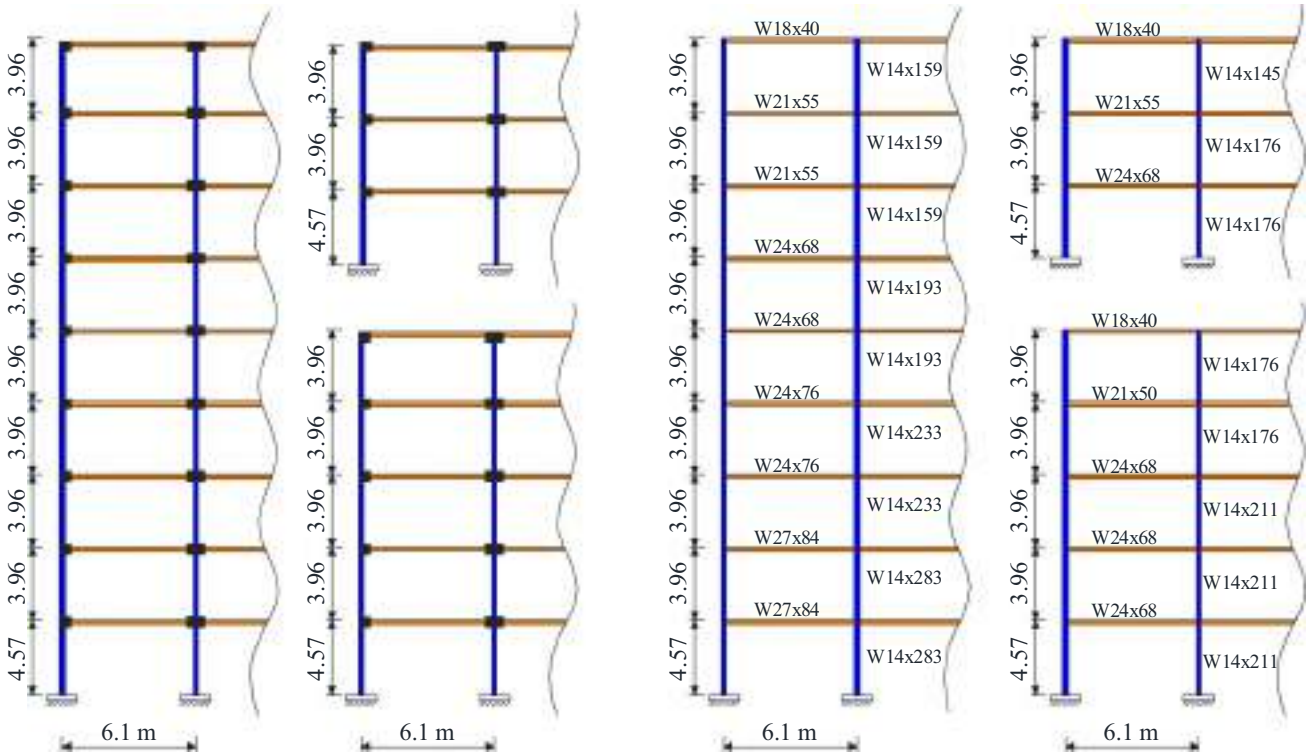

Fig. 2 Structural elements and geometry of the selected steel and RC structures

Table 1 Detail of the column members of RC

Model	Floor	Exterior					Interior				
		h (m)	b (m)	s (m)	ρ_{tot}(%)	ρ_{sh}(%)	h (m)	b (m)	s (m)	ρ_{tot}(%)	ρ_{sh}(%)
3-story RC	1st	0.762	0.711	0.127	1.33	0.98	0.762	0.711	0.127	1.7	0.98
	2nd	0.762	0.711	0.127	1	0.98	0.762	0.711	0.127	1.7	0.98
	3rd	0.762	0.711	0.127	1	0.98	0.762	0.711	0.127	1.7	0.98
5-story RC	1st	0.762	0.813	0.089	2.1	0.85	0.762	0.813	0.089	1.6	1.12
	2nd	0.762	0.813	0.089	2.1	0.85	0.762	0.813	0.089	1.6	0.8
	3rd	0.762	0.813	0.102	1	0.61	0.762	0.813	0.102	1	0.8
	4th	0.762	0.813	0.102	1	0.61	0.762	0.813	0.102	1	0.8
	5th	0.762	0.813	0.102	1	0.61	0.762	0.813	0.102	1	0.8
9-story RC	1st	0.711	0.661	0.089	2	0.97	0.711	0.661	0.089	1.8	1.2
	2nd	0.711	0.661	0.089	1.5	0.97	0.711	0.661	0.089	1.3	1.2
	3rd	0.711	0.661	0.089	1.5	0.97	0.711	0.661	0.089	1.3	1.2
	4th	0.711	0.661	0.102	1.3	0.97	0.711	0.661	0.102	1.3	1.2
	5th	0.711	0.661	0.102	1.3	0.69	0.711	0.661	0.102	2.2	0.69
	6th	0.711	0.661	0.102	1	0.69	0.711	0.661	0.102	1.5	0.69
	7th	0.711	0.661	0.102	1	0.69	0.711	0.661	0.102	1.4	0.69
	8th	0.711	0.661	0.102	1	0.69	0.711	0.661	0.102	1	0.69
	9th	0.711	0.661	0.102	1	0.69	0.711	0.661	0.102	1	0.69

Table 2 Detail of the beam members of RC

Model	Floor	Exterior and interior					
		h (cm)	b (cm)	s (cm)	ρ_{tot}	ρ'	$\rho_{sh}t$
3-story RC	1st	71.1	71.1	12.7	0.0065	0.0075	0.0039
	2nd	71.1	71.1	12.7	0.0065	0.0075	0.0039
	3rd	71.1	71.1	12.7	0.0065	0.0075	0.0039
5-story RC	1st	61	81.3	12.7	0.0108	0.0123	0.0051
	2nd	61	81.3	12.7	0.01	0.0115	0.0048
	3rd	16	81.3	12.7	0.0093	0.0180	0.0039
	4th	61	81.3	12.7	0.0048	0.0060	0.0029
	5th	61	81.3	12.7	0.0048	0.0060	0.0029
9-story RC	1st	76.2	66.1	12.7	0.0068	0.0075	0.0042
	2nd	76.2	66.1	16.5	0.0073	0.0083	0.0045
	3rd	76.2	66.1	12.7	0.0068	0.0080	0.0043
	4th	76.2	66.1	13.9	0.0063	0.0075	0.0041
	5th	76.2	66.1	15.2	0.0055	0.0068	0.0037
	6th	76.2	66.1	16.5	0.0049	0.0055	0.0031
	7th	76.2	66.1	13.9	0.0032	0.0040	0.0025
	8th	76.2	66.1	15.2	0.0032	0.0032	0.0024
	9th	76.2	66.1	15.2	0.0032	0.0032	0.0024

shows numerical models of structures used in this study with assumed SDs between them.

There are many impact element models that can be used to model impact force due to colliding between adjacent structures. They can be sorted from the high accuracy of modeling this phenomenon such as linear and nonlinear viscoelastic model to the lower accuracy such as using spring element [50, 51]. The equation of linear viscoelastic element can be presented as follows:

$$F(t) = K_i\delta(t) + C_i\dot{\delta}(t), \quad C_i = \frac{-2\times\ln(e)}{\sqrt{\pi^2+(\ln e)^2}}\sqrt{K_i\frac{m_1m_2}{m_1+m_2}}, \tag{2}$$

where the impact force, F(t), can be calculated by the contact stiffness, K_i, and the damping coefficient of the contact model, C_i, having the amount of δ(t) and $\dot{\delta}(t)$, relative deformation and velocity of adjacent structures, respectively. In addition, m_1 and m_2 are the masses of structures in the level

Table 3 SDs assumed between numerical models of steel and RC structures

Numerical models	δ_{M1} *	δ_{M2}	0.0	$0.5SD_{min}$ (m)	$1.0SD_{min}$ (m)
3-story RC with 3-story steel	0.013	0.024	0.0	0.083	0.147
3-story RC with 5-story steel	0.013	0.025	0.0	0.077	0.155
3-story RC with 9-story steel	0.013	0.027	0.0	0.074	0.166
5-story RC with 3-story steel	0.017	0.027	0.0	0.088	0.176
5-story RC with 5-story steel	0.023	0.041	0.0	0.129	0.259
5-story RC with 9-story steel	0.023	0.044	0.0	0.138	0.275
9-story RC with 3-story steel	0.012	0.027	0.0	0.830	0.166
9-story RC with 5-story steel	0.020	0.041	0.0	0.125	0.250
9-story RC with 9-story steel	0.028	0.073	0.0	0.216	0.431

*$C_d = 5.5$ and $I = 1.0$ have been used

of implementing contact element. The coefficient of restitution, denoted as "e" signifies the ratio of the final relative velocity to the initial relative velocity of impacting bodies. It assumes a value between 0.0 and 1.0, representing fully elastic or fully plastic impacts, respectively. In the adopted models, the floor levels were treated as instances of concrete-to-concrete pounding, and a coefficient of restitution of 0.65 was presumed, aligning with findings from various other studies (for more details, see [5, 26–28, 31]).

The impact stiffness and damping coefficients of contact elements are contingent upon the material properties involved in the collision, and there is no singular relationship for their calculation. Nevertheless, Polycarpou et al. [52] proposed the methodology of three-dimensional colliding simulation that considers a simple approximation of the impact stiffness and damping coefficients assuming the plan geometry and material properties. This methodology prepares the requirements of this study for modeling of contact element. They proposed Eq. (3) to calculate the impact stiffness along the colliding side, K, as follows:

$$K = \left[\frac{1-\nu_1^2}{E_{\text{Dynamic},1}} + \frac{1-\nu_2^2}{E_{\text{Dynamic},2}}\right]^{-1}, \quad E_{\text{Dynamic}} = 5.82\left(E_{\text{Static}}\right)^{0.63} \tag{3}$$

where E_{Dynamic} is concrete dynamic elastic modulus that can be determined from static modulus of concrete, E_{Static} equal to 21 GPa. ν_i is Poisson's ratio and assumed equal to 0.2. Therefore, K can be calculated from Eq. (3) equal to $K = 20.96 \times 10^6$ kN/m^2. According to Fig. 1, the colliding length (9.15 m) multiplying by K can be used as K_i, which is 1.9185×10^8 kN/m, and from then, the impact damping coefficient C_i equal to 7576 kN. s/m was obtained [26–28].

3 Results of analysis

3.1 Moment and rotation of hinges

In this section, the effects of colliding on the moment and rotation of hinges of beams and columns were investigated. Sudden impact force in the floor level can considerably affect response of adjacent structures, and then can cause damages in beams and columns. The damage state can be achieved by evaluation of moment and rotation curves of hinges. It should be noted that the collision time could vary during the analysis due to lateral behavior of the structures, while the collision occurs during lateral displacement more than the separation distance. In this part, a nonlinear time-history analysis was performed using Duzce Turkey record (11/12/1999, Duzce, RSN No. 1605) selected from Near-Fault Pulse Like (NF-PL) ground motion subset suggested by FEMA-P695 [53]. The 9-Story steel colliding with 3-Story RC was selected from models to use for nonlinear time-history analysis assuming $S_a\,(T_1) = 1.27$ g given SD of 0.0. Figures 3 and 4 compare moment curves of column and beam hinges of the third floor of the 9-Story steel in alone and colliding with the 3-Story RC assuming SD of 0.0, respectively. According to results, colliding can cause sudden changes in the moment curve compared to the excluding model. These changes in some time step of analysis can increase the amount of moment value suddenly, which causes damages in the structural element. According to Figs. 3 and 4, the maximum moment value of column and beam hinges increased by 37.96% (from 797.86 to 1100.75 kN. m) and 13.22% (from 1145 to 1296.4 kN. m), respectively.

Figures 5 and 6 compare rotation curves of column and beam hinges of the third floor of the 9-Story steel in alone and colliding with the 3-Story RC assuming SD of 0.0, respectively. It is obvious that in the same time step of increasing the moment values, the rotation values

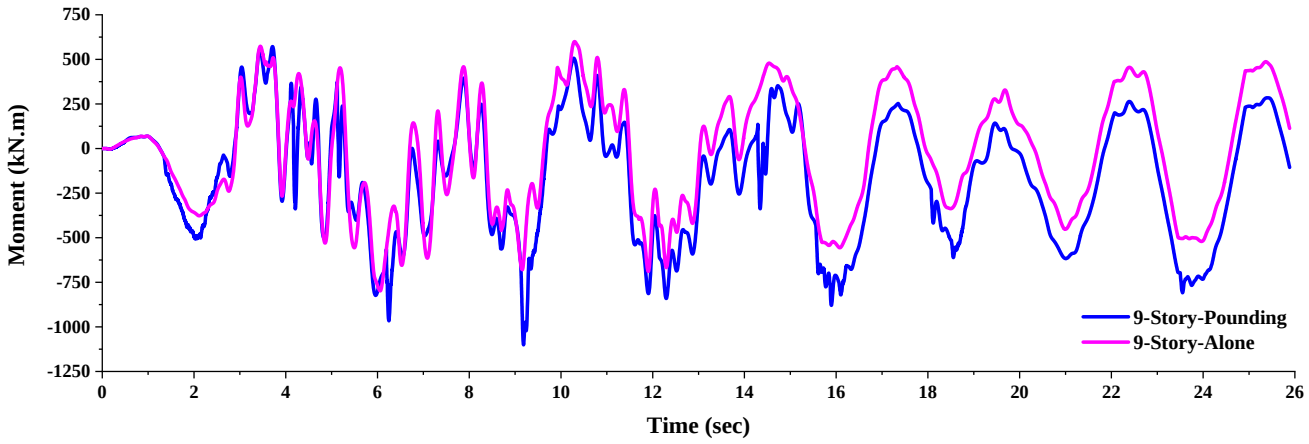

Fig. 3 Comparison between the moments of the third-floor column hinge of 9-Story steel in collision with the 3-Story RC given SD = 0.0

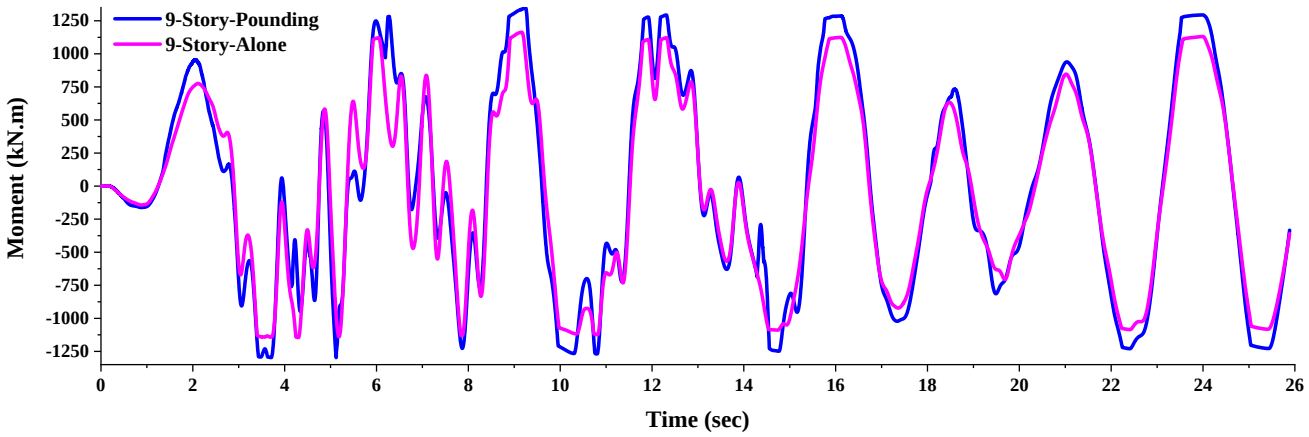

Fig. 4 Comparison between the moments of the third-floor beam hinge of 9-Story steel in collision with the 3-story RC given SD = 0.0

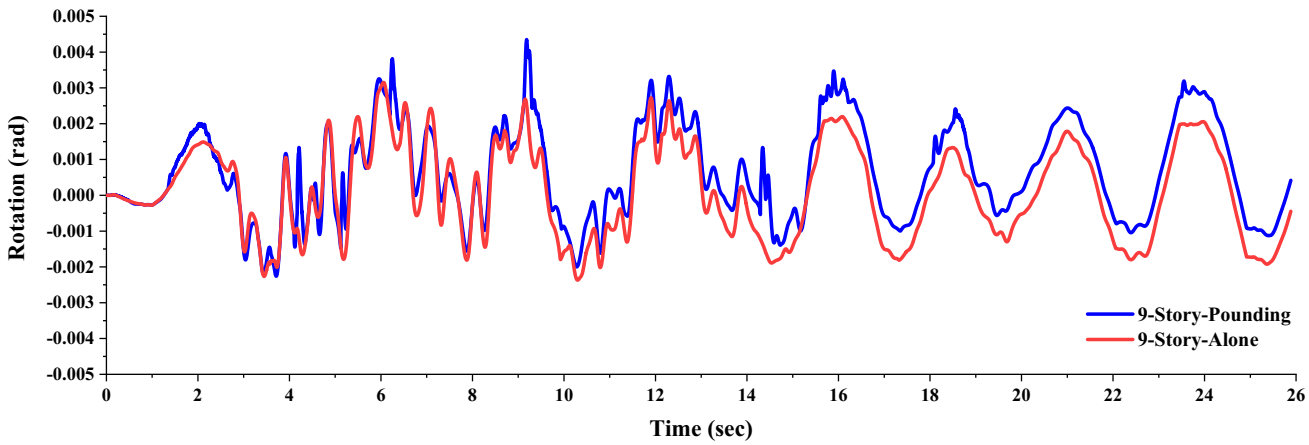

Fig. 5 Comparison between the rotations of the third-floor column hinge of 9-Story steel in collision with the 3-Story RC given SD = 0.0

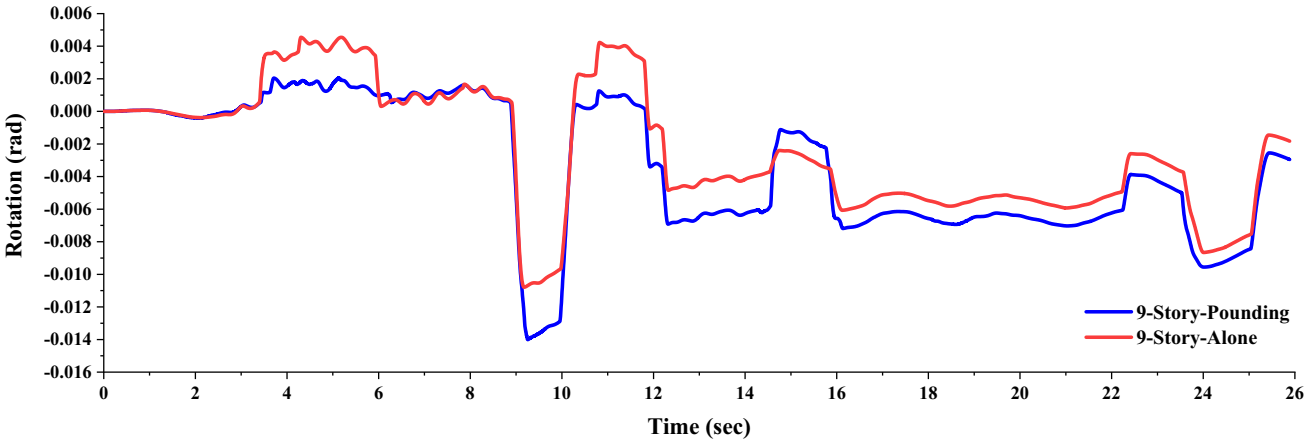

Fig. 6 Comparison between the rotations of the third-floor beam hinge of 9-story steel in collision with 3-story RC given SD = 0.0

experienced sudden changes. This means that the hinges of the selected column and beam entered into a nonlinear state. In addition, according to the results, the maximum rotation value of column and beam hinges increased by 31.25% (from 0.0032 rad to 0.0043 rad) and 29.62% (from 0.0108 rad to 0.0140 rad), respectively. It is noteworthy that results concern all of the hinges of columns and beams in the considered analytical models.

3.2 Analysis procedure

Incremental Dynamic Analysis (IDA) method establishes a probabilistic framework for evaluating structural fragility through the creation of numerous response curves aligned with varying intensity levels. Gradually escalating the ground motion intensity enables IDA to encapsulate the nonlinear dynamics and eventual collapse mechanisms of structures, thereby facilitating the derivation of fragility curves that accommodate uncertainties in ground motion attributes and structural behavior [54]. Previous section emphasized that colliding structures may experience a sudden impact force in the colliding level and this force affected the moment and rotation of the structural members' hinges. To extent the results, IDA is employed that uses IM to increase the intensity of records in each step until the total destruction of the structure, and in each step, EDP controls stability of structure. According to Kazemi et al. [55], various non-structure-specific IMs, including acceleration, velocity, and displacement-related IMs, were compared, revealing that the spectral-based IM, S_a (T_1), exhibited superior performance. Additionally, the analysis of the variations in standard deviation of natural logarithm of IMs indicated that S_a (T_1) demonstrated lower values, suggesting its efficiency as a scalar-valued IM for conducting IDA. Sufficiency, defined as the ability of an IM to render seismic response independent of other characteristics of seismic ground motion records, was evaluated by calculating the p value with respect to ground motion characteristics, such as M (magnitude), R (distance), and Vs30 (shear wave velocity). The results indicate that S_a (T_1) exhibits proper sufficiency, with p values ≥ 0.05, concerning M, R, and Vs30. For this purpose, spectral acceleration in the structure's period, S_a (T_1), is selected as IM, and maximum Interstory Drift Ratio (IDR) is selected as EDP. Therefore, in each step, IM and EDP values can be used for drawing the IDA curve. In this research, two ground motion sets of NF-PL and Near-Fault No Pulse (NF-NP) are considered regarding FEMA-P695 [53]. The NF records comprises 28 records (i.e., 56 individual components) sourced from the PEER NGA database, following the criteria outlined in Section A.7 in FEMA P-695 [53]. Among these, 14 records exhibit pulses (classified as NF-PL), while the remaining 14 records do not display pulses (classified as NF-NP). The selection of records is based on the maximum values of as-recorded Peak Ground Acceleration (PGA_{max}) and Peak Ground Velocity (PGV_{max}), which significantly influence the collision of adjacent structures. The mean spectrum of the chosen records aligns with the target spectrum specified for soil class D across the structural periods of colliding structures. Figure 7 presents the response spectrum of NF-PL and NF-NP record sets.

It is obvious that the real condition of colliding structures should be considered during analysis. Regarding this, in this research, the real condition of colliding structures has been investigated. In the real colliding between two adjacent structures, differences between fundamental periods of adjacent structures (e.g., $T_{1,1}$ and $T_{1,2}$) can cause each of the structures to have different collapse IM. Therefore, one of them should be collapsed before the second one. Moreover, S_a ($T_{1,1}$) and S_a ($T_{1,2}$) should be assumed for selecting the IM. A Tcl algorithm improved in MATLAB [37] and OpenSees [38] software to assume these characteristics in the models, and capture the results of

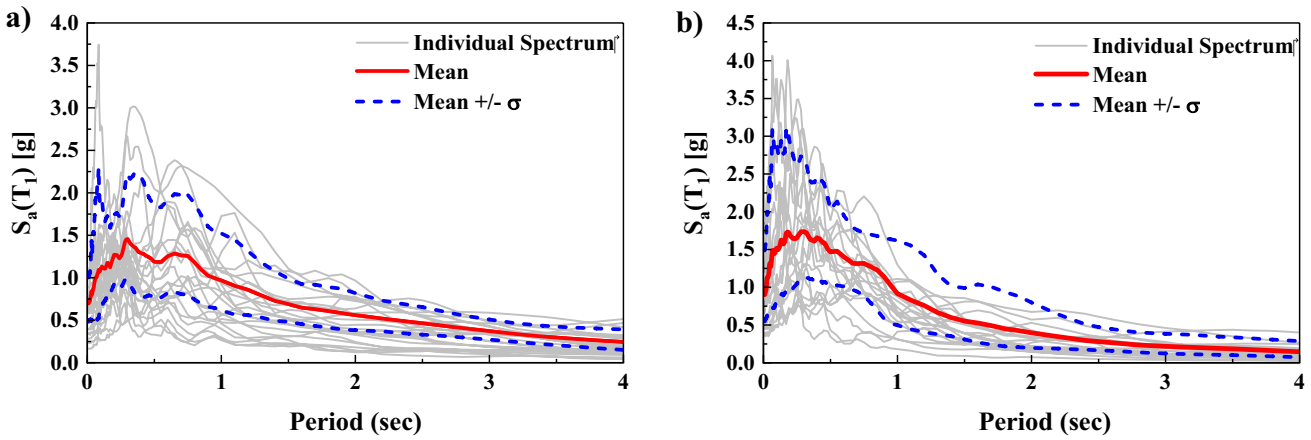

Fig. 7 Response spectrum of **a** NF-PL and **b** NF-NP records

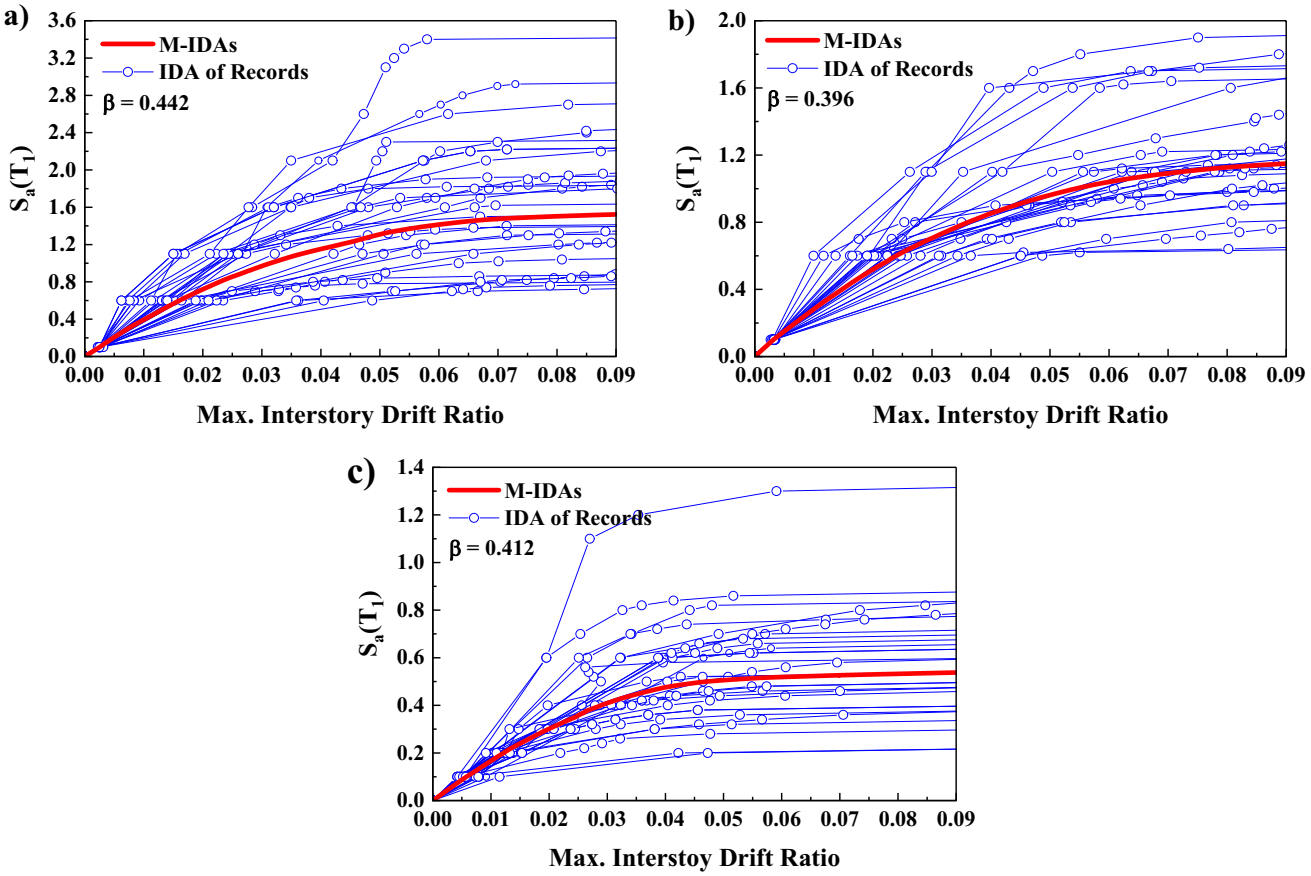

Fig. 8 IDAs of **a** 3-, **b** 5-, and **c** 9-Story RC including NF-NP record subset

each structures separately with considering their effects on each other. Therefore, it is possible to capture both structure's IDA curves at the same time in one model, which reduces the analytical time and efforts. Figures 8 and 9 present IDA curves and the median of IDA curves (M-IDA) of selected steel and RC structures including NF-NP record subset, respectively.

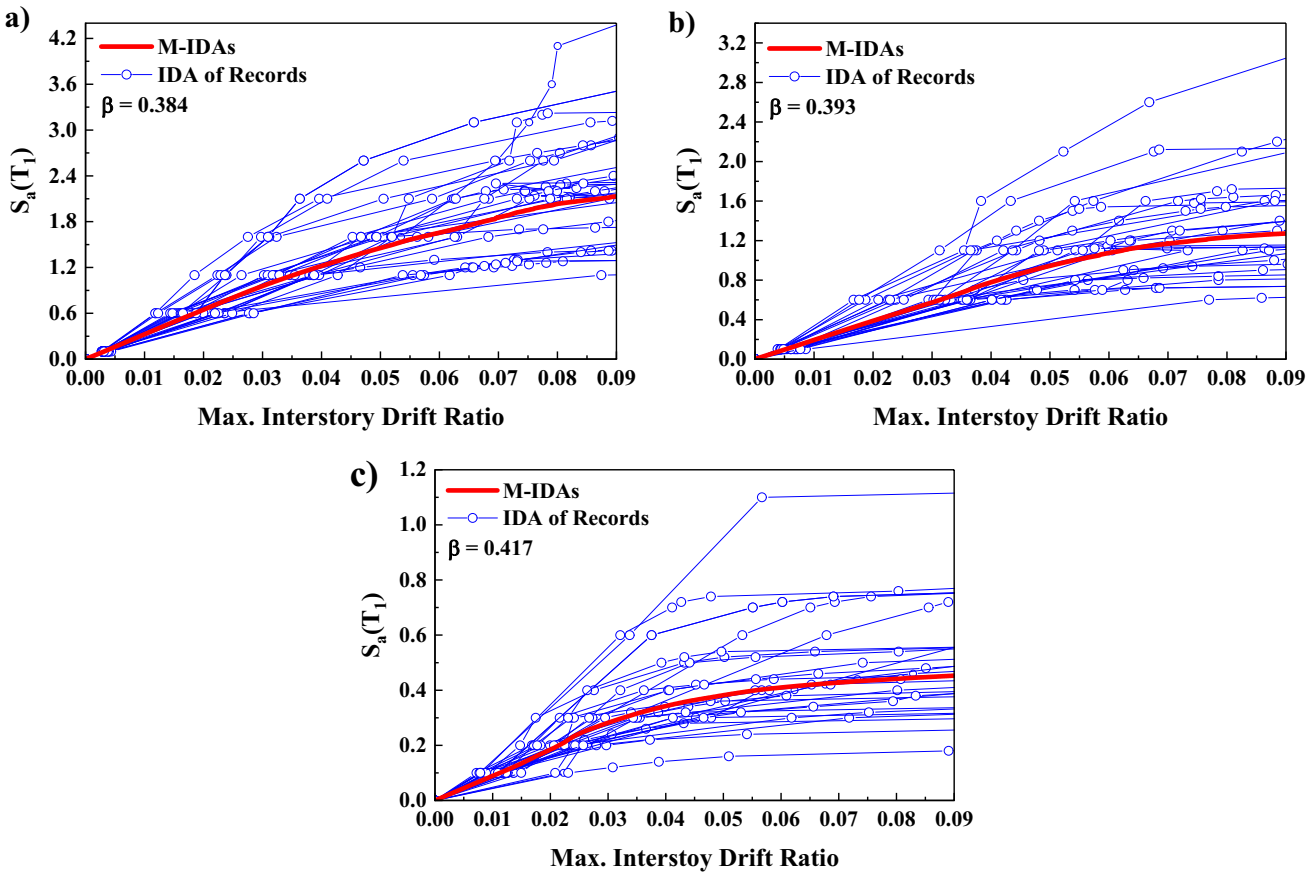

Fig. 9 IDAs of **a** 3-, **b** 5-, and **c** 9-Story steel including NF-NP record subset

3.3 Seismic performance level

In accordance with the descriptions provided in the preceding section, it is feasible to concurrently evaluate IDA curves for both adjacent structures. In this section, seismic limit state capacities of the aforementioned structures were achieved from IDA curves. Four seismic performances of Immediate Occupancy (IO), Life Safety (LS), Collapse Prevention (CP), and Total Collapse (TC) were defined in accordance with FEMA 356 [56]. To determine these performance levels for steel structures, the allowable IDR of 0.7%, 2.5%, and 5.0% represented for primary members and performance levels of IO, LS, and CP, respectively, were considered. In addition, for RC, the allowable IDR of 1.0%, 2.0%, and 4.0% represented for primary members and performance levels of IO, LS, and CP, respectively, were assumed. Moreover, the seismic performance level of TC was selected in the flat part of IDAs of steel and RC structures. Table 4 presents performance levels of steel and RC structures in alone condition including NF-NP and NF-PL record subsets. According to Table 1, in all seismic performance levels, S_a (T_1) values for RC including NF-NP records were higher than those including NF-PL records, correspondingly. The same result can be seen for the 3-Story

Table 4 Seismic performance of steel and RC structures in alone state including NF-NP and NF-PL records

Record subset	IO*	LS	CP	TC	IO	LS	CP	TC	IO	LS	CP	TC
	3-Story RC				5-Story RC				9-Story RC			
NF-PL	0.33	0.56	0.84	1.11	0.27	0.46	0.73	0.99	0.16	0.29	0.45	0.53
NF-NP	0.39	0.72	1.15	1.54	0.28	0.52	0.85	1.17	0.17	0.30	0.48	0.54
	3-Story steel				5-Story steel				9-Story steel			
NF-PL	0.28	0.81	1.37	1.89	0.15	0.50	0.95	1.27	0.08	0.28	0.46	0.55
NF-NP	0.28	0.80	1.46	2.22	0.13	0.48	0.94	1.30	0.06	0.24	0.38	0.47

*Unit of all values are (g)

Table 5 Performance of steel structures in collision with RC structures including seismic records for SD of 0.0

Steel models	Record	RC structures colliding with SD of 0.0											
		IO*	LS	CP	TC	IO	LS	CP	TC	IO	LS	CP	TC
		3-Story				5-Story				9-Story			
3-Story	NF-PL	0.26	0.78	1.29	1.71	0.23	0.73	1.23	1.64	0.29	0.76	1.25	1.77
	NF-NP	0.25	0.80	1.398	2.07	0.26	0.80	1.40	2.06	0.27	0.79	1.52	2.17
5-Story	NF-PL	0.14	0.50	0.86	1.17	0.17	0.52	0.88	1.16	0.18	0.52	0.81	1.07
	NF-NP	0.13	0.50	0.91	1.25	0.15	0.50	0.94	1.27	0.17	0.50	0.91	1.27
9-Story	NF-PL	0.08	0.28	0.54	0.70	0.06	0.24	0.42	0.53	0.10	0.28	0.48	0.56
	NF-NP	0.06	0.25	0.42	0.49	0.06	0.25	0.45	0.59	0.08	0.27	0.44	0.52

*Unit of all values are (g)

Table 6 Performance of steel structures in collision with RC structures including seismic records for $1.0SD_{min}$

Steel models	Record	RC structures colliding with SD of $1.0SD_{min}$											
		IO*	LS	CP	TC	IO	LS	CP	TC	IO	LS	CP	TC
		3-Story				5-Story				9-Story			
3-Story	NF-PL	0.25	0.81	1.36	1.85	0.25	0.81	1.35	1.81	0.26	0.80	1.29	1.86
	NF-NP	0.25	0.81	1.45	2.17	0.25	0.82	1.44	2.13	0.24	0.79	1.38	2.16
5-Story	NF-PL	0.17	0.52	0.895	1.20	0.16	0.52	0.91	1.22	0.17	0.53	0.88	1.25
	NF-NP	0.14	0.49	0.95	1.30	0.14	0.48	0.99	1.30	0.14	0.51	0.98	1.30
9-Story	NF-PL	0.08	0.29	0.54	0.63	0.08	0.28	0.53	0.69	0.09	0.28	0.52	0.70
	NF-NP	0.07	0.25	0.43	0.50	0.07	0.244	0.43	0.53	0.07	0.25	0.43	0.57

*Unit of all values are (g)

steel, while for the 5-Story and 9-Story steel, S_a (T_1) for performance levels including NF-PL record subset are higher.

Tables 5 and 6 present seismic performance levels of colliding steel and RC structures including considered records for SD of 0.0 and $1.0SD_{min}$, respectively. According to Table 5, in the colliding 3-Story steel with RC structures, the S_a (T_1) values in NF-PL record subsets are lower than those in NF-NP records, correspondingly. Except in performance level of IO for in collision with 3-, and 9-Story RC structures, the S_a (T_1) values in NF-PL record subsets are higher than in NF-NP record subsets. In addition, it can be seen that seismic performance level of TC in the 3-Story steel colliding with the 3-, 5-, and 9-Story RC structures decreased from 1.892 to 1.848, 1.812, and 1.861, respectively, in NF-PL record subset assuming $1.0SD_{min}$. Therefore, the 3-Story steel is more vulnerable to structural damages in NF-PL record subsets. In the 5-Story steel colliding with RC structures, the S_a (T_1) values in the seismic performance levels of IO and LS in NF-PL record subsets are higher than those in NF-NP record subsets, while S_a (T_1) values in seismic performance levels of CP and TC in NF-PL record subsets are lower than those in NF-NP record subsets. It means that due to the seismic performance level, the seismic vulnerability of the 5-Story steel changes from NF-NP record subsets to NF-PL record subsets. Seismic TC performance in 5-Story steel colliding with 3-, 5-, and 9-Story RC structures decreased from 1.269 to 1.202, 1.216, and 1.245, respectively, in NF-PL record subset assuming $1.0SD_{min}$. In the 9-Story steel colliding with 3-, and 9-Story RC structures, the S_a (T_1) values in NF-PL record subsets are higher than those in NF-NP record subsets correspondingly, while in the colliding with 5-Story RC structure, the S_a (T_1) values in NF-NP record subsets are higher than those in NF-PL record subsets correspondingly.

The results showed that TC performance in 9-Story steel in collision with the 3-, 5-, and 9-Story RC structures increased from 0.547 to 0.626, 0.690, and 0.697, respectively, in NF-PL record subset assuming $1.0SD_{min}$. Therefore, in the 9-Story steel, the kind of adjacent structures can change the seismic vulnerability from NF-NP record subsets to NF-PL record subsets.

According to Table 6, similar results were achieved for 3-, and 5-Story steel structures in collision with RC structures given $1.0SD_{min}$. Therefore, increasing the distance between 3-, and 5-Story steel in collision with RC structures had no effects on their vulnerability according to the type of record subsets, while in the general view, the S_a (T_1) values in the $1.0SD_{min}$ were higher than those in 0.0, correspondingly. The comparison of results derived from contact elements under colliding conditions verifies that

the acceleration response is influenced by the separation distance.

These variations in acceleration values have the potential to alter the extent of damage in structural elements. Consequently, as the separation distance increases to $1.0SD_{min}$, the occurrences of pounding decrease accordingly. Therefore, the separation distance of 0.0 is more critical than $1.0SD_{min}$. In 9-Story steel in collision with 3-, and 9-Story RC structures given SD of $1.0SD_{min}$, similar results were obtained, while the S_a (T_1) values in the $1.0SD_{min}$ were higher than those in 0.0, correspondingly. For 9-Story steel colliding with 5-Story RC structure, the S_a (T_1) values in NF-PL record subsets are higher than those in NF-NP record subsets correspondingly. Tables 7 and 8 present seismic performance levels of RC in collision with steel structures including NF-NP and NF-PL records for SD of 0.0 and $1.0SD_{min}$, respectively. According to Table 7, in 3-, and 5-Story RC structures colliding with steel structures, S_a (T_1) values in NF-PL record subsets are lower than those in NF-NP record subsets correspondingly. Thus, 3-, and 5-Story RC structures are more vulnerable to structural damages in NF-PL records. In 9-Story RC colliding with steel structures, S_a (T_1) values in NF-PL records are upper than NF-NP records.

According to Table 8, similar results were obtained for selected RC colliding with steel structure given SD of $1.0SD_{min}$. Therefore, increasing the distance between RC colliding with steel structures had no effects on their vulnerability according to the type of record subsets. In the general view, S_a (T_1) values of selected RC structures colliding with 3-Story steel witnessed an increase in both record subsets by changing the SD to $1.0SD_{min}$. In addition, S_a (T_1) values of 3-Story RC in collision with 5-Story steel decreased in both record subsets by changing the SD from 0.0 to $1.0SD_{min}$, while experienced an increase in colliding with 9-Story steel in both record subsets.

The S_a (T_1) values of 9-Story RC colliding with 9-Story steel decreased in both record subsets by changing the SD from 0.0 to $1.0SD_{min}$. Therefore, the elevation and T_1 can significantly affect the performance levels of structures. This means that during the applied record subsets, the adjacent structure may collapse earlier and affect the response of the remained structure. It is important to highlight that due to some preliminary analysis on the pounding cases having $0.5SD_{min}$, the results are approximately between those 0.0 and $1.0SD_{min}$. Therefore, for brevity, only results of 0.0 and $1.0SD_{min}$ have been presented in the manuscript. Moreover,

Table 7 Seismic performance of RC in collision with steel structures including seismic records for SD of 0.0

RC models	Subset	Steel structures colliding with SD of 0.0											
		IO*	LS	CP	TC	IO	LS	CP	TC	IO	LS	CP	TC
		3-Story				5-Story				9-Story			
3-Story	NF-PL	0.284	0.494	0.793	1.066	0.306	0.524	0.844	1.195	0.309	0.534	0.949	1.274
	NF-NP	0.348	0.644	1.151	1.518	0.379	0.697	1.163	1.548	0.379	0.719	1.157	1.563
5-Story	NF-PL	0.245	0.466	0.753	1.021	0.265	0.469	0.796	1.116	0.289	0.521	0.909	1.409
	NF-NP	0.283	0.536	0.947	1.289	0.286	0.539	0.945	1.314	0.302	0.572	1.040	1.439
9-Story	NF-PL	0.159	0.276	0.478	0.621	0.160	0.280	0.490	0.633	0.163	0.288	0.493	0.612
	NF-NP	0.143	0.268	0.478	0.553	0.145	0.270	0.484	0.563	0.161	0.275	0.481	0.597

*Unit of all values are (g)

Table 8 Seismic performance of RC in collision with steel structures including seismic records for $1.0SD_{min}$

RC models	Subset	Steel structures colliding with SD of $1.0SD_{min}$											
		IO*	LS	CP	TC	IO	LS	CP	TC	IO	LS	CP	TC
		3-Story				5-Story				9-Story			
3-Story	NF-PL	0.285	0.493	0.817	1.106	0.287	0.490	0.796	1.124	0.280	0.503	0.896	1.166
	NF-NP	0.357	0.663	1.142	1.606	0.355	0.658	1.142	1.583	0.377	0.685	1.296	1.667
5-Story	NF-PL	0.268	0.471	0.805	1.148	0.268	0.464	0.768	1.142	0.274	0.491	0.864	1.203
	NF-NP	0.297	0.559	0.956	1.332	0.297	0.561	0.946	1.326	0.303	0.612	1.086	1.441
9-Story	NF-PL	0.162	0.284	0.475	0.643	0.164	0.278	0.458	0.615	0.158	0.260	0.406	0.536
	NF-NP	0.150	0.278	0.464	0.573	0.155	0.284	0.459	0.550	0.147	0.253	0.400	0.524

*Unit of all values are (g)

the outcomes of pounding for $0.5SD_{min}$ can be approximated through linear interpolation of the results as detailed in Tables 5–8. It should be added that these tables are comprehensive source for designers to predict the effects of the collision phenomenon regarding structures' type, record subsets, and seismic code prescribed distance.

3.4 Seismic fragility curve for SD of 0.0

Seismic fragility curves express the seismic vulnerability of structure for different damage states at different ground motion intensities. These curves are a typical tool for the physical understanding of functionally level of structures. The damage states play a pivotal role in illustrating the condition of a compromised structure and assessing the feasibility of retrofitting and repair options. In the Sect. 3.3, four seismic performances (e.g., IO, LS, CP, and TC) were defined that show the structural damage states prescribed in FEMA 356 [56]. Seismic fragility curves were derived for aforementioned performance levels for both adjacent colliding structures given two record subsets. Comparison was made between the structure in alone condition and colliding one to clearly show the pounding effect on the seismic fragility curves. Figure 10 illustrates the procedure done to determine fragility curve. It should be mentioned that fragility curves of colliding structures achieved considering the influence of collapsed structure into the analyses. Therefore, due to assuming the real conditions of buildings, these results can be used for buildings with similar structural characteristics.

According to the analytical procedure, the seismic fragility curves were generated from obtained IDA curves. Figures 11, 12, and 13 present fragilities of 3-Story steel in collision with 3-, 5-, and 9-Story RC structures for different drift thresholds given SD of 0.0, including NF-PL records, respectively. Capacity level probability of 3-Story steel increased in LS, CP, and TC performances, while it reached a reduction in IO performance. Therefore, adjacent RC structures have a negative effect on capacity level probability of 3-Story steel. On the other side of colliding structures, capacity level probability of 3-Story RC increased for all different drift thresholds. Capacity level probability of 5-Story and 9-Story RC structures experienced an improvement in IO and LS performances, while this value decreased in CP and TC performances.

Figures 14, 15, and 16 present the fragilities of 5-Story steel in collision with 3-, 5-, and 9-Story RC structures for different drift thresholds given SD of 0.0, including NF-PL record, respectively. Capacity level probability of 5-Story steel increased in IO, LS, CP, and TC performances. It is obvious that adjacent RC structures have a negative effect on capacity level probability of 5-Story steel.

Whereas, limit state probability of 3-Story RC increased in IO and LS performance levels, and remained unchanged in the CP and TC performance levels. It should be noted that limit state probability of 5-, and 9-Story RC were significantly decreased in CP and TC performance levels that shows the positive effects of being adjacent to 5-Story steel. Although 5-Story steel achieved a higher limit state probability, it helped the adjacent RC to achieve a lower limit state probability (e.g., 5-, and 9-Story RC).

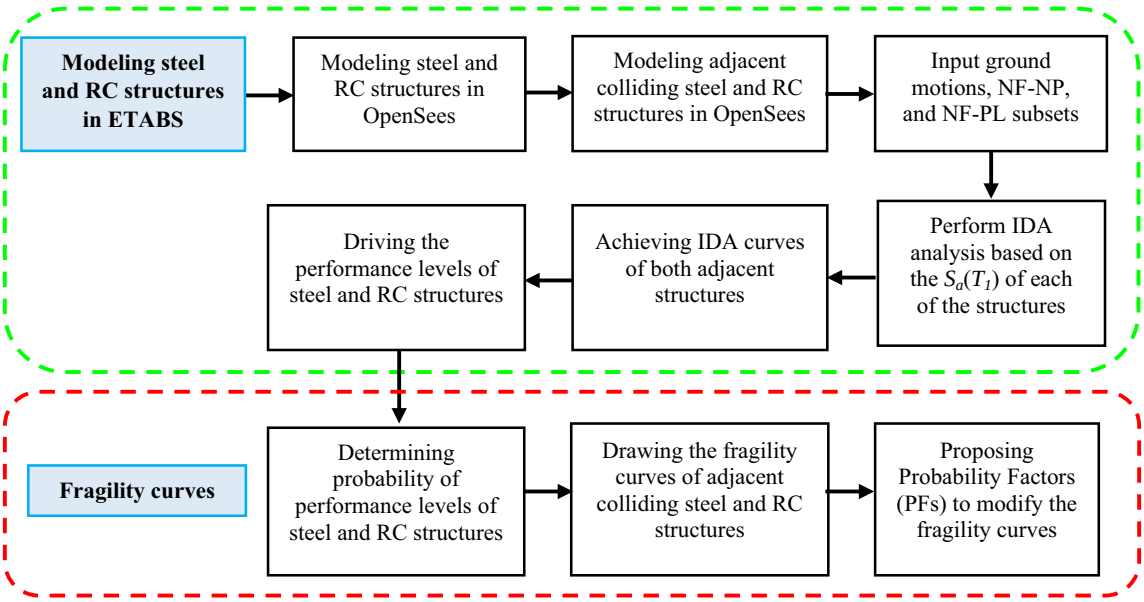

Fig. 10 Analytical procedures of this study

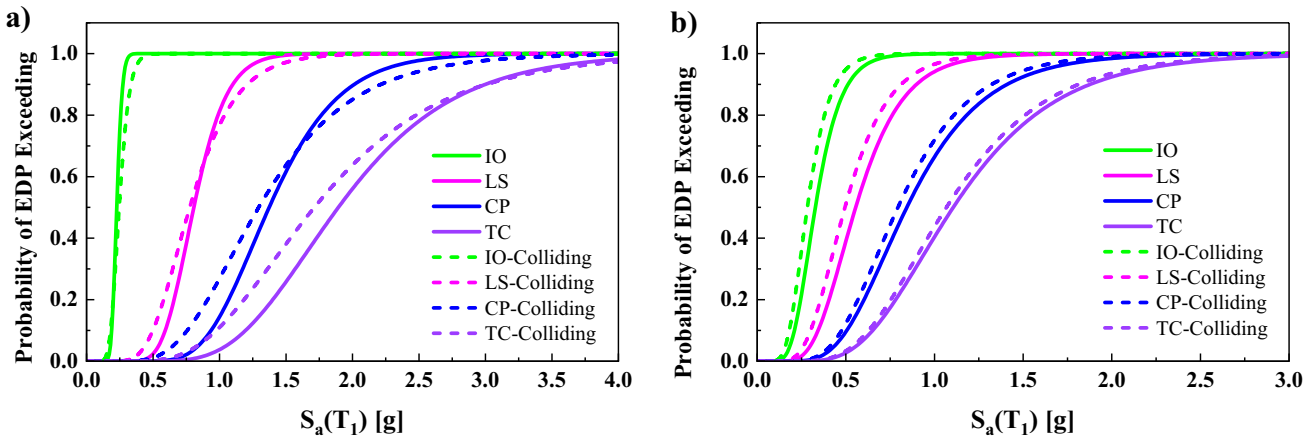

Fig. 11 Seismic fragilities of **a** 3-Story steel, and **b** 3-Story RC for drift thresholds given SD of 0.0, including NF-PL records

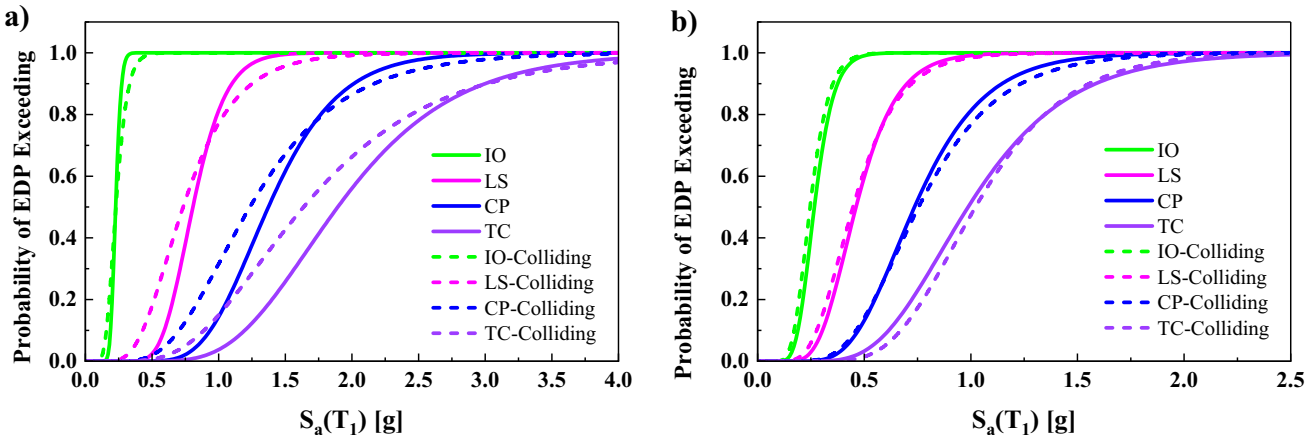

Fig. 12 Seismic fragilities of **a** 3-Story steel, and **b** 5-Story RC for drift thresholds given SD of 0.0, including NF-PL records

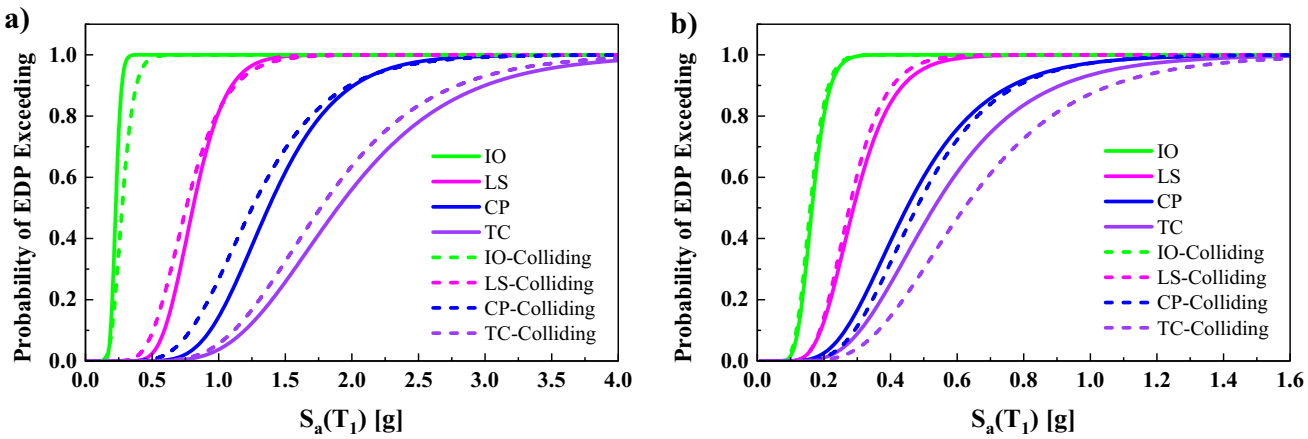

Fig. 13 Seismic fragilities of **a** 3-Story steel, and **b** 9-Story RC for drift thresholds given SD of 0.0, including NF-PL records

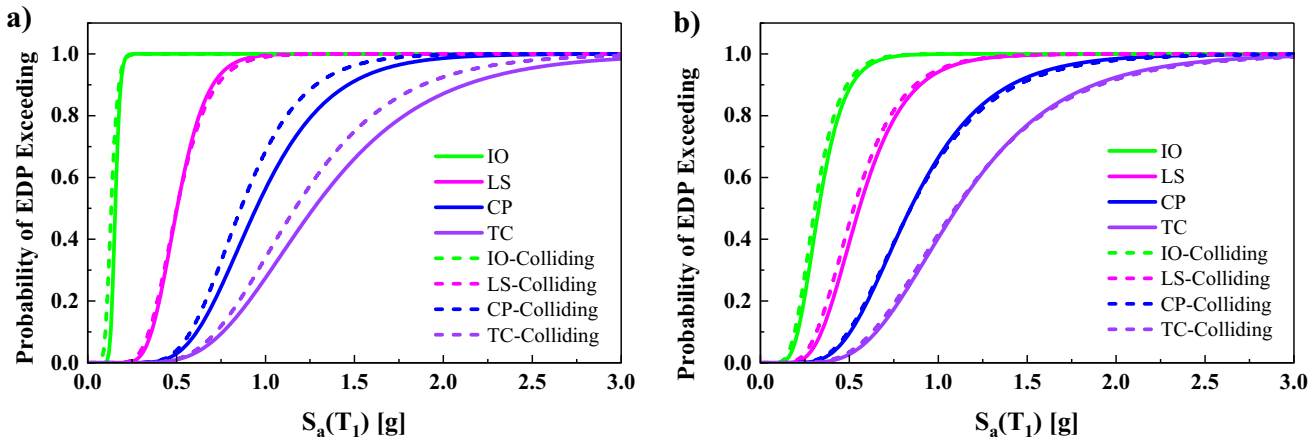

Fig. 14 Seismic fragilities of **a** 5-Story steel, and **b** 3-Story RC for drift thresholds given SD of 0.0, including NF-PL records

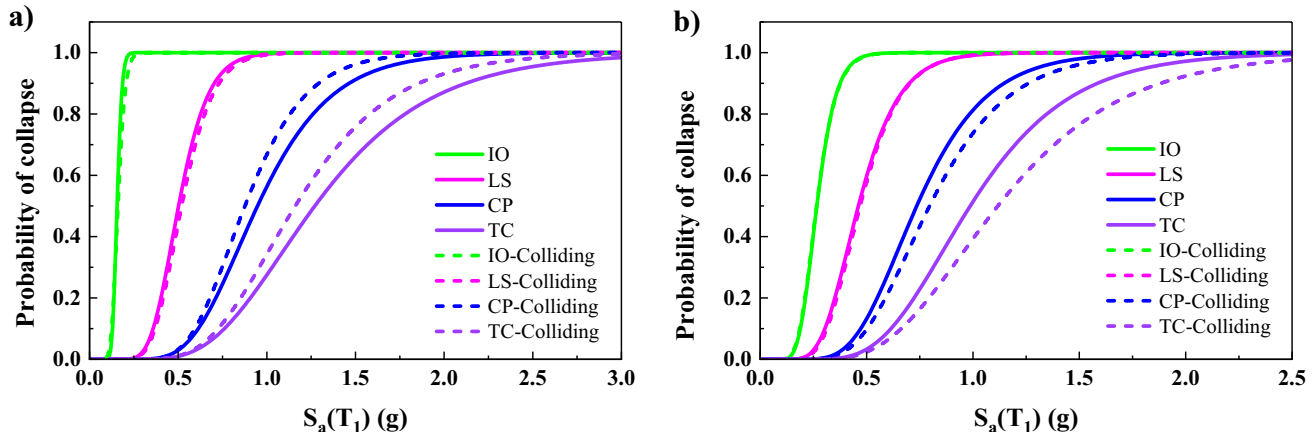

Fig. 15 Seismic fragilities of **a** 5-Story steel, and **b** 5-Story RC for drift thresholds given SD of 0.0, including NF-PL records

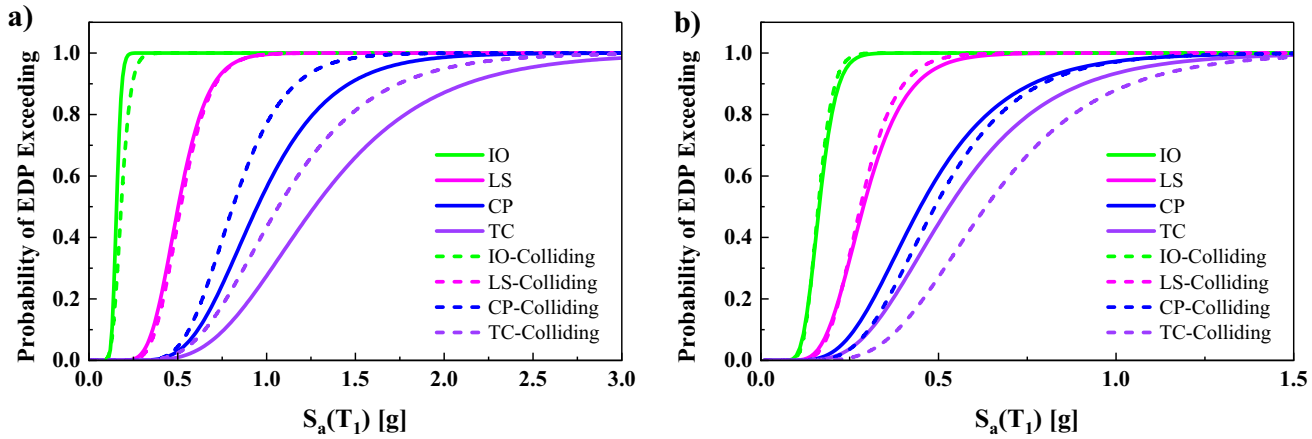

Fig. 16 Seismic fragilities of **a** 5-Story steel, and **b** 9-Story RC for drift thresholds given SD of 0.0, including NF-PL records

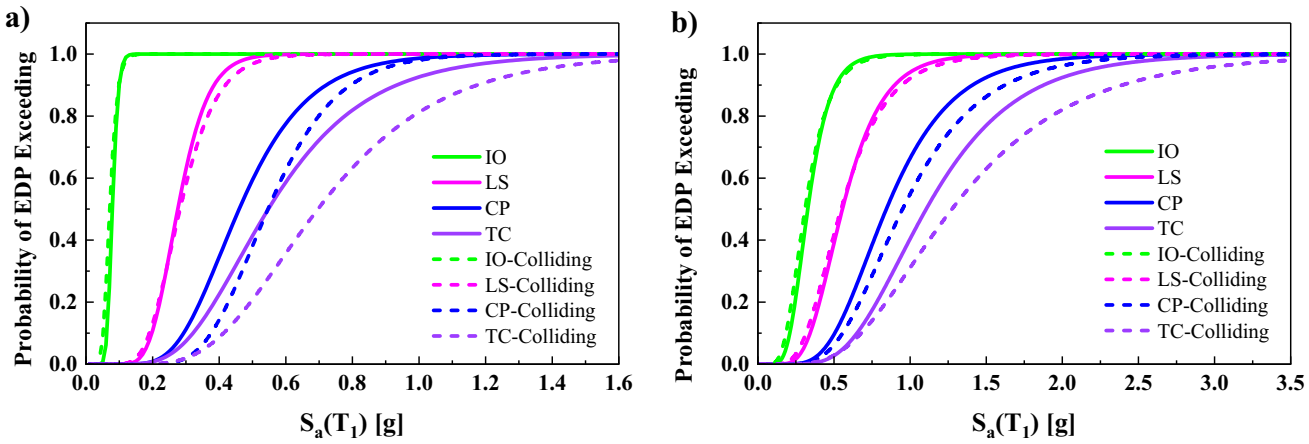

Fig. 17 Seismic fragilities of **a** 9-Story steel, and **b** 3-Story RC for drift thresholds given SD of 0.0, including NF-PL records

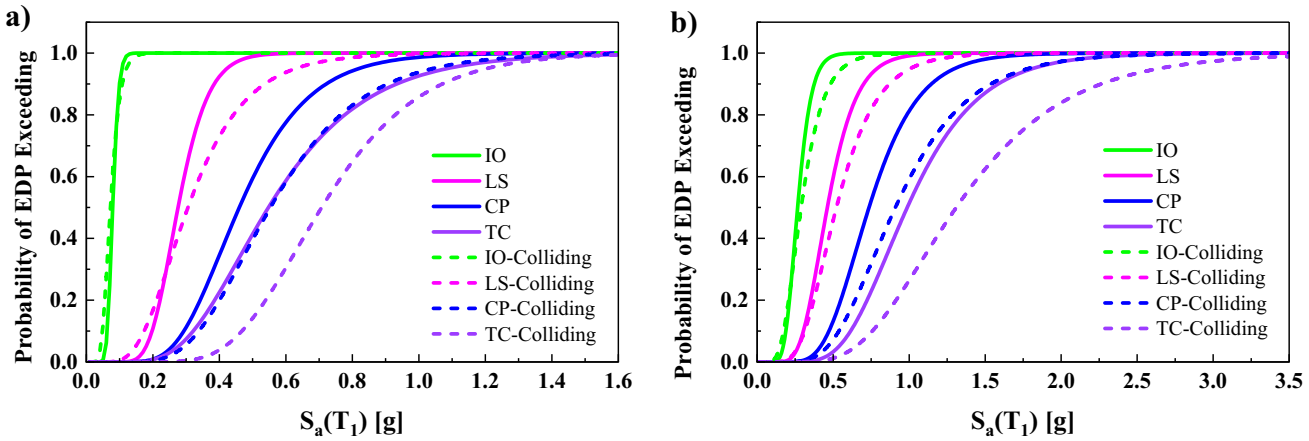

Fig. 18 Seismic fragilities of **a** 9-Story steel, and **b** 5-Story RC for drift thresholds given SD of 0.0, including NF-PL records

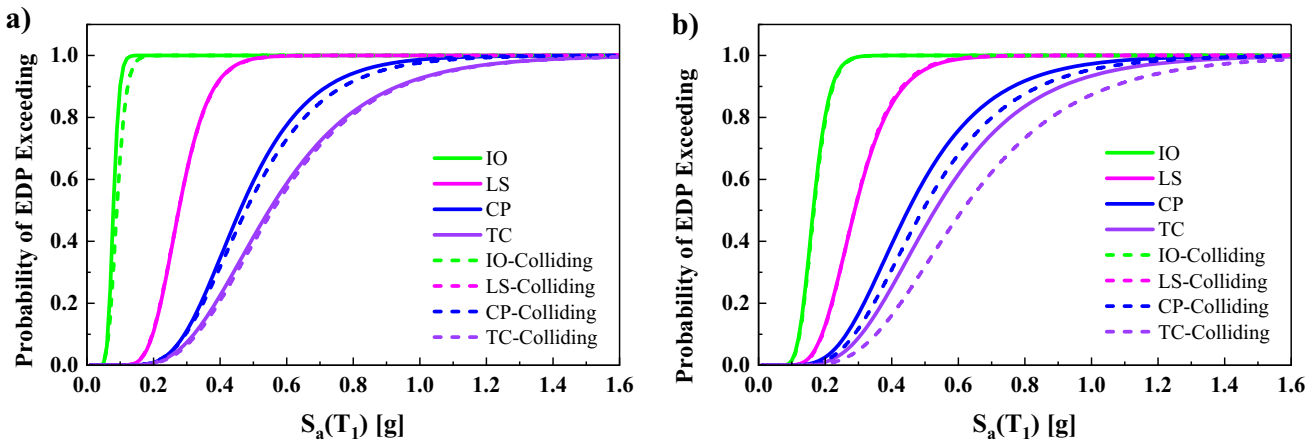

Fig. 19 Seismic fragilities of **a** 9-Story steel, and **b** 9-Story RC for drift thresholds given SD of 0.0, including NF-PL records

Figures 17, 18, and 19 present the fragilities of 9-Story steel colliding with selected RC structures for different drift thresholds given SD of 0.0, including NF-PL subset, respectively. Figure 17 shows that limit state probability of 9-Story

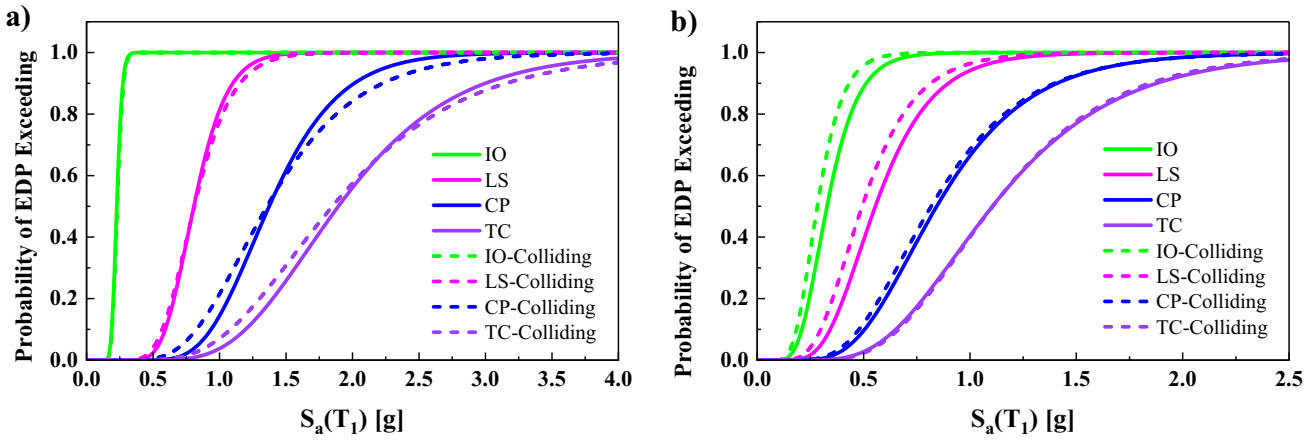

Fig. 20 Seismic fragilities of **a** 3-Story steel, and **b** 3-Story RC for drift thresholds given SD of $1.0SD_{min}$, including NF-PL records

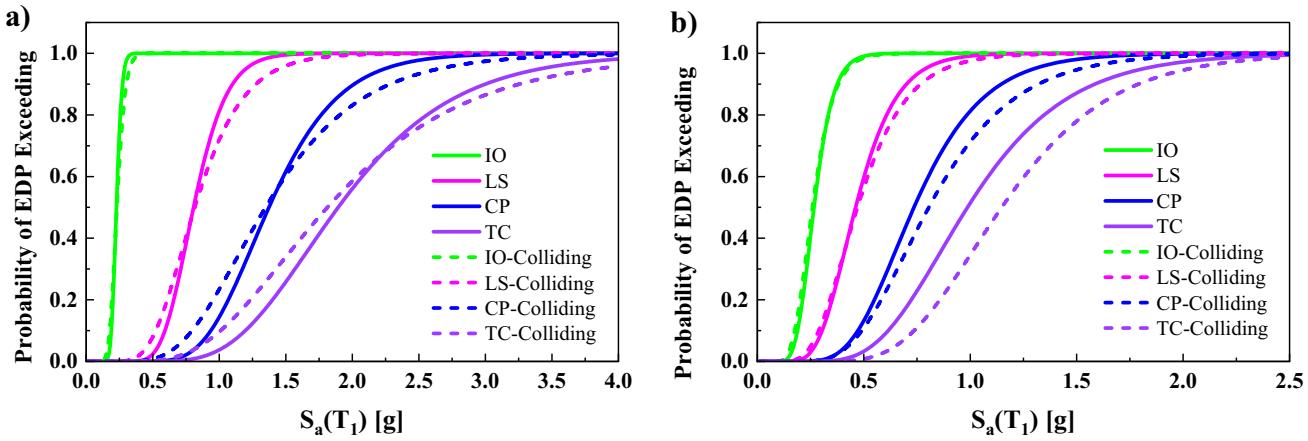

Fig. 21 Seismic fragilities of **a** 3-Story steel, and **b** 5-Story RC for drift thresholds given SD of $1.0SD_{min}$, including NF-PL records

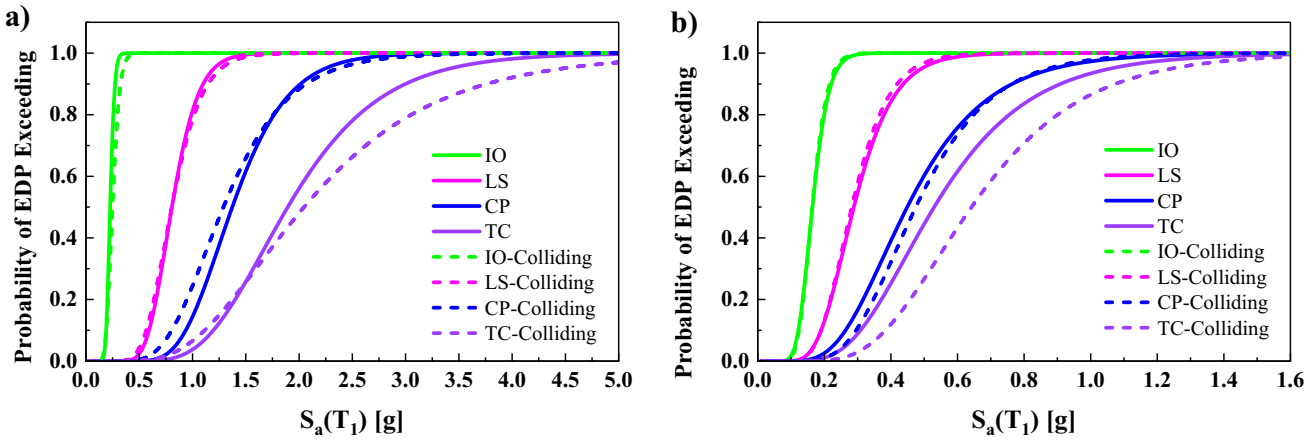

Fig. 22 Seismic fragilities of **a** 3-Story steel, and **b** 9-Story RC for drift thresholds given SD of $1.0SD_{min}$, including NF-PL records

steel significantly reduced LS, CP, and TC performance levels, while the same reduction was observed in the adjacent 3-Story RC. The same results were observed from Fig. 18 for 9-Story steel colliding with 5-Story RC. According to Fig. 19, limit state probability of 9-Story steel reduced in IO, CP, and TC performances, while limit state probability of 9-Story RC significantly reduced in CP and TC performances. Therefore, 9-Story steel prevents adjacent RC from destruction during the seismic events and decreases their seismic limit state probabilities. According to the results, this phenomenon can be considered in the seismic evaluation of the adjacent structures.

3.5 Seismic fragility curve for SD of 1.0SD$_{min}$

Figures 20, 21, and 22 present fragilities of 3-Story steel colliding with selected RC structures for various drift thresholds given SD of 1.0SD$_{min}$, including NF-PL record subset, respectively. Fragilities of 3-Story steel in all performances were steeper than the colliding values and limit state probability of 3-Story steel can be achieved according to S_a (T_1) values. Limit state probability of 3-Story RC increased during the colliding in all performance levels, while limit state probability of 5-, and 9-Story RC structures significantly decreased in CP and TC performances. Although the slope of fragility curves of 3-Story steel reduced during collision, adjacent RC achieve a lower limit state probability (e.g., 5-, and 9-Story RC); thus, colliding effects can be considered in their seismic evaluation in the conservative way.

Figures 23, 24, and 25 present fragilities of 5-Story steel colliding with selected RC for different drift thresholds given SD of 1.0SD$_{min}$, including NF-PL record subset, respectively. According to results, limit state probability of 5-Story steel remained unchanged in IO performance, while decreasing in LS performance level. Limit state probability of 5-Story steel in collision with 3-, and 5-Story RC increased in CP and TC performances, and CP performance increased in colliding with 9-Story RC. On the other side, all

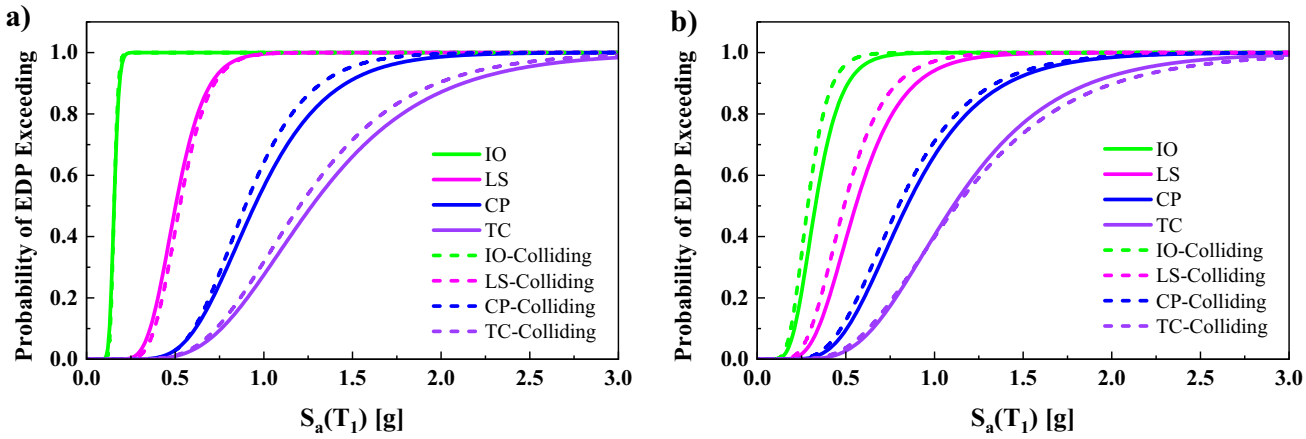

Fig. 23 Seismic fragilities of **a** 5-Story steel, and **b** 3-Story RC for drift thresholds given SD of 1.0SD$_{min}$, including NF-PL records

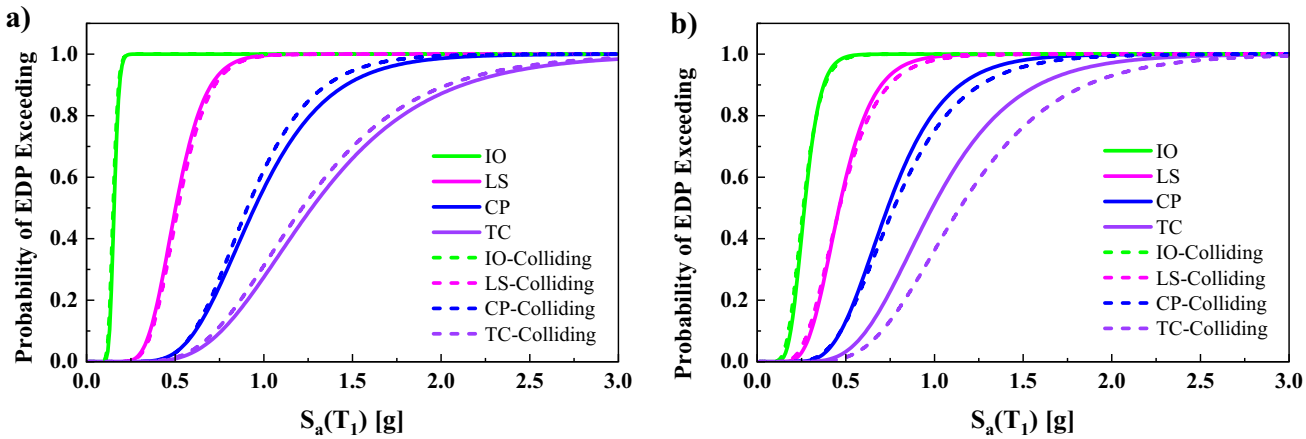

Fig. 24 Seismic fragilities of **a** 5-Story steel, and **b** 5-Story RC for drift thresholds given SD of 1.0SD$_{min}$, including NF-PL records

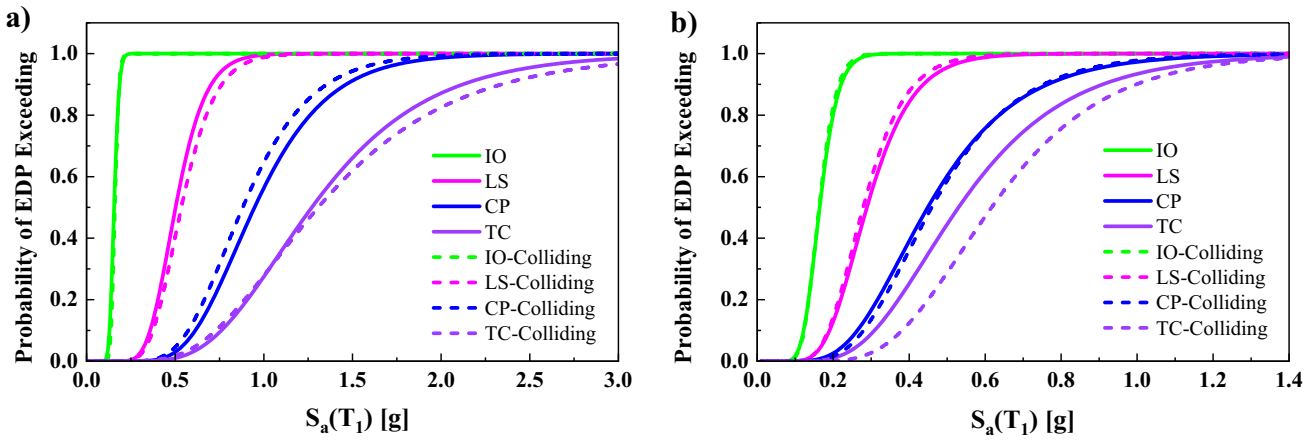

Fig. 25 Seismic fragilities of **a** 5-Story steel, and **b** 9-Story RC for drift thresholds given SD of $1.0SD_{min}$, including NF-PL records

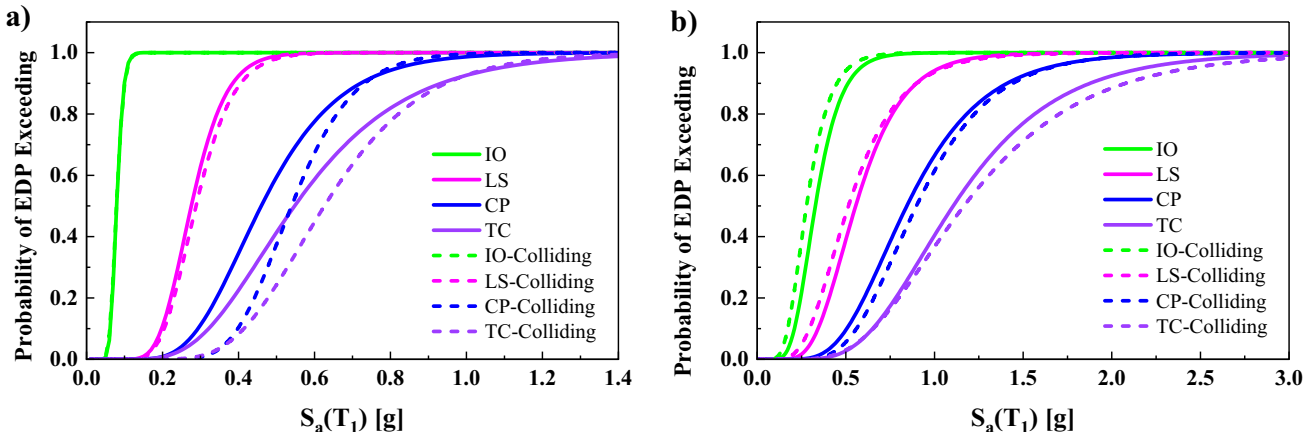

Fig. 26 Seismic fragilities of **a** 9-Story steel, and **b** 3-Story RC for drift thresholds given SD of $1.0SD_{min}$, including NF-PL records

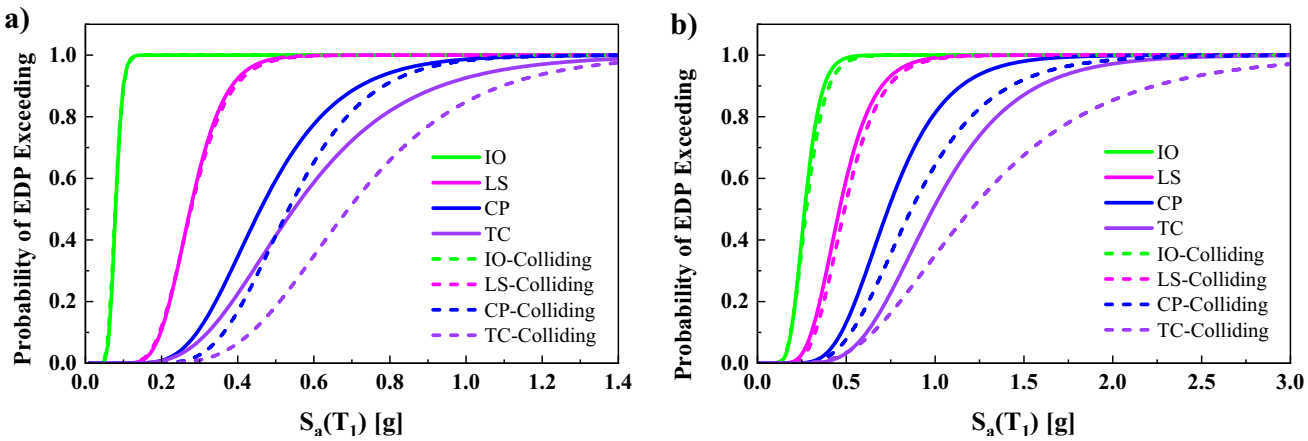

Fig. 27 Seismic fragilities of **a** 9-Story steel, and **b** 5-Story RC for drift thresholds given SD of $1.0SD_{min}$, including NF-PL records

performance levels of 3-Story RC affected by collision and 5-, and 9-Story RC-MRFs experienced a significant decrease in TC performance.

Figures 26, 27, and 28 present the fragilities of 9-Story steel colliding with selected RC structures for different drift thresholds given SD of $1.0SD_{min}$, including NF-PL record subset, respectively. According to Fig. 26, limit state probability of 9-Story steel remained unchanged in IO performance, while significantly decreasing in LS, CP, and TC performances. Although seismic limit state probability of 3-Story RC decreased in IO and LS performances, values showed a reduction in CP and TC performances. Figure 27 shows that the seismic limit state probability of 9-Story steel and 5-Story RC significantly decreased. Therefore, these adjacent structures can help each other to remain more stable and achieve higher performance levels. Figure 28 shows that limit state probability of 9-Story steel and 9-Story RC increased during colliding and they have a negative effect on their performance levels.

Similar results hold true for aforementioned colliding cases, but due to brevity, seismic limit state fragility curves were presented for NF-PL record subset. In addition,

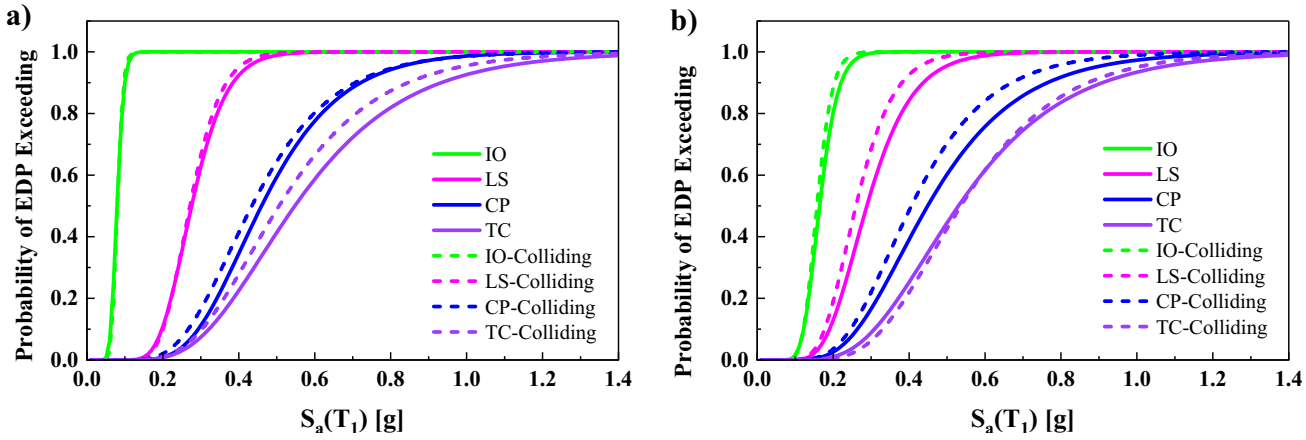

Fig. 28 Seismic fragilities of **a** 9-Story steel, and **b** 9-Story RC for drift thresholds given SD of $1.0SD_{min}$, including NF-PL records

Table 9 Seismic limit state probability of for RC and steel structures in alone state including NF-NP and NF-PL records

Record subset	IO*	LS	CP	TC	IO	LS	CP	TC	IO	LS	CP	TC
	3-Story RC				5-Story RC				9-Story RC			
NF-PL	0.507	0.490	0.496	0.504	0.465	0.496	0.491	0.503	0.454	0.506	0.502	0.500
NF-NP	0.488	0.498	0.498	0.501	0.483	0.475	0.496	0.490	0.436	0.497	0.488	0.492
NF-PL	0.536	0.507	0.497	0.498	0.404	0.493	0.491	0.492	0.523	0.468	0.500	0.486
NF-NP	0.540	0.497	0.505	0.498	0.449	0.499	0.495	0.497	0.445	0.491	0.495	0.485

*Unit of all values are (g)

Table 10 Seismic limit state probability of for steel in collision with RC including seismic records for SD of 0.0

Steel models	Subset	RC structures colliding with SD of 0.0											
		IO*	LS	CP	TC	IO	LS	CP	TC	IO	LS	CP	TC
		3-Story				5-Story				9-Story			
3-Story	NF-PL	0.324	0.535	0.554	0.588	0.444	0.583	0.594	0.618	0.193	0.574	0.600	0.575
	NF-NP	0.396	0.492	0.543	0.577	0.367	0.503	0.543	0.566	0.300	0.514	0.458	0.520
5-Story	NF-PL	0.715	0.498	0.611	0.581	0.367	0.443	0.591	0.588	0.205	0.448	0.699	0.668
	NF-NP	0.673	0.448	0.527	0.543	0.399	0.441	0.503	0.527	0.266	0.443	0.538	0.530
9-Story	NF-PL	0.471	0.442	0.278	0.266	0.629	0.389	0.315	0.201	0.321	0.470	0.460	0.468
	NF-NP	0.605	0.430	0.396	0.402	0.586	0.461	0.322	0.274	0.301	0.481	0.472	0.493

*Unit of all values are (g)

Table 11 Seismic limit state probability of for steel in collision with RC including seismic records for $1.0SD_{min}$

Steel models	Subset	RC structures colliding with SD of $1.0SD_{min}$											
		IO*	LS	CP	TC	IO	LS	CP	TC	IO	LS	CP	TC
		3-Story				5-Story				9-Story			
3-Story	NF-PL	0.361	0.480	0.510	0.521	0.409	0.477	0.516	0.536	0.275	0.491	0.565	0.433
	NF-NP	0.405	0.467	0.495	0.525	0.408	0.464	0.508	0.540	0.500	0.524	0.567	0.527
5-Story	NF-PL	0.376	0.419	0.563	0.547	0.502	0.452	0.546	0.534	0.285	0.404	0.576	0.468
	NF-NP	0.447	0.462	0.486	0.499	0.498	0.503	0.447	0.500	0.445	0.439	0.451	0.406
9-Story	NF-PL	0.534	0.404	0.251	0.323	0.548	0.461	0.310	0.248	0.497	0.491	0.537	0.564
	NF-NP	0.458	0.437	0.371	0.416	0.445	0.494	0.401	0.356	0.028	0.302	0.362	0.508

*Unit of all values are (g)

Table 12 Seismic limit state probability of for RC in collision with steel including seismic records for SD of 0.0

RC models	Subset	Steel structures colliding with SD of 0.0											
		IO*	LS	CP	TC	IO	LS	CP	TC	IO	LS	CP	TC
		3-Story				5-Story				9-Story			
3-Story	NF-PL	0.671	0.608	0.557	0.529	0.577	0.530	0.465	0.449	0.513	0.519	0.414	0.334
	NF-NP	0.616	0.605	0.499	0.507	0.478	0.416	0.348	0.322	0.638	0.626	0.550	0.475
5-Story	NF-PL	0.584	0.548	0.495	0.503	0.473	0.474	0.405	0.373	0.482	0.548	0.387	0.305
	NF-NP	0.533	0.529	0.488	0.494	0.458	0.404	0.352	0.309	0.633	0.623	0.513	0.458
9-Story	NF-PL	0.562	0.505	0.384	0.382	0.395	0.377	0.296	0.248	0.436	0.508	0.393	0.352
	NF-NP	0.531	0.489	0.401	0.479	0.357	0.345	0.238	0.224	0.453	0.551	0.455	0.385

*Unit of all values are (g)

Table 13 Seismic limit state probability of for RC in collision with steel including seismic records for $1.0SD_{min}$

RC models	Subset	Steel structures colliding with SD of $1.0SD_{min}$											
		IO*	LS	CP	TC	IO	LS	CP	TC	IO	LS	CP	TC
		3-Story				5-Story				9-Story			
3-Story	NF-PL	0.681	0.609	0.526	0.494	0.507	0.477	0.399	0.324	0.456	0.535	0.442	0.316
	NF-NP	0.589	0.575	0.505	0.450	0.414	0.369	0.337	0.272	0.590	0.604	0.515	0.439
5-Story	NF-PL	0.678	0.621	0.551	0.480	0.501	0.492	0.444	0.342	0.466	0.551	0.479	0.343
	NF-NP	0.591	0.578	0.505	0.466	0.410	0.370	0.361	0.293	0.538	0.560	0.523	0.480
9-Story	NF-PL	0.675	0.561	0.428	0.448	0.424	0.422	0.329	0.334	0.533	0.598	0.581	0.487
	NF-NP	0.535	0.544	0.389	0.419	0.367	0.296	0.209	0.200	0.546	0.684	0.646	0.507

*Unit of all values are (g)

Tables 9, 10, 11, 12, and 13 present the seismic limit state probability of RC and steel structures with and without colliding conditions for SDs of 0.0 and $1.0SD_{min}$, including NF-NP and NF-PL record subsets. Then, it is possible to find out limit state probability in aforementioned performances for all types of models considered in this study. Then, it will be possible to compare limit state probability of a structure before and after colliding. For example, according to Table 9, 5-Story RC achieved probability of 0.503 in TC performance. Then, to find out the effects of colliding with SD of 0.0, the seismic probabilities presented in Table 12 can be used for any adjacent steel with all performance levels.

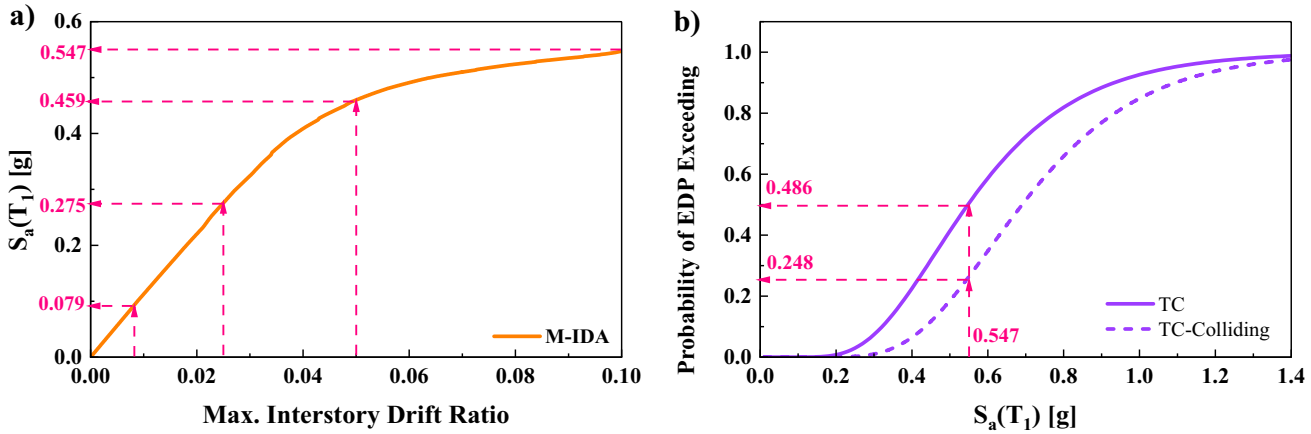

Fig. 29 Procedure to calculate the seismic probability factors using **a** M-IDA curve of 9-Story steel, and **b** fragility curves of 9-Story steel including and excluding colliding with 5-Story RC in TC performance, given SD of $1.0SD_{min}$, including NF-PL records

3.6 Modification factors

Results confirm that colliding between structures even in the prescribed SD (i.e., seismic code) affects both performance levels of structures; however, the designer does not consider these effects in design process that can cause severe damages to structures. Therefore, it is hard for the structural designer to find out the external forces that can exert by colliding. To overcome this problem, researchers proposed modification factors that could be considered to estimate limit state capacities of adjacent structures (e.g., see [27, 28]). In this study, seismic Probability Factors (PFs) proposed to predict probability of colliding steel and RC structures in four performances. Figure 29 presents procedure used in this study for calculating the PF for the 9-Story steel including and excluding colliding with 5-Story RC in TC performance, given SD of $1.0SD_{min}$ including NF-PL record subset. In the first step, IO, LS, CP, and TC performances with the allowable IDR described in Sect. 3.3 were shown in M-IDA curve of the 9-Story steel (Fig. 29a). The S_a (T_1) values corresponding to IO, LS, CP, and TC performances were calculated by 0.079, 0.275, 0.459, and 0.547, respectively (these values are determined in Table 4). Then, these values can be assumed to determine seismic limit state probability. For instance, a value corresponding to the TC performance (i.e., 0.547) connected to limit state probability of 9-Story steel including and excluding collision with 5-Story RC (Fig. 29b), and the values of 0.248 and 0.486 were achieved, respectively. Comparing probability values of colliding and alone conditions show that colliding can decrease failure probability by 51%. Therefore, a seismic PF of 0.51 is obtained and can be easily used by designers to calculate the colliding effects on the seismic limit state probability.

Seismic PFs proposed in this study significantly reduced the time and analysis efforts for designers, and help them to consider the colliding effect in their analyses. Tables 14, 15, 16, and 17 present seismic PFs for colliding steel and RC structures including NF-NP and NF-PL record subsets, given SD of 0.0 and SD_{min}. For example, to calculate colliding effects on limit state probability of 5-Story steel including NF-NP records given SD of 0.0, the values presented in Table 14 can be used. According to Table 14, adjacent

Table 14 Seismic probability factors of steel structures in collision with RC including seismic records for SD of 0.0

Steel models	Subset	RC structures colliding with SD of 0.0											
		IO	LS	CP	TC	IO	LS	CP	TC	IO	LS	CP	TC
		3-Story				5-Story				9-Story			
3-Story	NF-PL	0.604	1.055	1.115	1.181	0.828	1.150	1.195	1.241	0.360	1.132	1.207	1.155
	NF-NP	0.733	0.990	1.075	1.159	0.680	1.012	1.075	1.137	0.556	1.034	0.907	1.044
5-Story	NF-PL	1.770	1.010	1.244	1.181	0.908	0.899	1.204	1.195	0.392	0.957	1.398	1.372
	NF-NP	1.499	0.898	1.065	1.093	0.889	0.884	1.016	1.060	0.598	0.902	1.087	1.093
9-Story	NF-PL	0.901	0.944	0.556	0.546	1.203	0.831	0.630	0.413	0.614	1.004	0.920	0.961
	NF-NP	1.360	0.876	0.800	0.829	1.317	0.939	0.651	0.565	0.676	0.980	0.954	1.016

Table 15 Seismic probability factors of steel structures in collision with RC including seismic records for $1.0SD_{min}$

Steel models	Subset	Colliding with SD of $1.0SD_{min}$											
		IO	LS	CP	TC	IO	LS	CP	TC	IO	LS	CP	TC
		3-Story				5-Story				9-Story			
3-Story	NF-PL	0.674	0.947	1.026	1.046	0.763	0.941	1.038	1.076	0.513	0.968	1.137	0.869
	NF-NP	0.750	0.940	0.980	1.054	0.756	0.934	1.006	1.084	0.926	1.054	1.123	1.058
5-Story	NF-PL	0.931	0.850	1.147	1.112	1.243	0.917	1.112	1.085	0.545	0.863	1.152	0.961
	NF-NP	0.996	0.926	0.982	1.004	1.109	1.008	0.903	1.006	1.000	0.894	0.911	0.837
9-Story	NF-PL	1.021	0.863	0.502	0.663	1.048	0.985	0.620	0.510	0.950	1.049	1.074	1.158
	NF-NP	1.029	0.890	0.749	0.858	1.000	1.006	0.810	0.734	0.063	0.615	0.731	1.047

Table 16 Seismic probability factors of RC in collision with steel structures including seismic records for SD of 0.0

RC models	Subset	Steel structures colliding with SD of 0.0											
		IO	LS	CP	TC	IO	LS	CP	TC	IO	LS	CP	TC
		3-Story				5-Story				9-Story			
3-Story	NF-PL	1.323	1.241	1.123	1.050	1.138	1.082	0.938	0.891	1.012	1.059	0.835	0.663
	NF-NP	1.262	1.215	1.002	1.012	0.980	0.835	0.699	0.643	1.307	1.257	1.104	0.948
5-Story	NF-PL	1.256	1.105	1.008	1.000	1.017	0.956	0.825	0.742	1.062	1.083	0.771	0.610
	NF-NP	1.104	1.114	0.984	1.008	0.948	0.851	0.710	0.631	1.452	1.254	1.051	0.931
9-Story	NF-PL	1.238	0.998	0.765	0.764	0.870	0.745	0.590	0.496	0.960	1.004	0.783	0.704
	NF-NP	1.218	0.984	0.822	0.974	0.819	0.694	0.488	0.455	1.039	1.109	0.932	0.783

Table 17 Seismic probability factors of RC in collision with steel structures including seismic records for $1.0SD_{min}$

RC models	Subset	Steel structures colliding with SD of $1.0SD_{min}$											
		IO	LS	CP	TC	IO	LS	CP	TC	IO	LS	CP	TC
		3-Story				5-Story				9-Story			
3-Story	NF-PL	1.343	1.243	1.060	0.980	1.000	0.973	0.804	0.643	0.899	1.092	0.891	0.627
	NF-NP	1.207	1.155	1.014	0.898	0.848	0.741	0.677	0.543	1.209	1.213	1.034	0.876
5-Story	NF-PL	1.458	1.252	1.122	0.954	1.077	0.992	0.904	0.680	1.026	1.089	0.954	0.686
	NF-NP	1.224	1.217	1.018	0.951	0.849	0.779	0.728	0.598	1.234	1.127	1.072	0.976
9-Story	NF-PL	1.487	1.109	0.853	0.896	0.934	0.834	0.655	0.668	1.174	1.182	1.157	0.974
	NF-NP	1.227	1.095	0.797	0.852	0.842	0.596	0.428	0.407	1.252	1.376	1.324	1.030

3-Story RC can improve limit state probability of 5-Story steel by a factor of 1.499 in IO performance. Therefore, designers can use these tables to find out about the effects of adjacent structures and take them into account.

4 Conclusions

This study aimed to evaluate the limit state probability of steel structures in collision with RC structures including NF-PL and NF-NP records introduced by FEMA-P695 [53] given SDs of 0.0, $0.5SD_{min}$, and $1.0SD_{min}$. According to developed analytical model, it is possible to perform IDAs for adjacent colliding structures with different fundamental periods (e.g., $T_{1,1}$ and $T_{1,2}$) assuming the effects of collapsed structure as it happens in real conditions. M-IDA curves and fragilities of selected structures have been determined and PFs have been proposed to estimate limit state probability of considered colliding structures. The results are summarized as follows:

- The findings validate that the S_a (T_1) values for RC structures, across various drift thresholds, including the NF-PL record subset, are lower compared to the NF-NP record subset. Consequently, it is evident that the NF-PL record subset has the potential to heighten the vulnerability of adjacent structures. Similar outcomes were observed for 3-story steel structure, while the S_a (T_1) values of 5-story and 9-story steel structures exhibited distinct trends across different drift thresholds.
- It is evident that structural collisions can exert external forces on the contact level of adjacent structures. These external forces may lead to sudden changes in the moment and rotation curves compared to the isolated condition of the structure. Examination of these external forces for 9-story steel structures colliding with 3-story RC structures, assuming a SD of 0.0, revealed that the maximum moment values of column and beam hinges increased by 37.96% and 13.22%, respectively. Additionally, the maximum rotation values of column and beam hinges increased by 31.25% and 29.62%, respectively.
- The analysis results indicate that structural pounding can affect performance levels. For instance, in 3-story and 5-story steel structures in collision with 5-story RC structures, the TC performance decreased by 4.22% and 4.17%, respectively, while the TC performance improved by 26.14% in 9-story steel structures in the NF-PL record subset under the assumption of 1.0SDmin. Thus, accounting for the effects of collisions on performance levels is deemed necessary.
- To apply the findings of this study, the authors propose seismic PFs to estimate the probability of capacity levels in various performance states such as IO, LS, CP, and TC, assuming 0.0 and 1.0SD_{min}, including both NF-PL and NF-NP record subsets. These proposed seismic PFs can significantly streamline the analysis process and reduce the modeling efforts required by designers to account for collision phenomena. Furthermore, the authors suggest that these PFs could be widely adopted for retrofitting existing buildings by considering the additional capacity that collisions might provide. In addition, for 0.5SD_{min}, the PFs can be approximated through linear interpolation.

Although this study tried to include a wide range of results, the findings are applicable for those low- to mid-rise adjacent structures including near-field records that present floor-to-floor collision. For future research, the authors suggested to include far-field records as well as more pounding cases having floor-to-column collision. In addition, it is suggest including different structural plan to see the influence of various floor weight.

Funding The authors declare that no financial support received for the research.

Declarations

Conflict of interest The authors declare that there is no conflict of interest with relation to the paper '**Seismic probabilistic assessment of steel and reinforced concrete structures including earthquake-induced pounding**' submitted for publication in ***Archives of Civil and Mechanical Engineering***.

Ethics approval Research Ethics Committee of Gdansk University of Technology approved this study on October 21, 2023.

Statement of originality This is to certify that the research paper submitted by me is an outcome of my independent and original work. I have duly acknowledged all the sources from which the ideas and extracts have been taken. The project is free from any plagiarism and has not been submitted elsewhere for publication.

Open Access This article is licensed under a Creative Commons Attribution 4.0 International License, which permits use, sharing, adaptation, distribution and reproduction in any medium or format, as long as you give appropriate credit to the original author(s) and the source, provide a link to the Creative Commons licence, and indicate if changes were made. The images or other third party material in this article are included in the article's Creative Commons licence, unless indicated otherwise in a credit line to the material. If material is not included in the article's Creative Commons licence and your intended use is not permitted by statutory regulation or exceeds the permitted use, you will need to obtain permission directly from the copyright holder. To view a copy of this licence, visit http://creativecommons.org/licenses/by/4.0/.

References

1. Favvata MJ. Minimum required separation gap for adjacent RC frames with the potential inter-story seismic pounding. Eng Struct. 2017;152:643–59.
2. Miari M, Jankowski R. Seismic gap between buildings founded on different soil types experiencing pounding during earthquakes. Earthq Spectra. 2022;38(3):2183–206.
3. Kazemi F, Asgarkhani N, Manguri A, Lasowicz N, Jankowski R. Introducing a computational method to retrofit damaged buildings under seismic mainshock-aftershock sequence. In international conference on computational science 2023, (pp. 180–187).
4. Elwardany H, Seleemah A, Jankowski R, El-Khoriby S. Influence of soil-structure interaction on seismic pounding between steel frame buildings considering the effect of infill panels. Bull Earthq Eng. 2019;17(11):6165–202.
5. Mohebi B, Yazdanpanah O, Kazemi F, Formisano A. Seismic damage diagnosis in adjacent steel and RC-MRFs considering pounding effects through improved wavelet-based damage-sensitive feature. J Build Eng. 2021;33:101847.
6. Sołtysik B, Falborski T, Jankowski R. Preventing of earthquake-induced pounding between steel structures by using polymer elements – experimental study. Proced Eng. 2017;199:278–83.
7. Kazemi F, Asgarkhani N, Manguri A, Jankowski R. Investigating an optimal computational strategy to retrofit buildings with implementing viscous dampers. In international conference on computational science 2022, (pp. 184–191).
8. Kandemir-Mazanoglu EC, Mazanoglu K. An optimization study for viscous dampers between adjacent buildings. Mech Syst Signal Process. 2017;89:88–96.

9. Karayannis CG, Favvata MJ. Earthquake-induced interaction between adjacent reinforced concrete structures with non-equal heights. Earthquake Eng Struct Dynam. 2005;34(1):1–20.
10. Bantilas KE, Naoum MC, Kavvadias IE, Karayannis CG, Elenas A. Structural pounding effect on the seismic performance of a multistorey reinforced concrete frame structure. Infrastructures. 2023;8(8):122.
11. Mohamed H, Romão X. Analysis of the performance of strut models to simulate the seismic behavior of masonry infills in partially infilled RC frames. Eng Struct. 2020;222:111124.
12. Karayannis CG, Naoum MC. Torsional behavior of multistory RC frame structures due to asymmetric seismic interaction. Eng Struct. 2018;163:93–111.
13. Jankowski R. Experimental study on earthquake-induced pounding between structural elements made of different building materials. Earthquake Eng Struct Dynam. 2010;39(3):343–54.
14. Favvata MJ, Naoum MC, Karayannis CG. Earthquake induced interaction between RC frame and steel frame structures. WIT Trans Built Environ. 2013;134:839–51.
15. Kazemi F, Mohebi B, Yakhchalian M. Predicting the seismic collapse capacity of adjacent structures prone to pounding. Can J Civ Eng. 2020;47(6):663–77.
16. Zain M, Usman M, Farooq SH. A framework with reduced computational burden for seismic fragility assessment of reinforced concrete buildings in high-intensity seismic zones. Structures. 2021;33:3055–65.
17. Mohamed H, Romão X. Seismic fragility functions for non-seismically designed RC structures considering pounding effects. Buildings. 2021;11(12):665.
18. Tubaldi E, Freddi F, Barbato M. Probabilistic seismic demand model for pounding risk assessment. Earthquake Eng Struct Dynam. 2016;45(11):1743–58.
19. Barbato M, Tubaldi E. A probabilistic performance-based approach for mitigating the seismic pounding risk between adjacent buildings. Earthquake Eng Struct Dynam. 2013;42(8):1203–19.
20. Ruggieri S, Tosto C, Rosati G, Uva G, Ferro GA. Seismic vulnerability analysis of masonry churches in piemonte after 2003 valle scrivia earthquake: post-event screening and situation 17 years later. Int J Archit Herit. 2020;16:1–29.
21. Ruggieri S, Perrone D, Leone M, Uva G, Aiello MA. A prioritization RVS methodology for the seismic risk assessment of RC school buildings. Int J Disaster Risk Reduct. 2020;51:101807.
22. Asgarkhani N, Kazemi F, Jankowski R. Optimal retrofit strategy using viscous dampers between adjacent RC and SMRFs prone to earthquake-induced pounding. Arch Civ Mech Eng. 2023;23(1):7.
23. Ruggieri S, Porco F, Uva G. A practical approach for estimating the floor deformability in existing RC buildings: evaluation of the effects in the structural response and seismic fragility. Bull Earthq Eng. 2020;18(5):2083–113.
24. Sabouniaghdam M, Mohammadi Dehcheshmeh E, Safari P, Broujerdian V. Probabilistic collapse assessment of steel frame structures considering the effects of soil-structure interaction and height. Scientia Iranica. 2022;29:2979.
25. Brunelli A, de Silva F, Cattari S. Site effects and soil-foundation-structure interaction: derivation of fragility curves and comparison with codes-conforming approaches for a masonry school. Soil Dyn Earthq Eng. 2022;154:107125.
26. Kazemi F, Mohebi B, Yakhchalian M. Evaluation the P-delta effect on collapse capacity of adjacent structures subjected to far-field ground motions. Civ Eng J. 2018;4(5):1066. https://doi.org/10.28991/cej-0309156.
27. Kazemi F, Miari M, Jankowski R. Investigating the effects of structural pounding on the seismic performance of adjacent RC and steel MRFs. Bull Earthq Eng. 2021;19(1):317–43.
28. Kazemi F, Mohebi B, Jankowski R. Predicting the seismic collapse capacity of adjacent SMRFs retrofitted with fluid viscous dampers in pounding condition. Mech Syst Signal Process. 2021;161:107939.
29. Miano A, Mele A, Prota A. Fragility curves for different classes of existing RC buildings under ground differential settlements. Eng Struct. 2022;257:114077.
30. Wang JH, Sun YP. Seismic fragility and post-earthquake reparability of concrete frame with low-bond high-strength reinforced concrete column. Structures. 2022;37:185–202.
31. Yazdanpanah O, Mohebi B, Kazemi F, Mansouri I, Jankowski R. Development of fragility curves in adjacent steel moment-resisting frames considering pounding effects through improved wavelet-based refined damage-sensitive feature. Mech Syst Signal Process. 2022;173:109038.
32. Flenga MG, Favvata MJ. Probabilistic seismic assessment of the pounding risk based on the local demands of a multistory RC frame structure. Eng Struct. 2021;245:112789.
33. Flenga MG, Favvata MJ. A risk-targeted decision model for the verification of the seismic performance of RC structures against structural pounding. Soil Dyn Earthq Eng. 2023;175:108229.
34. Sinha R, Rao BN. Seismic fragility of non-ductile RC frames for pounding risk assessment. Structures. 2023;56:104865.
35. Kazemi F, Asgarkhani N, Jankowski R. Machine learning-based seismic fragility and seismic vulnerability assessment of reinforced concrete structures. Soil Dyn Earthq Eng. 2023;166:107761.
36. Kazemi F, Asgarkhani N, Jankowski R. Machine learning-based seismic response and performance assessment of reinforced concrete buildings. Arch Civ Mech Eng. 2023;23(2):94.
37. MATLAB/Simulink as a technical computing language. Engineering computations and modeling in MATLAB, 2018.
38. McKenna, F., Fenves, G. L., Filippou, F. C., Scott, M. H. Open system for earthquake engineering simulation (OpenSees). Berkeley: pacific earthquake engineering research center, University of California, Web page, 2016. http://OpenSees.berkeley.edu.
39. ASCE/SEI 7-16. Minimum design loads and associated criteria for buildings and other structures. Reston, VA: American society of civil engineers, 2017.
40. AISC Committee. Specification for structural steel buildings (ANSI/AISC 360-16). American institute of steel construction, Chicago-Illinois, 2016.
41. AISC, A. AISC 341-16, seismic provisions for structural steel buildings. Chicago, IL: American institute of steel construction, 2016.
42. ACI Committee, and international organization for standardization. Building code requirements for structural concrete (ACI 318-14) and commentary. American Concrete Institute, 2014.
43. Asgarkhani N, Yakhchalian M, Mohebi B. Evaluation of approximate methods for estimating residual drift demands in BRBFs. Eng Struct. 2020;224:110849.
44. Kazemi F, Asgarkhani N, Jankowski R. Enhancing seismic performance of steel buildings having semi-rigid connection with infill masonry walls considering soil type effects. Soil Dyn Earthq Eng. 2024;177:108396.
45. Asgarkhani N, Kazemi F, Jakubczyk-Gałczyńska A, Mohebi B, Jankowski R. Seismic response and performance prediction of steel buckling-restrained braced frames using machine-learning methods. Eng Appl Artif Intell. 2024;128:107388.
46. Lignos DG, Krawinkler H. Deterioration modeling of steel components in support of collapse prediction of steel moment frames under earthquake loading. J Struct Eng. 2010;137(11):1291–302.
47. Haselton CB. Assessing seismic collapse safety of modern reinforced concrete moment frame buildings (Doctoral dissertation, Stanford University), 2006.

48. Ibarra LF, Medina RA, Krawinkler H. Hysteretic models that incorporate strength and stiffness deterioration. Earthquake Eng Struct Dynam. 2005;34(12):1489–511.
49. Altoontash, A. Simulation and damage models for performance assessment of reinforced concrete beam-column joints (Doctoral dissertation, Stanford University), 2004.
50. Mahmoud S, Chen X, Jankowski R. Structural pounding models with Hertz spring and nonlinear damper. J Appl Sci. 2008;8(10):1850–8.
51. Rezaei H, Moayyedi SA, Jankowski R. Probabilistic seismic assessment of RC box-girder highway bridges with unequal-height piers subjected to earthquake-induced pounding. Bull Earthq Eng. 2020;18(4):1547–78.
52. Polycarpou PC, Papaloizou L, Komodromos P. An efficient methodology for simulating earthquake-induced 3D pounding of buildings. Earthquake Eng Struct Dynam. 2014;43(7):985–1003.
53. Applied Technology Council, and United States. Federal Emergency Management Agency (FEMA P-695). Quantification of building seismic performance factors. US Department of Homeland Security, FEMA, 2009.
54. Vamvatsikos D, Cornell CA. Incremental dynamic analysis. Earthquake Eng Struct Dynam. 2002;31(3):491–514.
55. Kazemi F, Mohebi B, Asgarkhani N, Yousefi A. Advanced scalar-valued intensity measures for residual drift prediction of SMRFs with fluid viscous dampers. Int J Struct Integr. 2023;12:20–5.
56. FEMA-356. Prestandard and commentary for the seismic rehabilitation of buildings. Washington, DC: Federal Emergency Management Agency, 2000.

Publisher's Note Springer Nature remains neutral with regard to jurisdictional claims in published maps and institutional affiliations.

Paper II:

Asgarkhani, N., Kazemi, F., & Jankowski, R. (2022). Optimal retrofit strategy using viscous dampers between adjacent RC and SMRFs prone to earthquake-induced pounding. Archives of Civil and Mechanical Engineering, 23(1), 7. doi.org/10.1007/s43452-022-00542-1

Archives of Civil and Mechanical Engineering (2023) 23:7
https://doi.org/10.1007/s43452-022-00542-1

ORIGINAL ARTICLE

Optimal retrofit strategy using viscous dampers between adjacent RC and SMRFs prone to earthquake-induced pounding

N. Asgarkhani[1] · F. Kazemi[1] · R. Jankowski[1]

Received: 9 June 2022 / Revised: 3 September 2022 / Accepted: 1 October 2022 / Published online: 17 October 2022
© The Author(s) 2022

Abstract
Nowadays, retrofitting-damaged buildings is an important challenge for engineers. Finding the optimal placement of Viscous Dampers (VDs) between adjacent structures prone to earthquake-induced pounding can help designers to implement VDs with optimizing the cost of construction and achieving higher performance levels for both structures. In this research, the optimal placement of linear and nonlinear VDs between the 3-story, 5-story, and 9-story Steel and RC Moment-Resisting Frames (SMRFs and RC MRFs) is investigated. It is shown that the pounding phenomenon can significantly affect the seismic performance capacities of buildings during earthquakes, and using VDs can improve the seismic limit-state capacities of buildings for retrofitting purposes. For this goal, the seismic limit-state capacities of both colliding structures were assessed using Incremental Dynamic Analysis (IDA) assuming Near-fault Pulse-Like, Near-fault No-Pulse, and Far-Fault seismic records suggested by FEMA-P695. To perform IDAs, structures were modeled according to the seismic codes using a developed algorithm in Matlab and OpenSees software with the ability to remove a collapsed structure during the analysis. The results present an optimal placement for using VDs between structures and also compare the possible conditions to implement VDs. Using these results, engineers can approximately predict the seismic performance levels of both structures prone to earthquake-induced pounding and their final performance after retrofitting. Finally, retrofitting modification factors were proposed to help designers to predict the limit-state performance levels of retrofitted colliding structures without involving complicated and time-consuming analyses.

Keywords Viscous dampers · Structural pounding · Seismic retrofitting · Retrofitting modification factor · Seismic limit-state capacity · Incremental dynamic analysis

1 Introduction

Researchers have investigated the earthquake-induced pounding phenomenon, especially the influence of the impact force as an unexpected additional force for structures [1–4]. The importance of these studies is related to the fact that many buildings were constructed without sufficient in-between Separation Distance (SD) and pounding between them during earthquakes can impose crucial damages or total destruction. In addition, the design process of structures in the past neglected this external force, as the minimum SD between adjacent structures was not considered in the old seismic codes. Neglecting the SD between the newly constructed buildings also takes place because of the land price in populated cities and lack of a proper monitoring system of construction of buildings [1–3]. There are many examples of such a situation, as it can be seen in Fig. 1.

Although the current seismic codes prescribe a minimum SD, some factors such as an irregular plan or different center of rigidity, which can lead to a torsional movement, make this distance ineffective. Researchers categorized structural pounding as: the floor-to-floor or the floor-to-column pounding [4–8], pounding due to difference in weight of adjacent structures [5, 9, 10], eccentric or non-eccentric pounding [11, 12], and pounding between unequal-height buildings in series [13, 14].

✉ F. Kazemi
farzin.kazemi@pg.edu.pl

N. Asgarkhani
neda.asgarkhani@pg.edu.pl

R. Jankowski
jankowr@pg.edu.pl

[1] Faculty of Civil and Environmental Engineering, Gdańsk University of Technology, ul. Narutowicza 11/12, 80-233 Gdansk, Poland

Fig. 1 Newly constructed adjacent buildings without sufficient SD, and with different base and floors levels (Qazvin, Iran)

The nature of the earthquake-induced pounding phenomenon is a highly-complex engineering problem that should be solved by engineers. Due to this complexity, researchers proposed some ways to control collisions between adjacent structures. One possible solution is to increase the stiffness of the structural members and finally reduce the lateral displacements. Although this approach can be used in all types of structures, this may impose the increase in the construction cost and architectural issues. Therefore, researchers proposed using energy dissipation devices due to their ability to control both displacements and accelerations that are the main features of the pounding phenomenon [15–17]. Raheem [18] conducted the parametric study on the adjacent buildings exposed to earthquakes using linear and nonlinear contact models for different SDs. He proposed to use a shock absorber that reduces the acceleration peaks and finally the impact force. In a more general work, Raheem et al. [19] investigated the effects of eccentric alignment of three, six, and twelve-story adjacent structures under nine earthquakes using a viscoelastic impact model. Their results confirm that the eccentric alignments make the design more complicated and the corners of buildings play a key role against the torsional response of eccentric pounding. Impact-absorbing materials were also considered and a number of studies were carried out using polystyrene bumpers and polymer elements [20–22] and rubber shock absorbers [23, 24]. To overcome the pounding impact, Jankowski and Mahmoud [25] connected the three-story adjacent structures with link elements using spring, dashpots, and viscoelastic elements. The results showed that using viscoelastic elements reduced the peak displacement response of structures compared to dashpot or spring elements applied alone. Regarding this approach, other studies were also carried for viscous dampers (VDs) [26–31], tuned mass dampers [32], friction dampers [33], and multi-link viscoelastic elements [34] installed at the floor levels of buildings where larger probability of collisions is expected. The Linear or Nonlinear Viscous Dampers (LVDs or NVDs) may have different properties. Martinez-Rodrigo and Romero [35] compared the use of the LVDs and NVDs, and found out that the larger reduction occurred in the case of LVDs while the NVDs achieved smaller damping force. Increasing the number of VDs would not certainly be related to their efficiency [36, 37], while the distribution of VDs had significant effects on structural modal properties [38]. Adding LVDs at all floor levels of the adjacent steel and reinforced concrete structures were proposed by Kazemi et al. [39]. This approach eliminates the sudden changes in impact force, and therefore reduces the possibility of structural damages due to the pounding phenomenon.

The purpose of this study is to investigate an optimal placement of LVDs or NVDs between Steel and RC Moment-Resisting Frames (SMRFs and RC MRFs) prone to earthquake-induced pounding considering the optimized cost of implementation and the seismic limit-state capacity performance level as targets. Therefore, the seismic performance levels of both adjacent structures were investigated, while implementing LVDs or NVDs can affect the seismic behavior of both of them. In addition, based on the results of this study, modification factors for retrofitted structures are determined that can provide a practical tool for estimating proposed retrofitting strategy on the newly constructed or existing structures.

2 Methods of modeling

2.1 Modeling approach of adjacent buildings

To study the pounding phenomenon, the 3-, 5-, and 9-story SMRFs and RC MRFs were considered to be constructed in California with seismic design parameters of $SD_S = 1.0$ g

and $SD_1 = 0.6$ g and soil type of D (see Fig. 2 for their structural plan). To model the structures, the seismic codes of ASCE 7-16 [40], ANSI/AISC 360-16 [41], ANSI/AISC 341-16 [42], and ACI 318-14 [43] were used. The design coefficients and factors for assumed structures were considered according to the seismic code of ASCE 7-16 [40] (Table 12.2-1), having dead and live loads of 8.379 kN/m^2 and 2.39 kN/m^2, respectively. Based on the procedures of modeling used by Kitayama and Constantinou [44] and Haselton and Deierlein [45], it is possible to model three-dimensional building by a two-dimensional structure. For this purpose, the main columns of MRFs are used (columns with thick blue lines in Fig. 2 show the MRFs in the *X* direction), which are connected to the leaning column taking into account the other gravity columns effects. Using the leaning column provides the possibility of considering the *P*-delta effects with acceptable accuracy of modeling (e.g. see [7, 9, 46]). For modeling structures, the concrete compressive strength of 34.5 MPa, the steel yield strength and Young's modulus of 345 MPa and 200 GPa, respectively, were assumed in the analysis. Figures 3 and 4 show the three-dimensional view of the 3-, 5-, and 9-story SMRFs and RC MRFs, respectively.

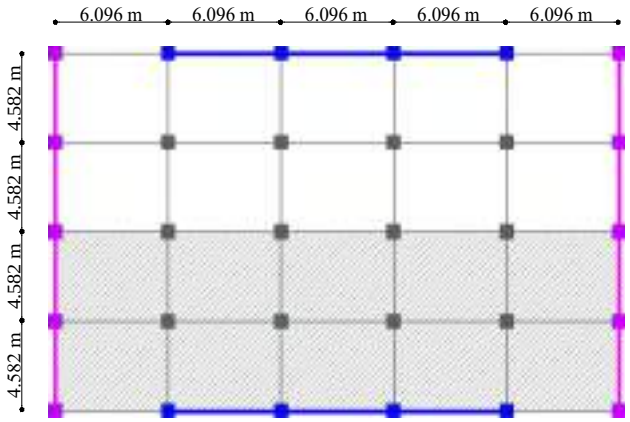

Fig. 2 Considered plan for modeling steel and RC MRFs

For SMRFs, the moment-rotation behavior of the structural elements were defined considering a nonlinear rotational spring at both ends of each member. The behavior of the spring was simulated based on the modified Ibarra–Krawinkler bilinear-hysteretic model (for more detail see [39, 46]) and it was assigned using the zero-length element. The Ibarra–Krawinkler model can

Fig. 3 Three-dimensional view of the 3-, 5-, and 9-story SMRFs

Fig. 4 Three-dimensional view of the 3-, 5-, and 9-story RC MRFs

simulate the cyclic deterioration including unloading and reloading stiffness, strength and post-capping strength. Figure 5 presents the two-dimensional model and the modified Ibarra–Krawinkler model used for defining the nonlinear behavior of elements. It should be noted that 316 specimens were used to calibrate the model with wide range of *W*-sections [39–46]. Therefore, it is possible to calculate the parameters of hysteresis curves using formula introduced by Lignos and Krawinkler [47].

To model beams and columns of RC MRFs, a trilinear backbone curve of deterioration model, mainly developed by Ibarra et al. [48] and implemented in Opensees [49] software by Altoontash [50], was used. This model can capture the modes of cyclic degradation and collapse states. Two main sources were used for determining the model parameters: the

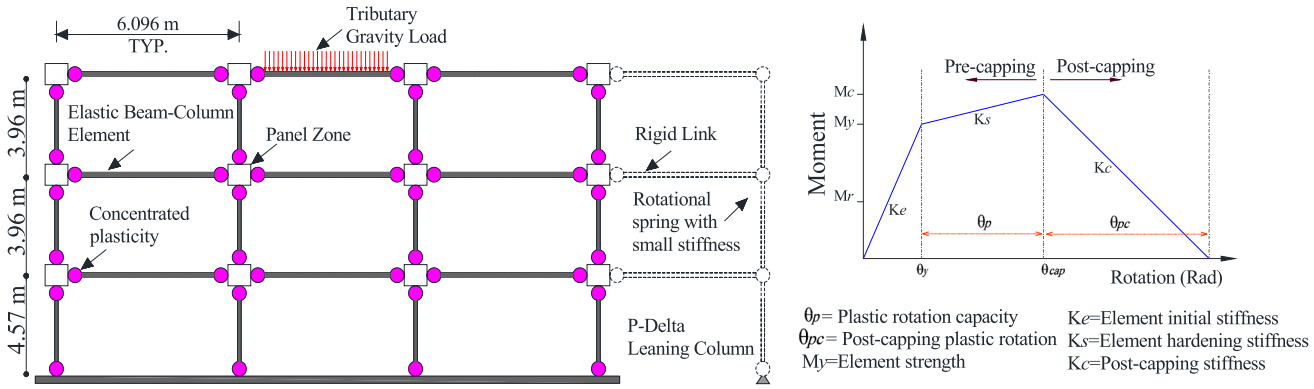

Fig. 5 Two-dimensional model and the modified Ibarra–Krawinkler model used for defining the nonlinear behavior of elements

first one is based on the relationships introduced by Fardis and Biskinis [51], and the second one is based on the experimental specimens of columns investigated by Berry et al. [52]. A number of studies were performed based on this model to capture the seismic collapse capacity of the RC MRFs (e.g. see [39, 53, 54]). Structural documentation of the columns and beams of RC MRFs and SMRFs are presented in Tables 1 and 2.

2.2 Impact contact element

To simulate the structural pounding phenomenon, researchers used different element force models that can precisely model the impact force with high accuracy. The viscoelastic contact element (Kelvin-Voigt element) with high acceptable accuracy was used in this study [54, 55]. The implementation of viscoelastic contact element was validated by Kazemi et al. [5] using the following formula:

$$F(t) = K_{\text{imp}}\delta(t) + C_{\text{imp}}\dot{\delta}(t) \tag{1}$$

$$C_{\text{imp}} = 2\xi\sqrt{K_{\text{imp}}\frac{m_1 m_2}{m_1 + m_2}} \tag{2}$$

$$\xi = \frac{-\ln(e)}{\sqrt{\pi^2 + (\ln e)^2}} \tag{3}$$

where $F(t)$ is the impact force, C_{imp} and K_{imp} are impact damping and stiffness coefficients, and relative deformation and velocity are expressed as $\delta(t)$ and $\dot{\delta}(t)$. m_1 and m_2 are masses of particular stories of adjacent structures, and ξ is the impact damping ratio [56–58]. The coefficient of restitution, e, was assumed equal to 0.65 (e.g. see [39, 46, 54–59]). According to Polycarpou et al. [12] approach for modeling the three-dimensional adjacent structure, the dimensionless impact stiffness, K_i, in the contact region can be determined as follows:

$$K_i = \left[\frac{1-\nu_1^2}{E_{\text{Dyn},1}} + \frac{1-\nu_2^2}{E_{\text{Dyn},2}}\right]^{-1} \tag{4}$$

$$E_{\text{Dyn, i}} = 5.82\left(E_{\text{Static},i}\right)^{0.63} \tag{5}$$

where ν_i and $E_{\text{Dyn, }i}$ are the Poisson's ratio and the dynamic elastic modulus of contact material. Considering the $E_{\text{Static}} = 21$ GPa and $\nu_i = 0.2$ are used for normal strength concrete, the dimensionless impact stiffness, K_i, can be calculated from Eqs. 4 and 5 as equal to $K_i = 209.6 \times 10^5$ kN/m^2. Moreover, assuming the half of structural plan (see Fig. 2) in pounding condition (9.144 m), the impact damping and

Table 1 Structural documentation of the columns of RC MRFs

Model	Story	Exterior					Interior				
		h (cm)	b (cm)	s* (cm)	ρ_{tot}**	ρ_{sh}***	h (cm)	b (cm)	s (cm)	ρ_{tot}	ρ_{sh}
3-Story RC MRF	1st	76.2	71.1	12.7	0.0135	0.01	76.2	71.1	12.7	0.017	0.01
	2nd	76.2	71.1	12.7	0.01	0.01	76.2	71.1	12.7	0.017	0.01
	3rd	76.2	71.1	12.7	0.01	0.01	76.2	71.1	12.7	0.017	0.01
5-Story RC MRF	1st	76.2	81.3	8.9	0.02	0.0085	96.5	81.3	8.9	0.016	0.0112
	2nd	76.2	81.3	8.9	0.02	0.0085	96.5	81.3	8.9	0.016	0.008
	3rd	76.2	81.3	10.2	0.01	0.006	96.5	81.3	8.9	0.01	0.008
	4th	76.2	81.3	10.2	0.01	0.006	96.5	81.3	8.9	0.01	0.008
	5th	76.2	81.3	10.2	0.01	0.006	96.5	81.3	8.9	0.01	0.008
9-Story RC MRF	1st	71.1	66.05	8.9	0.02	0.01	86.4	66.05	8.9	0.018	0.012
	2nd	71.1	66.05	8.9	0.015	0.01	86.4	66.05	8.9	0.013	0.012
	3rd	71.1	66.05	8.9	0.015	0.01	86.4	66.05	8.9	0.013	0.012
	4th	71.1	66.05	10.2	0.015	0.01	86.4	66.05	8.9	0.013	0.012
	5th	71.1	66.05	10.2	0.015	0.007	86.4	66.05	8.9	0.022	0.007
	6th	71.1	66.05	10.2	0.01	0.007	71.1	66.05	10.2	0.015	0.007
	7th	71.1	66.05	10.2	0.01	0.007	71.1	66.05	10.2	0.014	0.007
	8th	71.1	66.05	10.2	0.01	0.007	71.1	66.05	10.2	0.01	0.007
	9th	71.1	66.05	10.2	0.01	0.007	71.1	66.05	10.2	0.01	0.007

*s spacing of transverse reinforcement

**ρ_{tot} ratio of total longitudinal reinforcement area

***ρ_{sh} ratio of transverse reinforcement area

Table 2 Structural documentation of SMRFs and RC MRFs

Model	Story	RC MRF						SMRF		
		Exterior and interior beam						Interior column	Exterior column	Beam
		h (cm)	b (cm)	s (cm)	ρ	ρ'*	ρ_{sh}			
3-Story	1st	71.1	71.1	12.7	0.0065	0.0075	0.004	W14X176	W14X176	W24X68
	2nd	71.1	71.1	12.7	0.0065	0.0075	0.004	W14X176	W14X176	W21X55
	3rd	71.1	71.1	12.7	0.0065	0.0075	0.004	W14X145	W14X145	W18X40
5-Story	1st	61	81.3	12.7	0.0108	0.012	0.005	W14X211	W14X211	W24X68
	2nd	61	81.3	12.7	0.01	0.0115	0.005	W14X211	W14X211	W24X68
	3rd	61	81.3	12.7	0.009	0.018	0.004	W14X211	W14X211	W24X68
	4th	61	81.3	12.7	0.005	0.006	0.003	W14X176	W14X176	W21X50
	5th	61	81.3	12.7	0.005	0.006	0.003	W14X176	W14X176	W18X40
9-Story	1st	76.2	66.05	12.7	0.007	0.0075	0.004	W14X283	W14X283	W27X84
	2nd	76.2	66.05	16.5	0.007	0.0085	0.0045	W14X283	W14X283	W27X84
	3rd	76.2	66.05	12.7	0.007	0.008	0.004	W14X233	W14X233	W24X76
	4th	76.2	66.05	14	0.006	0.0075	0.004	W14X233	W14X233	W24X76
	5th	76.2	66.05	15.25	0.0055	0.007	0.0037	W14X193	W14X193	W24X68
	6th	76.2	66.05	16.5	0.005	0.005	0.003	W14X193	W14X193	W24X68
	7th	76.2	66.05	14	0.003	0.004	0.0025	W14X159	W14X159	W21X55
	8th	76.2	66.05	15.25	0.003	0.003	0.0025	W14X159	W14X159	W21X55
	9th	76.2	66.05	15.25	0.003	0.003	0.0025	W14X159	W14X159	W18X40

*ρ' ratio of longitudinal reinforcement in compression

stiffness coefficients, C_{imp} and K_{imp}, can be obtained from the equations equal to $C_k = 7576$ kNs/m and $K_{imp} = 19.17 \times 10^7$ kN/m, respectively.

2.3 Models of pounding

Modeling pounding is a very complicated process, including factors such as the local deformation effects, the yielding area, the material of impact area and ductility effects. Although these factors can complicate the modeling process, it has been seen that different damping coefficients and impact stiffness do not significantly affect the results [60]. Hence, the determined values can be approximately considered as appropriate values for the analysis.

To consider the allowable SD, the approach proposed by ASCE 7-16 [40] was used. The adjacent buildings should be separated by the allowable SD, which can be calculated as follows:

$$\mathrm{SD} = \sqrt{\left(\frac{C_d \cdot \delta_M}{I}\right)_1^2 + \left(\frac{C_d \cdot \delta_M}{I}\right)_2^2} \quad (6)$$

where δ_M is the maximum inelastic response displacement and C_d and I are the deflection amplification factor and the importance factor, respectively. δ_M for both RC MRFs and SMRFs can be calculated from the nonlinear static analysis (i.e. pushover) having the lateral load distribution of the first mode shape. This value is used as $1.0D$ between adjacent structures and two other values of 0.0 and $0.5D$ can be assumed. Table 3 presents the considered SDs between RC MRFs and SMRFs.

Table 3 SDs between adjacent RC MRFs and SMRFs

Models	0.0 (cm)	$0.5D$ (cm)	$1.0D$ (cm)
3-Story RC MRFs and 3-story SMRFs	0.0	8.3	16.6
3-Story RC MRFs and 5-story SMRFs	0.0	7.7	15.5
3-Story RC MRFs and 9-story SMRFs	0.0	7.4	14.7
5-Story RC MRFs and 3-story SMRFs	0.0	8.8	17.6
5-Story RC MRFs and 5-story SMRFs	0.0	12.9	25.9
5-Story RC MRFs and 9-story SMRFs	0.0	13.8	27.5
9-Story RC MRFs and 3-story SMRFs	0.0	8.3	16.6
9-Story RC MRFs and 5-story SMRFs	0.0	12.5	25.0
9-Story RC MRFs and 9-story SMRFs	0.0	21.6	43.1

2.4 Using VDs between structures

VD is a kind of energy dissipation device that transforms kinetic energy into heat energy to dissipate the seismic energy due to earthquakes. Equation (7) shows the relation between the VD force, F_{VD}, the damping coefficient, $C(\alpha)$, the relative velocity, $\dot{x}$, the signum function, sgn, and the damper velocity exponent, α [26–39].

$$F_{FVD} = C(\alpha)|\dot{x}|^{\alpha}\mathrm{sgn}(\dot{x}) \tag{7}$$

The damper velocity exponent can take values from 0.0 to 1.0 for NVDs or LVDs, respectively. To calculate the supplemental damping ratio, ξ_{VD}, of VDs implemented between adjacent RC MRFs and SMRFs, modified equation introduced by Kandemir-Mazanoglu and Mazanoglu [30] was used:

$$\xi_{VD} = \frac{\left(\max\left\{T_{1,1}, T_{1,2}\right\}\right)\sum_j C(\alpha)_j\left(\phi_{j,1} - \phi_{j,2}\right)^2}{4\pi\sum_i m_i\phi_i^2} \tag{8}$$

$$C(\alpha) = \frac{C(\alpha = 1)\left(\min\left\{\omega_{1,1}, \omega_{1,2}\right\}X_0\right)^{1-\alpha}}{\beta} \tag{9}$$

$$\beta = \frac{2^{2+\alpha}\Gamma^2\left(1 + \frac{\alpha}{2}\right)}{\pi\Gamma(2+\alpha)} \tag{10}$$

where $T_{1,1}$, $T_{1,2}$ are the fundamental period for the structures, the relative horizontal deformation corresponding to the first mode shape between floor levels of adjacent RC MRFs and SMRFs is obtained by $\left(\phi_{j,1} - \phi_{j,2}\right)$. Moreover, X_0 is the maximum relative displacement of the adjacent structures, $\omega_{1,1}$ and $\omega_{1,2}$ are the natural frequencies of the adjacent buildings, and Γ is the gamma function. To model VDs, it was considered that the VDs with rigid supporting do not reach their stroke limits during seismic excitations due to assumption of their large enough stroke limits.

In this research, both of NVDs or LVDs were considered between the aforementioned adjacent structures. Assuming three SDs, three ground motion data sets of Near-fault Pulse-Like (NPL), Near-fault No-Pulse (NNP), and Far-Fault (FF) seismic records suggested by FEMA-P695 [61] were used to find out the effects of earthquake events. Table 4 presents all the considered conditions (1086 models). In addition, all structures were analyzed in alone condition.

3 Results of analysis

3.1 Moment-rotation curve

Modified Ibarra–Krawinkler bilinear-hysteretic model (see [62–64]) was used to model the plastic hinges of structural elements. To compare the effects of pounding and implementing LVDs between the structures, the moment-rotation curves were used. Figures 6 and 7 present a comparison between beam and column hinges of the 3-story SMRF colliding with 5-story RC MRF in pounding situation and implementing LVDs between structures, respectively, subjected to NNP record (Northridge, 1/17/1994, Sepulveda VA Hospital station) assuming SD equal to 0.0 and $S_a(T_1) = 0.92$ g. According to results, pounding can increase the maximum rotation of beam and column by 16% and 29.1% (for the beam from 0.042 to 0.050 rad, and for the column from 0.034 to 0.048 rad), respectively. In a structure, columns play a crucial role in the total collapse and the results show that 29.1% of column rotation will be added due to collisions. So it is important to find a solution to resist this sudden force. According to this result, adding VDs between the colliding structures is an alternative. The results confirm that using LVDs between structures can decrease the maximum values of the moment-rotation curves for beams and columns by 48% and 31.25% (for the beam from 0.050 to 0.026 rad, and the column from 0.048 to 0.033 rad), respectively. It is worth mentioning that this reduction can cause overall improvement in performance levels. Similar results were also observed for beams and column hinges of other colliding structures with different SDs and VDs.

3.2 IDA curves of pounding structures

To better investigate the effects of adding VDs on the seismic limit-state capacity of the colliding structures, the Incremental Dynamic Analysis (IDA) was used. Although many intensity measures were introduced by the researchers, $S_a(T_1)$ was selected for this purpose, and IDAs were performed assuming three ground motion sets of NPL, NNP, and FF suggested by FEMA-P695 [61]. OpenSees [49] software is an open-source developed program that can be used for accomplishing computational simulations in earthquake engineering to obtain the structural performances. The structural elements can be defined in interpreter (e.g. Python or Tcl) and different types of numerical solutions can be used for seismic analysis, which includes nonlinear time-history analysis or IDAs. It should be noted that new materials and structural elements have been added in this software to determine seismic behavior

Table 4 Considered adjacent pounding RC MRFs and SMRFs for optimal placement of NVDs or LVDs

Structure 1	Structure 2	Seismic ground motion (FEMA-P695)	SD	Linear or nonlinear VDs	Implementation stories	Model name
3-Story SMRF	3-Story RC MRF	NPL	0.0	Alpha 0.3*	2	3St-3RC-1
		NNP	0.5D	Alpha 0.7	3	3St-3RC-2
		FF	1.0D	Alpha 1.0	1, 3	3St-3RC-3
					1, 2, 3	3St-3RC-4
3-Story SMRF	5-Story RC MRF	NPL	0.0	Alpha 0.3	2	3St-5RC-1
		NNP	0.5D	Alpha 0.7	3	3St-5RC-2
		FF	1.0D	Alpha 1.0	1, 3	3St-5RC-3
					1, 2, 3	3St-5RC-4
3-Story SMRF	9-Story RC MRF	NPL	0.0	Alpha 0.3	2	3St-9RC-1
		NNP	0.5D	Alpha 0.7	3	3St-9RC-2
		FF	1.0D	Alpha 1.0	1, 3	3St-9RC-3
					1, 2, 3	3St-9RC-4
5-Story SMRF	3-Story RC MRF	NPL	0.0	Alpha 0.3	2	5St-3RC-1
		NNP	0.5D	Alpha 0.7	3	5St-3RC-2
		FF	1.0D	Alpha 1.0	1, 3	5St-3RC-3
					1, 2, 3	5St-3RC-4
5-Story SMRF	5-Story RC MRF	NPL	0.0	Alpha 0.3	5	5St-5RC-1
		NNP	0.5D	Alpha 0.7	2, 5	5St-5RC-2
		FF	1.0D	Alpha 1.0	1, 3, 5	5St-5RC-3
					1, 2, 3, 4, 5	5St-5RC-4
5-Story SMRF	9-Story RC MRF	NPL	0.0	Alpha 0.3	5	5St-9RC-1
		NNP	0.5D	Alpha 0.7	2, 5	5St-9RC-2
		FF	1.0D	Alpha 1.0	1, 3, 5	5St-9RC-3
					1, 2, 3, 4, 5	5St-9RC-4
9-Story SMRF	3-Story RC MRF	NPL	0.0	Alpha 0.3	2	9St-3RC-1
		NNP	0.5D	Alpha 0.7	3	9St-3RC-2
		FF	1.0D	Alpha 1.0	1, 3	9St-3RC-3
					1, 2, 3	9St-3RC-4
9-Story SMRF	5-Story RC MRF	NPL	0.0	Alpha 0.3	5	9St-5RC-1
		NNP	0.5D	Alpha 0.7	2, 5	9St-5RC-2
		FF	1.0D	Alpha 1.0	1, 3, 5	9St-5RC-3
					1, 2, 3, 4, 5	9St-5RC-4
9-Story SMRF	9-Story RC MRF	NPL	0.0	Alpha 0.3	9	9St-9RC-1
		NNP	0.5D	Alpha 0.7	5	9St-9RC-2
		FF	1.0D	Alpha 1.0	9, 5	9St-9RC-3
					9, 5, 1	9St-9RC-4
					9, 6, 3	9St-9RC-5
					8, 6, 4, 2	9St-9RC-6
					9, 7, 5, 3, 1	9St-9RC-7
					9, 8, 7, 6, 5, 4, 3, 2, 1	9St-9RC-8

*Alpha presents the damper velocity exponent

of members. To control, monitor and classify the output results, MATLAB [65] was used, which is a programming platform with wide range of capabilities. In real condition, it is possible that RC MRF and SMRF are constructed next to each other. Taking into account the pounding phenomenon, the adjacent structures may have different collapse states, in which, one of the structures may experience total failure before the next one. Therefore, it is important to consider the real condition of two colliding structures and take into account that one of the structures would collapse before the other one. To tackle this issue, the Tcl programing code, that uses MATLAB [65] and OpenSees [49]

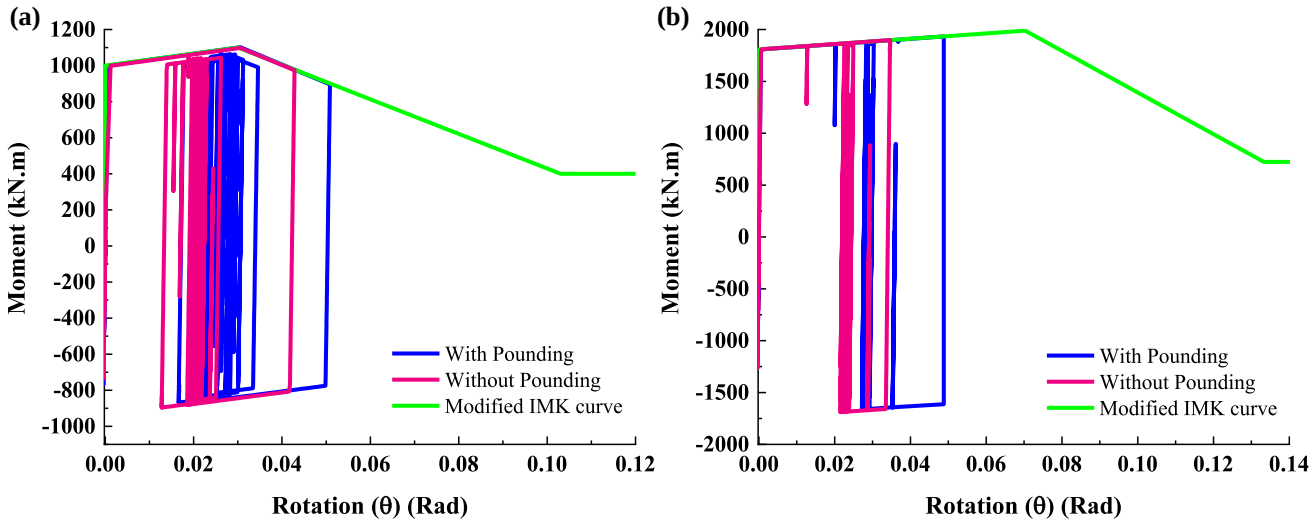

Fig. 6 Comparison between hinges of **a** beam, **b** column of 3rd floor of the 3-story SMRF colliding with 5-story RC MRF assuming SD of 0.0

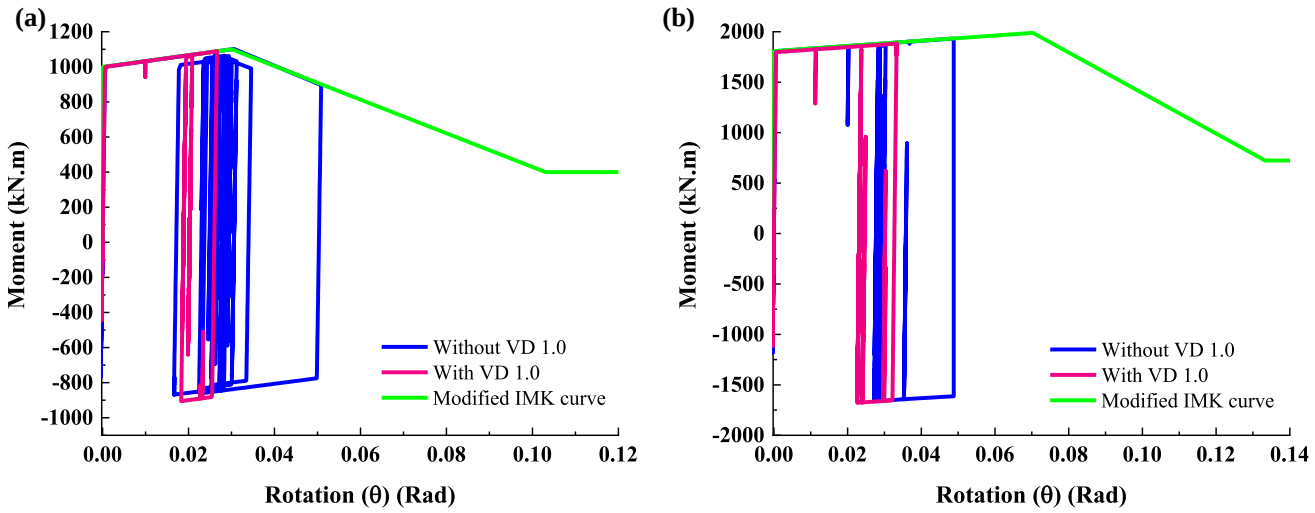

Fig. 7 Comparison between hinges of **a** beam, **b** column of 3rd floor of the 3-story SMRF colliding with 5-story RC MRF considering LVDs in all floor levels for SD of 0.0

softwares simultaneously, was developed. This program allowed us to consider the effects of collapsed structure during the analysis, and this structure was not removed during further analysis until the total collapse of the second structure. In this way, the real condition of pounding phenomenon could be simulated. Using the program, both limit-state capacities of colliding structures can be obtained in one model that decreases the analysis time, and the effects of collapsed structure can be considered in the response of the second structure that can increase the accuracy of modeling. Figure 8 presents the IDA curves (black lines) and the median IDA curves (pink lines) (M-IDAs) of the 9-story RC MRFs (a) and the 9-story SMRFs (b) subjected to NPL records for SD of 1.0.

3.3 Performance level of structures

Following recommendations of FEMA 356 [66], the allowable interstory drift for primary structural elements were assumed for performance levels of Immediate Occupancy (IO), Life Safety (LS), Collapse Prevention (CP), and total Collapse (C) according to defined damages.

The allowable values of interstory drift ratio of 1.0%, 2.0%, and 4.0%, were assumed for the performance of IO,

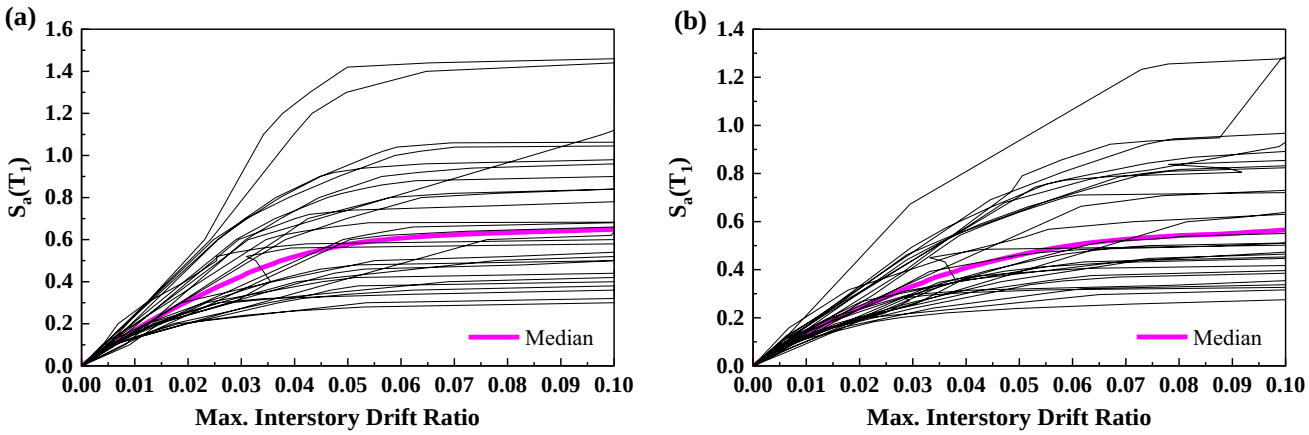

Fig. 8 IDA curves for, **a** the 9-story RC MRFs, **b** the 9-story SMRFs assuming LVDs between all stories subjected to NPL records for SD of 1.0

LS, and CP for RC MRFs, respectively. In addition, for SMRFs, the allowable values of interstory drift ratio of 0.7%, 2.5%, and 5.0%, respectively, were considered. In both structures, the flat part of M-IDAs presents the total collapse of the structure (C). Table 5 shows the performance levels of RC MRFs and SMRFs in no pounding condition considering three record subsets. It can be seen that, in the case of RC MRFs, the values of M-IDAs for assumed performance levels in NNP subset are higher than for other subsets. It is also correct for the 3-story SMRF, while for in the 5-, and 9-story SMRFs, the assumed performance levels in FF subset are higher than for other subsets.

3.4 Comparing implementing NVDs or LVDs

Figure 9 compares the results of using NVDs or LVDs in the floor levels of all stories on M-IDAs of the 3-story SMRF colliding with 3-story RC MRF subjected to NPL for SD of 1.0D. According to Fig. 9, using LVDs between structures prone to pounding can increase M-IDAs of the RC MRFs by 33.06% (from 1.104 to 1.469), while decreasing M-IDAs of the SMRFs by 16.22% (from 1.892 to 1.585). The results confirm that using NVDs or LVDs has the same effect in M-IDAs that increases M-IDAs of RC MRFs and decreases M-IDAs of SMRFs. In other words, there is no difference between using NVDs or LVDs. These VDs can decrease M-IDAs of 3-story SMRF while increasing M-IDAs of 3-story RC MRF. The amount of M-IDAs in the aforementioned performance levels obtained from the analysis is presented in Table 6. According to this table, in each performance level, M-IDAs can show which kind of VDs have better performance. It can be seen that the LVDs added to all story levels have better performance levels, as compared to the NVDs.

Figure 10 compares the results of using NVDs or LVD in the second-floor level on M-IDAs of the 3-story SMRF colliding with 3-story RC MRF subjected to NPL for SD of 1.0D. It can be seen that the LVD added at the second-floor level increases M-IDAs of the 3-story RC MRF more than NVDs. In addition, LVD added at the second-floor level of the 3-story SMRF causes less reduction in M-IDAs, as compared to NVDs. LVD can also prevent further damages. To better compare the results, Table 7 presents the values of the performance levels of colliding structures in detail. It can be seen from the table that using LVD at the second level of colliding structures results in better performance levels increasing M-IDAs of the 3-story RC MRF by 15.67% (from 1.104 to 1.277) or decreasing M-IDAs of the 3-story

Table 5 Limited state capacities of the RC MRFs and SMRFs in alone condition assuming three record subsets

Subset	3-Story RC				5-Story RC				9-Story RC			
	IO	LS	CP	C	IO	LS	CP	C	IO	LS	CP	C
NPL	0.330	0.556	0.844	1.104	0.264	0.460	0.734	0.988	0.163	0.290	0.450	0.530
NNP	0.395	0.721	1.153	1.539	0.280	0.518	0.853	1.167	0.165	0.302	0.476	0.545
FF	0.375	0.673	1.082	1.338	0.265	0.492	0.850	1.102	0.174	0.318	0.483	0.552
	3-Story steel				5-Story steel				9-Story steel			
NPL	0.226	0.807	1.374	1.893	0.153	0.502	0.946	1.270	0.080	0.274	0.460	0.548
NNP	0.226	0.805	1.454	2.221	0.135	0.481	0.945	1.304	0.061	0.241	0.382	0.465
FF	0.223	0.795	1.454	2.085	0.142	0.546	1.075	1.409	0.065	0.243	0.415	0.513

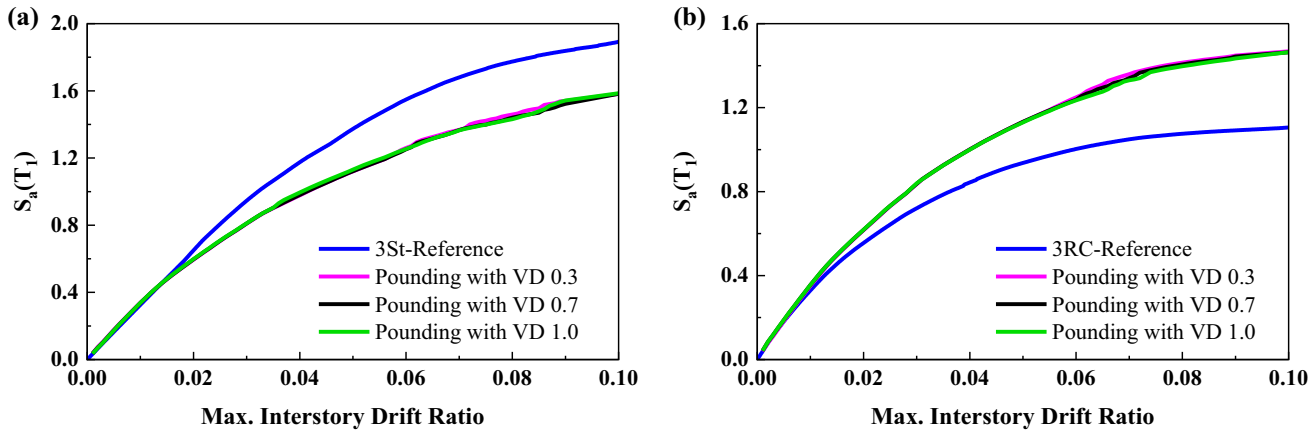

Fig. 9 Comparing the effects of the NVDs or LVDs implemented in all story levels on M-IDAs of **a** the 3-story SMRF, **b** the 3-story RC MRF including NPL record subset for SD of 1.0D

Table 6 Limited state capacities of the 3-story SMRF and the 3-story RC MRF structures with different VDs implemented in all story levels subjected to NPL record subsets for SD of 1.0D

Model name	3-Story SMRF				3-Story RC MRF			
	IO	LS	CP	C	IO	LS	CP	C
3St-3RC-SD1.0D	0.229	0.806	1.373	1.892	0.329	0.555	0.843	1.104
3St-3RC-4-VD 0.3-SD1.0D	0.243	0.705	1.120	1.581	0.350	0.616	1.00	1.468
3St-3RC-4-VD 0.7-SD 1.0D	0.241	0.707	1.121	1.582	0.355	0.618	1.00	1.463
3St-3RC-4-VD 1.0-SD1.0D	**0.245**	**0.709**	**1.131**	**1.585**	**0.357**	**0.619**	**1.01**	**1.469**

Bold values indicate the best results obtained from implementing VDs

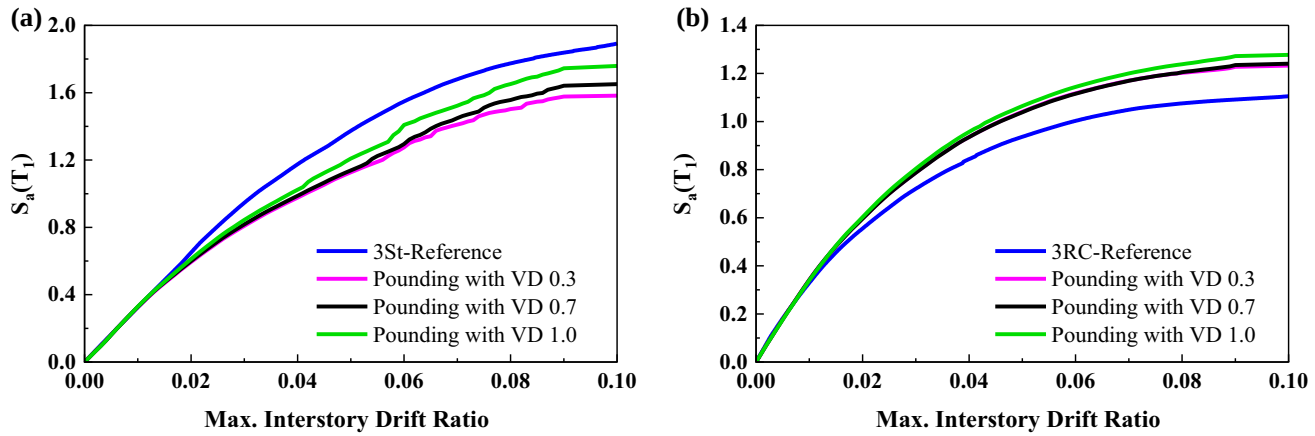

Fig. 10 Comparing the effects of the NVDs or LVDs implemented in 2nd story level on M-IDAs of **a** the 3-story SMRF, **b** the 3-story RC MRF including NPL record subset for SD of 1.0D

Table 7 Limited state capacities of the 3-story SMRF and the 3-story RC MRF assuming different VDs implemented in 2nd story level subjected to NPL record subsets for SD of 1.0D

Model name	3-Story SMRF				3-Story RC MRF			
	IO	LS	CP	C	IO	LS	CP	C
3St-3RC-SD1.0D	0.229	0.806	1.373	1.892	0.329	0.555	0.843	1.104
3St-3RC-1-VD 0.3-SD1.0D	0.229	0.708	1.127	1.582	0.341	0.597	0.936	1.232
3St-3RC-1-VD 0.7-SD1.0D	0.229	0.716	1.138	1.651	0.341	0.596	0.935	1.240
3St-3RC-1-VD 1.0-SD1.0D	**0.229**	**0.736**	**1.208**	**1.759**	**0.341**	**0.602**	**0.957**	**1.277**

Bold values indicate the best results obtained from implementing VDs

SMRF by 7.02% (from 1.892 to 1.759). Therefore, according to this sensitivity analysis, the placement of LVDs between adjacent structures will be investigated due to their better performance, as compared to NVDs. It is worth noting that similar results were also observed for other record subsets.

3.5 Comparing M-IDAs of 3-story SMRF pounding with RC MRFs

Figure 11 presents the effects of using LVDs on M-IDAs of the 3-story SMRF and 3-story RC MRF subjected to NPL for SD of 1.0D. The models were defined according to Table 4. Using LVDs at all floor levels (3St-3RC-4) increases M-IDAs for the 3-story RC MRF by 32.48% (from 1.105 to 1.464) which is more than other assumed models considering LVD at the second-floor level (3St-3RC-1), at the third-floor level (3St-3RC-2), and at both first and third-floor level simultaneously (3St-3RC-3) by 12.4%, 13.4%, and 7.3%, respectively. Therefore, the best model to improve the performance levels of the 3-story RC MRF is implementing the LVDs according to the condition defined for 3St-3RC-4 in Table 4. The values of the four performance levels are presented in Table 8. On other side, for improving the performance levels of IO and LS for the 3-story SMRF, using the condition of 3St-3RC-2, and for the performance levels of CP and C, using the condition of 3St-3RC-3 can be a good alternative. Because these conditions, 3St-3RC-2 and 3St-3RC-3, can cause less reduction in M-IDAs, as compared to other models. Although using the 3St-3RC-4 is the best alternative for the 3-story RC MRF, this condition can cause the largest reduction in M-IDAs of the 3-story SMRF. Therefore, it is suggested to consider both structures' performance levels in retrofitting approach and choose the best model according to required performance levels.

Figure 12 presents the results of using LVDs on M-IDAs of the 3-story SMRF and 5-story RC MRF subjected to NPL for SD of 1.0D. Using LVD at the third-floor level (3St-5RC-2) increases M-IDAs for the 5-story RC MRF by 26.8% (from 0.987 to 1.252) which is more than other assumed models considering LVD at second-floor level (3St-5RC-1), at both first and third-floor level simultaneously (3St-5RC-3), and at all floor levels (3St-5RC-4) by 5.4%, 13.8%, and 12.4%, respectively. Therefore, the best model to improve the performance levels of the 5-story RC MRF is implementing the LVD according to the condition defined for 3St-3RC-2 in Table 4. In addition, for other performance levels, the values are presented in Table 9. For the 3-story SMRF, the 3St-5RC-1 condition is a better alternative in

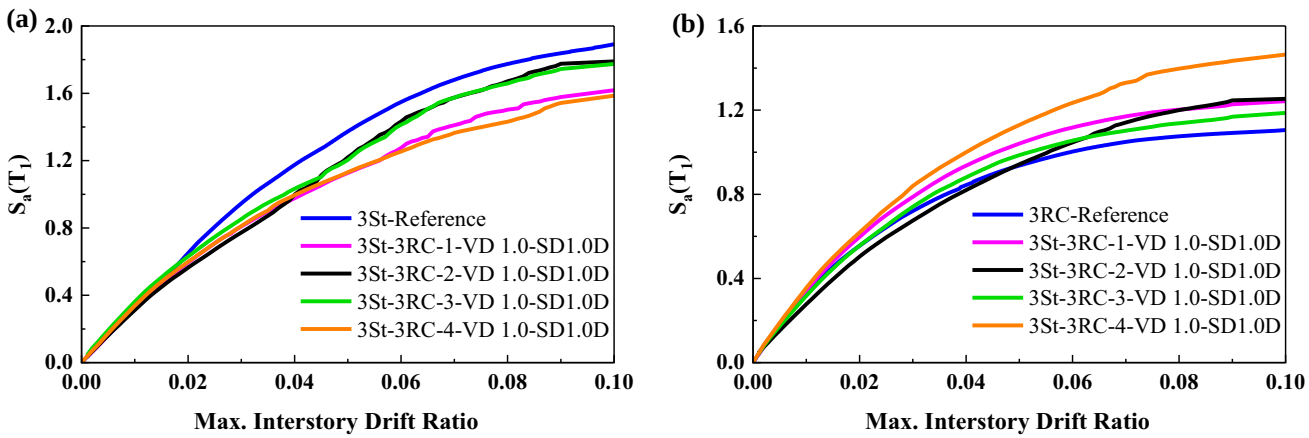

Fig. 11 Comparison M-IDAs of **a** the 3-story SMRF, **b** the 3-story RC MRF in pounding condition including NPL record subset for SD of 1.0D

Table 8 Limited state capacities of the 3-story SMRF and the 3-story RC MRF structures subjected to NPL record subsets for SD of 1.0D

Model name	3-Story SMRF				3-Story RC MRF			
	IO	LS	CP	C	IO	LS	CP	C
3St-3RC-SD1.0D	0.229	0.806	1.373	1.892	0.329	0.555	0.843	1.105
3St-3RC-1-VD 1.0-SD1.0D	0.229	0.708	1.127	1.618	0.341	0.597	0.936	1.242
3St-3RC-2-VD 1.0-SD1.0D	0.222	0.670	**1.219**	**1.789**	0.277	0.504	0.819	1.253
3St-3RC-3-VD 1.0-SD1.0D	**0.261**	**0.747**	1.203	1.774	0.317	0.555	0.880	1.186
3St-3RC-4-VD 1.0-SD1.0D	0.241	0.709	1.131	1.585	**0.355**	**0.618**	**0.999**	**1.464**

Bold values indicate the best results obtained from implementing VDs

performance levels of IO and LS with improvements in M-IDAs values by 17% and 4.8%, respectively, while this can cause smaller reduction in the performance level of CP by 13.32%. For the performance level of C, the results confirm that the 3St-5RC-3 condition, with the reduction by 4.75%, is the best alternative among all models. Adding LVDs between the structures can cause an increase or decrease due to the assumed performance levels and the kind of implementation.

Figure 13 presents the results of using LVDs on M-IDAs of the 3-story SMRF and the 9-story RC MRF subjected to NPL for SD of 1.0D. Using LVDs at all floor levels (3St-9RC-4) increases M-IDAs for the 9-story RC MRF in performance levels of IO, LS, and CP by 5.5%, 2.1%, and 12.7%,

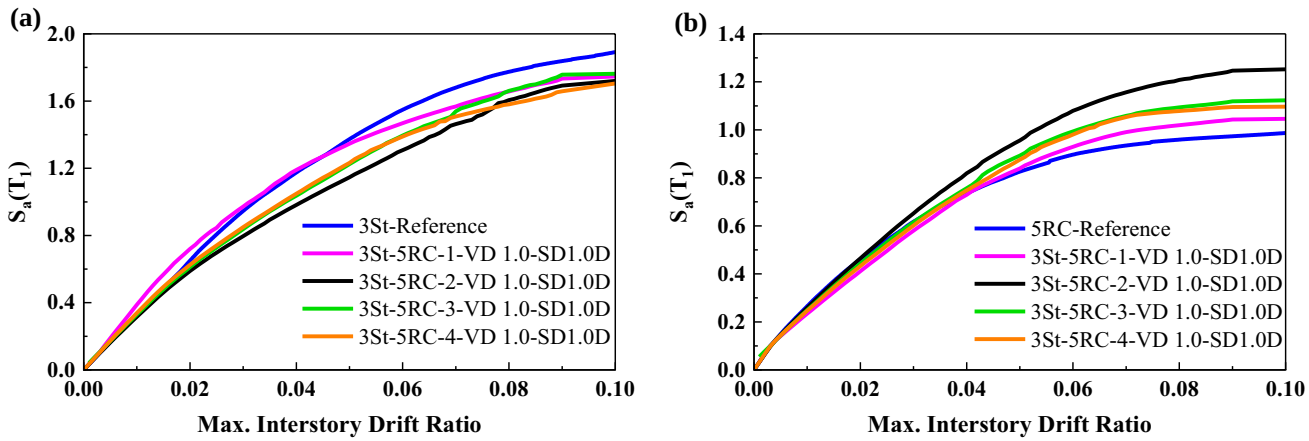

Fig. 12 Comparison M-IDAs of **a** 3-story SMRF, **b** 5-story RC MRF in pounding condition including NPL record subset for SD of 1.0D

Table 9 Limited state capacities of the 3-story SMRF and 5-story RC MRF structures subjected to NPL record subsets for SD of 1.0D

Model name	3-Story SMRF				5-Story RC MRF			
	IO	LS	CP	C	IO	LS	CP	C
3St-5RC-SD1.0D	0.229	0.806	1.373	1.892	0.265	0.461	0.734	0.987
3St-5RC-1-VD 1.0-SD1.0D	**0.268**	**0.845**	**1.190**	1.746	0.234	0.411	0.729	1.040
3St-5RC-2-VD 1.0-SD1.0D	0.225	0.697	0.981	1.699	**0.258**	**0.464**	**0.818**	**1.252**
3St-5RC-3-VD 1.0-SD1.0D	0.230	0.728	1.036	**1.802**	0.248	0.443	0.756	1.123
3St-5RC-4-VD 1.0-SD1.0D	0.240	0.740	1.048	1.664	0.246	0.432	0.747	1.109

Bold values indicate the best results obtained from implementing VDs

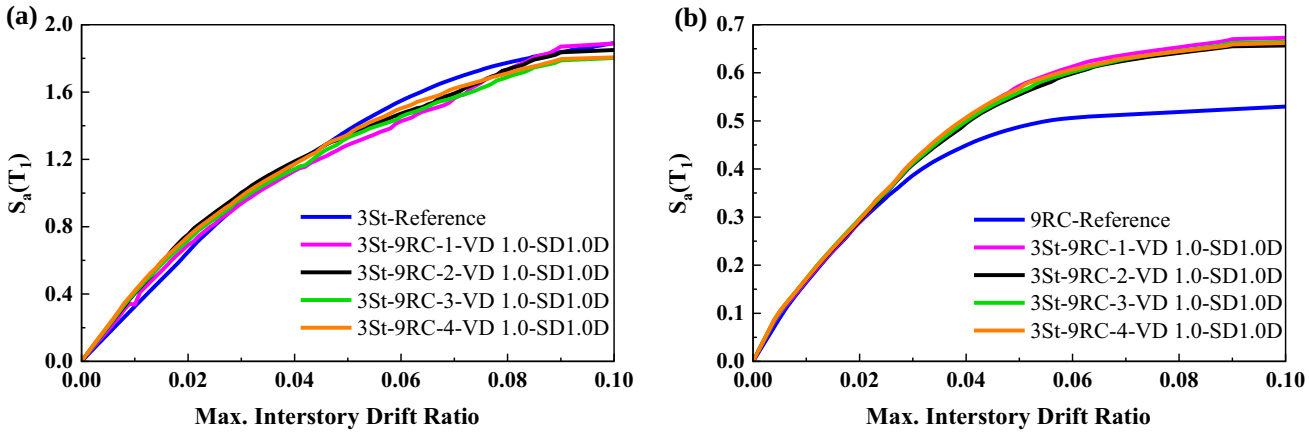

Fig. 13 Comparison M-IDAs of **a** the 3-story SMRF, **b** the 9-story RC MRF in pounding condition including NPL record subset for SD of 1.0D

respectively, and for the performance level of C, the 3St-9RC-1 condition has the highest increase, i.e. by 27.03% (from 0.529 to 0.672). Therefore, the best model to enhance the performance levels of the 9-story RC MRF is 3St-9RC-4 and 3St-9RC-1 according to the condition defined in Table 4. It can also be seen that adding LVDs does not have a significant effect on M-IDAs of the 3-story SMRF. Although in previous models of pounding between the 3-story SMRF and 3-, and 5-story RC MRF, the M-IDAs of the 3-story SMRF significant reduction was obtained, pounding between the 3-story SMRF and the 9-story RC MRF has smaller effect on M-IDAs of the 3-story SMRF. Therefore, by increasing the height of the adjacent structure, M-IDAs of the 3-story SMRF will have fewer changes. Table 10 provides information on M-IDAs of the 3-story SMRF in detail. The results can also be used for retrofitting both adjacent structures. For example, if the 3St-9RC-4 condition is selected for retrofitting the 9-story RC MRF adjacent to the 3-story SMRF, it will have a significant influence on M-IDAs of the 9-story RC MRF according to the information presented in Table 10. On other side, it will increase M-IDAs of the 3-story SMRF in performance levels of IO and LS, while decreasing the values of performance levels of CP and C. In this condition in retrofitting, it is suggested to check and retrofit the adjacent structure for the performance levels of CP and C, while it can be neglected in conservative way for other performances. It is worth noting that similar results were also observed for other record subsets.

3.6 Comparing M-IDAs of 5-story SMRF pounding with RC MRFs

Figure 14 presents the results of using LVDs on M-IDAs of the 5-story SMRF and the 5-story RC MRF subjected to NPL for SD of 1.0D. Using LVDs at all floor levels (5St-5RC-4) increases M-IDAs for the 5-story RC MRF by 30.3% (from 0.987 to 1.286) which is more than for other assumed models considering LVD at the 5th floor level (5St-5RC-1), at both 2nd and 5th floor levels (5St-5RC-2), and at the 1st, 3rd and 5th floor levels (5St-5RC-3) by 15.5%, 23.6%, and 21.3%, respectively. Therefore, the condition of 5St-5RC-4 is the best alternative to implement LVDs between structures. Table 11 presents details of M-IDAs of colliding structures in all performance levels. For the 5-story SMRF, the condition of 5St-5RC-1 is a better alternative due to the fact that it increases M-IDAs of the 5-story SMRF in IO and LS by 19.2% and 12.2%, respectively, while it decreases the values of CP and C by 1.5% and 0.39%, respectively. It can be seen that the reduction values of performance levels of CP and C do not significantly influence M-IDAs of the 5-story SMRF.

Table 10 Limited state capacities of the 3-story SMRF and the 9-story RC MRF subjected to NPL record subsets for SD of 1.0D

Model name	3-Story SMRF				9-Story RC MRF			
	IO	LS	CP	C	IO	LS	CP	C
3St-9RC-SD1.0D	0.229	0.806	1.373	1.892	0.164	0.289	0.449	0.529
3St-9RC-1-VD 1.0-SD1.0D	0.263	0.815	1.285	**1.891**	0.167	0.289	0.501	**0.672**
3St-9RC-2-VD 1.0-SD1.0D	0.286	**0.884**	1.342	1.850	0.170	0.291	0.494	0.656
3St-9RC-3-VD 1.0-SD1.0D	0.291	0.845	1.328	1.802	0.172	0.294	0.499	0.664
3St-9RC-4-VD 1.0-SD1.0D	**0.299**	0.865	**1.344**	1.806	**0.173**	**0.295**	**0.506**	0.662

Bold values indicate the best results obtained from implementing VDs

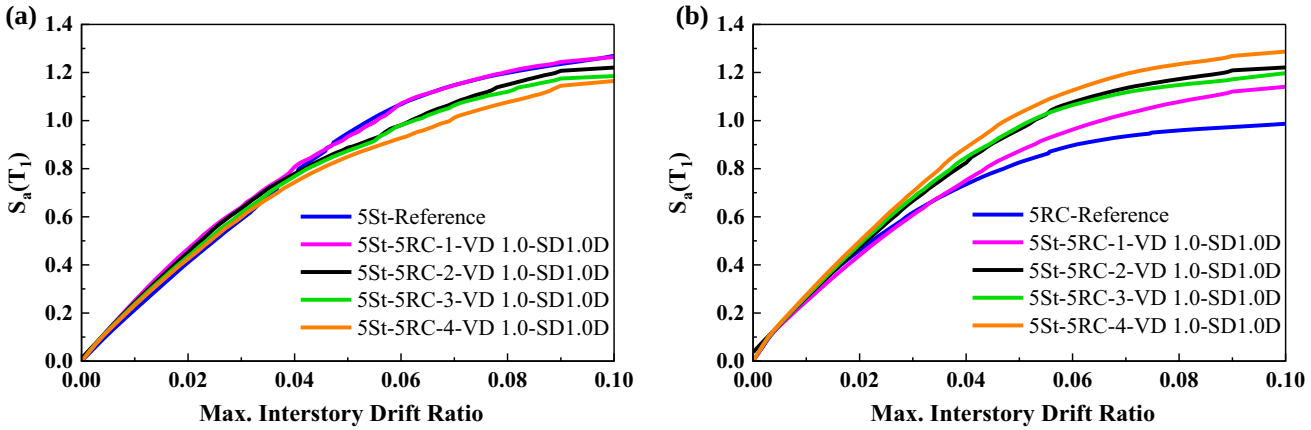

Fig. 14 Comparison M-IDAs of **a** the 5-story SMRF, **b** the 5-story RC MRF in pounding condition including NPL record subset for SD of 1.0D

For retrofitting purposes, using condition of 5St-5RC-4 can be the best suggestion for the 5-story RC MRF due to its increasing effects in all performance levels, but it should be said that this condition has a reduction effect on the CP and C performances of the 5-story SMRF. Therefore, it is suggested to check and retrofit the adjacent structure for the CP and C performances.

Figure 15 presents the results of using LVDs on M-IDAs of the 5-story SMRF and the 5-story RC MRF subjected to NNP for SD of 0.0. Using LVDs in all floor levels (5St-5RC-4) increases M-IDAs for the 5-story RC MRF by 59.6% (from 0.987 to 1.575) which is more than for other assumed models considering LVD at the 5th floor level (5St-5RC-1), at both 2nd and 5th floor levels (5St-5RC-2), and at the 1st, 3rd and 5th floor levels (5St-5RC-3) by 40.4%, 48.3%, and 48.3%, respectively. It can be noted that by decreasing the SD from 1.0 to 0.0, the performance of LVDs implemented at all floor levels (5St-5RC-4) between the 5-story SMRF and the 5-story RC MRF increases by 37.71% (from 23.25% for SD of 1.0 to 37.33% for SD of 0.0). Therefore, this strategy is more useful to retrofit the 5-story RC MRF in any adjacency condition. Table 12 presents details of M-IDAs of colliding structures in all performance levels.

For the 5-story SMRF, the condition of 5St-5RC-3 is a better alternative due to the increased M-IDAs of the 5-story SMRF in performance levels of IO, LS, and CP by 5.9%, 13.2%, and 1.86%, respectively, while it decreases the value of performance level of C by 0.39%. According to retrofitting criteria (Seismic Evaluation and Retrofit of Existing Buildings), there were some retrofitting purposes that the designer regarding the knowledge about the structure can choose for a building to check them. Most of the purposes of retrofitting

Table 11 Limited state capacities of the 5-story SMRF and the 5-story RC MRF subjected to NPL record subsets for SD of 1.0D

Model name	5-Story SMRF				5-Story RC MRF			
	IO	LS	CP	C	IO	LS	CP	C
5St-5RC-SD1.0D	0.151	0.501	0.947	1.269	0.265	0.461	0.734	0.987
5St-5RC-1-VD 1.0-SD1.0D	**0.180**	**0.562**	**0.933**	**1.264**	0.248	0.439	0.752	1.140
5St-5RC-2-VD 1.0-SD1.0D	0.176	0.552	0.887	1.220	0.264	0.474	0.824	1.220
5St-5RC-3-VD 1.0-SD1.0D	0.172	0.528	0.874	1.185	0.268	0.485	0.846	1.197
5St-5RC-4-VD 1.0-SD1.0D	0.168	0.515	0.849	1.165	**0.275**	**0.498**	**0.887**	**1.286**

Bold values indicate the best results obtained from implementing VDs

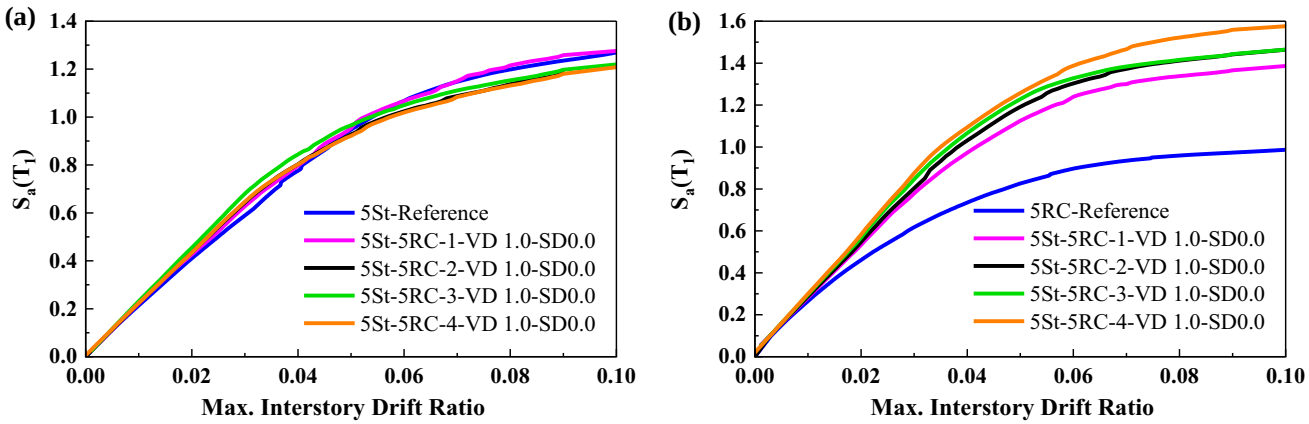

Fig. 15 Comparison M-IDAs of **a** the 5-story SMRF, **b** the 5-story RC MRF in pounding condition including NNP record subset for SD of 0.0

Table 12 Limited state capacities of the 5-story SMRF and the 5-story RC MRF subjected to NNP record subsets for SD of 0.0D

model name	5-Story SMRF				5-Story RC MRF			
	IO	LS	CP	C	IO	LS	CP	C
5St-5RC-SD0.0D	0..153	0.501	0.947	1.269	0.265	0.461	0.734	0.987
5St-5RC-1-VD 1.0-SD0.0D	0.156	0.522	0.953	**1.275**	0.282	0.533	0.972	1.386
5St-5RC-2-VD 1.0-SD0.0D	0.157	0.541	0.927	1.220	0.287	0.547	1.031	1.464
5St-5RC-3-VD 1.0-SD0.0D	**0.162**	**0.567**	**0.965**	1.219	0.296	0.567	1.066	1.464
5St-5RC-4-VD 1.0-SD0.0D	0.159	0.543	0.921	1.208	**0.299**	**0.582**	**1.094**	**1.575**

Bold values indicate the best results obtained from implementing VDs

are directed to achieve the performance levels of IO and LS. Therefore, in these performance levels, the designer should consider both structures' performances to assure choosing the best alternative in implementing the LVDs between the structures. In addition, the designer can choose the condition of 5St-5RC-1 regarding the details presented in Table 12. In this condition, although the performance levels of the 5-story SMRF were more or less unchanged (fluctuating between + 4.02% and − 0.47%), the performance levels of IO, LS, CP, and C for the 5-story RC MRF increased by 6.4%, 15.6%, 32.4%, and 40.4%, respectively.

Figure 16 presents the results of using LVDs on M-IDAs of the 5-story SMRF and the 9-story RC MRF subjected to NPL for SD of 1.0D. Using LVDs at both 2nd and 5th floor levels (5St-9RC-2) can be a good alternative for the 9-story RC MRF that causes a reduction in performance levels of IO and LS by 4.3% and 6.6%, respectively, while increasing the performance levels of CP and C by 2.39% and 23.3%, respectively. Other conditions of considering LVD at 5th floor level (5St-9RC-1), at the 1st, 3rd, and 5th floor levels (5St-9RC-3), and at all floor levels (5St-9RC-4) increase M-IDAs for the 9-story RC MRF by 6.8%, 11.9%, and 12.9%, respectively. Table 13 presents details of M-IDAs of colliding structures in all performance levels.

For the 5-story SMRF, the conditions of 5St-9RC-3 and 5St-9RC-4 are better alternatives due to increasing M-IDAs of the 5-story SMRF in performance levels of IO and LS by 30.1% and 10.2%, respectively. While for other performance levels, the conditions of 5St-9RC-1 can be chosen that decrease the values of the performance level of CP and C by 6.8% and 5.59%, respectively, less than for other conditions. Table 13 presents useful information concerning retrofitting these two adjacent structures. For example, the designer can decide to choose one of the conditions to implement the LVDs between the structures relying on the details provided in Table 13 and checking the effects of retrofitting one structure (e.g. the 5-story SMRF) on the other one (e.g. the 9-story RC MRF).

3.7 Comparing M-IDAs of 9-story SMRF pounding with RC MRFs

Figure 17 presents the results of using LVDs on M-IDAs of the 9-story SMRF and the 3-story RC MRF subjected to NPL for SD of 0.0. Using LVDs at all floor levels (9St-3RC-4) increases M-IDAs for the 3-story RC MRF in

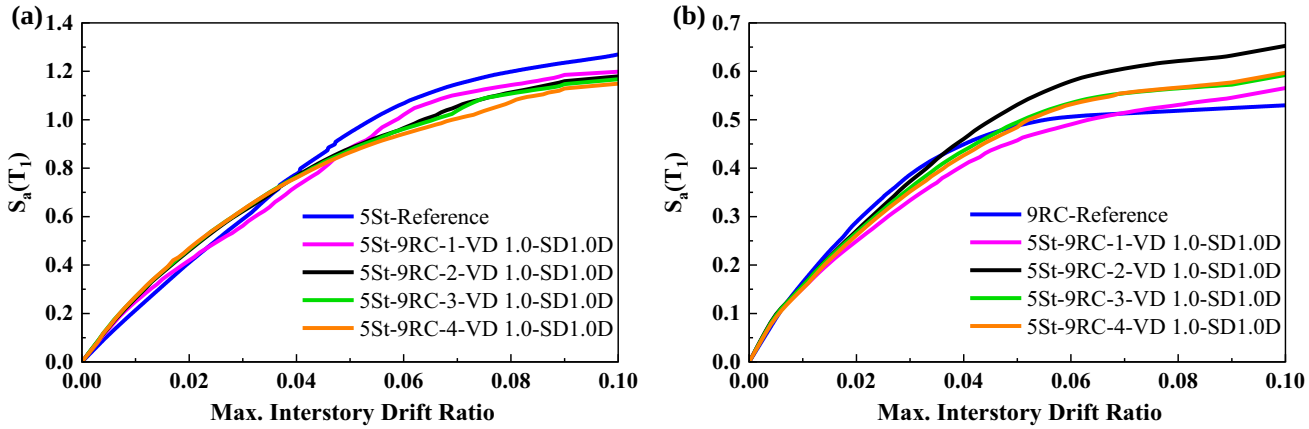

Fig. 16 Comparison M-IDAs of **a** the 5-story SMRF, **b** the 9-story RC MRF in pounding condition including NPL record subset for SD of 1.0D

Table 13 Limited state capacities of the 5-story SMRF and 9-story RC MRF subjected to NPL record subsets for SD of 1.0D

Model name	5-Story SMRF				9-Story RC MRF			
	IO	LS	CP	C	IO	LS	CP	C
5St-9RC-SD1.0D	0.153	0.501	0.947	1.269	0.164	0.289	0.449	0.529
5St-9RC-1-VD 1.0-SD1.0D	0.187	0.493	**0.883**	**1.198**	0.151	0.249	0.406	0.565
5St-9RC-2-VD 1.0-SD1.0D	0.193	0.546	0.881	1.179	**0.157**	**0.270**	**0.460**	**0.652**
5St-9RC-3-VD 1.0-SD1.0D	**0.199**	**0.552**	0.875	1.167	0.156	0.266	0.436	0.592
5St-9RC-4-VD 1.0-SD1.0D	**0.199**	**0.552**	0.865	1.149	0.151	0.261	0.426	0.597

Bold values indicate the best results obtained from implementing VDs

performance levels of IO, LS, CP, and C by 11.2%, 18%, 42.5%, and 32.8%, respectively. Moreover, other conditions of considering LVD at the 2nd floor level (9St-3RC-1), at the 3rd floor level (9St-3RC-2), and at the 1st and 3rd floor levels (9St-3RC-3) increase M-IDAs for the 3-story RC MRF by 16.7%, 19.9%, and 7.3%, respectively. Table 14 presents details of M-IDAs of colliding structures in all performance levels. For the 9-story SMRF, the conditions of 9St-3RC-3 and 9St-3RC-1 are better alternatives due to increasing M-IDAs of the 9-story SMRF in performance levels of IO and LS by 30.4% and 8%, respectively, and increasing the performance levels of CP and C by 21.1% and 36%, respectively. Although using the condition of (9St-3RC-4) is the best alternative for the 3-story RC MRF, this condition also stands in the second rate for the 9-story SMRF. Therefore, according to Table 14, for retrofitting purposes, the designer can decide to choose one of the conditions to implement the LVDs between the structures.

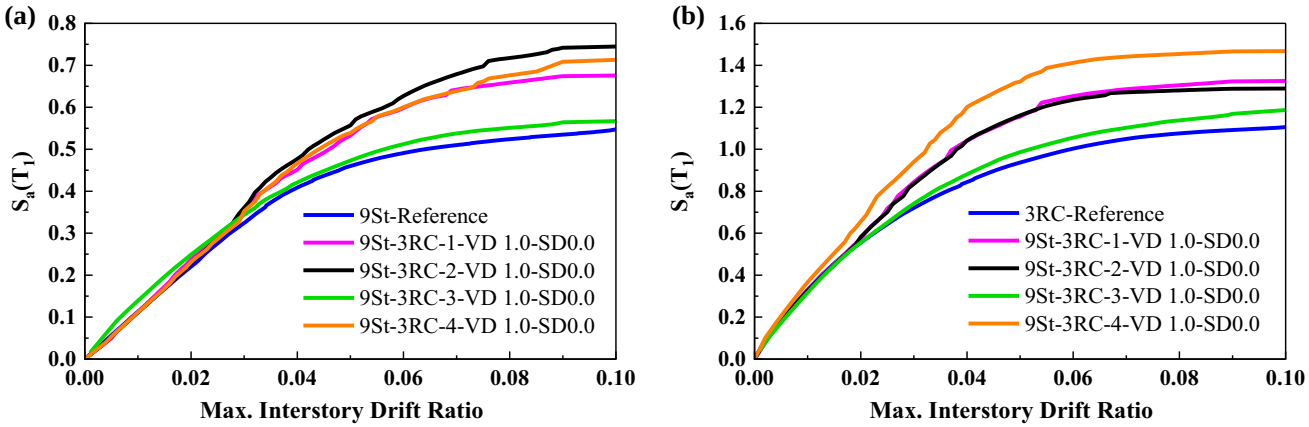

Fig. 17 Comparison M-IDAs of **a** the 9-story SMRF, **b** the 3-story RC MRF in pounding condition including NPL record subset for SD of 0.0

Table 14 Limited state capacities of the 9-story SMRF and 3-story RC MRF subjected to NPL record subsets for SD of 0.0D

Model name	9-Story SMRF				3-Story RC MRF			
	IO	LS	CP	C	IO	LS	CP	C
9St-3RC-SD0.0D	0.079	0.275	0.459	0.547	0.329	0.555	0.843	1.105
9St-3RC-1-VD 1.0-SD0.0D	0.076	0.284	**0.556**	**0.744**	0.325	0.581	1.041	1.289
9St-3RC-2-VD 1.0-SD0.0D	0.076	0.283	0.532	0.675	0.328	0.574	1.040	1.325
9St-3RC-3-VD 1.0-SD0.0D	**0.103**	**0.297**	0.472	0.566	0.317	0.555	0.880	1.186
9St-3RC-4-VD 1.0-SD0.0D	0.079	0.285	0.538	0.713	**0.366**	**0.655**	**1.201**	**1.467**

Bold values indicate the best results obtained from implementing VDs

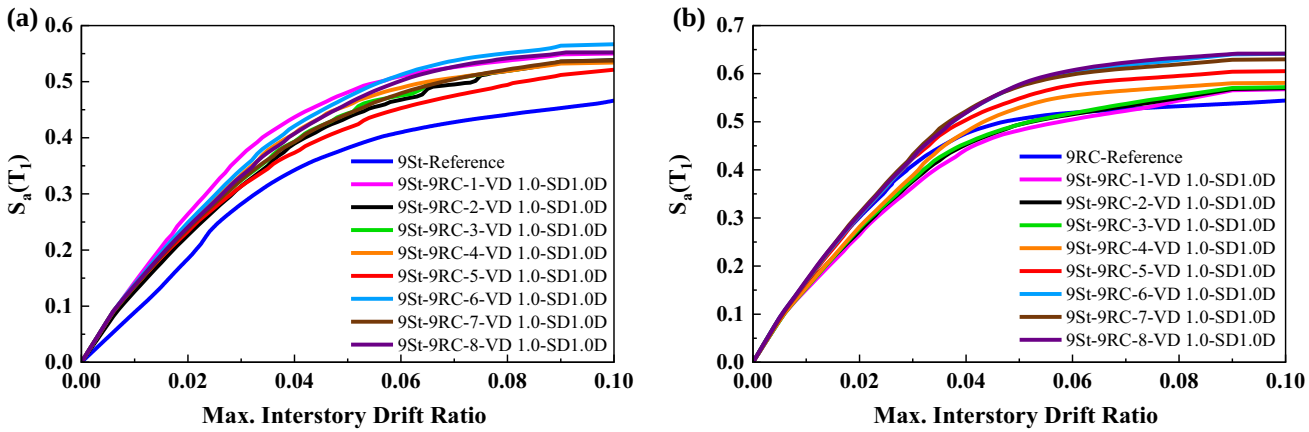

Fig. 18 Comparison M-IDAs of **a** the 9-story SMRF, **b** the 9-story RC MRF in pounding condition including NPL record subset for SD of 1.0D

Table 15 Limited state capacities of the 9-story SMRF and 9-story RC MRF structures subjected to NPL record subsets for SD of 1.0D

Model name	9-Story RC MRF				9-Story SMRF			
	IO	LS	CP	C	IO	LS	CP	C
9St-9RC-SD1.0D	0.062	0.242	0.381	0.466	0.166	0.301	0.475	0.544
9St-9RC-1-VD 1.0-SD1.0D	**0.103**	**0.317**	**0.480**	0.550	0.151	0.265	0.442	0.567
9St-9RC-2-VD 1.0-SD1.0D	0.094	0.271	0.436	0.538	0.157	0.272	0.452	0.569
9St-9RC-3-VD 1.0-SD1.0D	0.102	0.281	0.443	0.536	0.154	0.278	0.455	0.572
9St-9RC-4-VD 1.0-SD1.0D	**0.103**	0.289	0.457	0.534	0.155	0.281	0.479	0.581
9St-9RC-5-VD 1.0-SD1.0D	0.102	0.275	0.417	0.521	0.165	0.304	0.503	0.605
9St-9RC-6-VD 1.0-SD1.0D	**0.103**	0.297	0.472	**0.566**	0.168	0.305	0.519	0.641
9St-9RC-7-VD 1.0-SD1.0D	0.101	0.282	0.442	0.537	**0.170**	**0.310**	**0.522**	0.629
9St-9RC-8-VD 1.0-SD1.0D	**0.103**	0.286	0.460	0.553	0.168	0.307	0.518	**0.649**

Bold values indicate the best results obtained from implementing VDs

Figure 18 presents the results of using LVDs on M-IDAs of the 9-story SMRF and the 9-story RC MRF subjected to NPL for SD of 1.0D. Implementing LVDs at the floor levels of the 1st, 3rd, 5th, 7th, and 9th (9St-9RC-7) increases M-IDAs for the 9-story RC MRF in performance levels of IO, LS, and CP by 2.4%, 2.9%, and 9.9%, respectively. While for the performance level of C, the condition of 9St-9RC-8 increases M-IDAs for the 9-story RC MRF by 19.3%, which is more than for other conditions. Table 15 presents details of M-IDAs of colliding structures in all performance levels.

For the 9-story SMRF, all the conditions increase the amount of M-IDAs and they can be chosen for retrofitting purposes. The conditions of 9St-9RC-1, 9St-9RC-4, 9St-9RC-6, and 9St-9RC-8 are good alternatives to increase the performance level of IO by 66.1%. The only difference between them is the cost of implementation of LVDs. In the condition of 9St-9RC-1, only one LVD at the top floor can increase M-IDAs of the 9-story SMRF in the performance level of IO by the same value as in the case of other conditions (e.g. 9St-9RC-4, 9St-9RC-6, and 9St-9RC-8) with a lower cost of the implementation. In addition, the condition of 9St-9RC-1 is the best alternative for increasing the performance levels of LS and CP by 31% and 26%, respectively. Moreover, the condition of 9St-9RC-6 increases the performance level of C by 21.5%. It can be noted that using Table 15 can help designers to choose and compare the alternatives of adding LVDs between the structures by considering the amount of increased values of performance levels and the cost of the implementation. Also, it is suggested that the performance levels of the adjacent structure should be checked based on the influence of adding LVDs that were presented in the figures.

4 Seismic failure probability

To evaluate the effects of implemented VDs, the seismic fragility curves were plotted for the performance level of C. Figure 19 illustrates the seismic fragility curves of the

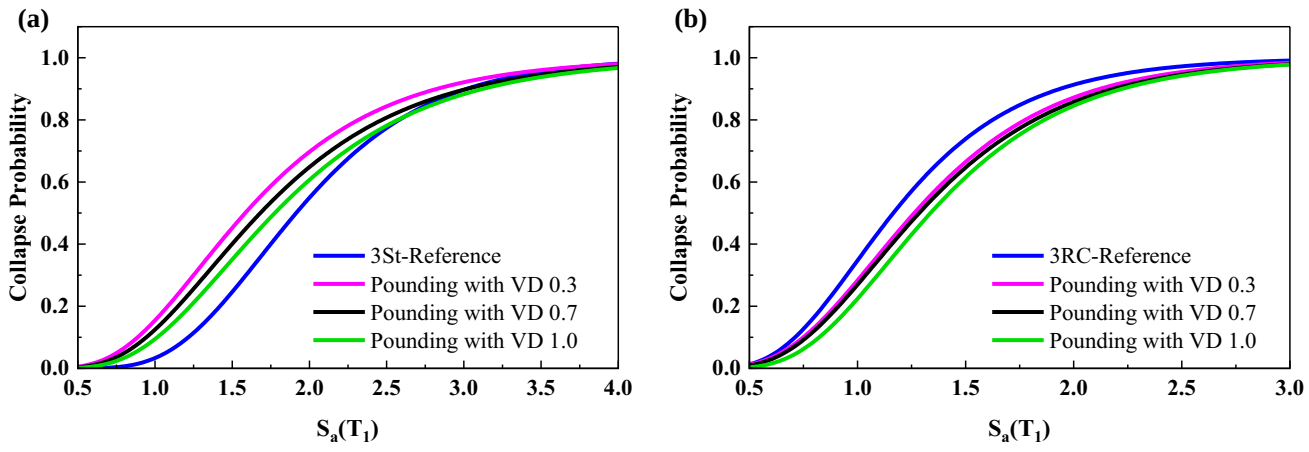

Fig. 19 Seismic fragility curves of **a** the 3-story SMRF, **b** the 3-story RC MRF assuming implemented NVDs or LVDs in second story level including NNP record subset for SD of 1.0D

3-story SMRF and RC MRF with different types of VDs implemented on second story level including NNP records given SD of 1.0D. The $S_a(T_1)$ corresponding to the failure probability of 50% for the 3-story SMRF in the performance level of C assuming VDs with damper velocity exponent of 0.3, 0.7, and 1.0 were determined by 1.61, 1.71, and 1.79, respectively, in which, the LVDs achieved higher values of $S_a(T_1)$ that shows the lower value of the failure probability. On the other side, the $S_a(T_1)$ corresponding to the failure probability of 50% for the 3-story RC MRF in the performance level of C assuming VDs with damper velocity exponent of 0.3, 0.7, and 1.0 were determined by 1.27, 1.29, and 1.35, respectively. The results confirmed that the structures with implemented LVDs achieved higher values of $S_a(T_1)$ in the failure probability of 50%.

Figures 20 and 21 illustrate the seismic fragility curves of the 3-story and 5-story SMRFs colliding with RC MRFs of similar height assuming different types of implementing VDs including NNP and NPL records and SD of 1.0D, respectively. It is obvious that adding LVDs can significantly decrease the seismic failure probability of RC MRFs, while it can increase the seismic failure probability of SMRFs. Therefore, it can be concluded that different types of lateral resisting systems can affect the results of implementing VDs between the adjacent structures with similar heights. In addition, implementing VDs in all story levels can be the best alternative for retrofitting the RC MRFs, while this condition can significantly increase the seismic failure probability of SMRFs. Thus, it is recommended that the condition of adjacent structure should be considered in the retrofitting process.

Figures 22 and 23 illustrate the fragility curves of the 3-story SMRF and 5-story RC MRF, and the 5-story SMRF and 9-story RC MRF including NNP records and SD of

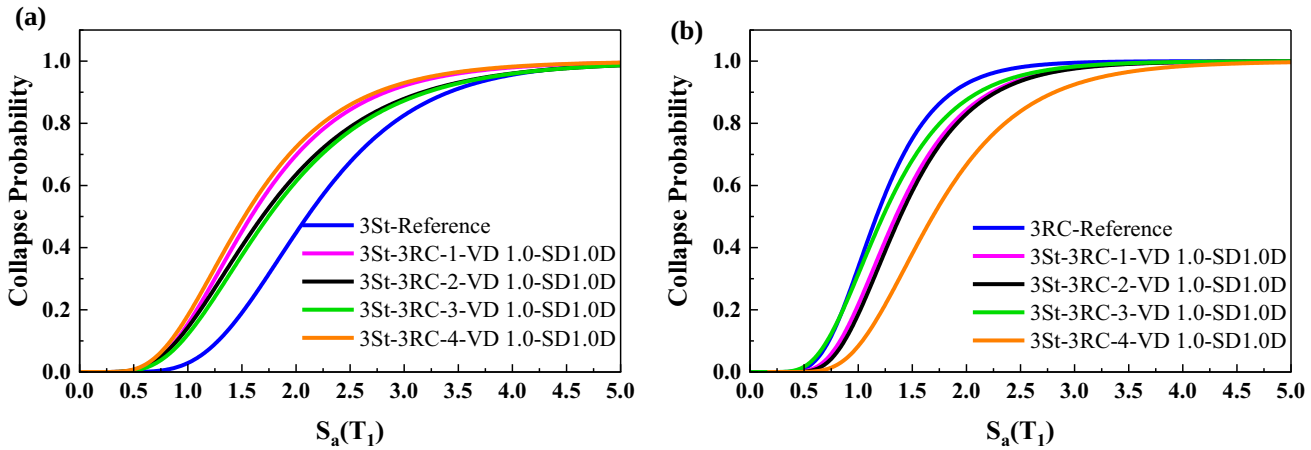

Fig. 20 Seismic fragility curves of **a** the 3-story SMRF, **b** the 3-story RC MRF in pounding condition including NNP record subset for SD of 1.0D

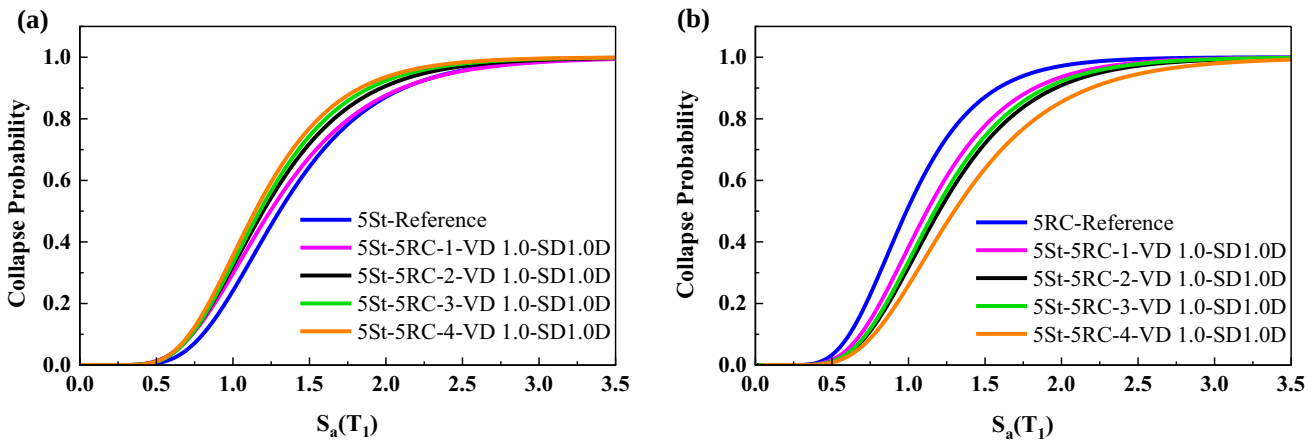

Fig. 21 Seismic fragility curves of **a** the 5-story SMRF, **b** the 5-story RC MRF in pounding condition including NPL record subset for SD of 1.0D

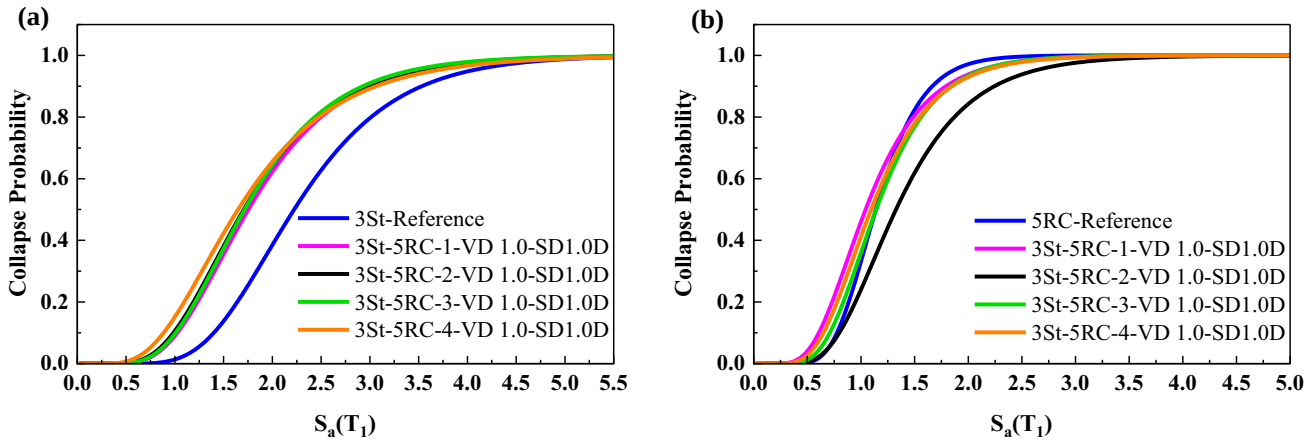

Fig. 22 Seismic fragility curves of **a** the 3-story SMRF, **b** the 5-story RC MRF in pounding condition including NNP record subset for SD of 1.0D

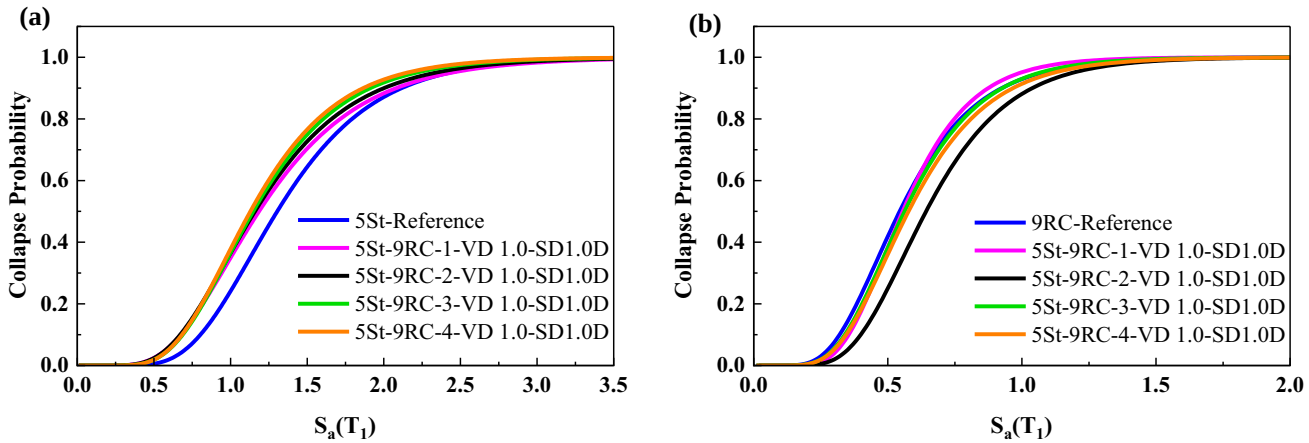

Fig. 23 Seismic fragility curves of **a** the 5-story SMRF, **b** the 9-story RC MRF in pounding condition including NNP record subset for SD of 1.0D

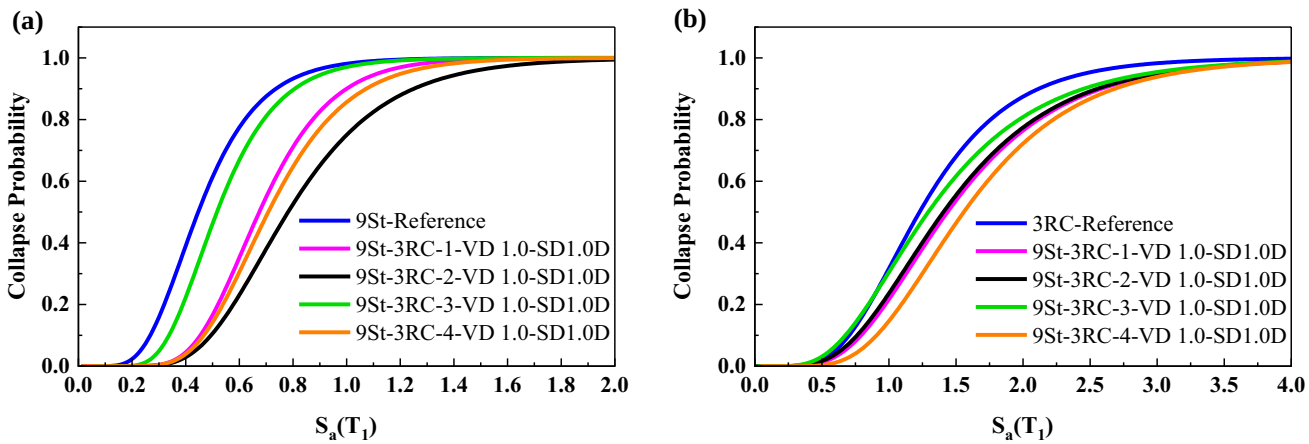

Fig. 24 Seismic fragility curves of **a** the 9-story SMRF, **b** the 3-story RC MRF in pounding condition including NNP record subset for SD of 0.0

1.0D, respectively. It is presented that implementing VDs can increase the failure probability of shorter structures (i.e. the 3-, and 5-story SMRFs), while the failure probability of taller structure remains more or less unchanged, except for placement of condition two (see Table 4). In the case of pounding between taller and shorter structures, results of failure probability for the 9-story SMRF and 3-story RC MRF, including NNP records for SD of 0.0, were compared in Fig. 24. It can be observed from the figure that implementing VDs in this condition can help both structures and improve their failure probabilities. It can be said that, due to possibility of collapse in the middle of the 9-story SMRF, implementing the VD in the top floor of the 3-story RC MRF prevents the failure of the 9-story SMRF; then, as a result, the failure probability is reduced. On the other hand, this situation helped the 3-story RC MRF to decrease the failure probability.

5 Retrofitting modification factors

Based on the results concerning the M-IDAs of colliding structures, Retrofitting Modification Factors (RMFs) were calculated after dividing the M-IDAs of the colliding structures in the retrofitted condition (presented in Table 4) by the corresponding values of M-IDAs without any retrofitting devices (e.g. VDs). The RMFs can be applied to the structures with the same conditions and structural elements

Table 16 RMF of the 3-story SMRF and the 3-story RC MRF subjected to all record subsets for SD of 0.0 and 1.0D

Model name	SD	3-Story SMRF				3-Story RC MRF			
		IO	LS	CP	C	IO	LS	CP	C
3St-3RC-1-VD 1.0	1.0D	1.000	0.878	0.821	0.855	1.036	1.076	1.110	1.124
	0.0	0.997	0.869	0.816	0.848	1.029	1.068	1.105	1.119
3St-3RC-2-VD 1.0	1.0D	0.969	0.831	0.888	0.946	0.842	0.908	0.972	1.134
	0.0	0.960	0.823	0.875	0.940	0.834	0.898	0.967	1.129
3St-3RC-3-VD 1.0	1.0D	1.140	0.927	0.876	0.938	0.964	1.000	1.044	1.073
	0.0	1.138	0.921	0.871	0.931	0.958	0.993	1.038	1.067
3St-3RC-4-VD 1.0	1.0D	1.052	0.880	0.824	0.838	1.079	1.114	1.185	1.325
	0.0	1.049	0.874	0.817	0.831	1.071	1.107	1.178	1.319

Table 17 RMF of the 3-story SMRF and the 5-story RC MRF subjected to all record subsets for SD of 0.0 and 1.0D

Model name	SD	3-Story SMRF				5-Story RC MRF			
		IO	LS	CP	C	IO	LS	CP	C
3St-5RC-1-VD 1.0	1.0D	1.170	1.048	0.867	0.923	0.883	0.892	0.993	1.054
	0.0	1.167	1.052	0.873	0.921	0.889	0.899	1.003	1.059
3St-5RC-2-VD 1.0	1.0D	0.983	0.865	0.714	0.898	0.974	1.007	1.114	1.268
	0.0	0.985	0.869	0.719	0.905	0.978	1.014	1.119	1.276
3St-5RC-3-VD 1.0	1.0D	1.004	0.903	0.755	0.952	0.936	0.961	1.030	1.138
	0.0	1.000	0.896	0.750	0.948	0.930	0.965	1.035	1.145
3St-5RC-4-VD 1.0	1.0D	1.048	0.918	0.763	0.879	0.928	0.937	1.018	1.124
	0.0	1.046	0.915	0.758	0.875	0.923	0.938	1.022	1.128

Table 18 RMF of the 3-story SMRF and the 9-story RC MRF subjected to all record subsets for SD of 0.0 and 1.0D

Model name	SD	3-Story SMRF				9-Story RC MRF			
		IO	LS	CP	C	IO	LS	CP	C
3St-9RC-1-VD 1.0	1.0D	1.148	1.011	0.936	0.999	1.018	1.000	1.116	1.270
	0.0	1.155	1.017	0.944	1.021	1.010	0.998	1115	1.268
3St-9RC-2-VD 1.0	1.0D	1.249	1.097	0.977	0.978	1.037	1.007	1.100	1.240
	0.0	1.245	1.090	0.979	0.988	1.044	1.015	1.110	1.251
3St-9RC-3-VD 1.0	1.0D	1.271	1.048	0.967	0.952	1.049	1.017	1.111	1.255
	0.0	1.266	1.044	0.960	0.945	1.048	1.014	1.106	1.250
3St-9RC-4-VD 1.0	1.0D	1.306	1.073	0.979	0.955	1.055	1.021	1.127	1.251
	0.0	1.300	1.067	0.970	0.947	1.059	1.028	1.129	1.258

Table 19 RMF of the 5-story SMRF and the 3-story RC MRF subjected to all record subsets for SD of 0.0 and 1.0D

Model name	SD	5-Story SMRF				3-Story RC MRF			
		IO	LS	CP	C	IO	LS	CP	C
5St-3RC-1-VD 1.0	1.0D	1.192	1.122	0.985	0.996	0.936	0.952	1.025	1.155
	0.0	1.188	1.118	0.989	0.999	0.933	0.960	1.032	1.161
5St-3RC-2-VD 1.0	1.0D	1.166	1.102	0.937	0.961	0.996	1.028	1.123	1.236
	0.0	1.161	1.002	0.944	0.967	0.990	1.032	1.126	1.239
5St-3RC-3-VD 1.0	1.0D	1.139	1.054	0.923	0.934	1.011	1.052	1.153	1.213
	0.0	1.136	1.040	0.934	0.944	1.003	1.062	1.156	1.219
5St-3RC-4-VD 1.0	1.0D	1.113	1.028	0.897	0.918	1.038	1.080	1.208	1.303
	0.0	1.109	1.027	0.902	0.926	1.033	1.072	1.198	1.295

Table 20 RMF of the 5-story SMRF and the 5-story RC MRF subjected to all record subsets for SD of 0.0 and 1.0D

Model name	SD	5-Story SMRF				5-Story RC MRF			
		IO	LS	CP	C	IO	LS	CP	C
5St-5RC-1-VD 1.0	1.0D	1.020	1.042	1.006	1.005	1.064	1.156	1.324	1.404
	0.0	1.025	1.044	1.010	1.011	1.066	1.159	1.329	1.409
5St-5RC-2-VD 1.0	1.0D	1.026	1.080	0.979	0.961	1.083	1.187	1.405	1.483
	0.0	1.027	1.088	0.983	0965	1.088	1.191	1.409	1.486
5St-5RC-3-VD 1.0	1.0D	1.059	1.132	1.019	0.961	1.117	1.230	1.452	1.483
	0.0	1.061	1.135	1.022	0.965	1.120	1.233	1.455	1.486
5St-5RC-4-VD 1.0	1.0D	1.039	1.084	0.973	0.952	1.128	1.262	1.490	1.596
	0.0	1.043	1.088	0.979	0.958	1.133	1.266	1.492	1.599

Table 21 RMF of the 5-story SMRF and the 9-story RC MRF subjected to all record subsets for SD of 0.0 and 1.0D

Model name	SD	5-Story SMRF				9-Story RC MRF			
		IO	LS	CP	C	IO	LS	CP	C
5St-9RC-1-VD 1.0	1.0D	1.222	0.984	0.932	0.944	0.921	0.862	0.904	1.068
	0.0	1.220	0.988	0.936	0.946	0.922	0.865	0.908	1.072
5St-9RC-2-VD 1.0	1.0D	1.261	1.090	0.930	0.929	0.957	0.934	1.024	1.233
	0.0	1.256	1.099	0.937	0.933	0.961	0.937	1.028	1.238
5St-9RC-3-VD 1.0	1.0D	1.301	1.102	0.924	0.920	0.951	0.920	0.971	1.119
	0.0	1.298	1.106	0.927	0.924	0.956	0.922	0.976	1.122
5St-9RC-4-VD 1.0	1.0D	1.301	1.102	0.913	0.905	0.921	0.903	0.949	1.129
	0.0	1.293	1.06	0.916	0.908	0.925	0.908	0.953	1.133

Table 22 RMF of the 9-story SMRF and the 3-story RC MRF subjected to all record subsets for SD of 0.0 and 1.0D

Model name	SD	9-Story SMRF				3-Story RC MRF			
		IO	LS	CP	C	IO	LS	CP	C
9St-3RC-1-VD 1.0	1.0D	0.962	1.033	1.211	1.360	0.988	1.047	1.235	1.167
	0.0	0.966	1.036	1.217	1.362	0.993	1.052	1.239	1.171
9St-3RC-2-VD 1.0	1.0D	0.962	1.029	1.159	1.234	0.997	1.034	1.234	1.199
	0.0	0.966	1.035	1.167	1.237	1.008	1.039	1.238	1.205
9St-3RC-3-VD 1.0	1.0D	1.304	1.080	1.028	1.035	0.964	1.000	1.044	1.073
	0.0	1.308	1.085	1.032	1.037	0.969	0.993	1.038	1.068
9St-3RC-4-VD 1.0	1.0D	1.000	1.036	1.172	1.303	1.112	1.180	1.425	1.328
	0.0	0.993	1.039	1.177	1.305	1.119	1.174	1.420	1.323

Table 23 RMF of the 9-story SMRF and the 5-story RC MRF subjected to all record subsets for SD of 0.0 and 1.0D

Model name	SD	9-Story SMRF				5-Story RC MRF			
		IO	LS	CP	C	IO	LS	CP	C
9St-5RC-1-VD 1.0	1.0D	0.977	1.102	1.126	1.129	0.908	1.117	1.247	1.178
	0.0	0.982	1.109	1.129	1.135	0.917	1.123	1.254	1.184
9St-5RC-2-VD 1.0	1.0D	0.950	1.003	1.212	1.108	0.999	1.056	1.235	1.201
	0.0	0.957	1.005	1.208	1.116	1.009	1.065	1.242	1.208
9St-5RC-3-VD 1.0	1.0D	1.211	1.121	1.045	1.110	0.989	1.023	1.078	1.088
	0.0	1.208	1.127	1.049	1.117	0.994	1.029	1.083	1.094
9St-5RC-4-VD 1.0	1.0D	1.130	1.250	1.081	1.124	1.108	1.230	1.455	1.342
	0.0	1.125	1.255	1.089	1.129	1.111	1.234	1.459	1.347

Table 24 RMF of the 9-story SMRF and the 9-story RC MRF subjected to all record subsets for SD of 0.0 and 1.0D

Model name	SD	9-Story SMRF				9-story RC MRF			
		IO	LS	CP	C	IO	LS	CP	C
9St-9RC-1-VD 1.0	1.0D	1.661	1.310	1.260	1.180	0.910	0.880	0.931	1.042
	0.0	1.668	1.312	1.266	1.189	0.918	0.888	0.933	1.040
9St-9RC-2-VD 1.0	1.0D	1.516	1.120	1.144	1.155	0.946	0.904	0.952	1.046
	0.0	1.508	1.122	1.149	1.159	0.951	0.911	0.956	0.044
9St-9RC-3-VD 1.0	1.0D	1.645	1.161	1.163	1.150	0.928	0.924	0.958	1.051
	0.0	1.649	1.163	1.166	1.148	0.927	0.929	0.962	1.049
9St-9RC-4-VD 1.0	1.0D	1.661	1.194	1.199	1.146	0.934	0.934	1.008	1.068
	0.0	1.668	1.197	1.203	1.147	0.933	0.938	1.018	1.067
9St-9RC-5-VD 1.0	1.0D	1.645	1.136	1.094	1.118	0.994	1.010	1.059	1.112
	0.0	1.649	1.138	1.099	1.121	0.999	1.014	1.066	1.110
9St-9RC-6-VD 1.0	1.0D	1.661	1.227	1.239	1.215	1.012	1.013	1.093	1.178
	0.0	1.668	1.232	1.244	1.219	1.018	1.017	1.099	1.169
9St-9RC-7-VD 1.0	1.0D	1.629	1.165	1.160	1.152	1.024	1.030	1.099	1.156
	0.0	1.631	1.169	1.163	1.163	1.033	1.038	1.103	1.155
9St-9RC-8-VD 1.0	1.0D	1.661	1.182	1.207	1.187	1.012	1.020	1.091	1.193
	0.0	1.668	1.185	1.213	1.196	1.019	1.028	1.098	1.195

to help designers approximately calculate the performance levels of the colliding structures when using LVDs. RMFs can be used for all kinds of assumed structures and aforementioned SDs. According to the results for different record subsets, the difference between the performance levels of M-IDAs for the colliding structures with and without retrofitting devices are approximately equal. Therefore, RMFs can be successfully used for colliding structures subjected to three aforementioned record subsets. In addition, RMFs can help designers to estimate the amount of M-IDAs after retrofitting. To calculate RMFs, the pounding model and the condition of retrofitting according to the Table 4 should be firstly selected. Then the values obtained from Tables 16, 17, 18, 19, 20, 21, 22, 23 and 24 can be applied to the pounding condition of models. For example, for the condition of 9St-3RC-3 for SD of 1.0D, M-IDAs of the 9-story SMRF and 3-story RC MRF colliding structures should be multiplied by 1.035 and 1.073 (RMFs according to Table 22), respectively, to achieve the performance level of C of the retrofitted structures.

6 Conclusions

This study has been focused on seismic limit-states of SMRFs and RC MRFs prone to earthquake-induced pounding. The effects of adding VDs between adjacent structures have been carried out and proper RMFs for retrofitting purposes have been determined assuming three SDs of 0.0, 0.5D, and 1.0D. In this study, a Tcl code was developed to assess the limit-state capacity of adjacent pounding structures taking into account the collapsed structure. The results are summarized as follows:

- The results confirm that pounding between adjacent structures can cause an increase in the maximum values of the moment-rotation curves of beams and columns

(e.g. beam and column of the 3-story SMRF colliding with 5-story RC MRF experienced an increase by 16% and 29.1%, respectively). The placement of LVDs between structures can be effective to reduce the values of the moment-rotation curves for beams and columns by 48% and 31.25%, respectively.

- Regarding RC MRFs and SMRFs without any adjacent structure, the values of M-IDAs for the IO, LS, CP, and C performance levels of RC MRFs including the NNP records were higher than for other subsets. While this was correct for the 3-story SMRF, in the case of 5-, and 9-story SMRFs, the assumed performance levels in the FF subset were higher than for other subsets.
- Comparing the results of using NVDs and LVDs, it can be seen that LVDs attain better performance levels, as compared to the NVDs, for three different record subsets and SDs.
- The results confirm that implementing LVDs between adjacent structures play a crucial role in increasing the performance levels of RC MRFs. For example, in the condition of 3St-3RC-4, M-IDAs for the 3-story RC MRF increased by 32.48%, in the condition of 3St-5RC-2, M-IDAs for the 5-story RC MRF increased by 26.8%, in the condition of 3St-9RC-1, M-IDAs for the 9-story RC MRF increased by 27.03%. Although RC MRFs achieved higher performance levels, the alternative conditions were caused by the reduction in M-IDAs of the 3-story SMRF. Therefore, it is suggested to consider both structures' performance levels in retrofitting approach and choose the best model according to required performance levels.
- RMFs were proposed to approximately predict the M-IDAs of the structures after retrofitting. The RMFs can be easily applied to the structures with the same structural elements to help designers approximately calculate the performance levels of the colliding structures when using LVDs between the structures without involving analytical difficulties.
- Comparing pounding between MRFs of similar height (i.e. the 3-, and 5-story) shows that adding VDs can significantly decrease the seismic failure probability of RC MRFs, while it can increase the seismic failure probability of SMRFs. The results confirm that implementing VDs can increase the failure probability of shorter structures (i.e. the 3-, and 5-story SMRFs), while the failure probability of taller structure remains more or less unchanged, except for placement of condition two. Comparing pounding between taller SMRF and shorter RC MRF shows that implementing the VD at the top of the shorter RC MRF prevents the failure of the taller SMRF; then, as a result, the failure probability is reduced.
- To address the reason behind this, it can be said that pounding phenomenon leads to complex situation that any changes, such as lateral resisting system, total weight of structure, fundamental period, and implementing VDs, can affect the impact forces at the floor levels, which may change the seismic behavior of both structures. Therefore, it is recommended that the condition of adjacent structure should be considered in the retrofitting process of the building under investigation.

Author contributions All authors contributed to the study conception and design. Material preparation, data collection and analysis were performed by NA, FK, and RJ. The first draft of the manuscript was written by FK and all authors commented on previous versions of the manuscript. All authors read and approved the final manuscript. NA: Writing-original draft preparation, analysis, and investigation. FK: Methodology, Conceptualization, Writing. RJ: Review and editing, Supervision.

Declarations

Conflict of interest All authors declare that they have no conflict of interest.

Ethical approval This material is the authors' own original work, which has not been previously published elsewhere. The paper is not currently being considered for publication elsewhere. The paper reflects the authors' own research and analysis in a truthful and complete manner.

Open Access This article is licensed under a Creative Commons Attribution 4.0 International License, which permits use, sharing, adaptation, distribution and reproduction in any medium or format, as long as you give appropriate credit to the original author(s) and the source, provide a link to the Creative Commons licence, and indicate if changes were made. The images or other third party material in this article are included in the article's Creative Commons licence, unless indicated otherwise in a credit line to the material. If material is not included in the article's Creative Commons licence and your intended use is not permitted by statutory regulation or exceeds the permitted use, you will need to obtain permission directly from the copyright holder. To view a copy of this licence, visit http://creativecommons.org/licenses/by/4.0/.

References

1. Sołtysik B, Jankowski R. Non-linear strain rate analysis of earthquake-induced pounding between steel buildings. Int J Earth Sci Eng. 2013;6(3):429–33.
2. Elwardany H, Seleemah A, Jankowski R, El-Khoriby S. Influence of soil–structure interaction on seismic pounding between steel frame buildings considering the effect of infill panels. Bull Earthq Eng. 2019;17(11):6165–202.
3. Rezaei H, Moayyedi SA, Jankowski R. Probabilistic seismic assessment of RC box-girder highway bridges with unequal-height piers subjected to earthquake-induced pounding. Bull Earthq Eng. 2020;18(4):1547–78.
4. Kazemi F, Asgarkhani N, Manguri A, Jankowski R. Investigating an optimal computational strategy to retrofit buildings with implementing viscous dampers. Int Conf Comput Sci ICCS Proc, Lecture Notes in Compu Sci, vol. 13351. 2022. p. 184–91. https://doi.org/10.1007/978-3-031-08754-7_25.

5. Kazemi F, Mohebi B, Yakhchalian M. Predicting the seismic collapse capacity of adjacent structures prone to pounding. Can J Civ Eng. 2020;47(6):663–77.
6. Cole G, Dhakal RP, Carr AJ, Bull D. Building pounding state of the art: Identifying structures vulnerable to pounding damage. In: Proceedings of New Zealand society for earthquake engineering annual conference, 2010.
7. Kazemi F, Mohebi B, Yakhchalian M. Evaluation the *P*-delta effect on collapse capacity of adjacent structures subjected to far-field ground motions. Civ Eng J. 2018;4(5):1066. https://doi.org/10.28991/cej-0309156.
8. Favvata MJ. Minimum required separation gap for adjacent RC frames with potential inter-story seismic pounding. Eng Struct. 2017;152:643–59.
9. Mohebi B, Kazemi F, Yakhchalian M. Investigating the *P*-Delta effects on the seismic collapse capacity of adjacent structures. In: 16th European conference on earthquake engineering (16ECEE), 18–21, June, Thessaloniki, Greece, 2018.
10. Jankowski R. Experimental study on earthquake-induced pounding between structural elements made of different building materials. Earthq Eng Struct Dyn. 2010;39(3):343–54.
11. Leibovich E, Rutenberg A, Yankelevsky DZ. On eccentric seismic pounding of symmetric buildings. Earthq Eng Struct Dyn. 1996;25(3):219–33.
12. Polycarpou PC, Papaloizou L, Komodromos P. An efficient methodology for simulating earthquake-induced 3D pounding of buildings. Earthq Eng Struct Dyn. 2014;43(7):985–1003.
13. Skrekas P, Sextos A, Giaralis A. Influence of bi-directional seismic pounding on the inelastic demand distribution of three adjacent multi-storey R/C buildings. Earthq Struct. 2014;6(1):71–87.
14. Raheem SEA, Fooly MY, Shafy AGA, Taha AM, Abbas YA, Latif MMA. Numerical simulation of potential seismic pounding among adjacent buildings in series. Bull Earthq Eng. 2019;17(1):439–71.
15. Yahyazadeh A, Yakhchalian M. Probabilistic residual drift assessment of SMRFs with linear and nonlinear viscous dampers. J Constr Steel Res. 2018;148:409–21.
16. Pavlou E, Constantinou MC. Response of nonstructural components in structures with damping systems. J Struc Eng. 2006;132(7):1108–17.
17. Lavan O, Dargush GF. Multi-objective evolutionary seismic design with passive energy dissipation systems. J Earthq Eng. 2009;13(6):758–90.
18. Raheem SEA. Mitigation measures for earthquake induced pounding effects on seismic performance of adjacent buildings. Bull Earthq Eng. 2014;12(4):1705–24.
19. Raheem SEA, Fooly MY, Omar M, Zaher AKA. Seismic pounding effects on the adjacent symmetric buildings with eccentric alignment. Earthq Struct. 2019;16(6):715–26.
20. Rezavandi A, Moghadam AS. Experimental and numerical study on pounding effects and mitigation techniques for adjacent structures. Adv Struct Eng. 2007;10(2):121–34.
21. Lasowicz N, Kwiecień A, Jankowski R. Experimental study on the effectiveness of polymer damper in damage reduction of temporary steel grandstand. J Phys Conf Ser. 2015;628(1):012051.
22. Stręk AM, Lasowicz N, Kwiecień A, Zając B, Jankowski R. Highly dissipative materials for damage protection against earthquake-induced structural pounding. Materials. 2021;14(12):3231.
23. Polycarpou PC, Komodromos P, Polycarpou AC. A nonlinear impact model for simulating the use of rubber shock absorbers for mitigating the effects of structural pounding during earthquakes. Earthq Eng Struct Dyn. 2013;42(1):81–100.
24. Takabatake H, Yasui M, Nakagawa Y, Kishida A. Relaxation method for pounding action between adjacent buildings at expansion joint. Earthq Eng Struct Dyn. 2014;43(9):1381–400.
25. Jankowski R, Mahmoud S. Linking of adjacent three-storey buildings for mitigation of structural pounding during earthquakes. Bull Earthq Eng. 2016;14(11):3075–97.
26. Patel CC, Jangid RS. Seismic response of dynamically similar adjacent structures connected with viscous dampers. IES J Part A Civ Struct Eng. 2010;3(1):1–13.
27. Pratesi F, Sorace S, Terenzi G. Seismic pounding mitigation of a modern heritage R/C bell tower. WIT Trans Built Environ. 2013;131:303–14.
28. Sorace S, Terenzi G. Damped interconnection-based mitigation of seismic pounding between adjacent R/C buildings. Int J Eng Technol. 2013;5(3):406.
29. Pratesi F, Sorace S, Terenzi G. Analysis and mitigation of seismic pounding of a slender R/C bell tower. Eng Struct. 2014;71:23–34.
30. Kandemir-Mazanoglu EC, Mazanoglu K. An optimization study for viscous dampers between adjacent buildings. Mech Syst Signal Process. 2017;89:88–96.
31. Kazemi F, Mohebi B, Yakhchalian M. Enhancing the seismic performance of adjacent pounding structures using viscous dampers. In: The 16th European conference on earthquake engineering (16ECEE); 2018, pp. 18–21.
32. Bekdaş G, Nigdeli SM. Preventing the pounding of adjacent buildings with harmony search optimized tuned mass damper. In: 3rd European conference of civil engineering; 2012, pp. 2–4.
33. Licari M, Sorace S, Terenzi G. Nonlinear modeling and mitigation of seismic pounding between R/C frame buildings. J Earthq Eng. 2015;19(3):431–60.
34. Tubaldi E, Barbato M, Ghazizadeh S. A probabilistic performance-based risk assessment approach for seismic pounding with efficient application to linear systems. Struct Saf. 2012;36:14–22.
35. Martinez-Rodrigo M, Romero ML. An optimum retrofit strategy for moment resisting frames with nonlinear viscous dampers for seismic applications. Eng Struct. 2003;25(7):913–25.
36. Bigdeli K, Hare W, Tesfamariam S. Configuration optimization of dampers for adjacent buildings under seismic excitations. Eng Optim. 2012;44(12):1491–509.
37. Dall′Asta A, Tubaldi E, Ragni L. Influence of the nonlinear behavior of viscous dampers on the seismic demand hazard of building frames. Earthq Eng Struct Dyn. 2015;45(1):149–69.
38. Mansoori MR, Moghadam AS. Using viscous damper distribution to reduce multiple seismic responses of asymmetric structures. J Constr Steel Res. 2009;65(12):2176–85.
39. Kazemi F, Miari M, Jankowski R. Investigating the effects of structural pounding on the seismic performance of adjacent RC and steel MRFs. Bull Earthq Eng. 2021;19(1):317–43.
40. ASCE 7-16. Minimum design loads and associated criteria for buildings and other structures. Reston, VA: American Society of Civil Engineers; 2017.
41. AISC Committee. Specification for structural steel buildings (ANSI/AISC 360-16). Chicago-Illinois: American Institute of Steel Construction; 2016.
42. AISC A. AISC 341-16, seismic provisions for structural steel buildings. Chicago, IL: American Institute of Steel Construction; 2016.
43. ACI Committee, International Organization for Standardization. Building code requirements for structural concrete (ACI 318-14) and commentary. American Concrete Institute; 2014.
44. Kitayama S, Constantinou MC. Seismic performance of buildings with viscous damping systems designed by the procedures of ASCE/SEI 7-16. J Struct Eng. 2018;144(6):04018050.
45. Haselton CB. Assessing seismic collapse safety of modern reinforced concrete moment frame buildings. Doctoral dissertation, Stanford University; 2006.
46. Kazemi F, Mohebi B, Jankowski R. Predicting the seismic collapse capacity of adjacent SMRFs retrofitted with fluid viscous

dampers in pounding condition. Mech Syst Signal Process. 2021;161: 107939.
47. Lignos DG, Krawinkler H. Deterioration modeling of steel components in support of collapse prediction of steel moment frames under earthquake loading. J Struct Eng. 2010;137(11):1291–302.
48. Ibarra LF, Medina RA, Krawinkler H. Hysteretic models that incorporate strength and stiffness deterioration. Earthq Eng Struct Dyn. 2005;34(12):1489–511.
49. McKenna F, Fenves GL, Filippou FC, Scott MH. Open system for earthquake engineering simulation (OpenSees). Berkeley: Pacific Earthquake Engineering Research Center, University of California; 2016.
50. Altoontash A. Simulation and damage models for performance assessment of reinforced concrete beam–column joints. Doctoral dissertation, Stanford University; 2004.
51. Fardis MN, Biskinis DE. Deformation capacity of RC members, as controlled by flexure or shear. In: Otani symposium, vol. 511530; 2003.
52. Berry M, Parrish M, Eberhard M. PEER structural performance database user's manual. Berkeley: University of California; 2004.
53. Deierlein GG, Haselton CB. Benchmarking the collapse safety of code-compliant reinforced concrete moment frame building systems. In: ATC/JSCA US-Japan workshop on improvement of structural design and construction practices, proceedings of an international workshop; 2005, pp. 17–9.
54. Mohebi B, Yazdanpanah O, Kazemi F, Formisano A. Seismic damage diagnosis in adjacent steel and RC MRFs considering pounding effects through improved wavelet-based damage-sensitive feature. J Build Eng. 2021;33:101847.
55. Mahmoud S, Jankowski R. Modified linear viscoelastic model of earthquake-induced structural pounding. Iran J Sci Technol Trans Civ Eng. 2011;35(C1):51–62.
56. Yazdanpanah O, Mohebi B, Kazemi F, Mansouri I, Jankowski R. Development of fragility curves in adjacent steel moment-resisting frames considering pounding effects through improved wavelet-based refined damage-sensitive feature. Mech Syst Signal Process. 2022;173: 109038.
57. Anagnostopoulos SA. Equivalent viscous damping for modeling inelastic impacts in earthquake pounding problems. Earthq Eng Struct Dyn. 2004;33(8):897–902.
58. Mahmoud S, Jankowski R. Elastic and inelastic multi-storey buildings under earthquake excitation with the effect of pounding. J Appl Sci. 2009;9(18):3250–62.
59. Polycarpou PC, Komodromos P. Earthquake-induced poundings of a seismically isolated building with adjacent structures. Eng Struct. 2010;32(7):1937–51.
60. Karayannis CG, Naoum MC. Torsional behavior of multistory RC frame structures due to asymmetric seismic interaction. Eng Struct. 2018;163:93–111.
61. Applied Technology Council, United States. Federal Emergency Management Agency. Quantification of building seismic performance factors. US Department of Homeland Security, FEMA; 2009.
62. Asgarkhani N, Yakhchalian M, Mohebi B. Evaluation of approximate methods for estimating residual drift demands in BRBFs. Eng Struct. 2020;224: 110849.
63. Kazemi F, Jankowski R. Enhancing seismic performance of rigid and semi-rigid connections equipped with SMA bolts incorporating nonlinear soil–structure interaction. Eng Struct. 2022;114896.
64. Kazemi F, Jankowski R. Machine learning-based prediction of seismic limit-state capacity of steel moment-resisting frames considering soil–structure interaction. Comput Struct. 2022. https://doi.org/10.1016/j.compstruc.2022.106886.
65. MATLAB. Simulink as a Technical Computing Language. Engineering Computations and Modeling in MATLAB; 2018.
66. FEMA-356. Prestandard and commentary for the seismic rehabilitation of buildings. Washington, DC: Federal Emergency Management Agency; 2000.

Publisher's Note Springer Nature remains neutral with regard to jurisdictional claims in published maps and institutional affiliations.

Paper III:

Kazemi, F., & Jankowski, R. (2023). Enhancing seismic performance of rigid and semi-rigid connections equipped with SMA bolts incorporating nonlinear soil-structure interaction. Engineering Structures, 274, 114896. doi.org/10.1016/j.engstruct.2022.114896

Engineering Structures 274 (2023) 114896

Contents lists available at ScienceDirect

Engineering Structures

journal homepage: www.elsevier.com/locate/engstruct

Enhancing seismic performance of rigid and semi-rigid connections equipped with SMA bolts incorporating nonlinear soil-structure interaction

F. Kazemi *, R. Jankowski

Faculty of Civil and Environmental Engineering, Gdańsk University of Technology, ul. Narutowicza 11/12, 80-233 Gdansk, Poland

ARTICLE INFO

Keywords:
Rigid connection
Semi-rigid connection
Shape memory alloys
Soil–structure interaction
Seismic retrofit
Seismic limit-state capacity

ABSTRACT

Nowadays, using smart connections can improve the performance of buildings with some recentering features that are from the superelastic behavior of Shape Memory Alloys (SMAs). It seems that there is different rigidity between the designed connection and the real one in Steel Moment-Resisting Frames (SMRFs), which can be considered as a problematic issue due to the importance of connections in seismic performance assessment. This paper aims to investigate the seismic limit-state capacities of rigid and semi-rigid connections implemented in the 3-Story, 5-Story, 7-Story, and 9-Story SMRFs considering the nonlinear Soil-Structure Interaction (SSI) effects. A Tcl programming code was developed to model semi-rigid connection and SSI effects using Opensees. Incremental Dynamic Analyses (IDAs) were employed to assess the seismic performance levels of SMRFs considering Near-Fault Pulse-Like (NF-PL) and Near-Fault No-Pulse (NF-NP) records suggested by FEMA-P695. The results showed that assuming semi-rigid connections with rigidity of 80%, 70%, and 60%, significantly decreased the median values of IDA curves compared to rigid connection. Considering the SSI effects can considerably decrease the $S_a(T_1)$ values of IDA curves and seismic collapse probability in all soil types; therefore, it is suggested to assume the real condition of the structure by modeling the connection rigidity and the SSI effects. It can be concluded that SMA bolts have the ability to improve the seismic performance of connection to compensate the lack of rigidity in semi-rigid connections of SMRFs; as well as, they can be used as a retrofitting strategy for existing buildings.

1. Introduction

During the design process of steel structures, the beam-to-column joints are assumed as pinned or rigid connections to simplify the modeling and analysis, while in the actual cases most of them are semi-rigid connections and behave between these two extreme conditions. Semi-rigid connections have significant effects on the moment distribution along with the structural elements and can affect the Maximum Interstory Drift Ratio (M−IDR) of the steel frames [1–3]. Due to the importance of connection behavior, some researchers experimentally investigated rigid and semi-rigid connections. Abidelah et al. [4] investigated eight specimens of extended and flush end-plates for beam-to-beam and beam-to-column bolted connections, and showed that Eurocode 3 overestimates the initial stiffness of connections. To use the experimental results in the modeling process, analytical and numerical investigations were performed by Sherbourne and Bahaari [5], and Bahaari and Sherbourne [6]. They provided parametric formula to assess the moment-rotation curve of the end-plate bolted connections. Shi et al. [7] proposed a numerical procedure for modeling the end-plate connection with prestressed bolts. It can be possible to use their numerical results for generating the moment-rotation curve, simulating the end-plate connection with prestressed bolts, the behavior of the end-plate, and the panel zone. Reliability evaluation based on the probability of collapse is an important factor that should be considered due to uncertainties of applied loads, the behavior of the material, and the properties of geometry. Some investigations were carried out to access the reliability index of structural elements of steel structures and to estimate the failure probability, which significantly affected by semi-rigid connections [8,9].

The superelastic behavior of the Shape Memory Alloys (SMAs) made them a unique tool for enhancing the response of structural elements. Nickel-Titanium (Ni-Ti) alloys have acceptable superelasticity characteristics and can be widely used in structural members [10]. Speicher et al. [11] performed experimental investigation on the Ni-Ti alloys in the interior beam-to-column connection and find out the significant performance of Ni-Ti alloys to reduce the residual drift. The

* Corresponding author.
E-mail address: farzin.kazemi@pg.edu.pl (F. Kazemi).

https://doi.org/10.1016/j.engstruct.2022.114896
Received 5 April 2022; Received in revised form 18 August 2022; Accepted 26 August 2022
Available online 25 October 2022
0141-0296/© 2022 Elsevier Ltd. All rights reserved.

experimental investigation considering eight full-scale tests done by Fang et al. [12], which the normal bolts replaced by SMA bolts on the end-plate connections. They concluded that the recentring ability of SMA bolts can improve the energy dissipation capability. Wang et al. [13] introduced a novel beam-to-column connection based on using SMA and steel tendons. Their novel connection showed moderate energy dissipation and recentering capability under cyclic loads up to drift of 6 %. Nowadays, SMA materials are widely investigated for bolt connections that may decrease the amount of residual displacements. SMA bolts have become a useful element to retrofit damaged structures in severe earthquakes. Their superelastic effects allow them to be deformed after unloading up to 10 % strain, and this can help the connection to behave more effectively than using regular bolts [14,15].

Many attempts have been undertaken by researchers to accurately model the Soil-Structure Interaction (SSI) assuming different soil types beneath the foundation. The approaches can be categorized starting from using simple elastic models and finishing with using nonlinear models with the ability to consider soil parameters [16–18]. Ghandil and Behnamfar [19,20] proposed a modified linear method to consider the shear modulus of soil near the foundation that can be used for modeling of SSI effects. Elwardany et al. [21,22] investigated SSI effects on the Steel Moment-Resisting Frames (SMRFs) by assuming infill masonry walls, and find out that SSI effects can significantly influence the seismic response of the SMRFs. The vulnerability assessment of structures based on the probabilistic seismic collapse capacity is an important topic that many researchers followed [23–28]. Some studies investigated the influence of SSI on the seismic fragility curves of Reinforced Concrete (RC) buildings. Mitropoulou et al. [29] developed seismic fragility curves for three systems of fixed-based, Winkler spring model and two-dimensional finite element for pile foundation. Then, Forcellini [30] investigated the SSI effects on the seismic fragility curves of the RC buildings, and showed that the SSI effects can increase the failure probability of RC buildings. Kamal et al. [31] introduced a novel combination of multiple earthquakes parameters to reflect the damage potential of RC buildings. In addition, they investigated the effects of SSI and structure-soil-structure interaction on the adjacent RC buildings [32]. Soil nonlinearity is another important factor that can affect the response of structures; thus, models should be accurate enough to consider this influence. Rajeev and Tesfamariam [33] performed analysis on RC buildings with the foundation modeling approach of Beam on Nonlinear Winkler Foundation (BNWF) model to find the nonlinearity effects of SSI assuming soil parameters such as cohesion, density, Poisson's ratio, and friction angle. Harden et al. [34] proposed a simulation methodology for nonlinearity modeling of shallow foundation using BNWF.

The current paper aims to explore the seismic performance levels of SMRFs with different rigidity of connections assuming steel bolts. Then, different soil types and SSI effects were considered to investigate their influence on the seismic performance of semi-rigid connections, and evaluate the vulnerability of semi-rigid connections in the case of seismic excitations. Since the rigidity reduction can significantly affect the seismic performance and limit-state capacity of SMRFs, SMA bolts with similar diameters, as compared to steel bolts, were replaced in models to investigate their effects on the seismic response of SMRFs. Using SMA bolts can help to improve the seismic performance of buildings with semi-rigid connections without any additional changes, and can be considered as a retrofitting strategy to overcome the issue of weak connection in existing buildings.

2. Modeling methods

2.1. Modeling of SMRFs

Fig. 1 presents the regular plan of buildings with three, five, seven, and nine story levels (3-Story, 5-Story, 7-Story, and 9-Story) considering SMRFs in four outer frames (blue color). It was assumed that buildings were located in California with a latitude of 34.039° and longitude of −118.324°, and then, four soil types were considered for buildings according to the USGS website [35]. For designing the structures, the design parameters of R = 8, C_d = 5.5, and Ω_0 = 3 and steel yield strength of 345 MPa were assumed. Table 1 presents seismic design parameters and soil parameter values for the soil types B, C, D, and E, which were introduced by Haghollahi and Behnamfar (see [36]). To calculate the shear modulus of all soil types, the equations considered by Madani et al. [37] were used.

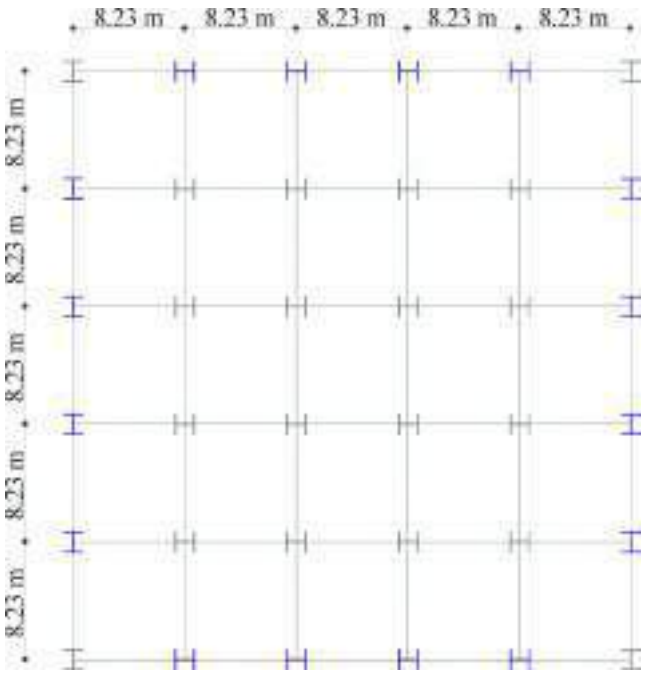

Fig. 1. Structural plan for modeling of SMRFs.

S_{DS} and S_{D1} are numeric seismic design values at 0.2 and 1.0 s, respectively, G_0 is the initial shear modulus of soil, Φ, c, γ, v_s are friction angle, cohesion coefficient, unit weight, and shear wave velocity, respectively. Three-dimensional buildings were modeled in ETABS 2016 software with the floor dead and live loads of 3.35 kN/m^2 and 1.68 kN/m^2, respectively, and considering the provisions of ASCE 7–16 [38], AISC 360–16 [39], and AISC 341–10 [40]. Table 2 presents the designed structural members of SMRFs assuming different soil types.

Some approaches were used by researchers to model two-dimensional SMRFs in Opensees [41] with respect to three-dimensional building. The paramount of analytical tools is able to model strength and stiffness deterioration of structural elements, which is suitable for two-dimensional modeling of structures. According to this approach, to model the P-Delta effects, all columns were assumed to be the leaning columns neglecting the columns in the SMRF (e.g. see [42–44]). Then, the two-dimensional models were verified by the fundamental periods of three-dimensional buildings modeled in ETABS 2016 software. The Modified Ibarra–Krawinkler bilinear hysteretic model (IMK Hinge) [25–28,45–47] was used for modeling the structural

Table 1
Soil parameters used for modeling SMRFs.

Soil type	B	C	D	E
S_{DS}	1.306	1.567	1.576	1.623
S_{D1}	0.463	0.648	0.653	0.659
G_0 (MPa)	6000	280	60	30
Φ (Degree)	45	42	38	35
c (kPa)	0	0	5	5
γ (kN/m^3)	24	21	19	18
υ	0.25	0.35	0.4	0.45
v_s (m/s)	1565	360	175	120

Table 2
Structural members of SMRFs assuming different soil types.

SMRF	Story level	Soil type B		Soil type C		Soil type D		Soil type E	
		Beam	Column	Beam	Column	Beam	Column	Beam	Column
3-story	1st	W24X68	W14X132	W24X94	W14X159	W24X94	W14X159	W24X94	W14X159
	2nd	W21X68	W14X120	W24X84	W14X120	W24X94	W14X120	W24X94	W14X120
	3rd	W18X46	W14X120	W18X50	W14X120	W18X50	W14X120	W18X55	W14X120
5-story	1st	W24X76	W14X145	W24X94	W14X159	W27X102	W14X159	W27X102	W14X159
	2nd	W24X76	W14X120	W24X94	W14X132	W27X102	W14X132	W27X102	W14X159
	3rd	W24X76	W14X120	W24X84	W14X120	W24X84	W14X120	W24X84	W14X120
	4th	W24X55	W14X120	W24X84	W14X120	W24X84	W14X120	W24X84	W14X120
	5th	W24X55	W14X120	W24X55	W14X120	W24X55	W14X120	W24X55	W14X120
7-story	1st	W24X84	W14X145	W27X102	W14X176	W27X102	W14X176	W27X102	W14X176
	2nd	W24X84	W14X145	W27X102	W14X159	W27X102	W14X159	W27X102	W14X159
	3rd	W24X84	W14X145	W27X94	W14X145	W27X102	W14X145	W27X102	W14X145
	4th	W24X84	W14X120	W27X94	W14X120	W27X94	W14X120	W24X84	W14X145
	5th	W24X68	W14X120	W24X84	W14X120	W24X84	W14X120	W24X84	W14X120
	6th	W21X50	W14X120	W21X68	W14X120	W21X68	W14X120	W21X68	W14X120
	7th	W21X50	W14X120	W21X50	W14X120	W21X50	W14X120	W21X50	W14X120
9-story	1st	W27X94	W14X233	W27X114	W14X233	W27X114	W14X233	W27X114	W14X233
	2nd	W27X94	W14X233	W27X114	W14X233	W27X114	W14X233	W27X114	W14X233
	3rd	W27X94	W14X176	W27X114	W14X176	W27X114	W14X176	W27X114	W14X233
	4th	W24X94	W14X176	W27X102	W14X176	W27X102	W14X176	W27X114	W14X176
	5th	W24X94	W14X176	W27X102	W14X176	W27X102	W14X176	W27X114	W14X176
	6th	W24X84	W14X120	W24X84	W14X120	W27X94	W14X159	W27X94	W14X120
	7th	W24X84	W14X120	W24X84	W14X120	W24X84	W14X120	W24X84	W14X120
	8th	W21X50	W14X120	W21X68	W14X120	W21X68	W14X120	W24X84	W14X120
	9th	W21X50	W14X120	W21X50	W14X120	W21X50	W14X120	W21X50	W14X120

elements due to the validation of this model by more than 300 experimental tests and its implementation in OpenSees software. Beams and columns of SMRFs were modeled with two nonlinear rotational springs at both ends of the elastic beam-column element. It was shown that the IMK model had the ability to model structural elements with high accuracy, while significantly increase the time of analysis and reduce the computational efforts.

2.2. Numerical modeling of SSI

The BNWF model can be assume to estimate the response of foundation, piles, and retaining walls by considering the slide and settlement with a hysteretic model with defined rules of loading, unloading, and reloading. This model has shown a good predictive ability for capturing the experimentally observed behavior of foundations by employing a series of nonlinear springs and dashpots. Fig. 2 presents the implementation of the springs and dashpots in the BNWF model. As it is shown in Fig. 2, three types of springs known as the q-z spring, p-x spring, and *t*-x spring were used to capture the vertical and rotational resistance, and

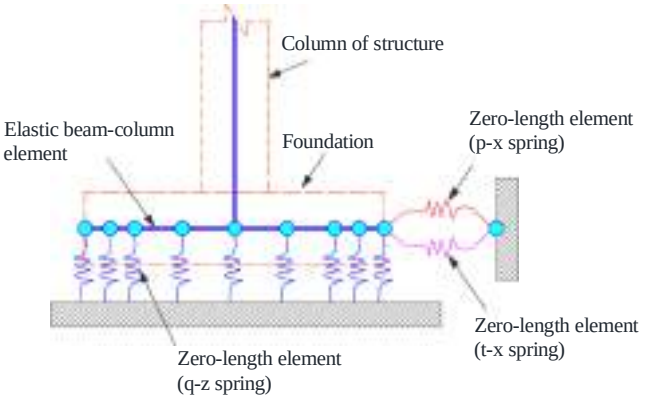

Fig. 2. Implementation of the springs and dashpots in the BNWF model.

the sliding and passive resistance of the foundation, respectively. Fig. 3 presents the normalized load-normalized displacement curves of the q-z spring, p-x spring, and *t*-x spring used in the BNWF model. For modeling the BNWF model in Opensees [41], the material model of *QzSimple*, *PxSimple*, *and TxSimple* were used for q-z spring, p-x spring, and *t*-x spring [17,18,33,34]. Then, a nonlinear zero-length element was used for modeling *QzSimple*, *PxSimple*, and *TxSimple* material models. The foundation of the 3-Story, 5-Story, 7-Story, and 9-Story SMRFs were modeled using SAFE 2016 software and their dimensions are presented in Table 3.

To provide sliding and passive resistance, two lateral springs showed in Fig. 2 (t–x and p–x) were used. Assuming different factors, such as depth, foundation area and shape, soil cohesion, load intensity, and friction angle between soil and foundation [37], the equations proposed by Terzaghi [48] and Meyerhof [49] were applied to determine the vertical load bearing and horizontal sliding capacities for SSI modelling.

Boulanger et al. [50] presented equations for defining the materials used in the BNWF model. It was assumed that in the elastic region of *the QzSimple* material model, the assumed load, q_e, has linear behavior with the displacement, z, and the initial elastic stiffness, k_{ini}.

$$q_e = k_{ini} z \tag{1}$$

It is experimentally proved that the maximum load in the elastic region, q_0, is a factor C_r of the ultimate load, q_{ult}, as follows:

$$q_0 = C_r q_{ult} \tag{2}$$

Then, the nonlinear part of the curve can be rewritten as follows:

$$q = q_{ult} - (q_{ult} - q_0)\left[\frac{Cz_{50}}{Cz_{50} + |z - z_0|}\right]^n \tag{3}$$

where cz_{50} is the displacement in the 50 % of the ultimate load, *and* z_0 is displacement in the yield point. To control the post-yield portion and shape of the curve, constitutive values of C and n can be used. For *PxSimple* and *TxSimple* material models, calculation of *QzSimple* material model can be used with assuming various values of C_r, n, C. for calculating the vertical stiffness and lateral stiffness of springs, k_v, and k_h, respectively, following equations can be determined [51]:

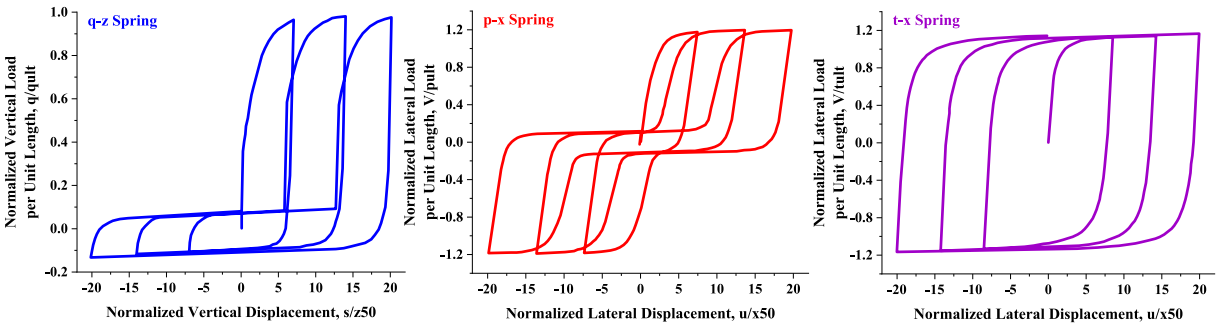

Fig. 3. Normalized load-normalized displacement curves of the q-z spring, p-x spring, and *t*-x spring.

Table 3
Dimensions of SMRFs foundation for different soil types.

SMRF	Soil type	Width (m)	Length (m)	Height (m)
3-story	B	1	26	0.6
	C	1	26	0.6
	D	1.1	27	0.7
	E	1.1	27	0.7
5-story	B	1.3	26	0.7
	C	1.3	26	0.7
	D	1.3	27	0.7
	E	1.3	27	0.7
7-story	B	1.5	27	0.8
	C	1.5	27	0.8
	D	2	27	0.8
	E	2	27	0.8
9-story	B	2.5	27	1.0
	C	2.5	27	1.0
	D	3	27	1.1
	E	3	27	1.1

$$k_v = \frac{GL}{1-\upsilon}\left[0.73 + 1.54\left(\frac{B}{L}\right)^{0.75}\right]$$
$$k_h = \frac{GL}{2-\upsilon}\left[2 + 2.5\left(\frac{B}{L}\right)^{0.85}\right] \quad (4)$$

where G and υ are shear moduli and Poisson's ratio of the soil, respectively, and B and L are the foundation width and length, respectively.

2.3. Numerical modeling of connections

The top and seat angles with double web-angle connections are widely used in the construction of SMRFs. Fig. 4 shows the normalized moment-rotation curve for different types of connections, in which the top and seat angles with double web-angle connections are considered a semi-rigid connection. Calado et al. [52] investigated the behavior of 15 full-scale tests and find out that the ultimate moment and rotation values of monotonic loading are bigger than those of cyclic loading, while a similar failure mode was observed. Some researchers proved that the top and seat angles with double web-angle connection had higher ductility and plastic moment compared to the predictions. Many pioneer studies were performed to verify the experimental results with finite element models and investigated the effects of materials, angles, bolts, residual stress, and plastic hinge location (e.g. see [53,54]).

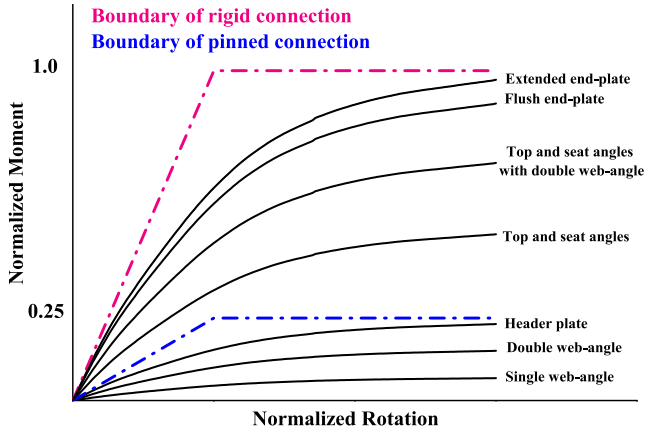

Fig. 4. Comparison of the moment-rotation curve for different types of connections.

Although they have investigated the effects of top and seat angles with double web-angle connection, little attention is paid to real earthquake excitations, the large scale limit state capacity, seismic collapse mode, and seismic performance of SMRFs with these types of connections. Therefore, the top and seat angles with double web-angle connection was selected to investigate the semi-rigid connection effects. Geometric configurations of semi-rigid beam-to-column known as top and seat angles with double web-angle connection is presented in Fig. 5.

According to the designed sections presented in Table 2, various types of beam sections were used in SMRFs, and according to Fig. 5, the type of the top and seat angles with double web-angle connection depends on the beam section. Therefore, regarding the beam sections used in the models, the placement of bolts and distances can be determined according to Table 4.

It is confirmed that the moment-rotation behavior of the semi-rigid connection is related to the connection details, such as properties of beam and column, placement of bolts, the end-plate thickness, and the bolts diameter. To define the rigidity of the connections, the moment-rotation curve of the rigid connection should be calculated based on the plastic bending capacity of beam. Then, it is possible to calculate the moment-rotation curve of a rigid connection based on the formula introduced by Sherbourne and Bahaari [5] and Bahaari and Sherbourne [6]. It should be noted that the initial stiffness and strength of this curve is associated with a fully rigid connection; therefore, it is possible to achieve relative rigidities of 80 %, 70 %, and 60 % with respect to the initial stiffness and strength of fully rigid connections. Having the initial stiffness and strength corresponding to rigidities of 80 %, 70 %, and 60 %, the thickness of angles and the bolt diameter were calculated based on the equation proposed by Sherbourne and Bahaari [5] and Bahaari and Sherbourne [6]. Tables 5 to 8 present the thickness of angles and bolt diameter used for the three semi-rigid connections of SMRFs assuming four soil types of B, C, D, and E, respectively.

Panel zone is the joint region of beam-to-column intersect, which deforms primarily in shear due the opposing moments in beams and columns. In this study, the procedure introduced by Gupta and Krawinkler [3] was considered to capture the deformations. According to this procedure, eight very stiff elements (e.g. rigid element) with a zero-length element (e.g. rotational spring) were used in a rectangle area that

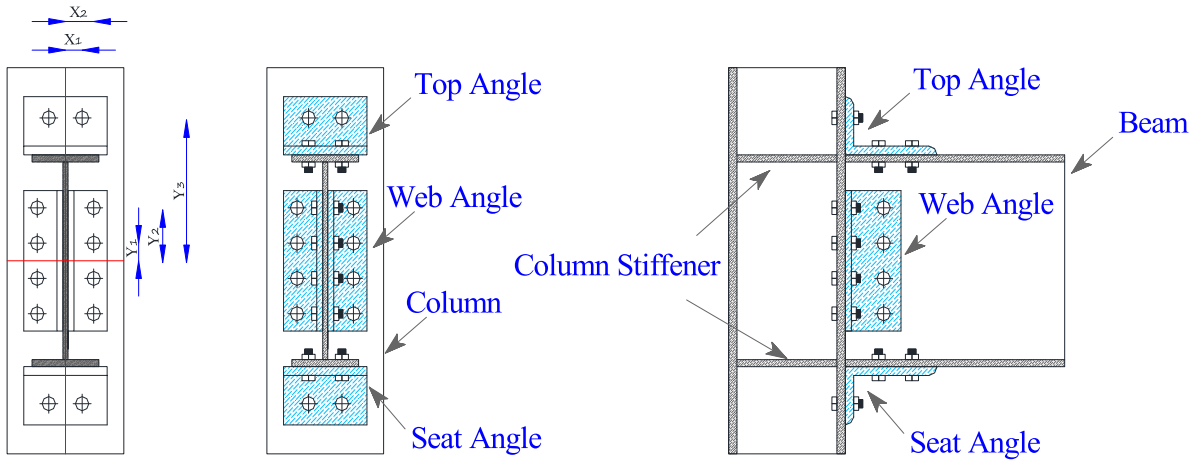

Fig. 5. Geometric configurations of semi-rigid beam-to-column steel connection known as top and seat angles with double web-angle.

Table 4
Placement of bolts and distances for semi-rigid connection.

Column	Height (cm)	Widths (cm)	X_1 (cm)	Y_2 (cm)	Y_1 (cm)	X_2 (cm)	Y_3 (cm)
W18X46	45.97	15.39	5	15	5	7	29.50
W18X50	45.72	19.05	5	15	5	7	29.50
W21X50	52.83	16.50	5	15	5	7	33.40
W21X68	53.59	21.00	5	15	5	7	33.75
W24X55	59.94	17.80	5	15	5	7	37.00
W24X68	60.19	22.78	6	15	5	7	37.00
W24X76	60.70	22.83	6	15	5	7	37.50
W24X84	61.21	22.91	6	15	5	7	37.60
W24X94	61.72	23.03	6	15	5	7	37.85
W27X94	68.32	25.40	7	15	5	7	41.20
W27X102	68.83	25.40	7	15	5	7	41.50
W27X114	69.34	25.65	7	15	5	7	41.65

is shown in Fig. 6. The rotational spring have a trilinear backbone curve based on the principle of a deformed panel zone investigated by Gupta and Krawinkler [3], and other three corners of panel zone have pin connections (showed by green color).

To model the fully rigid connection, it is expected that the rigid connection can transfer all the moments from the beams into the columns; therefore, the rigid element was used instead of connection spring in the numerical models. While for semi-rigid connection, the moment-rotation curve calculated for the assumed rigidities were assigned to the connection spring.

2.4. Numerical modeling of SMAs

The SMA materials used in this study are Ni-Ti (Ni = 49.3 % and Ti = 50.4 %) alloys manufactured based on the ASTM. In Ni-Ti alloys, the percentage of nickel, carbon, hydrogen, oxygen, and nitrogen are 56.01 %, 0.009 %, 0.0006 %, 0.024 %, and 0.003 %, respectively. Fig. 7 presents the stress–strain hysteresis curve of SMA material and the main phases of austenite and martensite. The main feature of SMA material is the ability to change between austenite and martensite phases due to internal forces or temperature, and its flag-shape loop has the ability to dissipate energy without residual drift. For defining this material in Opensees [41], the modulus of elasticity for the austenite phase, E_{SMA}, the secondary slope of the loading phase, R_S, martensite to austenite starting stress,F_{MS}, austenite to martensite finishing stress,F_{MF}, martensite to austenite starting stress, F_{AS}, martensite to austenite finishing stress,F_{AF}, and strain at which the transformation to martensite is complete, d_L, should be determined [55,56].

SMA materials are widely used as structural members in smart buildings. They helped designers to improve the response of smart buildings. In this study, some approaches were used to model the hysteresis curve of SMA materials, and for verifying this approach, the result of an experimental test performed by Ke et al. [56] and Fang et al. [14] was used. They used SMA bolts with a diameter of 8 mm and a total length of 290.5 mm installed with four washers in series (specimen D8L290W8). After applying cyclic load in the maximum drift of 4 %, structural members remained elastic without any failure and SMA bolts stayed tightened which can be used for further excitations (e.g. see [14,55,56]). For brevity, Fig. 8 presents the stress–strain curve of modeled SMA bolts in Opensees [41] with those of experimental tests performed by Eatherton et al. [55] and Ke et al. [56]. It should be noted that this comparison has good agreement with the test results and approves the modeling approach of SMA materials. In this study, SMA material with mechanical properties ofE_{SMA} = 76530 MPa,R_S = 0.033E_{SMA}, F_{MS}=308 MPa,F_{AS} = 221 MPa, F_{AF}=124 MPa, andd_L = 0.0412 m/m were considered [55].

3. Seismic limit-state performance

In this section, the results of Incremental dynamic analysis (IDA) were compared. IDAs were employed to determine the seismic limit-state capacities of the 3-Story, 5-Story, 7-Story, and 9-Story SMRFs founded on the four soil types assuming different rigidity connections. According to the previous studies [23,25–28], the spectral acceleration in the fundamental period, $S_a(T_1)$, which is a suitable Intensity Measure (IM) for seismic limit-state capacity assessment, was selected as IM and M−IDR in each step on analysis was assumed as Engineering Demand Parameter (EDP). Therefore, IDA curves were plotted according to the IM and EDP in each step of analysis using Near-Fault Pulse-like (NF-PL) and Near-Fault No-Pulse (NF-NP) record subsets suggested by FEMA-P695 [57]. Table 9 presents the summary of record subsets. Fig. 9(a)-(d) present IDA curves of the 7-story SMRF founded on soil type B assuming rigid connection, 80 % rigidity, 70 % rigidity, and 60 % rigidity, respectively, subjected to NF-PL ground motions.

Seismic provisions proposed seismic performance levels according to the structural and non-structural state of damages. Therefore, in each M−IDR it is possible to find the seismic performance level of the structure. In this study, three seismic performance levels of Immediate Occupancy (IO), Life Safety (LS), and Collapse Prevention (CP) with M−IDR of 0.7 %, 2.5 %, and 5.0 %, respectively, were selected in accordance with FEMA 356 [58] (see Table C1-3, page 1–14). In addition, in the flat part of the M−IDA curve, the structure is not capable of resisting and this M−IDR can be assumed as the seismic performance of Total Collapse (TC).

Table 5
Steel profile and bolt diameter for SMRFs with semi-rigid connection in soil type B.

SMRF	Story level	Soil type B		60 % Rigid		70 % Rigid		80 % Rigid	
		Beam	Column	Thickness of angles (mm)	Bolt Diameter (mm)	Thickness of angles (mm)	Bolt Diameter (mm)	Thickness of angles (mm)	Bolt Diameter (mm)
3-story	1st	W24X68	W14X132	20	20	24	22	26	24
	2nd	W21X68	W14X120	20	20	22	22	24	24
	3rd	W18X46	W14X120	20	20	22	20	24	22
5-story	1st	W24X76	W14X145	22	20	22	22	24	24
	2nd	W24X76	W14X120	20	20	22	22	24	24
	3rd	W24X76	W14X120	20	20	22	22	24	24
	4th	W24X55	W14X120	20	20	22	22	24	24
	5th	W24X55	W14X120	20	20	22	22	24	24
7-story	1st	W24X84	W14X145	20	20	22	22	24	24
	2nd	W24X84	W14X145	20	20	22	22	24	24
	3rd	W24X84	W14X145	20	20	22	22	24	24
	4th	W24X84	W14X120	20	20	22	22	24	24
	5th	W24X68	W14X120	20	20	20	22	24	24
	6th	W21X50	W14X120	20	20	20	22	22	22
	7th	W21X50	W14X120	20	20	20	20	22	22
9-story	1st	W27X94	W14X233	24	24	26	26	28	28
	2nd	W27X94	W14X233	24	24	26	26	28	28
	3rd	W27X94	W14X176	24	24	26	26	28	28
	4th	W24X94	W14X176	22	24	26	26	28	28
	5th	W24X94	W14X176	22	24	26	26	28	28
	6th	W24X84	W14X120	22	22	22	24	24	26
	7th	W24X84	W14X120	22	22	22	24	24	26
	8th	W21X50	W14X120	20	20	20	22	22	24
	9th	W21X50	W14X120	20	20	20	22	22	24

Table 6
Steel profile and bolt diameter for SMRFs with semi-rigid connection in the soil type C.

SMRF	Story level	Soil type B		60 % Rigid		70 % Rigid		80 % Rigid	
		Beam	Column	Thickness of angles (mm)	Bolt Diameter (mm)	Thickness of angles (mm)	Bolt Diameter (mm)	Thickness of angles (mm)	Bolt Diameter (mm)
3-story	1st	W24X94	W14X159	20	22	24	24	26	26
	2nd	W24X84	W14X120	20	22	24	22	26	26
	3rd	W18X50	W14X120	20	20	22	22	24	24
5-story	1st	W24X94	W14X159	22	22	22	24	24	26
	2nd	W24X94	W14X132	20	22	22	24	24	26
	3rd	W24X84	W14X120	20	22	22	24	24	26
	4th	W24X84	W14X120	20	22	22	24	24	26
	5th	W24X55	W14X120	20	20	22	22	24	24
7-story	1st	W27X102	W14X176	22	26	22	28	24	30
	2nd	W27X102	W14X159	22	26	22	28	24	30
	3rd	W27X94	W14X145	22	26	22	28	24	30
	4th	W27X94	W14X120	22	26	22	28	24	30
	5th	W24X84	W14X120	22	24	22	26	24	28
	6th	W21X68	W14X120	20	24	22	24	24	26
	7th	W21X50	W14X120	20	22	22	24	24	26
9-story	1st	W27X114	W14X233	24	26	26	28	28	30
	2nd	W27X114	W14X233	24	26	26	28	28	30
	3rd	W27X114	W14X176	24	26	26	28	28	30
	4th	W27X102	W14X176	22	24	26	26	28	28
	5th	W27X102	W14X176	22	24	26	26	28	28
	6th	W24X84	W14X120	22	22	22	24	24	26
	7th	W24X84	W14X120	22	22	22	24	24	26
	8th	W21X68	W14X120	20	20	20	22	22	24
	9th	W21X50	W14X120	20	20	20	22	22	24

Table 7
Steel profile and bolt diameter for SMRFs with semi-rigid connection in the soil type D.

SMRF	Story level	Soil type B		60 % Rigid		70 % Rigid		80 % Rigid	
		Beam	Column	Thickness of angles (mm)	Bolt Diameter (mm)	Thickness of angles (mm)	Bolt Diameter (mm)	Thickness of angles (mm)	Bolt Diameter (mm)
3-story	1st	W24X94	W14X159	20	22	24	24	26	26
	2nd	W24X94	W14X120	20	22	24	24	26	26
	3rd	W18X50	W14X120	20	20	22	22	24	24
5-story	1st	W27X102	W14X159	22	24	24	26	26	28
	2nd	W27X102	W14X132	22	24	24	26	26	28
	3rd	W24X84	W14X120	20	22	22	24	24	26
	4th	W24X84	W14X120	20	22	22	24	24	26
	5th	W24X55	W14X120	20	20	22	22	24	24
7-story	1st	W27X102	W14X176	22	26	22	28	24	30
	2nd	W27X102	W14X159	22	26	22	28	24	30
	3rd	W27X102	W14X145	22	26	22	28	24	30
	4th	W27X94	W14X120	22	26	22	28	24	30
	5th	W24X84	W14X120	22	24	22	26	24	28
	6th	W21X68	W14X120	20	24	22	26	24	28
	7th	W21X50	W14X120	20	22	22	24	22	26
9-story	1st	W27X114	W14X233	24	26	26	28	28	30
	2nd	W27X114	W14X233	24	26	26	28	28	30
	3rd	W27X114	W14X176	24	26	26	28	28	30
	4th	W27X102	W14X176	24	26	26	28	28	30
	5th	W27X102	W14X176	24	26	26	28	28	30
	6th	W27X94	W14X159	22	24	24	26	26	28
	7th	W24X84	W14X120	22	22	22	24	24	26
	8th	W21X68	W14X120	20	20	20	22	22	24
	9th	W21X50	W14X120	20	20	20	22	22	24

Table 8
Steel profile and bolt diameter for SMRFs with semi-rigid connection in the soil type E.

SMRF	Story level	Soil type B		60 % Rigid		70 % Rigid		80 % Rigid	
		Beam	Column	Thickness of angles (mm)	Bolt Diameter (mm)	Thickness of angles (mm)	Bolt Diameter (mm)	Thickness of angles (mm)	Bolt Diameter (mm)
3-story	1st	W24X94	W14X159	20	22	24	24	26	26
	2nd	W24X94	W14X120	20	22	24	24	26	26
	3rd	W18X55	W14X120	20	20	22	22	24	24
5-story	1st	W27X102	W14X159	22	24	24	26	26	28
	2nd	W27X102	W14X159	22	24	24	26	26	28
	3rd	W24X84	W14X120	20	22	22	24	24	26
	4th	W24X84	W14X120	20	22	22	24	24	26
	5th	W24X55	W14X120	20	20	22	22	24	24
7-story	1st	W27X102	W14X176	22	26	22	28	24	30
	2nd	W27X102	W14X159	22	26	22	28	24	30
	3rd	W27X102	W14X145	22	26	22	28	24	30
	4th	W24X84	W14X145	22	26	22	28	24	30
	5th	W24X84	W14X120	22	26	22	28	24	30
	6th	W21X68	W14X120	20	24	22	26	24	28
	7th	W21X50	W14X120	20	24	20	26	24	28
9-story	1st	W27X114	W14X233	24	28	26	30	28	32
	2nd	W27X114	W14X233	24	28	26	30	28	32
	3rd	W27X114	W14X233	24	28	26	30	28	32
	4th	W27X114	W14X176	24	28	26	30	28	32
	5th	W27X114	W14X176	24	28	26	30	28	32
	6th	W27X94	W14X120	22	24	24	26	26	28
	7th	W24X84	W14X120	22	22	22	24	24	26
	8th	W24X84	W14X120	22	22	22	24	24	26
	9th	W21X50	W14X120	20	20	20	22	22	24

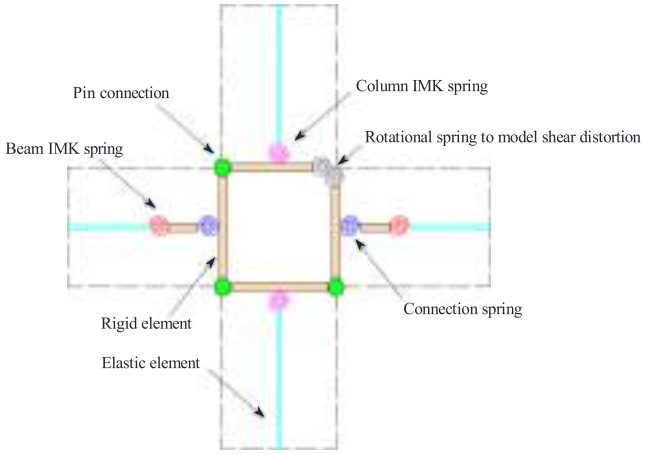

Fig. 6. Configuration of internal joints with panel zone and semi-rigid connection.

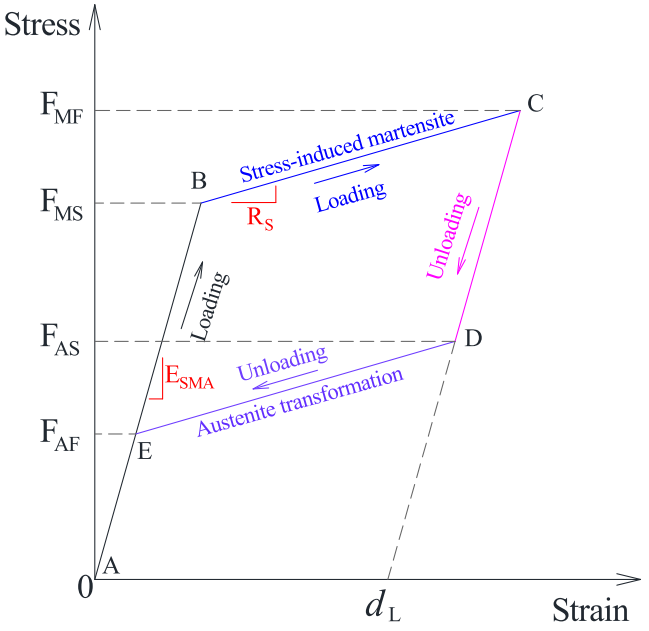

Fig. 7. Stress–strain hysteresis curve of SMA material and main phases of austenite and martensite.

3.1. M−IDA curves

To show the results of analyses, M−IDA curves of SMRFs in each soil type assuming different rigidity were compared. Fig. 10(a)-(d) present M−IDA curves of the 3-Story SMRF considering four cases of rigidity and four soil types subjected to NF-PL ground motions. It is shown that semi-rigid connections significantly decreased the values of M−IDA curves. The 60 % rigidity had the lowest values of M−IDAs in all soil types, while rigid connection achieved higher values of M−IDAs. Although in each soil type similar trends were observed, the values of $S_a(T_1)$ were different corresponding to the type of rigidity. In other words, the M−IDA curve of the 3-Story SMRF founded on soil type E had higher $S_a(T_1)$ values than the 3-Story SMRF founded on soil type B.

Tables 10 and 11 illustrate the seismic limit-state capacities of the 3-Story SMRF in four cases of rigidity and soil types assuming NF-PL and NF-NP ground motions, respectively. According to results presented in Table 10, assuming the rigidity of 80 %, 70 %, and 60 % for the 3-Story SMRF founded on soil type B can decrease the $S_a(T_1)$ values of the performance level of LS by 17.16 %, 23.82 %, and 28.55 %, respectively.

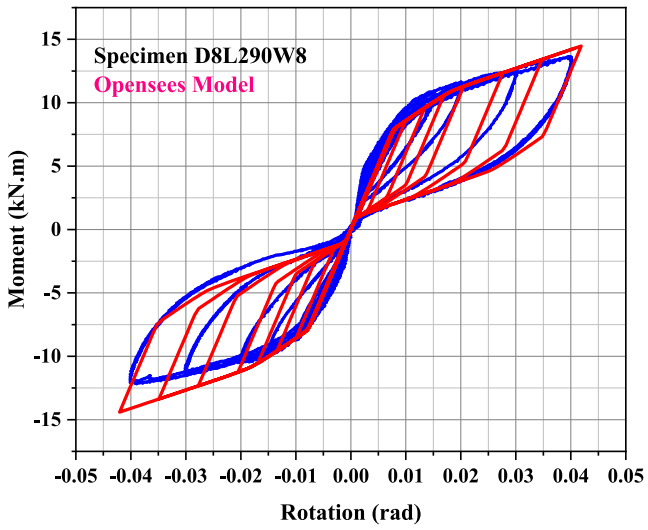

Fig. 8. Stress–strain curve of SMA bolts was used in this study with the result of specimen D8L290W8 [55,56].

Table 9
Summary of earthquake events suggested by FEMA-P695 [57].

RSN	M	Year	Name	Fault Type	PGA_{max} (g)	PGV_{max} (cm/s.)
NF-PL record subset						
181	6.5	1979	Imperial Valley-06	Strike-slip	0.44	111.9
182	6.5	1979	Imperial Valley-06	Strike-slip	0.46	108.9
292	6.9	1980	Irpinia, Italy-01	Normal	0.31	45.5
723	6.5	1987	Superstition Hills-02	Strike-slip	0.42	106.8
802	6.9	1989	Loma Prieta	Strike-slip	0.38	55.6
821	6.7	1992	Erzican, Turkey	Strike-slip	0.49	95.5
828	7	1992	Cape Mendocino	Thrust	0.63	82.1
879	7.3	1992	Landers	Strike-slip	0.79	140.3
1063	6.7	1994	Northridge-01	Thrust	0.87	167.3
1086	6.7	1994	Northridge-01	Thrust	0.73	122.8
1165	7.5	1999	Kocaeli, Turkey	Strike-slip	0.22	29.8
1503	7.6	1999	Chi-Chi, Taiwan	Thrust	0.82	127.7
1529	7.6	1999	Chi-Chi, Taiwan	Thrust	0.29	106.6
1605	7.1	1999	Duzce, Turkey	Strike-slip	0.52	79.3
NF-NP record subset						
126	6.8	6.8	Gazli, USSR	Thrust	0.71	71.2
160	6.5	1979	Imperial Valley-06	Strike-slip	0.76	44.3
165	6.5	1979	Imperial Valley-06	Strike-slip	0.28	30.5
495	6.8	1985	Nahanni, Canada	Thrust	1.18	43.9
496	6.8	1985	Nahanni, Canada	Thrust	0.45	34.7
741	6.9	1989	Loma Prieta	Strike-slip	0.64	55.9
753	6.9	1989	Loma Prieta	Strike-slip	0.51	45.5
825	7	1992	Cape Mendocino	Thrust	1.43	119.5
1004	6.7	1994	Northridge-01	Thrust	0.73	70.1
1048	6.7	1994	Northridge-01	Thrust	0.42	53.2
1176	7.5	1999	Kocaeli, Turkey	Strike-slip	0.31	73
1504	7.6	1999	Chi-Chi, Taiwan	Thrust	0.56	91.8
1517	7.6	1999	Chi-Chi, Taiwan	Thrust	1.16	115.1
2114	7.9	2002	Denali, Alaska	Strike-slip	0.33	126.4

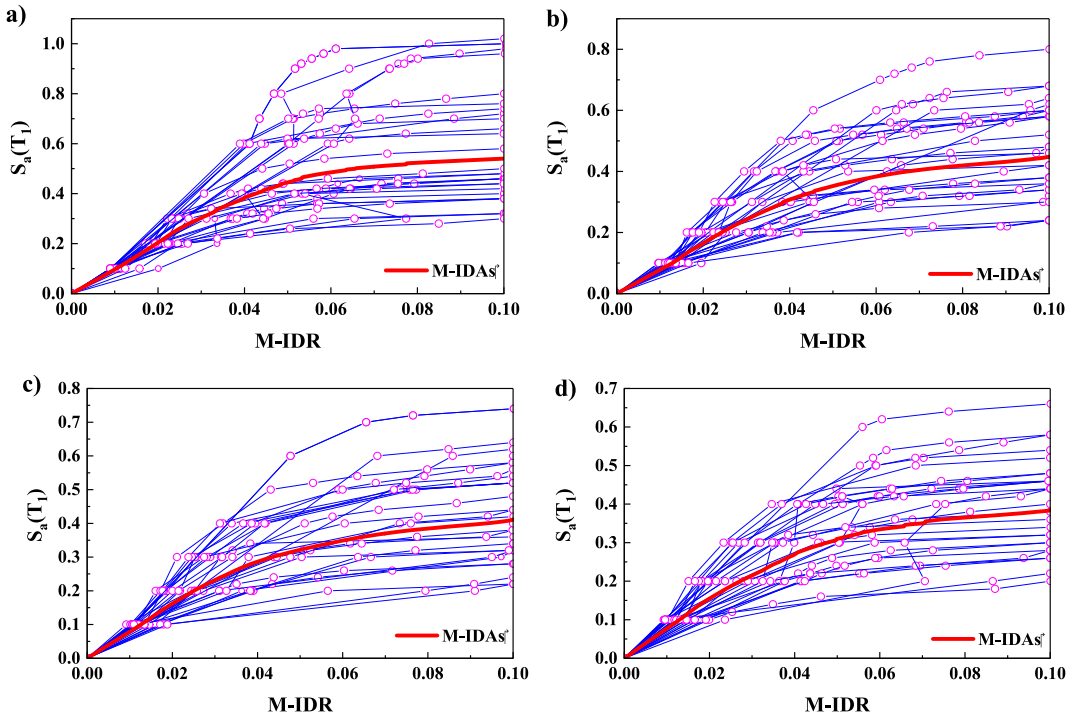

Fig. 9. IDA curves of the 7-story SMRF founded on soil type B assuming, a) rigid connection, b) 80% rigidity, c) 70% rigidity, d) 60% rigidity, subjected to NF-PL ground motions.

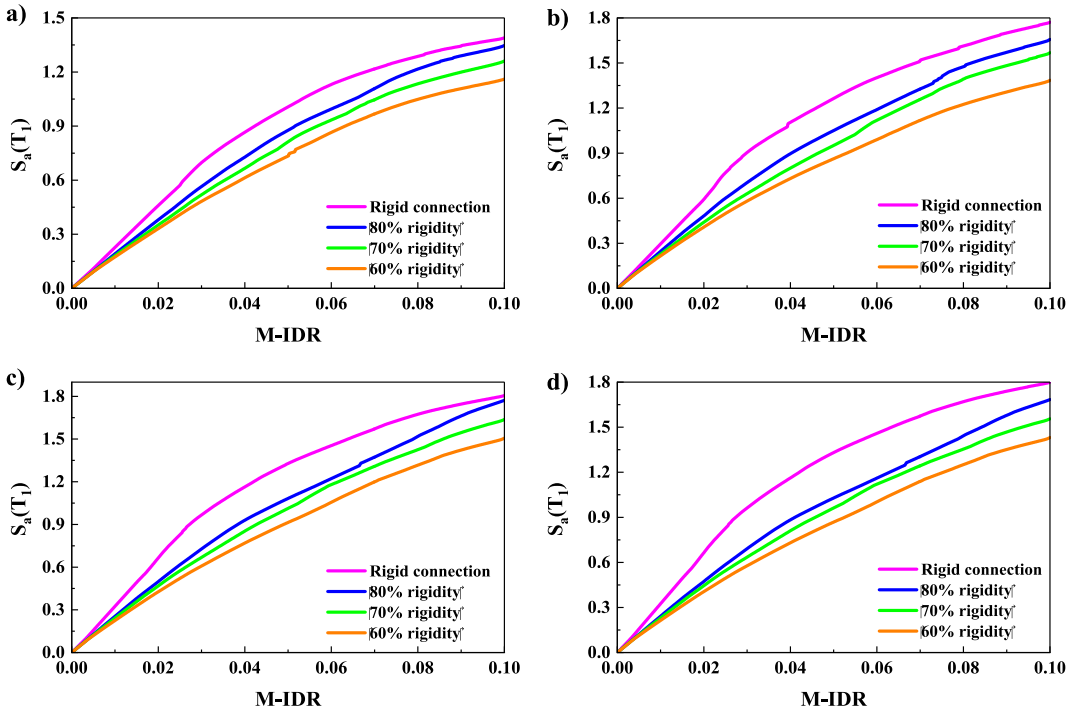

Fig. 10. M−IDA curves of the 3-Story SMRF considering four cases of rigidity, a) soil type B, b) soil type C, c) soil type D, and d) soil type E, subjected to NF-PL ground motions.

In addition, for the 3-Story SMRF founded on soil type C, assuming the rigidity of 80 %, 70 %, and 60 % can decrease the $S_a(T_1)$ values of the performance level of LS by 21.98 %, 29.78 %, and 35.24 %, respectively, and for soil type D, the $S_a(T_1)$ values of the performance level of LS decreased by 25.51 %, 30.71 %, and 37.12 %, respectively. In soil type E, the $S_a(T_1)$ values of the performance level of LS experienced a reduction of 29.18 %, 34.02 %, and 40.19 %, respectively. Therefore, the highest reduction occurred in the 3-Story SMRF founded on soil type E. Moreover, similar trends were observed in Table 11 for NF-NP ground motions. According to results, assuming a semi-rigid connection can widely affect the seismic performance levels and may result in wrong evaluations in seismic vulnerability assessment of SMRFs. Results presented in the Tables 10 and 11 can be used for the initial estimation of the rigidity effects.

Table 10
Seismic limit-state capacities of the 3-Story SMRF in four cases of rigidity and soil types assuming NF-PL ground motions.

Performance level	IO	LS	CP	TC	IO	LS	CP	TC
3-Story SMRF	Soil type B				Soil type C			
Rigid connection	0.156	0.571	1.006	1.389	0.206	0.769	1.263	1.771
80 % rigidity	0.133	0.473	0.876	1.347	0.172	0.600	1.050	1.657
70 % rigidity	0.128	0.435	0.813	1.261	0.162	0.540	0.951	1.568
60 % rigidity	0.125	0.408	0.733	1.160	0.155	0.498	0.862	1.385
3-Story SMRF	Soil type D				Soil type E			
Rigid connection	0.224	0.827	1.328	1.805	0.223	0.826	1.330	1.800
80 % rigidity	0.178	0.616	1.082	1.772	0.169	0.585	1.028	1.683
70 % rigidity	0.171	0.573	1.013	1.637	0.162	0.545	0.962	1.555
60 % rigidity	0.162	0.520	0.914	1.506	0.154	0.494	0.868	1.431

Table 11
Seismic limit-state capacities of the 3-Story SMRF in four cases of rigidity and soil types assuming NF-NP ground motions.

Performance level	IO	LS	CP	TC	IO	LS	CP	TC
3-Story SMRF	Soil type B				Soil type C			
Rigid connection	0.152	0.580	1.070	1.553	0.192	0.716	1.251	1.917
80 % rigidity	0.127	0.477	0.897	1.489	0.168	0.612	1.139	1.816
70 % rigidity	0.124	0.443	0.836	1.352	0.163	0.598	1.121	1.780
60 % rigidity	0.122	0.432	0.811	1.260	0.154	0.583	1.106	1.756
3-Story SMRF	Soil type D				Soil type E			
Rigid connection	0.203	0.752	1.416	2.156	0.203	0.752	1.416	2.116
80 % rigidity	0.177	0.649	1.175	2.036	0.179	0.649	1.179	2.042
70 % rigidity	0.172	0.616	1.114	1.930	0.174	0.610	1.154	1.965
60 % rigidity	0.166	0.569	1.056	1.763	0.162	0.559	1.121	1.801

Fig. 11(a)-(d) present M−IDA curves of the 5-Story SMRF considering four cases of rigidity and four soil types subjected to NF-PL ground motions. It is shown that semi-rigid connections significantly decreased the values of M−IDA curves, similar to the previous results. Changing the type of connection after constructing the structure is not possible; therefore, it is suggested to consider the rigidity of connection as much as similar to the kind of connection. For the existing building, it is proposed to use SMA bolts with same size of steel bolts used for applying the connections. Tables 12 and 13 illustrate the seismic limit-state capacities of the 5-Story SMRF in four cases of rigidity and soil types assuming NF-PL and NF-NP ground motions, respectively. Comparing the results showed that a similar trend was observed for the 5-Story SMRF in all soil types.

Fig. 12(a)-(d) present M−IDA curves of the 7-Story SMRF considering four cases of rigidity and four soil types subjected to NF-PL ground motions. It is shown that semi-rigid connections can decrease the values of M−IDA curves. The 60 % rigidity had the lowest values of M−IDAs in all soil types, while rigid connection achieved higher values of M−IDAs.

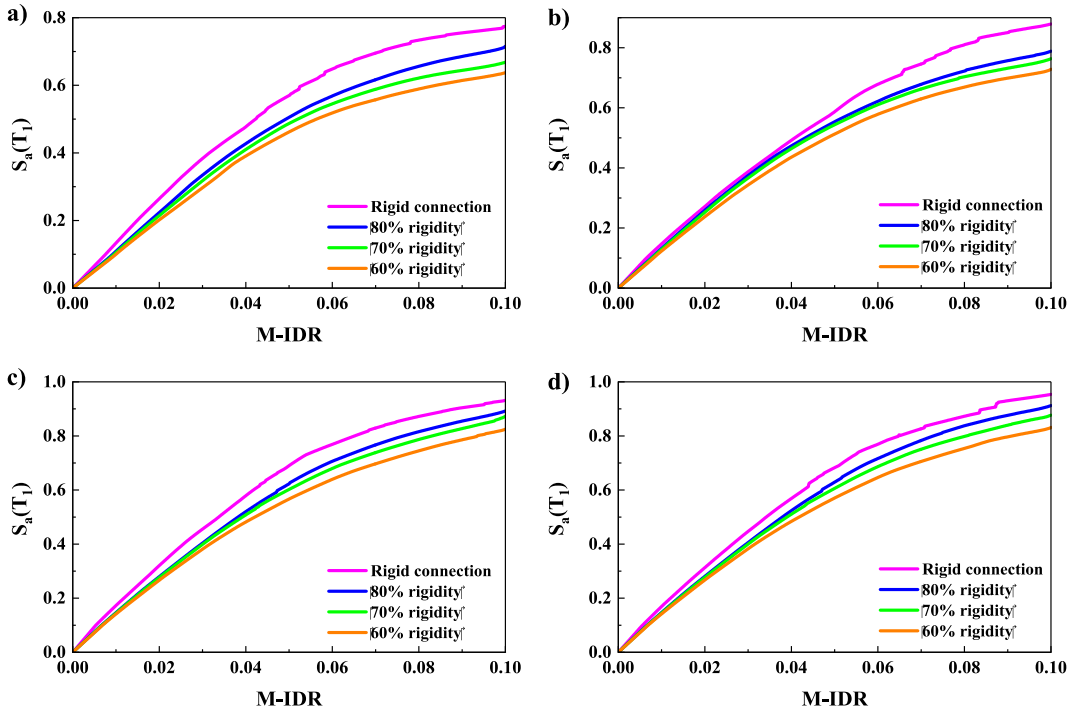

Fig. 11. M−IDA curves of the 5-Story SMRF considering four cases of rigidity, a) soil type B, b) soil type C, c) soil type D, and d) soil type E, subjected to NF-PL ground motions.

Table 12
Seismic limit-state capacities of the 5-Story SMRF in four cases of rigidity and soil types assuming NF-PL ground motions.

Performance level	IO	LS	CP	TC	IO	LS	CP	TC
5-Story SMRF	Soil type B				Soil type C			
Rigid connection	0.092	0.326	0.569	0.774	0.107	0.332	0.586	0.878
80 % rigidity	0.075	0.280	0.505	0.715	0.092	0.318	0.553	0.788
70 % rigidity	0.072	0.266	0.487	0.668	0.089	0.311	0.543	0.763
60 % rigidity	0.069	0.248	0.461	0.637	0.085	0.292	0.512	0.728
5-Story SMRF	Soil type D				Soil type E			
Rigid connection	0.126	0.392	0.690	0.931	0.122	0.381	0.682	0.953
80 % rigidity	0.104	0.342	0.623	0.892	0.105	0.344	0.629	0.912
70 % rigidity	0.103	0.338	0.602	0.872	0.103	0.339	0.605	0.876
60 % rigidity	0.101	0.324	0.566	0.824	0.101	0.325	0.570	0.831

Table 13
Seismic limit-state capacities of the 5-Story SMRF in four cases of rigidity and soil types assuming NF-NP ground motions.

Performance level	IO	LS	CP	TC	IO	LS	CP	TC
5-Story SMRF	Soil type B				Soil type C			
Rigid connection	0.077	0.293	0.538	0.684	0.083	0.347	0.558	0.754
80 % rigidity	0.067	0.242	0.436	0.645	0.079	0.303	0.524	0.704
70 % rigidity	0.065	0.245	0.430	0.613	0.078	0.284	0.509	0.700
60 % rigidity	0.063	0.227	0.405	0.568	0.077	0.272	0.490	0.681
5-Story SMRF	Soil type D				Soil type E			
Rigid connection	0.104	0.355	0.685	0.937	0.105	0.365	0.705	0.950
80 % rigidity	0.090	0.337	0.612	0.855	0.090	0.341	0.622	0.861
70 % rigidity	0.088	0.320	0.583	0.839	0.088	0.323	0.587	0.857
60 % rigidity	0.086	0.229	0.544	0.807	0.086	0.290	0.529	0.819

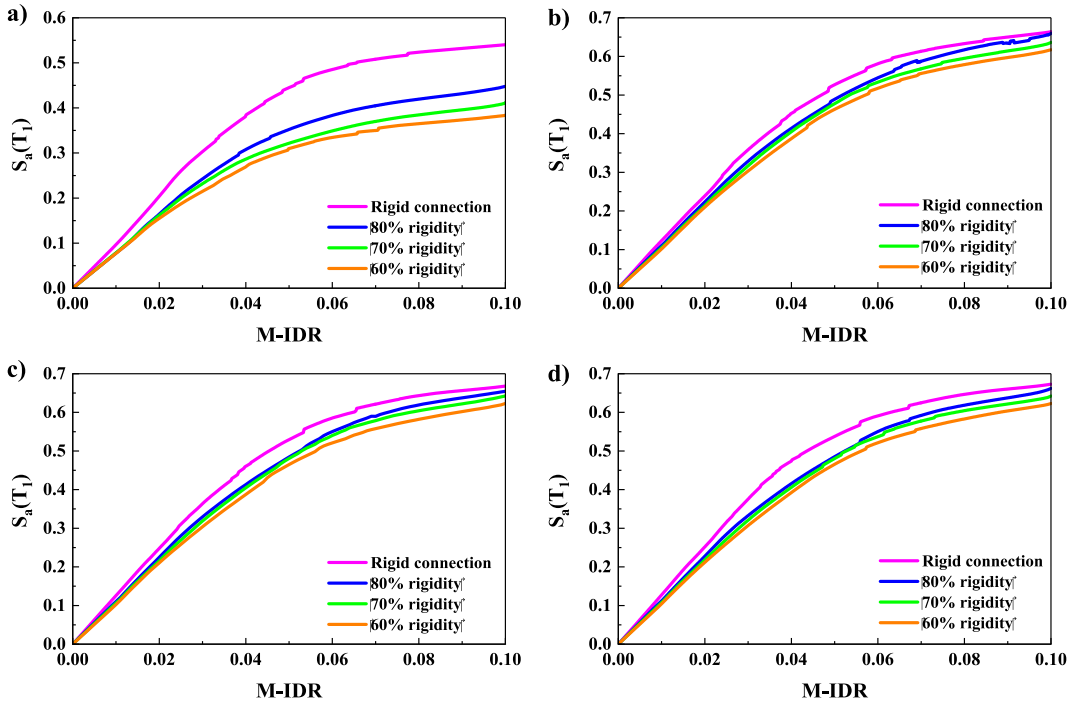

Fig. 12. M−IDA curves of the 7-Story SMRF considering four cases of rigidity, a) soil type B, b) soil type C, c) soil type D, and d) soil type E, subjected to NF-PL ground motions.

Tables 14 and 15 illustrate the seismic limit-state capacities of the 7-Story SMRF in four cases of rigidity and soil types assuming NF-PL and NF-NP ground motions, respectively. According to results presented in Table 14, assuming the rigidity of 80 %, 70 %, and 60 % for the 7-Story SMRF founded on soil type B can decrease the $S_a(T_1)$ values of the performance level of LS by 20.77 %, 23.46 %, and 28.46 %, respectively. In addition, for the 7-Story SMRF founded on soil type C, assuming the rigidity of 80 %, 70 %, and 60 % can decrease the $S_a(T_1)$ values of the performance level of LS by 8.25 %, 11.88 %, and 14.85 %, respectively, and for soil type D, the $S_a(T_1)$ values of the performance level of LS decreased by 9.68 %, 13.23 %, and 16.77 %, respectively. In soil type E, the $S_a(T_1)$ values of the performance level of LS experienced a reduction of 11.43 %, 13.97 %, and 17.46 %, respectively. Therefore, the highest reduction occurred in the 7-Story SMRF founded on soil type B. Moreover, similar trends were observed in Table 15 for NF-NP ground motions. By improving the connections of the 7-Story SMRF found on soil type B with rigidity of 80 %, 70 %, and 60 %, the performance level of TC significantly increased by 27.74 %, 40.63 %, and 49.08 %,

Table 14
Seismic limit-state capacities of the 7-Story SMRF in four cases of rigidity and soil types assuming NF-PL ground motions.

Performance level	IO	LS	CP	TC	IO	LS	CP	TC
7-Story SMRF	Soil type B				Soil type C			
Rigid connection	0.067	0.260	0.445	0.540	0.087	0.303	0.526	0.664
80 % rigidity	0.054	0.206	0.352	0.447	0.077	0.278	0.489	0.659
70 % rigidity	0.055	0.199	0.321	0.411	0.073	0.267	0.477	0.636
60 % rigidity	0.054	0.186	0.309	0.383	0.070	0.258	0.463	0.617
7-Story SMRF	Soil type D				Soil type E			
Rigid connection	0.088	0.310	0.529	0.668	0.089	0.315	0.537	0.672
80 % rigidity	0.077	0.280	0.484	0.649	0.077	0.279	0.475	0.649
70 % rigidity	0.074	0.269	0.480	0.642	0.075	0.271	0.480	0.642
60 % rigidity	0.071	0.258	0.464	0.623	0.072	0.260	0.465	0.623

Table 15
Seismic limit-state capacities of the 7-Story SMRF in four cases of rigidity and soil types assuming NF-NP ground motions.

Performance level	IO	LS	CP	TC	IO	LS	CP	TC
7-Story SMRF	Soil type B				Soil type C			
Rigid connection	0.051	0.208	0.367	0.440	0.063	0.241	0.456	0.573
80 % rigidity	0.048	0.174	0.301	0.367	0.056	0.230	0.407	0.552
70 % rigidity	0.047	0.170	0.282	0.339	0.055	0.227	0.402	0.531
60 % rigidity	0.045	0.161	0.255	0.305	0.054	0.220	0.392	0.490
7-Story SMRF	Soil type D				Soil type E			
Rigid connection	0.061	0.231	0.451	0.579	0.065	0.244	0.452	0.594
80 % rigidity	0.058	0.237	0.411	0.547	0.059	0.236	0.409	0.555
70 % rigidity	0.057	0.232	0.404	0.535	0.058	0.238	0.405	0.525
60 % rigidity	0.055	0.223	0.391	0.499	0.057	0.229	0.402	0.502

respectively.

It can be seen that SMA bolts used in the 7-Story SMRF founded on soil type E with 80 %, 70 %, and 60 % of rigidity significantly increased the performance level of TC by 23.72 %, 27.10 %, and 30.97 %, respectively.

Fig. 13(a)-(d) present M−IDA curves of the 9-Story SMRF considering four cases of rigidity and four soil types subjected to NF-PL ground motions. It is shown that semi-rigid connections significantly decreased the values of M−IDA curves, similar to the previous results. In addition, Tables 16 and 17 illustrate the seismic limit-state capacities of the 9-Story SMRF in four cases of rigidity and soil types assuming NF-PL and NF-NP ground motions, respectively. A similar trend was observed for the 9-Story SMRF in all soil types.

3.2. SSI effects

In this section, SSI effects on M−IDA curves of the 3-Story and 7-Story SMRFs were investigated. Figs. 14 and 15 present M−IDA curves

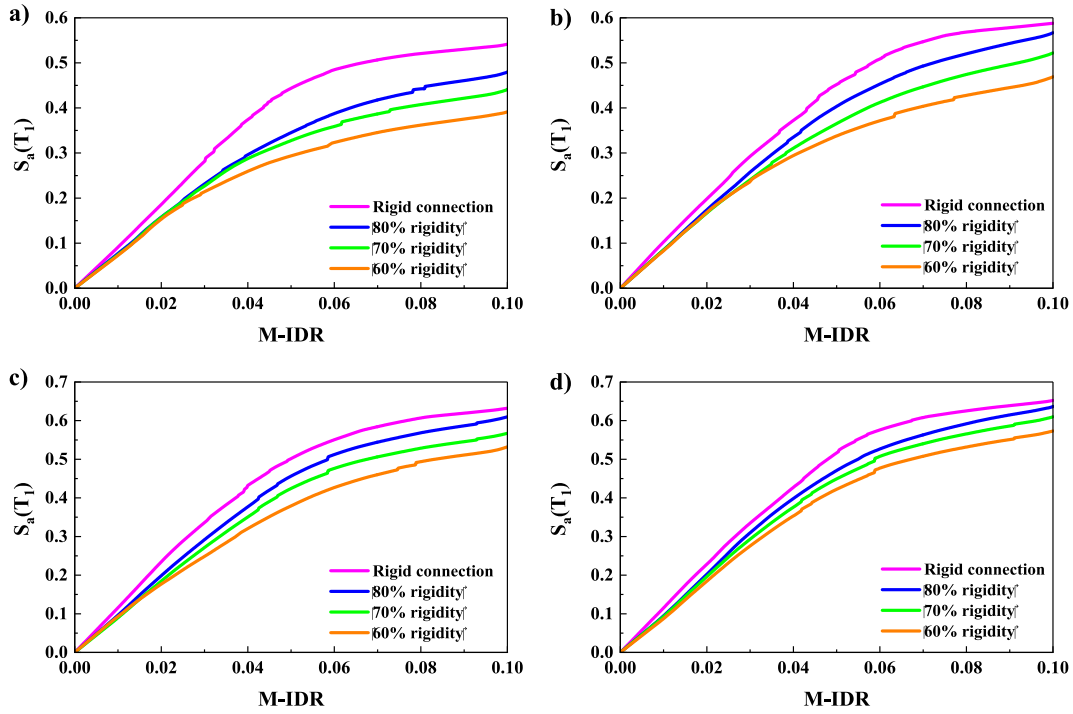

Fig. 13. M−IDA curves of the 9-Story SMRF considering four cases of rigidity, a) soil type B, b) soil type C, c) soil type D, and d) soil type E, subjected to NF-PL ground motions.

Table 16
Seismic limit-state capacities of the 9-Story SMRF in four cases of rigidity and soil types assuming NF-PL ground motions.

Performance level	IO	LS	CP	TC	IO	LS	CP	TC
9-Story SMRF	Soil type B				Soil type C			
Rigid connection	0.063	0.234	0.443	0.541	0.072	0.244	0.451	0.587
80 % rigidity	0.054	0.195	0.345	0.479	0.059	0.215	0.403	0.566
70 % rigidity	0.052	0.192	0.327	0.441	0.059	0.204	0.365	0.522
60 % rigidity	0.050	0.186	0.293	0.391	0.058	0.203	0.337	0.469
9-Story SMRF	Soil type D				Soil type E			
Rigid connection	0.080	0.288	0.501	0.632	0.080	0.284	0.516	0.652
80 % rigidity	0.067	0.246	0.456	0.609	0.065	0.257	0.470	0.637
70 % rigidity	0.065	0.229	0.424	0.567	0.064	0.246	0.449	0.609
60 % rigidity	0.062	0.0.213	0.379	0.532	0.061	0.231	0.422	0.573

Table 17
Seismic limit-state capacities of the 9-Story SMRF in four cases of rigidity and soil types assuming NF-NP ground motions.

Performance level	IO	LS	CP	TC	IO	LS	CP	TC
9-Story SMRF	Soil type B				Soil type C			
Rigid connection	0.046	0.177	0.348	0.411	0.050	0.190	0.400	0.532
80 % rigidity	0.045	0.173	0.283	0.375	0.050	0.188	0.325	0.437
70 % rigidity	0.045	0.170	0.272	0.352	0.048	0.185	0.307	0.402
60 % rigidity	0.044	0.164	0.246	0.316	0.047	0.180	0.296	0.377
9-Story SMRF	Soil type D				Soil type E			
Rigid connection	0.056	0.232	0.418	0.520	0.057	0.239	0.424	0.556
80 % rigidity	0.055	0.211	0.360	0.472	0.053	0.212	0.371	0.486
70 % rigidity	0.054	0.210	0.342	0.450	0.052	0.211	0.356	0.471
60 % rigidity	0.054	0.205	0.329	0.431	0.052	0.206	0.332	0.460

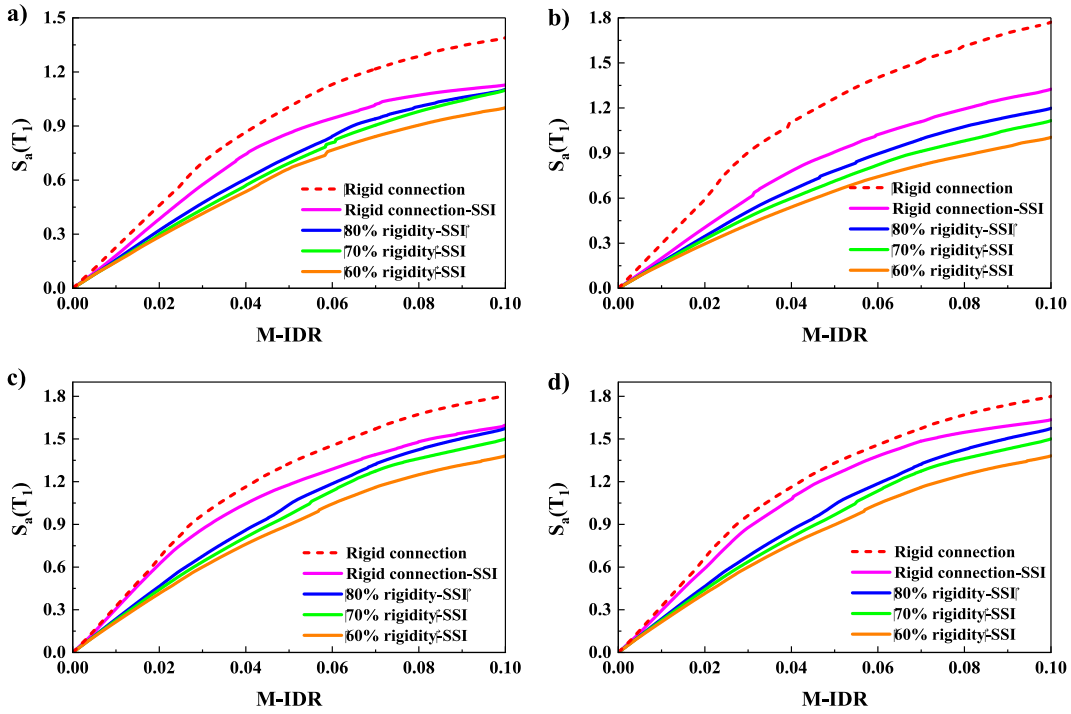

Fig. 14. M−IDA curves of the 3-Story SMRF considering four cases of rigidity and SSI effects, a) soil type B, b) soil type C, c) soil type D, and d) soil type E, subjected to NF-PL ground motions.

of the 3-Story and 7-Story SMRF considering four cases of rigidity and four soil types with SSI effect subjected to NF-PL ground motions, respectively. It can be seen that SSI effects can significantly decrease the $S_a(T_1)$ values of M−IDA curves in all soil types. Therefore, it is suggested to consider the SSI effect for modeling and investigating the limit-state performance levels. In addition, semi-rigid connections can decrease the values of M−IDA curves, while the 60 % rigidity had the lowest values of M−IDAs in all soil types.

Tables 18 and 19 illustrate the seismic limit-state capacities of the 3-Story and 7-Story SMRFs in four cases of rigidity and soil types with SSI effects assuming NF-PL ground motions, respectively. According to Table 18, considering the rigidity of 80 %, 70 %, and 60 % for the 3-Story SMRF founded on soil type B with SSI effects decreased the $S_a(T_1)$ values of the performance level of LS by 17.26 %, 22.87 %, and 27.23 %, respectively. In addition, for the 3-Story SMRF founded on soil type C with SSI effects, considering the rigidity of 80 %, 70 %, and 60 %

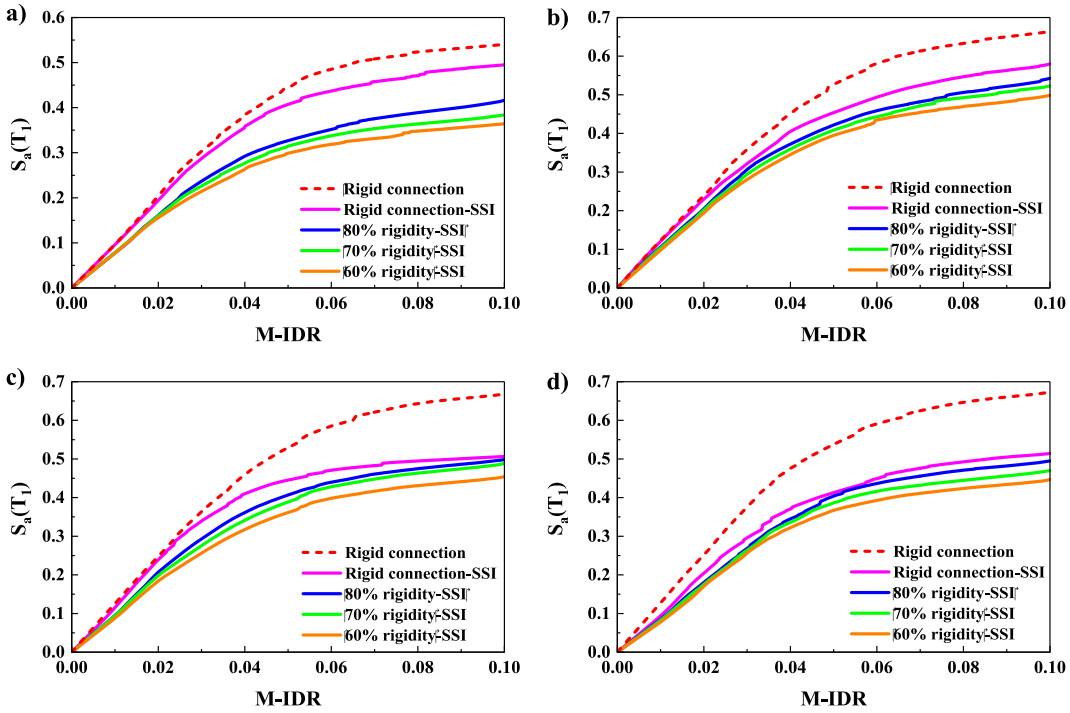

Fig. 15. M−IDA curves of the 7-Story SMRF considering four cases of rigidity and SSI effects, a) soil type B, b) soil type C, c) soil type D, and d) soil type E, subjected to NF-PL ground motions.

Table 18
Seismic limit-state capacities of the 3-Story SMRF in four cases of rigidity and soil types with SSI effects assuming NF-PL ground motions.

Performance level	IO	LS	CP	TC	IO	LS	CP	TC
3-Story SMRF	Soil type B				Soil type C			
Rigid connection-SSI	0.123	0.481	0.860	1.128	0.139	0.502	0.907	1.325
80 % rigidity-SSI	0.108	0.398	0.729	1.102	0.120	0.430	0.782	1.198
70 % rigidity-SSI	0.105	0.371	0.694	1.099	0.117	0.400	0.713	1.116
60 % rigidity-SSI	0.104	0.350	0.663	1.002	0.113	0.360	0.647	1.005
3-Story SMRF	Soil type D				Soil type E			
Rigid connection-SSI	0.209	0.756	1.178	1.597	0.202	0.742	1.249	1.635
80 % rigidity-SSI	0.164	0.578	1.038	1.574	0.164	0.578	1.038	1.574
70 % rigidity-SSI	0.159	0.543	0.967	1.501	0.159	0.543	0.967	1.501
60 % rigidity-SSI	0.153	0.509	0.897	1.381	0.153	0.509	0.897	1.381

Table 19
Seismic limit-state capacities of the 7-Story SMRF in four cases of rigidity and soil types with SSI effects assuming NF-PL ground motions.

Performance level	IO	LS	CP	TC	IO	LS	CP	TC
7-Story SMRF	Soil type B				Soil type C			
Rigid connection-SSI	0.067	0.245	0.407	0.494	0.086	0.279	0.453	0.579
80 % rigidity-SSI	0.054	0.202	0.326	0.416	0.074	0.258	0.421	0.542
70 % rigidity-SSI	0.055	0.197	0.314	0.383	0.073	0.248	0.408	0.522
60 % rigidity-SSI	0.054	0.186	0.298	0.364	0.068	0.240	0.394	0.498
7-Story SMRF	Soil type D				Soil type E			
Rigid connection-SSI	0.079	0.296	0.445	0.506	0.065	0.255	0.412	0.514
80 % rigidity-SSI	0.066	0.252	0.406	0.498	0.059	0.224	0.403	0.494
70 % rigidity-SSI	0.065	0.237	0.388	0.488	0.057	0.218	0.386	0.470
60 % rigidity-SSI	0.061	0.221	0.361	0.454	0.054	0.213	0.366	0.447

decreased the $S_a(T_1)$ values of the performance level of LS by 14.34 %, 20.32 %, and 28.29 %, respectively. While for soil type D with SSI effects, the $S_a(T_1)$ values of the performance level of LS decreased by 23.54 %, 28.17 %, and 32.67 %, respectively. In addition, using SMA bolts increased the performance levels of three assumed rigidities and can be used for retrofitting the semi-rigid connections.

In soil type E with SSI effects, the $S_a(T_1)$ values of the performance level of LS experienced a reduction of 22.10 %, 26.82 %, and 31.40 %, respectively. Therefore, the highest reduction occurred in the 3-Story SMRF founded on soil type D with SSI effects.

According to Table 19, considering the rigidity of 80 %, 70 %, and 60 % for the 7-Story SMRF founded on soil type B with SSI effects decreased the $S_a(T_1)$ values of the performance level of LS by 17.55 %, 19.59 %, and 24.08 %, respectively. In addition, for the 7-Story SMRF founded on soil type C with SSI effects, considering the rigidity of 80 %, 70 %, and 60 % decreased the $S_a(T_1)$ values of the performance level of LS by 7.53

%, 11.11 %, and 13.98 %, respectively. While for soil type D with SSI effects, the $S_a(T_1)$ values of the performance level of LS decreased by 14.86 %, 19.93 %, and 25.34 %, respectively. In soil type E with SSI effects, the $S_a(T_1)$ values of the performance level of LS experienced a reduction of 12.16 %, 14.51 %, and 16.47 %, respectively. Therefore, the highest reduction occurred in the 7-Story SMRF founded on soil type D with SSI effects. Assuming a semi-rigid connection can significantly affect the idea of SMRFs with rigid connections. In other words, in design procedures, it was assumed that SMRFs would have rigid connections, while in the real condition the type of the connection cannot fulfill the rigidity. Then, two factors of rigidity of connections and SSI effects can change the expected performance level and this may impose wrong seismic vulnerability assessment. Moreover, it is shown that the rigidity and SSI effect play a key role in the vulnerability assessment of SMRFs and should be considered in the modeling process.

4. Seismic fragility curves

Seismic fragility curves are the most common way of comparing the seismic collapse probability of the structures. Using these curves, it is possible to achieve the probability of exceeding a considered damaged state. In this section, four performance levels were considered to achieve seismic fragility curves. Fig. 16(a)-(d) present the seismic fragility curves of the 5-Story SMRF founded on soil type B considering four cases of rigidity subjected to NF-PL ground motions. The results showed that reducing the rigidity of the connection could significantly reduce the seismic probability of collapse of the 5-Story SMRF. In the performance level of IO, the seismic collapse probability of 50 % in the rigid connection, 80 % rigidity, 70 % rigidity, and 60 % rigidity were achieved equal to 0.092, 0.075, 0.072, and 0.069, respectively.

In the performance level of LS, the seismic collapse probability of 50 % in the rigid connection, 80 % rigidity, 70 % rigidity, and 60 % rigidity were achieved equal to 0.326, 0.280, 0.266, and 0.248, respectively. In addition, in the performance level of CP, the seismic collapse probability of 50 % in the rigid connection, 80 % rigidity, 70 % rigidity, and 60 % rigidity were achieved equal to 0.569, 0.505, 0.487, and 0.461, respectively, while for the performance level of TC, values were equal to 0.774, 0.715, 0.668, and 0.637, respectively. Therefore, it can be concluded that the percentage of the connection rigidity can highly affect the seismic probability of collapse, and it should be considered in the seismic response analysis. Similar results were obtained from comparing the results of other considered SMRFs.

Fig. 17(a)-(d) present the seismic fragility curves of the 7-Story SMRF founded on soil type E considering four cases of rigidity with and without SSI effects subjected to NF-PL ground motions. It can be seen that in all cases, the SSI effect can significantly decrease the seismic collapse probability of the 7-Story SMRF. For example, In the performance level of LS, the seismic collapse probability of 50 % in the rigid connection, 80 % rigidity, 70 % rigidity, and 60 % rigidity were achieved equal to 0.315, 0.279, 0.271, and 0.260, respectively, while the SSI effects reduced the values to 0.255, 0.224, 0.218, and 0.213, correspondingly. Moreover, in the performance level of TC, the seismic collapse probability of 50 % in the rigid connection, 80 % rigidity, 70 % rigidity, and 60 % rigidity were achieved equal to 0.672, 0.649, 0.642, and 0.623, respectively, while the SSI effects reduced the values to 0.514, 0.494, 0.470, and 0.447, correspondingly. Therefore, it is suggested to consider the SSI effects in the modeling due to their significant influence on the seismic collapse probability. To improve the seismic collapse probability of semi-rigid connections, SMA bolts can be replaced. For example, using this strategy in the 80 % rigidity increased the seismic collapse probability of 50 % in the performance levels of IO, LS, CP and TC by 1.8 % (from 0.054 to 0.055), 1.45 % (from 0.206 to 0.209), 12.5 % (from 0.352 to 0.396), and 31.76 % (from 0.447 to 0.589), respectively. For the 70 % rigidity, the performance levels of IO, LS, CP and TC increased by 1.81 % (from 0.055 to 0.056), 1 % (from 0.199 to 0.201), 14.64 % (from 0.321 to 0.368), and 36 % (from 0.411 to 0.559), respectively. While for the 60 % rigidity, the performance levels of IO, LS, CP and TC increased by 7.4 % (from 0.054 to 0.058), 0.5 % (from 0.186 to 0.187), 20.06 % (from 0.309 to 0.371), and 62.66 % (from 0.383 to 0.623), respectively. Similar results were obtained from comparing the results of other considered SMRFs.

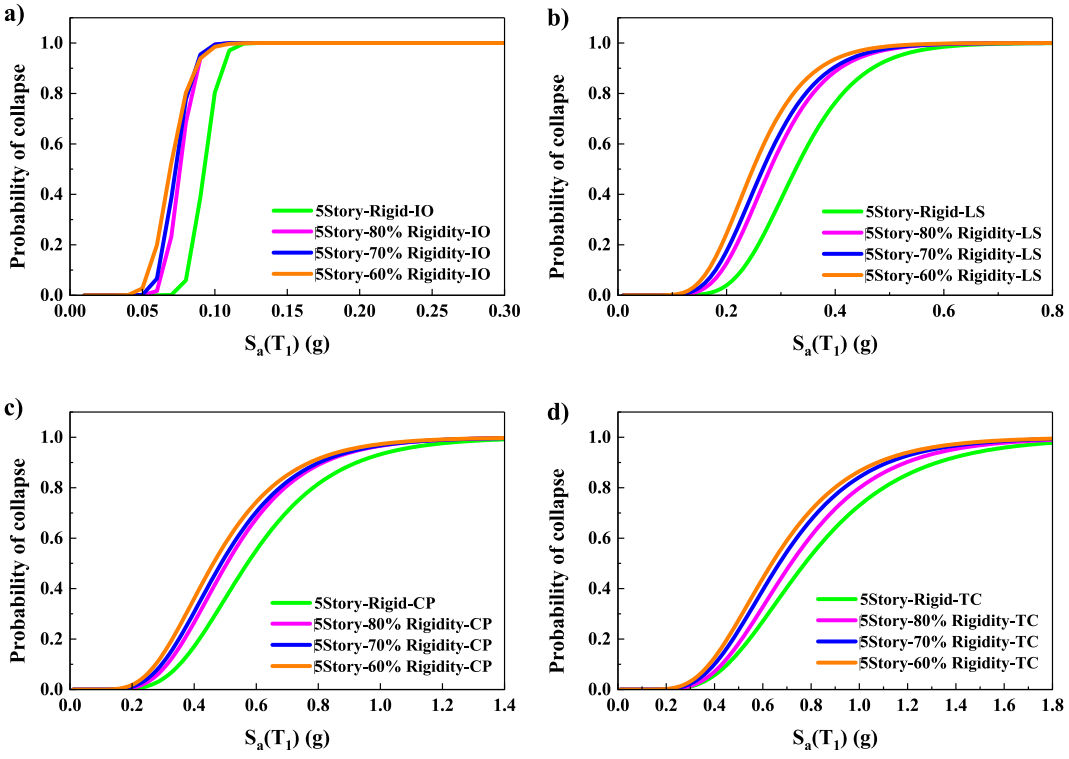

Fig. 16. Seismic fragility curves of the 5-Story SMRF founded on soil type B considering four cases of rigidity subjected to NF-PL ground motions.

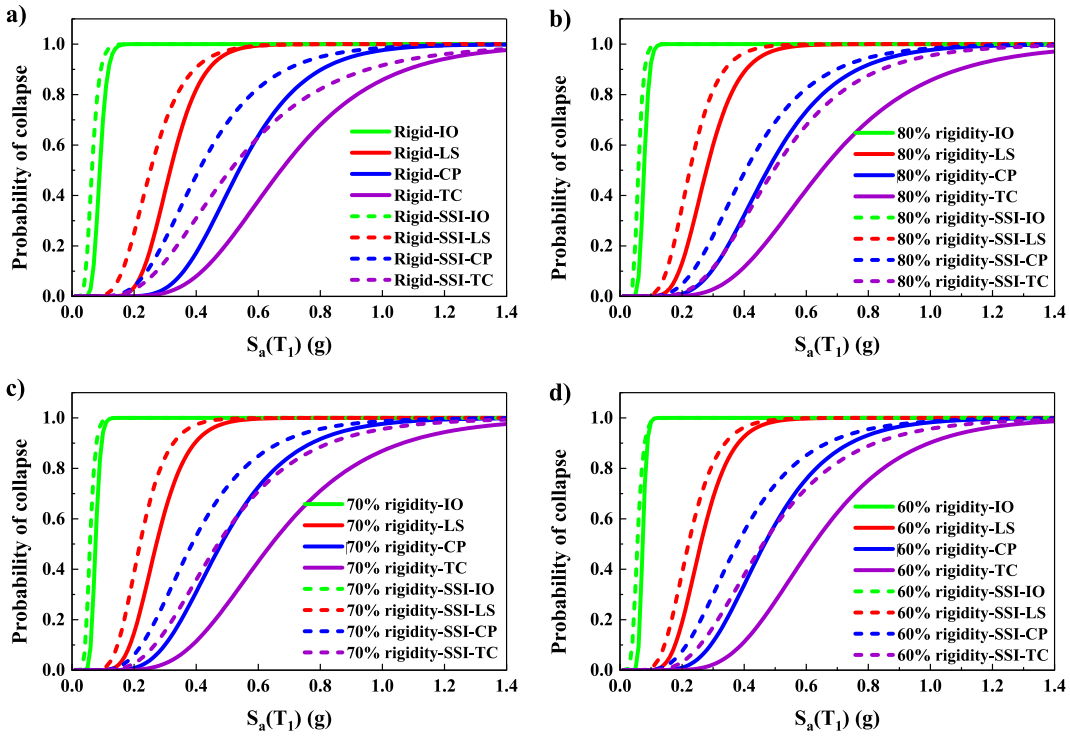

Fig. 17. Seismic fragility curves of the 7-Story SMRF founded on soil type E considering four cases of rigidity with and without SSI effects subjected to NF-PL ground motions.

5. Conclusion

Since the rigidity of connections can be a major issue for SMRFs during severe earthquakes, this paper has been focused on the seismic limit-state capacities of the rigid and semi-rigid connections of the 3-Story, 5-Story, 7-Story, and 9-Story SMRFs considering the SSI effects. Moreover, to improve the seismic limit-state capacities of the semi-rigid connections, SMA bolts have been used to control the EDPs and increase the performance levels. The results are summarized as follows:

- Comparing the results of the 3-Story, 5-Story, 7-Story, and 9-Story SMRFs showed that assuming semi-rigid connections significantly decreased the values of M−IDA curves and the rigidity of 60 % had the lowest values of M−IDAs in all soil types, while rigid connection achieved higher values of M−IDAs. For instance, assuming the rigidity of 80 %, 70 %, and 60 % for the 3-Story SMRF founded on soil type E can decrease the $S_a(T_1)$ values of the performance level of LS by 29.18 %, 34.02 %, and 40.19 %, respectively.
- Considering the SSI effects can considerably decrease the $S_a(T_1)$ values of M−IDA curves in all soil types. For example, for the 3-Story SMRF founded on soil type D with the SSI effects, considering the rigidity of 80 %, 70 %, and 60 % decreased the $S_a(T_1)$ values of the performance level of LS by 23.54 %, 28.17 %, and 32.67 %, respectively.
- It seems that there is different rigidity between the designed connection and the real one, which can be considered as a problematic issue due to the importance of connections in the seismic performance of SMRFs. Therefore, it is suggested to consider the real condition of the structure by assuming the rigidity of the connections in modeling process.
- Seismic fragility curves were compared to investigate the seismic probability of exceeding an assumed damage state of SMRFs. Assuming the semi-rigid connection can significantly reduce the seismic collapse probability. For example, the seismic probability of collapse of the 5-Story SMRF in the rigidity of 60 % for the performance level of IO, LS, CP, and TC experienced a reduction of 25 %, 23.92 %, 18.98 %, and 17.70 %, respectively, compared to the rigid connection.
- Assuming the SSI effect in modeling process allows us to simulate real condition of building. In addition, the results showed that the SSI effects could significantly decrease the seismic collapse probability; thus, it is recommended to take into account the SSI effects in the seismic vulnerability assessment of SMRFs.
- The superelastic behavior of SMA materials can widely help designers to compensate for the gap between the design process and construction conditions. This paper proposed SMA bolts for semi-rigid connections that can improve the seismic limit-state performance levels of SMRFs under severe earthquakes. Moreover, SMA bolts can be replaced in semi-rigid connections of existing buildings for retrofitting purposes. For brevity, implementing SMA bolts in the 7-Story SMRF founded on soil type B with 80 %, 70 %, and 60 % of rigidity significantly increased the performance level of TC by 23.72 %, 27.10 %, and 30.97 %, respectively. In addition, using SMA bolts for the 80 %, 70 %, and 60 % rigidity connections in the 7-Story SMRF founded on soil type B increased the seismic collapse probability of 50 % in the performance levels of TC by 31.76 %, 36 %, and 62.66 %, respectively.

CRediT authorship contribution statement

F. Kazemi: Conceptualization, Methodology, Software, Validation, Formal analysis, Writing – original draft. **R. Jankowski:** Conceptualization, Methodology, Writing – review & editing.

Declaration of Competing Interest

The authors declare that they have no known competing financial interests or personal relationships that could have appeared to influence the work reported in this paper.

Data availability

No data was used for the research described in the article.

Acknowledgments

Numerical calculations were carried out at the Tri-City Academic Supercomputer and Network (*CI TASK*) in Gdańsk, Poland.

References

[1] Elnashai AS, Elghazouli AY. Seismic behaviour of semi-rigid steel frames. J Constr Steel Res 1994;29(1–3):149–74.
[2] Kameshki ES, Saka MP. Optimum design of nonlinear steel frames with semi-rigid connections using a genetic algorithm. Comput Struct 2001;79(17):1593–604.
[3] Gupta A., Krawinkler H. Seismic Demands for Performance Evaluation of Steel Moment Resisting Frame Structures, Technical Report 132. Stanford, CA: The John A. Blume Earthquake Engineering Research Center, Department of Civil Engineering, Stanford University; 1999.
[4] Abidelah A, Bouchaïr A, Kerdal DE. Experimental and analytical behavior of bolted end-plate connections with or without stiffeners. J Constr Steel Res 2012;76:13–27.
[5] Sherbourne AN, Bahaari MR. Finite element prediction of end plate bolted connection behavior. I: Parametric study. J Struct Eng 1997;123(2):157–64.
[6] Bahaari MR, Sherbourne AN. Finite element prediction of end plate bolted connection behavior. II: Analytic formulation. J Struct Eng 1997;123(2):165–75.
[7] Shi G, Shi Y, Wang Y, Bradford MA. Numerical simulation of steel pretensioned bolted end-plate connections of different types and details. Eng Struct 2008;30(10):2677–86.
[8] Kang WH, Hicks S, Uy B. Safety factors for the resistance of steel sections. Aust J Struct Eng 2015;16(2):116–28.
[9] Thai HT, Uy B, Kang WH, Hicks S. System reliability evaluation of steel frames with semi-rigid connections. J Constr Steel Res 2016;121:29–39.
[10] Wilde K, Gardoni P, Fujino Y. Base isolation system with shape memory alloy device for elevated highway bridges. Eng Struct 2000;22(3):222–9.
[11] Speicher MS, DesRoches R, Leon RT. Experimental results of a NiTi shape memory alloy (SMA)-based recentering beam-column connection. Eng Struct 2011;33(9):2448–57.
[12] Fang C, Yam MC, Lam AC, Xie L. Cyclic performance of extended end-plate connections equipped with shape memory alloy bolts. J Constr Steel Res 2014;94:122–36.
[13] Wang W, Chan TM, Shao H, Chen Y. Cyclic behavior of connections equipped with NiTi shape memory alloy and steel tendons between H-shaped beam to CHS column. Eng Struct 2015;88:37–50.
[14] Fang C, Yam MC, Chan TM, Wang W, Yang X, Lin X. A study of hybrid self-centring connections equipped with shape memory alloy washers and bolts. Eng Struct 2018;164:155–68.
[15] Chowdhury MA, Rahmzadeh A, Moradi S, Alam MS. Feasibility of using reduced length superelastic shape memory alloy strands in post-tensioned steel beam–column connections. J Intell Mater Syst Struct 2019;30(2):283–307.
[16] Fatahi B, Tabatabaiefar SHR. Fully nonlinear versus equivalent linear computation method for seismic analysis of midrise buildings on soft soils. Int J Geomech 2014;14(4):04014016.
[17] Raychowdhury P. Seismic response of low-rise steel moment-resisting frame (SMRF) buildings incorporating nonlinear soil–structure interaction (SSI). Eng Struct 2011;33(3):958–67.
[18] Petridis C, Pitilakis D. Fragility curve modifiers for reinforced concrete dual buildings, including nonlinear site effects and soil–structure interaction. Earthquake Spectra 2020;36(4):1930–51.
[19] Ghandil M, Behnamfar F. The near-field method for dynamic analysis of structures on soft soils including inelastic soil–structure interaction. Soil Dyn Earthquake Eng 2015;75:1–17.
[20] Ghandil M, Behnamfar F. Ductility demands of MRF structures on soft soils considering soil-structure interaction. Soil Dyn Earthquake Eng 2017;92:203–14.
[21] Elwardany H, Seleemah A, Jankowski R. Seismic pounding behavior of multi-story buildings in series considering the effect of infill panels. Eng Struct 2017;144:139–50.
[22] Elwardany H, Seleemah A, Jankowski R, El-Khoriby S. Influence of soil–structure interaction on seismic pounding between steel frame buildings considering the effect of infill panels. Bull Earthq Eng 2019;17(11):6165–202.
[23] Kazemi F, Mohebi B, Yakhchalian M. Predicting the seismic collapse capacity of adjacent structures prone to pounding. Can J Civ Eng 2020;47(6):663–77.
[24] Asgarkhani N, Yakhchalian M, Mohebi B. Evaluation of approximate methods for estimating residual drift demands in BRBFs. Eng Struct 2020;224:110849.
[25] Kazemi F, Miari M, Jankowski R. Investigating the effects of structural pounding on the seismic performance of adjacent RC and steel MRFs. Bull Earthq Eng 2021;19(1):317–43.
[26] Kazemi F, Mohebi B, Jankowski R. Predicting the seismic collapse capacity of adjacent SMRFs retrofitted with fluid viscous dampers in pounding condition. Mech Syst Sig Process 2021;161:107939.
[27] Yazdanpanah O, Mohebi B, Kazemi F, Mansouri I, Jankowski R. Development of fragility curves in adjacent steel moment-resisting frames considering pounding effects through improved wavelet-based refined damage-sensitive feature. Mech Syst Sig Process 2022;173:109038.
[28] Kazemi F, Asgarkhani N, Manguri A, Jankowski R. Investigating an optimal computational strategy to retrofit buildings with implementing viscous dampers, International Conference on Computational Science, Lecture Notes in Computer Science,13351. Cham: Springer; 2022. p. 184–91.
[29] Mitropoulou CC, Kostopanagiotis C, Kopanos M, Ioakim D, Lagaros ND. Influence of soil–structure interaction on fragility assessment of building structures. Structures 2016;6:85–98.
[30] Forcellini D. Analytical fragility curves of shallow-founded structures subjected to Soil-Structure Interaction (SSI) effects. Soil Dyn Earthquake Eng 2021;141:106487.
[31] Kamal M, Inel M. Correlation between Ground Motion Parameters and Displacement Demands of Mid-Rise RC Buildings on Soft Soils Considering Soil-Structure-Interaction. Buildings 2021;11(3):125.
[32] Kamal M, Inel M, Cayci BT. Seismic behavior of mid-rise reinforced concrete adjacent buildings considering soil-structure interaction. Journal of Building Engineering 2022;51:104296.
[33] Rajeev P, Tesfamariam S. Seismic fragilities of non-ductile reinforced concrete frames with consideration of soil structure interaction. Soil Dyn Earthquake Eng 2012;40:78–86.
[34] Harden CW, Hutchinson TC. Beam-on-nonlinear-Winkler-foundation modeling of shallow, rocking-dominated footings. Earthquake Spectra 2009;25(2):277–300.
[35] USGS. US Geological Survey; 2012. http://usgs.gov.
[36] Haghollahi S, Behnamfar F. Performance evaluation of special RC moment frames against collapse considering soil–structure interaction. Int J Geomech 2020;20(2):04019176.
[37] Madani B, Behnamfar F, Riahi HT. Dynamic response of structures subjected to pounding and structure–soil–structure interaction. Soil Dyn Earthquake Eng 2015;78:46–60.
[38] ASCE. Minimum design loads and associated criteria for buildings and other structures. Reston, VA: American Society of Civil Engineers; 2017. p. 7–16.
[39] Committee AISC. Specification for structural steel buildings (ANSI/AISC 360–10). Chicago-Illinois: American Institute of Steel Construction; 2016.
[40] AISC 341–10, seismic provisions for structural steel buildings. Chicago, IL: American Institute of Steel Construction; 2016.
[41] McKenna F, Fenves GL, Filippou FC, Scott MH. Open system for earthquake engineering simulation (OpenSees). Berkeley: Pacific Earthquake Engineering Research Center, University of California; 2016. berkeley.edu.
[42] Kazemi F, Mohebi B, Yakhchalian M. Evaluation the P-delta effect on collapse capacity of adjacent structures subjected to far-field ground motions. Civil Engineering Journal 2018;4(5):1066. https://doi.org/10.28991/cej-0309156.
[43] Mohebi B., Kazemi F., Yakhchalian M. Investigating the P-Delta effects on the seismic collapse capacity of adjacent structures, 16th European Conference on Earthquake Engineering (16ECEE), 18-21, June, Thessaloniki, Greece, 2018.
[44] Yakhchalian M, Asgarkhani N, Yakhchalian M. Evaluation of deflection amplification factor for steel buckling restrained braced frames. Journal of Building Engineering 2020;30:101228.
[45] Yakhchalian M, Yakhchalian M, Asgarkhani N. An advanced intensity measure for residual drift assessment of steel BRB frames. Bull Earthq Eng 2021;19(4):1931–55.
[46] Kazemi F., Mohebi B., Yakhchalian M. Enhancing the seismic performance of adjacent pounding structures using viscous dampers. In The 16th European Conference on Earthquake Engineering (16ECEE), 18-21, June, Thessaloniki, Greece, 2018.
[47] Mohebi B, Yazdanpanah O, Kazemi F, Formisano A. Seismic damage diagnosis in adjacent steel and RC MRFs considering pounding effects through improved wavelet-based damage-sensitive feature. Journal of Building Engineering 2021;33:101847.
[48] Terzaghi K. Theoretical Soil Mechanics, 314. New York: John Wiley and Sons Inc. p.1943.
[49] Meyerhof GG. Some recent research on the bearing capacity of foundations. Can Geotech J 1963;1(1):16–26.
[50] Boulanger RW, Curras CJ, Kutter BL, Wilson DW, Abghari A. Seismic soil-pile-structure interaction experiments and analyses. J Geotech Geoenviron Eng 1999;125(9):750–9.
[51] Gazetas G. Formulas and charts for impedances of surface and embedded foundations. Journal of geotechnical engineering 1991;117(9):1363–81.
[52] Calado L, De Matteis G, Landolfo R. Experimental response of top and seat angle semi-rigid steel frame connections. Mater Struct 2000;33(8):499–510.
[53] AlHendi H, Mahmoud M, Celikag M. Numerical study of top-and seat-angle with double web-angle connection with high-strength steel. J Constr Steel Res 2020;174:106297.
[54] Rigi A, JavidSharifi B, Hadianfard MA, Yang TY. Study of the seismic behavior of rigid and semi-rigid steel moment-resisting frames. J Constr Steel Res 2021;186:106910.
[55] Eatherton MR, Fahnestock LA, Miller DJ. Computational study of self-centering buckling-restrained braced frame seismic performance. Earthquake Eng Struct Dyn 2014;43(13):1897–914.
[56] Ke K, Zhou X, Zhu M, Yam MC, Wang Y, Zhang H. Seismic evaluation of industrial steel moment resisting frames with shape memory alloys using performance-spectra-based method. Journal of Building. Engineering 2021;103950.
[57] Applied Technology Council, & United States. Federal Emergency Management Agency. Quantification of building seismic performance factors. FEMA: US Department of Homeland Security; 2009.
[58] Fema-356.. Prestandard and commentary for the seismic rehabilitation of buildings. Washington, DC: Federal Emergency Management Agency; 2000.

Paper IV:

Kazemi, F., Asgarkhani, N., & Jankowski, R. (2023). Probabilistic assessment of SMRFs with infill masonry walls incorporating nonlinear soil-structure interaction. Bulletin of Earthquake Engineering, 21(1), 503-534. doi.org/10.1007/s10518-022-01547-0

Bulletin of Earthquake Engineering (2023) 21:503–534
https://doi.org/10.1007/s10518-022-01547-0

ORIGINAL ARTICLE

Probabilistic assessment of SMRFs with infill masonry walls incorporating nonlinear soil-structure interaction

F. Kazemi[1] · **N. Asgarkhani**[1] · **R. Jankowski**[1]

Received: 9 June 2022 / Accepted: 17 October 2022 / Published online: 8 November 2022
© The Author(s) 2022

Abstract
Infill Masonry Walls (IMWs) are used in the perimeter of a building to separate the inner and outer space. IMWs may affect the lateral behavior of buildings, while they are different from those partition walls that separate two inner spaces. This study focused on the seismic vulnerability assessment of Steel Moment-Resisting Frames (SMRFs) assuming different placement of IMWs incorporating nonlinear Soil-Structure Interaction (SSI). The aim is to explore the damage states of IMWs and use their ability for improving the vulnerability of SMRFs. For this purpose, the three, five, seven, and nine story levels (3-Story, 5-Story, 7-Story, and 9-Story) SMRFs were modeled considering four soil types. Incremental Dynamic Analyses (IDAs) were performed to determine the seismic performance limit-state capacities of SMRFs considering the Far-Fault (FF) record subset suggested by FEMA P695. To accurately model the influence of IMWs on the seismic response of SMRFs, a Tcl programming algorithm was developed to intelligently monitor the damage states of IMWs in each floor level. Results of the analysis show that assuming different placement of IMWs can significantly increase the seismic limit-state capacities of SMRFs with and without considering SSI effects. In addition, IMWs can play a crucial role to improve the seismic performances as well as the seismic collapse probability, which may be suggested for retrofitting purposes.

Keywords Infill masonry wall · Nonlinear soil-structure interaction · Seismic limit-state capacity · Seismic collapse probability · Seismic retrofit · Damage identification

1 Introduction

The Infill Masonry Walls (IMWs) have been considered as nonstructural members and were neglected in the modeling of buildings with their strength and stiffness. In addition, seismic provisions prescribed a factor to consider IMWs effects on the fundamental period of the buildings. Engineers do not consider the IMWs in their designing procedures and this may affect their models. To overcome this issue, some experimental investigations

✉ F. Kazemi
farzin.kazemi@pg.edu.pl

[1] Faculty of Civil and Environmental Engineering, Gdańsk University of Technology, ul. Narutowicza 11/12, 80-233 Gdansk, Poland

were made to find out the effects of IMWs on the structural response (e.g. Ramos et al. 2010, Preti et al. 2012, Salmanpour et al. 2015, Carpine et al. 2021). Brodsky and Yankelevsky (Brodsky and Yankelevsky 2017) focused on the effects of IMWs in the Reinforced Concrete (RC) frame by using half-scale specimens subjected to monotonic loads. Their results showed that IMWs increased the vertical loading resistance of the frame by an amount of 280% on average, and affected the failure mode. Nicoletti et al. (Nicoletti et al. 2020) proposed a procedure to determine the stiffness of IMWs in the modeling of RC frame and validated through an experimental work based on the in-situ impact load test. Uva et al. (Uva et al. 2012) investigated the effects of IMWs for an existing RC building located in Calabria, Italy, and proposed some factors to refine the structural response. Recently, scientific studies proved that the stiffness and strength provided by IMWs should be considered in the modeling process due to their effects on the global behavior of buildings (Mohamed and Romão 2020). In addition, the interaction between nonstructural components and structural members may lead to local damages in columns of buildings (Fardis et al. 1999; Perrone et al. 2017; Merino et al. 2020).

It is worth noting that the opening dimensions, boundary condition, geometry of wall (e.g. thickness and height), out-of-plane behavior, previous damage of IMWs, and double-leaf infills can highly influence the seismic behavior of buildings. Ozturkoglu et al. (Ozturkoglu et al. 2017) noted that the position and dimensions of openings could considerably influence the lateral stiffness and nonlinear behavior of RC structures, as compared to fully infilled and bare frames. Zuo et al. (Zuo et al. 2022) performed a parametric study to take the aspect ratio and opening dimensions of IMWs into account. Single and double-leaf infills were investigated under the in-plane and out-of-plane loads (Onat et al. 2018; Mazza and Donnici 2021). Misir et al. (Misir et al. 2016) proposed Z-ties as improving method that can help the double-leaf infills to withstand high lateral deformations. Furtado et al. (Furtado et al. 2016a, 2017) performed comprehensive experimental and numerical studies on lateral behavior and the out-of-plane failure of IMWs. They concluded that openings could reduce the frequency of IMWs by 20–40%, and the axial loads of lateral columns could increase the frequency of IMWs. In addition, they showed that the width of wall support and previous damages could considerably decrease the strength capacity of IMWs, even up to 60% (Furtado et al. 2020). Some investigations were carried out to evaluate the effects of material and geometry of IMWs, effects of lateral columns stiffness on the IMWs behavior, effects of the connection between IMWs and frame, as well as mechanical characteristics of IMWs on the seismic performance of buildings (Mazza and Donnici 2021; Wararuksajja et al. 2020; Huang et al. 2021). It was confirmed that previous damages of IMWs could significantly reduce the frequency of wall up to 5% and 35% corresponding to in-plane and out-of-plane loads (Furtado et al. 2017). Therefore, this effect should be considered for seismic vulnerability assessment of structures.

Many studies were performed to investigate the seismic failure probability of structures, while the IMWs were assumed as non-structural elements and their effects on the seismic responses were neglected (e.g. see Kazemi and Jankowski 2023a, Kazemi et al. 2023). It should be noted that the IMWs could provide additional stiffness and strength that may highly affect seismic parameters such as fundamental structural period and interstory drift ratio (Gara et al. 2021). Also, IMWs showed different limit-state levels, as compared to the structural elements, which affect the overall performance of the building. Moreover, previous damages of IMWs (i.e. in-plane damages) and different workmanships can affect the performance level and collapse capacity of IMWs (Furtado et al. 2022).

Nowadays, the growing need for constructing buildings in urban areas leads to having buildings on different soil types. Although many improvements made to model buildings

with a high amount of accuracy, it is hard to take into account the effects of Soil-Structure Interaction (SSI) in the designing process. Therefore, designers used some simplified procedures proposed by seismic codes to consider the SSI effect. Many studies have been performed assuming the SSI effects on the buildings constructed in different soil types (Dutta et al. 2004; Pitilakis et al. 2008; Raychowdhury 2011; Petridis and Pitilakis 2020). Elwardany et al. (Elwardany et al. 2017, 2019) investigated the SSI effects on buildings with Steel Moment-Resisting Frames (SMRFs) with and without IMWs subjected to the earthquake-induced colliding. They concluded that SSI and IMWs could significantly alter the behavior and structural response of buildings. Recent studies focused on the seismic probabilities of collapse based on the fragility curves to assess the vulnerability of SMRFs and RC structures (Kazemi et al. 2020, 2021a, b). Some studies used finite element models to determine the fragility curves of RC structures and confirmed the key role of SSI effects in the seismic probabilities (Pitilakis et al. 2014; Karapetrou et al. 2015). In addition, Mitropoulou et al. (Mitropoulou et al. 2016) developed fragility curves for three systems of fixed-based, two-dimensional finite element for pile foundation and Winkler spring model. Approaches of modeling SSI is a fundamental principle and neglecting the soil nonlinearity may lead to an un-conservative prediction of the system response (Pecker et al. 2014). Rajeev and Tesfamariam (Rajeev and Tesfamariam 2012) investigated the nonlinearity effects of SSI and soil parameters such as cohesion, density, Poisson's ratio, and friction angle on the seismic vulnerability of RC structures using the Beam on Nonlinear Winkler Foundation (BNWF) model. Nonlinear behavior of shallow foundations may dissipate the seismic energy through soil yielding. Harden and Hutchinson (Harden and Hutchinson 2009) introduced a simulation methodology for modeling of nonlinearity of shallow foundations using BNWF, and the model was developed as a stand-alone module as a useful tool for designing purposes by Allotey and El Naggar (Allotey and Naggar 2008). Forcellini (Forcellini 2021) investigated the SSI effects on the fragility curves of the RC structures with and without IMWs and concluded that SSI effects increased the failure probability of both RC structures.

The present paper aims to investigate the effects of different placements of IMWs, and the nonlinearity effects of SSI on the seismic response of SMRFs. Due to different collapse states for IMWs and SMRFs, a Tcl programming algorithm was developed to control demand limitations during Incremental Dynamic Analysis (IDA). Therefore, it can be possible to determine the effects of IMWs on the seismic responses considering SSI effects assuming four soil types. To determine the seismic vulnerability of SMRFs, seismic limit state capacities and seismic fragility curves were plotted and the influence of assumed parameters were investigated. The results of this study can be widely used by civil engineers for design procedures or retrofitting purposes.

2 Modeling methods

2.1 Modeling of SMRFs

In this paper, buildings with three, five, seven, and nine story levels (3-Story, 5-Story, 7-Story, and 9-Story) with considering SMRFs in four outer frames were designed according to the regular plan presented in Fig. 1. In the design process, four soil types were

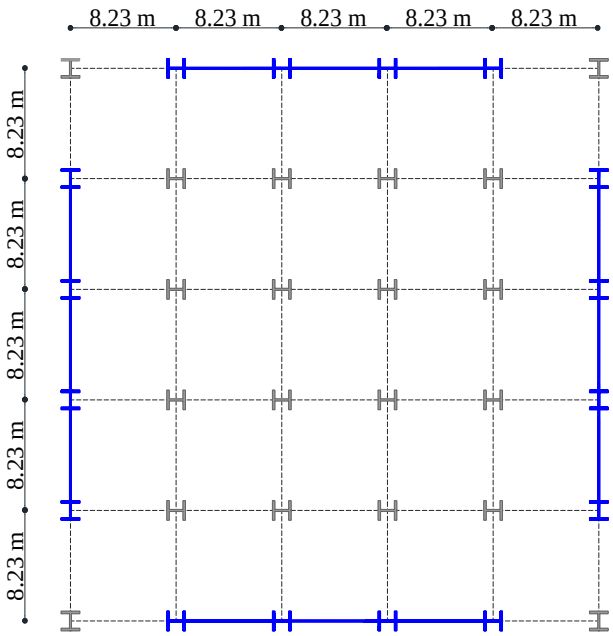

Fig. 1 Considered plan for modeling of SMRFs

considered to model buildings located in California with a latitude of 34.039º and longitude of − 118.324º.

Table 1 presents values of the soil parameters and seismic design parameters for selected soil types. These quantities are available both in ASCE 7–16 (ASCE 2017) and on the USGS website (USGS 2022). S_{DS} and S_{D1} are numeric seismic design values at 0.2 and 1.0 s, respectively, G_0 is the initial soil shear modulus, Φ, c, γ, V_s, υ are friction angle, cohesion coefficient, unit weight, shear wave velocity, and Poisson's ratio, respectively. According to the seismic force-resisting system selected for the buildings, design parameters of R, Ω_0 and C_d equal to 8, 3, and 5.5, respectively, were selected (see Table 12.2.1 ASCE 7–16 (ASCE 2017)). It is worth noting that the force-based design approach was used for designing SMRFs assuming spectral acceleration presented in Table 1 for considered soil types and provisions of ASCE 7–16 (ASCE 2017), AISC 360–16 (AISC 2016), and AISC 341–16 (see Section E3) (AISC 2016). To model three-dimensional buildings

Table 1 Soil and seismic design parameters

Soil	B	C	D	E
S_{DS}	1.306	1.567	1.576	1.623
S_{D1}	0.463	0.648	0.653	0.659
G_0 (MPa)	6000	280	60	30
Φ (Degree)	45	42	38	35
c (kPa)	0	0	5	5
γ (kN/m^3)	24	21	19	18
υ	0.25	0.35	0.4	0.45
V_s (m/s)	1565	360	175	120

using ETABS 2016 software, the floor dead and live loads of 3.35 kN/m^2 and 1.68 kN/m^2 were applied, respectively. For designing the SMRFs, the parameters of $F_y = 345$ MPa (yield strength), E = 200 GPa, and $\upsilon = 0.3$ were considered for steel, and the compressive strength of concrete for designing the foundation was considered equal to 30 MPa (Kazemi et al. 2021a).

Some studies used 2D structural models in Opensees (McKenna et al. 2016) for 3D buildings (e.g. see (Kazemi et al. 2018, 2020, 2021a, b; Mohebi et al. 2018; Asgarkhani et al. 2020; Yakhchalian et al. 2020, 2021)) since the regular plan of building can allow us to neglect the torsional effects. Regarding the improvements of analytical tools in Opensees (McKenna et al. 2016), it is possible to model the deterioration effects of strength and stiffness that are suitable for 2D modeling (Ibarra et al. 2005). In this study, the 2D models were verified with 3D buildings that were modeled in ETABS 2016 software. To reduce the complexity of models, 2D models were used (instead of 3D ones) and SSI effects were added to them. According to the plan, to model SMRFs in Opensees (McKenna et al. 2016), all columns, except for those in SMRF (blue colour), were assumed as leaning columns to consider the crucial role of the P-delta effects in seismic performance (Kazemi et al. 2018; Mohebi et al. 2018; Asgarkhani et al. 2020; Yakhchalian et al. 2020, 2021). All structural elements were modelled with an elastic beam-column element with two nonlinear rotational springs according to the Modified Ibarra–Krawinkler bilinear hysteretic model (IMK Hinge) (Ibarra et al. 2005; Kazemi and Jankowski 2023b; Mohebi et al. 2021; Yazdanpanah et al. 2022). Table 2 presents the design documentation for the assumed SMRFs considering four types of soil. The region of beam-to-column connection, that is known as panel zone, was modeled to capture the deformations. To model the panel zone, the procedure introduced in Opensees (McKenna et al. 2016) was used assuming eight rigid elements and one zero-length element with a trilinear backbone curve proposed by Gupta and Krawinkler (Gupta and Krawinkler 1999).

2.2 SSI modeling

The BNWF model, which can be widely used for modeling shallow foundations, retaining walls, and piles, have the degrading hysteretic behavior with the ability of defining rules. This model employs a series of nonlinear springs and dashpots in parallel to model soil beneath the foundation. Figure 2 presents the BNWF model and implementation of the springs and dashpots. The kind of springs used in this model plays a crucial role in soil responses. Therefore, three types of springs known as the q–z spring, p–x spring, and t–x spring were used to capture the vertical and rotational resistance, and the sliding and passive resistance of the foundation, respectively. Normalized load-normalized displacement curves of these springs were plotted in Fig. 3. The BNWF model was modeled in Opensees (McKenna et al. 2016) using material models of *QzSimple* for q–z spring, *PxSimple* for p–x spring, and *TxSimple* for t–x spring (Raychowdhury 2011; Rajeev and Tesfamariam 2012; Harden and Hutchinson 2009; Raychowdhury and Hutchinson 2009; Kazemi and Jankowski 2023b)

The BNWF consists of structural beam elements between foundation and soil nodes, and soil springs defined with zero-length element (Fig. 2). To define the BNWF model parameters, the foundation of the 3-Story, 5-Story, 7-Story, and 9-Story SMRFs were designed according to the soil parameters presented in Table 1 using SAFE 2016 software. It should be added that the dimensions of foundations were controlled based on the

Table 2 Design documentation of SMRFs for soil types

SMRF	Floor	Soil B		Soil C		Soil D		Soil E	
		Column	Beam	Column	Beam	Column	Beam	Column	Beam
3-story	1st	W14X132	W24X68	W14X159	W24X94	W14X159	W24X94	W14X159	W24X94
	2nd	W14X120	W21X68	W14X120	W24X84	W14X120	W24X94	W14X120	W24X94
	3rd	W14X120	W18X46	W14X120	W18X50	W14X120	W18X50	W14X120	W18X55
5-story	1st	W14X145	W24X76	W14X159	W24X94	W14X159	W27X102	W14X159	W27X102
	2nd	W14X120	W24X76	W14X132	W24X94	W14X132	W27X102	W14X159	W27X102
	3rd	W14X120	W24X76	W14X120	W24X84	W14X120	W24X84	W14X120	W24X84
	4th	W14X120	W24X55	W14X120	W24X84	W14X120	W24X84	W14X120	W24X84
	5th	W14X120	W24X55	W14X120	W24X55	W14X120	W24X55	W14X120	W24X55
7-story	1st	W14X145	W24X84	W14X176	W27X102	W14X176	W27X102	W14X176	W27X102
	2nd	W14X145	W24X84	W14X159	W27X102	W14X159	W27X102	W14X159	W27X102
	3rd	W14X145	W24X84	W14X145	W27X94	W14X145	W27X102	W14X145	W27X102
	4th	W14X120	W24X84	W14X120	W27X94	W14X120	W27X94	W14X145	W24X84
	5th	W14X120	W24X68	W14X120	W24X84	W14X120	W24X84	W14X120	W24X84
	6th	W14X120	W21X50	W14X120	W21X68	W14X120	W21X68	W14X120	W21X68
	7th	W14X120	W21X50	W14X120	W21X50	W14X120	W21X50	W14X120	W21X50
9-story	1st	W14X233	W27X94	W14X233	W27X114	W14X233	W27X114	W14X233	W27X114
	2nd	W14X233	W27X94	W14X233	W27X114	W14X233	W27X114	W14X233	W27X114
	3rd	W14X176	W27X94	W14X176	W27X114	W14X176	W27X114	W14X233	W27X114
	4th	W14X176	W24X94	W14X176	W27X102	W14X176	W27X102	W14X176	W27X114
	5th	W14X176	W24X94	W14X176	W27X102	W14X176	W27X102	W14X176	W27X114
	6th	W14X120	W24X84	W14X120	W24X84	W14X159	W27X94	W14X120	W27X94
	7th	W14X120	W24X84	W14X120	W24X84	W14X120	W24X84	W14X120	W24X84
	8th	W14X120	W21X50	W14X120	W21X68	W14X120	W21X68	W14X120	W24X84
	9th	W14X120	W21X50	W14X120	W21X50	W14X120	W21X50	W14X120	W21X50

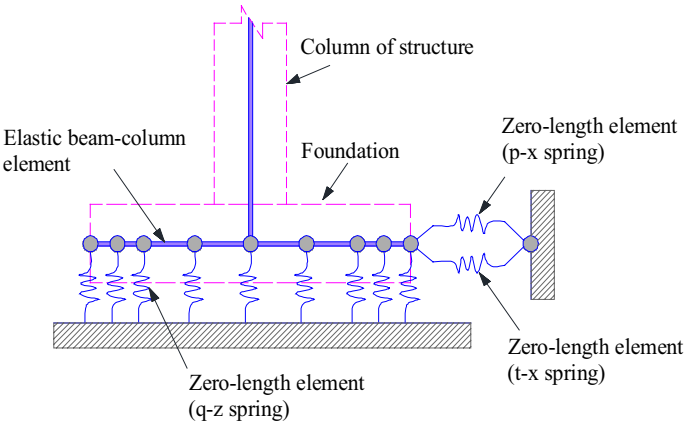

Fig. 2 BNWF model and implementation of the springs and dashpots

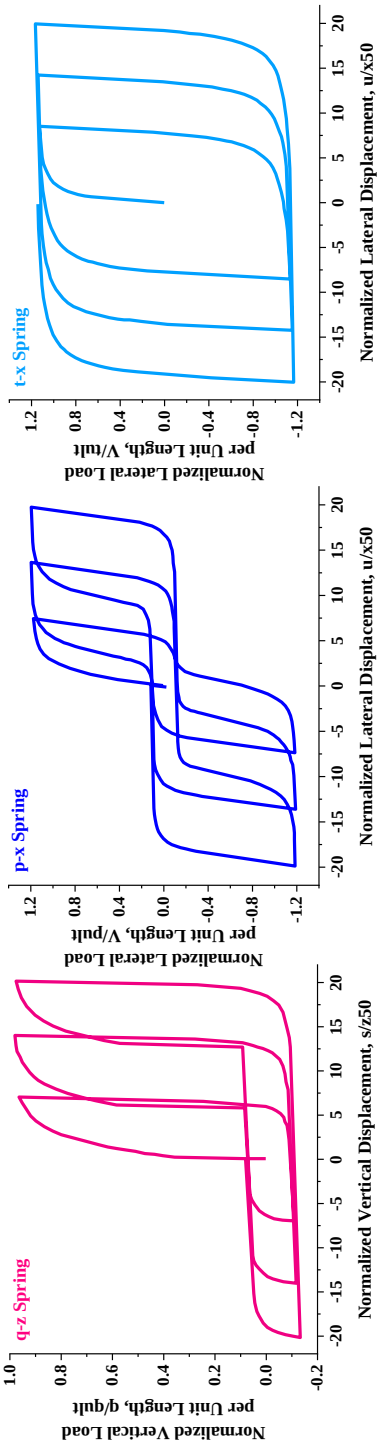

Fig. 3 Normalized load-normalized displacement curves of the nonlinear springs

Table 3 Foundations' dimensions considered for SMRFs

SMRF	Soil	Width (m)	Length (m)	Height (m)
3-story	B	1	26	0.6
	C	1	26	0.6
	D	1.1	27	0.7
	E	1.1	27	0.7
5-story	B	1.3	26	0.7
	C	1.3	26	0.7
	D	1.3	27	0.7
	E	1.3	27	0.7
7-story	B	1.5	27	0.8
	C	1.5	27	0.8
	D	2	27	0.8
	E	2	27	0.8
9-story	B	2.5	27	1.0
	C	2.5	27	1.0
	D	3	27	1.1
	E	3	27	1.1

assumed provisions and load combinations. Table 3 presents the dimensions of the foundation considered for SMRFs.

To define the materials used in the BNWF model, the equations presented by Boulanger et al. (Boulanger et al. 1999) were used. According to the definition, in the elastic region of *the QzSimple* material model, load q_e was assumed to have linear behavior regarding deformation, z.

$$q_e = k_{ini} z \tag{1}$$

where k_{ini} is the initial elastic stiffness. It is experimentally achieved that the elastic maximum load, q_0, is a factor C_r of the ultimate load, q_{ult}, then:

$$q_0 = C_r q_{ult} \tag{2}$$

Then, the nonlinear part of the curve can be defined by:

$$q = q_{ult} - (q_{ult} - q_0)\left[\frac{Cz_{50}}{Cz_{50} + |z - z_0|}\right]^n \tag{3}$$

where z_{50} is the displacement in the half of ultimate load, z_0 is displacement in the yield point, C and n are constitutive values to control the post-yield portion and curve shape. The calculation for *PxSimple* and *TxSimple* material models is similar to the *QzSimple* material model with assuming various values of C_r, n, C. Gazetas (Gazetas 1991) proposed the following equations for calculating the vertical stiffness and lateral stiffness of springs, k_v, and k_h, respectively, based on the width and length of foundation, B and L, respectively.

$$k_{\mathrm{v}} = \frac{GL}{1-\upsilon}\left[0.73 + 1.54\left(\frac{B}{L}\right)^{0.75}\right]$$
$$k_{\mathrm{h}} = \frac{GL}{2-\upsilon}\left[2 + 2.5\left(\frac{B}{L}\right)^{0.85}\right] \quad (4)$$

2.3 Numerical modeling approach to represent infill masonry wall

For decades, researchers experimentally studied the IMWs effects on the lateral response of RC and SMRFs (see (Buonopane and White 1999; Tasnimi and Mohebkhah 2011)), and proposed different types of numerical models (see Koutromanos et al. 2011, Trapani et al. 2018, Mazza 2019). For instance, the less complicated and simple model is a double strut element developed by Smyrou et al. (Smyrou et al. 2011), three nonparallel strut elements that consider the interaction between IMWs and frames were developed by El-Dakhakhni et al. (El-Dakhakhni et al. 2003). Crisafulli and Carr (Crisafulli and Carr 2007) developed four nodes panel connected to the beam and column joints to include both shear and compressive behavior of IMW. In this research, the model proposed by Rodrigues et al. (2010) that is commonly used for simulation of nonlinear behavior of IMWs was used. Figure 4 presents the schematic illustration of the IMW modeling approach in Opensees (McKenna et al. 2016). Some experimental tests assuming cyclic loads validated this model. Therefore, to validate the modeling process, the experimental test used by Kakaletsis and Karayannis (Kakaletsis and Karayannis 2008) was assumed. Figure 5 presents the shear-displacement curve of the IMW model validated with the result of Test S-full infill used by Kakaletsis and Karayannis (Kakaletsis and Karayannis 2008). The results show good agreement with the numerical modeling of IMW.

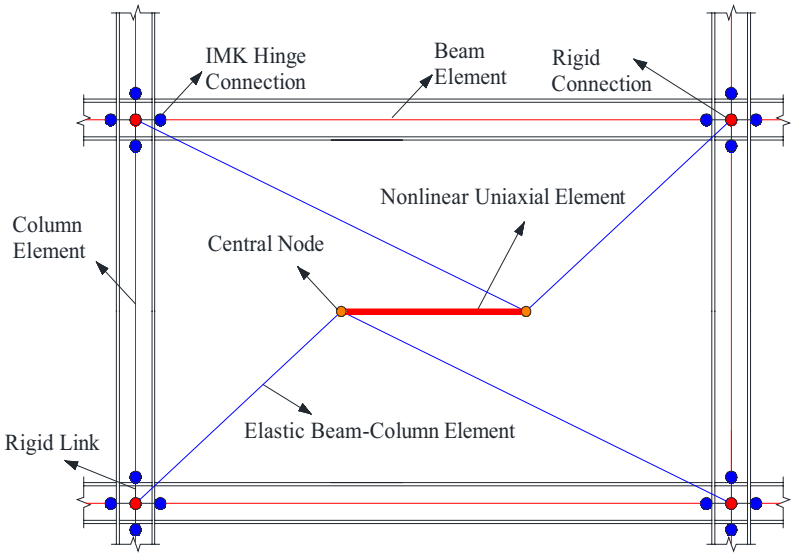

Fig. 4 Schematic illustration of IMW modeling approach in Opensees (McKenna et al. 2016)

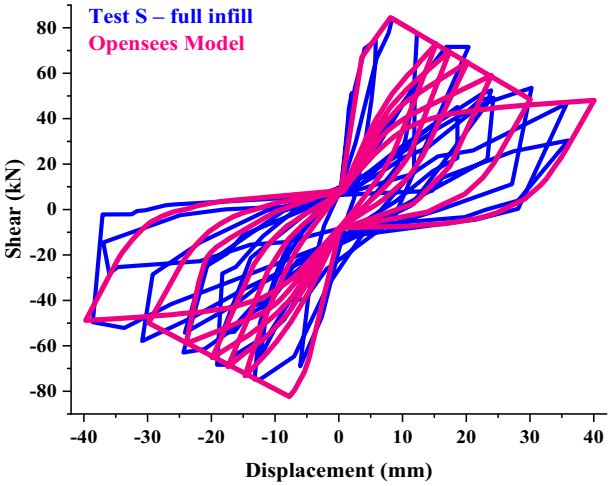

Fig. 5 Verification of shear-displacement curve of IMW model in Opensees with the result of Test S-full infill used by Kakaletsis and Karayannis (Kakaletsis and Karayannis 2008)

To define the IMW model, the nonlinear uniaxial element (see Fig. 4) should characterize by a multi-linear hysteresis curve defined as *uniaxial Material Pinching4* in Opensees (McKenna et al. 2016). Furtado et al. (Furtado et al. 2015, 2016b, 2018, 2021) numerically investigated the IMWs and their influences on the seismic structural behavior. They showed that the first cracks of IMW could appear between 0.075% and 0.12% drift (d_c). Therefore, in this study, d_c was selected equal to 0.1%, and the corresponding cracking force, F_c, was determined equal to 570 kPa, based on the relationship between elasticity modulus of IMW, E_m, and d_c. According to experimental tests and recommendations of seismic codes, the ratio of cracking strength and maximum strength (F_c/F_{cr}) for the IMW considering the brick and mortar properties can be adopted equal to 0.55 (Furtado et al. 2015). In addition, F_y and d_y are the yielding force and the corresponding displacement that can be assumed between 65 and 75% of F_{cr} and 0.35–0.50% of d_{cr}, while F_{cr} can occur for drift value of 0.5% (Furtado et al. 2021). Moreover, by estimating the diagonal compressive strength of IMW from experimental specimens, f_{IMW}, the maximum strength can be calculated from the following equations:

$$F_{cr} = 0.818\frac{L_{inf} \times t_{inf} \times f_{IMW}}{C_t}(1 + \sqrt{C_t^2 + 1})$$
$$C_t = 1.925\frac{L_{inf}}{h_{inf}} \quad (5)$$

where L_{inf}, h_{inf}, t_{inf} are the length, height, and thickness of the assumed IMW. Table 4 illustrates modeling properties used for IMWs. Figure 6 presents the uniaxial material model adopted for numerical modeling of IMW according to Table 4.

Table 4 Numerical properties adopted for modeling IMWs (Furtado et al. 2021)

d_c(%)	d_y(%)	d_{cr}(%)	d_u(%)	F_c(kPa)	F_y(kPa)	F_{cr}(kPa)	F_u(kPa)
0.1	0.25	0.5	1.5	570	750	1010	280

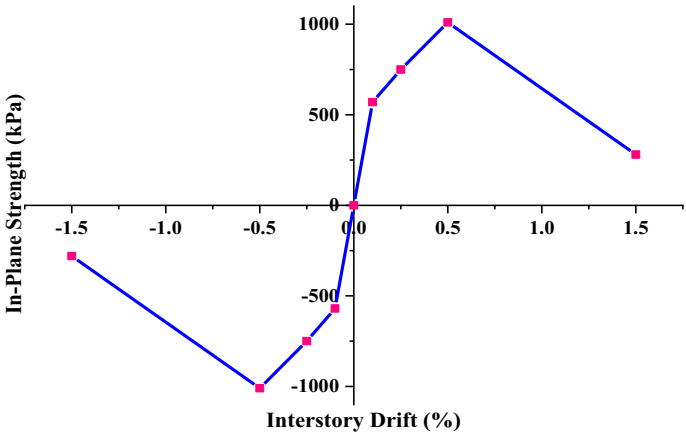

Fig. 6 The uniaxial material model was adopted for numerical modeling of IMW according to Table 4

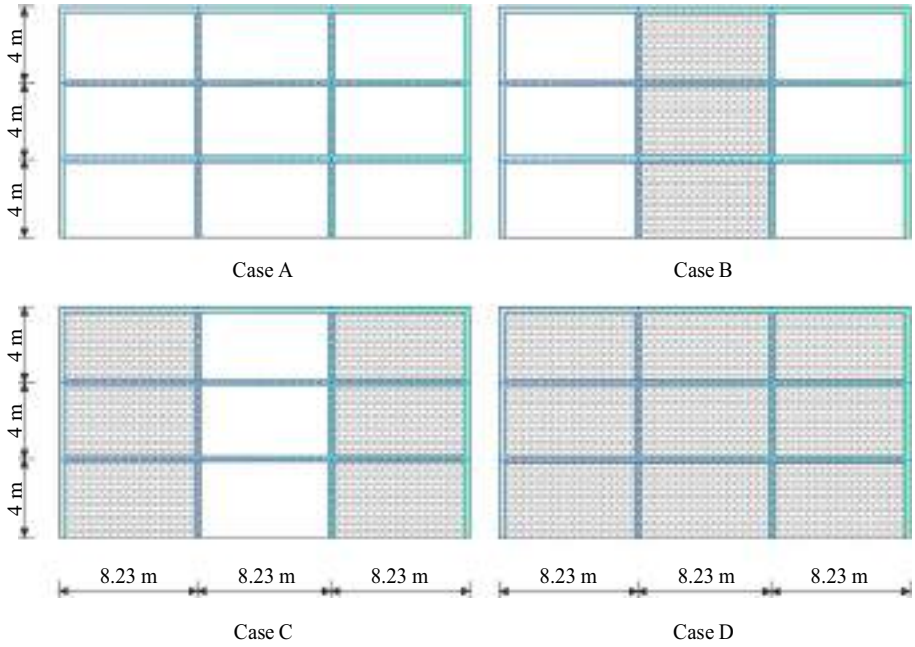

Fig. 7 Illustration of different placement of IMWs considered for the 3-Story SMRF model

2.4 Numerical models

To investigate the effects of assuming IMWs and SSI in the 3-Story, 5-Story, 7-Story, and 9-Story SMRFs, four placements of IMWs were considered. Figure 7 presents different placement of IMWs considered for the 3-Story SMRF. Similarly, all these placements were considered for other SMRFs with and without SSI effects.

Table 5 Fundamental periods of SMRFs with and without IMWs

SMRF	Soil type	Case A	Case B	Case C	Case D
3-story	B	1.17	1.09	1.0	0.95
	C	1.01	0.96	0.90	0.87
	D	1.0	0.96	0.90	0.87
	E	1.0	0.95	0.89	0.86
5-story	B	1.81	1.69	1.57	1.50
	C	1.66	1.57	1.48	1.42
	D	1.56	1.49	1.41	1.36
	E	1.56	1.49	1.41	1.36
7-story	B	2.44	2.28	2.12	2.02
	C	2.14	2.04	1.93	1.86
	D	2.12	2.02	1.91	1.85
	E	2.11	2.01	1.90	1.83
9-story	B	2.75	2.60	2.44	2.34
	C	2.55	2.43	2.31	2.23
	D	2.42	2.32	2.21	2.15
	E	2.40	2.35	2.24	2.17

Table 5 presents fundamental periods of SMRFs with and without IMWs assuming different cases and soil types. In each soil type, Case D had the lowest fundamental period and Case A had the highest one. It is worth noting that the vibration mode of structures were influenced by adding IMWs. For instance, in Case B, the values of the first vibration mode was increased by 2.33%, as compared to Case A. Moreover, in Case C and D, the values of the first vibration mode were increased by 4.67 and 6.07%, respectively. Regarding different placement of IMWs, structure founded on soil type E had the lowest fundamental period and structure founded on soil type B had the highest one. Therefore, the fundamental period of structures were affected by changing the soil types.

3 Incremental dynamic analysis

It is important to evaluate the current state of a building after a severe earthquake. The state of a building can be defined based on damage states of the non-structural and structural members. Seismic codes propose useful tools to determine the seismic performance levels of the structures. To investigate the seismic performance levels of SMRFs, IDA was employed to determine the seismic limit-states of SMRFs regarding the increasing amount of Intensity Measure (IM). In this study, the spectral acceleration in the fundamental period of the SMRF, $S_a(T_1)$, was selected as IM, and the Maximum Interstory Drift Ratio (M-IDR) as controlling parameter. Then, the seismic limit-state capacity assessment of SMRFs was conducted by performing IDAs assuming the Far-Fault (FF) records introduced by FEMA-P695 (FEMA P695 2009). In addition, FEMA 356 (FEMA-356. 2000) propose three performance levels of Immediate Occupancy (IO), Life Safety (LS), and Collapse Prevention (CP) for corresponding M-IDR of 0.7%, 2.5%, and 5.0%, respectively, which can be used for limit-state assessment. Moreover, the Total Collapse (TC) limit of the structure can be achieved by considering the flat part of the IDA curve.

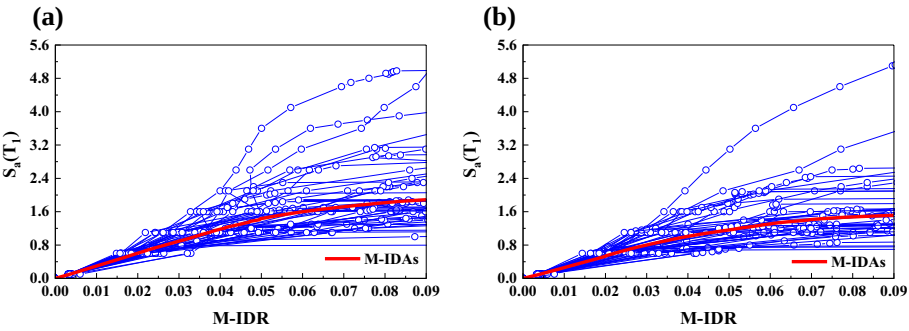

Fig. 8 IDA curves of the 3-story SMRF, **a** without SSI, and, **b** with SSI, in the soil D subjected to FF record subset

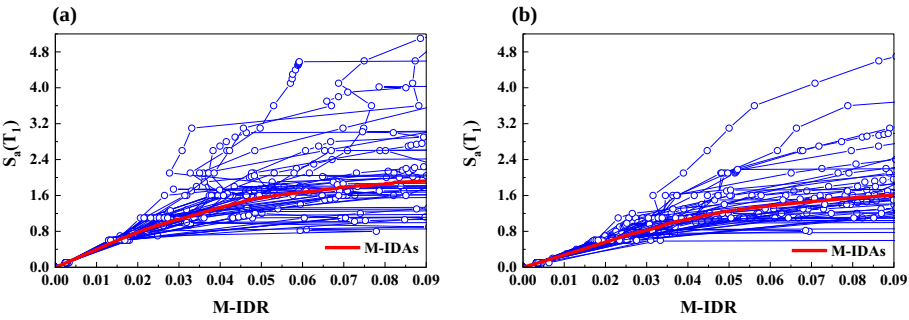

Fig. 9 IDA curves of the 3-story SMRF, **a** with IMWs (Case D), and, **b** without IMWs (Case A), in the soil C subjected to FF record subset

According to a full-scale experimental test of RC structure done by Pujol and Fick (Pujol and Fick 2010), IMWs that were assumed to fill all bays from bottom to top witnessed initial cracks with the width of 4 mm in M-IDR of 0.25%. Their results confirmed that IMWs were in the collapse state at an M-IDR of 1.75%. Therefore, in this M-IDR, IMWs were collapsed and could not be considered in the numerical model. To assume the collapse effects of IMWs, a Tcl programming algorithm was developed in OpenSees (McKenna et al. 2016) to control the collapse of IMWs in each story assuming M-IDR of the collapse limit of IMWs equal to 1.75%. Figure 8 presents IDAs of the 3-story SMRF neglecting and including SSI effects in the soil D subjected to FF record subset. Figure 9 presents IDAs of the 3-story SMRF with IMWs (Case D) and without IMWs (Case A) in soil C subjected to FF record subset.

3.1 Seismic performance level

To evaluate the influence of considering IMWs in modeling, the seismic performance levels of each aforementioned case based on the median IDA curves (M-IDAs) were compared. Figure 10a–d present M-IDA curves of the 3-Story SMRF considering four cases of IMWs placement and four soil types of B, C, D, and E, respectively, subjected to FF record subset. According to Fig. 10a–b, Case D had higher values of M-IDAs and showed

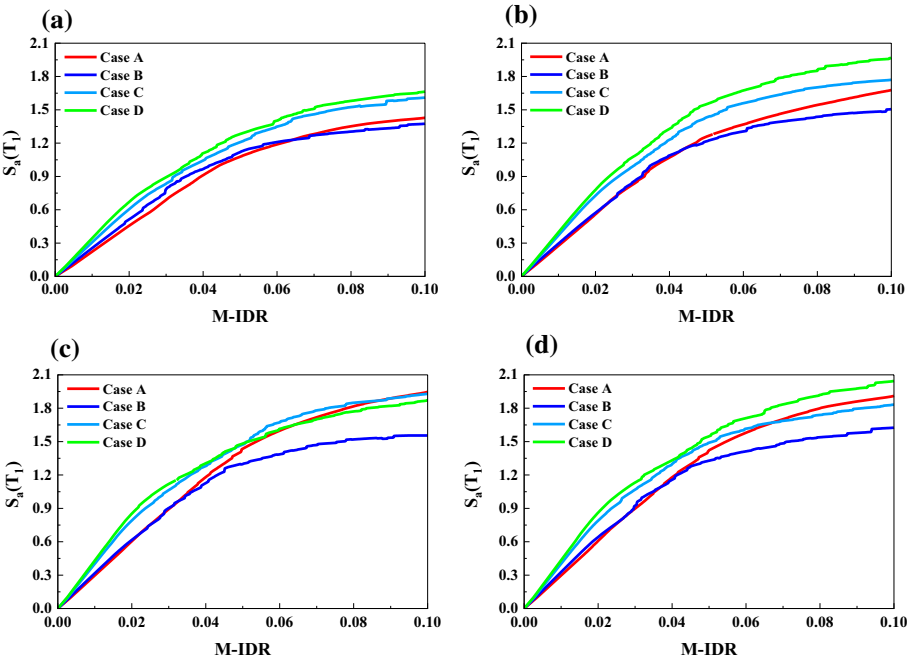

Fig. 10 M-IDAs of the 3-Story SMRF considering four cases of IMWs, **a** soil B, **b** soil C, **c** soil D, and **d** soil E, subjected to FF record subset

that the placement of IMWs in all floor levels increased the lateral resisting strength of the 3-Story SMRF. While, the placement of IMWs according to Case C had lower values of M-IDAs compared to Case D, and higher values than other cases. Therefore, increasing the placement of IMWs in the 3-Story SMRF with soil types of B and C showed an increase in the values of $S_a(T_1)$ in M-IDA curves. For cases in the soil types of D and E presented in Fig. 10c, d, respectively, the placement of IMWs in the 3-Story SMRF increased the values of $S_a(T_1)$ in M-IDA curves. In all soil types, the placement of IMWs according to Case B had lower values of $S_a(T_1)$ in M-IDA curves that show the negative effects of using this case for the 3-Story SMRF. It can be concluded that having an opening in the 3-Story SMRF (i.e. Case B) can significantly decrease the values of $S_a(T_1)$. Similar results were obtained from M-IDA curves of the 3-Story SMRF considering four cases of IMWs with SSI effect presented in Fig. 11a–d.

To compare between results of all cases and soil types, the seismic limit-state capacities of the 3-Story SMRF in four soil types according to the aforementioned seismic performance level are presented in Table 6. It is possible to compare the values of $S_a(T_1)$ in four performance levels of IO, LS, CP, and TC, and four soil types, assuming different placement of IMWs. For instance, assuming Case D in soil types of B, C, D, and E, the limit-state capacities of the 3-Story SMRF experienced an increase by 16.45% (from 1.428 to 1.663), 17.22% (from 1.428 to 1.663), − 3.9% (from 1.428 to 1.663), and 6.95% (from 1.428 to 1.663), respectively.

Table 7 presents the seismic limit-state capacities of the 3-Story SMRF in four soil types with SSI effects subjected to FF record subset. This table prepares the effects of

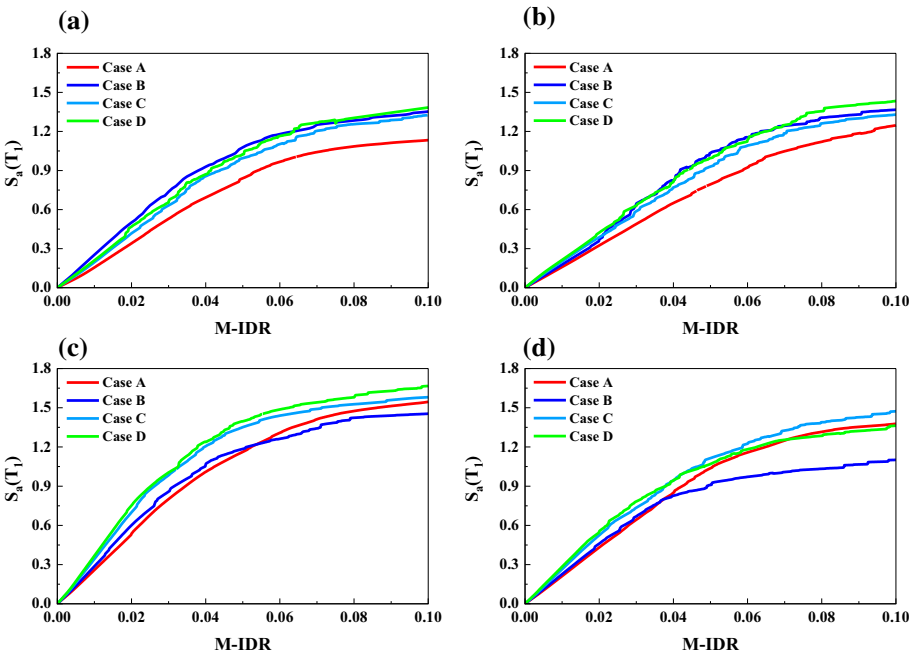

Fig. 11 M-IDAs of the 3-Story SMRF considering four cases of IMWs with SSI effect on the, **a** soil B, **b** soil C, **c** soil D, and **d** soil E, subjected to FF record subset

Table 6 Seismic limit-state capacities of the 3-Story SMRF in four cases assuming FF record subset

Performance level	IO	LS	CP	TC	IO	LS	CP	TC
3-Story SMRF	Soil B				Soil C			
Case A	0.152	0.564	1.077	1.428	0.191	0.708	1.258	1.678
Case B	0.177	0.645	1.118	1.374	0.209	0.700	1.216	1.505
Case C	0.213	0.735	1.208	1.610	0.257	0.869	1.431	1.770
Case D	0.238	0.792	1.281	1.663	0.277	0.936	1.550	1.967
3-Story SMRF	Soil D				Soil E			
Case A	0.206	0.754	1.436	1.948	0.206	0.761	1.422	1.911
Case B	0.222	0.752	1.298	1.555	0.228	0.766	1.328	1.625
Case C	0.277	0.931	1.473	1.930	0.277	0.932	1.490	1.832
Case D	0.297	1.006	1.482	1.872	0.299	1.015	1.547	2.044

SSI and can be easily used for comparing assumed cases. For example, in Case A with and without assuming SSI effects, the performance level of TC in soil B decreased from 1.428 (Table 6) to 1.133 (Table 7). Moreover, the values of $S_a(T_1)$ in four performance levels of IO, LS, CP, and TC, similarly decreased due to SSI effects. Therefore, the SSI effects can significantly affect the limit-state capacities.

Figure 12a–d present M-IDA curves of the 5-Story SMRF considering four cases of IMWs placement and four soil types of B, C, D, and E, respectively, subjected to

Table 7 Seismic limit-state capacities of the 3-Story SMRF with SSI effects assuming FF record subset

Performance level	IO	LS	CP	TC	IO	LS	CP	TC
3-Story SMRF	Soil B				Soil C			
Case A	0.102	0.438	0.840	1.133	0.111	0.406	0.794	1.247
Case B	0.174	0.631	1.077	1.352	0.124	0.502	1.035	1.366
Case C	0.133	0.520	0.994	1.326	0.144	0.483	0.930	1.329
Case D	0.145	0.570	1.023	1.384	0.154	0.518	0.995	1.435
3-Story SMRF	Soil D				Soil E			
Case A	0.177	0.679	1.162	1.545	0.146	0.534	1.037	1.378
Case B	0.197	0.724	1.185	1.454	0.158	0.553	0.909	1.101
Case C	0.233	0.873	1.351	1.581	0.183	0.645	1.114	1.473
Case D	0.250	0.895	1.396	1.666	0.198	0.673	1.069	1.362

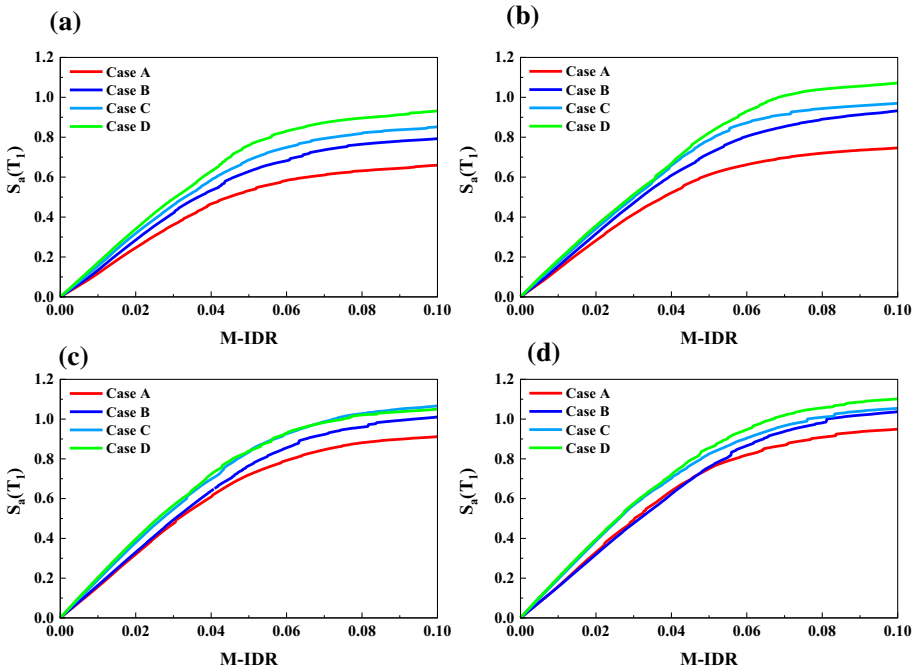

Fig. 12 M-IDAs of the 5-Story SMRF considering four cases of IMWs, **a** soil B, **b** soil C, **c** soil D, and **d** soil E, subjected to FF record subset

FF record subset. According to Fig. 12a, b, Case D had higher values of M-IDAs and showed that the placement of IMWs in all floor levels significantly increased the lateral resisting strength of the 5-Story SMRF. In addition, the placement of IMWs according to Case C had lower values of M-IDAs compared to Case D, and higher values than other cases. It can be noted that increasing the IMWs can significantly affect the $S_a(T_1)$ values of M-IDA of the 5-Story SMRF with soil types of B and C. Similar results were observed for soil D and soil E in Fig. 12c, d, respectively. Moreover, it can be show that

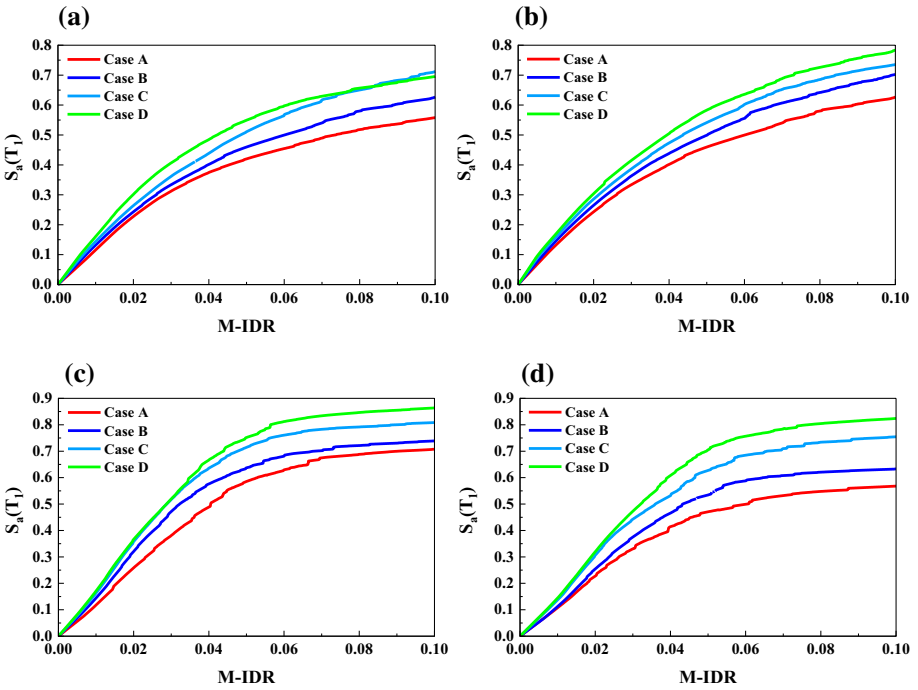

Fig. 13 M-IDAs of the 5-Story SMRF considering four cases of IMWs with SSI effect on the, **a** soil B, **b** soil C, **c** soil D, and **d** soil E, subjected to FF record subset

the effects of the placement of IMWs in the 5-Story SMRF in soil types of B and C is more than those in soil types of D and E. The main reason for this may be lie in the type of structural elements. The 5-Story SMRF had higher structural strength in soil type E comparing with soil type B and for this reason, fundamental period of the 5-Story SMRF in soil E is less than in soil B (e.g. 1.56 and 1.81, respectively, according to Case

Table 8 Seismic limit-state capacities of the 5-Story SMRF in four cases assuming FF record subset

Performance level	IO	LS	CP	TC	IO	LS	CP	TC
3-Story SMRF	Soil B				Soil C			
Case A	0.090	0.305	0.532	0.659	0.094	0.351	0.612	0.746
Case B	0.090	0.356	0.628	0.792	0.104	0.395	0.718	0.933
Case C	0.106	0.389	0.686	0.852	0.122	0.422	0.786	0.970
Case D	0.119	0.420	0.759	0.932	0.131	0.435	0.821	1.071
3-Story SMRF	Soil D				Soil E			
Case A	0.109	0.401	0.719	0.912	0.109	0.417	0.751	0.949
Case B	0.114	0.412	0.765	1.010	0.109	0.399	0.758	1.037
Case C	0.135	0.467	0.834	1.066	0.137	0.478	0.824	1.054
Case D	0.143	0.485	0.839	1.049	0.143	0.486	0.854	1.101

A in Table 5). Therefore, the structural elements are important factor in the collapse of structure and can increase the values of $S_a(T_1)$ in M-IDA curves.

Figure 13a–d present M-IDA curves of the 5-Story SMRF considering four cases of IMWs and four soil types with SSI effect subjected to FF record subset. The SSI effects can significantly reduce the values of $S_a(T_1)$ in M-IDA curves of all cases. Therefore, it is suggested to consider the SSI effects in the evaluation process due to its high influence.

Table 8 presents seismic limit-state capacities of the 5-Story SMRF in four cases of IMWs and four soil types assuming FF record subset. It can be seen that the placement of IMWs in all cases can significantly affect the values of $S_a(T_1)$ in M-IDA curves in all seismic limit-state capacities. For instance, in soil type B, assuming IMWs placement of Case B, Case C, and Case D increased the performance level of TC of the 5-Story SMRF by 41.42%, 29.28%, and 20.18%, respectively. In addition, for soil type C, the performance level of TC of the 5-Story SMRF increased by 43.56%, 30.02%, and 25.06%, respectively. Table 9 presents seismic limit-state capacities of the 5-Story SMRF with SSI effects subjected to FF record subset. The SSI effects can significantly reduce the $S_a(T_1)$ values in M-IDA curves. For instance, in soil type E, the $S_a(T_1)$ values in the performance level of CP for Cases of A to D decreased by 37.41% (from 0.751 to 0.470), 29.55% (from 0.758 to 0.534), 24.27% (from 0.828 to 0.627), and 17.44% (from 0.854 to 0.705), respectively. Therefore, it is suggested to the designers for assuming the effects of IMWs and SSI in their evaluations, and Tables 8 and 9 can be easily used for the prediction of IMWs and SSI effects.

Figure 14a–d present M-IDA curves of the 7-Story SMRF considering four cases of IMWs placement and four soil types of B, C, D, and E, respectively, subjected to FF record subset. Results presented by Fig 14a and b showed that Case D had higher values of M-IDAs compared to other cases. While Case B decreased the values of M-IDAs of the 7-Story SMRF founded on soil type B, other cases had a positive influence on the values of M-IDAs of the 7-Story SMRF. Therefore, the placement of IMWs can significantly increase the values of $S_a(T_1)$ in M-IDA curves of the 7-Story SMRF founded on soil types of B and C. Figure 14c and d show that the placement of IMWs can affect the values of $S_a(T_1)$ in M-IDA curves in a positive way, while the number of values between cases has small differences. It should be noted that the 7-Story SMRF founded on soil types of D and E had higher structural strength compared to corresponding to the 7-Story SMRF founded

Table 9 Seismic limit-state capacities of the 5-Story SMRF with SSI effects assuming FF record subset

Performance level	IO	LS	CP	TC	IO	LS	CP	TC
3-Story SMRF	Soil B				Soil C			
Case A	0.070	0.273	0.420	0.557	0.093	0.025	0.459	0.626
Case B	0.104	0.315	0.499	0.702	0.104	0.315	0.499	0.702
Case C	0.103	0.314	0.510	0.711	0.117	0.338	0.541	0.735
Case D	0.116	0.359	0.549	0.696	0.125	0.364	0.583	0.783
3-Story SMRF	Soil D				Soil E			
Case A	0.079	0.319	0.585	0.707	0.074	0.285	0.470	0.567
Case B	0.098	0.396	0.637	0.739	0.075	0.318	0.534	0.632
Case C	0.110	0.440	0.714	0.808	0.094	0.384	0.627	0.754
Case D	0.116	0.444	0.751	0.863	0.099	0.401	0.705	0.823

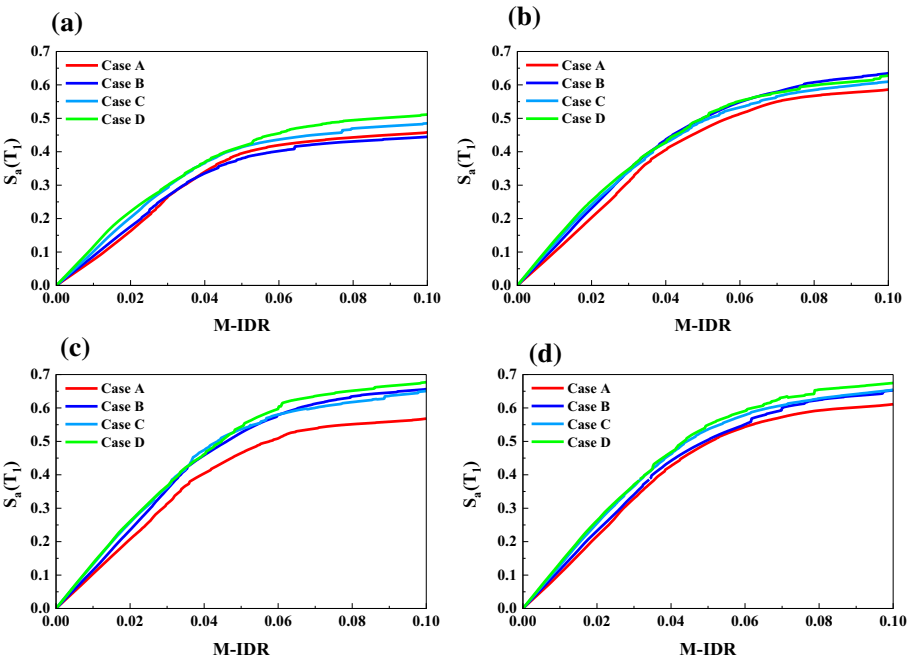

Fig. 14 M-IDAs of the 7-Story SMRF considering four cases of IMWs, **a** soil B, **b** soil C, **c** soil D, and **d** soil E, subjected to FF record subset

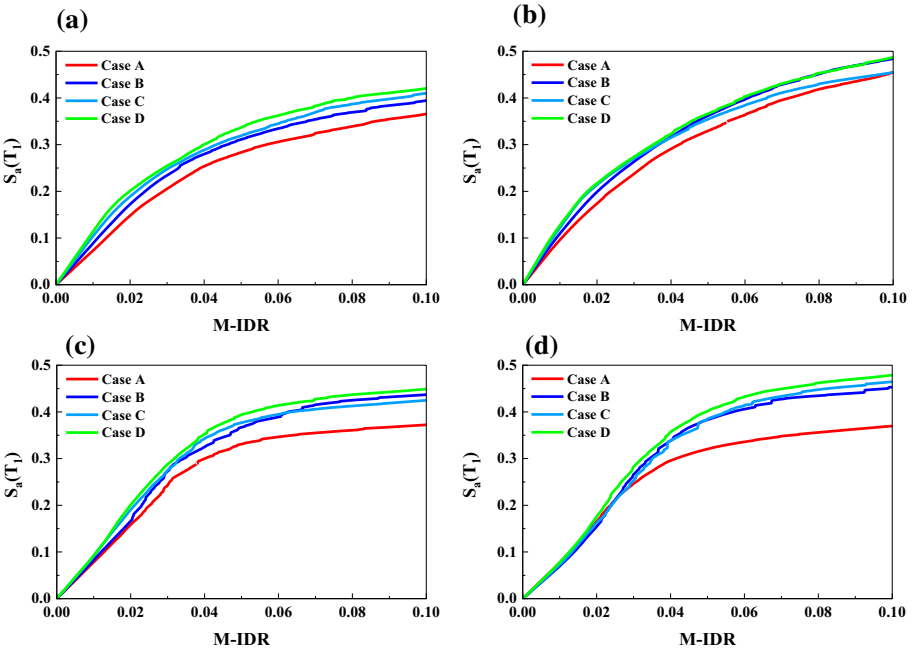

Fig. 15 M-IDAs of the 7-Story SMRF considering four cases of IMWs with SSI effect on the, **a** soil B, **b** soil C, **c** soil D, and **d** soil E, subjected to FF record subset

Table 10 Seismic limit-state capacities of the 7-Story SMRF in four cases assuming FF record subset

Performance level	IO	LS	CP	TC	IO	LS	CP	TC
3-Story SMRF	Soil B				Soil C			
Case A	0.053	0.209	0.395	0.458	0.069	0.253	0.466	0.586
Case B	0.061	0.219	0.380	0.444	0.079	0.286	0.499	0.634
Case C	0.070	0.251	0.413	0.484	0.088	0.290	0.492	0.609
Case D	0.081	0.261	0.415	0.511	0.094	0.303	0.501	0.627
3-Story SMRF	Soil D				Soil E			
Case A	0.072	0.257	0.464	0.568	0.071	0.272	0.495	0.611
Case B	0.080	0.294	0.525	0.656	0.081	0.285	0.504	0.652
Case C	0.093	0.309	0.536	0.650	0.090	0.312	0.536	0.654
Case D	0.095	0.315	0.544	0.677	0.095	0.318	0.549	0.674

on soil types of B and C (see Table 2). It can be concluded that the placement of IMWs effects can increase the structural strength of the SMRF. Figure 15a–d present M-IDA curves of the 7-Story SMRF considering four cases of IMWs and four soil types with SSI effect subjected to FF record subset. Although the SSI effect decreased the $S_a(T_1)$ values of bare frames in all soil types (e.g. Case A), assuming SSI significantly affects M-IDA curves of the SMRFs with IMWs (e.g. Case B, Case C, and Case D). In other words, the $S_a(T_1)$ values of M-IDAs for the 7-Story SMRF considering SSI effects were lower than those for the 7-Story SMRF neglecting SSI effects. Therefore, SSI effects play a key role in seismic capacity evaluations and should be taken into account.

Table 10 presents seismic limit-state capacities of the 7-Story SMRF in four cases of IMWs and four soil types assuming FF record subset. Results showed that the placement of IMWs in all the cases increased the values of $S_a(T_1)$ in M-IDA curves of the 7-Story SMRF founded on soil type B. For instance, assuming IMWs placement of Case C and Case D, the performance level of TC of the 7-Story SMRF founded on soil type B increased by 5.67% and 11.57%, respectively. Table 11 presents seismic limit-state capacities of the 7-Story SMRF with SSI effects subjected to FF record subset. Compared to Table 10, SSI effects significantly decrease the values of $S_a(T_1)$ in M-IDA curves. In IMWs placement of Case B, Case C, and Case D, the performance level of TC

Table 11 Seismic limit-state capacities of the 7-Story SMRF with SSI effects assuming FF record subset

Performance level	IO	LS	CP	TC	IO	LS	CP	TC
3-Story SMRF	Soil B				Soil C			
Case A	0.051	0.179	0.283	0.365	0.068	0.207	0.329	0.455
Case B	0.062	0.206	0.311	0.394	0.078	0.233	0.362	0.484
Case C	0.073	0.220	0.319	0.410	0.087	0.243	0.354	0.455
Case D	0.080	0.229	0.337	0.420	0.093	0.247	0.366	0.487
3-Story SMRF	Soil D				Soil E			
Case A	0.054	0.198	0.330	0.372	0.053	0.210	0.320	0.369
Case B	0.057	0.224	0.367	0.436	0.048	0.211	0.383	0.453
Case C	0.063	0.234	0.376	0.424	0.050	0.209	0.385	0.464
Case D	0.064	0.246	0.394	0.449	0.053	0.233	0.401	0.478

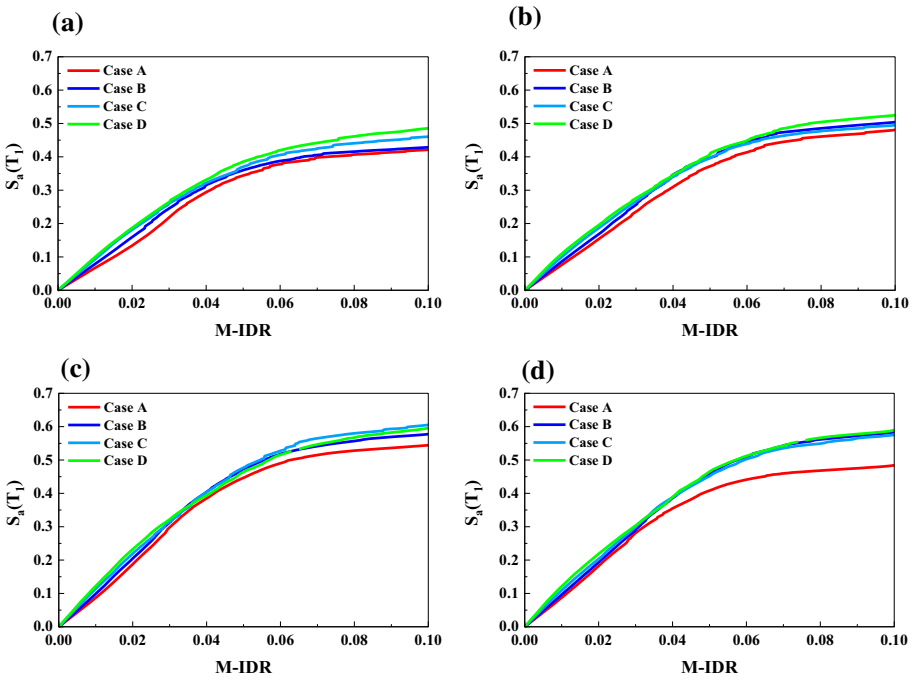

Fig. 16 M-IDAs of the 9-Story SMRF considering four cases of IMWs, **a** soil B, **b** soil C, **c** soil D, and **d** soil E, subjected to FF record subset

of the 7-Story SMRF founded on soil type B decreased by 7.94%, 12.32%, and 15.06%, respectively, assuming SSI effects. Similar trends were observed for other soil types.

Figure 16a–d present M-IDA curves of the 9-Story SMRF considering four cases of IMWs placement and four soil types of B, C, D, and E, respectively, subjected to FF record subset. Case D had higher values of M-IDAs compared to other cases in the four soil types, and Case A had the lowest values among other cases. Similar to other SMRFs, it can be seen that the placement of IMWs can significantly increase the values of $S_a(T_1)$ in M-IDA curves of the 9-Story SMRF. Figure 17a–d present M-IDA curves of the 9-Story SMRF considering four cases of IMWs and four soil types with SSI effect subjected to FF record subset. Compared to Fig. 16a–d, differences between Case D and Case A increased. In other words, the SSI effects had a lower influence on the cases with IMWs placement than the bare frame (e.g. Case A).

Tables 12 and 13 present seismic limit-state capacities of the 7-Story SMRF in four cases of IMWs and four soil types assuming FF record subset without and with SSI effects, respectively. Results confirm the increasing trends of the values of $S_a(T_1)$ in M-IDA curves of the 9-Story SMRF with the IMWs placement of Case B, Case C, and Case D. For instance, assuming IMWs placement of Case D, the performance level of TC of the 9-Story SMRF founded on soil type B increased by 15.2%, and with assuming the SSI effects, the performance level of TC increased by 15.48%. Results of tables can be used for estimating the effects of IMWs and SSI on the performance levels of the 9-Story SMRF.

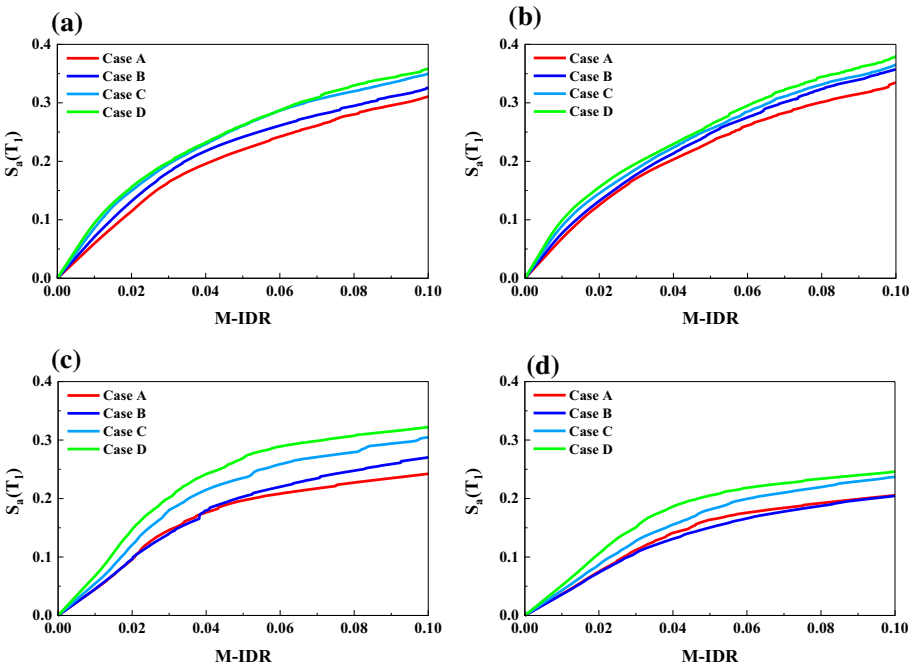

Fig. 17 M-IDAs of the 9-Story SMRF considering four cases of IMWs with SSI effect on the, **a** soil B, **b** soil C, **c** soil D, and **d** soil E, subjected to FF record subset

Table 12 Seismic limit-state capacities of the 9-Story SMRF in four cases assuming FF record subset

Performance level	IO	LS	CP	TC	IO	LS	CP	TC
3-Story SMRF	Soil B				Soil C			
Case A	0.047	0.172	0.334	0.421	0.053	0.194	0.371	0.481
Case B	0.055	0.202	0.360	0.428	0.060	0.213	0.397	0.503
Case C	0.065	0.218	0.370	0.460	0.071	0.227	0.396	0.494
Case D	0.070	0.226	0.385	0.485	0.079	0.238	0.407	0.524
3-Story SMRF	Soil D				Soil E			
Case A	0.060	0.239	0.446	0.544	0.060	0.229	0.408	0.484
Case B	0.068	0.256	0.473	0.577	0.067	0.242	0.458	0.583
Case C	0.080	0.265	0.477	0.605	0.077	0.253	0.451	0.575
Case D	0.087	0.281	0.464	0.595	0.087	0.262	0.465	0.589

4 Seismic fragility curves

In this section, the fragility curves of the aforementioned SMRFs were compared based on the analytical procedures and probability of reaching or exceeding the aforementioned damages states. It is important to evaluate the influence of IMWs placement and their effects on the seismic performance. Therefore, the performance levels of IO and LS, which present nonstructural damages without death or serious structural failure, were considered.

Table 13 Seismic limit-state capacities of the 9-Story SMRF with SSI effects assuming FF record subset

Performance level	IO	LS	CP	TC	IO	LS	CP	TC
3-Story SMRF	Soil B				Soil C			
Case A	0.041	0.141	0.220	0.310	0.048	0.148	0.233	0.334
Case B	0.049	0.157	0.241	0.326	0.055	0.155	0.247	0.357
Case C	0.060	0.173	0.260	0.350	0.065	0.166	0.255	0.365
Case D	0.067	0.179	0.261	0.358	0.073	0.177	0.262	0.379
3-Story SMRF	Soil D				Soil E			
Case A	0.031	0.127	0.196	0.242	0.025	0.093	0.163	0.205
Case B	0.031	0.120	0.203	0.270	0.025	0.090	0.150	0.204
Case C	0.038	0.152	0.235	0.304	0.030	0.106	0.181	0.237
Case D	0.047	0.177	0.269	0.322	0.035	0.131	0.205	0.246

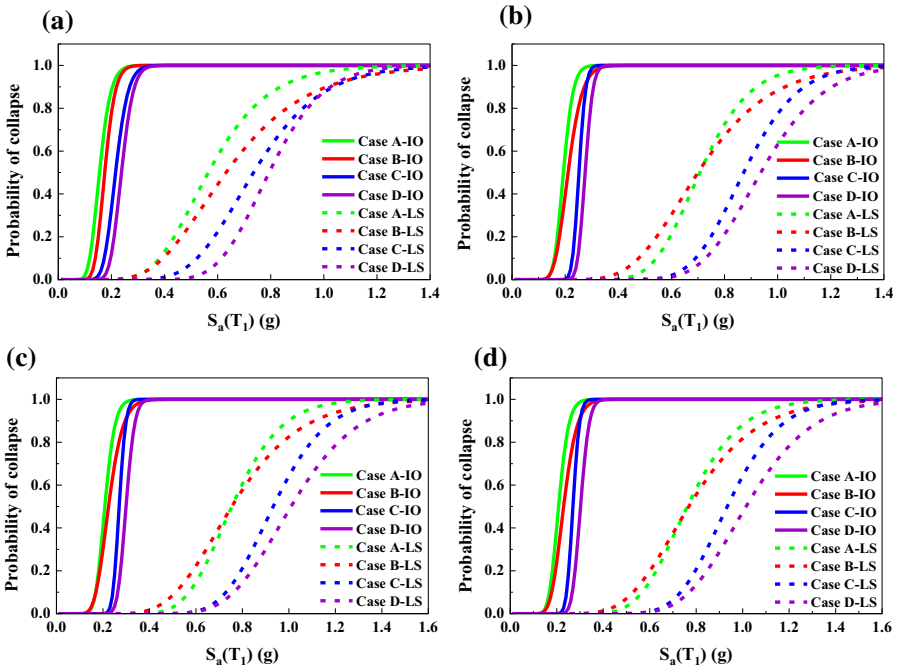

Fig. 18 Seismic fragility curves of the 3-Story SMRF considering four cases of IMWs on the, **a** soil type B, **b** soil type C, **c** soil type D, and **d** soil type E, subjected to FF record subset

According to the aforementioned performance levels, the probability of exceedance of a limit state (i.e. IO or LS) was determined and different cases were compared. It is worth noting that the difference between seismic fragility curves of IO and LS performance levels for the 9-story SMRF can be justified due to difference between their corresponding M-IDR.

Figure 18a–d illustrate seismic fragility curves in the performance of IO and LS of the 3-Story SMRF considering four cases of IMWs founded on the four soil types subjected

to FF record subset. The result shows that in the performance of IO for all soil types, the $S_a(T_1)$ values of Case D corresponding to the seismic failure probability of 50% are higher than those for Case C, Case B, Case A, respectively. According to Fig. 18a, in soil type B, the $S_a(T_1)$ values of Case A, Case B, Case C, and Case D, corresponding to the seismic collapse probability of 50% in the performance level of IO are 0.15, 0.17, 0.21, and 0.24, respectively, and in the performance level of LS are 0.56, 0.64, 0.74, and 0.79, respectively. Therefore, Case D with the full placement of IMWs can increase the seismic failure probability of the 3-Story SMRF founded on soil type B by 60% and 41.07%, in the performance of IO and LS, respectively. According to Fig. 18b, in soil type C, the $S_a(T_1)$ values of Case A, Case B, Case C, and Case D, corresponding to the seismic collapse probability of 50% in the performance level of IO are 0.19, 0.21, 0.25, and 0.27, respectively, and in the performance of LS are 0.70, 0.70, 0.87, and 0.94, respectively. Therefore, Case D with the full placement of IMWs can increase the seismic failure probability of the 3-Story SMRF founded on soil type C by 42.10% and 34.28%, in the performance of IO and LS, respectively. According to Fig. 18c, in soil type D, the $S_a(T_1)$ values of Case A, Case B, Case C, and Case D, corresponding to the seismic collapse probability of 50% in the performance level of IO are 0.21, 0.22, 0.28, and 0.30, respectively, and in the performance of LS are 0.75, 0.75, 0.93, and 1.01, respectively. Therefore, Case D with the full placement of IMWs can increase the seismic failure probability of the 3-Story SMRF founded on soil type D by 42.85% and 34.66%, in the performance of IO and LS, respectively. According to Fig. 18d, in soil type E, the $S_a(T_1)$ values of Case A, Case B, Case C, and Case D, corresponding to the seismic collapse probability of 50% in the performance level of IO are 0.21, 0.23, 0.28, and 0.30, respectively, and in the performance level of LS are 0.76, 0.77, 0.93, and 1.02, respectively. Therefore, Case D with the full placement of IMWs can increase the seismic

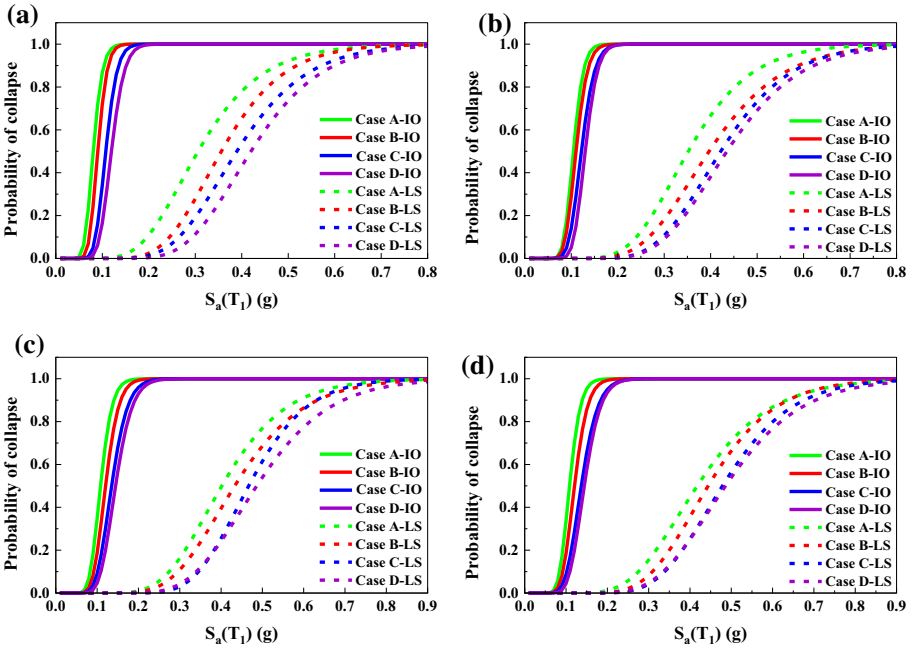

Fig. 19 Seismic fragility curves of the 5-Story SMRF considering four cases of IMWs on the, **a** soil type B, **b** soil type C, **c** soil type D, and **d** soil type E, subjected to FF record subset

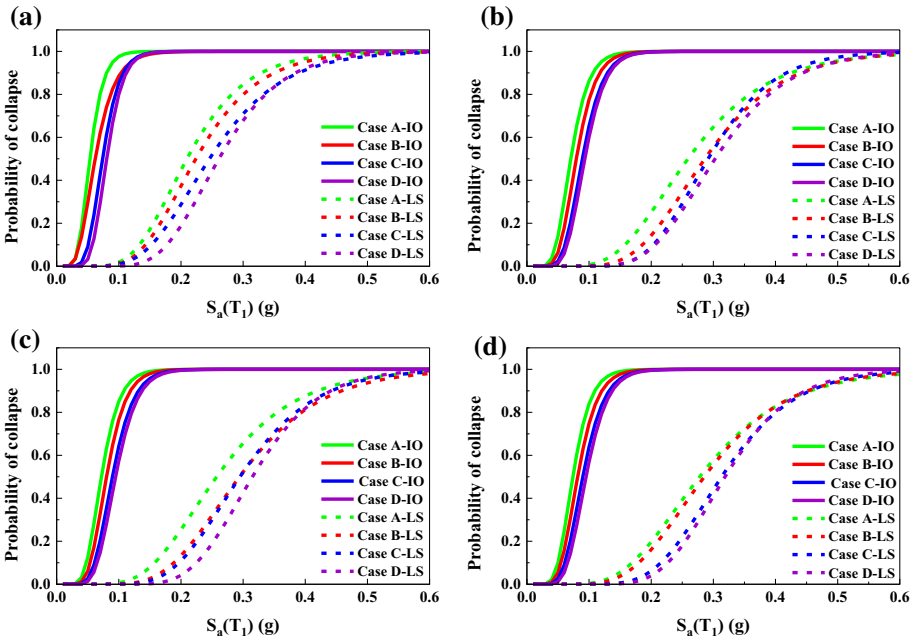

Fig. 20 Seismic fragility curves of the 7-Story SMRF considering four cases of IMWs on the, **a** soil type B, **b** soil type C, **c** soil type D, and **d** soil type E, subjected to FF record subset

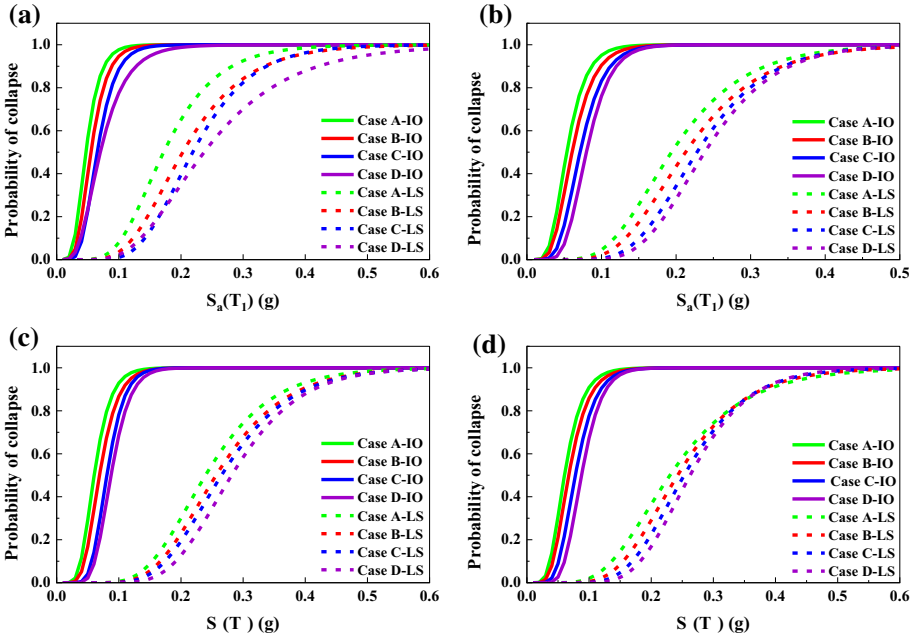

Fig. 21 Seismic fragility curves of the 9-Story SMRF considering four cases of IMWs on the, **a** soil type B, **b** soil type C, **c** soil type D, and **d** soil type E, subjected to FF record subset

failure probability of the 3-Story SMRF founded on soil type E by 33.33% and 34.21%, in the performance of IO and LS, respectively.

Figures 19a–d, 20a–d, and 21a–d illustrate seismic fragility curves in the performance levels of IO and LS of the 5-Story, 7-Story, and 9-Story SMRFs considering four cases of IMWs founded on the four soil types subjected to FF record subset, respectively. According to Fig. 19a–d, comparing the Case A and Case D in the performance level of IO show that the seismic failure probability of the 5-Story SMRF founded on soil type B, C, D, and E increased by 48.75%, 39.36%, 31.19%, and 31.19%, respectively. Moreover, the performance level of LS experienced an increase by a factor of 37.70%, 23.93%, 20.94%, and 16.54%, respectively. According to Fig. 20a–d, comparing the Case A and Case D in the performance level of IO show that the seismic failure probability of the 7-Story SMRF founded on soil type B, C, D, and E increased by 52.83%, 36.23%, 31.94%, and 33.80%, respectively. Moreover, the performance level of LS experienced an increase by a factor of 24.88%, 19.76%, 22.56%, and 16.91%, respectively. According to Fig. 21a–d, comparing the Case A and Case D in the performance level of IO show that the seismic failure probability of the 9-Story SMRF founded on soil type B, C, D, and E increased by 48.93%, 49.05%, 45%, and 45%, respectively. Moreover, the performance level of LS experienced an increase by a factor of 31.39%, 22.68%, 17.57%, and 14.41%, respectively.

In all soil types and SMRFs, the $S_a(T_1)$ values in the seismic failure probability of 50% corresponding to the performance levels of IO and LS in Case D were higher than those for Case C, Case B, and Case A. Moreover, it can be seen that assuming Case D for SMRFs founded on soil type B (e.g. 5-Story SMRF) resulted in the highest increase in the $S_a(T_1)$ values of seismic failure probability of 50% (e.g. 48.75%), as compared to the SMRFs founded in soil type E (e.g. 31.19%).

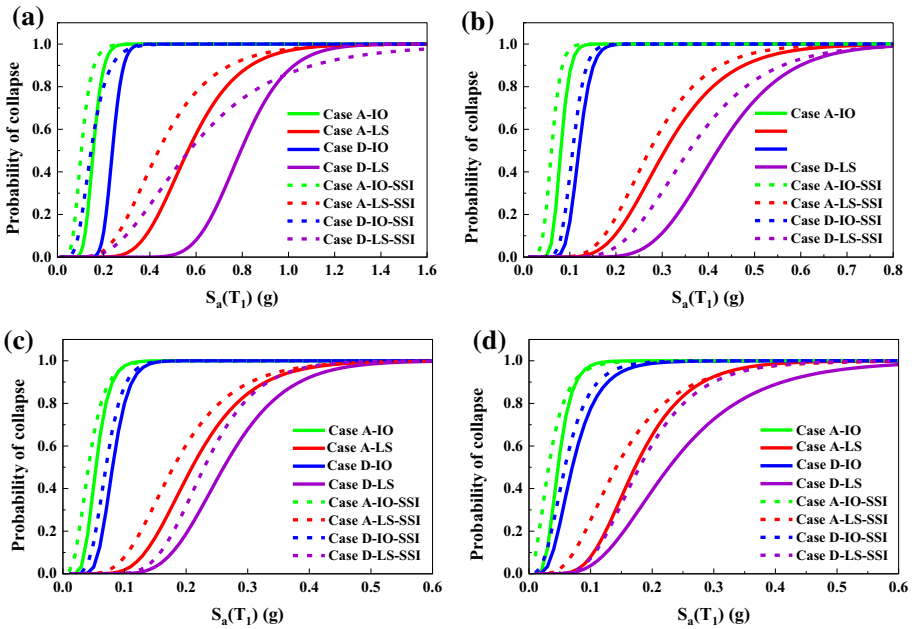

Fig. 22 Comparison of the seismic fragility curves of Case A and Case D on the soil type B with SSI effects, **a** the 3-Story, **b** the 5-Story, **c** the 7-Story, and **d** the 9-Story SMRFs, subjected to FF record subset

Therefore, it can be concluded that the IMWs can significantly decrease the seismic failure probability of the SMRFs and it should be assumed in the modeling process. The IMWs effects on the SMRFs founded on different soil types cannot be neglected and civil engineers should consider this effect to improve the seismic performance levels.

Figure 22a–d present the seismic fragility curves of the 3-Story, 5-Story, 7-Story, and 9-Story SMRFs in Case A and Case D on the soil type B with SSI effects, respectively, subjected to FF record subset. According to the results presented by Fig. 22a–d, SSI effects decreased the seismic failure probability in both performance levels of IO and LS. In the performance level of IO, the seismic failure probability of the 3-Story SMRF in the Case A and Case D decreased by 32.89% (from 0.152 to 0.102) and 60.92% (from 0.238 to 0.145), respectively, and in the performance level of LS, decreased by 22.34% (from 0.564 to 0.438) and 28.03% (from 0.792 to 0.570), respectively. In the performance level of IO, the seismic probability of collapse of the 5-Story SMRF in the Case A and Case D decreased by 22.22% (from 0.09 to 0.07) and 10.92% (from 0.119 to 0.106), respectively, and in the performance level of LS, decreased by 10.49% (from 0.305 to 0.273) and 14.52% (from 0.420 to 0.359), respectively. In the performance level of IO, the seismic probability of collapse of the 7-Story SMRF in the Case A and Case D decreased by 30.55% (from 0.072 to 0.050) and 15.78% (from 0.095 to 0.080), respectively, and in the performance level of LS, decreased by 30.35% (from 0.257 to 0.179) and 27.30% (from 0.315 to 0.229), respectively. In the performance level of IO, the seismic failure probability of the 9-Story SMRF in the Case A and Case D decreased by 14.89% (from 0.047 to 0.040) and 111% (from 0.07 to 0.06), respectively, and in the performance level of LS, decreased by (from 0.172 to 0.141) and 14.28% (from 0.226 to 0.179), respectively. For brevity, the results of SSI effects for soil type B were presented, while similar trends were observed for other soil types and SMRFs.

According to Fig. 22a–d, it can be observed that the $S_a(T_1)$ values in the seismic failure probability of 50% corresponding to the performance levels of IO and LS in Case D were higher than those for Case A considering the SSI effects. Therefore, the results of analysis can be used for SMRFs considering the SSI effects. In addition, in both situation of Case A and Case D, it is shown that the SSI effects increased the seismic failure probability. Therefore, the negative effects of considering SSI should be assumed in modeling process.

5 Conclusions

This research evaluates the seismic performance levels of 3-Story, 5-Story, 7-Story, and 9-Story SMRFs founded on the four soil types assuming four cases of IMWs placement prone to FF subset used by FEMA-P695 (FEMA P695 2009; Yazdanpanah et al. 2022). The results have been focused on the effects of considering IMWs and their significant influence on the fundamental period and seismic responses. To accurately model the IMWs and their effects on the structural response, a Tcl programming algorithm was developed in OpenSees (McKenna et al. 2016) to intelligently control the collapse state of IMWs in each floor level assuming M-IDR of the collapse limit of IMWs equal to 1.75%. It worth noting that, due to considering 2D models, the results of analysis can be used for 2D structures within the context of assumptions. The main remarks can be summarized as follows:

- According to the results of the fundamental period of SMRFs (Table 5), the placement of IMWs can add more stiffness to SMRFs and this can significantly decrease the fundamental periods. For instance, in soil type B, assuming Case D in the 3-Story SMRF can cause the fundamental period to decrease by 18.80% (from 1.17 to 0.95). Therefore, in each soil type, Case D with the full placement of IMWs has a lower fundamental period.
- The $S_a(T_1)$ values in M-IDA curves for the aforementioned SMRFs increased by adding IMWs (i.e. Case B, Case C, and Case D) into the bare frame (i.e. Case A). Therefore, the results confirm that the placement of IMWs in all floor levels increased the lateral resisting strength and this can cause an increase in the seismic performance levels. For soil type B, the $S_a(T_1)$ values in the performance level of TC for the 5-Story SMRF assuming IMWs placement of Case B, Case C, and Case D increased by 41.42%, 29.28%, and 20.18%, respectively.
- The SSI effects on the seismic limit-state capacities of the aforementioned SMRFs have been investigated. The results show that considering the SSI effects significantly decreased the $S_a(T_1)$ values in all performance levels compared to neglecting the SSI effects. For example, assuming SSI effects in the soil type E, the $S_a(T_1)$ values in the performance level of CP for the 5-Story SMRF with IMWs placement of Case B, Case C, and Case D decreased by 37.41% (from 0.751 to 0.470), 29.55% (from 0.758 to 0.534), 24.27% (from 0.828 to 0.627), and 17.44% (from 0.854 to 0.705), respectively. Therefore, it is suggested to consider the SSI effects on the modeling process and seismic vulnerability evaluation.
- Comparing the seismic probability of collapse for the performance levels of IO and LS showed that the $S_a(T_1)$ values corresponding to the seismic collapse probability of 50% for the placement of IMWs in all floor levels (i.e. Case D) are higher than those for the bare frame (i.e. Case A). For brevity, the results of 3-Story SMRF founded on soil type B showed that assuming Case D could increase the seismic collapse probability of the performance levels of IO and LS by 60% and 41.07%, respectively.
- Assuming SSI effects had a reduction influence on the seismic failure probability. Thus, this is important to model SSI and assume its significant influence on the seismic responses. In soil type B and the seismic performance level of LS, assuming SSI effects can decrease the collapse probability of the 5-Story SMRF by 10.49% (from 0.305 to 0.273) and 14.52% (from 0.420 to 0.359), for the Case A and Case D, respectively.
- According to results of analysis presented for SMRFs, IMWs have considerable influence on the fundamental period of SMRFs, which can change the seismic behavior of structures. In addition, the significant effects of IMWs on the seismic performance levels and seismic failure probability cannot be ignored. For future work, three-dimensional modeling of buildings with possibility of out-of-plane failure of IMWs is recommended. In addition, it is suggested to investigate previous damages of IMWs (i.e. in-plane damages), different workmanships and the effects of near-fault seismic records.

Acknowledgements Numerical calculations were carried out at the Tri-City Academic Supercomputer and Network (*CI TASK*) in Gdańsk, Poland.

Author contributions FK: Conceptualization, Methodology, Software, Writing—Original draft preparation, Validation. NA: Data curation, Methodology, Software, Writing—Original draft preparation. RJ: Supervision, Writing—Reviewing and Editing.

Funding The authors have not disclosed any funding.

Declarations

Conflict of interest The authors declare that there is no conflict of interest, and all authors named in the manuscript are aware of the submission and have agreed for the paper in title of 'Probabilistic assessment of SMRFs with infill masonry walls incorporating nonlinear soil–structure interaction' to be submitted for publication in *Bulletin of Earthquake Engineering*.

Open Access This article is licensed under a Creative Commons Attribution 4.0 International License, which permits use, sharing, adaptation, distribution and reproduction in any medium or format, as long as you give appropriate credit to the original author(s) and the source, provide a link to the Creative Commons licence, and indicate if changes were made. The images or other third party material in this article are included in the article's Creative Commons licence, unless indicated otherwise in a credit line to the material. If material is not included in the article's Creative Commons licence and your intended use is not permitted by statutory regulation or exceeds the permitted use, you will need to obtain permission directly from the copyright holder. To view a copy of this licence, visit http://creativecommons.org/licenses/by/4.0/.

References

AISC A (2016). Seismic provisions for structural steel buildings. Chicago, IL: American Institute of Steel Construction. 341–16

Allotey N, El Naggar MH (2008) Generalized dynamic Winkler model for nonlinear soil–structure interaction analysis. Can Geotech J 45(4):560–573

Applied Technology Council, & United States. Federal Emergency Management Agency, (FEMA P695) (2009) Quantification of building seismic performance factors. US Department of Homeland Security, FEMA

ASCE 7-16 (2017) Minimum design loads and associated criteria for buildings and other structures. Reston, VA: American Society of Civil Engineers.

Asgarkhani N, Yakhchalian M, Mohebi B (2020) Evaluation of approximate methods for estimating residual drift demands in BRBFs. Eng Struct 224:110849

Boulanger RW, Curras CJ, Kutter BL, Wilson DW, Abghari A (1999) Seismic soil-pile-structure interaction experiments and analyses. J Geotech Geoenviron Eng 125(9):750–759

Brodsky A, Yankelevsky DZ (2017) Resistance of reinforced concrete frames with masonry infill walls to in-plane gravity loading due to loss of a supporting column. Eng Struct 140:134–150

Buonopane SG, White RN (1999) Pseudodynamic testing of masonry infilled reinforced concrete frame. J Struct Eng 125(6):578–589

Carpine R, Ientile S, Vacca N, Boscato G, Rospars C, Cecchi A, Argoul P (2021) Modal identification in the case of complex modes–Use of the wavelet analysis applied to the after-shock responses of a masonry wall during shear compression tests. Mech Syst Signal Process 160:107753

AISC Committee. (2016). Specification for structural steel buildings (ANSI/AISC 360–16). American Institute of Steel Construction, Chicago-Illinois

Crisafulli FJ, Carr AJ (2007) Proposed macro-model for the analysis of infilled frame structures. Bull N Z Soc Earthq Eng 40(2):69–77

Di Trapani F, Shing PB, Cavaleri L (2018) Macroelement model for in-plane and out-of-plane responses of masonry infills in frame structures. J Struct Eng 144(2):04017198

Dutta SC, Bhattacharya K, Roy R (2004) Response of low-rise buildings under seismic ground excitation incorporating soil–structure interaction. Soil Dyn Earthq Eng 24(12):893–914

El-Dakhakhni WW, Elgaaly M, Hamid AA (2003) Three-strut model for concrete masonry-infilled steel frames. J Struct Eng 129(2):177–185

Elwardany H, Seleemah A, Jankowski R (2017) Seismic pounding behavior of multi-story buildings in series considering the effect of infill panels. Eng Struct 144:139–150

Elwardany H, Seleemah A, Jankowski R, El-Khoriby S (2019) Influence of soil–structure interaction on seismic pounding between steel frame buildings considering the effect of infill panels. Bull Earthq Eng 17(11):6165–6202

Fardis MN, Bousias SN, Franchioni G, Panagiotakos TB (1999) Seismic response and design of RC structures with plan-eccentric masonry infills. Earthq Eng Struct Dyn 28(2):173–191

FEMA-356. (2000) Prestandard and commentary for the seismic rehabilitation of buildings. Washington, DC: Federal Emergency Management Agency.
Forcellini D (2021) Analytical fragility curves of shallow-founded structures subjected to soil-structure interaction (SSI) effects. Soil Dyn Earthq Eng 141:106487
Furtado A, Rodrigues H, Arêde A (2015) Modelling of masonry infill walls participation in the seismic behaviour of RC buildings using OpenSees. Int J Adv Struct Eng (IJASE) 7(2):117–127
Furtado A, Rodrigues H, Arêde A, Varum H (2016a) Experimental evaluation of out-of-plane capacity of masonry infill walls. Eng Struct 111:48–63
Furtado A, Rodrigues H, Arêde A, Varum H (2016b) Simplified macro-model for infill masonry walls considering the out-of-plane behaviour. Earthq Eng Struct Dyn 45(4):507–524
Furtado A, Rodrigues H, Arêde A, Varum H (2017) Modal identification of infill masonry walls with different characteristics. Eng Struct 145:118–134
Furtado A, Rodrigues H, Arêde A (2018) Calibration of a simplified macro-model for infilled frames with openings. Adv Struct Eng 21(2):157–170
Furtado A, Rodrigues H, Arêde A, Varum H (2020) Effect of the panel width support and columns axial load on the infill masonry walls out-of-plane behavior. J Earthq Eng 24(4):653–681
Furtado A, Rodrigues H, Arede A, Varum H (2022) Experimental investigation on the possible effect of previous damage, workmanship and test setup on the out-of-plane behaviour of masonry infill walls. J Earthq Eng 26(11):5647–5678
Furtado A, Rodrigues H, & Arêde A. (2021). Effect of the infill panels in the floor response spectra of an 8-storey RC building. In: structures. Elsevier (Vol 34, pp 2476–2498)
Gara F, Carbonari S, Roia D, Balducci A, Dezi L (2021) Seismic retrofit assessment of a school building through operational modal analysis and fe modeling. J Struct Eng 147(1):04020302
Gazetas G (1991) Formulas and charts for impedances of surface and embedded foundations. J Geotech Eng 117(9):1363–1381
Gupta, A., and Krawinkler, H. (1999). Seismic demands for performance evaluation of steel moment resisting frame structures, technical report 132, The John A. Blume earthquake engineering research Center, department of civil engineering, Stanford University, Stanford, CA.
Harden CW, Hutchinson TC (2009) Beam-on-nonlinear-Winkler-foundation modeling of shallow, rocking-dominated footings. Earthq Spectra 25(2):277–300
Huang X, Zhou Z, Wang Y (2021) Investigation of the seismic behaviour of masonry infilled self-centring beam moment frames using a new infill material model. Bull Earthq Eng 19(12):4887–4910
Ibarra LF, Medina RA, Krawinkler H (2005) Hysteretic models that incorporate strength and stiffness deterioration. Earthq Eng Struct Dyn 34(12):1489–1511
Kakaletsis DJ, Karayannis CG (2008) Influence of masonry strength and openings on infilled R/C frames under cycling loading. J Earthq Eng 12(2):197–221
Karapetrou ST, Fotopoulou SD, Pitilakis KD (2015) Seismic vulnerability assessment of high-rise non-ductile RC buildings considering soil–structure interaction effects. Soil Dyn Earthq Eng 73:42–57
Kazemi F, Mohebi B, Yakhchalian M (2018) Evaluation the P-delta effect on collapse capacity of adjacent structures subjected to far-field ground motions. Civil Eng J 4(5):1066. https://doi.org/10.28991/cej-0309156
Kazemi F, Mohebi B, Yakhchalian M (2020) Predicting the seismic collapse capacity of adjacent structures prone to pounding. Can J Civ Eng 47(6):663–677
Kazemi F, Miari M, Jankowski R (2021a) Investigating the effects of structural pounding on the seismic performance of adjacent RC and steel MRFs. Bull Earthq Eng 19(1):317–343
Kazemi F, Mohebi B, Jankowski R (2021b) Predicting the seismic collapse capacity of adjacent SMRFs retrofitted with fluid viscous dampers in pounding condition. Mech Syst Signal Process 161:107939
Kazemi F, Jankowski R (2023a) Enhancing seismic performance of rigid and semi-rigid connections equipped with SMA bolts incorporating nonlinear soil-structure interaction. Eng Struct 274:114896. https://doi.org/10.1016/j.engstruct.2022.114896
Kazemi F, Jankowski R (2023b) Machine learning-based prediction of seismic limit-state capacity of steel moment-resisting frames considering soil-structure interaction. Comput Struct 274:106886
Kazemi F, Asgarkhani N, Jankowski R (2023) Predicting seismic response of SMRFs founded on different soil types using machine learning techniques. Eng Struct 274:114953
Koutromanos I, Stavridis A, Shing PB, Willam K (2011) Numerical modeling of masonry-infilled RC frames subjected to seismic loads. Comput Struct 89(11–12):1026–1037
Mazza F (2019) In-plane–out-of-plane non-linear model of masonry infills in the seismic analysis of RC-framed buildings. Earthq Eng Struct Dyn 48(4):432–453
Mazza F, Donnici A (2021) In-plane and out-of-plane seismic damage of masonry infills in existing rc structures: the case study of De Gasperi-Battaglia school in Norcia. Bull Earthq Eng 19(1):345–376

McKenna F, Fenves GL, Filippou, FC, & Scott MH (2016) Open system for earthquake engineering simulation (open sees) Berkeley: pacific Earthquake engineering research center, University of California, Web page. http://opensees.berkeley.edu.
Merino RJ, Perrone D, Filiatrault A (2020) Consistent floor response spectra for performance-based seismic design of nonstructural elements. Earthq Eng Struct Dyn 49(3):261–284
Misir IS, Ozcelik O, Girgin SC, Yucel U (2016) The behavior of infill walls in RC frames under combined bidirectional loading. J Earthq Eng 20(4):559–586
Mitropoulou CC, Kostopanagiotis C, Kopanos M, Ioakim D, & Lagaros ND. (2016). Influence of soil–structure interaction on fragility assessment of building structures. In: Structures (Vol 6, pp 85–98).
Mohamed H, Romão X (2020) Analysis of the performance of strut models to simulate the seismic behaviour of masonry infills in partially infilled RC frames. Eng Struct 222:111124
Mohebi B, Yazdanpanah O, Kazemi F, Formisano A (2021) Seismic damage diagnosis in adjacent steel and RC MRFs considering pounding effects through improved wavelet-based damage-sensitive feature. J Build Eng 33:101847
Mohebi B, Kazemi F, Yakhchalian M (2018) Investigating the P-Delta effects on the seismic collapse capacity of adjacent structures. In: 16th European Conference on Earthquake Engineering (16ECEE), 18–21 June, Thessaloniki, Greece
Nicoletti V, Arezzo D, Carbonari S, Gara F (2020) Expeditious methodology for the estimation of infill masonry wall stiffness through in-situ dynamic tests. Constr Build Mater 262:120807
Onat O, Correia AA, Lourenço PB, Koçak A (2018) Assessment of the combined in-plane and out-of-plane behavior of brick infill walls within reinforced concrete frames under seismic loading. Earthq Eng Struct Dyn 47(14):2821–2839
Ozturkoglu O, Ucar T, Yesilce Y (2017) Effect of masonry infill walls with openings on nonlinear response of reinforced concrete frames. Earthq Struct 12(3):333–347
Pecker A, Paolucci R, Chatzigogos C, Correia AA, Figini R (2014) The role of non-linear dynamic soil-foundation interaction on the seismic response of structures. Bull Earthq Eng 12(3):1157–1176
Perrone D, Leone M, Aiello MA (2017) Non-linear behaviour of masonry infilled RC frames: influence of masonry mechanical properties. Eng Struct 150:875–891
Petridis C, Pitilakis D (2020) Fragility curve modifiers for reinforced concrete dual buildings, including nonlinear site effects and soil–structure interaction. Earthq Spectra 36(4):1930–1951
Pitilakis D, Dietz M, Wood DM, Clouteau D, Modaressi A (2008) Numerical simulation of dynamic soil–structure interaction in shaking table testing. Soil Dyn Earthq Eng 28(6):453–467
Pitilakis KD, Karapetrou ST, Fotopoulou SD (2014) Consideration of aging and SSI effects on seismic vulnerability assessment of RC buildings. Bull Earthq Eng 12(4):1755–1776
Preti M, Bettini N, Plizzari G (2012) Infill walls with sliding joints to limit infill-frame seismic interaction: large-scale experimental test. J Earthq Eng 16(1):125–141
Pujol S, Fick D (2010) The test of a full-scale three-story RC structure with masonry infill walls. Eng Struct 32(10):3112–3121
Rajeev P, Tesfamariam S (2012) Seismic fragilities of non-ductile reinforced concrete frames with consideration of soil structure interaction. Soil Dyn Earthq Eng 40:78–86
Ramos LF, Marques L, Lourenço PB, De Roeck G, Campos-Costa A, Roque J (2010) Monitoring historical masonry structures with operational modal analysis: two case studies. Mech Syst Signal Process 24(5):1291–1305
Raychowdhury P (2011) Seismic response of low-rise steel moment-resisting frame (SMRF) buildings incorporating nonlinear soil–structure interaction (SSI). Eng Struct 33(3):958–967
Raychowdhury P, Hutchinson TC (2009) Performance evaluation of a nonlinear Winkler-based shallow foundation model using centrifuge test results. Earthq Eng Struct Dyn 38(5):679–698
Rodrigues H, Varum H, Costa A (2010) Simplified macro-model for infill masonry panels. J Earthq Eng 14(3):390–416
Salmanpour AH, Mojsilović N, Schwartz J (2015) Displacement capacity of contemporary unreinforced masonry walls: an experimental study. Eng Struct 89:1–16
Smyrou E, Blandon C, Antoniou S, Pinho R, Crisafulli F (2011) Implementation and verification of a masonry panel model for nonlinear dynamic analysis of infilled RC frames. Bull Earthq Eng 9(5):1519–1534
Tasnimi AA, Mohebkhah A (2011) Investigation on the behavior of brick-infilled steel frames with openings, experimental and analytical approaches. Eng Struct 33(3):968–980
USGS (2022) US geological survey. http://usgs.gov. Accessed 6 July 2022
Uva G, Porco F, Fiore A (2012) Appraisal of masonry infill walls effect in the seismic response of RC framed buildings: a case study. Eng Struct 34:514–526

Wararuksajja W, Srechai J, Leelataviwat S (2020) Seismic design of RC moment-resisting frames with concrete block infill walls considering local infill-frame interactions. Bull Earthq Eng 18(14):6445–6474
Yakhchalian M, Asgarkhani N, Yakhchalian M (2020) Evaluation of deflection amplification factor for steel buckling restrained braced frames. J Build Eng 30:101228
Yakhchalian M, Yakhchalian M, Asgarkhani N (2021) An advanced intensity measure for residual drift assessment of steel BRB frames. Bull Earthq Eng 19(4):1931–1955
Yazdanpanah O, Mohebi B, Kazemi F, Mansouri I, Jankowski R (2022) Development of fragility curves in adjacent steel moment-resisting frames considering pounding effects through improved wavelet-based refined damage-sensitive feature. Mech Syst Signal Process 173:109038
Zuo H, Zhang W, Wang B, Gu X (2022) Force–displacement relationship modelling of masonry infill walls with openings in hinged steel frames. Bull Earthq Eng 20(1):349–382

Publisher's Note Springer Nature remains neutral with regard to jurisdictional claims in published maps and institutional affiliations.

Paper V:

Kazemi, F., Asgarkhani, N., & Jankowski, R. (2024). Enhancing seismic performance of steel buildings having semi-rigid connection with infill masonry walls considering soil type effects. Soil Dynamics and Earthquake Engineering, 177, 108396.

doi.org/10.1016/j.soildyn.2023.108396

Paper V

Soil Dynamics and Earthquake Engineering 177 (2024) 108396

Contents lists available at ScienceDirect

Soil Dynamics and Earthquake Engineering

journal homepage: www.elsevier.com/locate/soildyn

Enhancing seismic performance of steel buildings having semi-rigid connection with infill masonry walls considering soil type effects

F. Kazemi [a,b,*], N. Asgarkhani [a], R. Jankowski [a]

[a] Faculty of Civil and Environmental Engineering, Gdańsk University of Technology, ul. Narutowicza 11/12, 80-233 Gdansk, Poland
[b] Department of Civil, Environmental & Geomatic Engineering, University College London, London, UK

ARTICLE INFO

Keywords:
Steel damaged building
Infill masonry wall
Rigidity of connection
Soil type effects
Seismic performance assessment
Seismic retrofit.

ABSTRACT

Unpreventable constructional defects are the main issues in the case of steel Moment-Resisting Frames (MRFs) that mostly occur in the rigidities of beam-to-column connections. The present article aims to investigate the effects of different rigidities of structures and to propose Infill Masonry Walls (IMWs) as retrofitting strategy for the steel damaged buildings. A fault or failure to meet a certain consideration of the soil type beneath the building and the current rigidity of connections can cause mistake in determining the performance of building. Therefore, this study comprehensively explores different conditions of soil types, connection rigidities, and implementing IMWs on the 3-, 5-, 7-, and 9-story MRFs. Two nonlinear analyses, namely Nonlinear Dynamic Analysis (NDA) and Incremental Dynamic Analysis (IDA) were performed on 384 steel MRFs having different conditions of defects and the results of the analysis include 3456 performance curves assuming three ground motion subsets recommended by FEMA P695. The results confirm that the proposed retrofitting procedure can effectively improve the performance levels of MRFs, which the connections rigidity of 90 %, 80 %, 70 %, 60 %, and 50 % can reduce the collapse performance level by 2.86 %, 5.35 %, 9.31 %, 16.56 %, and 34.65 %, respectively.

1. Introduction

Infill Masonry Walls (IMWs) are non-structural features that serve as a mean of separating architectural spaces while providing heat, sound, and fire insulation. There is no doubt that exterior IMWs are ones of the most frequently damaged non-structural systems in severe earthquakes. Some buildings that were structurally damaged by an earthquake as a result of failure in IMWs could not be used anymore, and they were demolished following the earthquake. There has been extensive research conducted through both experimental and analytical methods to understand the seismic response of IMWs during earthquakes. It is generally accepted that wall panels are not taken into consideration in structural seismic design, even though they have a considerable impact on the building's safety and functionality. There have been several seismic hazard investigations demonstrated that enclosure wall damage and collapse are responsible for many casualties and property damage when earthquakes occur [1]. It is also important to note that the irrational connector and arrangement of the IMWs contributed to the poor integrity as well (e.g., see Refs. [2,3]). Several studies have been conducted on wall panels to evaluate their ability to accommodate structural deformations and the way in which they contribute to the structural behavior of the building. According to results of shaking table tests, Fiorino et al. [4] classified the damaged state of wall panels according to the level of repair, and performed fragility analyses based on the classified damages. According to Hou et al. [5], a new type of IMW implemented with inter-panel energy absorbers was proposed and the lateral behavior of system was examined. Hu et al. [6] tested a precast IMW with damage-control capabilities for steel buildings and found out that it performed well in earthquakes. Flexible connections, known as semi-rigid connections, reduce the stiffness of the frame systems and degrade their bearing capacity. Fig. 1 presents examples of rigid and semi-rigid connections that were used in steel building, which some of them have less expected rigidity due to constructional defects while it was assumed as rigid connections in the design process.

There have been several proposals to improve the strength and lateral stiffness of structures, including strengthening connections [7] and substituting regular bolts with shape memory alloy bolts [8]. Despite the potential improvement in seismic response by this method, the intervention of traditional infill may make it difficult for an accurate estimation of actual structural response because the effects of IMWs are

* Corresponding author. Faculty of Civil and Environmental Engineering, Gdańsk University of Technology, ul. Narutowicza 11/12, 80-233 Gdansk, Poland;
E-mail address: farzin.kazemi@pg.edu.pl (F. Kazemi).

https://doi.org/10.1016/j.soildyn.2023.108396
Received 12 May 2023; Received in revised form 22 November 2023; Accepted 1 December 2023
Available online 11 December 2023
0267-7261/© 2023 Elsevier Ltd. All rights reserved.

uncertain. An experimental investigation by Zhang et al. [9] was conducted to evaluate the working mechanism and behavior of prefabricated IMWs installed on semi-rigid steel frames. According to their findings, the IMWs can improve the steel frame's energy dissipation capacity by approximately 23.3 %. A new partitioning technique was also proposed by Cheng et al. [10] for IMWs that demonstrated good in-plane and out-of-plane seismic performance as well as low damages. Farahani et al. [11] proposed new formulas for accurately predicting responses of infilled MRFs and introduces a novel non-uniform out-of--plane force distribution pattern including aspect ratio, window opening size, and frame flexibility in a wide-ranging parametric study.

Previous studies showed that opening position (i.e. door and window) and wall geometry could considerably affect the IMWs behavior [12,13]. In addition, workmanships, double-leaf infills, and pre-damaged IMWs have been investigated by researchers [14,15]. Furtado et al. [16–18] investigated the in-plane and out-of-plane collapse of IMWs and the reduction in strength and stiffness as a result of the pre-damage. It was agreed that the material and geometry of IMWs could influence the total behavior of buildings, while the pre-damaged IMWs can reduce the frequency by up to even 35 % [17]. Although some studies have been performed for vulnerability assessment of buildings by neglecting the IMWs effects assuming them as non-structural elements (e.g., see Refs. [19–23]), the additional stiffness of IMWs cannot be neglected in the seismic performance of structures [12]. Therefore, the IMWs should be considered in the modelling and analysis of buildings.

Yekrangnia and Mohammadi [24] performed a comprehensive analysis of a newly introduced strut model designed for IMWs within steel Moment-Resisting Frames (MRFs). The basis of the model lies in meticulously calibrated finite element analyses, ensuring a realistic depiction of the behavior of infilled MRFs. The findings clearly demonstrated a substantial enhancement in accurately capturing the internal forces acting on the frame members and the force-displacement diagram of infilled MRFs when employing the proposed model, as opposed to the existing models. Furthermore, the robustness of the newly proposed model is underscored by its accurate predictions aligning with the performance of numerous experimental results involving IMWs within MRFs. Moreover, a multi-strut macro-model aimed at accurately simulating the force-displacement behavior of infilled frames with various opening configurations was proposed by Yekrangnia and Asteris [25]. The research highlights the significant impact of opening size and position relative to the IMWs on the behavior of infilled MRFs. The proposed model is rigorously validated through parametric evaluations, highlighting its reliability in approximating lateral responses of infilled MRFs with openings. Nowadays, with the increasing need to build low-, to mid-rise buildings, retrofitting existing structures is of great importance. In addition, retrofitting idea prevents the creation of unusual concrete materials resulting from destruction of the existing structure, which is valuable from an environmental point of view. By adding hysteric elements to improve structure's seismic performance, better results can be demonstrated in the structural behavior.

Fig. 1. Examples of rigid and semi-rigid connections that were used in steel building and they are revealed in retrofitting procedure.

Previous studies have implemented passive dissipation devices, such as viscous dampers [26–28] and buckling restrained braces [29–31], to control the lateral behavior of buildings to achieve higher performance of lateral system.

Due to damage to buildings during earthquakes, it has been observed that the connections have a great influence to meet the performance of the building. Constructional defects may not be considered in the design process; however, considering the rigid beam-to-column connection seems to be an ideal assumption. As shown in Fig. 1, in some cases, the connection of the structural elements has different rigidities compared to the designed assumption. In other words, it may have less rigidity than the assumed rigid connection in design process and this may reduce the capability of the structure in lateral loads. One effective method to enhance the seismic performance is to use all the available capacities of the structural members that can significantly save on retrofitting costs. In this regard, manufacturing defects, including problems in the behavior of connecting structural elements (i.e., semi-rigidity), should also be considered. This research aims to investigate the effects of IMWs and the type of structural connections on the behavior of steel Moment-Resisting Frames (MRFs) by considering all the possibilities including the rigidity of connections, soil type effects, and the placement of IMWs. The result of current research can help to evaluate the structural behavior. In addition, this research provides information for estimating the structural behavior and improvements in the performance of MRFs. The novelty lies in the holistic approach to retrofitting, accounting for various factors that impact structural performance, and thereby, contributing to cost-effective and environmentally conscious solutions for the construction industry. Finally, by providing the Graphical User Interface (GUI), it helps structural designers to find out the effects of each parameters and to compare and choice the optimal approach regarding the existing condition of the building.

2. Modeling process

2.1. Modeling of buildings

To evaluate the influence of IMWs and connection's rigidity of structures, buildings with 3-, 5-, 7-, and 9-Story elevations, having MRFs in the outer frames were designed considering the structural plan illustrated in Fig. 2. For designing buildings, four soil types with details presented in Table 1 were considered, in which, the lateral load and design spectrum were considered based on these soil types. To achieve the details of soil type, the location of buildings was assumed in Los Angeles, USA, having longitude and latitude of −118.32° and 34.04°, respectively [32]. It should be noted that the outer frames presented in Fig. 1 were assumed as MRFs, while other columns were modelled as gravity columns. According to Table 12.2.1 ASCE 7–16 [33], the selected seismic force-resisting systems have the design parameters of R, Ω_0 and C_d equal to 8.0, 3.0, and 5.5, respectively. ETABS 2016 software was employed to model structures having dead and live loads of 3.35 kN/m^2 and 1.68 kN/m^2, respectively, and steel material with a yield strength of 345 MPa. In addition, for the design process, the provisions of AISC 360-16 [34], and AISC 341-16 (i.e., see Section E3) [35] were used.

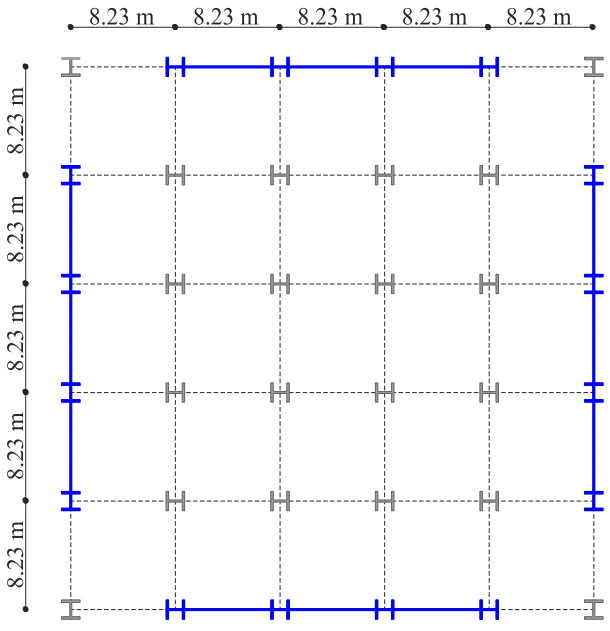

Fig. 2. Plan of modelled buildings assuming four MRFs in outer frames.

It has been reported that numerous studies used 2D models in OpenSees [36] software instead of 3D buildings (e.g., see Refs. [37–39]), since the regularity of building plan can neglect the torsional movements. Considering the improvements to OpenSees [36] software, 2D models have the ability to model the deterioration effects, which allows us to precisely consider the collapse state of structural elements. Therefore, in this study, the 2D models were used and the verification was done by comparing the fundamental periods of 2D models with those of 3D models that were created in ETABS 2016 software. It should be added that in each direction, there are two MRFs that each of them should resist the seismic loads of half of the plan. It is important to note that all columns except columns in MRFs were considered as leaning column with the role of the P-Delta effect and modelled in 2D structures in OpenSees [26]. To model the deterioration effects, the modified Ibarra–Krawinkler bilinear hysteretic model was used in the zero-length element at both ends of the beam elements [27–29,40,41], which the spring and elastic elements are work together to provide the entire strength and stiffness of the modelled structural element. In addition, the nonlinear-Beam-Column element was considered for columns in order to consider the interaction of axial and bending loads. Structural section of MRFs assuming four soil types was presented in Figs. A-1 to A-4 in *Appendix*. Although it is possible to neglect the panel zone effects and model it with four rigid elements to assume the rigid area of the panel zone, in this research, the panel zone was modelled using eight rigid elements and one nonlinear rotational spring having a trilinear backbone curve considering the doubler plate effect [8].

The aim is to investigate how placements of IMWs and connection rigidity affect the seismic response of MRFs. During Incremental Dynamic Analysis (IDA), demand limitations are controlled with a programming algorithm in Tcl to account for the different collapse states between IMWs and MRFs. As a part of the evaluation of the seismic vulnerability of MRFs, seismic responses of MRFs such as lateral permanent and interstory drifts, seismic capacities, and seismic fragility curves were plotted. This study provides civil engineers with valuable information that can be used in designing procedures or retrofitting existing buildings.

Table 1
Parameters of considered soils.

	Soil B	Soil C	Soil D	Soil E
S_{DS}	1.306	1.507	1.576	1.623
S_{D1}	0.463	0.637	0.653	0.659
Soil shear modulus (MPa)	6000	280	60	30
Friction angle (Degree)	45°	42°	38°	35°
Cohesion coefficient (Pa)	0	0	5000	5000
Unit weight (N/m^3)	24000	21000	19000	18000
Poisson's ratio	0.25	0.35	0.4	0.45
Shear wave velocity (m/s)	1565	360	175	120

2.2. Modeling of IMWs

Several numerical models have been proposed over the past few decades to describe IMWs effects on the lateral behavior of buildings (e.g., see Refs. [41,42]), as well as experimental studies that have been conducted for lateral behavior evaluations. Smyrou et al. [43] developed a simpler model based on the use of two struts, while El-Dakhakhni et al. [44] proposed a model based on three nonparallel struts that considers the interaction between IMWs and frames. To account for both the shear and compressive response of IMW, Crisafulli and Carr [45] a four-node panel attached to beam and column was developed. In addition, Rodrigues et al. [46] used the modeling approach and validated by experimental test, which the model is used for simulating nonlinear response of IMWs. Therefore, in this research, the IMWs modelling approach in OpenSees [36] software and the panel zone model are schematically demonstrated in Fig. 3. For defining the material of the IMWs, the values proposed in literature review has been considered. Moreover, the IMW modeling has been verified with an experimental test to find out the capability of the considered modeling approach.

2.3. Verification of IMW modeling

It was assumed that the experimental test used by Kakalestis and Karayannis [47] would serve as a validating test (i.e., *Test S-full infill*) since the IMW without opening is considered in this research. For this purpose, the experimental test has been used to prepare an OpenSees model given the information of IMW and structural elements. In this model, the weak material was selected with compressive strength of mortar and brick equal to 1.53 MPa and 3.10 MPa, respectively, and a thickness of 60 mm. Then, the cyclic analysis has been performed to compare the shear-displacement of both experimental and numerical models. Based on *Test S-full infill* considered by Kakaletsis and Karayannis [47], Fig. 4 depicts the pushover curve of IMW using OpenSees [36] for the *Test B-Reinforced Concrete (RC) frame* and *Test S-full infill*. It seems that the numerical model can perfectly present the symmetric behavior of the test specimen. Moreover, the backbone curve of the both pushover curves has fitted that confirms the capability of the numerical model. It is noteworthy that the inside crash of *Test S-full infill* [47] makes it suitable for modeling of IMWs in 2D MRFs in OpenSees [36], which follows the aims of this study.

It is recommended that the uniaxial nonlinear element (see Fig. 3) be characterized by a multi-linear hysteresis curve that is defined in OpenSees [36] as *uniaxial Material Pinching4*. Several numerical investigations have been done by Furtado et al. [16–18] on influence of IMWs on structural behavior. According to their findings, cracks in IMW can be observed between 0.075 % and 0.12 % drift (d_c). According to the elasticity modulus of IMW, E_m, the $d_c = 0.1$ %, and cracking force, $F_c = 0.57$ MPa were determined. For IMW with brick-and-mortar properties, the cracking strength divided to maximum strength (F_c/F_{cr}) can be adopted equal to 0.55 based on experimental results and seismic code recommendations [12,16]. Following are the equations that can be used to calculate the maximum strength for IMW by determining its diagonal compressive strength, f_{IMW}, based on experimental tests:

$$F_{cr} = 0.818 \frac{L_{IMW} \times t_{IMW} \times f_{IMW}}{C_t} \left(1 + \sqrt{C_t^2 + 1}\right)$$
$$C_t = 1.925 \frac{L_{IMW}}{h_{IMW}} \quad (1)$$

where L_{IMW}, h_{IMW}, t_{IMW} can be defined as the length, height, and thickness of the IMW, respectively. The parameters for defining the *uniaxial Material Pinching4* in OpenSees [36] are presented in Table 2 and Fig. 5 having the pinching effects. To evaluate the influence of IMWs, three configuration types were assumed that stem from using IMWs with and without opening. For example, the assumed configuration for the 3-Story MRFs is presented in Fig. 6.

2.4. Modeling of beam-to-column connections

Bolted Unstiffened Endplate (BUEP) connections can be used as semi-rigid connections implemented in MRFs. In comparison to predictions, scientists found the BUEP connection to be more ductile and to have a greater plastic moment. Numerous researches investigated to verify the experimental results with numerical models, as well as studies to investigate how materials, bolt size, endplate thickness, and location of plastic hinge may affect the results (e.g., see Refs. [48–50]). In this study, the BUEP connection was considered to model the MRFs having different connection rigidities. The general configuration of BUEP semi-rigid beam-to-column connection is presented in Fig. 7. Since the configuration of BUEP depends on the section of beam used in the MRFs (Figs. A-1 to A-4 in *Appendix*), for different sections, the bolt placements were calculated and illustrated in Table 3.

It is clear that the MRFs were constructed from a variety of beam sections, and it is apparent from Fig. 7 that the type of connections depends on the type of beam section used. As a result, it is possible to determine the location of bolts and distances within the beam sections used in the models. A semi-rigid connection's moment-rotation behavior can be related to details of the connection, such as the beam and column properties, the bolt placement, the thickness of the endplates, and the diameter of the bolts. Using the plastic bending capacity of the beam as a basis for calculating rigidity, calculation of moment-rotation curve for a rigid connection is an essential step in analyzing the seismic behavior of steel frames. This requires applying the formulas presented by Sherbourne and Bahaari [51], and Bahaari and Sherbourne [52]. The moment-rotation curve can be used to determine the initial stiffness and strength of the fully rigid connection. It is important to note that the

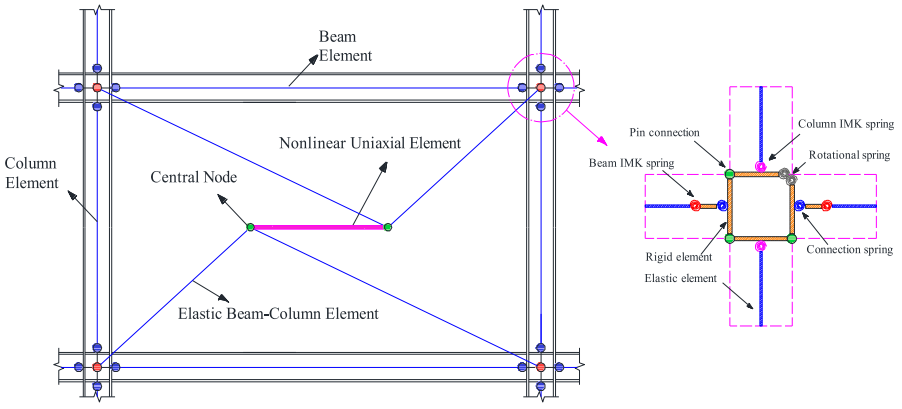

Fig. 3. Schematic view of modeling of IMW and panel zone with and semi-rigid connection in OpenSees [36].

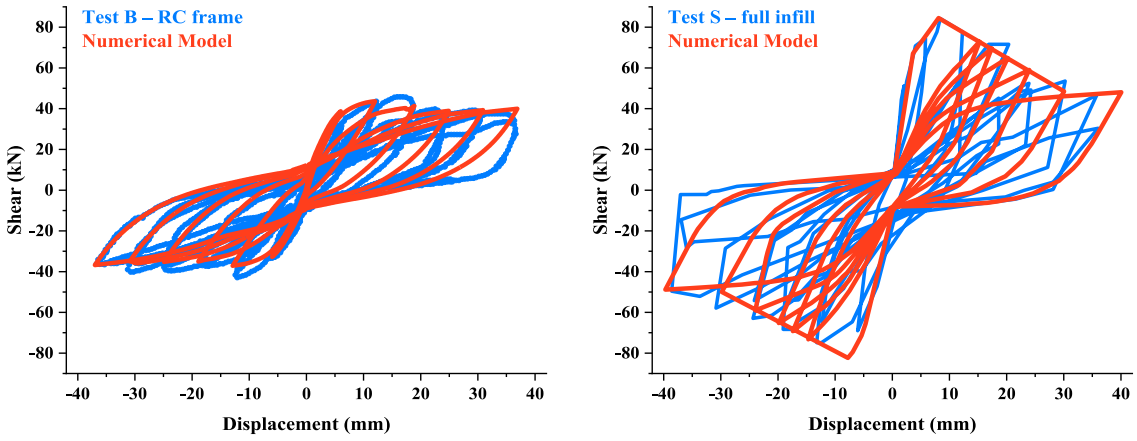

Fig. 4. Verifying the pushover curve of IMW modelled in OpenSees [36] with experimental results of Test B-RC frame and Test S-full infill [47].

Table 2
Material properties used for modeling IMW [12,16].

d_c (%)	d_y (%)	d_{cr} (%)	d_u (%)	F_c (MPa)	F_y (MPa)	F_{cr} (MPa)	F_u (MPa)
0.1	0.25	0.5	1.5	0.57	0.75	0.101	0.28

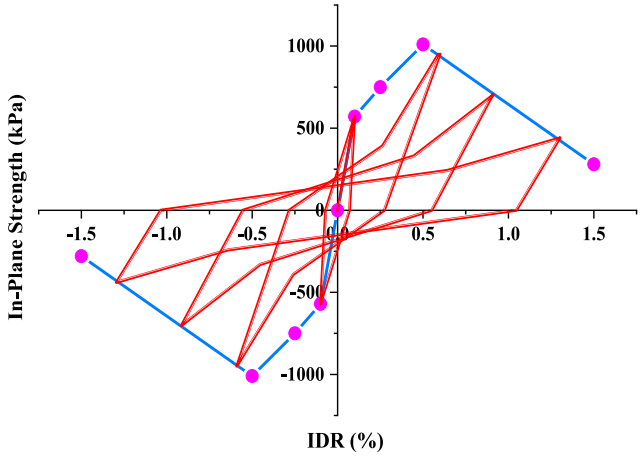

Fig. 5. Backbone curve and pinching effect of uniaxial material considered for modeling of IMW in OpenSees [36].

moment-rotation curve is specific to a fully rigid connection, and should be used accordingly. Once the moment-rotation curve is obtained, it can be used to evaluate the stiffness and strength of connection; therefore, relative rigidities can be achieved as high as 90 %, 80 %, 70 %, 60 %, and 50 % based on the initial stiffness and strength of fully rigid connections. Using Sherbourne and Bahaari's [51] and Bahaari and Sherbourne's [52] equations corresponding to rigidities of 90 %, 80 %, 70 %, 60 %, and 50 %, the diameter of bolts and the thickness of endplates were measured.

The panel zone is the region of intersection between beams and columns which is deformed primarily in shear, as a result of the opposition of moments between beams and columns. As a method of capturing deformations, Gupta and Krawinkler [53] proposed a method. The rectangle area that is shown in Fig. 3 is formed by eight rigid elements with a rotational spring to consider doubler plate effects. Using Gupta and Krawinkler [53] theory, the trilinear backbone curve is exhibited by the rotational spring that doubler plate has been considered in the stiffness of the spring, and pin connections assumed for other three corners of the panel zone. Assuming all the moments can be transferred by rigid connections, a model of a fully rigid connection was created. As a result, the numerical models utilized a rigid element instead of the connection spring to represent the fully rigid connection. With semi-rigid connections, the moment-rotation behavior was assigned to the spring where rigidities were assumed. For the semi-rigid connections considering four soil types, the thickness of endplate and bolts diameter are presented in Tables A-1 to A-4 in *Appendix*.

3. Results and discussions

3.1. Analysis methods

Since considering the beam-to-column connections of steel MRFs as a rigid connection is an ideal assumption and may not be applied in constructing buildings, this research investigates the effects of rigidities on performance levels and aims to propose retrofitting strategies for

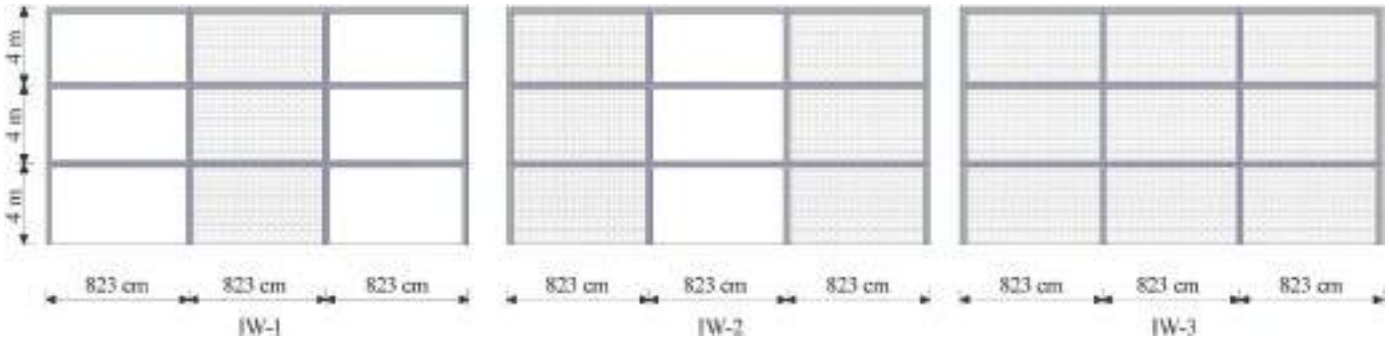

Fig. 6. Three configuration types of IMWs assumed for the 3-Story SMRF and other models.

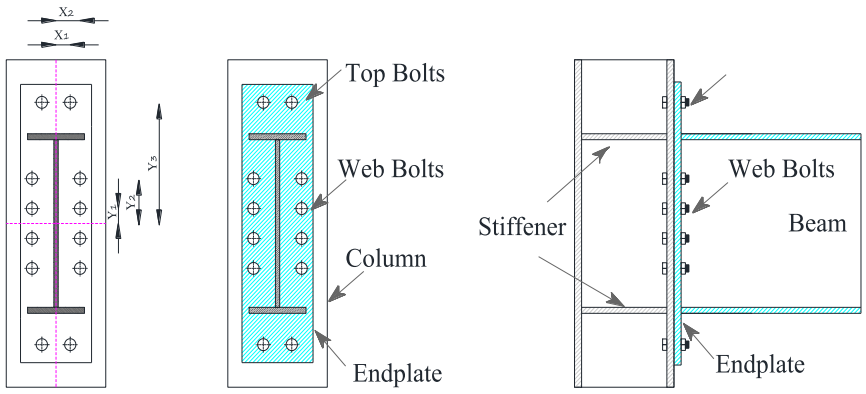

Fig. 7. General configurations of BUEP beam-to-column connection.

Table 3
Bolt placement distances of BUEP connection.

Section	Height (mm)	Flange (mm)	X_1 (mm)	X_2 (mm)	Y_1 (mm)	Y_2 (mm)	Y_3 (mm)
W18X46	460	154	50	70	50	150	295
W18X50	457	191	50	70	50	150	295
W21X50	528	165	50	70	50	150	334
W21X68	536	210	50	70	50	150	338
W24X55	599	178	50	70	50	150	370
W24X68	602	228	60	70	50	150	370
W24X76	607	228	60	70	50	150	375
W24X84	612	229	60	70	50	150	376
W24X94	617	230	60	70	50	150	379
W27X94	683	254	70	70	50	150	412
W27X102	688	254	70	70	50	150	415
W27X114	693	256	70	70	50	150	417

overcoming this issue. A comparison of the effectiveness of proposed systems was conducted using two types of analysis, namely Nonlinear Dynamic Analysis (NDA) and IDAs (for more details see Refs. [54–56]). The NDAs were carried out assuming Design-Based Earthquakes (DBE) as well as Maximum Considered Earthquake (MCE) levels. Noteworthy is the fact that the DBE and MCE levels were scaled in accordance with the target spectrum introduced in ASCE 7–10 [33]. In order to conduct IDAs, the amplitude of applied records was increased incrementally to reach the target values for Interstory Drift Ratio (IDR) and Residual Drift Ratio (RDR). In order to investigate the wide range of seismic records, three ground motion sets of Far-Fault (FF), Near-fault Pulse-like (NP), and Near-fault No-pulse (NN) were selected in accordance with FEMA P695 [57].

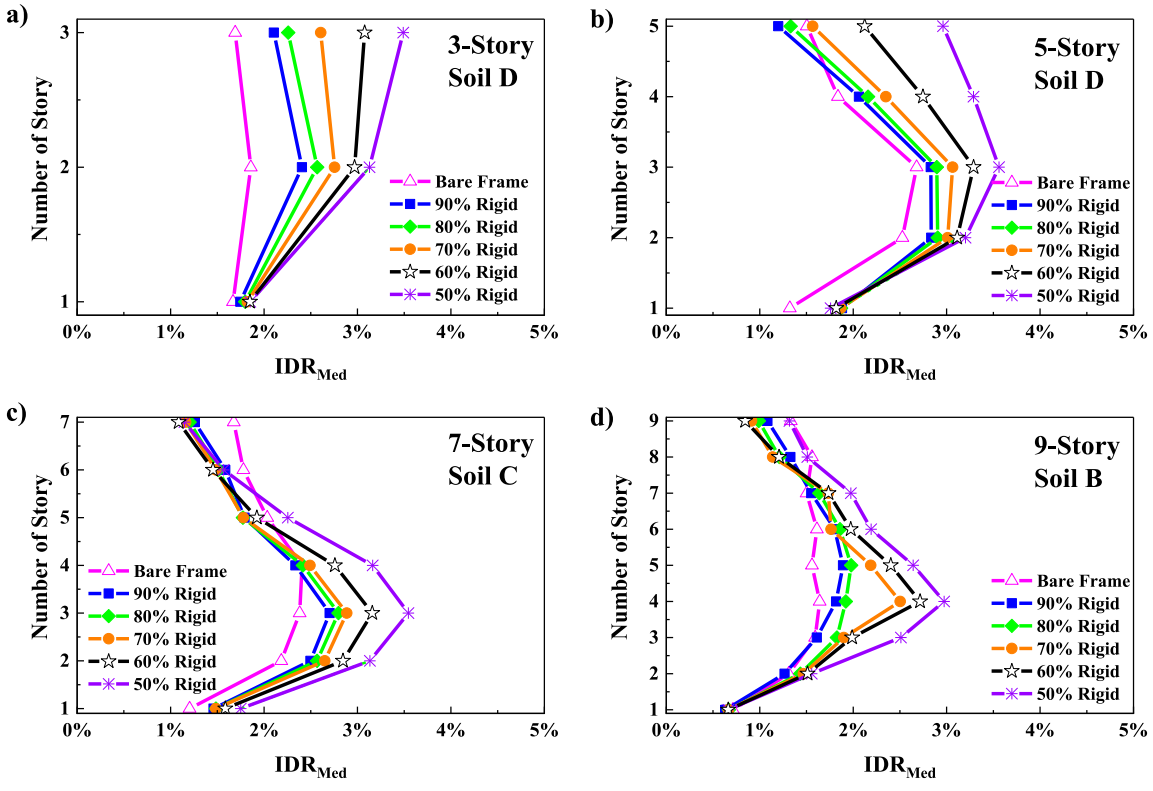

Fig. 8. IDR_{Med} of the steel MRFs considering different types of connection rigidities under DBE level of NP records.

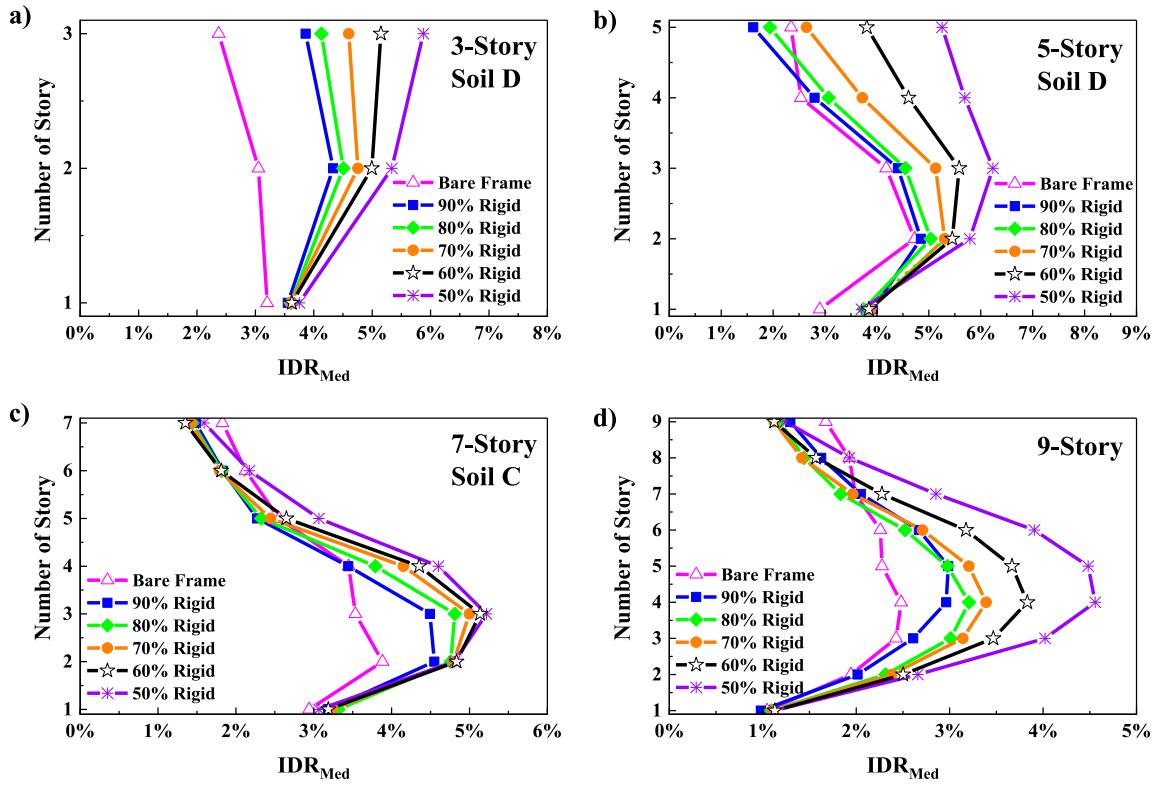

Fig. 9. IDR$_{Med}$ of the steel MRFs considering different types of connection rigidities under the MCE level of NP records.

3.2. Effects of connection rigidity

In this section, the rigidity of connections as the main issue of constructing buildings is discussed. Since the number of records had different outputs, the median of IDR (IDR$_{Med}$) and the median of RDR (RDR$_{Med}$) werevcalculated for comparing the results. Figs. 8 and 9 illustrate the distribution of IDR$_{Med}$ of the steel MRFs considering different types of connection rigidities under DBE and MCE levels of NP records, respectively. It is clear that the rigidity of connection has a great influence on the distribution of IDR$_{Med}$, however, the 50 % rigidity has the highest values of maximum IDR$_{Med}$ in all assumed structures. Under DBE and MCE levels, assuming 50 % rigidity of connections for the 9-Story MRF founded on soil B can increase the maximum IDR$_{Med}$ by 81.05 % and 83.71 %, respectively. Moreover, in the 90 % rigidity of connections, which may occur due to constructional defects, the IDR$_{Med}$ was increased, which confirms the importance of rigidity of connections in steel MRFs. Figs. 10 and 11 show the distribution of RDR$_{Med}$ of the steel MRFs considering different types of connection rigidities under DBE and MCE levels of NP records, respectively. For the 9-Story MRF founded on soil B, it can be seen that the maximum RDR$_{Med}$ increased by 2.12 and 3.03 times by considering the 50 % rigidity, which shows the great influence of rigidities on the performance of steel MRFs. Therefore, it can be observed that constructional defects have considerable influence on the lateral performance of the structure, since these defects may not be assumed in the design process. Although NP records are presented, it should be added that similar trends were observed for other record subsets.

3.3. Effects of soil types

Another issue that may affect the performance of buildings is the type of soil under the foundation. Although there may be some procedures for testing the soil beneath the structure to find the type of soil described by seismic provisions, it is possible to have some mistakes in properly selecting the type of soil due to the variability of soil types and their different behavior of them. Therefore, this section investigates different soil type effects on the distribution of IDR$_{Med}$ and RDR$_{Med}$ under DBE and MCE levels. Figs. 12 and 13 present the distribution of the IDR$_{Med}$ of the steel MRFs considering different soil types under DBE and MCE levels of NP records, respectively. It is noteworthy that the soil types can affect the distribution of IDR$_{Med}$, while soil B has lower values of IDR$_{Med}$. For instance, considering soil C for the 5-Story MRF increased the maximum of IDR$_{Med}$ by 66.76 % compared to soil B. Figs. 14 and 15 illustrate the distribution of the RDR$_{Med}$ of the steel MRFs considering different soil types under DBE and MCE levels of NP records, respectively. It can be seen that assuming different soil types can affect results of RDR$_{Med}$, which can influence the performance of the structure. Therefore, defects in the selection of soil type should be considered in retrofitting process. Although the results of NP records are presented, similar trends were observed for other record subsets.

3.4. Effects of IMWs

Figs. 16 and 17 illustrate the distribution of IDR$_{Med}$ of the steel MRFs considering different types of IMWs assuming DBE and MCE levels under NP records, respectively. The analysis results show that implementing IMWs can considerably decrease the distributed values of the IDR$_{Med}$ in all steel MRFs under DBE and MCE levels. In addition, the IW-3 condition can add more stiffness to the lateral-resisting system, and then, lower values were determined for the distribution of IDR$_{Med}$. For example, assuming the IW-3 condition in the 5-Story MRF, the maximum values of IDR$_{Med}$ were decreased by 12.72 % and 18.67 % under DBE and MCE levels, respectively. Figs. 18 and 19 illustrate the

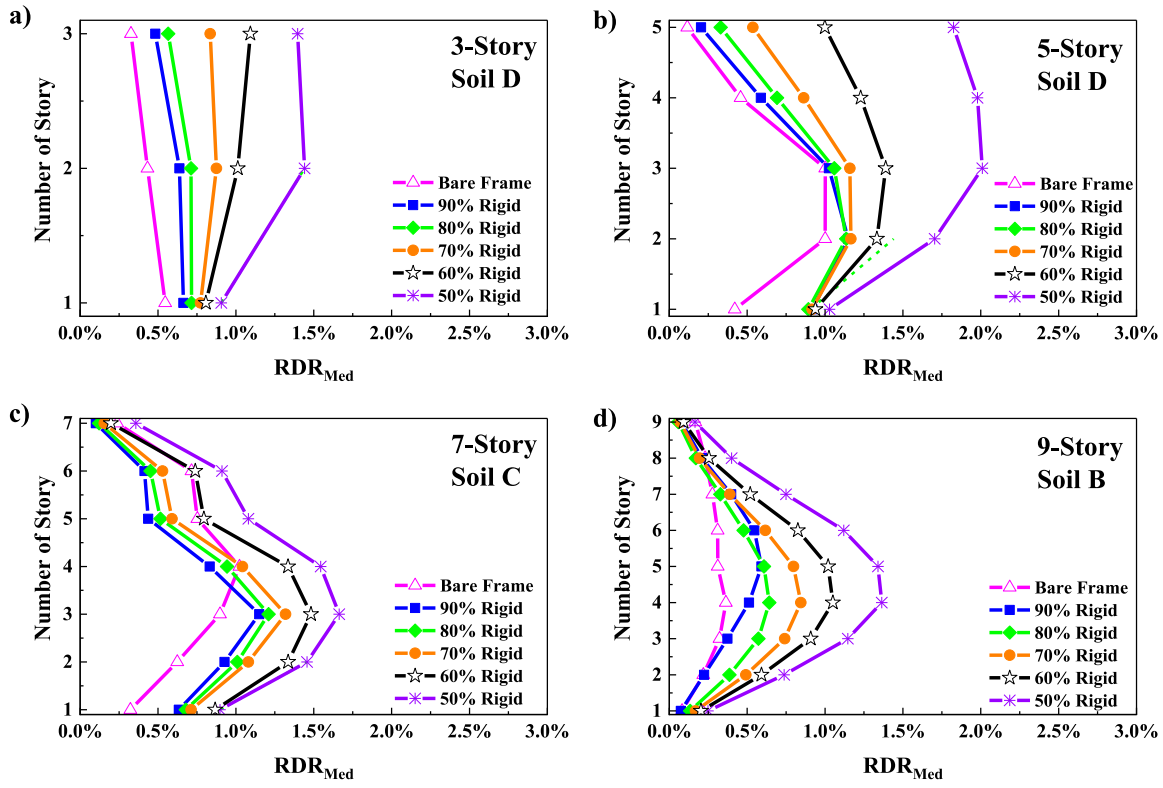

Fig. 10. RDR_{Med} of the steel MRFs considering different types of connection rigidities under DBE level of NP records.

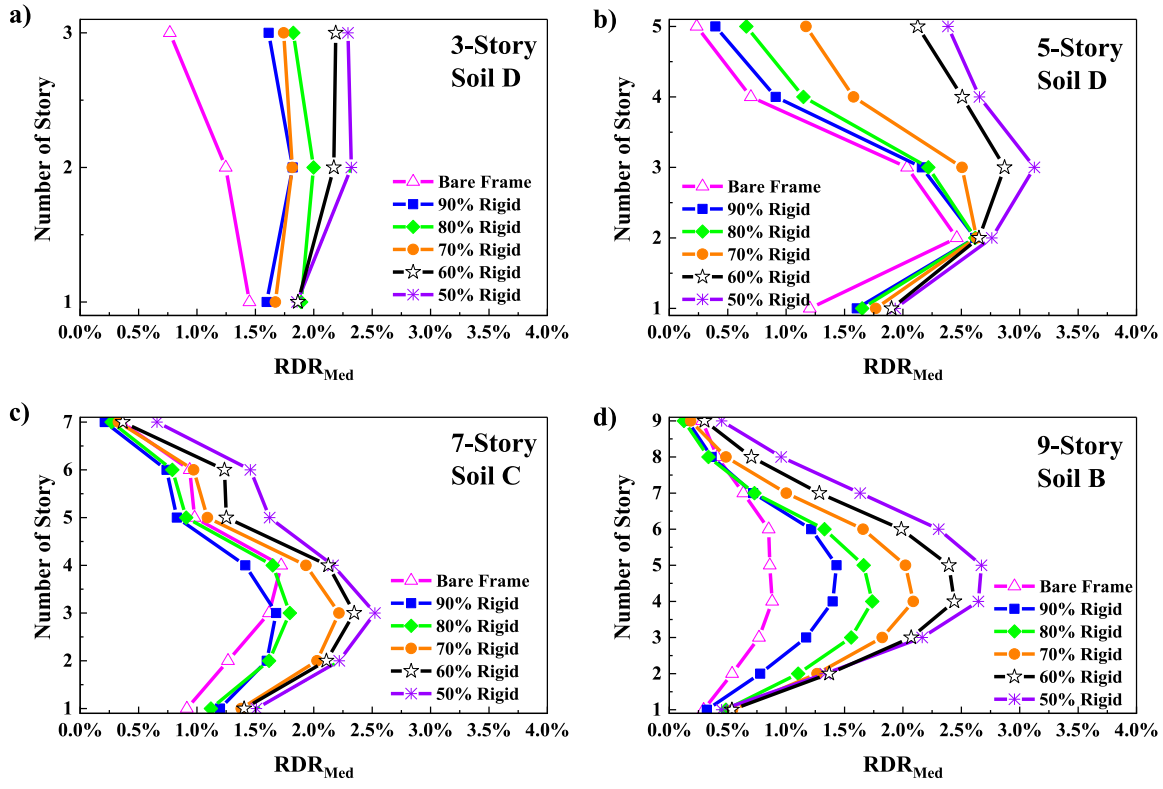

Fig. 11. RDR_{Med} of the steel MRFs considering different types of connection rigidities under the MCE level of NP records.

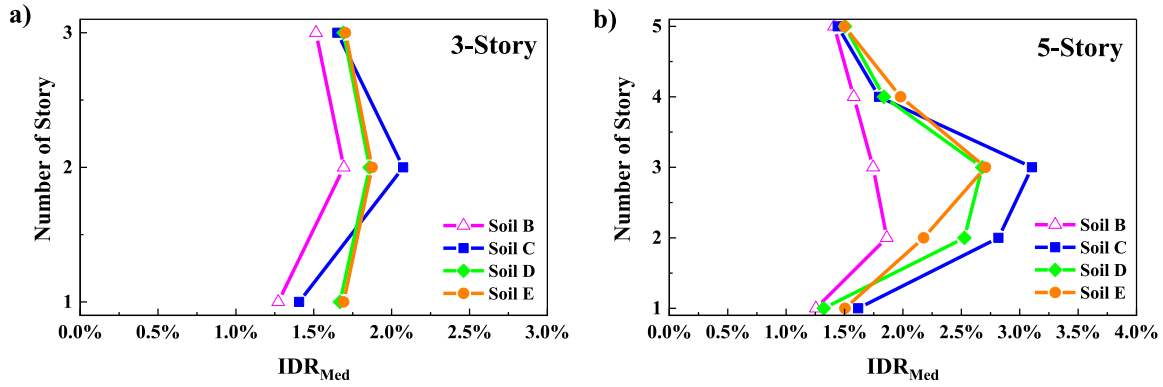

Fig. 12. IDR$_{Med}$ of the steel MRFs considering different soil types under DBE level of NP records.

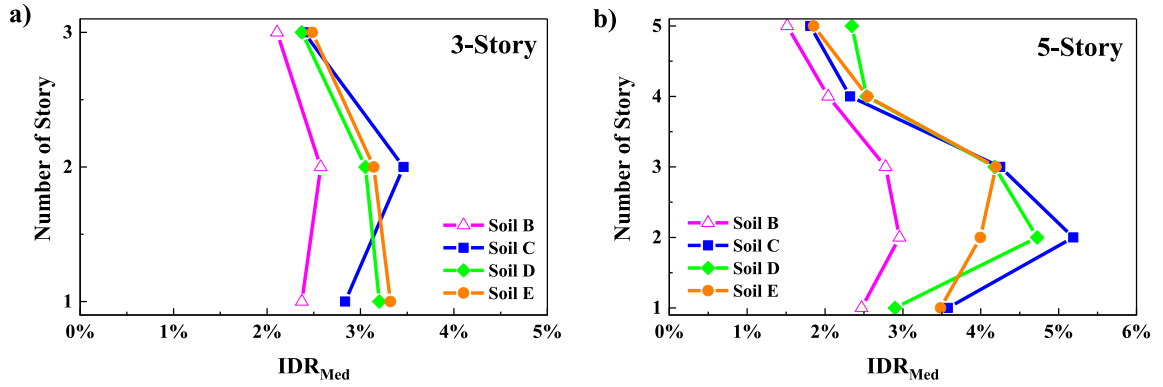

Fig. 13. IDR$_{Med}$ of the steel MRFs considering different soil types under MCE level of NP records.

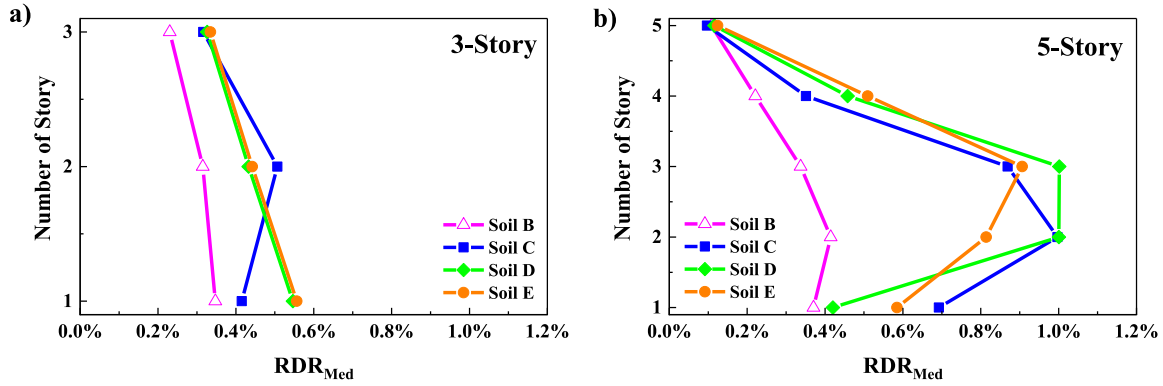

Fig. 14. RDR$_{Med}$ of the steel MRFs considering different soil types under DBE level of NP records.

distribution of RDR$_{Med}$ of the steel MRFs considering different types of IMWs assuming DBE and MCE levels of NP records. Similarly, it can be observed that implementing IMWs can more effectively reduce the distribution of RDR$_{Med}$ of the steel MRFs, and this reduction can control the RDR in allowable limitations. The results showed that assuming the IW-3 condition in the 5-Story MRF, the maximum values of RDR$_{Med}$ were reduced by 32.1 % and 21.77 % under DBE and MCE levels, respectively. As a result, using IMWs for retrofitting purposes can be useful for controlling the distribution of IDR and RDR in steel MRFs, which increases the performance of buildings. Finding of this research reveal that IMWs elevate ductility demands, consequently amplifying the IDR during more severe seismic events (e.g., MCE). Due to complex relationship of the IMWs and the behavior of structure in severe earthquakes, using IMWs to improve the seismic performance by reducing the IDR is not uniformly positive across all seismic intensity levels. Although the results of NP records are presented, similar trends were observed for other record subsets.

3.5. *Effects of IMWs and rigidity of connections*

Following the previous sections, there might be some problems to fulfill the performance of buildings due to defects in the connections and soil types, while using the IMWs can overcome this issue. In this section, the effects of using IMWs for retrofitting the steel MRFs with defects in the rigidity of connections are investigated. To clarify, two rigidity of 90 % and 50 % are selected that were retrofitted with the conditions of IW-1 and IW-3

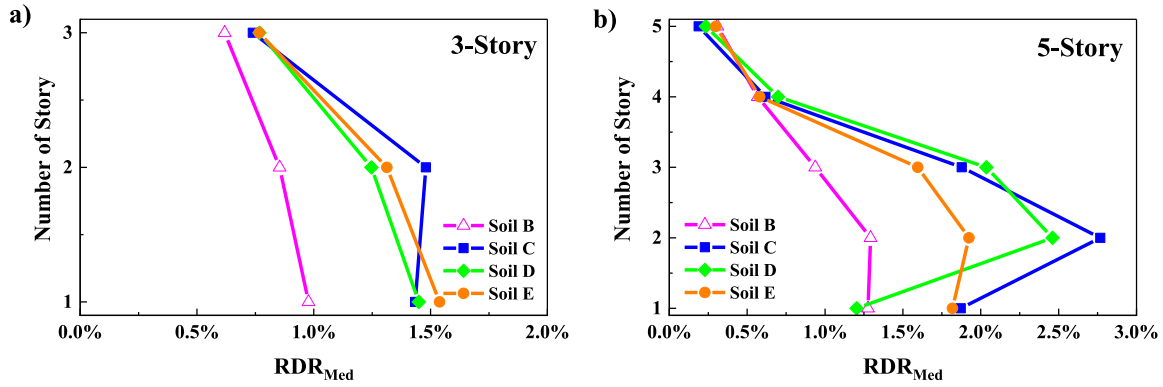

Fig. 15. RDR$_{Med}$ of the steel MRFs considering different soil types under MCE level of NP records.

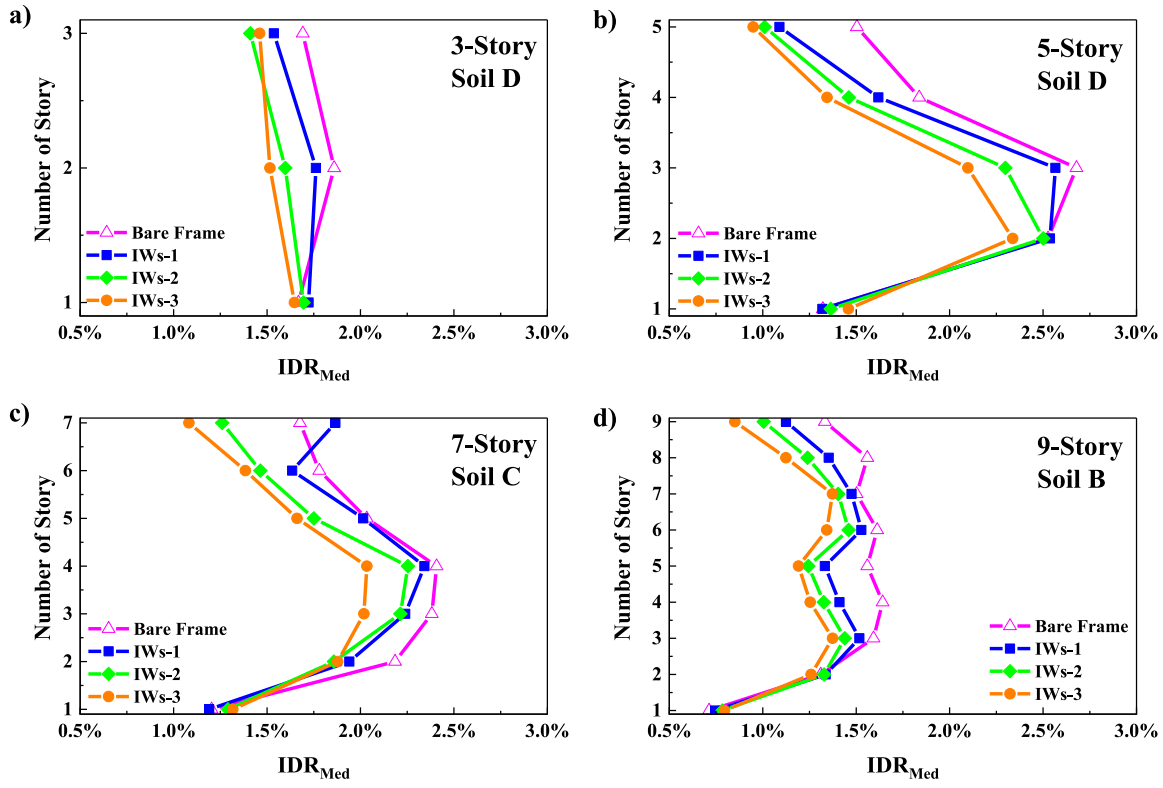

Fig. 16. IDR$_{Med}$ of the steel MRFs considering different types of IMWs assuming DBE level of NP records.

presented in Fig. 6. Figs. 20 and 21 illustrate the distribution of IDR$_{Med}$ of the steel MRFs considering different types of IMWs and connection rigidities under DBE and MCE levels of NP records, respectively. Results show that using conditions of IW-1 and IW-3 can reduce the values of IDR$_{Med}$, especially the maximum value IDR that has a considerable effect on performance level of structure. The 50 % rigidity in the 3-Story MRF experienced reductions of 16.47 % and 32.26 % for the conditions of IW-1 and IW-3 under the DBE level, respectively. In addition, for the 90 % rigidity, the IDR$_{Med}$ values were reduced by 9.1 % and 25.57 % for the conditions of IW-1 and IW-3 under the DBE level, respectively. Moreover, comparing the 90 % rigidity in the condition of IW-3 with the IDR$_{Med}$ for the bare frame of the 3-, 5-, 7-, and 9-Story MRFs showed that the proposed condition of IW-3 implemented in MRFs with 90 % rigidity reduced the IDR$_{Med}$ by 3.71 %, 19.55 %, 16.03 %, and 11.63 %, respectively.

Figs. 22 and 23 present the distribution of the RDR$_{Med}$ of steel MRFs considering different types of IMWs and of connection rigidities under DBE and MCE levels of NP records, respectively. Similar to IDR$_{Med}$, using conditions of IW-1 and IW-3 help to reduce the values of RDR$_{Med}$, which plays a key role in structure performance after the seismic event and retrofitting costs. The 50 % rigidity in the 7-Story MRF experienced reductions of 33.91 % and 42.69 % for the conditions of IW-1 and IW-3 under the DBE level, respectively. Moreover, for the 90 % rigidity, the RDR$_{Med}$ values were reduced by 22.38 % and 43.08 % for the conditions of IW-1 and IW-3 under the DBE level, respectively. In addition, comparing the 90 % rigidity in the condition of IW-3 with the RDR$_{Med}$ for the bare frame of the 3-, 5-, 7-, and 9-Story MRFs showed that the proposed condition of IW-3 implemented in MRFs with 90 % rigidity reduced the RDR$_{Med}$ by 47.80 %, 36.32 %, 44.08 %, and 55.09 %, respectively. Although the results of NP records are presented, similar trends were observed for other record subsets.

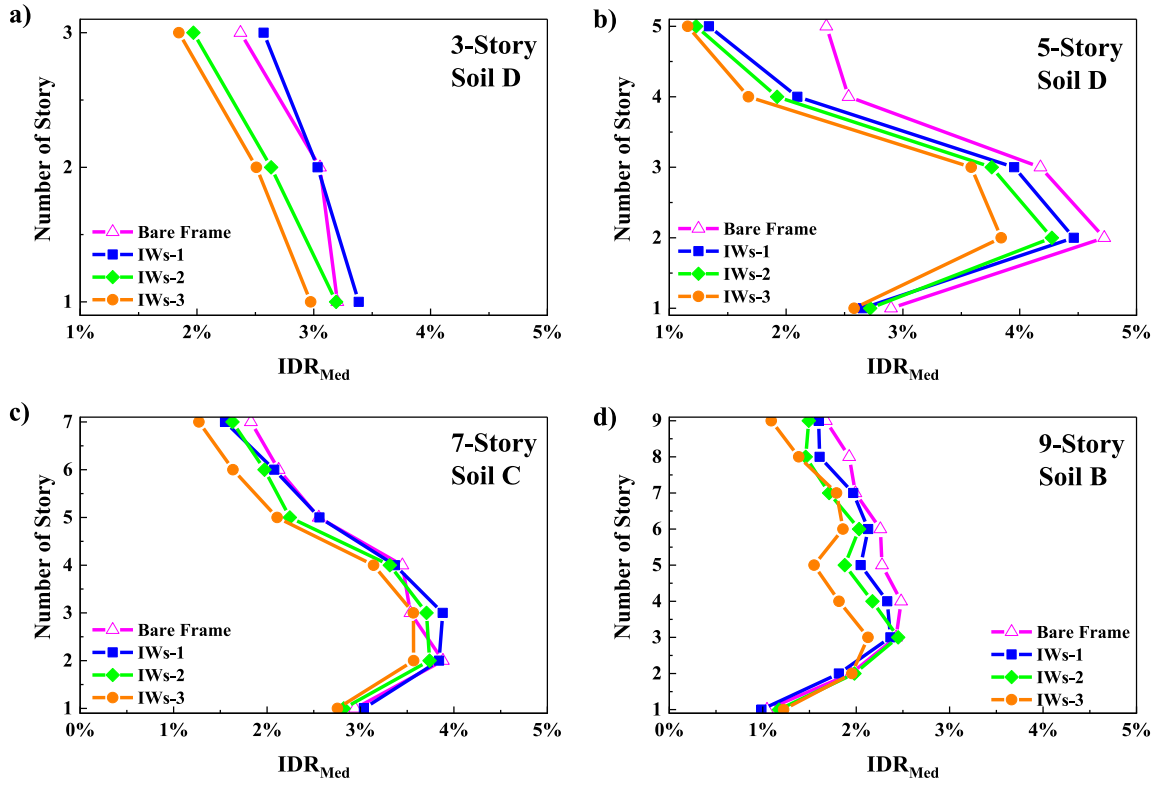

Fig. 17. IDR$_{Med}$ of the steel MRFs considering different types of IMWs assuming MCE level of NP records.

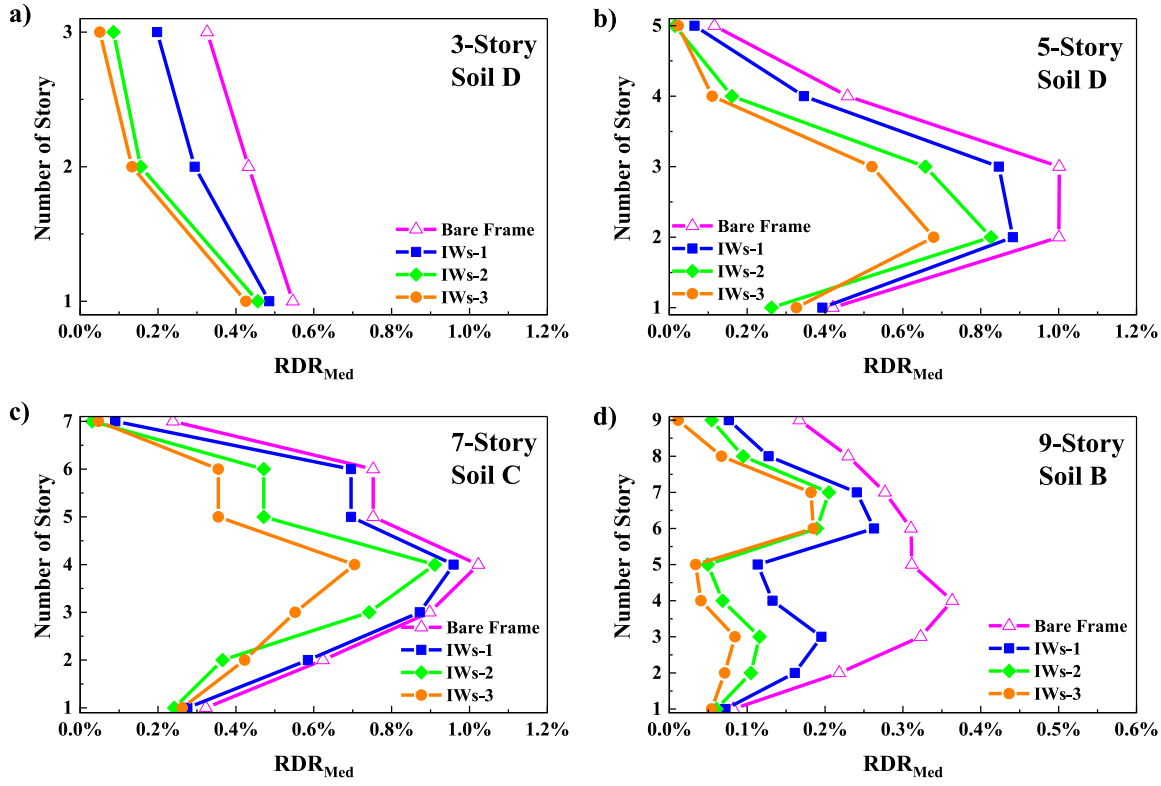

Fig. 18. RDR$_{Med}$ of the steel MRFs considering different types of IMWs assuming DBE level of NP records.

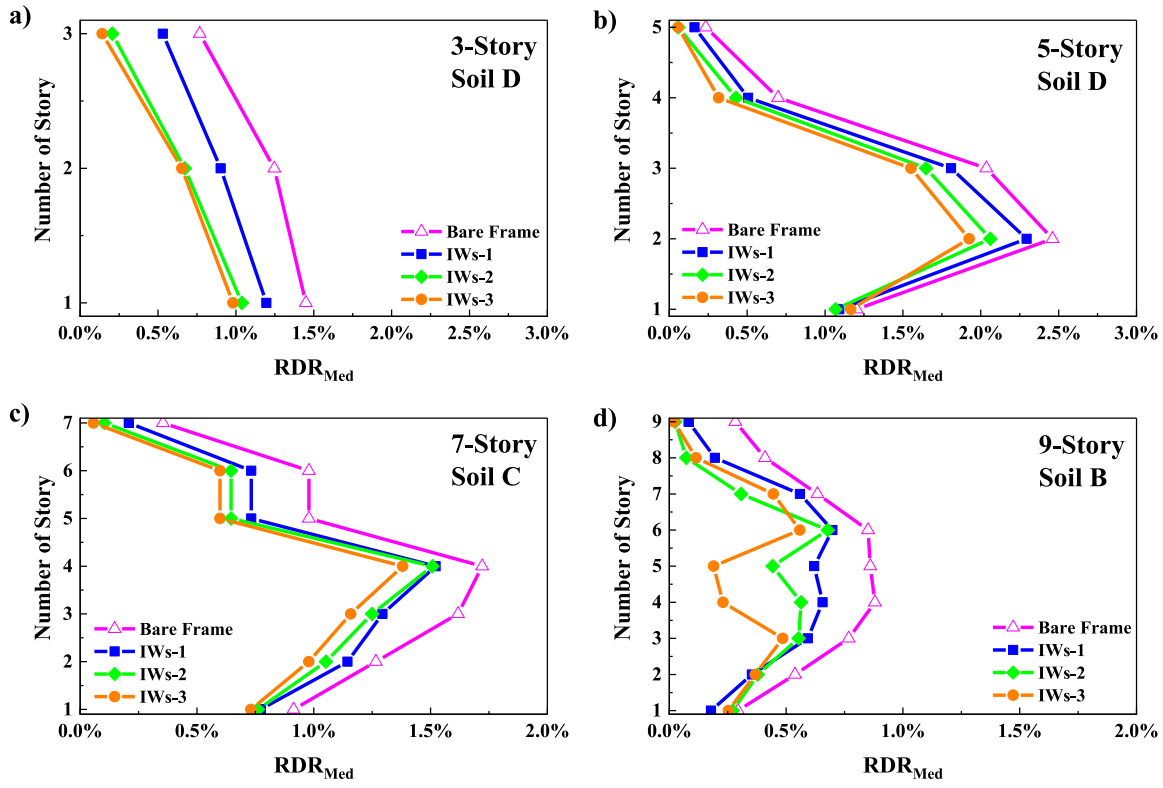

Fig. 19. RDR$_{Med}$ of the steel MRFs considering different types of IMWs assuming MCE level of NP records.

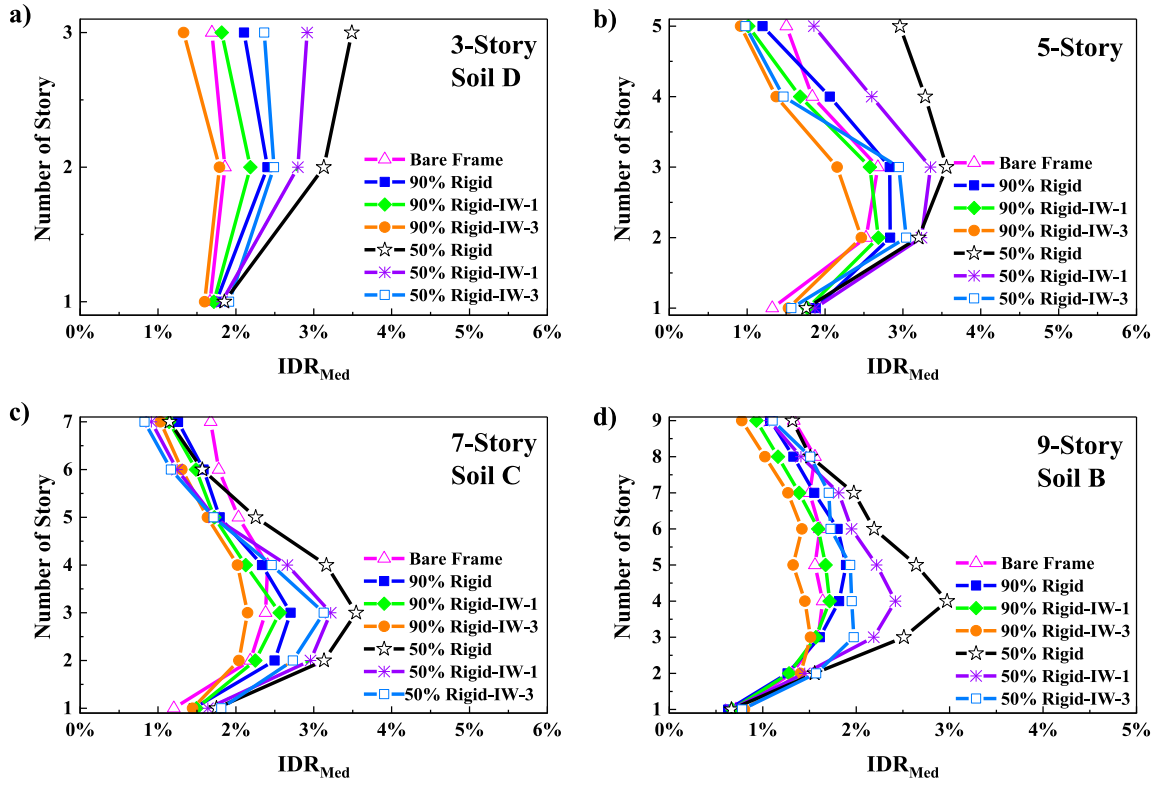

Fig. 20. IDR$_{Med}$ of the steel MRFs considering different types of IMWs and connection rigidities under the DBE level of NP records.

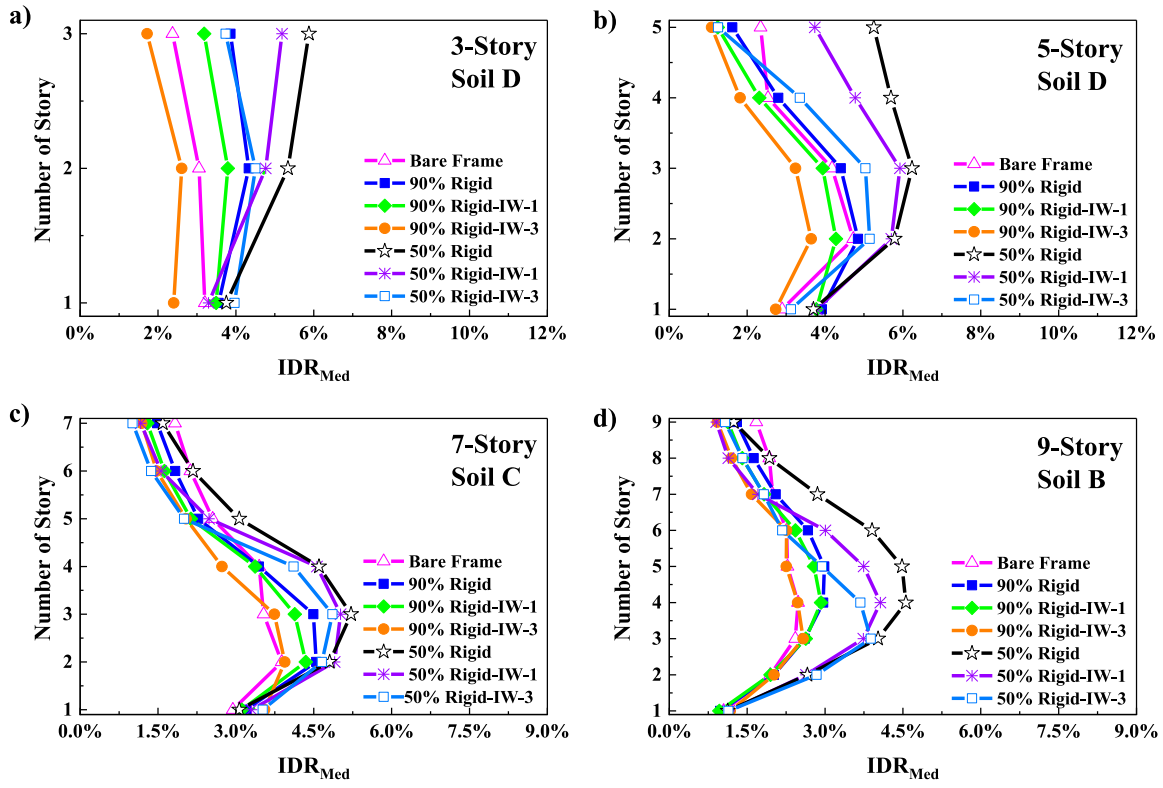

Fig. 21. IDR$_{Med}$ of the steel MRFs considering different types IMWs and of connection rigidities under MCE level of NP records.

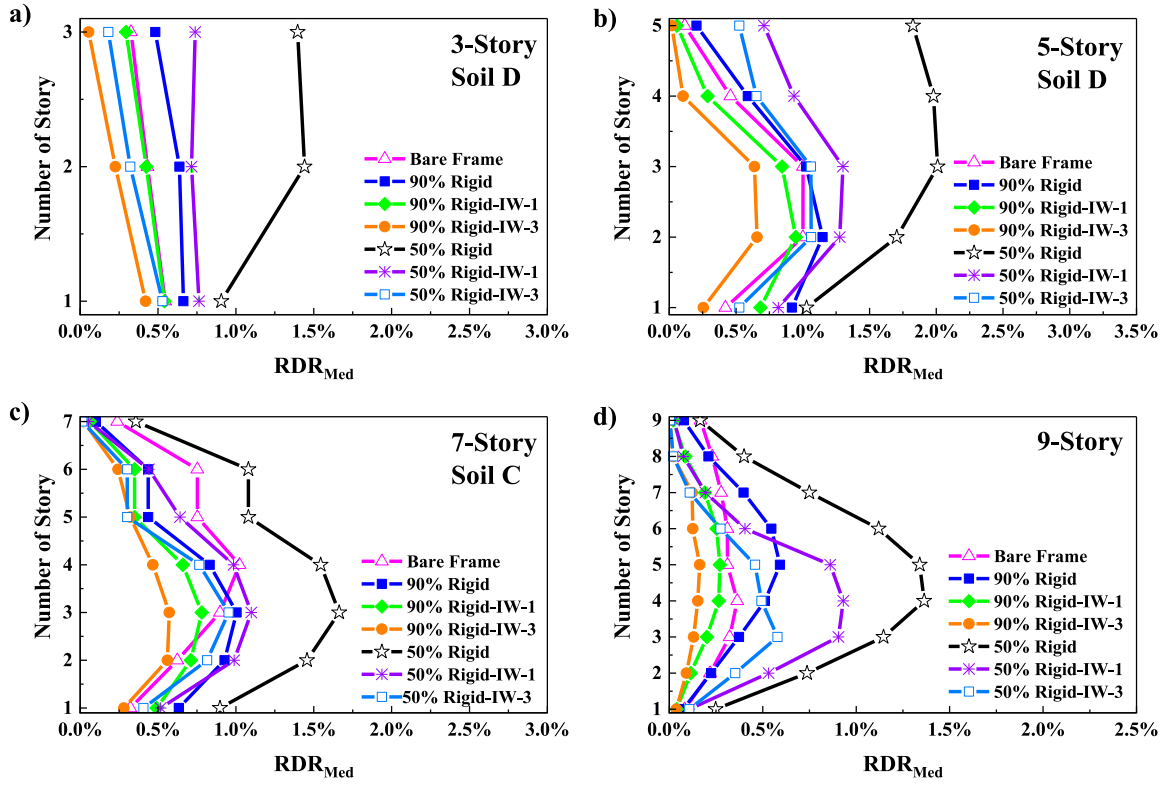

Fig. 22. RDR$_{Med}$ of the steel MRFs considering different types IMWs and of connection rigidities under DBE level of NP records.

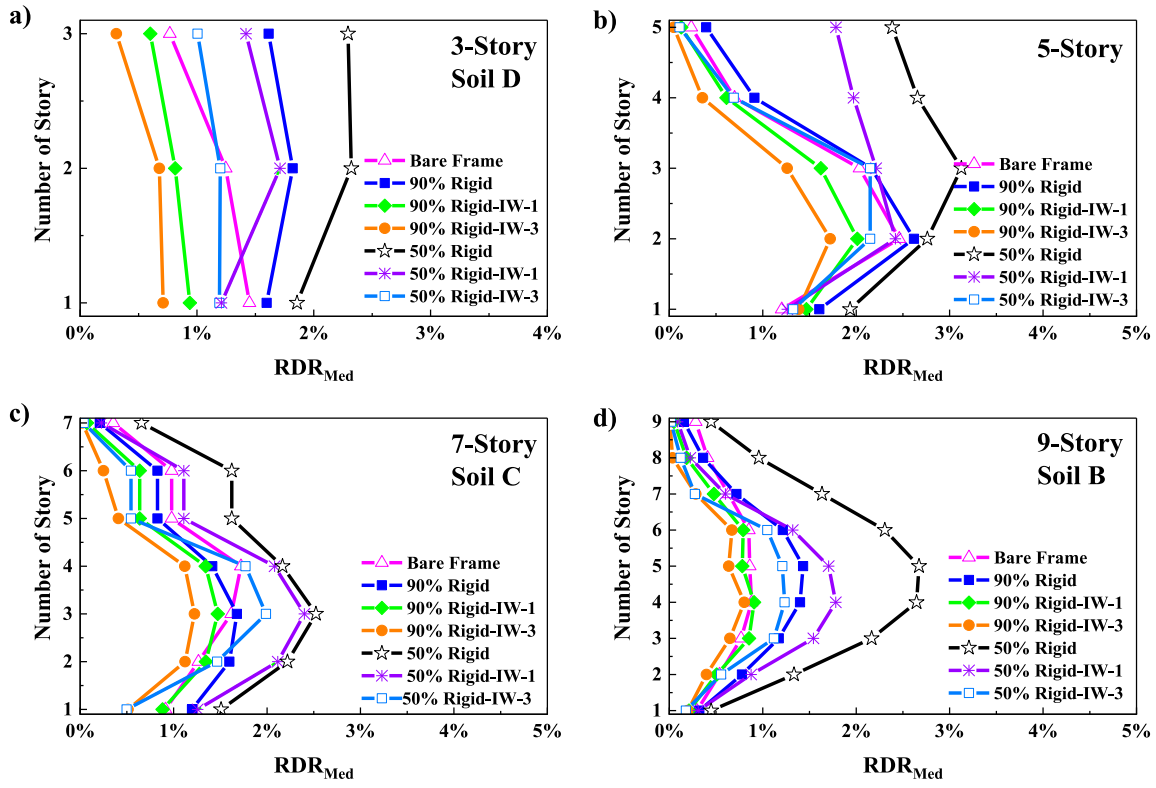

Fig. 23. RDR$_{Med}$ of the steel MRFs considering different types IMWs and of connection rigidities under MCE level of NP records.

3.6. *Box-plot distribution of IDR and RDR*

A box plot, also known as a box-and-whisker plot, is a commonly used graph for displaying the distribution of data since it provides information about the median, quartiles, and outliers of a set of numerical data. In the context of the interstory drift distribution along the floor levels of a structure, a Box-plot can be used to visualize the distribution of drift values for each floor level. The box of the plot represents the InterQuartile Range (IQR), which covers the middle 50 % of the data and is defined as the difference between the upper and lower quartile (i.e., 75th and 25th percentiles, respectively). The line inside the box is the median (i.e., 50th percentile) of the data. The whiskers extend from the box to the minimum and maximum values of the data, excluding outliers, which are plotted as individual points outside the whiskers. The Box-plot provides valuable information about the data distribution, including the skewness, symmetry, and the presence of outliers. By examining the box plot, engineers can gain insights into the performance of the structure and make decisions regarding its retrofit or improvement. For example, if the median is far from the center of the box, it suggests the data is skewed. If the box is symmetrical and the median is close to the center of the box, it indicates that the data is close to a normal distribution. Outliers outside the whiskers can indicate unusual behavior and warrant further investigation. Therefore, the box plot is a useful tool for visualizing and analyzing the distribution of IDR and RDR of the structure and provides engineers with valuable information to enhance performance and reduce seismic risk of the building.

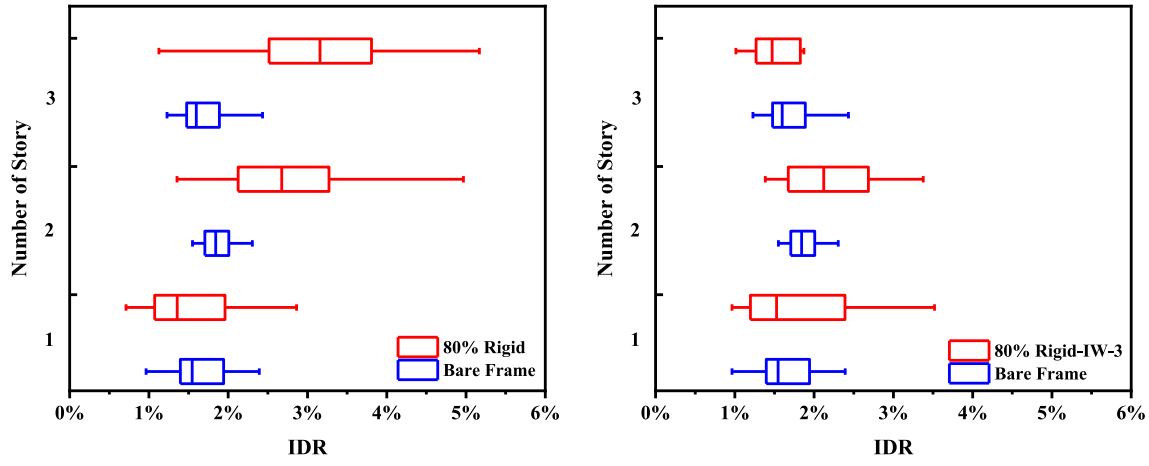

Fig. 24. Box-plot of the 3-Story MRFs founded on soil D to compare the IMW effects on the IDR under the DBE level of FF records.

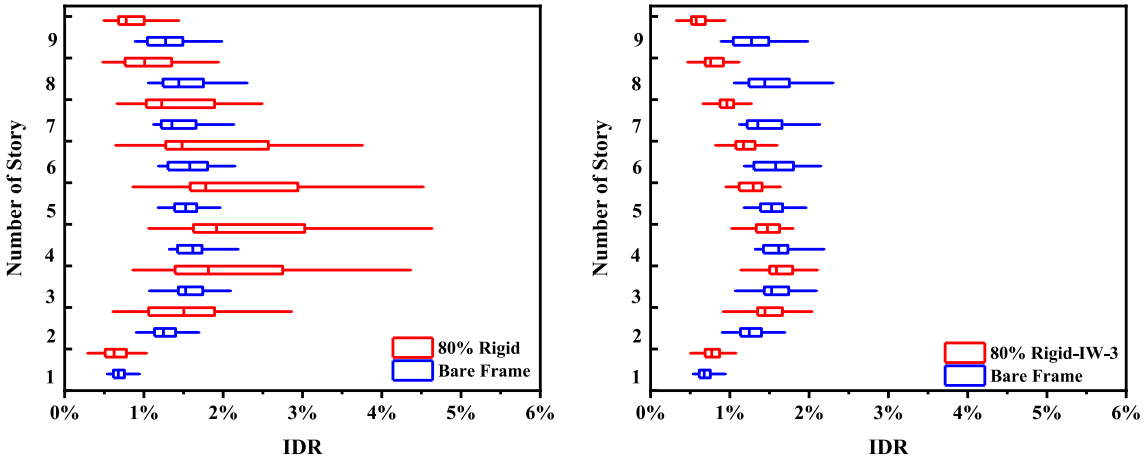

Fig. 25. Box-plot of the 9-Story MRFs founded on soil B to compare the IMW effects on the IDR under the DBE level of FF records.

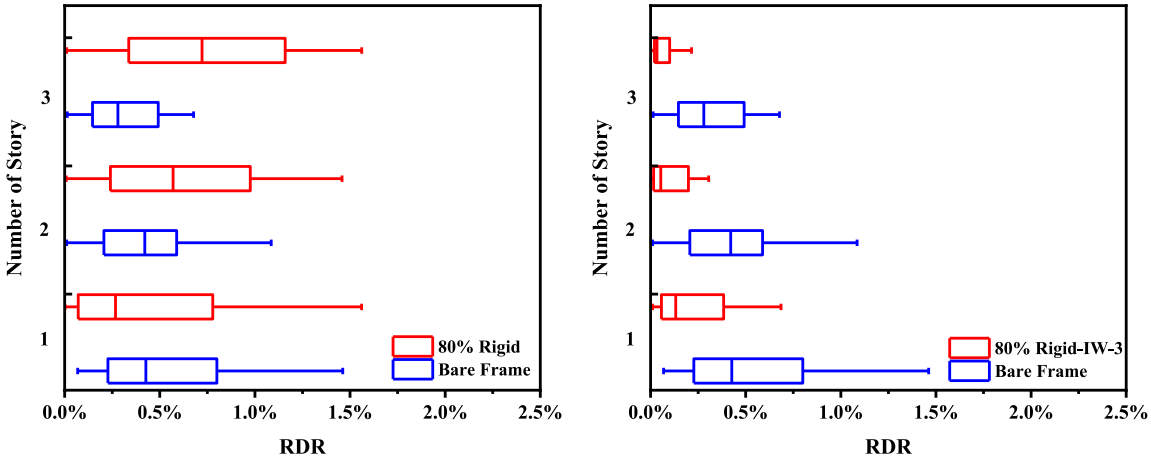

Fig. 26. Box-plot of the 3-Story MRFs founded on soil D to compare the IMW effects on the RDR under the DBE level of FF records.

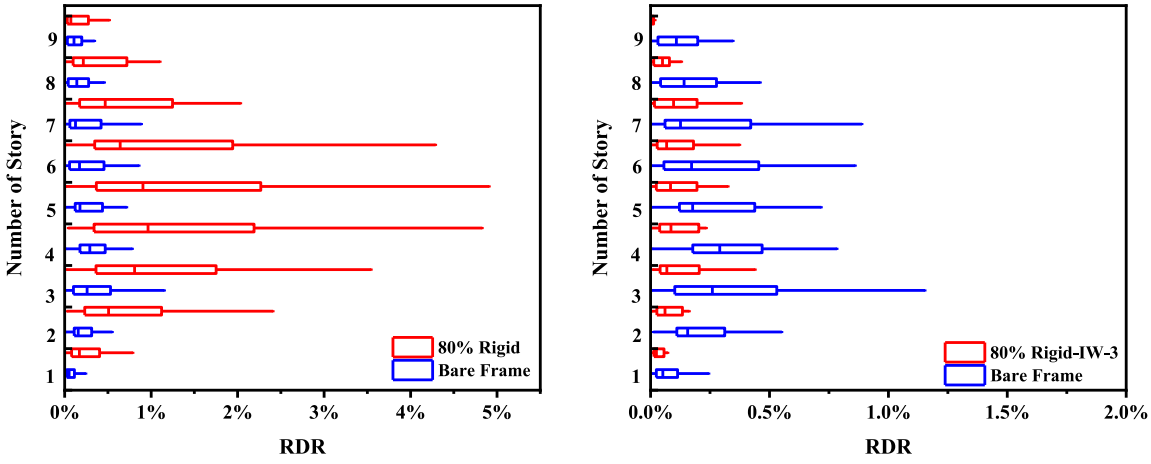

Fig. 27. Box-plot of the 9-Story MRFs founded on soil B to compare the IMW effects on the RDR under the DBE level of FF records.

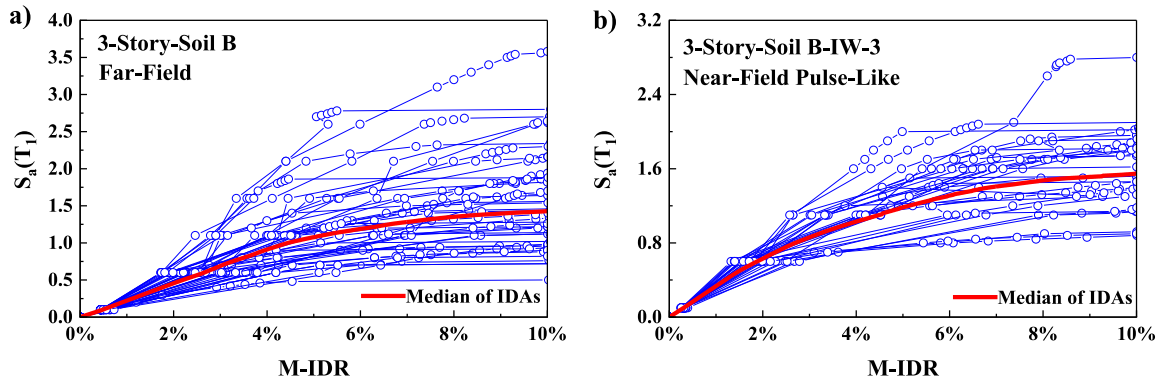

Fig. 28. IDAs of the 3-Story MRF founded on soil B, a) without IMWs under FF records, and, b) with IMWs under NP records.

Figs. 24 and 25 illustrate the box plot of the 3-Story MRFs founded on soil D and the 9-Story MRFs founded on soil B considering the IMW effects on the IDR under the DBE level of FF records, respectively. Figs. 26 and 27 illustrate the box plot of the 3-Story MRFs founded on soil D and the 9-Story MRFs founded on soil B considering the IMW effects on the RDR under the DBE level of FF records, respectively. In the context of the distribution of IDR along the floor levels of the structure, a lower box plot may indicate a smaller interquartile range, meaning that the data values are more tightly clustered around the median. This may suggest a lower level of variability in the IDR values for that floor level, compared to other floor levels with higher box plots. Distribution of IDR in box-plot can provide a large number of results, which can be useful for performance assessment. The median values of IDR and RDR of MRFs experienced a great increase by reducing their connections' rigidity to 80 %. In addition, the median values of IDR and RDR were considerably reduced by adding IW-3 to those MRFs having defects of 80 % rigidity in their connections. A magnificent reduction was observed for the mid-rise MRFs (i.e., 9-Story MRF) compared to the bare frames. To justify this performance, it can be note that the IMWs can resist lateral loads until the collapse condition of the infills, which can alter the lateral behavior of the MRFs by dissipating seismic energy and can provide a safeguard against damages of lateral loads.

3.7. IDA analysis

The assessment of a building's current condition following a significant earthquake is crucial. Seismic codes provide valuable tools to evaluate the seismic performance levels of structures. In this study, IDA was utilized to investigate the seismic performance levels of MRFs by determining their seismic limit states with increasing intensity measures. The spectral acceleration in the fundamental period of the MRF, $S_a(T_1)$, was chosen as the IM and the IDR was selected as the controlling demand parameter. The analysis has been done by hunt & fill algorithm to improve the computational time and the accuracy of capturing the collapse capacity. In addition, FEMA 356 [58] proposes three performance levels (i.e., Immediate Occupancy (IO), Life Safety (LS), and Collapse Prevention (CP)) for IDR values of 0.7 %, 2.5 %, and 5.0 % respectively, which can be utilized for limit-state assessment. Furthermore, the flat portion of IDA curve shows Total Collapse (TC) state [59]. An experimental test of RC structure conducted by Pujol and Fick [60] revealed that the IMWs experienced 4 mm cracks at the IDR of 0.25 %. The results indicated that IMWs were in collapse state at IDR of 1.75 %. To account for the collapse of the IMWs, an algorithm was implemented in Tcl programming using OpenSees [36] to simulate collapse of IMWs in floors, considering the collapse limit of 1.75 %. Using the developed Tcl code allows having the real condition of performance assessment of MRFs and IMWs having different collapse states. Fig. 28 presents the results of IDAs of the 3-Story MRF founded on soil B without IMWs under FF records, and with IMWs under NP records.

Considering the ability of models to have different collapse states of the structural elements, the IDAs were conducted for the assumed structures having a different configuration of placement of IMWs and rigidity of connections. Fig. 29(a)-(d) compares the median of IDAs of the 3-Story MRF implementing different arrangement of IMWs and the rigidity of connections under NP records. According to Fig. 29(a), adding IMWs can improve the collapse performance by 2.04 %, 5.74 %, and 12.48 %, for the conditions of IW-1, IW-2, and IW-3, respectively, compared to the bare frame. Whereas, Fig. 29(b) confirms that the rigidity of connections can considerably reduce $S_a(T_1)$ values in the collapse performance level by 2.86 %, 5.35 %, 9.31 %, 16.56 %, and 34.65 %, respectively, compared to the bare frame. Therefore, these two conditions can work vice versa in the performance level assessment of buildings. Regarding the proposed retrofitting strategy, the IMWs can be implemented in a way to enhance the seismic behavior. According to Fig. 29(c)–(d), considering the defects of rigidity in the steel MRF, implementing two conditions of IW-1 and IW-3 can significantly improve $S_a(T_1)$ values in all performance levels compared to Fig. 29(b), which shows only the rigidity effects. For example, in the collapse performance level of Fig. 29(d), implementing IMWs with the condition of IW-3 can improve the values of $S_a(T_1)$ by 15.04 %, 13.49 %, 11.07 %, 14.29 %, and 35.11 %, for rigidities of 90 %, 80 %, 70 %, 60 %, and 50 %, respectively. Fig. 30 compares the median of IDAs of the 5-Story MRF implementing different conditions of IMWs and the rigidity of connections under NP records. Similar trends were observed for assumed steel MRFs. For example, in the collapse performance level of Fig. 30(d), implementing IMWs with the condition of IW-3 can increase the $S_a(T_1)$ values of 5-Story MRF by 21.09 %, 27.93 %, 25.09 %, 23.52 %, and 23.46 %, for rigidities of 90 %, 80 %, 70 %, 60 %, and 50 %, respectively. Therefore, it is recommended to use the IMWs in the outer frames of the buildings as retrofitting elements to improve the defects of the construction process, while this can reduce the cost of retrofitting.

A seismic fragility curve represents the vulnerability of a structure or system to seismic events. It quantifies the probability of structural damage or failure at varying levels of ground motion intensity. This curve illustrates the relationship between the seismic intensity (i.e., $S_a(T_1)$), and the probability of exceeding (i.e., performance limit-states) [61]. Seismic fragility curves are commonly employed in seismic risk assessments, aiding in the development of risk mitigation strategies, the establishment of design guidelines, and the enhancement of structural resilience against seismic events. Some studies have been done to propose a novel non-parametric approach for seismic fragility assessment of buildings (e.g., see Ref. [62]) considering IDR and RDR demands [63]. They serve as valuable tools in evaluating the potential structural vulnerabilities and in making informed decisions related to seismic hazard mitigation and structural design improvements. For brevity, the seismic fragility curves have been included in the Graphical User Interface (GUI).

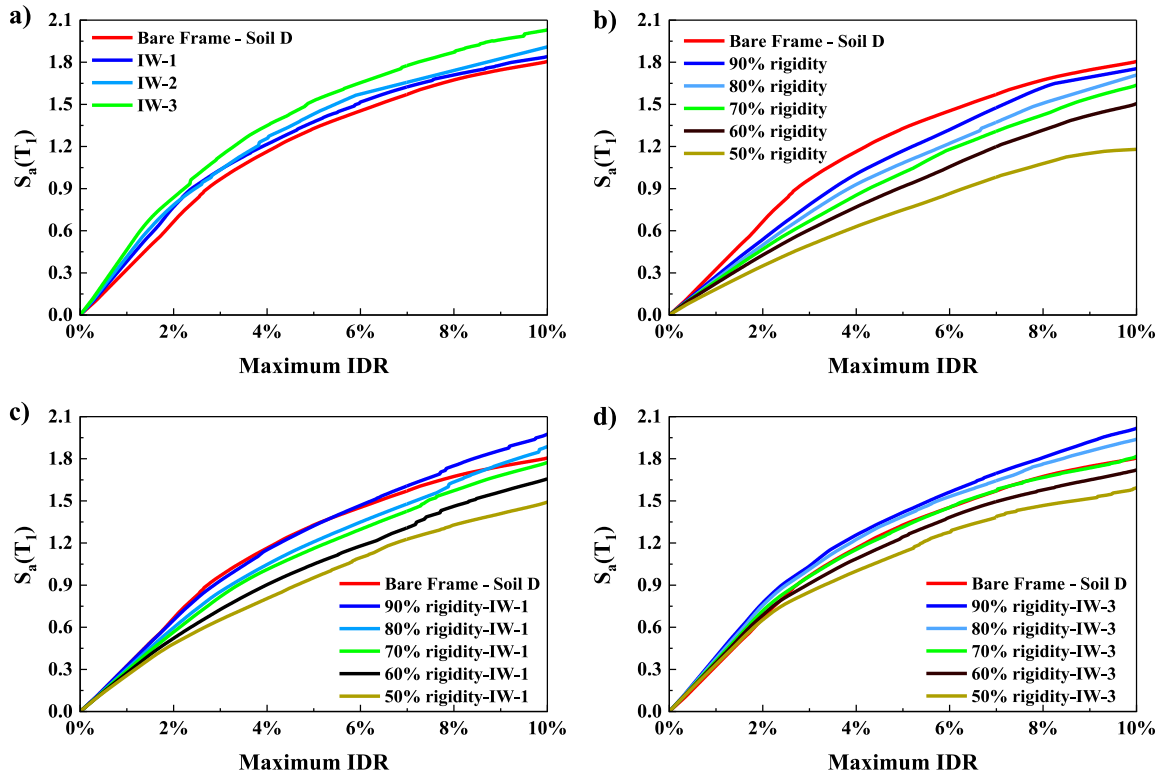

Fig. 29. Comparing the median of IDAs of the 3-Story MRF implementing different conditions of IMWs and rigidity of connections under NP records.

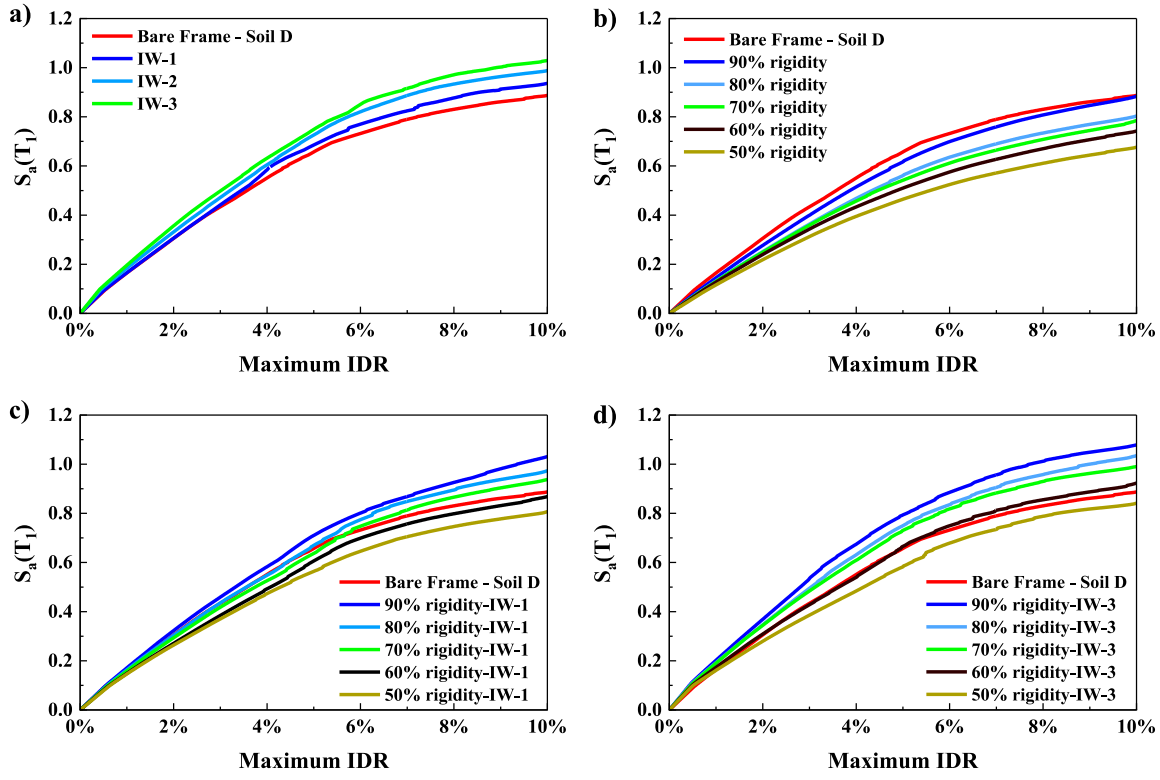

Fig. 30. Comparing the median of IDAs of the 5-Story MRF implementing different conditions of IMWs and rigidity of connections under NP records.

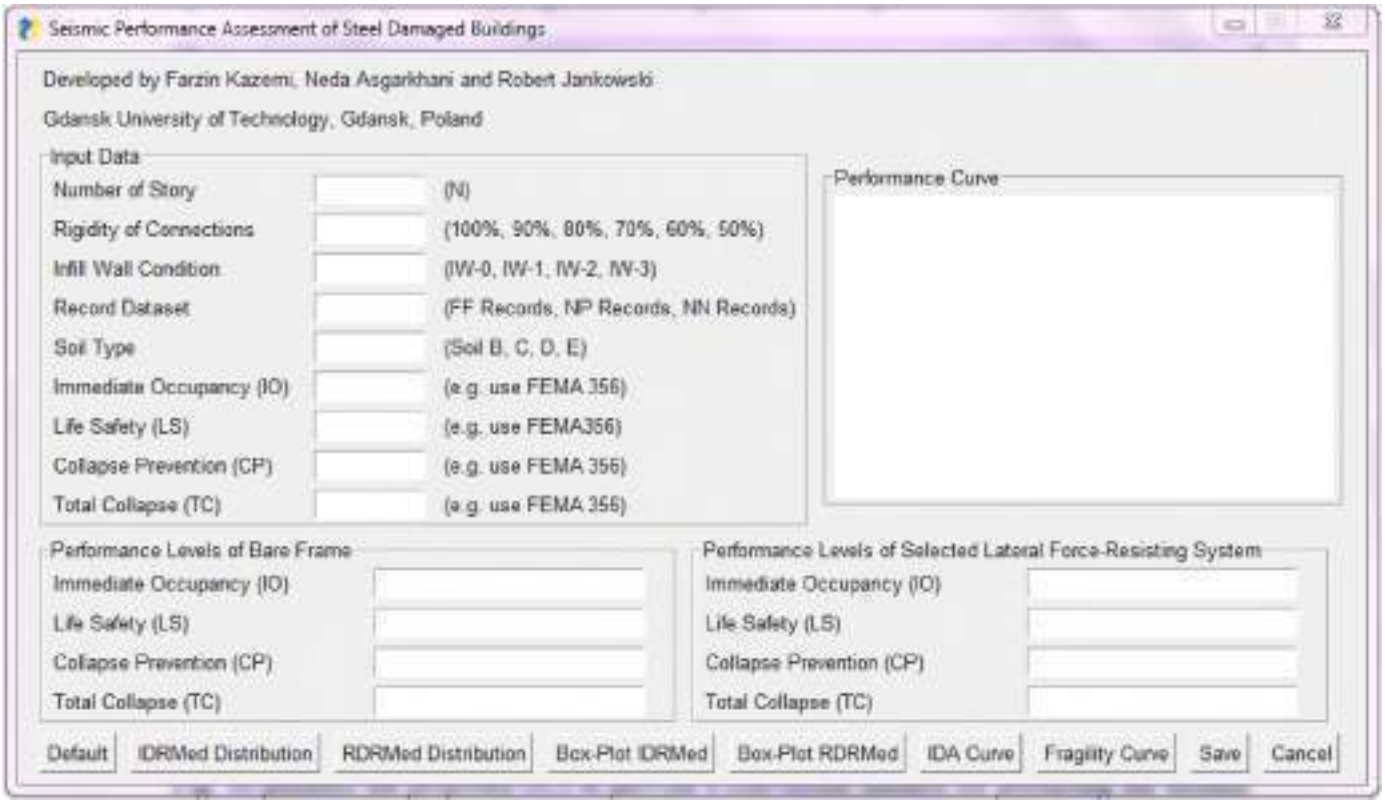

Fig. 31. Proposed GUI for predicting the seismic limit-state performance levels of steel MRFs with different conditions of rigidity, IMWs, soil types, and records (will be available at https://github.com/FarzinKazemi).

4. General use of results

This study investigates the possibility of using the IMWs for retrofitting buildings that have constructional defects, and the effects of defects on the performance levels. For this purpose, 384 steel MRFs were modelled and two types of analyses of NDAs (considering DBE and MCE levels) and IDAs were performed subjected to three record subsets. Since the results of the analysis include 3456 performance curves, it is not possible to plot all of them in this research. The results of this study can be used in practice through the development of a GUI. Fig. 31 presents the proposed GUI to provide a convenient method for predicting the seismic limit-state performance levels of steel MRFs with different levels of rigidity in connections, different soil types, different effects from implementing IMWs, and the effects of records.

The GUI has access to a large database that can be used for efficient predictions of different conditions of steel MRFs. Using this tool, it is possible to have the combination of constructional conditions (e.g., having different rigidity and IMWs); however, different performance curves such as IDR_{Med} and RDR_{Med} distribution, box-plot distribution of IDR_{Med} and RDR_{Med}, IDA curve, and fragility curve can be plotted to provide information for the users. In addition, the save button was considered to save the data points of the selected performance curve. With this tool, engineers and architects can evaluate the seismic performance of MRFs, taking into consideration the influence of various parameters, to ensure their safety and stability during earthquakes.

5. Conclusions

This research has investigated steel damaged buildings due to constructional defects on the rigidity of connections, and then, a retrofitting strategy for improving their performance levels has been proposed. To include all the possibilities of combinations of rigidity conditions, implementing IMWs, and effects of soil types, 384 steel MRFs were modelled having 3-, 5-, 7-, and 9-story floor levels and two types of analysis of NDAs (i.e., under DBE and MCE levels) and IDAs were performed subjected to three types of ground motion subsets. The comprehensive study included 3456 performance curves, therefore, to better use the results of this study, the GUI was introduced to have the ability for plotting different performance curves based on the NDAs and IDAs. The results of the study were discussed and the conclusions are as follows.

- Constructional defects are unpreventable and they may occur in the rigidities of connections of steel MRFs. This issue has a major effect on performance level of MRFs. According to the results, under DBE and MCE levels of NP records, assuming 50 % rigidity of connections for the 9-Story MRF founded on soil B can increase the maximum IDR_{Med} by 81.05 % and 83.71 %, respectively; however, the maximum RDR_{Med} increased by 2.12 and 3.03 times compared to MRF with the rigid connection.
- A fault or failure to meet a certain consideration of the soil type beneath the building can cause mistakes in calculating the value of the building's performance. The results confirm that assuming different soil types can affect the results of IDR_{Med} and RDR_{Med}, which can affect the performance of the building. For instance, considering soil C for the 5-Story MRF increased the maximum of IDR_{Med} by 66.76 % compared to soil B under the DBE level of NP records.
- As a method to improve the behavior of the building, it is suggested to use the sidewalls of the building in retrofitting models. Results confirm that implementing IMWs can considerably reduce the distributed values of the IDR_{Med} and RDR_{Med} in all steel MRFs under DBE and MCE levels. For example, assuming the IW-3 condition in the 5-Story MRF, the maximum values of IDR_{Med} were decreased by 12.72 % and 18.67 %, and the maximum values of RDR_{Med} were reduced by 32.1 % and 21.77 % under DBE and MCE levels, respectively.
- Implementing IMWs in a building, which has defects in their connections, can improve performance levels. For instance, implementing IW-1 and IW-3 conditions in the 3-Story MRF with 50 % rigidity can reduce the maximum value IDR by 16.47 % and 32.26 %

under the DBE level, respectively. In addition, implementing IW-3 in the MRFs with 90 % rigidity can decrease the IDR_{Med} of the 3-, 5-, 7-, and 9-Story MRFs by 3.71 %, 19.55 %, 16.03 %, and 11.63 %, respectively, and the RDR_{Med} by 47.80 %, 36.32 %, 44.08 %, and 55.09 %, respectively, under DBE level.

- Tcl programming code was developed to include different collapse states of the structural members and IMWs to accurately model the real condition of MRFs. Therefore, the results of IDAs take the collapsed IMWs into consideration for plotting the IDA curve. Compared to bare 3-Story MRF, it can be observe that adding IMWs can increase the collapse performance level by 2.04 %, 5.74 %, and 12.48 %, for the conditions of IW-1, IW-2, and IW-3, respectively. Whereas, the rigidity of connections can decrease $S_a(T_1)$ values in the collapse performance level by 2.86 %, 5.35 %, 9.31 %, 16.56 %, and 34.65 %, respectively.
- The proposed retrofitting strategy using IMWs can considerably improve $S_a(T_1)$ values in all performance levels. Implementing the IW-3 condition in the 3-Story MRF can improve the values of $S_a(T_1)$ by 15.04 %, 13.49 %, 11.07 %, 14.29 %, and 35.11 %, for rigidities of 90 %, 80 %, 70 %, 60 %, and 50 %, respectively, and the $S_a(T_1)$ values of 5-Story MRF increased by 21.09 %, 27.93 %, 25.09 %, 23.52 %, and 23.46 %, for rigidities of 90 %, 80 %, 70 %, 60 %, and 50 %, respectively.

CRediT authorship contribution statement

F. Kazemi: Conceptualization, Data curation, Formal analysis, Investigation, Methodology, Project administration, Resources, Software, Validation, Visualization, Writing – original draft, Writing – review & editing. **N. Asgarkhani:** Data curation, Formal analysis, Investigation, Software, Validation, Writing – original draft. **R. Jankowski:** Supervision, Writing – review & editing.

Declaration of competing interest

The authors declare that there is no conflict of interest, and all authors named in the manuscript are aware of the submission and have agreed for the paper in title of **Enhancing seismic performance of steel buildings having semi-rigid connection with infill masonry walls considering soil type effects** to be submitted for publication in *Soil Dynamics and Earthquake Engineering*.

Data availability

Data will be made available on request.

Acknowledgments

Numerical calculations were carried out at the Tri-City Academic Supercomputer and Network (*CI TASK*) in Gdańsk, Poland.

Appendix

The structural design sections of the SMRFs are illustrated in Figs. A-1 to A-4.

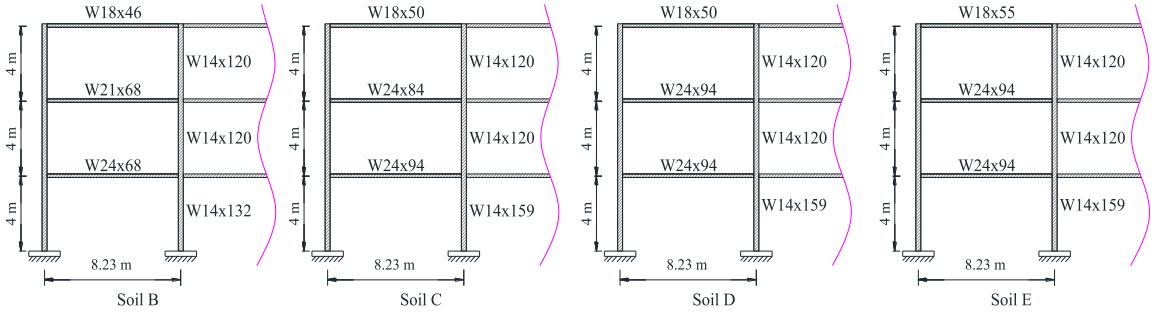

Fig. A-1. Design sections of the 3-Story SMRF assuming all soil types.

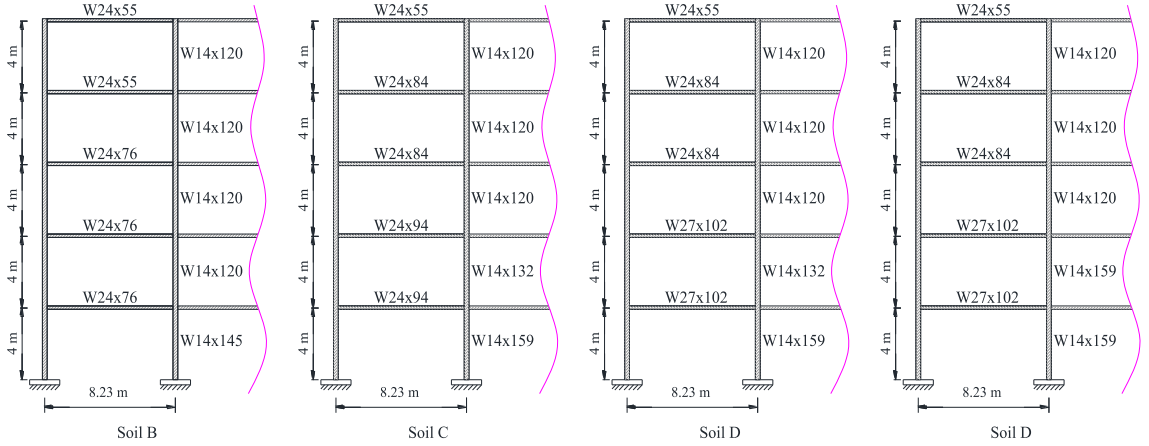

Fig. A-2. Design sections of the 5-Story SMRF assuming all soil types.

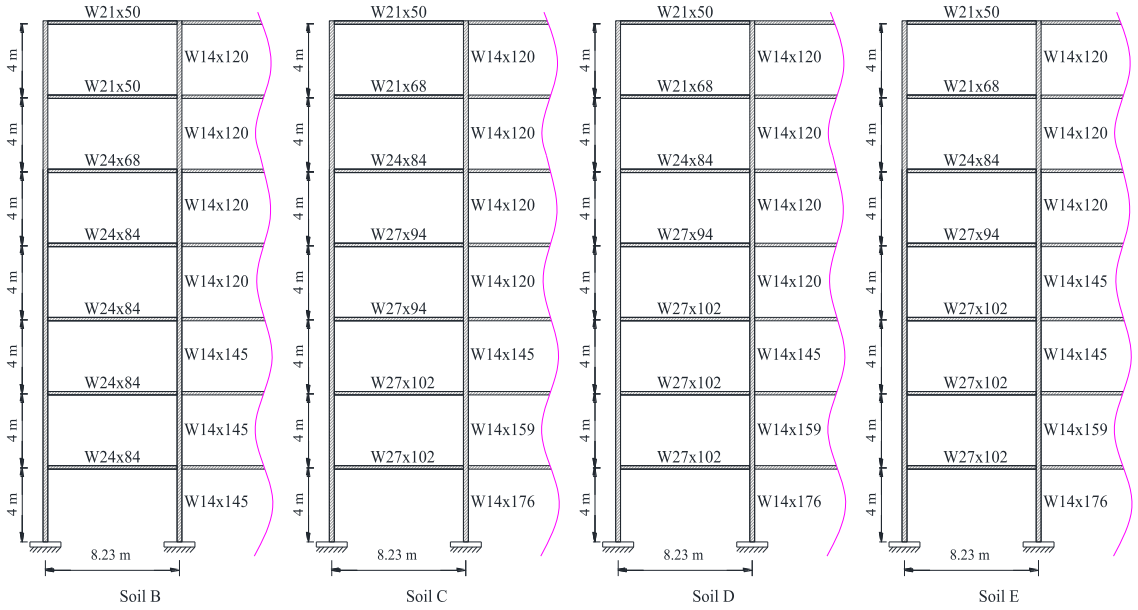

Fig. A-3. Design sections of the 7-Story SMRF assuming all soil types.

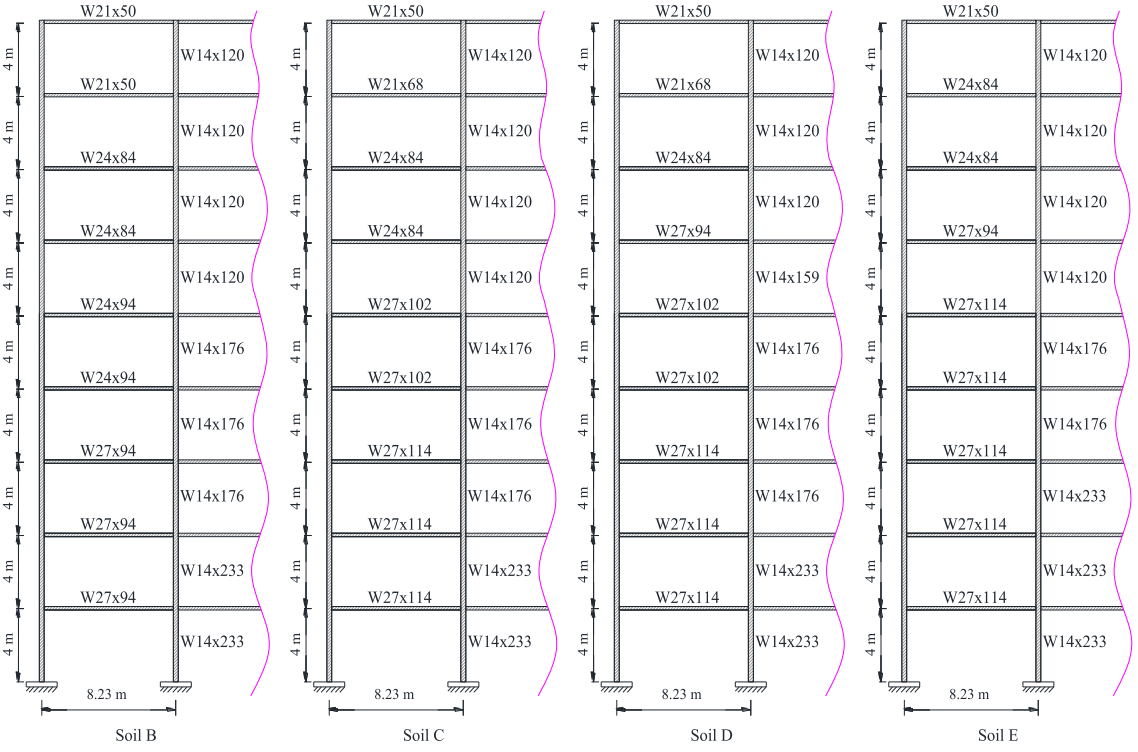

Fig. A-4. Design sections of the 9-Story SMRF assuming all soil types.

Table A-1
Details of bolts and endplates of BUEP connection used for MRFs founded on soil B.

SMRF	Story level	90 % Rigid		80 % Rigid		70 % Rigid		60 % Rigid		50 % Rigid	
		Bolt size (cm)	Endplate thickness (cm)	Bolt size (cm)	Endplate thickness (cm)	Bolt size (cm)	Endplate thickness (cm)	Bolt size (cm)	Endplate thickness (cm)	Bolt size (cm)	Endplate thickness (cm)
3-story	One	2.6	2.8	2.4	2.6	2.2	2.4	2	2	1.8	1.8
	Two	2.6	2.6	2.4	2.4	2.2	2.2	2	2	1.8	1.8
	Three	2.6	2.6	2.2	2.4	2.0	2.2	2	2	1.8	1.8
5-story	One	2.6	2.6	2.4	2.4	2.2	2.2	2	2.2	1.8	1.8
	Two	2.6	2.6	2.4	2.4	2.2	2.2	2	2	1.8	1.8
	Three	2.6	2.6	2.4	2.4	2.2	2.2	2	2	1.8	1.8
	Four	2.6	2.6	2.4	2.4	2.2	2.2	2	2	1.8	1.8
	Five	2.6	2.6	2.4	2.4	2.2	2.2	2	2	1.8	1.8
7-story	One	2.6	2.6	2.4	2.4	2.2	2.2	2	2	1.8	1.8
	Two	2.6	2.6	2.4	2.4	2.2	2.2	2	2	1.8	1.8
	Three	2.6	2.6	2.4	2.4	2.2	2.2	2	2	1.8	1.8
	Four	2.6	2.6	2.4	2.4	2.2	2.2	2	2	1.8	1.8
	Five	2.6	2.6	2.4	2.4	2.2	2	2	2	1.8	1.8
	Six	2.4	2.4	2.2	2.2	2.2	2	2	2	1.8	1.8
	Seven	2.4	2.4	2.2	2.2	2	2	2	2	1.8	1.8
9-story	One	3	3	2.8	2.8	2.6	2.6	2.4	2.4	2.2	2.2
	Two	3	3	2.8	2.8	2.6	2.6	2.4	2.4	2.2	2.2
	Three	3	3	2.8	2.8	2.6	2.6	2.4	2.4	2.2	2.2
	Four	3	3	2.8	2.8	2.6	2.6	2.4	2.2	2.2	2
	Five	3	3	2.8	2.8	2.6	2.6	2.4	2.2	2.2	2
	Six	2.8	2.6	2.6	2.4	2.4	2.2	2.2	2.2	2	2
	Seven	2.8	2.6	2.6	2.4	2.4	2.2	2.2	2.2	2	2
	Eight	2.6	2.4	2.4	2.2	2.2	2	2	2	1.8	1.8
	Nine	2.6	2.4	2.4	2.2	2.2	2	2	2	1.8	1.8

Table A-2
Details of bolts and endplates of BUEP connection used for MRFs founded on soil C.

SMRF	Story level	90 % Rigid		80 % Rigid		70 % Rigid		60 % Rigid		50 % Rigid	
		Bolt size (cm)	Endplate thickness (cm)	Bolt size (cm)	Endplate thickness (cm)	Bolt size (cm)	Endplate thickness (cm)	Bolt size (cm)	Endplate thickness (cm)	Bolt size (cm)	Endplate thickness (cm)
3-story	One	2.8	2.8	2.6	2.6	2.4	2.4	2.2	2	2	1.8
	Two	2.8	2.8	2.6	2.6	2.2	2.4	2.2	2	2	1.8
	Three	2.6	2.6	2.4	2.4	2.2	2.2	2	2	1.8	1.8
5-story	One	2.8	2.6	2.6	2.4	2.4	2.2	2.2	2.2	2	2
	Two	2.8	2.6	2.6	2.4	2.4	2.2	2.2	2	2	1.8
	Three	2.8	2.6	2.6	2.4	2.4	2.2	2.2	2	2	1.8
	Four	2.8	2.6	2.6	2.4	2.4	2.2	2.2	2	2	1.8
	Five	2.6	2.6	2.4	2.4	2.2	2.2	2	2	1.8	1.8
7-story	One	3.2	2.6	3	2.4	2.8	2.2	2.6	2.2	2.4	2
	Two	3.2	2.6	3	2.4	2.8	2.2	2.6	2.2	2.4	2
	Three	3.2	2.6	3	2.4	2.8	2.2	2.6	2.2	2.4	2
	Four	3.2	2.6	3	2.4	2.8	2.2	2.6	2.2	2.4	2
	Five	3	2.6	2.8	2.4	2.6	2.2	2.4	2.2	2.2	2
	Six	2.8	2.6	2.6	2.4	2.4	2.2	2.4	2	2.2	1.8
	Seven	2.8	2.6	2.6	2.4	2.4	2.2	2.2	2	2	1.8
9-story	One	3.2	3	3	2.8	2.8	2.6	2.6	2.4	2.4	2.2
	Two	3.2	3	3	2.8	2.8	2.6	2.6	2.4	2.4	2.2
	Three	3.2	3	3	2.8	2.8	2.6	2.6	2.4	2.4	2.2
	Four	3	3	2.8	2.8	2.6	2.6	2.4	2.2	2.2	2
	Five	3	3	2.8	2.8	2.6	2.6	2.4	2.2	2.2	2
	Six	2.8	2.6	2.6	2.4	2.4	2.2	2.2	2.2	2	2
	Seven	2.8	2.6	2.6	2.4	2.4	2.2	2.2	2.2	2	2
	Eight	2.6	2	2.4	2.2	2.2	2	2	2	1.8	1.8
	Nine	2.6	2	2.4	2.2	2.2	2	2	2	1.8	1.8

Table A-3
Details of bolts and endplates of BUEP connection used for MRFs founded on soil D.

SMRF	Story level	90 % Rigid		80 % Rigid		70 % Rigid		60 % Rigid		50 % Rigid	
		Bolt size (cm)	Endplate thickness (cm)	Bolt size (cm)	Endplate thickness (cm)	Bolt size (cm)	Endplate thickness (cm)	Bolt size (cm)	Endplate thickness (cm)	Bolt size (cm)	Endplate thickness (cm)
3-story	One	2.8	2.8	2.6	2.6	2.4	2.4	2.2	2	2	1.8
	Two	2.8	2.8	2.6	2.6	2.4	2.4	2.2	2	2	1.8
	Three	2.6	2.6	2.4	2.4	2.2	2.2	2	2	1.8	1.8
5-story	One	3	2.8	2.8	2.6	2.6	2.4	2.4	2.2	2.2	2
	Two	3	2.8	2.8	2.6	2.6	2.4	2.4	2.2	2.2	2
	Three	2.8	2.6	2.6	2.4	2.4	2.2	2.2	2	2	1.8
	Four	2.8	2.6	2.6	2.4	2.4	2.2	2.2	2	2	1.8
	Five	2.6	2.6	2.4	2.4	2.2	2.2	2	2	1.8	1.8
7-story	One	3.2	2.6	3	2.4	2.8	2.2	2.6	2.2	2.4	2
	Two	3.2	2.6	3	2.4	2.8	2.2	2.6	2.2	2.4	2
	Three	3.2	2.6	3	2.4	2.8	2.2	2.6	2.2	2.4	2
	Four	3.2	2.6	3	2.4	2.8	2.2	2.6	2.2	2.4	2
	Five	3	2.6	2.8	2.4	2.6	2.2	2.4	2.2	2.2	2
	Six	3	2.6	2.8	2.4	2.6	2.2	2.4	2	2.2	1.8
	Seven	2.8	2.4	2.6	2.2	2.4	2.2	2.2	2	2	1.8
9-story	One	3.2	3	3	2.8	2.8	2.6	2.6	2.4	2.4	2.2
	Two	3.2	3	3	2.8	2.8	2.6	2.6	2.4	2.4	2.2
	Three	3.2	3	3	2.8	2.8	2.6	2.6	2.4	2.4	2.2
	Four	3.2	3	3	2.8	2.8	2.6	2.6	2.4	2.4	2.2
	Five	3.2	3	3	2.8	2.8	2.6	2.6	2.4	2.4	2.2
	Six	3	2.8	2.8	2.6	2.6	2.4	2.4	2.2	2.2	2
	Seven	2.8	2.6	2.6	2.4	2.4	2.2	2.2	2.2	2	2
	Eight	2.6	2.4	2.4	2.2	2.2	2	2	2	1.8	1.8
	Nine	2.6	2.4	2.4	2.2	2.2	2	2	2	1.8	1.8

Table A-4
Details of bolts and endplates of BUEP connection used for MRFs founded on soil E.

SMRF	Story level	90 % Rigid		80 % Rigid		70 % Rigid		60 % Rigid		50 % Rigid	
		Bolt size (cm)	Endplate thickness (cm)	Bolt size (cm)	Endplate thickness (cm)	Bolt size (cm)	Endplate thickness (cm)	Bolt size (cm)	Endplate thickness (cm)	Bolt size (cm)	Endplate thickness (cm)
3-story	One	2.8	2.8	2.6	2.6	2.4	2.4	2.2	2	2	1.8
	Two	2.8	2.8	2.6	2.6	2.4	2.4	2.2	2	2	1.8
	Three	2.6	2.6	2.4	2.4	2.2	2.2	2	2	1.8	1.8
5-story	One	3	2.8	2.8	2.6	2.6	2.4	2.4	2.2	2.2	2
	Two	3	2.8	2.8	2.6	2.6	2.4	2.4	2.2	2.2	2
	Three	2.8	2.6	2.6	2.4	2.4	2.2	2.2	2	2	1.8
	Four	2.8	2.6	2.6	2.4	2.4	2.2	2.2	2	2	1.8
	Five	2.6	2.6	2.4	2.4	2.2	2.2	2	2	1.8	1.8
7-story	One	3.2	2.6	3	2.4	2.8	2.2	2.6	2.2	2.4	2
	Two	3.2	2.6	3	2.4	2.8	2.2	2.6	2.2	2.4	2
	Three	3.2	2.6	3	2.4	2.8	2.2	2.6	2.2	2.4	2
	Four	3.2	2.6	3	2.4	2.8	2.2	2.6	2.2	2.4	2
	Five	3.2	2.6	3	2.4	2.8	2.2	2.6	2.2	2.4	2
	Six	3	2.6	2.8	2.4	2.6	2.2	2.4	2	2.2	1.8
	Seven	3	2.6	2.8	2.4	2.6	2	2.4	2	2.2	1.8
9-story	One	3.4	3	3.2	2.8	3	2.6	2.8	2.4	2.6	2.2
	Two	3.4	3	3.2	2.8	3	2.6	2.8	2.4	2.6	2.2
	Three	3.4	3	3.2	2.8	3	2.6	2.8	2.4	2.6	2.2
	Four	3.4	3	3.2	2.8	3	2.6	2.8	2.4	2.6	2.2
	Five	3.4	3	3.2	2.8	3	2.6	2.8	2.4	2.6	2.2
	Six	3.4	2.8	2.8	2.6	2.6	2.4	2.4	2.2	2.2	2
	Seven	2.8	2.6	2.6	2.4	2.4	2.2	2.2	2.2	2	2
	Eight	2.8	2.6	2.6	2.4	2.4	2.2	2.2	2.2	2	2
	Nine	2.6	2.4	2.4	2.2	2.2	2	2	2	1.8	1.8

References

[1] Filiatrault A, Sullivan T. Performance-based seismic design of nonstructural building components: the next frontier of earthquake engineering. Earthq Eng Eng Vib 2014;13(1):17–46.

[2] Borsaikia AC, Dutta A, Deb SK. Evaluation of participation of masonry infill walls in the linear and nonlinear behaviour of RC buildings with open ground storey. J Build Eng 2021;44:103263.

[3] Wei Y, Zhai C, He Y, Jin W, Xie L. Modification methods for infilled RC frames with and without openings with slides and formed steel: experimental study. J Build Eng 2022;57:104936.

[4] Fiorino L, Bucciero B, Landolfo R. Evaluation of seismic dynamic behaviour of drywall partitions, façades and ceilings through shake table testing. Eng Struct 2019;180:103–23.
[5] Hou H, Yan X, Qu B, Du Z, Lu Y. Cyclic tests of steel tee energy absorbers for precast exterior wall panels in steel building frames. Eng Struct 2021;242:112561.
[6] Hu S, Wang W, Yu J. Experimental and design strategy of precast exterior wall panels with damage-control function for steel buildings. J Build Eng 2022;61:105205.
[7] Feizi MG, Mojtahedi A, Nourani V. Effect of semi-rigid connections in improvement of seismic performance of steel moment-resisting frames. Steel Compos Struct 2015;19(2):467–84.
[8] Kazemi F, Jankowski R. Enhancing seismic performance of rigid and semi-rigid connections equipped with SMA bolts incorporating nonlinear soil-structure interaction. Eng Struct 2023;274:114896.
[9] Zhang C, Wongso S, Wang H, Huang W, Shi F, Deng X, Liang Z. Seismic responses of infill walls with sliding joints and openings in semi-rigid steel frame. J Build Eng 2023;63:105457.
[10] Cheng X, Zou Z, Zhu Z, Huang X, Liang W, Mo Y, Chen W. Experimental study on a steel frame infill wall based on vertical partitioning technology. Eng Struct 2020;213:110565.
[11] Farahani EM, Yekrangnia M, Liberatore L. In-plane, out-of-plane, and in-plane/out-of-plane interactional behavior of masonry-infilled steel MRFs with different frame components flexibilities and considering openings. J Build Eng 2023;74:106899.
[12] Kazemi F, Asgarkhani N, Jankowski R. Probabilistic assessment of SMRFs with infill masonry walls incorporating nonlinear soil-structure interaction. Bull Earthq Eng 2023;21:503–34.
[13] Ozturkoglu O, Ucar T, Yesilce Y. Effect of masonry infill walls with openings on nonlinear response of reinforced concrete frames. Earthquakes and Structures 2017;12(3):333–47.
[14] Onat O, Correia AA, Lourenço PB, Koçak A. Assessment of the combined in-plane and out-of-plane behavior of brick infill walls within reinforced concrete frames under seismic loading. Earthq Eng Struct Dynam 2018;47(14):2821–39.
[15] Mazza F, Donnici A. In-plane and out-of-plane seismic damage of masonry infills in existing rc structures: the case study of De Gasperi-Battaglia school in Norcia. Bull Earthq Eng 2021;19(1):345–76.
[16] Furtado A, Rodrigues H, Arêde A. Modelling of masonry infill walls participation in the seismic behaviour of RC buildings using OpenSees. International Journal of Advanced Structural Engineering (IJASE) 2015;7(2):117–27.
[17] Furtado A, Rodrigues H, Arêde A. Calibration of a simplified macro-model for infilled frames with openings. Adv Struct Eng 2018;21(2):157–70.
[18] Furtado A, Rodrigues H, Arêde A. Effect of the infill panels in the floor response spectra of an 8-storey RC building. Structures 2021;34:2476–98.
[19] Asgarkhani N, Kazemi F, Jakubczyk-Gałczyńska A, Mohebi B, Jankowski R. Seismic response and performance prediction of steel buckling-restrained braced frames using machine-learning methods. Eng Appl Artif Intell 2024;128:107388.
[20] Yazdanpanah O, Mohebi B, Kazemi F, Mansouri I, Jankowski R. Development of fragility curves in adjacent steel moment-resisting frames considering pounding effects through improved wavelet-based refined damage-sensitive feature. Mech Syst Signal Process 2022;173:109038.
[21] Mohebi B, Sartipi M, Kazemi F. Enhancing seismic performance of buckling-restrained brace frames equipped with innovative bracing systems. Arch Civ Mech Eng 2023;23(4):1–21.
[22] Asgarkhani N, Kazemi F, Jankowski R. Machine learning-based prediction of residual drift and seismic risk assessment of steel moment-resisting frames considering soil-structure interaction. Comput Struct 2023;289:107181.
[23] Kazemi F, Asgarkhani N, Manguri A, Lasowicz N, Jankowski R. Introducing a computational method to retrofit damaged buildings under seismic mainshock-aftershock sequence. In: International conference on computational science; 2023. p. 180–7.
[24] Yekrangnia M, Mohammadi M. A new strut model for solid masonry infills in steel frames. Eng Struct 2017;135:222–35.
[25] Yekrangnia M, Asteris PG. Multi-strut macro-model for masonry infilled frames with openings. J Build Eng 2020;32:101683.
[26] Kazemi F, Mohebi B, Jankowski R. Predicting the seismic collapse capacity of adjacent SMRFs retrofitted with fluid viscous dampers in pounding condition. Mech Syst Signal Process 2021;161:107939.
[27] Kazemi F, Asgarkhani N, Manguri A, Jankowski R. Investigating an optimal computational strategy to retrofit buildings with implementing viscous dampers. In: International conference on computational science; 2022. p. 184–91.
[28] Asgarkhani N, Kazemi F, Jankowski R. Optimal retrofit strategy using viscous dampers between adjacent RC and SMRFs prone to earthquake-induced pounding. Arch Civ Mech Eng 2023;23:7.
[29] Yakhchalian M, Asgarkhani N, Yakhchalian M. Evaluation of deflection amplification factor for steel buckling restrained braced frames. J Build Eng 2020;30:101228.
[30] Asgarkhani N, Yakhchalian M, Mohebi B. Evaluation of approximate methods for estimating residual drift demands in BRBFs. Eng Struct 2020;224:110849.
[31] –>Kazemi F, Jankowski R. Seismic performance evaluation of steel buckling-restrained braced frames including SMA materials. J Constr Steel Res 2023;201:107750.
[32] USGS. US geological survey. http://usgs.gov; 2022. [Accessed 21 October 2022].
[33] ASCE 7-16. Minimum design loads and associated criteria for buildings and other structures. Reston, VA: American Society of Civil Engineers; 2017.
[34] AISC Committee. Specification for structural steel buildings (ANSI/AISC 360-10). Chicago-Illinois: American Institute of Steel Construction; 2016.
[35] AISC, A. AISC 341-16. Seismic provisions for structural steel buildings. Chicago, IL: American Institute of Steel Construction; 2016.
[36] McKenna F, Fenves GL, Filippou FC, Scott MH. Open system for earthquake engineering simulation (OpenSees). Pacific earthquake engineering research center. Berkeley: University of California; 2016.
[37] Kazemi F, Jankowski R. Machine learning-based prediction of seismic limit-state capacity of steel moment-resisting frames considering soil-structure interaction. Comput Struct 2023;274:106886.
[38] Kazemi F, Asgarkhani N, Jankowski R. Predicting seismic response of SMRFs founded on different soil types using machine learning techniques. Eng Struct; 2023, 114953.
[39] Manguri A, Saeed N, Kazemi F, Szczepanski M, Jankowski R. Optimum number of actuators to minimize the cross-sectional area of prestressable cable and truss structures. Structures 2023;47:2501–14.
[40] Kazemi F, Asgarkhani N, Jankowski R. Machine learning-based seismic fragility and seismic vulnerability assessment of reinforced concrete structures. Soil Dyn Earthq Eng 2023;166:107761.
[41] Buonopane SG, White RN. Pseudodynamic testing of masonry infilled reinforced concrete frame. J Struct Eng 1999;125(6):578–89.
[42] Tasnimi AA, Mohebkhah A. Investigation on the behavior of brick-infilled steel frames with openings, experimental and analytical approaches. Eng Struct 2011;33(3):968–80.
[43] Smyrou E, Blandon C, Antoniou S, Pinho R, Crisafulli F. Implementation and verification of a masonry panel model for nonlinear dynamic analysis of infilled RC frames. Bull Earthq Eng 2011;9(5):1519–34.
[44] El-Dakhakhni WW, Elgaaly M, Hamid AA. Three-strut model for concrete masonry-infilled steel frames. J Struct Eng 2003;129(2):177–85.
[45] Crisafulli FJ, Carr AJ. Proposed macro-model for the analysis of infilled frame structures. Bulletin of the New Zealand society for earthquake engineering 2007;40(2):69–77.
[46] Rodrigues H, Varum H, Costa A. Simplified macro-model for infill masonry panels. J Earthq Eng 2010;14(3):390–416.
[47] Kakaletsis DJ, Karayannis CG. Influence of masonry strength and openings on infilled R/C frames under cycling loading. J Earthq Eng 2008;12(2):197–221.
[48] Calado L, De Matteis G, Landolfo R. Experimental response of top and seat angle semi-rigid steel frame connections. Mater Struct 2000;33(8):499–510.
[49] AlHendi H, Mahmoud M, Celikag M. Numerical study of top-and seat-angle with double web-angle connection with high-strength steel. J Constr Steel Res 2020;174:106297.
[50] Rigi A, JavidSharifi B, Hadianfard MA, Yang TY. Study of the seismic behavior of rigid and semi-rigid steel moment-resisting frames. J Constr Steel Res 2021;186:106910.
[51] Sherbourne AN, Bahaari MR. Finite element prediction of end plate bolted connection behavior. I: parametric study. J Struct Eng 1997;123(2):157–64.
[52] Bahaari MR, Sherbourne AN. Finite element prediction of end plate bolted connection behavior. II: analytic formulation. J Struct Eng 1997;123(2):165–75.
[53] Gupta A, Krawinkler H. Seismic demands for performance evaluation of steel moment resisting frame structures (SAC Task 5.4. 3. John A. Blume Earthquake Engineering Center; 1999.
[54] Yakhchalian M, Yakhchalian M, Asgarkhani N. An advanced intensity measure for residual drift assessment of steel BRB frames. Bull Earthq Eng 2021;19(4):1931–55.
[55] Mohebi B, Kazemi F, Yousefi A. Seismic response analysis of knee-braced steel frames using Ni-Ti shape memory alloys (SMAs). In: Eurasian conference on OpenSees; 2022. p. 238–47.
[56] Mohebi B, Kazemi F, Yousefi A. Enhancing seismic performance of semi-rigid connection using shape memory alloy bolts considering nonlinear soil–structure interaction. In: Eurasian conference on OpenSees; 2022. p. 248–56.
[57] FEMA P695. Quantification of building seismic performance factors. Applied Technology Council, & United States, Federal Emergency Management Agency, US Department of Homeland Security; 2009.
[58] FEMA-356. Prestandard and commentary for the seismic rehabilitation of buildings. Washington, DC: Federal Emergency Management Agency; 2000.
[59] Cao XY, Feng DC, Li Y. Assessment of various seismic fragility analysis approaches for structures excited by non-stationary stochastic ground motions. Mech Syst Signal Process 2023;186:109838.
[60] Pujol S, Fick D. The test of a full-scale three-story RC structure with masonry infill walls. Eng Struct 2010;32(10):3112–21.
[61] Cao XY, Feng DC, Wu G. Seismic performance upgrade of RC frame buildings using precast bolt-connected steel-plate reinforced concrete frame-braces. Eng Struct 2019;195:382–99.
[62] Cao XY, Feng DC, Beer M. A KDE-based non-parametric cloud approach for efficient seismic fragility estimation of structures under non-stationary excitation. Mech Syst Signal Process 2023;205:110873.
[63] Cao XY, Xiong CZ, Feng DC, Wu G. Dynamic and probabilistic seismic performance assessment of precast prestressed reinforced concrete frames incorporating slab influence through three-dimensional spatial model. Bull Earthq Eng 2022;20(12):6705–39.

Paper VI:

Kazemi, F., & Jankowski, R. (2023). Seismic performance evaluation of steel buckling-restrained braced frames including SMA materials. Journal of Constructional Steel Research, 201, 107750. doi.org/10.1016/j.jcsr.2022.107750

Journal of Constructional Steel Research 201 (2023) 107750

Contents lists available at ScienceDirect

Journal of Constructional Steel Research

journal homepage: www.elsevier.com/locate/jcsr

Seismic performance evaluation of steel buckling-restrained braced frames including SMA materials

F. Kazemi *, R. Jankowski

Faculty of Civil and Environmental Engineering, Gdańsk University of Technology, ul. Narutowicza 11/12, 80-233 Gdansk, Poland

ARTICLE INFO

Keywords:
Buckling-restrained braced frame
Shape memory alloys
Viscous damper
Seismic retrofit
Seismic limit-state capacity
Residual drift

ABSTRACT

The permanent deformation of the building after seismic excitations can be determined by the Maximum Residual Interstory Drift Ratio (MR-IDR), which may be used for measuring the damage states. Low-post yield stiffness of the steel buckling-restrained braced frame (BRBF) makes this system vulnerable to large MR-IDR after a severe earthquake event. To overcome this issue, this paper investigates the seismic limit state performances of low- to mid-rise BRBFs with two- to eight-story levels (i.e. 2-Story, 4-Story, 6-Story, and 8-Story) adopting different lateral force-resisting systems using Viscous Dampers (VDs) and Shape Memory Alloys (SMAs). For this purpose, BRBFs improved with different implementation of SMAs and VDs, and Incremental Dynamic Analyses (IDAs) were performed based on Maximum Interstory Drift Ratio (M-IDR) and MR-IDR demands. Results showed that VDs and SMAs can decrease the values of maximum moment and rotation of hinges of structural members. Implementing both SMAs and VDs can significantly improve the seismic performance level and collapse failure probability of BRBFs more effectively than using one of the VDs or SMAs; then, it can be recommended to control the MR-IDR of BRBFs. To use the results, graphical user interface has been developed to estimate the improvements in the M-IDR and MR-IDR demands.

1. Introduction

Buckling-Restrained Braced Frame (BRBF) is known as structural lateral-resisting system that provide unbuckling condition during severe ground motion excitation. In this system, Buckling-Restrained Brace (BRB) is usually implemented as a concentrically braced frame and consists of two main components of a steel core inside of a hollow section filled by low-friction materials. This debonding material prohibits the steel core from buckling in compression conditions and allows for better and more symmetric cyclic performance [1]. The experimental studies confirmed that BRBs have shown stable and symmetric hysteretic behavior under cyclic load and lead to a large amount of energy dissipation during earthquakes [2–4]. Although this proper function made them high-performance structural elements, the main drawback of BRBs is the low post-yield stiffness of their cores that can cause large Maximum Residual Interstory Drift Ratio (MR-IDR) in story levels [5–7]. Therefore, some studies have been carried out to improve MR-IDR of BRBFs by using two different systems as dual-frame lateral resistance [8–11]. Fang et al. [12] investigated the seismic behavior of Steel Moment-Resisting Frames (SMRFs) and BRBF as a dual system. They mentioned that larger MR-IDR after the earthquake could cause that building might not be economically repairable. Therefore, it is better to find a solution to overcome MR-IDR in story levels. To find a solution, Sun et al. [13] investigated a double-stage yield BRB that uses a stopper mechanism to employ small and large core plates for enhancing the dissipated energy. Moreover, Barbagallo et al. [14] numerically investigated the double-stage yield BRB and formulated the design process based on the performance objectives of Eurocode 8 [15].

Using energy dissipation devices to enhance the performance level of BRBFs was studied by many researchers (e.g. [16,17]). They used this idea to prevent concentrated MR-IDR in story levels. Pollino et al. [18] proposed stiff rocking core as retrofitting strategy to redistribute lateral demands, and then, control the amount of MR-IDR. Some researchers used this strategy to prevent larger MR-IDR in story levels (see [19,20]). Although these innovative strategies can lead to a lower amount of MR-IDR, they can cause some restrictions from an architectural point of view. Viscous Dampers (VDs) are hydraulic devices that can dissipate the kinetic energy of seismic excitations. This ability of VDs makes them proper versatile devices that can be designed for building to control the damping of them and protect them from seismic events. Recently,

* Corresponding author.
E-mail address: farzin.kazemi@pg.edu.pl (F. Kazemi).

https://doi.org/10.1016/j.jcsr.2022.107750
Received 6 October 2022; Received in revised form 6 December 2022; Accepted 19 December 2022
Available online 3 January 2023
0143-974X/© 2022 Elsevier Ltd. All rights reserved.

Kazemi et al. [21] used VDs for enhancing the seismic performance levels of colliding structures. They find out that using linear VDs had more desirable results than nonlinear VDs. In addition, they implemented VDs in structures as diagonal braces [22] or between two adjacent structures [23–25]. Their results confirm that linear VDs can be used as retrofitting devices to improve the performance levels of buildings.

Shape Memory Alloys (SMAs) have the ability to return to their original shape before deformation by being heated. This ability makes them a unique material that can be used as structural elements. Although several dozen types of SMAs with characteristics of superelasticity have been used in industry, Nickel-Titanium (Ni-Ti) alloys are the best SMAs with a high shape recovery performance that can be suitable for structures. Fig. 1 illustrates the superelastic behavior of SMA. The superelasticity effects of Ni-Ti alloys are the result of thermoelastic transformation from the austenitic phase (high temperature) to the martensitic phase (low temperature) [26,27]. Eatherton et al. [28] investigated restoring mechanism of a self-centering BRB to implement it in the building, and find out that this system can limit the amount of MR-IDR. Ke et al. [29] proposed a performance based methodology to enhance the seismic performance of SMRFs with SMAs. The researchers investigated the various types of SMAs for the beam to column connections, columns, and braces [30–32] that can be used in SMRFs, and performed experimental analysis to justify using SMAs [33,34].

Since the ability of VDs and SMAs were investigated and both energy dissipation devices showed a good improvements in the seismic behavior of buildings, there is a need to provide a user friendly tool to estimate the improvements for purpose of reducing the time of complex modeling and analysis. In this research, a comprehensive study was performed to improve the seismic limit-state capacity of BRBFs using energy dissipation devices such as SMAs and linear VDs. The main purpose of this research is to minimize MR-IDR of story levels with implementing different kind of energy dissipation devices, and propose prediction factors to estimate seismic performance level of the improved lateral-resisting system. Moreover, to easily access the results of this study, a user friendly tool was developed that can be widely used by engineers for design or retrofitting purposes.

2. Modeling of BRBFs

In this research, buildings with two, four, six, and eight story levels (2-Story, 4-Story, 6-Story, and 8-Story) with BRBFs were designed according to the regular plan presented in Fig. 2, and the site and seismic parameters used by Asgarkhani et al. [5], Kazemi et al. [23], and Mohebi et al. [35]. To model three-dimensional buildings, ETABS 2016 software was used assuming the seismic codes of ASCE 7–16 [36], ANSI/AISC 360–16 [37], and ANSI/AISC 341–16 [38], and design coefficients of $R = 8$, $C_d = 5$, and $\Omega_0 = 2.5$. Fig. 3 presents the 4-Story building designed with ETABS 2016 software. For all the structural elements, the elastic modulus of 200 GPa was considered. In addition, for beams and columns, the yield stress of 379.2 MPa, and for the BRB core, the yield stress

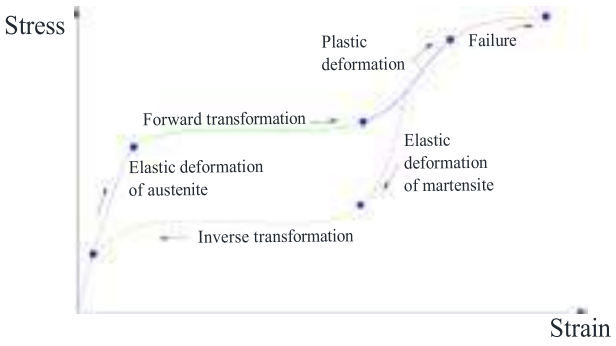

Fig. 1. Stress-strain diagram of superelastic behavior of SMA.

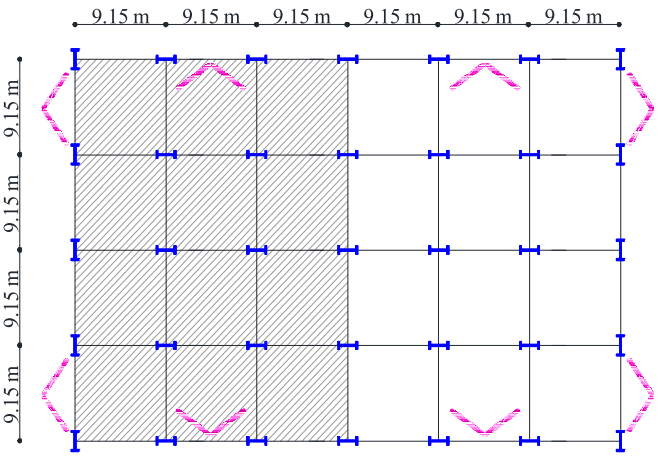

Fig. 2. Considered plan for modeling of BRBFs.

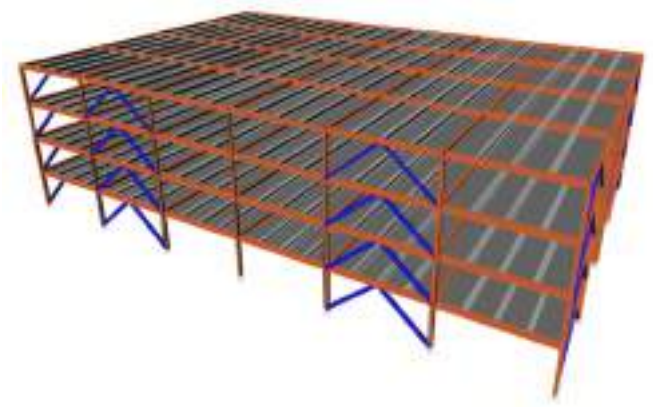

Fig. 3. 4-Story three-dimensional building modeled in ETABS 2016 software.

of 289.6 MPa was assumed [5]. It was assumed the length of BRB cores is equal to 0.7 times of the work point-to-work point brace length. To design the BRBFs, the procedures introduced in Section F-4 of ANSI/AISC 341–16 [38] and the performance-based design approach were used considering the target drift of 1.75%, which leads to the structural ductility from 3.94 to 6.25 [39]. It should be noted that beam-to-column connections as well as brace connections were assumed as pinned ones, and the yielding mechanism was limited to the braces; then, the maximum force demand on beams and columns were determined based on the expected yield of BRBs in tension and compression [5–7]. The BRBFs were assumed as reference structures to compare the performance of other systems combined with VDs and SMAs.

Due to the regularity of the plan, the two-dimensional model was created in Opensees [40] using Y-direction BRBF, and the gravity columns were modeled as leaning columns (which is conservative yet reliable for estimating the MR-IDR), as used by some researchers (for more detail see [5–7]). The leaning column, which consists of rigid elastic beam-column elements, was modeled for considering the P-Delta effects of gravity columns that can play a crucial role in predicting seismic performances [41–45].

Fig. 4 presents a schematic illustration of the modeling approach of BRBF in Opensees [40]. *Steel02* material with parameters of $R_0 = 20.0$, $CR_1 = 0.925$, and $CR_2 = 0.15$ were selected to obtain the kinematic hardening, and the *Hardening* material was assumed for isotropic hardening. Both materials were combined with *Parallel* material in Opensees [40] software. In addition, the stress-strain hardening ratio of 0.003 was selected for BRB cores to model the tension-compression behavior of the BRB. Fig. 5 presents the hysteretic behavior of the BRB used for the first

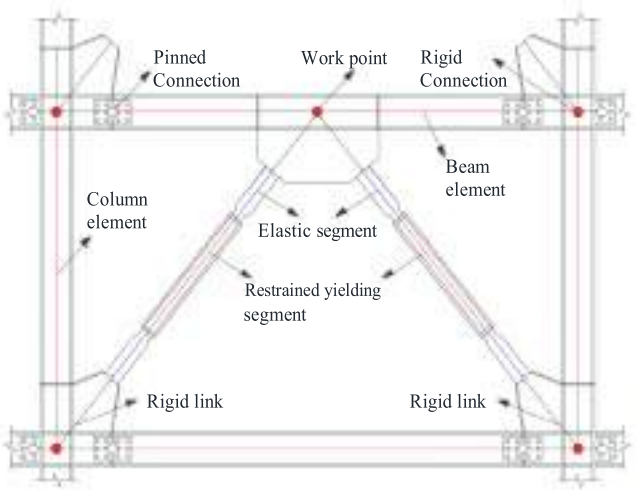

Fig. 4. Schematic illustration of the modeling approach of BRBF in Opensees [40].

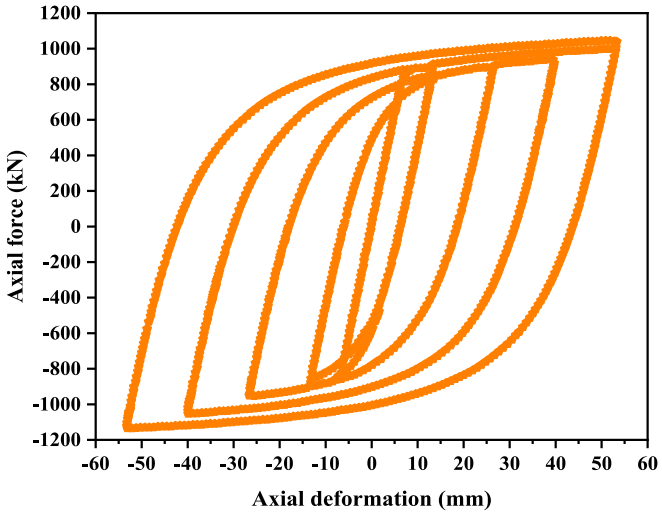

Fig. 5. Hysteretic behavior of the BRB implemented in the first floor of the 6-Story BRBF.

floor of the 6-Story BRBF. Fig. 6 presents design documentation of four bay BRBFs. It should be noted that sections of beams and columns and the area of BRB cores are similar to each story level.

3. Numerical models of SMAs and VDs implemented in BRBFs

VD is a kind of energy dissipation device that transforms kinetic energy into heat energy to dissipate the seismic energy due to earthquakes. According to Pollini et al. [46], a dashpot in series with two springs was considered to model the VD. The dashpot has the damping property of VD, the first spring accounts for the stiffness of the supporting brace, and the second spring is the stiffness of the VD. The general relation for VD was presented as follows:

$$F_{VD} = C(\alpha)\left|\dot{x}_{vd}\right|^{\alpha} sgn\left(\dot{x}_{vd}\right), F_{VD} = K_{vd}(x_{vd}), F_{Brace} = K_{Brace}(x_{Brace}) \quad (1)$$

where F_{VD} is VD force, $C(\alpha)$ is the damping coefficient, $\dot{x}_{vd}$ the relative velocity of damper ends, sgn is the signum function, K_{vd} is the damper stiffness, K_{Brace} is the brace stiffness, x_{Brace} is the elongation of the brace, and x_{vd} is the elongation of the VD [46,47]. The damper velocity exponent, α, can take values from 0.0 to 1.0 for nonlinear VDs or linear VDs, respectively.

Landi et al. [48,49] proposed a methodology to calculate the supplemental damping ratio provided by VDs, ξ_{VD}, based on comparing of the demand and capacity spectrums derived from the base shear-roof displacement curve (pushover curve). Hence, the effective damping of a structure,ξ_{eff},can be determined by following equation:

$$\xi_{eff} = \xi_h + \xi_{VD} + \xi_i \quad (2)$$

where ξ_i and ξ_h are the inherent damping ratio (i.e. Rayleigh damping with a ratio of 5% was assumed), and the hysteretic damping ratio, respectively. In the first mode of vibration, the supplemental viscous damping ratio, ξ_{VD}, can be achieved by following equation:

$$\xi_{VD} = \frac{\sum_{i=1}^{Nd} (2\pi)^{\alpha} \cdot T_1^{2-\alpha} \cdot \lambda_i \cdot C_i \cdot f_i^{1+\alpha} \cdot D_{roof}^{\alpha-1} \cdot \varphi_{ri1}^{1+\alpha}}{8\pi^3 \cdot \sum_{j=1}^{Ns} m_j \cdot \varphi_{j1}^2} \quad (3)$$

where N_d and N_s are the number of the VDs and the number of story levels, respectively. C_i is the damping coefficient of VD, λ_i is a constant value corresponding to the exponent of velocity, α, and T_1 is the fundamental period of the structure. θ_i is the angle of VD direction and f_i is equal to $\cos\theta_i$. The relative deformations of the horizontal degrees of freedom was defined by φ_{ri1}, the amplitude of the roof displacement was assumed by D_{roof}, and the mass of the stories was defined by m_j [23,35,49]. To model VDs, due to the assumption of VDs' large enough stroke limits, they do not reach their stroke limits during seismic excitations [23,50,51]. Since the idea of implementing the VDs is related to the increase in the effective damping (i.e. ξ_{eff}) of structures, the supplemental damping ratio of 0.1 with uniform distribution was assumed. Therefore, the damping coefficient of VDs can be calculated using Eq. (3) considering the target drift of 1.75%.

In this study, Ni-Ti SMA (Ni = 49.3% and Ti = 50.4%) was used that manufactured in accordance with the standard specification for wrought Ni-Ti SMA for medical devices and surgical implants (F2063) issued by ASTM. In this alloy, the percentage of the weight of nickel, carbon, hydrogen, oxygen, and nitrogen are 56.01%, 0.009%, 0.0006%, 0.024%, and 0.003%, respectively. The main crystal phase of SMAs is austenite and martensite. The changes between these phases occur due to internal forces or temperature. Fig. 7 shows the stress-strain hysteresis curve of SMA material. According to Fig. 7, E_{SMA} is a modulus of elasticity for the austenite phase, R_S is the second slope of the loading phase, F_{MS} is martensite to austenite starting stress, $F_{MF}$is austenite to martensite finishing stress, F_{AS} is martensite to austenite starting stress, F_{AF} is martensite to austenite finishing stress, and d_L is the strain at which the transformation to martensite is complete [27,51,52]. The flag-shaped loop of the graph shows the superelastic loading-unloading that dissipates energy with no residual strains. This SMA model was developed based on the six parameters to describe both positive and negative loading directions and a factor of $R_{esidual}$ equal to 0.00721 was considered for modeling the residual strain into the hysteresis curve [28].

To verify the modeling approach of SMA material, the result of the experimental test performed by Ke et al. [29] and Fang et al. [54] was used. The specimen D8L290W8 was an 8 mm diameter SMA bolt with a total length of 290.5 mm installed with four washers in series (see [29,54]). Fig. 8 presents the results of the experimental test compared with those of numerical Opensees [40] simulation used for verification. It can be seen that the numerical model has a good agreement and this proves the accuracy of modeling.

In this research, the SMA mechanical properties reported by Eatherton et al. [28] were used. According to Fig. 7, the values of E_{SMA}=76,530 MPa, R_S = 0.033E_{SMA}, F_{MS}=308 MPa, F_{AS}=221 MPa, F_{AF}=124 MPa, and d_L=0.0412 m/m were considered. Similarly, it is assumed that SMA braces are buckling restrained and can undergo compressive force without buckling. It should be noted that the SMA braces should be entered into the nonlinear behavior to dissipate the

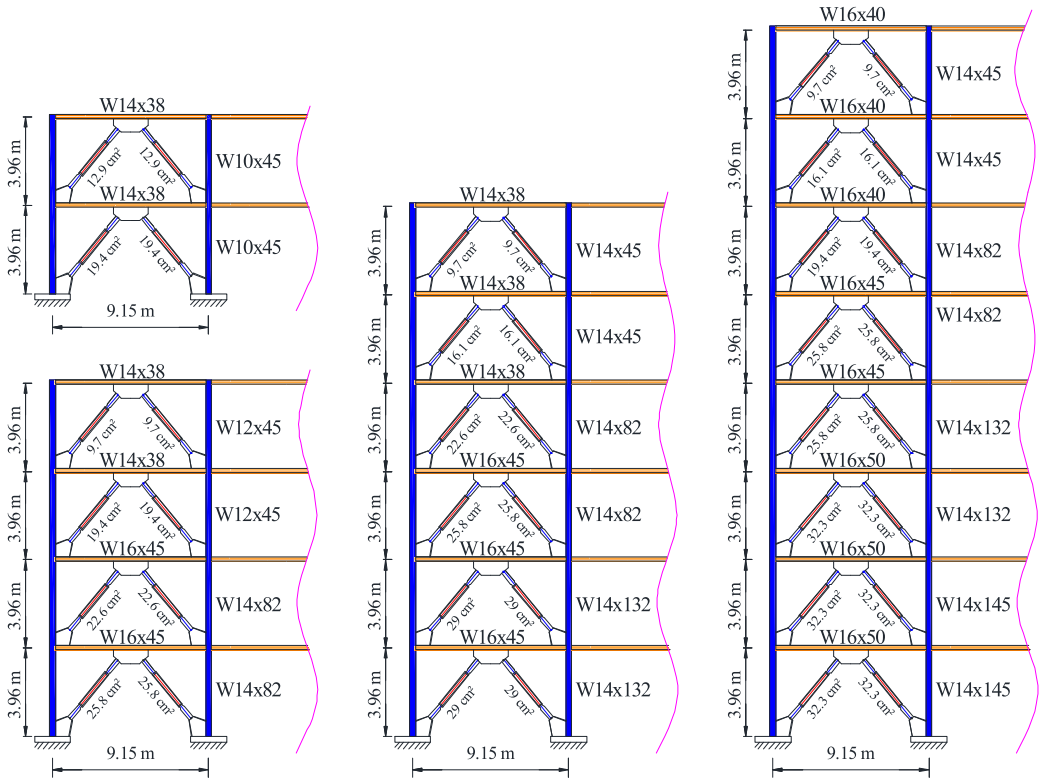

Fig. 6. Design documentation of BRBFs in Y-direction.

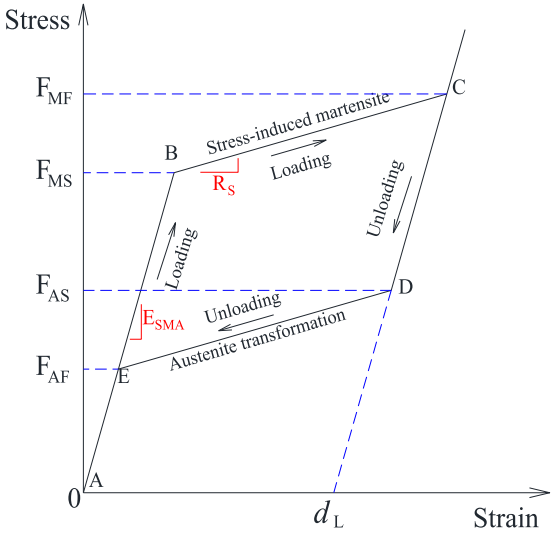

Fig. 7. The stress-strain hysteresis curve of SMA material.

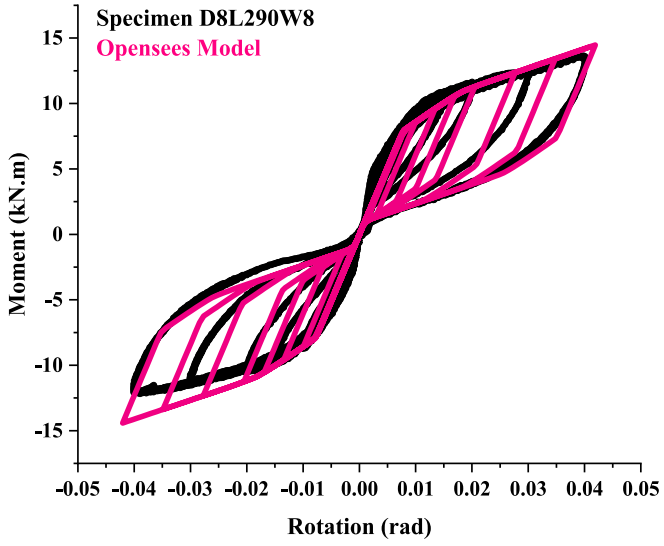

Fig. 8. Verification of stress-strain curve of SMA used in this study with the result of specimen D8L290W8 [28,53].

energy, while the nonlinearity should not extend to beams and columns due to assumption of limiting the yielding mechanism to the braces. Therefore, the axial strength of both SMA brace and BRB should be equal. To calculate the SMA brace area the following equation can be used:

$$A_{SMA} \times F_{MS} = F_{BRB} \times A_{BRB} \rightarrow A_{SMA} = A_{BRB} \frac{F_{BRB}}{F_{MS}} \tag{4}$$

where A_{SMA} is the cross-sectional area of the SMA brace, A_{BRB} and F_{BRB} are the cross-sectional area and yield stress of the BRB, respectively. In addition, the length of the SMA brace, L_{SMA}, can be calculated by the following equation:

$$\left(\frac{AE}{L}\right)_{SMA} = \left(\frac{AE}{L}\right)_{BRB} \tag{5}$$

According to Equations, the SMA brace can be defined and implemented in the models.

4. Nonlinear analysis

In this research, both nonlinear and linear VDs were considered in the sensitivity analysis, and results showed that the linear VDs had

higher effects than the nonlinear VDs (see also [21–25]). Therefore, the linear VDs selected for the rest of the analysis. To compare the results of the analysis, five types of systems were employed. Table 1 shows considered models and conditions of implementing VDs and SMAs. All BRBFs have two bracing bays with documentation presented in Fig. 6, and SMA cores were considered according to the calculation of *Section 3*. The results of the analysis will be discussed in the following sections.

Modified Ibarra–Krawinkler bilinear-hysteretic model [21–25,55,56] was used to model the plastic hinges of columns. Therefore, the moment and rotation curves of the 2-Story BRBF can be calculated according to this model. Figs. 9 and 10 present the moment and rotation of first floor column hinges of the 2-story BRBF assuming four types of BRBFs, respectively, subjected to Northridge record (1/17/1994, 17,645 Saticoy station, RSN number: 1048). According to Fig. 8, the 2-Story BRBF with implementing both BRBs and linear VDs has the lowest amount of maximum moment with 253.67 kN.m. The 2-Story BRBF with implementing SMAs has the highest amount of maximum moment with 346.48 kN.m. In addition, according to Fig. 10, this model has the highest amount of maximum rotation with 0.0411 rad. Table 2 illustrates the maximum moment and rotation values of the 2-Story BRBF and the percentage of differences of adding SMAs or linear VDs. Using linear VDs implemented with BRBs can significantly reduce the maximum moment and rotation values of the 2-Story BRBF by 25.69% and 39.29%, respectively. On the other hand, using SMAs increased the maximum moment and rotation values of the 2-Story BRBF. To overcome this issue, the linear VDs also used with SMAs, and results confirm that the maximum moment and rotation values of the 2-Story BRBF decreased by 11.74% and 28.57%, respectively. It is worth mentioning that this reduction can cause total improvement in performance levels. Similar results were observed from column hinges of other BRBFs with a different types of models.

5. Incremental dynamic analysis

Incremental Dynamic Analysis (IDA) is a procedure that consists of nonlinear dynamic analysis with the increasing amount of intensity measure until total collapse of the structure. This technique was used for seismic limit-state capacity assessment. In this procedure, the vertical axis depicts the amount of intensity measure that $S_a(T_1)$ was selected for this purpose, and the horizontal axis depicts the Engineering Demand Parameter (EDP) that Maximum Interstory Drift Ratio (M-IDR) and MR-IDR were selected. In addition, IDAs were performed using two seismic ground motion data sets of Near-fault Pulse-Like (NPL) and Near-fault No-Pulse (NNP) suggested by FEMA-P695 [57] to find out the effects of ground motion events. It is showed that each record subset includes 28 records in both directions. Fig. 11 illustrates the response spectra for 28 records in each subset introduced by FEMA-P695 [57].

A Tcl programming code was developed to assess EDPs of M-IDR and MR-IDR in each step of analysis using MATLAB [58] and OpenSees [40] simultaneously. In addition, to determine the MR-IDR of structures, zero acceleration values were added to the end of ground motions to let the structures oscillate; then, the permanent deformation of each floor level was considered as the MR-IDR. Fig. 12 presents IDA curves of 8-Story-BRB (blue lines) with considering EDPs of M-IDR and MR-IDR, respectively, subjected to NPL record subset. In addition, the median of IDA curves (M-IDAs) was plotted in the red line. Fig. 13 presents IDA curves of the 4-Story-BRB-VD with considering EDPs of M-IDR and MR-IDR, respectively, subjected to NNP record subset.

Seismic performance levels are useful tools to analyze the state of a building in seismic events. According to the type of EDPs, seismic codes proposed seismic performance levels. In this research, two types of EDPs were considered. Three seismic performance levels of Immediate Occupancy (IO), Life Safety (LS), and Collapse Prevention (CP) with M-IDR of 0.5%, 1.5%, and 2.0%, respectively, were selected in accordance with FEMA 356 [59]. In addition, the performance levels of IO, LS, and CP for the EDP of MR-IDR were assumed as 0.25%, 0.75%, and 1.25%, respectively, based on Veismoradi et al. [60]. Moreover, the seismic performance of Total Collapse (TC) was considered where M-IDA curve was flatted.

5.1. Performance level of 2-Story BRBF

To compare the results of analysis, M-IDAs of all 2-Story BRBFs were plotted assuming two EDPs of M-IDR and MR-IDR. Figs. 14 and 15 present the M-IDAs of the 2-Story BRBF with considering EDPs of the M-IDR and MR-IDR, subjected to NNP and NPL records, respectively. According to Fig. 14(a), the 2-Story-BRB, the 2-Story-BRB-SMA, and the 2-Story-SMA have approximately the same M-IDA curves based on the EDP of MR-IDR. Moreover, the 2-Story-BRB-VD is upper than the three aforementioned BRBFs, while the 2-Story-SMA-VD has the highest M-IDA curve among other BRBFs. According to Fig. 15(b), the 2-Story-BRB has the lowest M-IDA curve based on the EDP of MR-IDR. Whereas, the 2-Story-SMA-VD achieved the highest values of M-IDAs. Therefore, it can be concluded that implementing SMAs and VDs in the 2-Story BRBF significantly increases the M-IDA values compare to other implemented energy dissipation devices.

To better compare the BRBFs, the values of seismic limit state capacities were determined according to the seismic performance levels of IO, LS, CP, and TC. Tables 3 and 4 present the seismic limit-state capacities of the 2-Story BRBFs assuming two EDPs of the M-IDR and MR-IDR, respectively, subjected to two record subsets. According to Table 4, implementing VDs (e.g. the 2-Story-BRB-VD) can increase the IO, LS, CP, and TC performance levels by 2.90, 1.95, 1.77, and 1.27 times of that obtained in the 2-Story-BRB, respectively, subjected to NNP record subset. In addition, the IO, LS, CP, and TC performance levels had higher values in NNP record subset compared to NPL record subset, correspondingly. Implementing SMAs (e.g. the 2-Story-BRB-SMA and the 2-Story-SMA) had approximately no effects on the performance levels. Whereas, implementing both SMAs and VDs (e.g. the 2-Story-SMA-VD) significantly increased the IO, LS, CP, and TC performance levels by 3.35, 2.29, 2.07, and 1.54 times of that obtained in the 2-Story-BRB, respectively, subjected to NNP record subset. Similarly, the IO, LS, CP, and TC performance levels increased by 3.47, 2.65, 2.44, and 1.75 times of values obtained in the 2-Story-BRB, respectively, subjected to NPL record subset.

According to Table 4, implementing VDs (e.g. the 2-Story-BRB-VD) can increase the IO, LS, CP, and TC performance levels by 2.79, 2.20, 2.02, and 2.00 times of that obtained in the 2-Story-BRB, respectively, subjected to NNP record subset. Similarly, for NPL record subset, the IO, LS, CP, and TC performance levels increased by 2.92, 2.61, 2.50, and 2.49 times of values obtained in the 2-Story-BRB, respectively. In addition, implementing SMAs (e.g. the 2-Story-BRB-SMA) can increase the IO, LS, CP, and TC performance levels by 3.71, 2.35, 1.93, and 1.64 times of that obtained in the 2-Story-BRB, respectively, subjected to NNP record subset. The results confirm that implementing both SMAs and

Table 1
Considered different types of models for seismic performance assessment.

Model Name (X is the number of story level)	Number of bays in the BRBF			Description
	BRB	VD	SMA	
X-Story-BRB	Two bay	–	–	All BRBs in the models have steel cores
X-Story-BRB-VD	One bay	One bay	–	All BRBs in the models have steel cores and VDs are linear
X-Story-BRB-SMA	One bay	–	One bay	One bay of BRBs have steel cores and another BRBs have SMA cores
X-Story-SMA	–	–	Two bay	All BRBs in the models have SMA cores
X-Story-SMA-VD	–	One bay	One bay	All BRBs in the models have SMA cores and VDs are linear

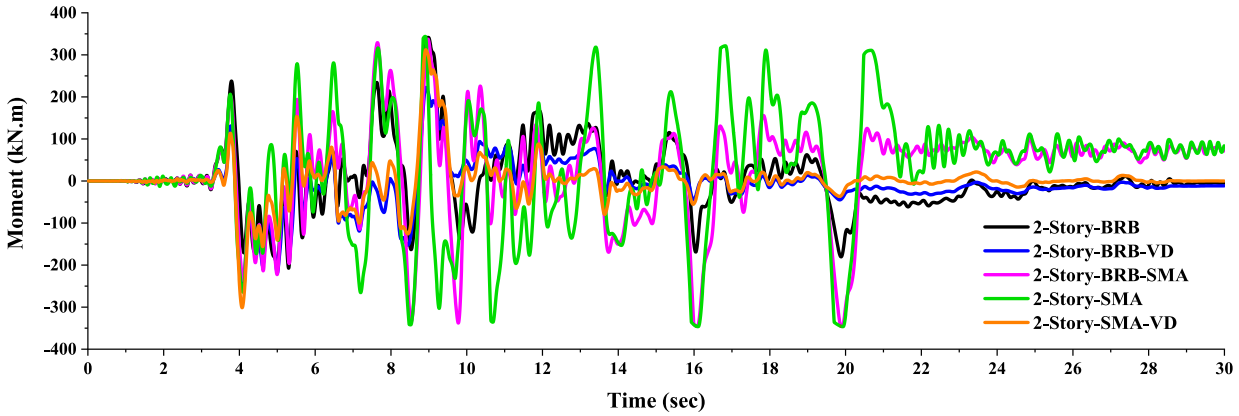

Fig. 9. Comparison between the maximum moment of first floor column hinges of the 2-Story BRBF with implemented VDs and SMAs subjected to the Northridge record.

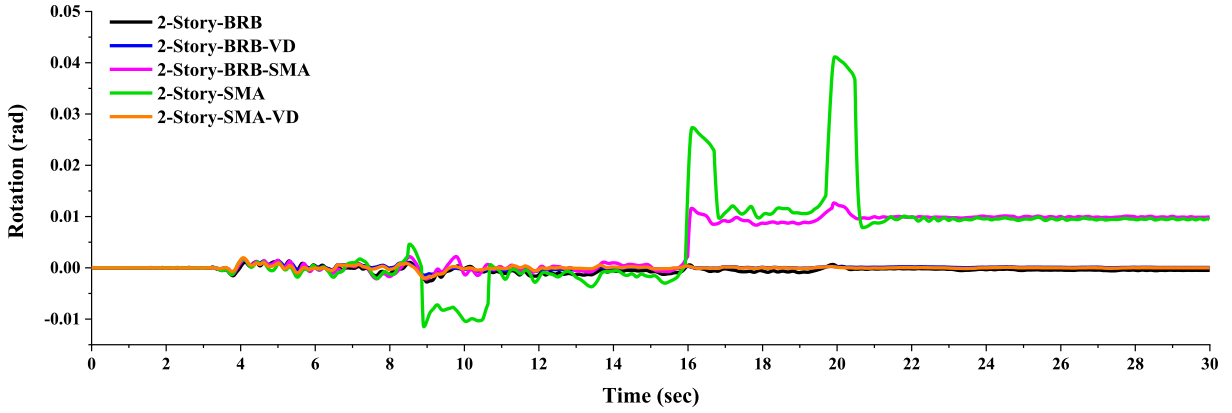

Fig. 10. Comparison between the maximum rotation of first floor column hinges of the 2-Story BRBF with implemented VDs and SMAs subjected to the Northridge record.

Table 2
Results of maximum moment and rotation of first floor column hinges of the 2-story BRBF implementing VDs and SMAs.

Results/Model Name	2-story BRBF with				
	BRB	BRB-VD	BRB-SMA	SMA	SMA-VD
Moment (kN.m)	341.37	253.67	345.37	346.48	301.29
Rotation (rad)	0.0028	0.0017	0.0127	0.0411	0.002
Percentage of differences (Moment)	–	−25.69%	1.17%	1.50%	−11.74%
Percentage of differences (Rotation)	–	−39.29%	353.57%	1367.86%	−28.57%

VDs (e.g. the 2-Story-SMA-VD) significantly increased the performance levels of IO, LS, CP, and TC by 6.68, 4.14, 3.37, and 2.81 times of that obtained in the 2-Story-BRB, respectively, subjected to NNP record subset.

5.2. Performance level of 4-Story BRBF

Figs. 16 and 17 present the M-IDAs of the 4-Story BRBF with considering EDPs of the M-IDR, and MR-IDR, subjected to NNP and NPL records, respectively. According to Fig. 16(a), the 4-Story-BRB-VD has the lowest M-IDA curve just under the 4-Story-BRB and the 4-Story-BRB-SMA and the 4-Story-SMA approximately are the same. Whereas, the 4-Story-BRB-SMA achieved the highest values of M-IDAs compared to other BRBFs. According to Fig. 16(b), the 4-Story-BRB has the lowest M-IDA curve based on MR-IDR just under the 4-Story-BRB-VD. Moreover, the 4-Story-SMA-VD stands upper than four BRBFs and shows that implementing SMAs and VDs can significantly affect the M-IDA curve.

Tables 5 and 6 present the seismic limit-state capacities of the 4-Story BRBFs assuming two EDPs of M-IDR and MR-IDR, respectively, subjected to two record subsets. According to Table 5, implementing VDs (e.g. the 4-Story-BRB-VD) can increase the IO, LS, and CP performance levels by 1.70, 1.25, and 1.16 times of that obtained in the 4-Story-BRB, and decrease the performance levels of TC by 0.84 times, correspondingly, subjected to NNP record subset. Implementing SMAs (e.g. the 4-Story-BRB-SMA) increased the IO, LS, CP, and TC performance levels by 1.27, 1.17, 1.20, and 1.48 times of that obtained in the 4-Story-BRB, respectively, subjected to NNP record subset. In addition, implementing both SMAs and VDs (e.g. the 4-Story-SMA-VD) significantly increased the IO, LS, CP, and TC performance levels by 3.34, 2.39, 2.20, and 1.67 times of that obtained in the 4-Story-BRB, respectively, subjected to NNP record subset. Similarly, the IO, LS, CP, and TC performance levels increased by 3.14, 2.72, 2.57, and 1.84 times of values obtained in the 4-Story-BRB, respectively, subjected to NPL record subset. Therefore, using both energy dissipation devices can be more effective than using one of them, and can increase the performance levels subjected to two record subsets.

According to Table 6, implementing VDs (e.g. the 4-Story-BRB-VD) can increase the IO, LS, and CP performance levels by 1.43, 1.18, and 1.06 times of M-IDA values based on MR-IDR obtained in the 4-Story-BRB, respectively, subjected to NNP record subset. Implementing

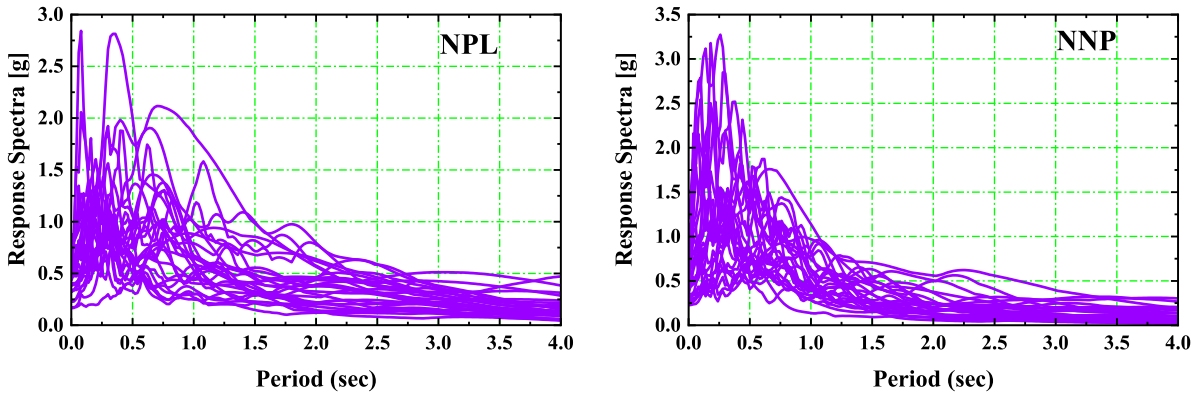

Fig. 11. Response spectra for NPL and NNP records [57].

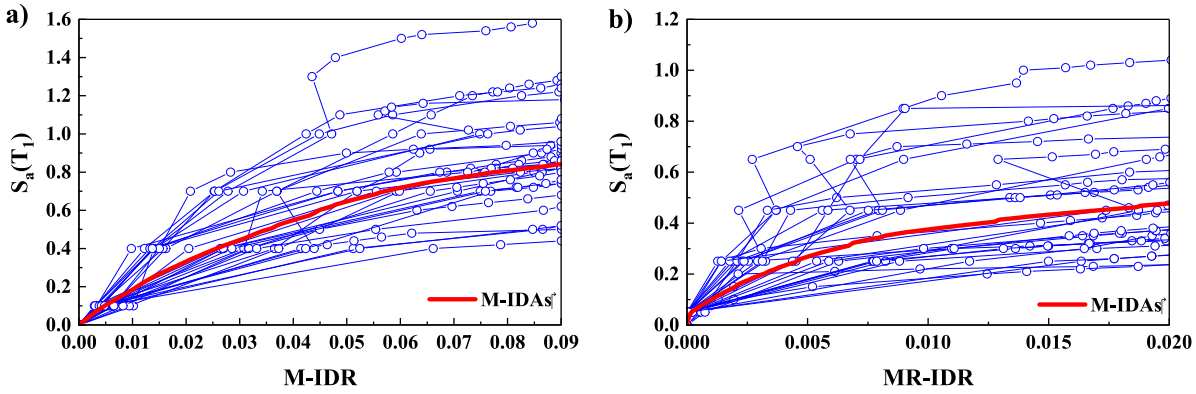

Fig. 12. IDA curves of the 8-Story-BRB assuming EDPs of, a) M-IDR, and, b) MR-IDR, subjected to NPL records.

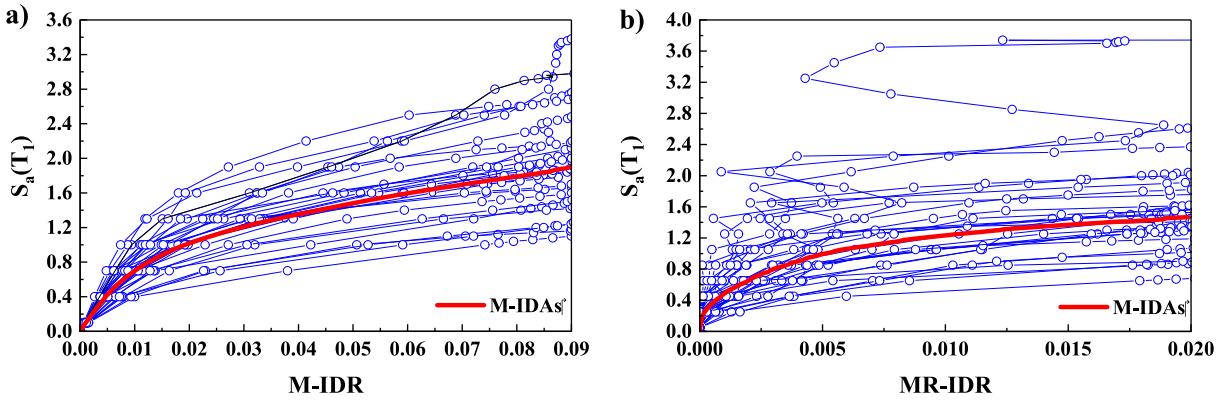

Fig. 13. IDA curves of the 4-Story-BRB-VD assuming EDPs of, a) M-IDR, and, b) MR-IDR, subjected to NNP records.

SMAs (e.g. the 4-Story-BRB-SMA) increased the IO, LS, CP, and TC performance levels by 4.71, 3.07, 2.44, and 2.04 times of that obtained in the 4-Story-BRB, respectively, subjected to NNP record subset. Moreover, implementing both SMAs and VDs (e.g. the 4-Story-SMA-VD) significantly increased the IO, LS, CP, and TC performance levels by 6.19, 3.70, 2.92, and 2.44 times of that obtained in the 4-Story-BRB, respectively, subjected to NNP record subset. Similarly, the IO, LS, CP, and TC performance levels increased by 6.84, 3.94, 2.67, and 1.84 times of values obtained in the 4-Story-BRB, respectively, subjected to NPL record subset.

5.3. Performance level of 6-Story BRBF

Figs. 18 and 19 present the M-IDAs of the 6-Story BRBF with considering EDPs of the M-IDR, and MR-IDR, subjected to NNP and NPL records, respectively. According to Fig. 18(a) and (b), the 6-Story-BRB has the lowest M-IDA curve just under the 6-Story-BRB-VD that shows adding VDs in one bay of the 6-Story-BRB can increase the values of M-IDAs in both EDPs. In both EDPs, the 6-Story-SMA-VD has the highest values of M-IDAs and stands than other BRBFs.

Tables 7 and 8 present the seismic limit-state capacities of the 6-Story BRBFs assuming two EDPs of M-IDR and MR-IDR, respectively, subjected to two record subsets. According to Table 7, implementing VDs (e.g. the 6-Story-BRB-VD) can increase the IO, LS, CP, and TC performance levels by 1.30, 1.32, 1.21, and 1.13 times of that obtained in the 6-Story-BRB, correspondingly, subjected to NNP record subset. Implementing SMAs (e.g. the 6-Story-BRB-SMA) increased the IO, LS, CP, and TC performance levels by 1.10, 1.43, 1.44, and 2.06 times of that obtained

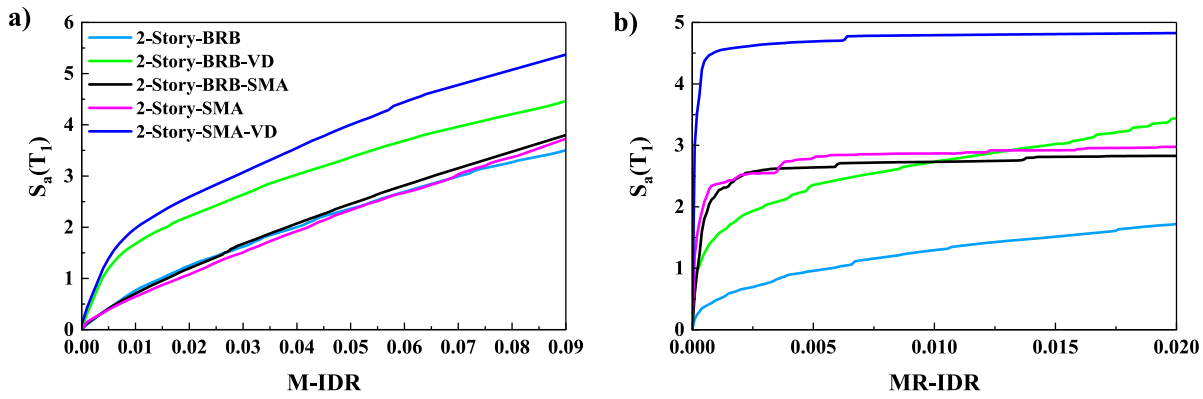

Fig. 14. M-IDAs of the 2-Story BRBF assuming EDPs of, a) M-IDR, and b) MR-IDR, subjected to NNP record subset.

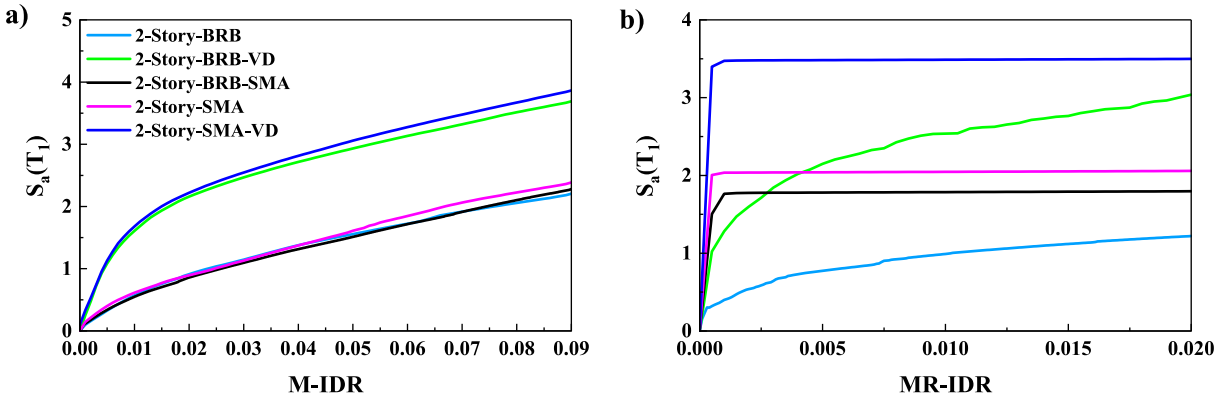

Fig. 15. M-IDAs of the 2-Story BRBF assuming EDPs of, a) M-IDR, and b) MR-IDR, subjected to NPL record subset.

Table 3
Seismic limit-state capacities of the 2-Story BRBFs given four M-IDR performance levels assuming two record subsets.

Model Name	IO	LS	CP	TC	IO	LS	CP	TC
	NNP record subset				NPL record subset			
2-Story-BRB	0.413	1.009	1.248	3.504	0.326	0.756	0.911	2.205
2-Story-BRB-VD	1.197	1.967	2.214	4.463	1.083	1.935	2.159	3.690
2-Story-BRB-SMA	0.410	0.957	1.198	3.801	0.338	0.704	0.858	2.276
2-Story-SMA	0.389	0.873	1.078	3.728	0.400	0.769	0.894	2.387
2-Story-SMA-VD	1.385	2.312	2.589	5.400	1.130	2.003	2.220	3.864

Table 4
Seismic limit-state capacities of the 2-Story BRBFs given four MR-IDR performance levels assuming two record subsets.

Model Name	IO	LS	CP	TC	IO	LS	CP	TC
	NNP record subset				NPL record subset			
2-Story-BRB	0.692	1.156	1.424	1.720	0.585	0.901	1.060	1.219
2-Story-BRB-VD	1.929	2.544	2.880	3.440	1.711	2.349	2.653	3.037
2-Story-BRB-SMA	2.570	2.718	2.746	2.828	1.776	1.782	1.787	1.795
2-Story-SMA	2.545	2.855	2.916	2.974	2.036	2.042	2.048	2.057
2-Story-SMA-VD	4.621	4.782	4.801	4.826	3.479	3.484	3.489	3.497

in the 6-Story-BRB, respectively, subjected to NNP record subset. In addition, implementing both SMAs and VDs (e.g. the 6-Story-SMA-VD) significantly increased the IO, LS, CP, and TC performance levels by 2.44, 2.37, 2.19, and 2.19 times of that obtained in the 6-Story-BRB, respectively, subjected to NNP record subset. Similarly, the IO, LS, CP, and TC performance levels increased by 1.45, 2.09, 1.97, and 1.27 times of values obtained in the 6-Story-BRB, respectively, subjected to NPL record subset.

According to Table 8 implementing VDs (e.g. the 6-Story-BRB-VD) can increase the performance levels of IO, LS, CP, and TC by 1.514, 1.155, 1.146, and 1.153 times of that obtained in M-IDA curves based on MR-IDR of the 6-Story-BRB, correspondingly, subjected to NNP record subset. Implementing SMAs (e.g. the 6-Story-BRB-SMA) significantly increased the performance levels of IO, LS, CP, and TC by 5.66, 3.50, 2.93, and 2.62 times of that obtained in the 6-Story-BRB, respectively, subjected to NNP record subset. Therefore, SMAs were more effective than the VDs to control MR-IDR values of the 6-Story-BRB. In addition, implementing both SMAs and VDs (e.g. the 6-Story-SMA-VD)

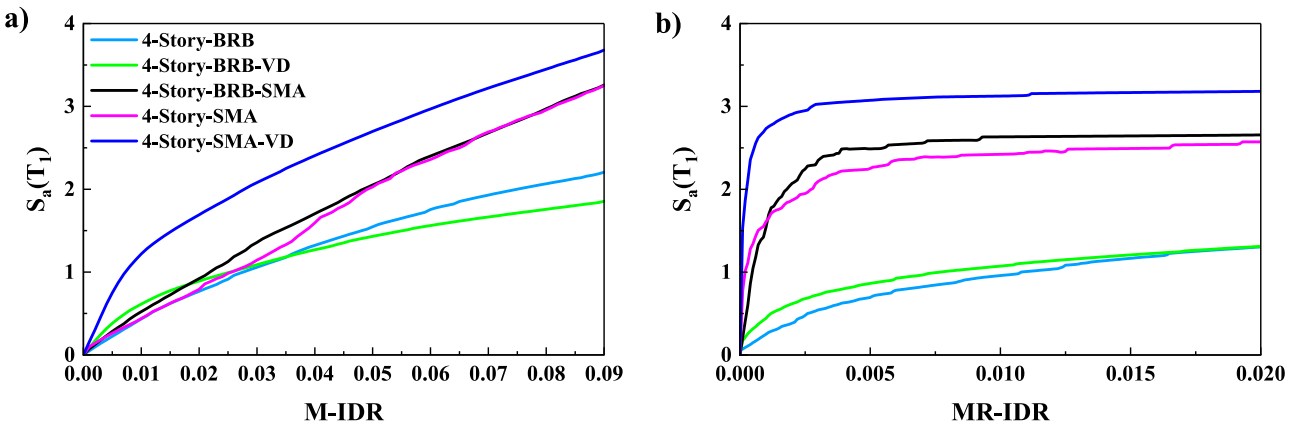

Fig. 16. M-IDAs of the 4-Story BRBF assuming EDPs of, a) M-IDR, and b) MR-IDR, subjected to NNP record subset.

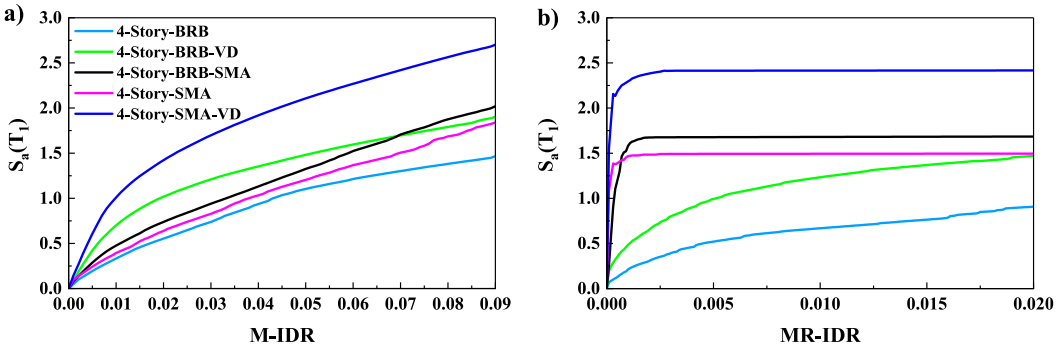

Fig. 17. M-IDAs of the 4-Story BRBF assuming EDPs of, a) M-IDR, and b) MR-IDR, subjected to NPL record subset.

Table 5
Seismic limit-state capacities of the 4-Story BRBFs given four M-IDR performance levels assuming two record subsets.

Model Name	IO	LS	CP	TC	IO	LS	CP	TC
	NNP record subset				NPL record subset			
4-Story-BRB	0.224	0.621	0.767	2.205	0.193	0.457	0.553	1.465
4-Story-BRB-VD	0.381	0.775	0.891	1.855	0.421	0.883	1.038	1.901
4-Story-BRB-SMA	0.284	0.724	0.920	3.258	0.286	0.611	0.737	2.019
4-Story-SMA	0.261	0.623	0.791	3.249	0.242	0.522	0.638	1.839
4-Story-SMA-VD	0.748	1.482	1.691	3.679	0.606	1.245	1.421	2.701

Table 6
Seismic limit-state capacities of the 4-Story BRBFs given four MR-IDR performance levels assuming two record subsets.

Model Name	IO	LS	CP	TC	IO	LS	CP	TC
	NNP record subset				NPL record subset			
4-Story-BRB	0.476	0.842	1.082	1.303	0.351	0.613	0.713	0.906
4-Story-BRB-VD	0.679	0.992	1.149	1.309	0.733	1.130	1.313	1.468
4-Story-BRB-SMA	2.243	2.586	2.637	2.655	1.675	1.678	1.680	1.684
4-Story-SMA	1.947	2.388	2.456	2.571	1.490	1.492	1.493	1.495
4-Story-SMA-VD	2.948	3.112	3.158	3.180	2.402	2.414	2.415	2.416

significantly increased the IO, LS, CP, and TC performance levels by 8.19, 4.06, 3.37, and 2.94 times of that obtained in the 6-Story-BRB, respectively, subjected to NNP record subset. It is concluded that SMAs and VDs can play a crucial role to control the values of MR-IDR of the 6-Story-BRB.

5.4. Performance level of 8-Story BRBF

Figs. 20 and 21 present the M-IDAs of the 8-Story BRBF with considering EDPs of the M-IDR, and MR-IDR, subjected to NNP and NPL records, respectively. According to Fig. 20(a), the 8-Story-BRB and the 8-Story-BRB-VD have approximately the same M-IDA curves. Implementing SMA material in the 8-Story-BRB significantly affects the M-IDA curve, and implementing VDs can improve the M-IDA curve more than other BRBFs. In addition, Fig. 20(b) confirms that implementing VDs in the 8-Story-BRB had approximately no effect on the values of M-IDA based on the MR-IDR, while implementing SMAs significantly increased the values of M-IDA. In addition, implementing both SMAs and VDs can

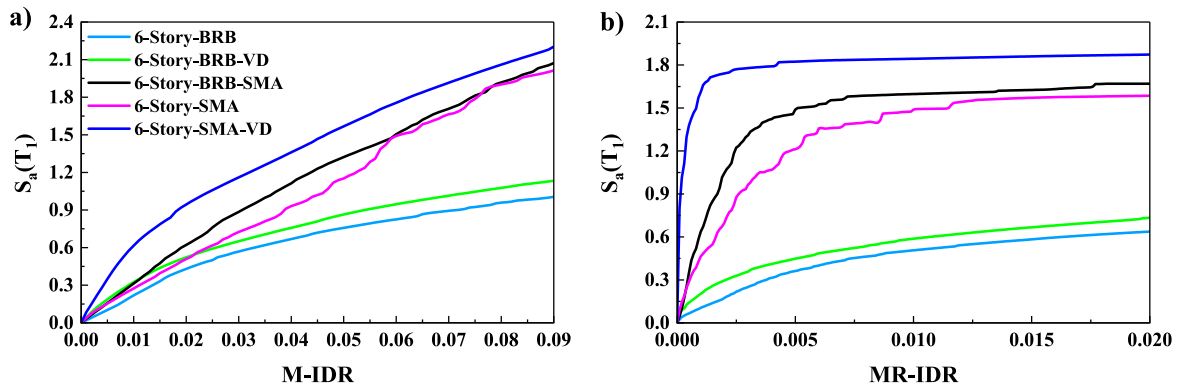

Fig. 18. M-IDAs of the 6-Story BRBF assuming EDPs of, a) M-IDR, and b) MR-IDR, subjected to NNP record subset.

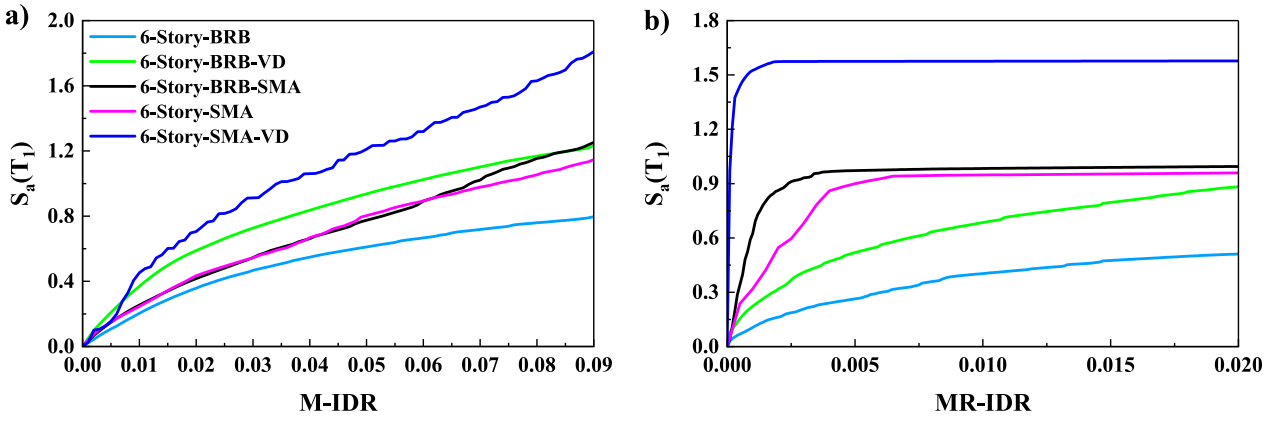

Fig. 19. M-IDAs of the 6-Story BRBF assuming EDPs of, a) M-IDR, and b) MR-IDR, subjected to NPL record subset.

Table 7
Seismic limit-state capacities of the 6-Story BRBFs given four M-IDR performance levels assuming two record subsets.

Model Name	IO	LS	CP	TC	IO	LS	CP	TC
	NNP record subset				NPL record subset			
6-Story-BRB	0.143	0.331	0.430	1.005	0.107	0.287	0.358	0.796
6-Story-BRB-VD	0.186	0.437	0.522	1.133	0.208	0.497	0.588	1.231
6-Story-BRB-SMA	0.157	0.474	0.621	2.072	0.148	0.340	0.416	1.252
6-Story-SMA	0.153	0.396	0.509	2.013	0.151	0.343	0.433	1.147
6-Story-SMA-VD	0.349	0.786	0.943	2.203	0.155	0.601	0.705	1.810

Table 8
Seismic limit-state capacities of the 6-Story BRBFs given four MR-IDR performance levels assuming two record subsets.

Model Name	IO	LS	CP	TC	IO	LS	CP	TC
	NNP record subset				NPL record subset			
6-Story-BRB	0.216	0.452	0.549	0.636	0.186	0.339	0.436	0.510
6-Story-BRB-VD	0.327	0.522	0.629	0.733	0.367	0.610	0.744	0.882
6-Story-BRB-SMA	1.223	1.582	1.608	1.669	0.910	0.978	0.986	0.994
6-Story-SMA	0.876	1.391	1.550	1.585	0.594	0.943	0.950	0.958
6-Story-SMA-VD	1.770	1.835	1.852	1.872	1.574	1.575	1.576	1.577

achieve the highest values of M-IDAs among other BRBFs.

Tables 9 and 10 present the seismic limit-state capacities of the 8-Story BRBFs assuming two EDPs of M-IDR and MR-IDR, respectively, subjected to two record subsets. According to Table 9, implementing VDs (e.g. the 8-Story-BRB-VD) can increase the performance levels of IO, LS, and CP by 1.30, 1.17, and 1.15 times of that obtained in the 8-Story-BRB, correspondingly, subjected to NNP record subset. Implementing SMAs (e.g. the 8-Story-BRB-SMA) increased the IO, LS, CP, and TC performance levels by 1.39, 1.56, 1.61, and 2.0 times of that obtained in the 8-Story-BRB, respectively, subjected to NNP record subset. In addition, implementing both SMAs and VDs (e.g. the 8-Story-SMA-VD) significantly increased the IO, LS, CP, and TC performance levels by 2.52, 2.43, 2.30, and 2.17 times of that obtained in the 8-Story-BRB, respectively, subjected to NNP record subset. Similarly, the IO, LS, CP, and TC performance levels increased by 2.03, 2.59, 2.57, and 2.28 times of values obtained in the 8-Story-BRB, respectively, subjected to NPL

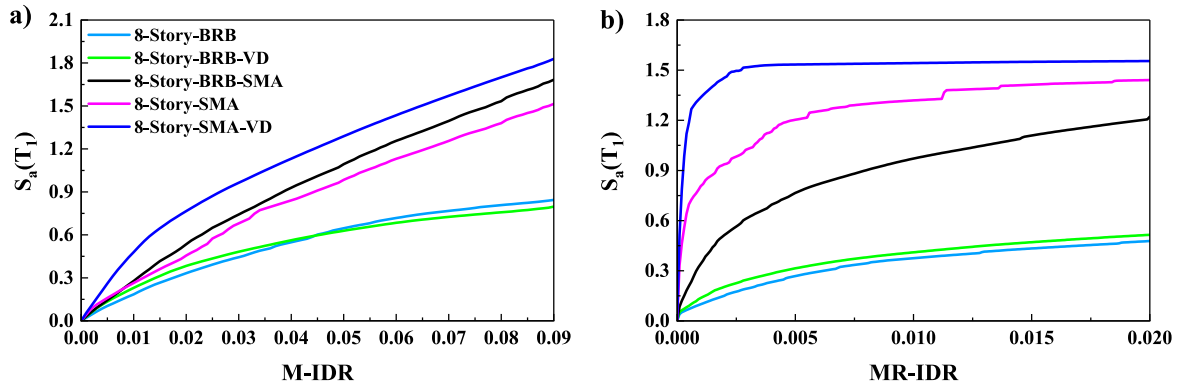

Fig. 20. M-IDAs of the 8-Story BRBF assuming EDPs of, a) M-IDR, and b) MR-IDR, subjected to NNP record subset.

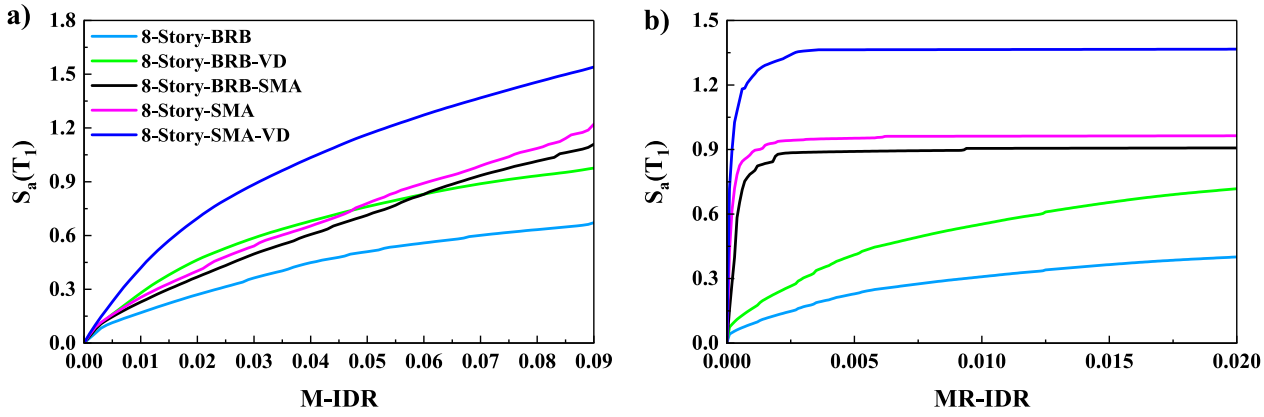

Fig. 21. M-IDAs of the 8-Story BRBF assuming EDPs of, a) M-IDR, and b) MR-IDR, subjected to NPL record subset.

Table 9
Seismic limit-state capacities of the 8-Story BRBFs given four M-IDR performance levels assuming two record subsets.

Model Name	IO	LS	CP	TC	IO	LS	CP	C
	NNP record subset				NPL record subset			
8-Story-BRB	0.103	0.266	0.332	0.843	0.113	0.221	0.270	0.671
8-Story-BRB-VD	0.134	0.313	0.383	0.797	0.160	0.380	0.463	0.971
8-Story-BRB-SMA	0.143	0.416	0.534	1.682	0.146	0.301	0.368	1.109
8-Story-SMA	0.159	0.360	0.455	1.514	0.158	0.331	0.401	1.221
8-Story-SMA-VD	0.260	0.646	0.765	1.828	0.229	0.572	0.695	1.531

Table 10
Seismic limit-state capacities of the 8-Story BRBFs given four MR-IDR performance levels assuming two record subsets.

Model Name	IO	LS	CP	TC	IO	LS	CP	C
	NNP record subset				NPL record subset			
8-Story-BRB	0.174	0.334	0.402	0.477	0.087	0.179	0.261	0.400
8-Story-BRB-VD	0.225	0.370	0.442	0.514	0.264	0.492	0.609	0.717
8-Story-BRB-SMA	0.564	0.880	1.037	1.220	0.884	0.894	0.905	0.907
8-Story-SMA	0.982	1.290	1.385	1.440	0.942	0.961	0.962	0.963
8-Story-SMA-VD	1.495	1.538	1.546	1.554	1.340	1.364	1.365	1.366

record subset.

According to Table 10, implementing VDs (e.g. the 8-Story-BRB-VD) can increase the performance levels of IO, LS, CP, and TC by 1.29, 1.108, 1.10, and 1.07 times of that obtained in M-IDA curves based on MR-IDR of the 8-Story-BRB, respectively, subjected to NNP record subset. Implementing SMAs (e.g. the 8-Story-BRB-SMA) significantly increased the IO, LS, CP, and TC performance levels by 3.24, 2.63, 2.58, and 2.56 times of that obtained in the 8-Story-BRB, respectively, subjected to NNP record subset. Therefore, SMAs were more effective than the VDs to control MR-IDR values of the 8-Story-BRB. In addition, implementing both SMAs and VDs (e.g. the 8-Story-SMA-VD) significantly increased the IO, LS, CP, and TC performance levels by 8.59, 4.60, 3.85, and 3.26 times of that obtained in the 8-Story-BRB, respectively, subjected to NNP record subset. It can be concluded that SMAs and VDs can play a crucial role to control the values of MR-IDR of the 8-Story-BRB. Moreover, using SMAs instead of BRBs (e.g. the 8-Story-SMA) significantly increased the IO, LS, CP, and TC performance levels by 5.64, 3.86, 3.45, and 3.02 times of that obtained in the 8-Story-BRB, respectively, subjected to NNP

record subset. The results showed that the self-centering characteristic of the SMA materials can help BRBFs to achieve a lower amount of MR-IDR and higher values of performance levels.

Comparing the results of all BRBFs, it can be concluded that the SMA-VD system had the highest values of the M-IDAs in both EDPs of the M-IDR and MR-IDR. Therefore, the self-centering ability of SMA materials and supplemental damping of VDs can work together to improve the M-IDA curves. By increasing the number of stories, the BRB-SMA system had better performance in improving the M-IDA curves assuming the EDP of M-IDR, while this system had good performance in the 4-, and 6-Story BRBFs considering the EDP of MR-IDR. It should be noted that implementing SMAs or VDs on all BRBFs showed that the assumed systems had positive influence on the M-IDA curves assuming the EDP of MR-IDR and, therefore, it can be considered as retrofitting strategy of the BRB system. It should be noted that the $S_a(T_1)$ values achieved in NPL records are lower than those achieved in NNP records, while the similar trend was observed for both assumed record subsets. Therefore, the records with pulse-like effects are more critical than no-pulse records.

6. Seismic fragility curves

In this section, the seismic fragility curves of considered BRBFs were compared. The seismic fragility curve is a lognormal distribution function that can show the probability of reaching or exceeding structural damage states (e.g. IO, LS, CP, and TC), given M-IDAs. In this study, the analytical procedure was used to plot the seismic fragility curves based on the performance levels of IO, LS, CP, and TC, and EDPs of M-IDR and MR-IDR. Fig. 22 presents the seismic fragility curves of the 2-Story BRBFs with considering EDP of M-IDR in the performance levels of a) IO, b) LS, c) CP, and d) TC, subjected to NPL record subset. It can be seen that the seismic fragility curves of the 2-Story-BRB-VD and the 2-Story-SMA-VD in all performance levels had a higher amount of the seismic collapse probability among other BRBFs. For example, in the performance level of IO, the $S_a(T_1)$ values corresponding to the seismic collapse probability of 50% are 0.33, 1.09, 0.34, 0.41, and 1.14 for the 2-Story-BRB, 2-Story-BRB-VD, 2-Story-BRB-SMA, 2-Story-SMA, and 2-Story-SMA-VD, respectively. In the performance level of LS, the $S_a(T_1)$ values corresponding to the seismic collapse probability of 50% are 0.76, 1.94, 0.71, 0.77, and 2.01 for the 2-Story-BRB, 2-Story-BRB-VD, 2-Story-BRB-SMA, 2-Story-SMA, and 2-Story-SMA-VD, respectively. In the performance level of CP, the $S_a(T_1)$ values corresponding to the seismic collapse probability of 50% are 0.92, 1.32, 0.86, 0.90, and 1.48 for the 2-Story-BRB, 2-Story-BRB-VD, 2-Story-BRB-SMA, 2-Story-SMA, and 2-Story-SMA-VD, respectively. In the performance level of TC, the $S_a(T_1)$ values corresponding to the seismic collapse probability of 50% are 2.21, 3.69, 2.29, 2.39, and 3.87 for the 2-Story-BRB, 2-Story-BRB-VD, 2-Story-BRB-SMA, 2-Story-SMA, and 2-Story-SMA-VD, respectively. Therefore, the 2-Story-SMA-VD had the higher seismic probability of collapse among other BRBFs, and implementing SMAs and VDs significantly increased the seismic collapse probability.

Fig. 23 presents the seismic fragility curves of the 4-Story BRBFs with considering EDP of M-IDR in the performance levels of a) IO, b) LS, c) CP, and d) TC, subjected to NPL record subset. It can be seen that the seismic fragility curves of the 4-Story-SMA-VD in all performance levels had a higher amount of the seismic collapse probability among other BRBFs. For example, in the performance level of IO, the $S_a(T_1)$ values corresponding to the seismic collapse probability of 50% are 0.19, 0.49, 0.29, 0.24, and 0.61 for the 4-Story-BRB, 4-Story-BRB-VD, 4-Story-BRB-SMA, 4-Story-SMA, and 4-Story-SMA-VD, respectively. In the performance level of LS, the $S_a(T_1)$ values corresponding to the seismic collapse probability of 50% are 0.24, 0.89, 0.61, 0.53, and 1.25 for the 4-

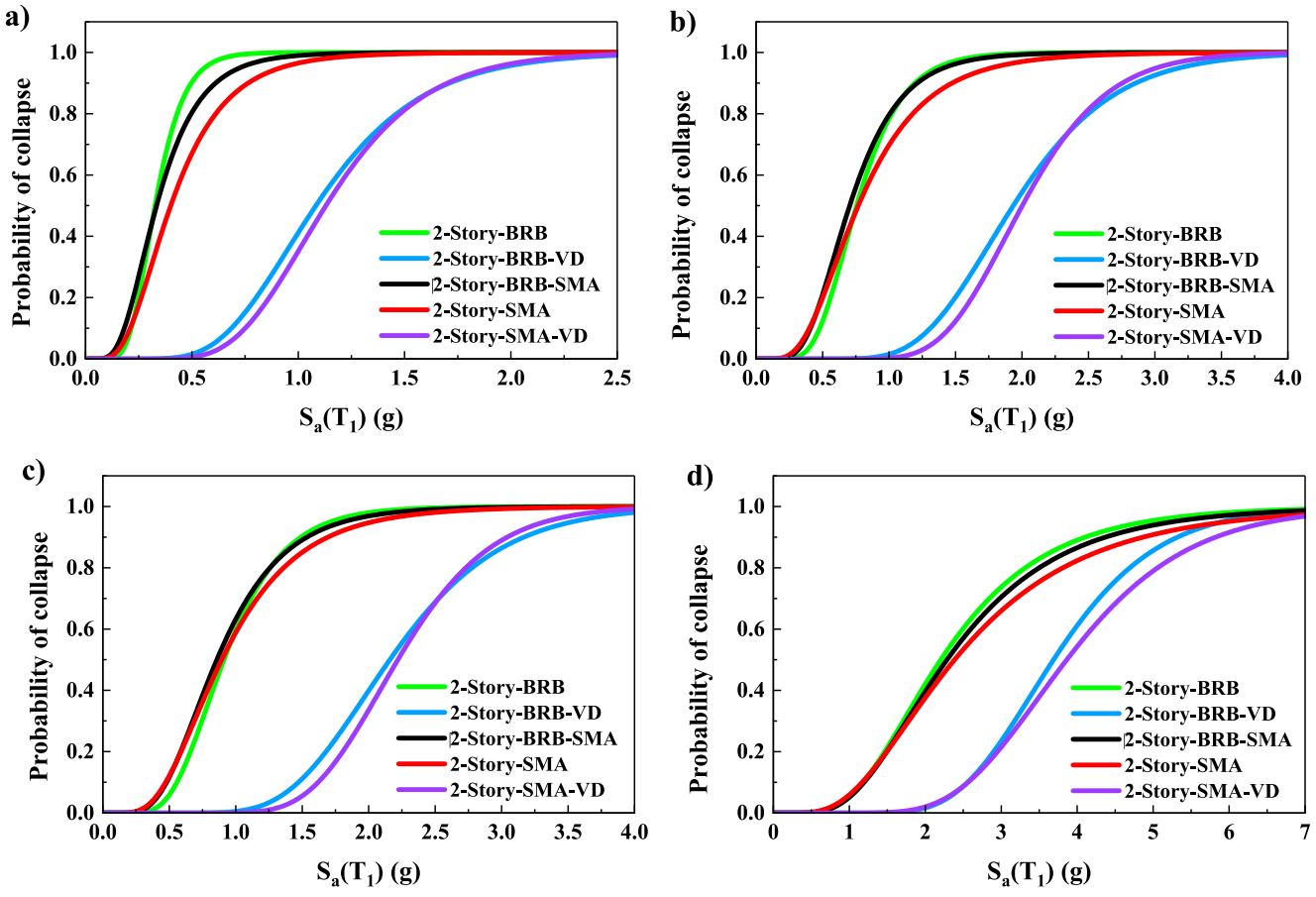

Fig. 22. Seismic fragility curves of the 2-Story BRBFs based on the M-IDR for the performance levels of, a) IO, b) LS, c) CP, and d) TC, subjected to NPL record subset.

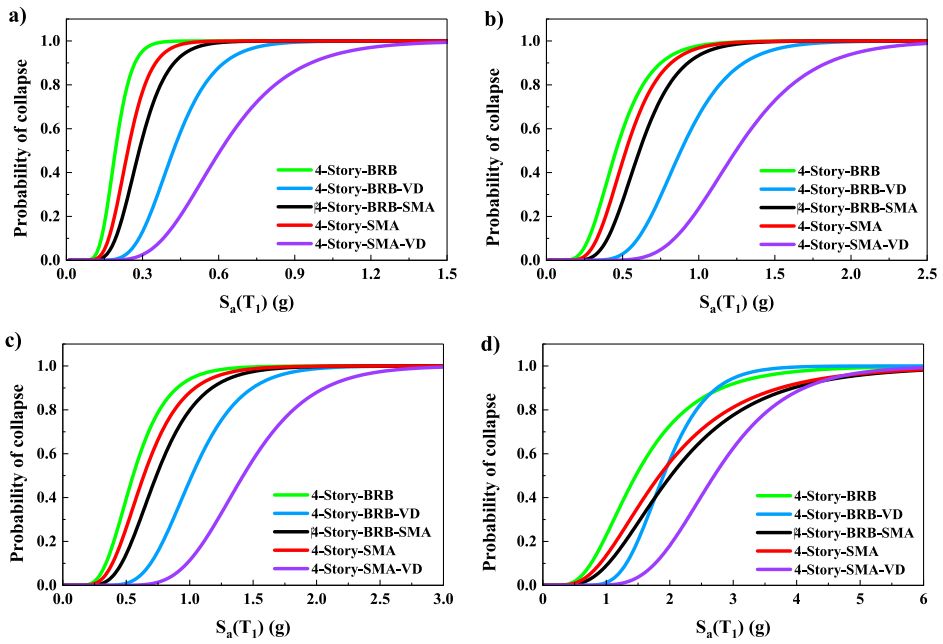

Fig. 23. Seismic fragility curves of the 4-Story BRBFs based on the M-IDR for the performance levels of a) IO, b) LS, c) CP, and d) TC, subjected to NPL record subset.

Story-BRB, 4-Story-BRB-VD, 4-Story-BRB-SMA, 4-Story-SMA, and 4-Story-SMA-VD, respectively. In the performance level of CP, the $S_a(T_1)$ values corresponding to the seismic collapse probability of 50% are 0.55, 1.02, 0.74, 0.64, and 1.43 for the 4-Story-BRB, 4-Story-BRB-VD, 4-Story-BRB-SMA, 4-Story-SMA, and 4-Story-SMA-VD, respectively. In the performance level of TC, the $S_a(T_1)$ values corresponding to the seismic collapse probability of 50% are 1.47, 1.91, 2.02, 1.84, and 2.71 for the 4-Story-BRB, 4-Story-BRB-VD, 4-Story-BRB-SMA, 4-Story-SMA, and 4-Story-SMA-VD, respectively. It can be noted that the 2-Story-SMA-VD had the higher seismic probability of collapse among other BRBFs, and implementing SMAs and VDs significantly increased the seismic collapse probability.

Fig. 24 presents the seismic fragility curves of the 6-Story BRBFs with considering EDP of M-IDR in the performance levels of a) IO, b) LS, c) CP, and d) TC, subjected to NPL record subset. It can be seen that the seismic fragility curves of the 6-Story-SMA-VD in all performance levels had a higher amount of the seismic collapse probability among other BRBFs. For example, in the performance level of IO, the $S_a(T_1)$ values corresponding to the seismic collapse probability of 50% are 0.103, 0.21, 0.15, 0.15, and 0.29 for the 6-Story-BRB, 6-Story-BRB-VD, 6-Story-

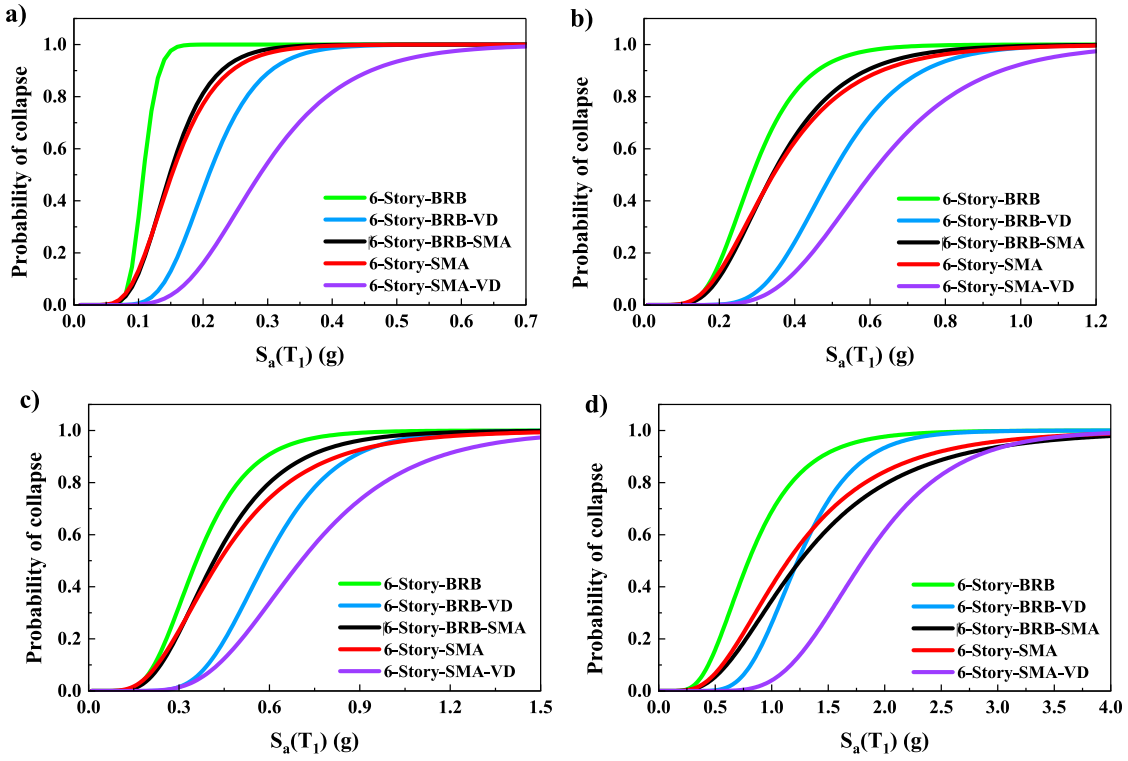

Fig. 24. Seismic fragility curves of the 6-Story BRBFs based on the M-IDR for the performance levels of a) IO, b) LS, c) CP, and d) TC, subjected to NPL record subset.

BRB-SMA, 6-Story-SMA, and 6-Story-SMA-VD, respectively. In the performance level of LS, the $S_a(T_1)$ values corresponding to the seismic collapse probability of 50% are 0.29, 0.50, 0.34, 0.34, and 0.61 for the 6-Story-BRB, 6-Story-BRB-VD, 6-Story-BRB-SMA, 6-Story-SMA, and 6-Story-SMA-VD, respectively. In the performance level of CP, the $S_a(T_1)$ values corresponding to the seismic collapse probability of 50% are 0.36, 0.59, 0.42, 0.44, and 0.71 for the 6-Story-BRB, 6-Story-BRB-VD, 6-Story-BRB-SMA, 6-Story-SMA, and 6-Story-SMA-VD, respectively. In the performance level of TC, the $S_a(T_1)$ values corresponding to the seismic collapse probability of 50% are 0.81, 1.24, 1.26, 1.15, and 1.81 for the 6-Story-BRB, 6-Story-BRB-VD, 6-Story-BRB-SMA, 6-Story-SMA, and 6-Story-SMA-VD, respectively. It can be noted that the 6-Story-SMA-VD had the higher seismic probability of collapse among other BRBFs, and implementing SMAs and VDs significantly increased the seismic collapse probability.

Fig. 25 presents the seismic fragility curves of the 8-Story BRBFs with considering EDP of M-IDR in the performance levels of a) IO, b) LS, c) CP, and d) TC, subjected to NPL record subset. It can be seen that similar to other results the seismic fragility curves of the 8-Story-SMA-VD in all performance levels had a higher amount of the seismic collapse probability among other BRBFs. For example, in the performance level of IO, the $S_a(T_1)$ values corresponding to the seismic collapse probability of 50% are 0.062, 0.124, 0.085, 0.1, and 0.235 for the 8-Story-BRB, 8-Story-BRB-VD, 8-Story-BRB-SMA, 8-Story-SMA, and 8-Story-SMA-VD, respectively. In the performance level of LS, the $S_a(T_1)$ values corresponding to the seismic collapse probability of 50% are 0.12, 0.26, 0.17, 0.21, and 0.47 for the 8-Story-BRB, 8-Story-BRB-VD, 8-Story-BRB-SMA, 8-Story-SMA, and 8-Story-SMA-VD, respectively. In the performance level of CP, the $S_a(T_1)$ values corresponding to the seismic collapse probability of 50% are 0.15, 0.33, 0.22, 0.27, and 0.55 for the 8-Story-BRB, 8-Story-BRB-VD, 8-Story-BRB-SMA, 8-Story-SMA, and 8-Story-SMA-VD, respectively. In the performance level of TC, the $S_a(T_1)$ values corresponding to the seismic collapse probability of 50% are 0.67, 0.98, 1.11, 1.23, and 1.55 for the 8-Story-BRB, 8-Story-BRB-VD, 8-Story-BRB-SMA, 8-Story-SMA, and 8-Story-SMA-VD, respectively.

The comparison of the seismic fragility curves for all types of BRBFs showed that the SMA-VD systems had the highest values of $S_a(T_1)$ corresponding to the seismic collapse probability of 50%, which shows the reliability of this system for the retrofitting purposes. While, the BRB system had the lowest values of $S_a(T_1)$ corresponding to the seismic collapse probability of 50% in all seismic fragility curves for four assumed performance levels. Although for brevity, the seismic fragility curves were plotted for NPL record subset, the similar trend was also observed for NNP record subset.

During severe earthquakes, it is important to control the lateral response of the structures. Seismic codes prescribed some limitations that if the structure exceeded them the damage states of the structure can be achieved. The performance level of LS shows that the nonstructural elements may be damaged but they would not cause death or serious damage. In this damage state, the decision of rehabilitation and normal use of the building depends on the structural evaluation. Therefore, it is important to find out how energy dissipation devices can improve the performance levels of structures and MR-IDR values. Seismic fragility can be used to compare the seismic probability of collapse of considered BRBFs. Due to the importance of MR-IDR values in the performance levels of LS, Fig. 26 presents seismic fragility curves of BRBFs with considering EDP of MR-IDR corresponding to LS performance subjected to NPL record subset. According to Fig. 26(a), the 2-Story-SMA-VD had the highest amount of seismic probability values. For example, in the seismic collapse probability of 50%, the 2-Story-BRB, 2-Story-BRB-VD, 2-Story-BRB-SMA, 2-Story-SMA, and 2-Story-SMA-VD achieved values of 0.8, 1.15, 1.79, 2.05, and 3.49, respectively. Therefore, implementing VDs or SMAs can increase the performance level of LS by 1.43 and 2.23 times of those achieved in the 2-Story-BRB, respectively. While changing the steel cores with SMAs (e.g. the 2-Story-SMA) and using both SMAs and VDs (e.g. the 2-Story-SMA-VD) can increase the performance level of LS by 2.56 and 4.36 times of those achieved in the 2-Story-BRB, respectively.

According to Fig. 26(b), the 4-Story-SMA-VD had the highest amount of seismic probability values. For example, in the seismic collapse probability of 50%, the 4-Story-BRB, 4-Story-BRB-VD, 4-Story-BRB-SMA, 4-Story-SMA, and 4-Story-SMA-VD achieved values of 0.25,

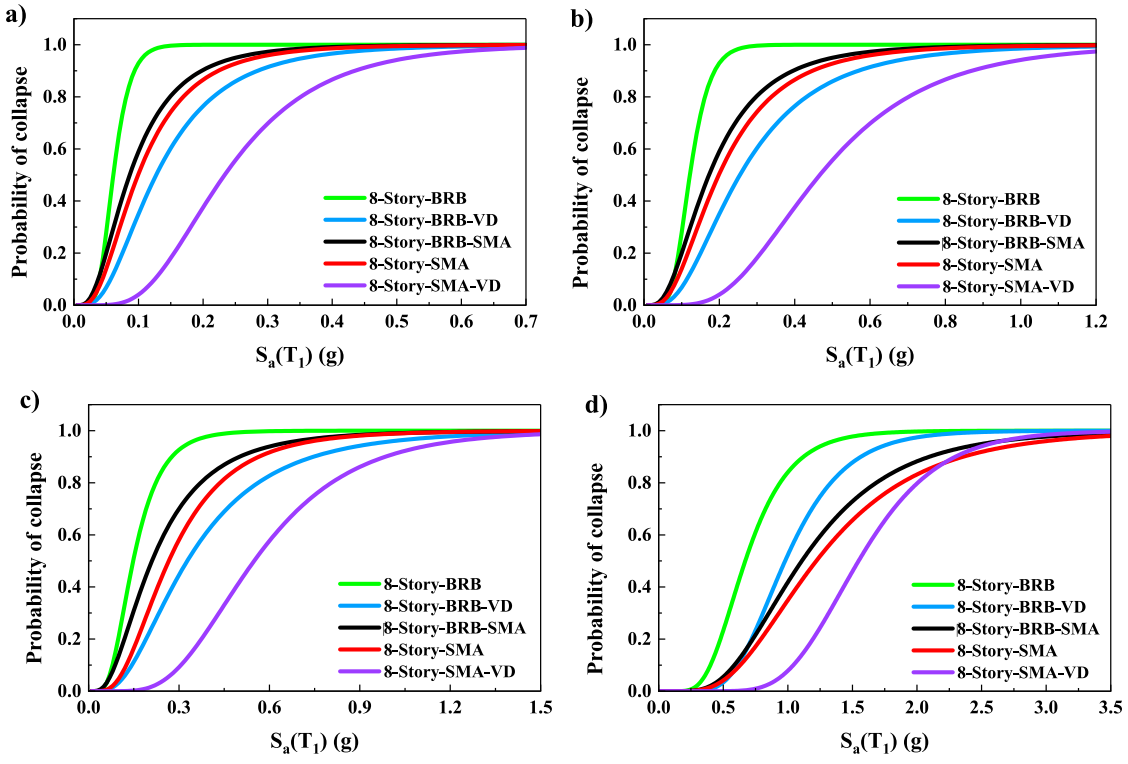

Fig. 25. Seismic fragility curves of the 8-Story BRBFs based on the M-IDR for the performance levels of a) IO, b) LS, c) CP, and d) TC, subjected to NPL record subset.

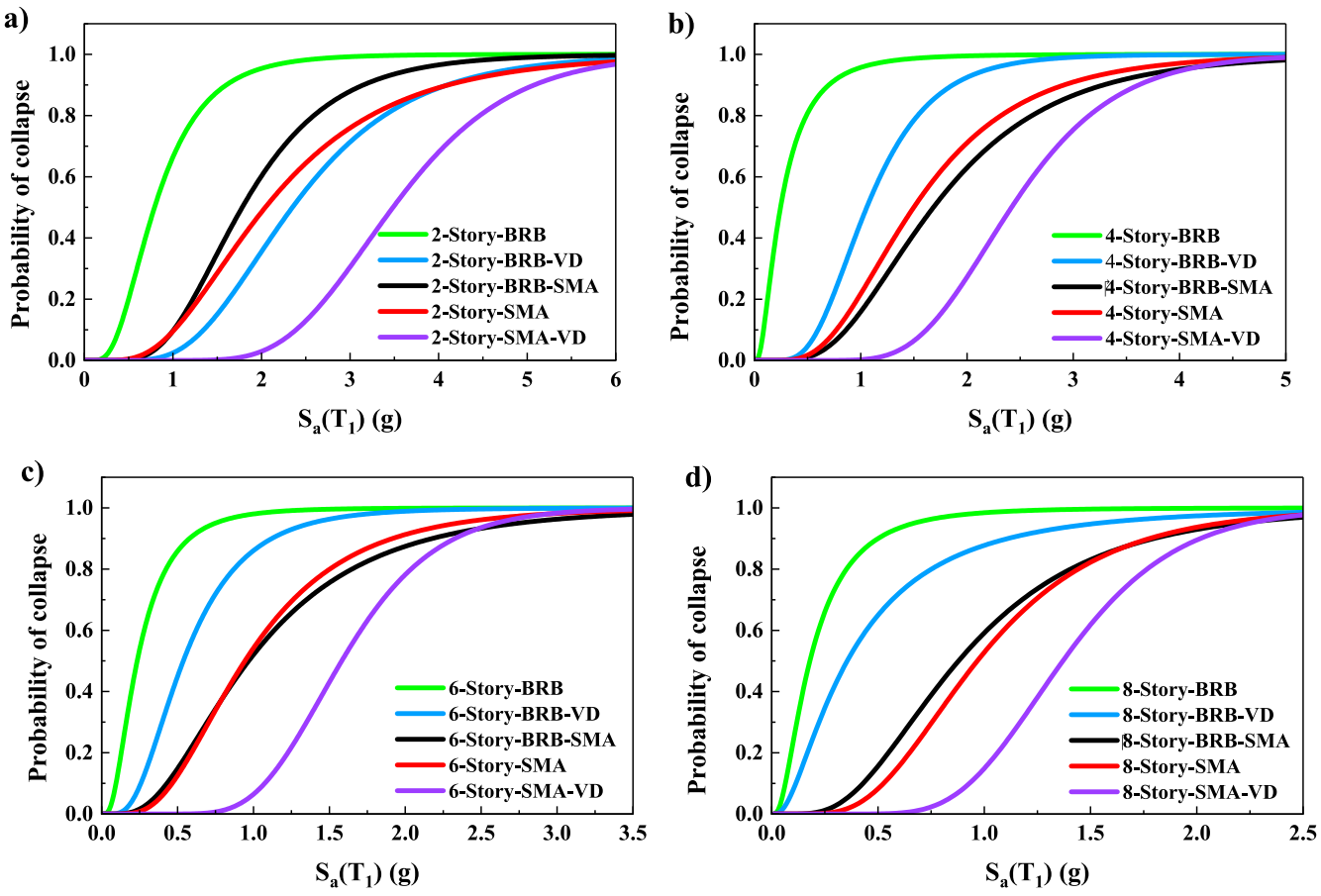

Fig. 26. Seismic fragility curve of BRBFs based on the MR-IDR for the performance level of LS subjected to NPL record subset.

1.06, 1.69, 1.5, and 2.42, respectively. Therefore, implementing VDs or SMAs can increase the performance level of LS by 4.24 and 6.76 times of those achieved in the 4-Story-BRB, respectively. While changing the steel cores with SMAs (e.g. the 4-Story-SMA) and using both SMAs and VDs (e.g. the 4-Story-SMA-VD) can increase the performance level of LS by 6.0 and 9.68 times of those achieved in the 4-Story-BRB, respectively. According to Fig. 26(c), similar to other results, the 6-Story-SMA-VD had the highest amount of seismic probability values. For example, in the seismic collapse probability of 50%, the 6-Story-BRB, 6-Story-BRB-VD, 6-Story-BRB-SMA, 6-Story-SMA, and 6-Story-SMA-VD achieved values of 0.24, 0.54, 0.97, 0.95, and 1.59, respectively. Therefore, implementing VDs or SMAs can increase the performance level of LS by 2.25 and 4.04 times of those achieved in the 6-Story-BRB, respectively. While changing the steel cores with SMAs (e.g. the 6-Story-SMA) and using both SMAs and VDs (e.g. the 6-Story-SMA-VD) can increase the performance level of LS by 3.95 and 6.62 times of those achieved in the 6-Story-BRB, respectively. According to Fig. 26(d), similar to other results, the 8-Story-SMA-VD had the highest amount of seismic probability values. For example, in the seismic collapse probability of 50%, the 8-Story-BRB, 8-Story-BRB-VD, 8-Story-BRB-SMA, 8-Story-SMA, and 8-Story-SMA-VD achieved values of 0.18, 0.36, 0.88, 0.97, and 1.38, respectively.

Therefore, implementing VDs or SMAs can increase the performance level of LS by 2.0 and 4.88 times of those achieved in the 8-Story-BRB, respectively. While changing the steel cores with SMAs (e.g. the 8-Story-SMA) and using both SMAs and VDs (e.g. the 8-Story-SMA-VD) can increase the performance level of LS by 5.38 and 7.66 times of those achieved in the 8-Story-BRB, respectively. Therefore, the results showed the impressive influence of SMAs and VDs to reduce the MR-IDR values and increase the performance levels of LS.

7. Estimating seismic performance level

For the benefits of readership, in this section, the Estimation Factors (EFs) are provided to predict the seismic performance levels of considered structures. To calculate the EFs, the seismic performance levels of each structures were divided into its corresponding performance level. It is noteworthy that the structures with BRB system (i.e. X-Story-BRB) are considered as base seismic performance and other EFs are calculated regarding to the performance levels of these structures. In other words, the EFs provided in Tables 11 and 12 can be used for estimating performance levels while the corresponding performance levels of the structure with BRB system are available. To clarify the process of using EFs, the EFs presented in Table 11 for 4-Story structure were selected. According to Table 11, the EFs for IO, LS, CP, and TC performances for the 4-Story-BRB-VD including NPL records were calculated as 2.181, 1.932, 1.877, and 1.298, respectively. To estimate the performance levels of the 4-Story-BRB-VD, the selected EFs should be multiplied by the corresponding performance levels of IO, LS, CP, and TC presented in Table 5 (Section 5.2) for the 4-Story-BRB (i.e. 1.465, 0.553, 0.457, and 0.193).

To avoid possible mistakes in the use of EFs, Graphical User Interface (GUI) has been developed, based on which the readers of this research can estimate the increase in structural capacities regarding the performance levels of selected lateral resisting system. Although Tables 11 and 12 provides EFs for the four predefined allowable performance levels, the GUI provides the possibility of using different performance thresholds. According to user defined thresholds and the base lateral resisting system, the performance levels are estimated in the output section. Fig. 27 presents the schematic view of GUI for estimating the performance levels of lateral resisting system. To include the IDA curves presented in this research, the plot curve possibility has been added to plot

Table 11
Estimation Factors of BRBFs given four M-IDR performance levels assuming two record subsets.

Model Name	IO	LS	CP	TC	IO	LS	CP	TC
	NPL record subset				NNP record subset			
2-Story-BRB-VD	3.322	2.560	2.370	1.673	2.898	1.949	1.774	1.274
2-Story-BRB-SMA	1.037	0.931	0.942	1.032	0.993	0.948	0.960	1.085
2-Story-SMA	1.227	1.017	0.981	1.083	0.942	0.865	0.864	1.064
2-Story-SMA-VD	3.466	2.649	2.437	1.752	3.354	2.291	2.075	1.541
4-Story-BRB-VD	2.181	1.932	1.877	1.298	1.701	1.248	1.162	0.841
4-Story-BRB-SMA	1.482	1.337	1.333	1.378	1.268	1.166	1.199	1.478
4-Story-SMA	1.254	1.142	1.154	1.255	1.165	1.003	1.031	1.473
4-Story-SMA-VD	3.140	2.724	2.570	1.844	3.339	2.386	2.205	1.668
6-Story-BRB-VD	1.944	1.732	1.642	1.546	1.301	1.320	1.214	1.127
6-Story-BRB-SMA	1.383	1.185	1.162	1.573	1.098	1.432	1.444	2.062
6-Story-SMA	1.411	1.195	1.209	1.441	1.070	1.196	1.184	2.003
6-Story-SMA-VD	1.449	2.094	1.969	2.274	2.441	2.375	2.193	2.192
8-Story-BRB-VD	1.416	1.719	1.715	1.447	1.301	1.177	1.154	0.945
8-Story-BRB-SMA	1.292	1.362	1.363	1.653	1.388	1.564	1.608	1.995
8-Story-SMA	1.398	1.498	1.485	1.820	1.544	1.353	1.370	1.796
8-Story-SMA-VD	2.027	2.588	2.574	2.282	2.524	2.429	2.304	2.168

Table 12
Estimation Factors of BRBFs given four MR-IDR performance levels assuming two record subsets.

Model Name	IO	LS	CP	TC	IO	LS	CP	TC
	NPL record subset				NNP record subset			
2-Story-BRB-VD	2.788	2.201	2.022	2.000	2.925	2.607	2.503	2.491
2-Story-BRB-SMA	3.714	2.351	1.928	1.644	3.036	1.978	1.686	1.473
2-Story-SMA	3.678	2.470	2.048	1.729	3.480	2.266	1.932	1.687
2-Story-SMA-VD	6.678	4.137	3.371	2.806	5.947	3.867	3.292	2.869
4-Story-BRB-VD	1.426	1.178	1.062	1.005	2.088	1.843	1.842	1.620
4-Story-BRB-SMA	4.712	3.071	2.437	2.038	4.772	2.737	2.356	1.859
4-Story-SMA	4.090	2.836	2.270	1.973	4.245	2.434	2.094	1.650
4-Story-SMA-VD	6.193	3.696	2.919	2.441	6.843	3.938	3.387	2.667
6-Story-BRB-VD	1.514	1.155	1.146	1.153	1.973	1.799	1.706	1.729
6-Story-BRB-SMA	5.662	3.500	2.929	2.624	4.892	2.885	2.261	1.949
6-Story-SMA	4.056	3.077	2.823	2.492	3.194	2.782	2.179	1.878
6-Story-SMA-VD	8.194	4.060	3.373	2.943	8.462	4.646	3.615	3.092
8-Story-BRB-VD	1.293	1.108	1.100	1.078	3.034	2.749	2.333	1.793
8-Story-BRB-SMA	3.241	2.635	2.580	2.558	10.161	4.994	3.467	2.268
8-Story-SMA	5.644	3.862	3.445	3.019	10.828	5.369	3.686	2.408
8-Story-SMA-VD	8.592	4.605	3.846	3.258	15.402	7.620	5.230	3.415

the IDA curves based on the demands of M-IDR and MR-IDR. The plotted curve shows the IDA curve of first structure that used for estimating the performance levels.

8. Conclusions

This research has been focused on the seismic performance levels of BRBFs prone to large MR-IDR after severe earthquakes. The effects of implementing different energy dissipation devices such as VDs and SMAs have been investigated assuming two EDPs of M-IDR and MR-IDR, and proper lateral resisting systems have been proposed to control assumed EDPs and increase the performance levels. The results are summarized as follows:

- The 2-Story-BRB-VD has the lowest amount of maximum moment with 253.67 kN.m, while the 2-Story-BRB-SMA has the highest amount of maximum moment with 346.48 kN.m. In addition, implemented VDs can significantly reduce the maximum moment and rotation values of the 2-Story-BRB, while these values increased by implementing SMAs in the 2-Story-BRB. Therefore, it is suggested that both of VDs and SMAs implemented in the BRBFs. For example, implementing VDs and SMAs decreased the maximum moment and rotation values of the 2-Story BRBF by 11.74% and 28.57%, respectively.
- Except for two models of the 2-Story-BRB-SMA and the 2-Story-SMA, replacing the steel cores of BRBs with SMA material can significantly affect the seismic performance levels of 4-Story, 6-Story, and 8-Story BRBFs assuming EDP of M-IDR (e.g. the 4-Story-BRB-SMA and the 4-Story-SMA). In addition, SMA material can significantly affect the seismic performance levels of 2-Story, 4-Story, 6-Story, and 8-Story BRBFs assuming EDP of MR-IDR subjected to NPL and NNP record subsets.
- Implementing both SMAs and VDs (e.g. the 4-Story-SMA-VD) can significantly affect the performance levels of BRBFs assuming both EDPs of M-IDR and MR-IDR subjected to NPL and NNP record subsets. This system had the highest $S_a(T_1)$ values among all considered BRBFs and can increase the performance levels more effectively than using one of the VDs or SMAs. Therefore, it is suggested to implement both of them in the BRBFs.
- Comparing the seismic fragility curves of BRBFs based on the performance levels of IO, LS, CP, and TC, and EDP of M-IDR showed that implementing both SMAs and VDs significantly increased the seismic collapse probability corresponding to the performance levels of IO, LS, CP, and TC. For example, in the performance levels of IO, LS, CP, and TC based on the M-IDR, the $S_a(T_1)$ values corresponding to the seismic collapse probability of 50% for the 2-Story-SMA-VD are 1.14, 2.01, 1.48, and 3,87 times of those the 2-Story-BRB.
- Moreover, implementing both SMAs and VDs had impressive results for controlling the MR-IDR of BRBFs. Comparing the seismic performance level of LS based on MR-IDR showed that the seismic collapse probability of 50% for the 2-Story-BRB, the 4-Story-BRB, the 6-Story-BRB, and the 8-Story-BRB can be increased by a factor of

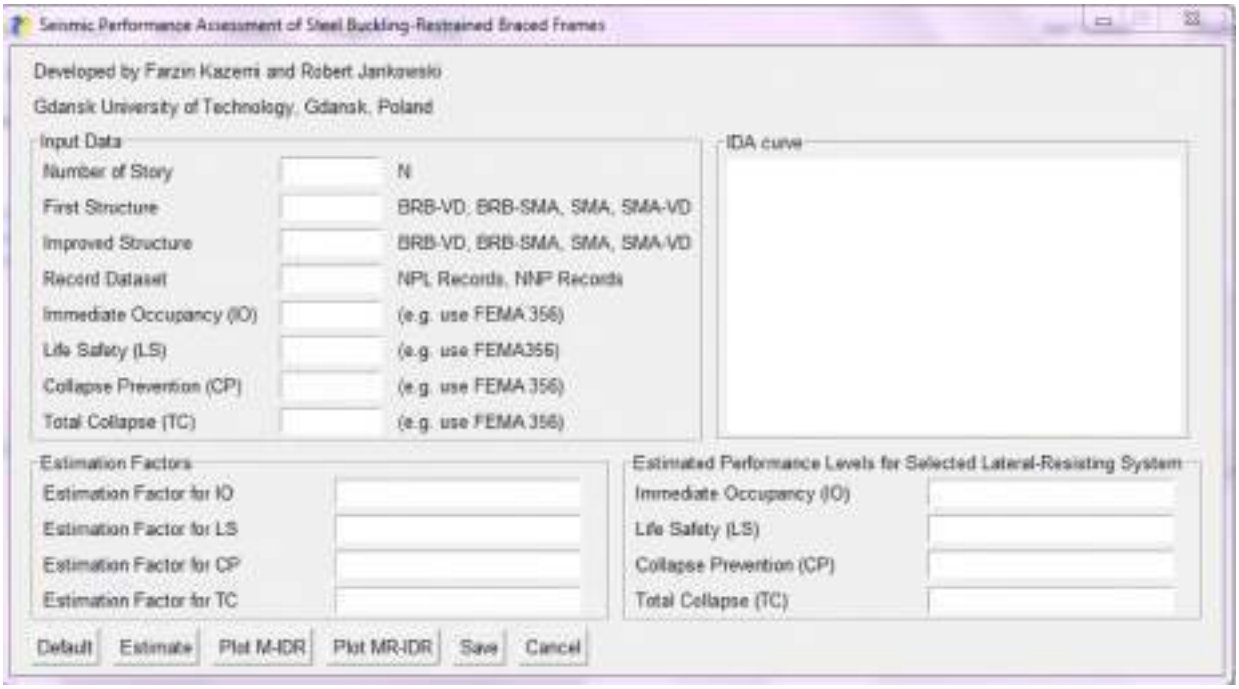

Fig. 27. Schematic view of GUI for estimating the performance levels of lateral-resisting systems.

4.36, 9.68, 6.62, and 7.66, respectively, due to using both SMAs and VDs.

- The results of IDA curves showed that the $S_a(T_1)$ values achieved in NPL records assuming both EDPs are lower than those achieved in NNP records, while the similar trend was observed for both assumed record subsets. In addition, NPL records achieved the lowest values of $S_a(T_1)$ corresponding to the seismic collapse probability of 50%. Therefore, it can be concluded that the records with pulse-like effects are more critical than no-pulse records.
- The EFs were calculated for estimating the seismic performance levels of structures. Using EFs can help engineers to estimate the improvements of selected lateral-resisting system compare to BRB structures. In addition, the GUI has been developed to provide information for estimating the seismic performance of user-defined thresholds. It is noteworthy that GUI facilitates the design and retrofitting process as well as lateral-resisting system selection.

CRediT authorship contribution statement

F. Kazemi: Conceptualization, Methodology, Software, Validation, Data curation, Formal analysis, Investigation, Project administration, Resources, Writing - original draft. **R. Jankowski:** Supervision, Writing – review & editing.

Declaration of Competing Interest

The authors declare that there is no conflict of interest with relation to the paper 'Seismic performance evaluation of steel buckling-restrained braced frames including SMA materials' submitted for publication in *Journal of Constructional Steel Research*.

Data availability

Data will be made available on request.

Acknowledgments

Numerical calculations were carried out at the Tri-City Academic Supercomputer and Network (*CI TASK*) in Gdańsk, Poland.

References

[1] S. Hosseinzadeh, B. Mohebi, Seismic evaluation of all-steel buckling restrained braces using finite element analysis, J. Constr. Steel Res. 119 (2016) 76–84.
[2] Q. Xie, State of the art of buckling-restrained braces in Asia, J. Constr. Steel Res. 61 (6) (2005) 727–748.
[3] Y. Bozorgnia, V.V. Bertero, Earthquake Engineering: From Engineering Seismology to Performance-Based Engineering, CRC Press, 2004.
[4] C. Ariyaratana, L.A. Fahnestock, Evaluation of buckling-restrained braced frame seismic performance considering reserve strength, Eng. Struct. 33 (1) (2011) 77–89.
[5] N. Asgarkhani, M. Yakhchalian, B. Mohebi, Evaluation of approximate methods for estimating residual drift demands in BRBFs, Eng. Struct. 224 (2020) 110849.
[6] M. Yakhchalian, N. Asgarkhani, M. Yakhchalian, Evaluation of deflection amplification factor for steel buckling restrained braced frames, J. Build. Eng. 30 (2020) 101228.
[7] M. Yakhchalian, M. Yakhchalian, N. Asgarkhani, An advanced intensity measure for residual drift assessment of steel BRB frames, Bull. Earthq. Eng. 19 (4) (2021) 1931–1955.
[8] T.J. Maley, T.J. Sullivan, G.D. Corte, Development of a displacement-based design method for steel dual systems with buckling-restrained braces and moment-resisting frames, J. Earthq. Eng. 14 (S1) (2010) 106–140.
[9] A. Deylami, M.A. Mahdavipour, Probabilistic seismic demand assessment of residual drift for Buckling-Restrained Braced Frames as a dual system, Struct. Saf. 58 (2016) 31–39.
[10] M. Baiguera, G. Vasdravellis, T.L. Karavasilis, Dual seismic-resistant steel frame with high post-yield stiffness energy-dissipative braces for residual drift reduction, J. Constr. Steel Res. 122 (2016) 198–212.
[11] R. Montuori, E. Nastri, V. Piluso, Theory of plastic mechanism control for MRF–EBF dual systems: closed form solution, Eng. Struct. 118 (2016) 287–306.
[12] C. Fang, Q. Zhong, W. Wang, S. Hu, C. Qiu, Peak and residual responses of steel moment-resisting and braced frames under pulse-like near-fault earthquakes, Eng. Struct. 177 (2018) 579–597.
[13] J. Sun, P. Pan, H. Wang, Development and experimental validation of an assembled steel double-stage yield buckling restrained brace, J. Constr. Steel Res. 145 (2018) 330–340.
[14] F. Barbagallo, M. Bosco, E.M. Marino, P.P. Rossi, Achieving a more effective concentric braced frame by the double-stage yield BRB, Eng. Struct. 186 (2019) 484–497.
[15] P. Code, Eurocode 8: Design of Structures for Earthquake Resistance-Part 1: General Rules, Seismic Actions and Rules for Buildings, Brussels, European Committee for Standardization, 2005.
[16] Y.W. Li, G.Q. Li, J. Jiang, Y.B. Wang, Use of energy-dissipative rocking columns to enhance seismic performance of buckling-restrained braced frames, J. Constr. Steel Res. 159 (2019) 548–559.

[17] P.S. Katsimpini, P.K. Askouni, G.A. Papagiannopoulos, D.L. Karabalis, Seismic drift response of seesaw-braced and buckling-restrained braced steel structures: a comparison study, Soil Dyn. Earthq. Eng. 129 (2020) 105925.
[18] M. Pollino, D. Slovenec, B. Qu, G. Mosqueda, Seismic rehabilitation of concentrically braced frames using stiff rocking cores, J. Struct. Eng. 143 (9) (2017), 04017080.
[19] D. Slovenec, A. Sarebanha, M. Pollino, G. Mosqueda, B. Qu, Hybrid testing of the stiff rocking core seismic rehabilitation technique, J. Struct. Eng. 143 (9) (2017), 04017083.
[20] Y. Feng, Z. Zhang, X. Chong, J. Wu, S. Meng, Elastic displacement spectrum-based design of damage-controlling BRBFs with rocking walls, J. Constr. Steel Res. 148 (2018) 691–706.
[21] F. Kazemi, B. Mohebi, M. Yakhchalian, Enhancing the seismic performance of adjacent pounding structures using viscous dampers, in: The 16th European Conference on Earthquake Engineering (16ECEE), 2018, pp. 18–21.
[22] F. Kazemi, B. Mohebi, R. Jankowski, Predicting the seismic collapse capacity of adjacent SMRFs retrofitted with fluid viscous dampers in pounding condition, Mech. Syst. Signal Process. 161 (2021) 107939.
[23] F. Kazemi, N. Asgarkhani, R. Jankowski, Probabilistic assessment of SMRFs with infill masonry walls incorporating nonlinear soil-structure interaction, Bull. Earthq. Eng. (2022) 1–32.
[24] N. Asgarkhani, F. Kazemi, R. Jankowski, Optimal retrofit strategy using viscous dampers between adjacent RC and SMRFs prone to earthquake-induced pounding, Arch. Civ. Mech. Eng. 23 (1) (2023) 7.
[25] F. Kazemi, N. Asgarkhani, A. Manguri, R. Jankowski, Investigating an optimal computational strategy to retrofit buildings with implementing viscous dampers, in: International Conference on Computational Science 13351, Lecture Notes in Computer Science, 2022, pp. 184–191,. Springer, Cham.
[26] R. DesRoches, B. Taftali, B.R. Ellingwood, Seismic performance assessment of steel frames with shape memory alloy connections. Part I—analysis and seismic demands, J. Earthq. Eng. 14 (4) (2010) 471–486.
[27] K. Wilde, P. Gardoni, Y. Fujino, Base isolation system with shape memory alloy device for elevated highway bridges, Eng. Struct. 22 (3) (2000) 222–229.
[28] M.R. Eatherton, L.A. Fahnestock, D.J. Miller, Computational study of self-centering buckling-restrained braced frame seismic performance, Earthq. Eng. Struct. Dyn. 43 (13) (2014) 1897–1914.
[29] K. Ke, X. Zhou, M. Zhu, M.C. Yam, Y. Wang, H. Zhang, Seismic evaluation of industrial steel moment resisting frames with shape memory alloys using performance-spectra-based method, J. Build. Eng. 103950 (2021).
[30] H.J. Kim, C. Christopoulos, Numerical models and ductile ultimate deformation response of post-tensioned self-centering moment connections, Earthq. Eng. Struct. Dyn. 38 (1) (2009) 1–21.
[31] E. Elettore, F. Freddi, M. Latour, G. Rizzano, Design and analysis of a seismic resilient steel moment resisting frame equipped with damage-free self-centering column bases, J. Constr. Steel Res. 179 (2021) 106543.
[32] Q. Xie, Z. Zhou, S.P. Meng, Experimental investigation of the hysteretic performance of self-centering buckling-restrained braces with friction fuses, Eng. Struct. 203 (2020) 109865.
[33] Y.C. Lin, R. Sause, J.M. Ricles, Seismic performance of steel self-centering, moment-resisting frame: hybrid simulations under design basis earthquake, J. Struct. Eng. 139 (11) (2013) 1823–1832.
[34] W. Wang, C. Fang, J. Liu, Large size superelastic SMA bars: heat treatment strategy, mechanical property and seismic application, Smart Mater. Struct. 25 (7) (2016), 075001.
[35] B. Mohebi, O. Yazdanpanah, F. Kazemi, A. Formisano, Seismic damage diagnosis in adjacent steel and RC MRFs considering pounding effects through improved wavelet-based damage-sensitive feature, J. Build. Eng. 33 (2021) 101847.
[36] ASCE 7–-16, Minimum Design Loads and Associated Criteria for Buildings and Other Structures, Reston, VA, American Society of Civil Engineers, 2017.
[37] A.I.S.C. Committee, Specification for Structural Steel Buildings (ANSI/AISC 360–16), American Institute of Steel Construction, Chicago-Illinois, 2016.
[38] AISC, A. AISC 341-16, Seismic Provisions for Structural Steel Buildings, American Institute of Steel Construction, Chicago, IL, 2016.
[39] D.R. Sahoo, S.H. Chao, Performance-based plastic design method for buckling-restrained braced frames, Eng. Struct. 32 (9) (2010) 2950–2958.
[40] F. McKenna, G.L. Fenves, F.C. Filippou, M.H. Scott, Open System for Earthquake Engineering Simulation (OpenSees), Pacific Earthquake Engineering Research Center, University of California, Berkeley, 2016.
[41] O. Yazdanpanah, B. Mohebi, F. Kazemi, I. Mansouri, R. Jankowski, Development of fragility curves in adjacent steel moment-resisting frames considering pounding effects through improved wavelet-based refined damage-sensitive feature, Mech. Syst. Signal Process. 173 (2022) 109038.
[42] F. Kazemi, B. Mohebi, M. Yakhchalian, Predicting the seismic collapse capacity of adjacent structures prone to pounding, Can. J. Civ. Eng. 47 (6) (2020) 663–677.
[43] F. Kazemi, R. Jankowski, Enhancing seismic performance of rigid and semi-rigid connections equipped with SMA bolts incorporating nonlinear soil-structure interaction, Eng. Struct. 274 (2023) 114896.
[44] F. Kazemi, N. Asgarkhani, R. Jankowski, Predicting seismic response of SMRFs founded on different soil types using machine learning techniques, Eng. Struct. 274 (2023) 114953.
[45] F. Kazemi, R. Jankowski, Machine learning-based prediction of seismic limit-state capacity of steel moment-resisting frames considering soil-structure interaction, Comput. Struct. 274 (2023) 106886.
[46] N. Pollini, O. Lavan, O. Amir, Minimum-cost optimization of nonlinear fluid viscous dampers and their supporting members for seismic retrofitting, Earthq. Eng. Struct. Dyn. 46 (12) (2017) 1941–1961.
[47] C.C. Patel, R.S. Jangid, Seismic response of dynamically similar adjacent structures connected with viscous dampers, IES J. A Civ. Struct. Eng. 3 (1) (2010) 1–13.
[48] L. Landi, S. Lucchi, P.P. Diotallevi, A procedure for the direct determination of the required supplemental damping for the seismic retrofit with viscous dampers, Eng. Struct. 71 (2014) 137–149.
[49] L. Landi, F. Conti, P.P. Diotallevi, Effectiveness of different distributions of viscous damping coefficients for the seismic retrofit of regular and irregular RC frames, Eng. Struct. 100 (2015) 79–93.
[50] C.Y. Seo, T.L. Karavasilis, J.M. Ricles, R. Sause, Seismic performance and probabilistic collapse resistance assessment of steel moment resisting frames with fluid viscous dampers, Earthq. Eng. Struct. Dyn. 43 (14) (2014) 2135–2154.
[51] A.S. Tzimas, A.I. Dimopoulos, T.L. Karavasilis, EC8-based seismic design and assessment of self-centering post-tensioned steel frames with viscous dampers, J. Constr. Steel Res. 105 (2015) 60–73.
[52] X. Xu, G. Cheng, J. Zheng, Tests on pretrained superelastic NiTi shape memory alloy rods: towards application in self-centering link beams, Adv. Civ. Eng. 2018 (2018).
[53] H. Beiraghi, H. Zhou, Dual-steel frame consisting of moment-resisting frame and shape memory alloy braces subjected to near-field earthquakes, Struct. Design Tall Spec. Build. 29 (14) (2020), e1784.
[54] C. Fang, M.C. Yam, T.M. Chan, W. Wang, X. Yang, X. Lin, A study of hybrid self-centring connections equipped with shape memory alloy washers and bolts, Eng. Struct. 164 (2018) 155–168.
[55] F. Kazemi, N. Asgarkhani, R. Jankowski, Machine learning-based seismic fragility and seismic vulnerability assessment of reinforced concrete structures, Soil Dynam. Earthq. Eng. 165 (2023).
[56] A. Altoontash, Simulation and damage models for performance assessment of reinforced concrete beam-column joints, Stanford University, Doctoral dissertation, 2004.
[57] Applied Technology Council, & United States. Federal Emergency Management Agency, Quantification of building seismic performance factors. US Department of Homeland Security, FEMA, 2009.
[58] MATLAB/Simulink as a Technical Computing Language, Engineering Computations and Modeling in MATLAB, 2018.
[59] FEMA-356, Prestandard and commentary for the seismic rehabilitation of buildings, Federal Emergency Management Agency, Washington, DC, 2000.
[60] S. Veismoradi, A. Cheraghi, E. Darvishan, Probabilistic mainshock-aftershock collapse risk assessment of buckling restrained braced frames, Soil Dyn. Earthq. Eng. 115 (2018) 205–216.

Paper VII:

Kazemi, F., Asgarkhani, N., Lasowicz, N., & Jankowski, R. (2024). Development and experimental validation of a novel double-stage yield steel slit damper-buckling restrained brace. Engineering Structures, 315, 118427. doi.org/10.1016/j.engstruct.2024.118427

Engineering Structures 315 (2024) 118427

Contents lists available at ScienceDirect

Engineering Structures

journal homepage: www.elsevier.com/locate/engstruct

Development and experimental validation of a novel double-stage yield steel slit damper-buckling restrained brace

F. Kazemi [a,b,*], N. Asgarkhani [a,b], N. Lasowicz [a], R. Jankowski [a]

[a] Faculty of Civil and Environmental Engineering, Gdańsk University of Technology, ul. Narutowicza 11/12, 80-233 Gdansk, Poland
[b] Department of Structures for Engineering and Architecture, School of Polytechnic and Basic Sciences, University of Naples "Federico II", Naples, Italy

ARTICLE INFO

Keywords:
Double-stage yield buckling-restrained brace
Steel slit damper
Experimental validation
Cyclic loading test
Novel bracing system
Seismic retrofit
Energy dissipation devices

ABSTRACT

This research is focused on the development and experimental validation of a novel double-stage yield steel slit damper-buckling restrained brace (SSD-DYB) system designed for seismic resistance of steel structures. The SSD-DYB integrates the energy dissipation capability of a steel slit damper (SSD) in its initial segment, enhancing performance in the case of lower seismic intensities levels while employing a larger segment for higher load resistance to maintain structural stability. The results of the study show that the proposed SSD-DYB is capable to reduce the weight of similar all-steel buckling restrained braces (BRBs) successfully addressing critical points through stiffeners and top and bottom plates. Additionally, the U-shaped element exhibits resilience during seismic loads, indicating its potential for replacing cores without failure which would be beneficial for seismic retrofitting of buildings. Experimental tests show that varying the number and shape of SSD strips significantly impacts the hysteresis curve's maximum load and dissipated energy (i.e., adding strips increased energy dissipation by 33.48 % for SSD-DYB-1), which can be used to control the proposed device for a specific performance target. Stopper mechanisms within the SSD-DYB regulate load distribution between segments and can be used to control the device and its transmitting capacities. Finally, an optimized SSD-DYB has been proposed with promising performance to be used by researchers for designing new structures or retrofit old ones.

1. Introduction

Seismic excitations are considered to be the most unpredictable and dangerous dynamic loads that can act on civil engineering structures. It was observed in the past that such situations might result in the death of hundreds of people and countless damage or even the collapse of structures. Steel buildings are common in most cities and are constructed with some lateral-resisting systems, such as steel moment resistance frames and concentrically braced frames, whose seismic behavior needs to be improved under a seismic retrofitting scheme. Some investigations proposed buckling-restrained braces (BRBs) for improving the performance of buildings (e.g., see [1,2]), while some novel investigations proposed column with replaceable SSD [3], box-shaped SSD [4], block slit damper [5], semi-active damper [6], and infill walls [7,8] for controlling the vibration of buildings. Moreover, some improvements in the behavior of the BRB are known as double-stage yield buckling-restrained brace (DYB) can be a novel energy dissipative device [9].

In DYB, a steel core is made of two BRB units known as small segment and large segment with different yield forces that are connected in series and are controlled by the length of small and large holes. When a DYB is subjected to an axial load (i.e., tension and compression), it behaves elastically under lower amount of loads, and then, the small segment deforms plastically when it yields, while the large segment is in elastic behavior. The control of this behavior depends on the size of small and large holes. Following to this, buckling-restrained mechanism recovers stiffness and restarts to deform elastically and then plastically until second yielding is achieved by a large segment of DYB [10]. This dual-stage behavior helps to prevent sudden and excessive deformation that may result in structural damage or failure during an earthquake while preventing the dissipative ability in lower-intensity seismic loads. Moreover, the steel core can be easily repaired or replaced by a new one after damage caused by seismic excitations, while the steel casing can be used repeatedly. The axial force is transferred through the steel core that yields and dissipates energy while the buckling-restraint mechanism avoids buckling of the core. Therefore, as proposed by researchers, both DYBs and BRBs can be used to improve the stiffness of existing structures that are erected in seismic regions as well as to repair buildings damaged

* Corresponding author at: Faculty of Civil and Environmental Engineering, Gdańsk University of ƤTechnology, ul. Narutowicza 11/12, 80-233 Gdansk, Poland.
E-mail address: farzin.kazemi@pg.edu.pl (F. Kazemi).

https://doi.org/10.1016/j.engstruct.2024.118427
Received 18 December 2023; Received in revised form 18 May 2024; Accepted 9 June 2024
Available online 25 June 2024
0141-0296/© 2024 Elsevier Ltd. All rights are reserved, including those for text and data mining, AI training, and similar technologies.

during earthquakes [11,12].

Cahís et al. [13] introduced a novel core of BRB consisting of a rectangular core shaped into two coplanar bands that can dissipate energy in acceptable promising efficiency. While the resistance of the core plays a key role in the behavior of BRB, Zheng et al. [14] investigated the BRB specimens having double restraints in around the core constructed from steel tubes to prevent buckling. Reducing the weight of the BRBs can help the device to be implemented easily and this leads to the invention of all-steel BRBs [15]. Studies show that the main concern in DYB is the performance of a small segment since this segment plays a crucial role in dissipating the energy of the seismic load. Therefore, Lu et al. [16] proposed adding a frictional damper in parallel to the small segment of DYB to improve the dissipative ability. Their experimental results confirmed the ability of the friction damper and improvements in the behavior of DYB. Zhang et al. [17] proposed to have two different cores for DYB, then, it would be possible to change each of them after seismic excitations. This can increase the reparability of the DYB and reduce the retrofitting cost. Yang et al. [18] proposed two parallel DYB cores to be installed in one element. This may reduce the number of DYBs in one bay just by implementing one DYB which may help to reduce the weight of the bracing system, while it can improve the seismic behavior and residual drift of the system [19].

The SSD is a passive energy dissipation device designed to enhance the seismic performance of structures. Its behavior is characterized by its ability to absorb and dissipate seismic energy, reducing the structural response during earthquakes. The SSD primarily operates through inelastic deformation and frictional sliding. The friction coefficient serves as a critical parameter influencing the performance characteristics of SSD, directly affecting their ability to absorb and dissipate energy during seismic events. Variations in the friction coefficient can significantly affect the dampers' effectiveness in mitigating structural vibrations and seismic forces. Over time, the repeated cycles of loading and unloading during seismic events can lead to wear and tear on the surfaces of the SSDs, affecting their frictional properties. As the SSDs experience more cycles of motion, the contact surfaces may undergo changes, potentially resulting in alterations in the friction coefficient. During the manufacturing process of SSDs, variations in material properties, surface finish, and fabrication techniques can lead to some differences in the friction coefficient among individual dampers. It is noteworthy that the friction behavior of device can change during each assembling; therefore, to provide a similar testing condition for all specimens, the frictional behavior of device between core and U-shape has been neglected due to the use of lubricant. More investigations were conducted by Ke et al. [20] using the behavior of SSD in a hybrid energy device attached to the end of a brace. Zhou et al. [21] applied SSDs on both ends of the brace and the results of investigation indicated that increasing the length of strips did not adversely affect the effectiveness of the SSDs. Oh and Park [22] examined the impact of unexpected tensile loads on a flexural yield SSD through experimental analysis. Results showed a parallelogram-shaped hysteresis under shear load and a butterfly-shaped curve under combined loading. Despite similarities in plastic deformation capacity and absorbed energy, the damper under additional tensile load exhibited unstable energy due to out-of-plane deformation. Although the SSD is mostly used for bracing systems, Naeem and Kim [23] used SSDs in parallel to be implemented in steel shear walls. Therefore, SSDs can be considered as the energy-dissipative devices in which the stiffness and deformations can be designed and controlled.

In this paper, the idea of using a novel double-stage yield steel slit damper-buckling restrained brace (SSD-DYB) is developed and experimentally tested to use both the ability of steel slit damper (SSD) and DYB in one device. Different shapes of SSD-DYB have been considered in the study to find out the effects of the number of strips, strip shape, and the width of a large segment. After some experimental tests, nine geometric configurations of steel cores have been optimized and introduced. To determine the hysteretic behavior and load-carrying mechanism of specimens, all specimens have been subjected to cyclic load. Moreover, the failure mechanism of each SSD-DYB has been determined and described in detail.

2. Modeling of SSD-DYB

2.1. SSD mechanism

The total dissipative device has two main parts, i.e. SSD in the small segment and DYB in the large one, which can provide a smooth transition from the energy dissipative segment of SSD to the stiffness segment of DYB. This section aims to provide a description of the design of SSD and the calculation of the number of strips that can play a key role in controlling the amount of dissipative energy. Fig. 1 illustrates the mechanism of SSD having one and two lines of strips under lateral load. Small height to width ratio (i.e., h/b) for strips can change the behavior of SSD mostly under the control of shear load, while increasing h/b can lead to both shear and bending behavior. Therefore, each strip can resist a specific shear load and bending moment during dissipating the energy under cyclic load. Fig. 2 illustrates the mechanism of one strip of SSD under lateral load. To control the failure part from the start of the strip, it is recommended to increase the width by r, which is the radius of holes in the plate.

According to Fig. 2, the deformation of shear and bending moment for one strip can be determined as:

$$\delta_t = \frac{Ph^3}{12EI} + \frac{Ph}{5/6 \times b \times t \times G} \tag{1}$$

where E is the elastic module which is approximately 2.5 times of shear modules, G, t is a strip thickness, and I is the moment inertia of the strip. By changing the parameters, Eqs. (2) and (3) can be used to determine the deformation, δ_t, and stiffness, K_{strip}, of one strip of SSD:

$$\delta_t = \frac{Ph^3}{Etb^3} \times \left(1 + 3\frac{b^2}{h^2}\right) \tag{2}$$

$$K_{strip} = \frac{Etb^3}{h^3\left(1 + 3\frac{b^2}{h^2}\right)} \tag{3}$$

It should be added that the height of the strip can be assumed based on the mechanism presented in Fig. 2, and the number of strips (n) can be multiplied by the stiffness determined in Eq. (3) to achieve the total stiffness of SSD with one line strips. Moreover, the calculations confirm that, for two lines of strips (see Fig. 1), the stiffness is determined as half of Eq. (3). Literature review shows that the concentration of shear force on the ends of strips can lead to a failure mechanism on the strips; hence, it could reduce the total capacity of the SSD [24]. This also can be expectable regarding the equations introduced. Therefore, in this research, different shapes of strips have been considered by increasing the width of strips' end to investigate the effects of strip shapes on the behavior of the SSD. It is expected by changing the shape of strips, the failure defects of end of strips would be improved. Fig. 3 presents different shapes and dimensions of strips used for SSDs.

2.2. DYB mechanism

The idea behind the use of DYB is to control and manage the ductility and energy dissipation capacity of a structure during seismic events. DYB is designed to provide two distinct stages of yielding under seismic loading, offering a controlled and gradual response to the applied forces. The first stage of yielding in a DYB brace allows for initial energy dissipation and deformation, while the second stage provides additional yielding and damping capacity. This dual-stage behavior is intended to prevent sudden and excessive deformation that could lead to structural

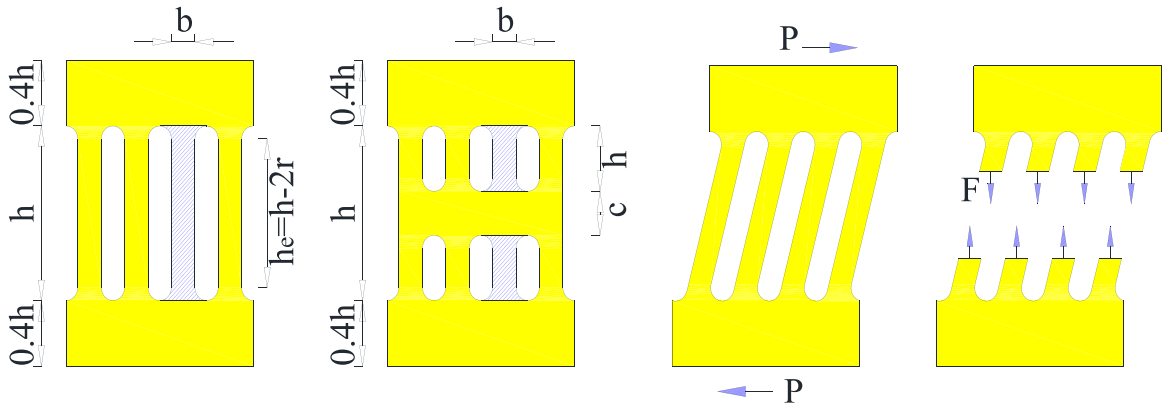

Fig. 1. Mechanism of SSD having one and two lines of strips under lateral load.

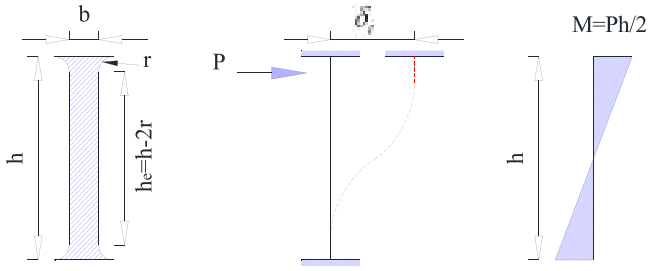

Fig. 2. Mechanism of one strip of SSD under lateral load.

damage or failure during an earthquake. Fig. 4 illustrates the ideal hysteretic behavior of DYB having small and large segments. The F_D and F_B values are depended to the width of cores in the small and large segments. However, the small and large holes in DYB play a crucial role on the changing part of hysteresis curve. It should be noted that it is possible to modify the size of small hole in a way to start the elastic behavior of large segment before reaching ultimate capacity of small segment. The skeleton curve (i.e., blue line) indicates the small segment yield (point B), the tolerance deformation of the small BRB (point C) that is controlled by small hole, the large segment yield (point D), and the tolerance deformation of the large BRB (point E) that is controlled by large hole. By controlling the ductility and energy dissipation through a double-stage yield mechanism, DYBs help enhance the seismic performance of a structure, reducing the risk of structural damage and ensuring the safety of the building and its occupants during a seismic event. In fact, DYB has the ability to control lower seismic events that may cause local damages mostly on non-structural components or even structural elements, while BRB remains elastic during these seismic loads and does not dissipate energy.

2.3. SSD-DYB behavior

The proposed SSD-DYB is an advanced structural element that can be implemented in seismic-resistant building design. It combines the features of a BRB with an SSD and provides a two-stage yield performance that can work as a fuse in the structure and reduce the risk of main structural damage. The SSD-DYB offers two distinct stages of energy dissipation and deformation capacity, which can help to control and enhance the seismic behavior of a building. Fig. 5 illustrates the ideal hysteretic behavior of SSD-DYB. In the first stage, the SSD component starts yielding and absorbing the energy (i.e., the green shadow in Fig. 5), allowing for further deformation of the brace while still

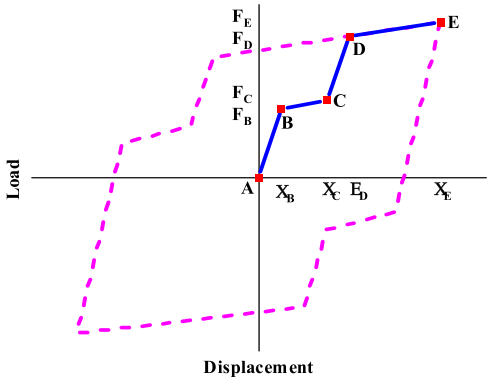

Fig. 4. Ideal hysteretic behavior of DYB.

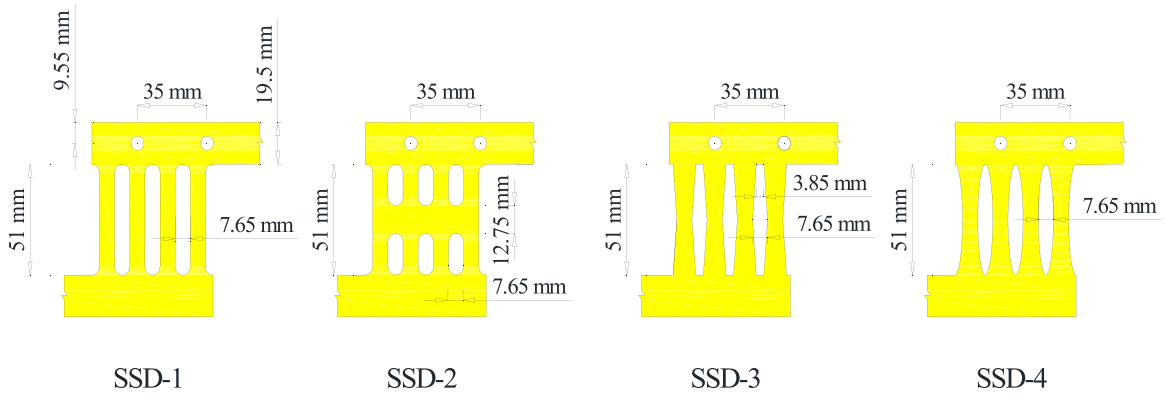

Fig. 3. Different shapes and dimensions of strips used for SSDs.

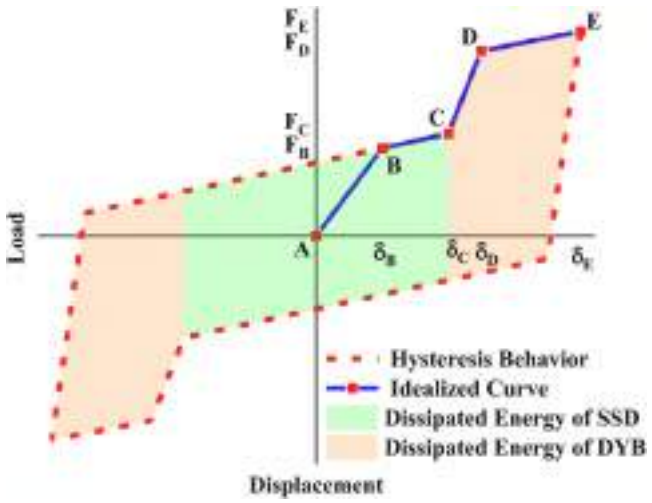

Fig. 5. Ideal hysteresis behavior of SSD-DYB.

providing resistance to lateral forces. This yielding is intended to prevent abrupt and excessive displacements during a large seismic event, increasing the structure's resilience. The amount of dissipated energy can be controlled by the number, size, and shape of the strips. In the second stage, the large segment behaves like a traditional BRB. It remains relatively stiff until reaching its specified yield strength. During this stage, the brace provides significant lateral stiffness to the structure, helping to limit lateral drift and displacement. The secondary yielding stage is characterized by the brace undergoing plastic deformation while maintaining its load-carrying capacity (i.e., the orange shadow in Fig. 5). The core size in the large segment can control the capacity of this part. The SSD-DYB's dual-stage behavior is advantageous for seismic design because it provides controlled energy dissipation and deformation capacity. It helps prevent the structure from experiencing excessive damage during a large earthquake by gradually releasing energy. This combination allows for effective seismic performance and enhances the building's safety by maintaining strength and stiffness while dissipating seismic forces. In addition, the cores of SSD-DYB can be replaced easily to provide a retrofit scheme and reduce the cost of implementing a new device. It is noteworthy that due to the formulation of each segment, engineers can select and design these elements to meet the performance objectives of buildings (i.e., seismic demand).

As presented in Fig. 5, the large segment is not activated in fist yield stage presented by ABC line, and due the series connection of the two segments, the first stiffness of the SSD-DYB can be calculated by:

$$K_{AB} = \frac{K_{SSD}.K_{DYB}}{K_{SSD} + K_{DYB}} \tag{4}$$

where K_{SSD} and K_{DYB} present the stiffness of small and large segments, respectively. It can be seen that SSD is yielded at point B; therefore, the deformation and force at yield point of SSD (i.e., δ_B and F_B) can be calculated as:

$$F_B = \delta_B \times \frac{nEtb^3}{h^3\left(1+3\frac{b^2}{h^2}\right)}$$
$$\delta_B = \delta_{\text{yieldSSD}} + \Delta_{\text{elasticDYB}} \tag{5}$$

where the δ_{yieldSSD}can be determined based on Eq. (2), and elastic deformation of DYB can be calculated by:

$$\Delta_{\text{elasticDYB}} = \frac{\sigma_{yield}A_{SSD}}{EA_{DYB}}L_{DYB} \tag{6}$$

where A_{SSD} and A_{DYB} illustrate sectional areas of SSD and DYB segments.

At point C presented in Fig. 5, the deformation reaches small hole and the DYB segment is activated. Therefore, the deformation and force at the end of the first stage (i.e., δ_C and F_C) can be calculated as:

$$F_C = F_B + \alpha K_{SSD}(H_{SSD} - \delta_B); \alpha = 0.01$$
$$\delta_C = \delta_B + \frac{F_C - F_B}{\alpha K_{SSD}} \tag{7}$$

where H_{SSD} is the clear length of small hole reducing the bolt size. In the second stage, the SSD has reached its limited deformation and the DYB is in elastic state until point D, which is the yield point of DYB. It is noteworthy that, in this stage, the stiffness of SSD-DYB, $K_{SSD\text{-}DYB}$, as well as the deformation and force at this point (i.e., δ_D and F_D) can be determined as follows:

$$K_{SSD-DYB} = \frac{K_{DYB}.K_{U-shape}}{K_{DYB} + K_{U-shape}}$$
$$F_D = \sigma_{yield}A_{DYB} \tag{8}$$
$$\delta_D = H_{SSD} + \frac{\sigma_{yield}}{E}L_{DYB}$$

Assuming point E as final stage of reaching to large hole of device, the deformation and force (i.e., δ_E and F_E) can be calculated as follows:

$$F_E = F_D + \alpha K_{DYB}(H_{SSD} + H_{DYB} - \delta_D); \alpha = 0.01$$
$$\delta_E = H_{SSD} + H_{DYB} \tag{9}$$

where H_{DYB} is the clear length of large hole reducing the bolt size. It should be clear that the small and large holes (i.e., H_{SSD} and H_{DYB}) can be used to adjust the behavior of the proposed SSD-DYB device.

3. Experimental test

3.1. Design procedure of SSD-DYB

For the purposes of experimental study, a single-span steel frame, as presented in Fig. 6, has been designed with a bay length of 6 m, and height of 3 m, in which, the inverted chevron SSD-DYBs with a length of 3.5 m (without connections length and gap for performance of bracing system) can be placed. Then, the SSD-DYB has been rescaled to 1/5 times its real size to be investigated in the experiment test. It should be noted that the scaling of elements has been done by considering the dimensional analysis. Due to limitation of the laboratory facilities, there was no possibility of conducting a full size test. However, a scaled size of a real device has been prepared and tested having different assembling of cores to provide a detailed description of device behavior.

According to the design approaches introduced by López and Sabelli [25] and Güner and Topkaya [26], the BRB elements have been designed and the specific parameters have been controlled. In addition, all

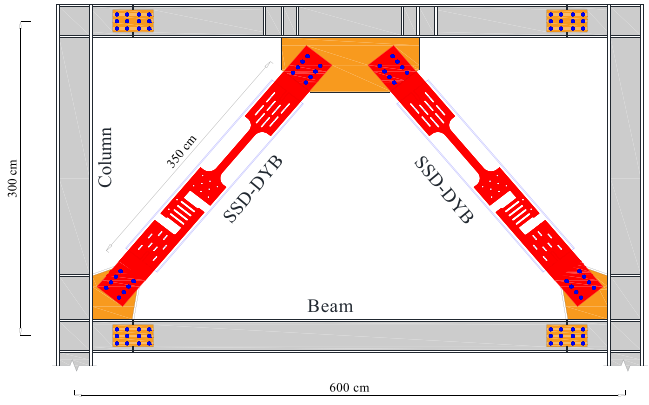

Fig. 6. Details of a single-span steel frame and SSD-DYB device used for the bracing system.

requirements for the design of steel structures according to ASCE 7–22 [27], AISC 360–22 [28], and AISC 341–22 [29] have been met. Different shapes of SSD-DYB have been considered to find out the effects of the number of strips, the shape of strips, and the length-to-width ratio of large segments. Fig. 7 illustrates the details of SSD-DYB specimens used for the experimental test. In each of the specimens, the shape and width of SSD-DYBs have been changed to investigate the difference between them.

The as-built U-shape case has been used to protect each cores of SSD-DYB from buckling and fulfill the need for the dissipative device. The core plates, as depicted in Fig. 7, adhere to a width of 90 mm and a length of 700 mm, which corresponds to the construction of the main cores of the SSD-DYBs. Furthermore, to control the width-to-length ratio of the cores, the width-to-length ratio of the small and large segments are limited to 0.153 and 0.157 that follows the investigation conducted by Sun et al. [10]. Fig. 8 presents the details of the as-built U-shape case used for the experimental test. It is noteworthy that the as-built U-shape case has two times the thickness of the cores to be sure the failure only occurs on the cores. However, Fig. 8 reveals that the U-shape encompasses the cores within its 110 mm width and 625 mm length, ensuring compatibility with the cyclic loading behavior. To control the inside buckling of the as-built U-shape case, some stiffeners have been considered in the small and large segments of the core. Moreover, to reduce the total weight of the dissipative device, the size of the top and bottom plates has been reduced based on the needs of the device. Therefore, one advantage of the novel SSD-DYB is its weight, since it has lower weight, as compared to other similar elements. While the core plates utilized in this investigation may be smaller in scale, comparing to a full-size test, they serve as an initial platform for comprehending the fundamental behavior of the proposed bracing system. Nonetheless, these models can potentially serve as verification tools for subsequent numerical simulations.

To prepare the dissipative device, the SSD-DYB core has been considered inside of the as-built U-shape case as presented in Fig. 9. Then, the top and bottom plates and bolts have been connected to fix the lateral buckling of the core. In addition, the inside bolts have been considered for three parts of holes named small holes, which control the movements of the small part, the middle holes, which fix the cores to the as-built U-shape case, and the large holes, which control the movements of large part. Except for the middle holes that are needed to fix the cores to the as-built U-shape case, the small and large holes can be defined according to the need for structure for the dissipative device and the capacity of the core.

In this research, the small holes equal to 19.5 mm have been

Fig. 7. Details of DYB and SSD-DYB specimens used for experimental test.

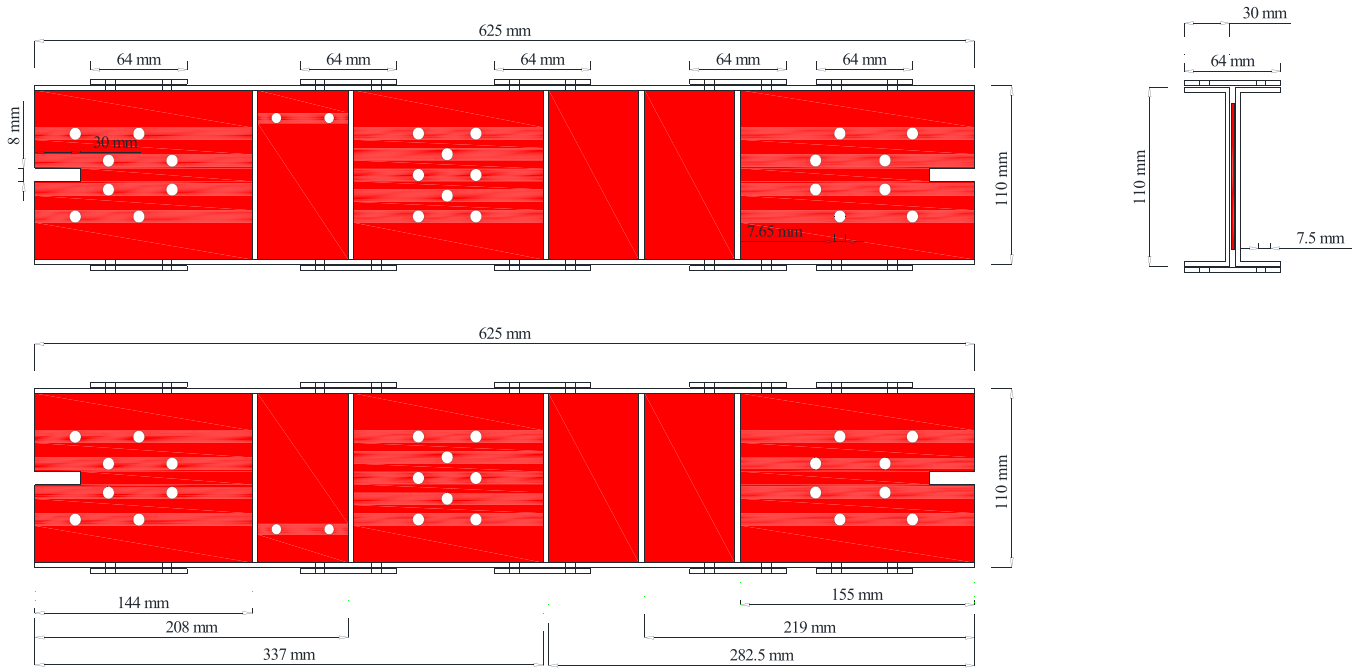

Fig. 8. Detail of the as-built U-shape case used for the experimental test.

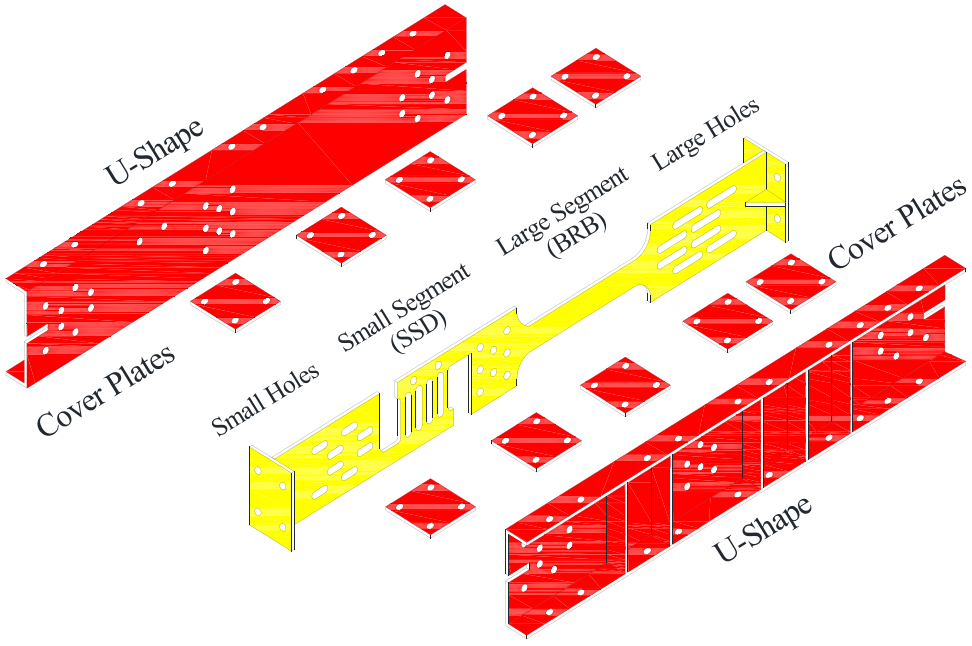

Fig. 9. 3D view and placement of the SSD-DYB core in the as-built U-shape case.

considered to have movements of ± 6.5 mm, and the large holes equal to 39.5 mm have been considered to have movements of ± 16.5 mm. These holes control the first and second stages of the SSD-DYB performance. It should be mentioned that the length of the holes for each segment has been calculated based on the capacity of SSD and DYB as discussed in previous sections. After providing the details for SSD-DYBs, the cores, and U-shape have been constructed by welding end-plates, and the cores have been placed in the U-shapes using high-strength bolts (i.e., M10–8.8) to be prepared for experimental tests. It should be mentioned that the laser cut has been done for all cores to avoid stress concentration. Fig. 10 illustrates the SSD-DYB cores for the first part of the experiment having five strips of SSD and a width of 50 mm for the large segment. After testing the first part, the cores have been updated with some changes. Fig. 11 presents the SSD-DYB cores for the second part of the experiment having four strips of SSD and a width of 20 mm and 30 mm for the large segment. Moreover, for experimenting with the SSD-DYB, the T-shapes have been connected to the end of the element and fixed to the universal testing machine. Fig. 12 illustrates the test setup using the universal testing machine (Zwick/Roell Z400) with ability to have both cyclic and tensile tests up to 400 kN loading force. Displacements have been measured using displacement sensor integrated with the machine traverse, while force has been measured by a measuring head integrated with the machine. The internal gauges have been used to check the failure of small and large segments during the test

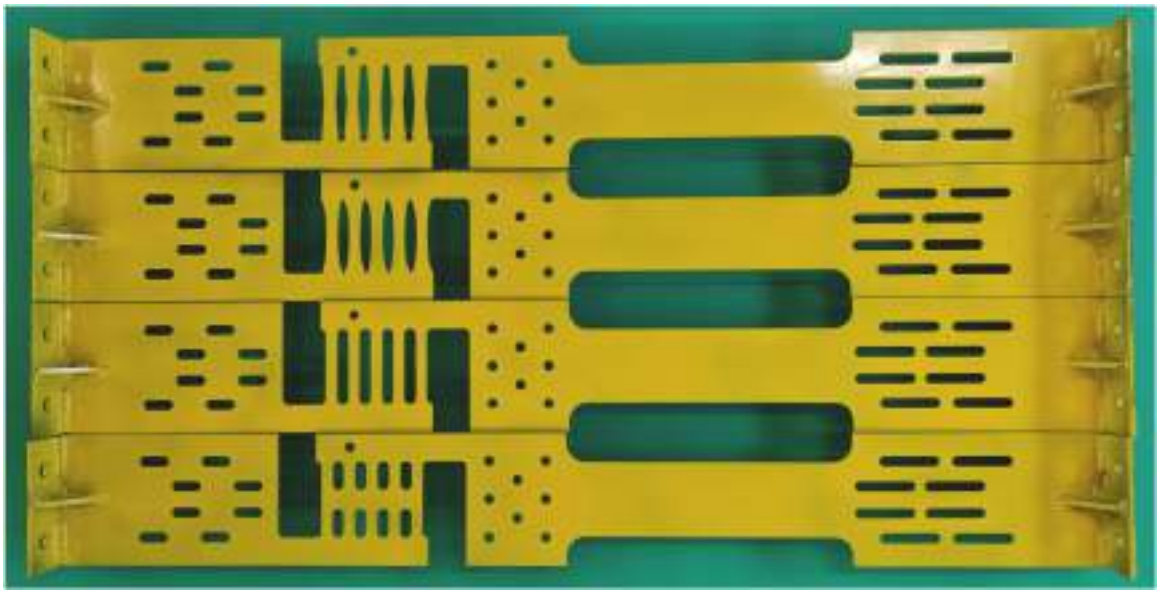

Fig. 10. SSD-DYB cores for the first part of experiment having five strips of SSD and width of 50 mm for the large segment.

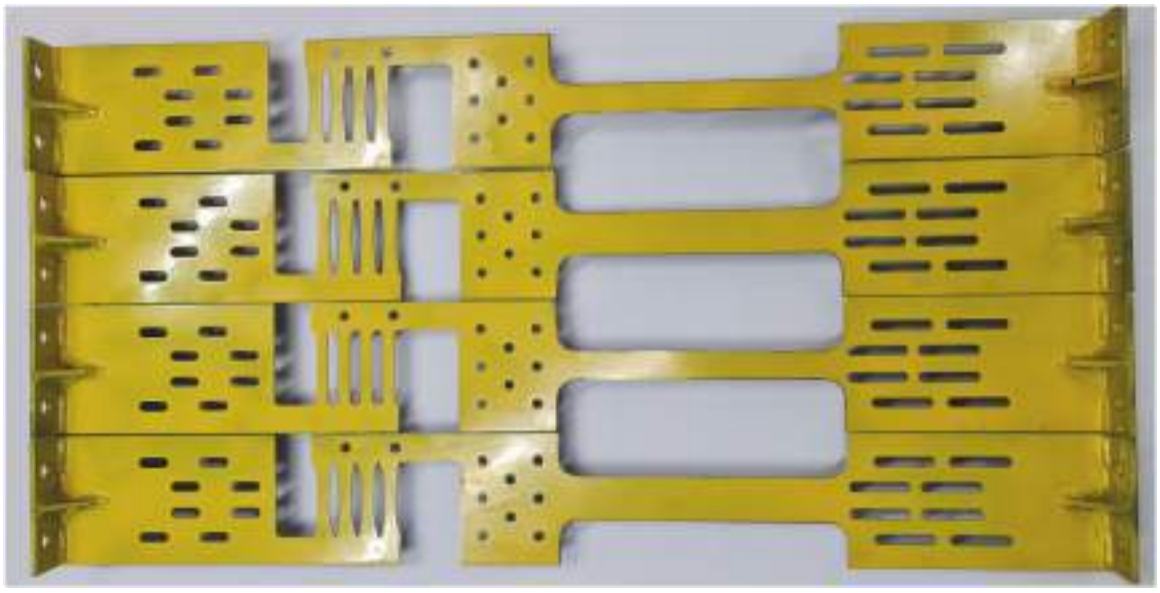

Fig. 11. SSD-DYB cores for the second part of experiment having four strips of SSD and width of 20 mm and 30 mm for the large segment.

and control the failure parts of element. The universal testing machine has the ability to collect data regarding the experiment and further preprocessing of data has been carried out by the authors.

Preparing the proposed SSD-DYB device to be useful either in lower-, or higher-intensity seismic loads can make it clear that the device can be used in any seismic-prone area with dissipative ability. However, using the proposed device provides this ability to control and construct devices having different stages of initial load capacity according to the design process, while the total weight of device has been reduced accordingly. Moreover, the steel core can be easily repaired or replaced by a new one after being damaged caused by seismic excitations, while the steel casing can be used repeatedly. Incorporating instrumentation into SSD-DYB for assessing their remaining service life aligns with the growing trend of structural health monitoring. By integrating sensors and monitoring devices into SSD-DYB device, engineers can gather real-time data on different factors, like strain and stress, enabling proactive maintenance and assessment of structural integrity. Furthermore, this approach enhances safety and allows for more informed decisions regarding the maintenance and replacement of SSD-DYBs, ultimately contributing to the overall reliability and performance of structures. The proposed SSD-DYB device has spaces between the top and bottom plates, as presented in Fig. 13, which can provide a vision-based control on the core as well as possibility of assembling controlling gauges on the device.

3.2. Loading protocol

The protocol used in this research is based on the assumption of three stages for the failure of the first segment and two stages for the failure of the second segment. To examine the low-cycle fatigue capability of the newly proposed SSD-DYB brace, loading protocol recommended in the seismic design code for buildings (GB50011–2010) and has been investigated by Sun et al. [10] was determined. In each stage, two cycles have been defined and applied for the first load protocol (i.e., see Fig. 14

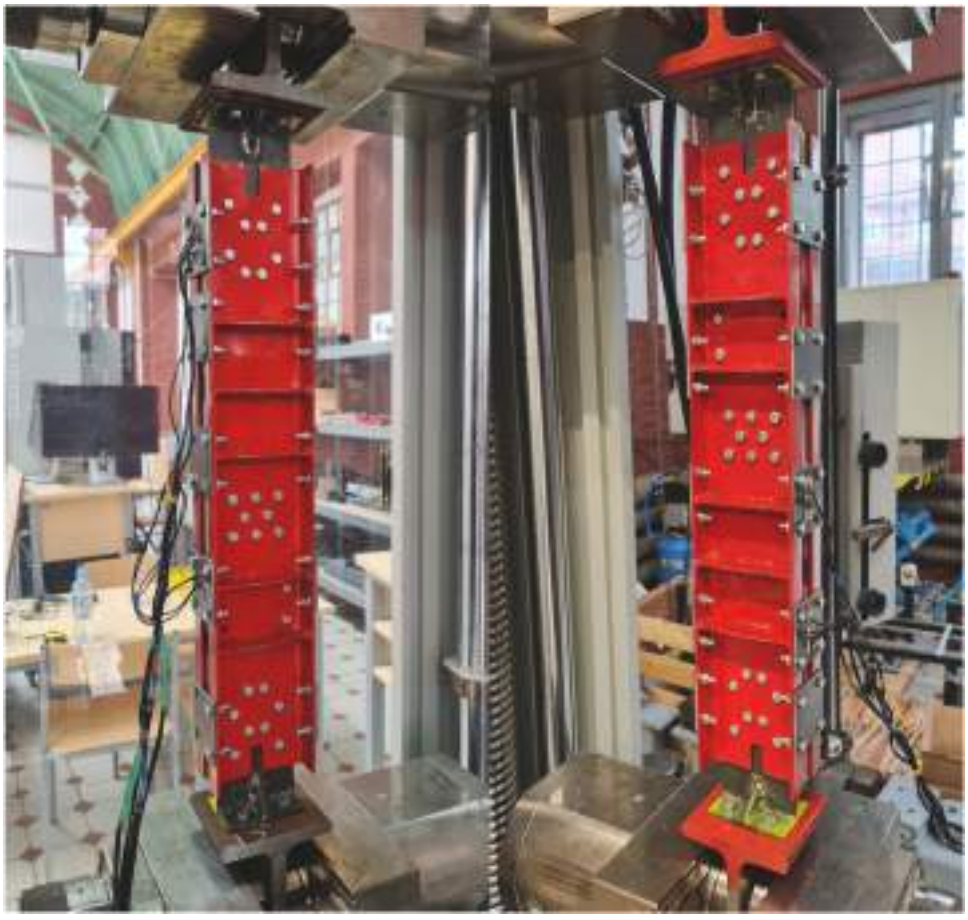

Fig. 12. Test setup of SSD-DYB device on the universal testing machine.

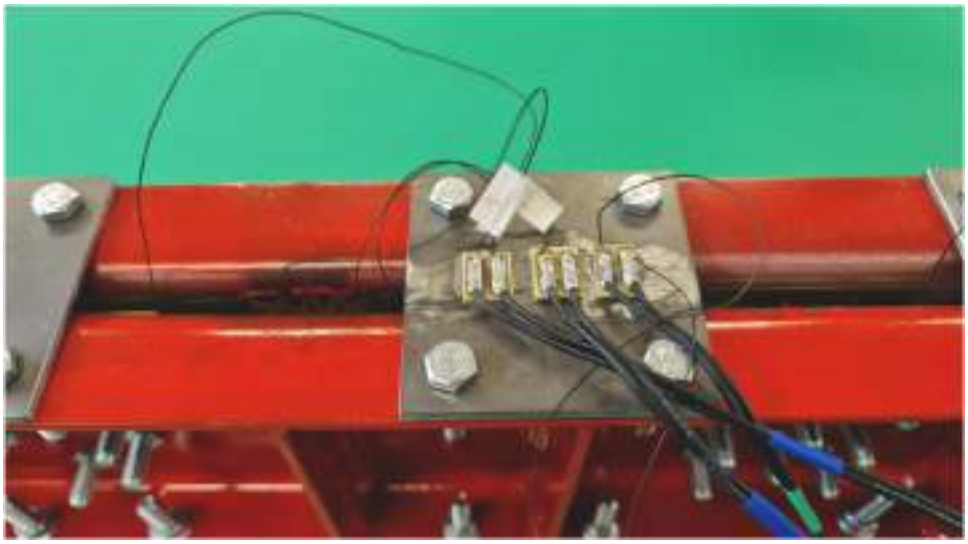

Fig. 13. Assembling of the gauges for controlling the core behavior and possibility of integrating sensors and monitoring devices into SSD-DYB device.

(a)), and to compare the effects of the loading protocol, the second loading protocol with five cycles in each stage has been defined (i.e., see Fig. 14(b)). At the end of the first stage, the maximum allowable deformation according to the holes of the small section is assumed as the controlling part, and then, the loads are moved to the large segment. This transition of loads between two segments can help the device to use the maximum capacity of each segment. Therefore, the SSD of the first segment is designed to have the maximum deformation, and based on this, the holes of the first segment are defined. It should be noted that the deformation of SSD can be determined based on Eq. (2) multiplied by the number of strips. According to the small and large holes of the cores, the loading protocol has been defined to simulate the behavior of the SSD-DYB under cyclic load.

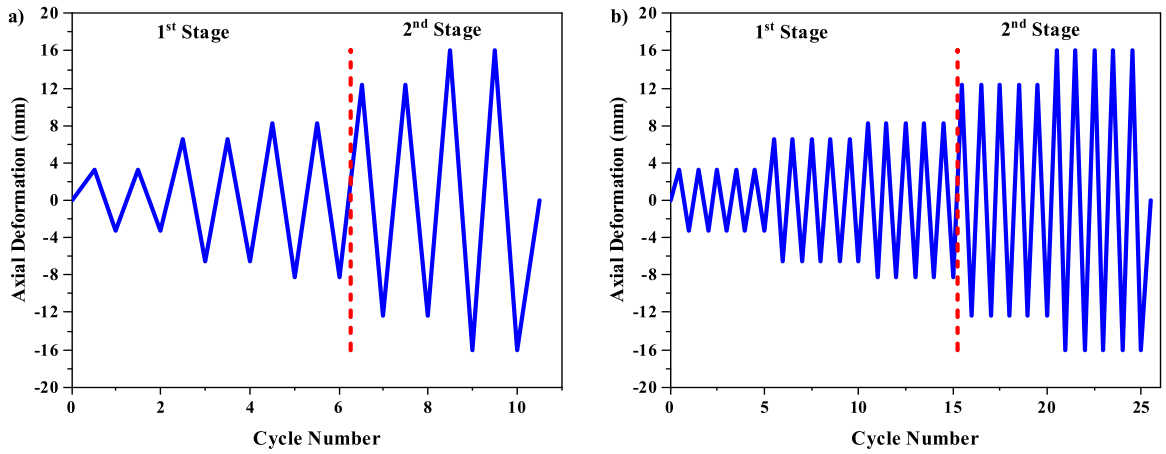

Fig. 14. Two loading protocols have been used in this research.

3.3. Tensile test of S235 and S355 steel materials

The steel material has a great influence on the behavior and failure mechanism of the SSD-DYB, and the correct selection of material properties can help designers to correctly estimate and design the device. In this section, two types of steel grades (i.e., S235 and S355) have been investigated to provide detailed information on the mechanical properties of the materials and how they can be used for designing the device. Meanwhile, in this research, the same material has been selected to have the confirmations of details of cores and U-shape, and control their ability to resist on different core material. Therefore, using the same material in the proposed device has been checked and it can work without local damages in U-shape. Fig. 15 presents the specimens used for material tests. For each material, two specimens have been used and the specimens have been prepared according to ASTM E8M-04. The specimens have been prepared with 2 mm thickness according to the thickness of SSD-DYB used in this research. The tensile test device has been controlled to have a speed of 0.1 mm/sec, and the result of the tensile test is illustrated in Fig. 16.

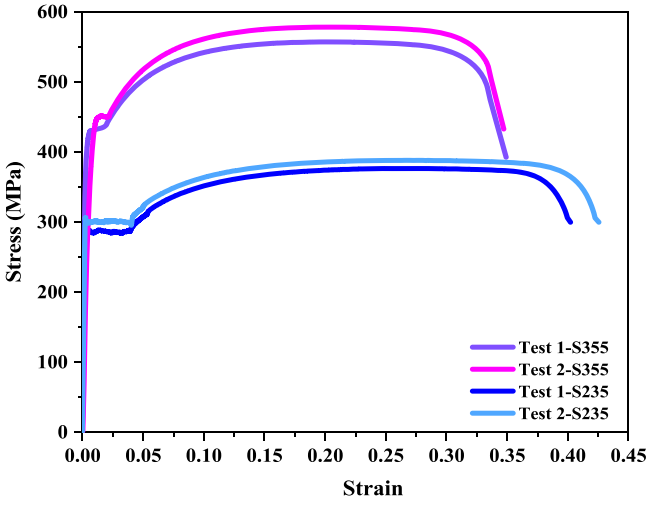

Fig. 16. Result of tensile test for four specimens.

Fig. 15. Tensile test of steel materials of S235 and S355.

4. Results of experimental test

4.1. Number of strips effects on hysteretic curve

As theoretically explained in Section 2, the number of strips can affect the stiffness of SSD, which can increase the loops of the hysteresis curve. The increase in the area of the loops of the hysteresis curve can lead to an increase in the dissipated energy. To investigate the influence of the number of strips, Figs. 17 and 18 illustrate the hysteretic curves of small segments of SSD-DYB-1 and SSD-DYB-2 having four and five strips, respectively. According to Fig. 17, the increasing number of strips has a great influence on the loop area of hysteresis curves, and the SSD-DYB-1 with five strips has a bigger hysteresis curve compared to SSD-DYB-1 with four strips. This can clearly show the effects of strip number on the stiffness and hysteresis curve. Additionally, according to Fig. 18, the increase in the stiffness of the SSD-DYB-2 with five strips is presented even though the amount of increase is lower than SSD-DYB-1 with five strips. The results confirm the idea of using strip numbers to control the small segment and its hysteresis curve for a specifically designed value that can be used for a selected performance level. This ability makes the SSD-DYB device a controlled device for designers that can ensure its specific performance in buildings.

To assess the energy content of the specimens (see Fig. 6), the dissipated energy in each loop of the hysteresis curve was determined. The total dissipated energy demonstrates the SSD-DYB's capacity to absorb energy during cyclic loading. The energy dissipated by SSD-DYB-1 with four strips amounts to 312.14 J, while for SSD-DYB-1 with five strips, it is 419.08 J. Thus, adding one strip to SSD-DYB-1 results in an increase in dissipated energy by 104.53 J, representing a percentage increase of approximately 33.5 %. Conversely, the energy dissipated by SSD-DYB-2 with four strips is 384.96 J, which is less than the dissipated energy of SSD-DYB-1 with five strips, measuring 431.93 J. Adding one strip to SSD-DYB-2 increases the dissipated energy by 46.97 J, indicating a percentage increase of around 12.2 %. Moreover, the results of experiments show that the SSD-DYB-1 has smaller initial stiffness compared to the SSD-DYB-2, which shows the effects of the shape of the SSD on the hysteresis behavior.

4.2. Effects of strip shape on hysteretic curve

The shape and size of the strips can influence the behavior of the hysteresis curve. This behavior can demonstrate the amount of energy dissipated and the performance of SSD-DYB. Fig. 19 compares different strip shapes of small segments of SSD-DYBs having four strips in the behavior of the hysteresis curve. It can be seen that the SSD-DYB-2 has larger loops and a steeper slope compared to other specimens. Accordingly, SSD-DYB-2 has the highest amount of dissipated energy among other specimens by 384.96 J. Comparing the SSD-DYB-1 with SSD-DYB-3 and SSD-DYB-4 reveals that the SSD-DYB-1 has lower amount of the dissipated energy by 312.14 J, while SSD-DYB-3 and SSD-DYB-4 have dissipated energies of 341.23 J and 347.16 J, respectively. The results confirm that taking different shapes of strips could influence the behavior of the hysteresis curve and correspondingly the amount of dissipated energy. Therefore, it is suggested to use the shape effects to achieve the desired capacity as expected in the design procedure. By selecting the SSD-DYB-1 as a reference, the specimens of SSD-DYB-2, SSD-DYB-3, and SSD-DYB-4 have increased the dissipated energy by 23.33 %, 9.32 %, and 11.22 %, respectively. In addition, by selecting the SSD-DYB-2 as a reference, changing the shape of strips can reduce the dissipated energy, for instance, the SSD-DYB-3 and SSD-DYB-4 reduced the amount of energy by 11.36 % and 9.82 %, respectively. Therefore, to increase or decrease the capability of SSD-DYBs, it is suggested to change the shape of strips rather than changing the numbers and thickness of the strips, since this can be used for optimizing the SSD-DYB for the expected performance.

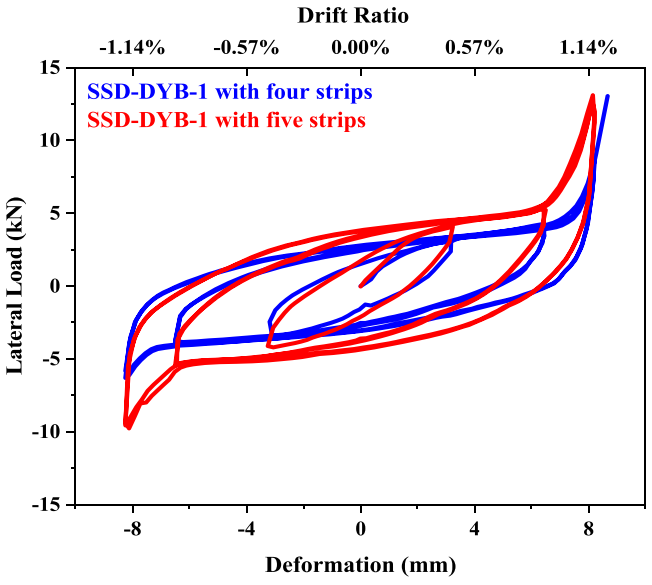

Fig. 17. Comparison of hysteretic curves of small segments of SSD-DYB-1 having four and five strips.

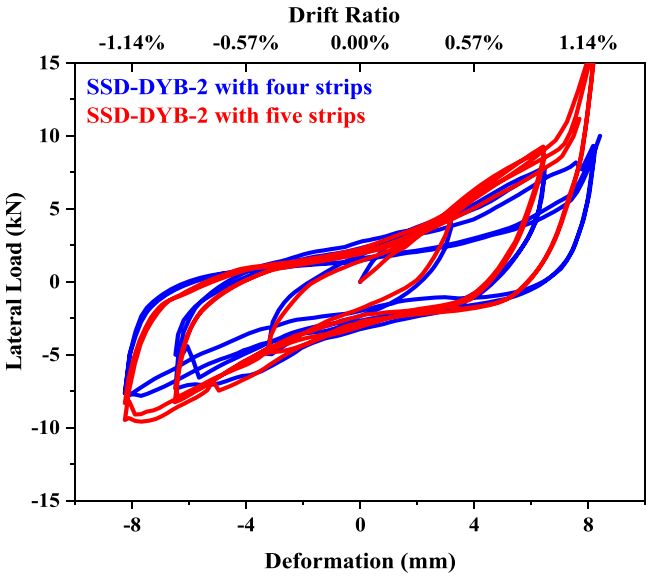

Fig. 18. Comparison of hysteretic curves of small segments of SSD-DYB-2 having four and five strips.

Fig. 20 illustrates types of failures of SSD-DYB-1 and SSD-DYB-5 after experimental tests under cyclic load. It is clear that the SSD-DYB-1 has failures on its strips and the proposed device is working in expected performance. In addition, the placement of holes and the number of holes for reaching this performance are well-selected and the failure of SSD occurs right before activating the large segment. In addition, considering the different widths of the large segments and their failure show that the large segment can carry on the excessive loads on the cyclic load to dissipate energy in the second stage. Furthermore, the number, length, and size of bolts for large segments satisfied the performance of the device.

4.3. Stopper effects on SSD-DYB behavior

The stopper of the SSD-DYB plays a crucial role in controlling the loads and deformation between two segments. The stopper works with the size of the small and large holes and the size of small and large holes

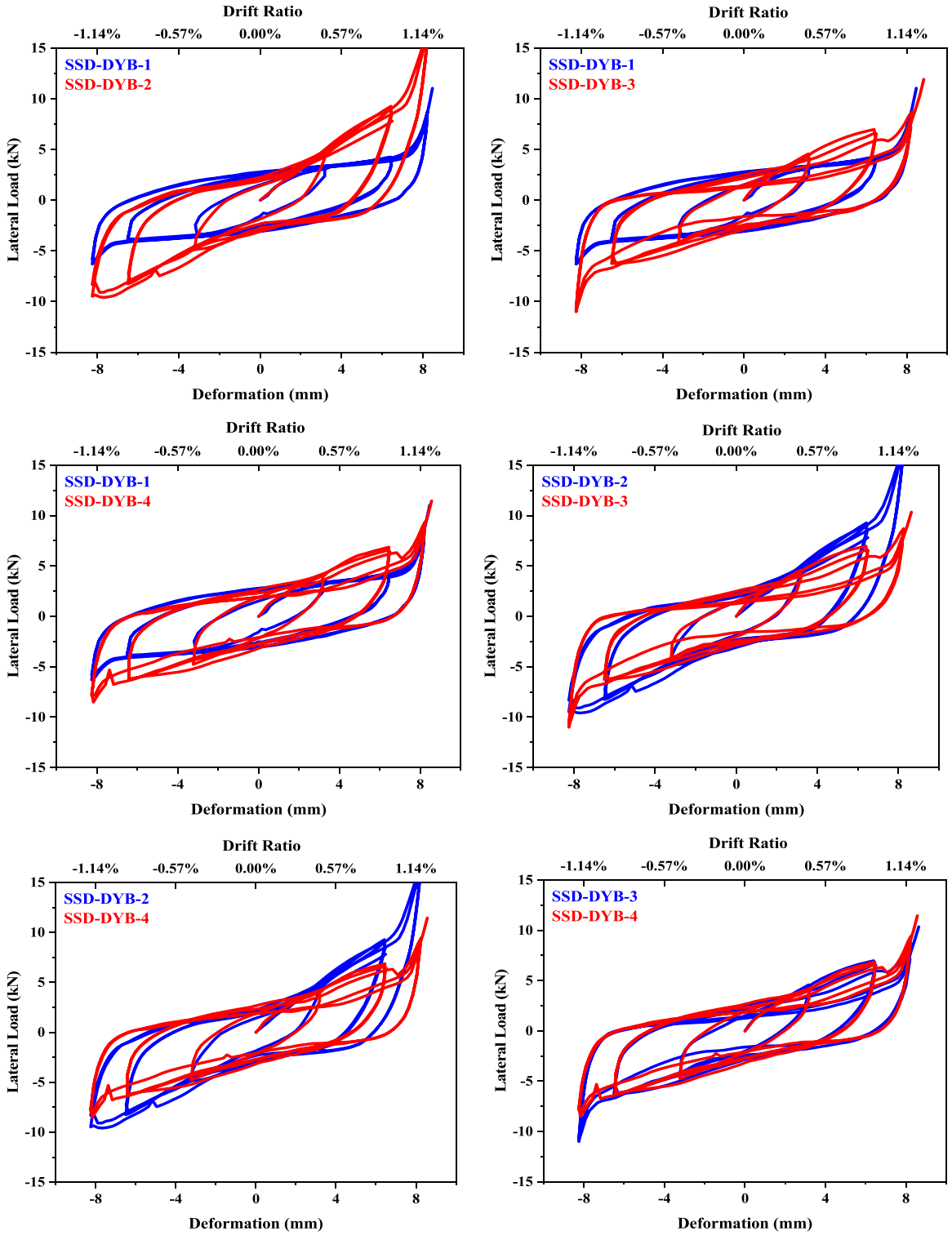

Fig. 19. Comparison of hysteresis curves of small segments of SSD-DYBs having four strips.

should be defined very precisely to use the maximum capacity of the first segment and transmit to the large segment just before failure of the first segment. The capacity of the SSD-DYB should be determined by structural designers, then, using this capacity and defining the performance of each segment, the maximum deformation of the SSD can be determined by equations presented in Section 2. The large segment holes can be considered based on the maximum capability of the DYB and the width of the large segment. In this study, the size of the small and large segments have been considered equal to 19.5 mm and 39.5 mm, respectively, in which, 6.5 mm has been added for bolt size. Therefore, the large hole is approximately 2.53 times the small one and they take the capacity of the SSD and DYB into account. Fig. 21 illustrates the hysteresis curves of SSD-DYBs under cyclic load. In Fig. 21(a), the difference of SSD-DYBs stems from the width of the large segments, and therefore, the second part of the hysteresis curves have different behavior. As expected, by increasing the width of the large segment from 20 mm to 30 mm (i.e., SSD-DYB-5 to SSD-DYB-1), the maximum capacity load has been increased from 18.68 kN to 27.06 kN (i.e.,

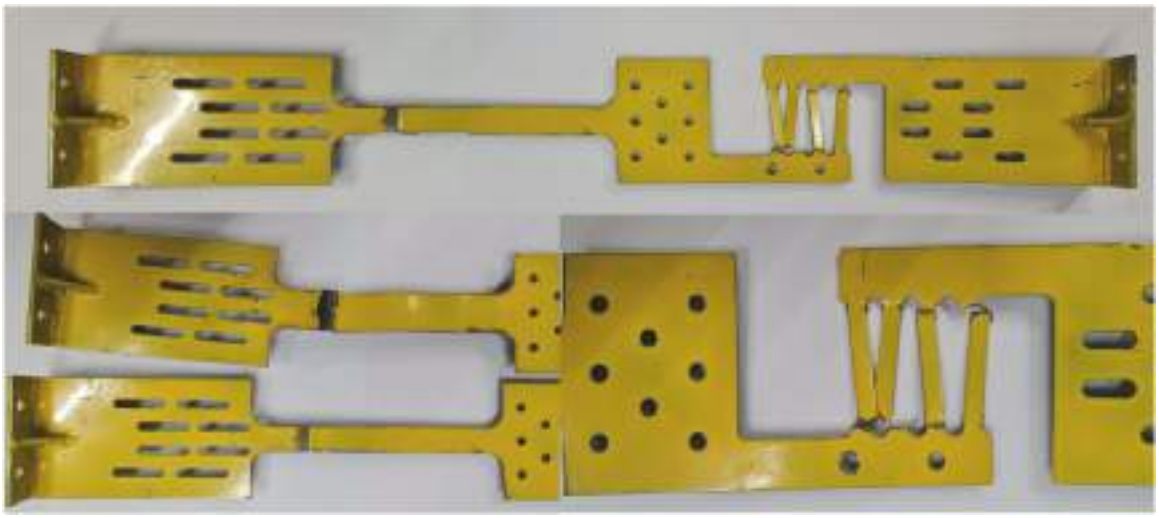

Fig. 20. Failures of small and large segments of the SSD-DYB-1 and SSD-DYB-5 after experimental test under cyclic load.

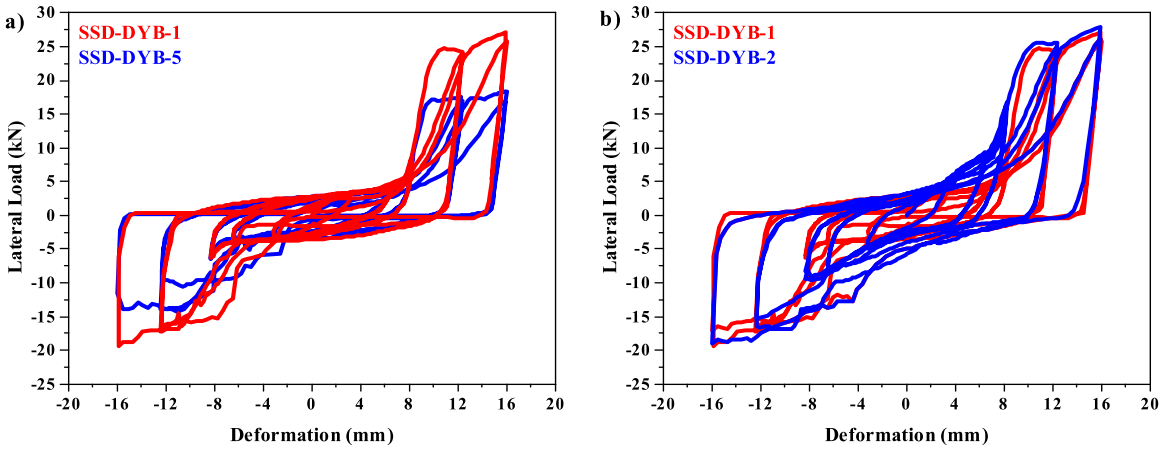

Fig. 21. Comparison of hysteresis curves of SSD-DYBs under cyclic load.

44.86 %). As presented in Fig. 21(b), by controlling the small segment, the pinching behavior of the total hysteresis curve of SSD-DYB-2 has been increased and the transition between the small segment and large segment is smoother than the hysteresis curve of SSD-DYB-1. This result shows that the proposed SSD-DYB device can be controlled by the designers and its performance can be estimated before designing of core. Moreover, it will be possible to change the size, shape, and number of strips to have different capacities and energy dissipation for the first and second segments. The dissipated energy of SSD-DYB-1 has been determined equal to 1513.44 J, which is higher than the dissipated energy of SSD-DYB-5 by 1128.63 J. In addition, by changing the shape of the SSD segment, the energy dissipated by SSD-DYB-2 has been increased to 1955.16 J, which is 29.18 % higher than the SSD-DYB-1.

Fig. 22 presents the elongation of large segments of SSD-DYB-2 and SSD-DYB-7 having widths of 30 mm and 20 mm, respectively, under cyclic load compared to unloaded SSD-DYB-1 specimens. It is clear that the elongation of 10 mm has been determined for the large segments of SSD-DYB, and these segments only have changes in their shape rather than the total failure that confirms their resistance for further cycles. In addition, there is no failure in the holes of the SSD-DYBs that show the correct number and size of bolts in all three zones.

4.4. Comparing DYB and SSD-DYB behavior

There are some main differences between the behavior of the DYB and the proposed SSD-DYB. In DYB, the failure of the first segment prevents to definition small width for the first segment of the core and there is no possibility of controlling the behavior of the small segment. This makes the DYB to be beneficial for a large initial load to get its yield capacity. In the proposed SSD-DYB, the small segment is definable and the designer can estimate the dissipative capacity of the small segment. As a result, the DYB behavior adds extra stiffness to the structures for the small deformations that can add extra unpredictable loads on the structural elements, while SSD-DYB behavior is different in this case. In the SSD-DYB element, the first segment works on the damping energy rather than adding extra stiffness to the structure. Therefore, in the same condition, the SSD-DYB dissipates energy in a small amount of load with its large deformations, while DYB just works in elastic behavior until reaching its yielding capacity. Fig. 23 presents the comparison of the hysteresis curves of the first segment of DYB compared to the SSD-DYB-1. It can be seen that the SSD-DYB-1 and DYB serve distinct roles in structural systems, and with lower applied force, the SSD-DYB-1 primarily contributes damping while the DYB provides stiffness. When the stiffness of a DYB is increased instead of enhancing its damping capacity, the dynamic response of the overall structural system undergoes specific changes because of increasing the overall stiffness of the structural system. This also can affect the structural elements of beams, columns, and connections to resist such loads as a result of being a displacement control element. Although it is possible to modify the dimensions of DYB to reach those lower initial stiffness and yield force, this may influence

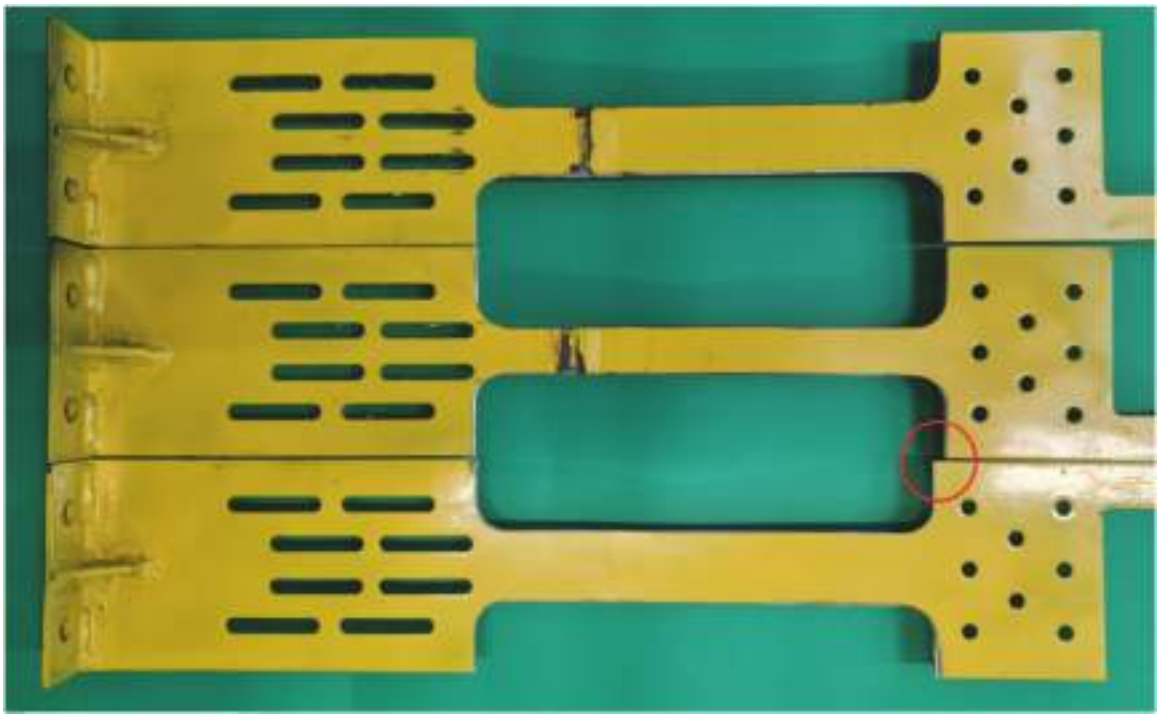

Fig. 22. Elongation of large segments of SSD-DYB-2 and SSD-DYB-7 having widths of 30 mm and 20 mm, respectively, under cyclic load compared to unloaded SSD-DYB-1 specimen.

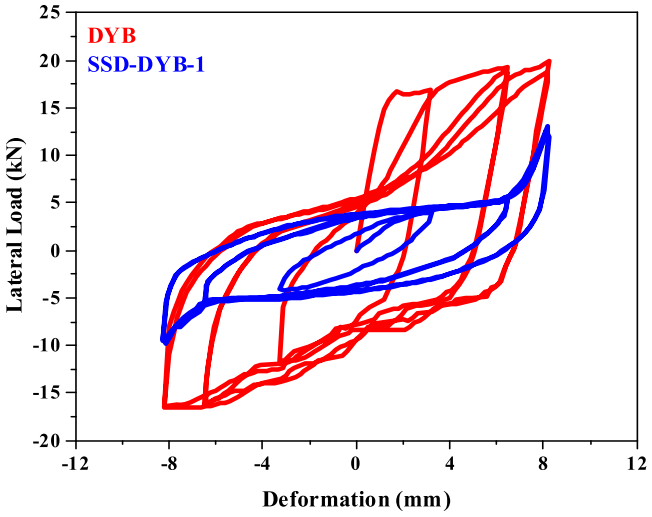

Fig. 23. Comparing the hysteresis curves of the first segments of DYB and SSD-DYB-1.

the possibility of buckling of internal segments of DYB as it is clear in Fig. 23 in compression loading. Therefore, there is a possibility that other components of the structure may experience heightened seismic forces, necessitating careful consideration in the design process. Moreover, the initial stiffness alters the natural frequencies of the system, potentially leading to a shift in the dominant vibration modes, and restricting its flexibility. As it is expected, the DYB has dissipated energy of 925.88 J which is approximately 2.2 times of SSD-DYB-1. It is noteworthy that the dissipated energy of SSD-DYB can be defined by different shapes, sizes, and strip numbers.

However, the DYB stiffness focuses on restraining lateral movements and enhancing structural rigidity, unlike the SSD segment which dissipates energy and reduces dynamic response. The proposed SSD-DYBs excel in dissipating seismic energy through the conversion of kinetic energy into heat. Their primary function is to enhance the structure's damping capacity during seismic events. In addition, the emphasis on damping contributes to a reduction in structural vibrations, thereby minimizing dynamic response and improving occupant comfort. If the deformation of the structure goes further, it can prevent this with the large segment of SSD-DYB. By adding damping to the structure by SSD-DYB we can increase total structural damping capacity to improve seismic resilience by reducing the structure's susceptibility to excessive deformations and accelerations. Moreover, it prevents sudden changes in structures since the large segment can add more stiffness to keep the structure in a stable condition. In addition to seismic benefits, SSDs can contribute to reducing wind-induced vibrations, enhancing the overall performance of the structure under service loads. On the benefit of the proposed SSD-DYB, the first segment (i.e., SSD) primarily affects damping characteristics that can result in lower impact on adjacent structural elements, potentially reducing the need for adjustments in their design. However, the large segment works to dissipate energy more than expected values in the large deformations.

4.5. Failure of SSD-DYB

In this section, the failure of SSD-DYBs and the way to prevent it have been discussed. To find out the effective width of the large segment of SSD-DYB, some additional experimental specimens have been considered, in which, the width of the large segment has been changed in the range of 20 mm, 30 mm, 40 mm, and 50 mm to find the effects of each width on the total behavior and failure of the SSD-DYB. Fig. 24 presents the failure of the connection of SSD-DYB having 50 mm width under cyclic load. It can be seen that the width of 50 mm can increase the total load capacity of the device and this leads to the failure of the connection.

Fig. 25 presents the failure of the U-shape and the connection of SSD-DYB having DYB width of 40 mm under cyclic load. The results show that increasing the width of the large segment to the total width of the SSD-DYB device by more than 38 % can increase the resistance of the total device more than the design load for connection and this has

Fig. 24. Failure of the connection of SSD-DYB having 50 mm width under cyclic load.

Fig. 25. Failure of the U-shape and the connection of SSD-DYB having 40 mm width under cyclic load.

resulted in a failure in the connection of the device to T-shape stand. Therefore, for having more values of width, the connection should be designed for the maximum load capacity of device or even 1.5 times to have safety factor. Due to assuming of U-shape as constant element of all tests, it should be noted that this failure may affect the U-shape case and there will be no possibility to use it anymore. To avoid this failure, the connection can be designed for carrying more loads. However, in this research, 1.5 time of maximum capacity of the SSD-DYB device (i.e., approximately 25 kN) has been selected as design force of connection (the connections have been designed for a maximum load of 40 kN). In addition, the buckling behavior of U-shape has been controlled by adding some stiffeners in the critical parts of device. To find the best placement, the effects of inner bolts to control bucking of U-shape have been considered. Therefore, the stiffeners have only been implemented on the small and large segments of the device to optimize the weight of total SSD-DYB. Experimental results confirm that the optimized placement of stiffeners can effectively resist the buckling behavior and there are no failure in these parts.

4.6. Optimized shape of SSD-DYB

In this section, the previously considered SSD-DYBs have been evaluated and the weaknesses of the proposed device have been improved. Since the core of SSD-DYB can resist different ranges of

seismic loads (i.e., earthquakes having different intensity levels), the failure of the core should be controlled in the area that dissipates more energy and prevents the failure. For this purpose, the corners of the large segment have been increased as presented in Fig. 26. This can help to move the failure section of the DYB to the middle of the length and helps to resist more cycles. In addition, previous results showed some failure in the connection of the element, hence, the device worked until the end of the loading protocol. To avoid this, the length of the connection stiffener has been increased taking the possible deformation of the core into account. Since the U-shape has no failure during the total test of specimens (except for final tests of increasing the length of large segments), there are no changes in the U-shape as it can resist loads in its current form. After preparing the optimized SSD-DYB, the test have been conducted to check the failure of the core. Fig. 27 presents the experimental test of the optimized SSD-DYB having five strips and a large segment width of 20 mm. It can be seen that, as expected, the failures occurred only in the small and large segments of the device what can guarantee the behavior of SSD-DYB under seismic loading.

To better illustrate the performance of the optimized SSD-DYB, it has been compared with BRB specimen with a segment width of 20 mm, as presented in Fig. 28. As it can be seen from the figure, the BRB specimen failed during the cyclic test while the optimized SSD-DYB remained until the end of cyclic loading, which confirms the superior resilience and durability of the optimized SSD-DYB. This outcome suggests that the design improvements made in the optimized SSD-DYB allow it to withstand cyclic stresses and strains more effectively, thereby enhancing its fatigue resistance and overall performance. This result is indicative of the potential benefits of incorporating such SSD-DYB device in seismic-resistant structural designs, leading to more robust and reliable systems for earthquake-prone areas.

Fig. 29 illustrates the hysteresis curve of small and large segments of optimized SSD-DYB (i.e., see Fig. 27) under cyclic load. The blue curve represents the hysteresis behavior of the small segment of the bracing system, which shows that the small segment has a relatively consistent energy dissipation capacity as indicated by the area enclosed within each loop. As it can be observed, the SSD behavior in small segment can work in symmetric way in both tensile and compressive load that can guarantee its response under cyclic loads. In addition, as it is discussed, it will be possible to control the behavior of small segment by modifying those parameters of SSD. The red curve depicts the hysteresis behavior of the large segment of the bracing system. As the loops progress from the origin, the slope decreases in both segments, indicating a reduction in stiffness, which is a typical behavior in hysteresis loops due to material yielding or damage. The inward bowing of the loops, especially noticeable in the large segment, could indicate buckling behavior in compressive loading. The nearly vertical lines during the unloading phase in both segments suggest that the unloading stiffness is relatively high, pointing to a quick return to near-zero deformation when the load is removed.

In addition, the hysteresis curves of the optimized SSD-DYB and BRB devices are compared in Fig. 30. It can be seen that the BRB device failed in the first stage of experimental test with deformation of 8 mm; however, the optimized SSD-DYB remained until the end of loading protocol with the deformation of 16 mm. This result confirm that the proposed SSD-DYB can resist more deformation, as compared to BRB device. Therefore, the optimized SSD-DYB has a higher capacity for energy dissipation and it can better accommodate inelastic deformations during seismic events. Consequently, this can lead to improved seismic performance in terms of reduced structural damage and lower risk of collapse during intense ground motions. It also suggests that incorporating DYBs into building designs could enhance the resilience and reparability of structures subjected to cyclic or seismic loading.

Fig. 31 compares the ideal hysteresis behavior expected for SSD-DYB with those obtained in optimized SSD-DYB, including the dissipated energy of both SSD and DYB components, and a hysteresis backbone curve that indicates the ideal expected behavior. The hysteresis curves are shown in blue and represent the actual response of the SSD-DYB to cyclic loading. The curves exhibit the characteristic pinched shape of hysteresis loops, which suggests that the system experiences stiffness degradation and pinching under cyclic loading. The loops are wide, indicating that the system can undergo significant deformation and is capable of dissipating energy through inelastic deformation. In addition, the shaded areas within the hysteresis loops represent the energy dissipated by the system during loading cycles by the SSD and DYB component. Larger shaded areas suggest greater energy dissipation capacity. The backbone curve traces the outermost points of the hysteresis loops and represents the idealized behavior of the system. This curve is expected to indicate the maximum capacity of the system to sustain

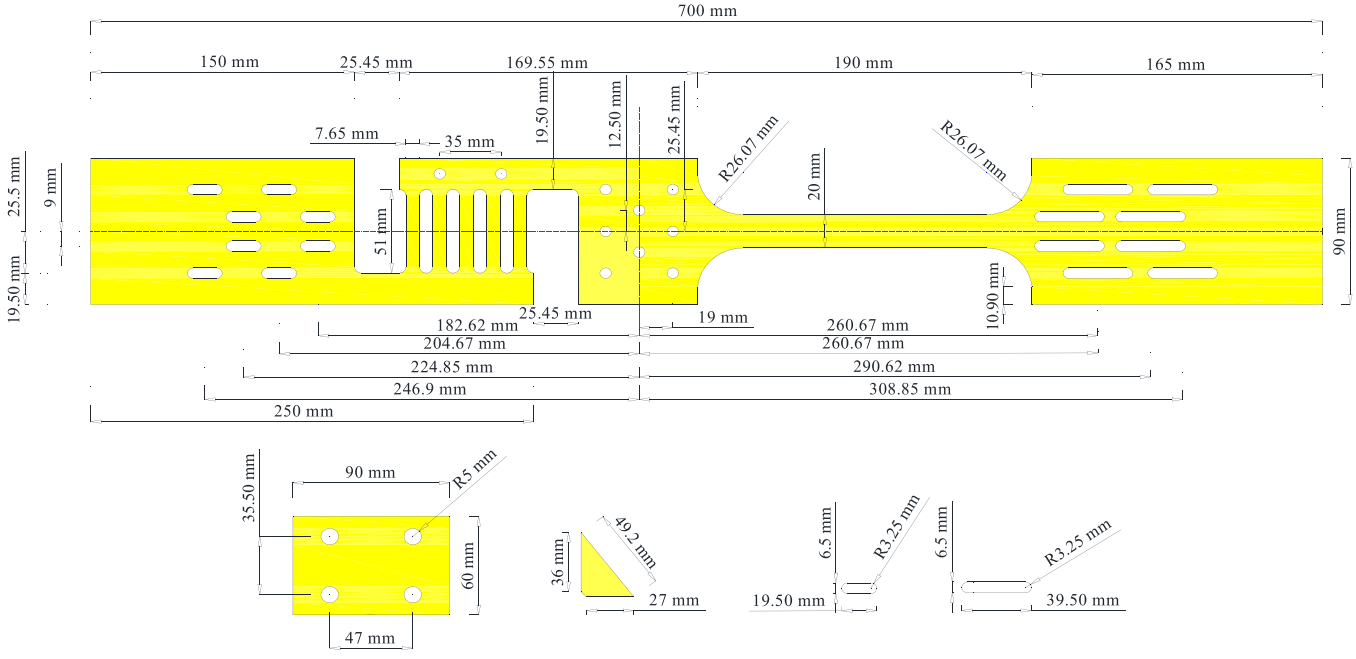

Fig. 26. Details of the optimized SSD-DYB having five strips and a large segment width of 20 mm.

Fig. 27. Experimental test of the optimized SSD-DYB having five strips and a large segment width of 20 mm.

Fig. 28. Experimental test of the optimized SSD-DYB and BRB specimens with a segment width of 20 mm.

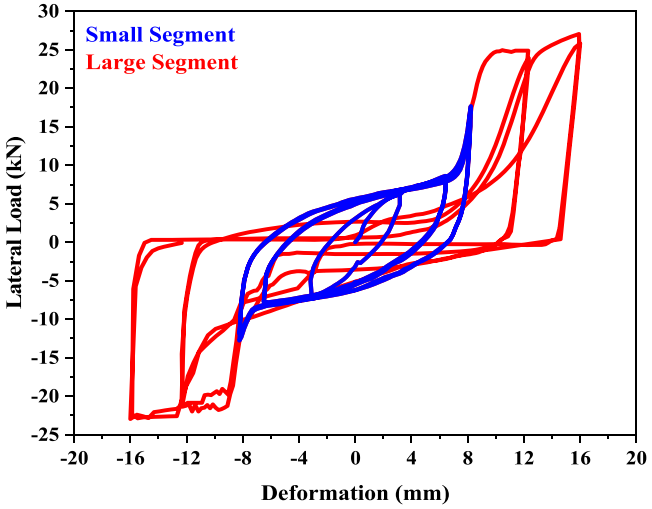

Fig. 29. Hysteresis curve of small and large segments of optimized SSD-DYB under cyclic load.

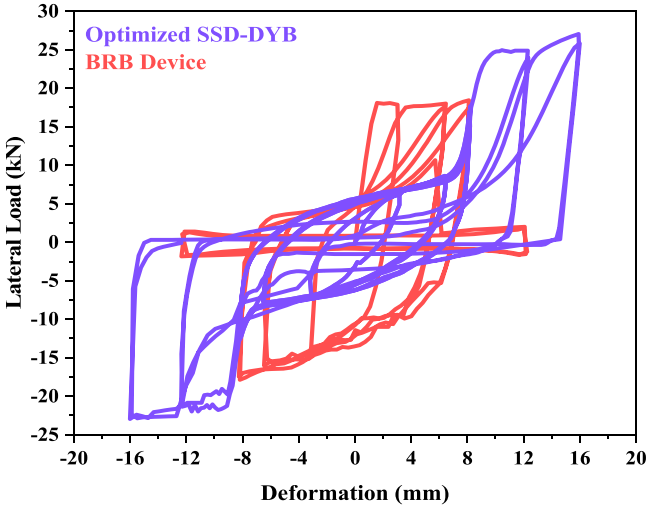

Fig. 30. Hysteresis curves of the optimized SSD-DYB and BRB devices under cyclic load.

loads at increasing levels of displacement. The backbone curve typically follows a path from the origin, ascending to the peak load capacity before softening or plateauing as the system yields and deforms plastically. The hysteresis behavior shown in the image, with its multiple loops and wide range of displacements, highlights the ability of the SSD-DYB.

The findings and conclusions presented herein are based on the research conducted to date, and future experimental programs involving full-scale and subassembly tests can provide additional information for the design of the proposed system.

5. Conclusions

This research has been focused on the development and experimental validation of a novel SSD-DYB device designed for seismic resistance of structures having bracing system. For this purpose, a single-span steel frame has been designed, and based on the real size of the bracing system, a 1/5 scaled SSD-DYB has been constructed. The main idea behind the proposed device is to use the energy dissipating capacity of SSD in the small segment of DYB so as to prepare the device to present a good performance in lower seismic intensity levels. At the same time, the large segment of SSD-DYB can resist higher loads to control the stability of the structure. The results of experimental tests are concluded as follows:

- Optimized placement of stiffeners as well as top and bottom plates confirm the workability of the U-shape during the tests, which shows the ability of the device to replace the cores after seismic events.

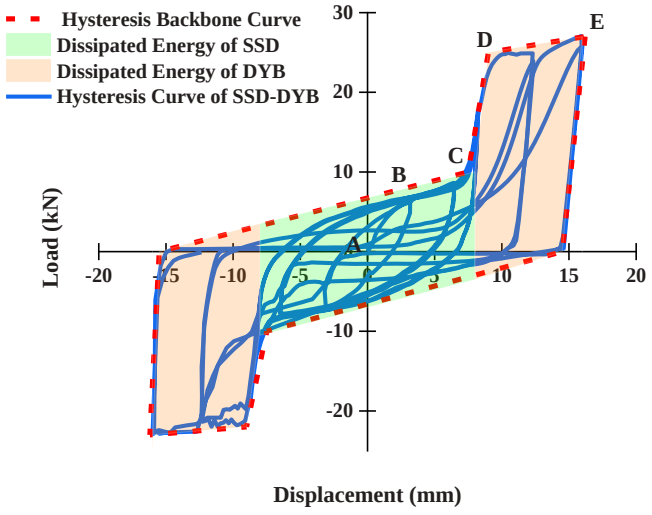

Fig. 31. Comparing the ideal hysteresis behavior expected for SSD-DYB with those obtained in optimized SSD-DYB.

- Experimental results reveal that the number of strips and shape of SSD can increase the maximum load of the hysteresis curve and this can help designers to adjust the size, shape, and number of strips to define different types of SSD-DYBs according to the target performance. For instance, increasing one strip to SSD-DYB-1 and SSD-DYB-2 can increase the dissipated energy by 33.48 % and 12.2 %, respectively. In addition, assuming the SSD-DYB-1 as a reference, the specimens of SSD-DYB-2, SSD-DYB-3, and SSD-DYB-4 have increased the dissipated energy by 23.33 %, 9.32 %, and 11.22 %, respectively.
- It is important to define small and large slotted holes based on the load-carrying capacity of each segment to use the maximum capacity of the device. As expected, by increasing the width of the large segment from 20 mm to 30 mm (i.e., SSD-DYB-5 to SSD-DYB-1), the maximum capacity load has been increased from 18.68 kN to 27.06 kN (i.e., 44.86 %). In total assessment of the proposed device, by changing the shape of the SSD segment, the energy dissipated by SSD-DYB-2 has been increased to 1955.16 J, which is 29.18 % higher than for SSD-DYB-1.
- The experimental results confirm that using a safety factor of 1.5 times of total capacity of device can guarantee the failure resistance of connections. In addition, assuming the width of the large segment equal to 38 % of the total width of the device can effectively protect the failure of connections.
- According to the results, the SSD-DYB can resist more deformation, as compared to the DYB having symmetric hysteresis curve, since this device has damping behavior in the small segment. In addition, it can be adjusted for the expected capacity from each parts of the device, while there will be no sudden rupture and buckling in the response of SSD-DYB.
- Optimized SSD-DYB has been proposed that has more compatibility with the design process and can be effectively used as an energy-dissipating device since the drawbacks of the other cores have been confirmed. It should be noted that the U-shape could be the same during the experiments since there is no failure in its ability to control and transmit the external loads.

Declaration of Competing Interest

The authors declare that there is no conflict of interest with relation to the paper "**Development and experimental validation of a novel double-stage yield steel slit damper-buckling restrained brace**" submitted for publication in *Engineering Structures*.

Data availability

Data will be made available on request.

Acknowledgments

The authors would like to thank Professor (Associate) Agnieszka Tomaszewska, Dr. Marcin Krajewski, Dr. Daniel Chuchała, and Eng. Denys Vinskyi for their efforts and help during the experiments. Experimental tests have been conducted at the laboratory of Department of Structural Mechanics, Gdańsk University of Technology, Poland.

References

[1] Kazemi F, Jankowski R. Seismic performance evaluation of steel buckling-restrained braced frames including SMA materials. J Constr Steel Res 2023;201:107750.
[2] Asgarkhani N, Kazemi F, Jakubczyk-Gałczyńska A, Mohebi B, Jankowski R. Seismic response and performance prediction of steel buckling-restrained braced frames using machine-learning methods. Eng Appl Artif Intell 2024;128:107388.
[3] Liu Y, Guo Z, Liu X, Chicchi R, Shahrooz B. An innovative resilient rocking column with replaceable steel slit dampers: Experimental program on seismic performance. Eng Struct 2019;183:830–40.
[4] Lee J, Kim J. Development of box-shaped steel slit dampers for seismic retrofit of building structures. Eng Struct 2017;150:934–46.
[5] Amiri HA, Najafabadi EP, Estekanchi HE, Ozbakkaloglu T. Performance-based seismic design and assessment of low-rise steel special moment resisting frames with block slit dampers using endurance time method. Eng Struct 2020;224:110955.
[6] Ginés R, Libanori R, Studart AR, Bergamini A, Motavalli M, Ermanni P. Ceramic–polymer composites with improved dielectric and tribological properties for semi-active damping. Compos Part B: Eng 2015;72:80–6.
[7] Kazemi F, Asgarkhani N, Jankowski R. Probabilistic assessment of SMRFs with infill masonry walls incorporating nonlinear soil-structure interaction. Bull Earthq Eng 2023;21(1):503–34.
[8] Mohebi B, Sartipi M, Kazemi F. Enhancing seismic performance of buckling-restrained brace frames equipped with innovative bracing systems. Arch Civ Mech Eng 2023;23(4):1–21.
[9] Kazemi F, Asgarkhani N, Jankowski R. Enhancing seismic performance of steel buildings having semi-rigid connection with infill masonry walls considering soil type effects. Soil Dyn Earthq Eng 2024;177:108396.
[10] Sun J, Pan P, Wang H. Development and experimental validation of an assembled steel double-stage yield buckling restrained brace. J Constr Steel Res 2018;145:330–40.
[11] Barbagallo F, Bosco M, Marino EM, Rossi PP. Achieving a more effective concentric braced frame by the double-stage yield BRB. Eng Struct 2019;186:484–97.
[12] Hu B, Min Y, Wang C, Xu Q, Keleta Y. Design, analysis and application of the double-stage yield buckling restrained brace. J Build Eng 2022;48:103980.
[13] Cahís Carola FX, Catalán Artigas A, Benavent-Climent A, Trias Mansilla D. A new Coplanar Dual Core Buckling-Restrained Brace. J Build Eng 2023;vol. 70:106286. 2023.
[14] Zheng SY, Yuan B, Wei MS, Liu XL, Liu XF, Zhou GY, Shi HW. Experimental & numerical investigation of all-steel assembled cruciform buckling-restrained braces. J Constr Steel Res 2023;207:107981.
[15] Shi QX, Wang F, Wang P, Chen K. Experimental and numerical study of the seismic performance of an all-steel assembled Q195 low-yield buckling-restrained brace. Eng Struct 2018;176:481–99.
[16] Lu Y, Liu Y, Wang Y, Liu J, Huang X. Development of a novel buckling-restrained damper with additional friction energy dissipation: Component tests and structural verification. Eng Struct 2023;274:115188.
[17] Zhang AL, Wang HW, Jiang ZQ, Guo K, Niu ZY. Numerical simulation analysis of double yield points assembled buckling-restrained brace with replaceable inner core. In Structures, Vol. 35. Elsevier,; 2022, January. p. 1278–94.
[18] Yang C, Xie L, An N, Li A, Liu Q, Wang X. Development of a novel parallel double-stage yielding buckling restrained brace: Theoretical, experimental, and numerical investigations. J Build Eng 2023;68:106089.
[19] Asgarkhani N, Yakhchalian M, Mohebi B. Evaluation of approximate methods for estimating residual drift demands in BRBFs. Eng Struct 2020;224:110849.
[20] Ke K, Chen Y, Zhou X, Yam MC, Hu S. Experimental and numerical study of a brace-type hybrid damper with steel slit plates enhanced by friction mechanism. Thin-Walled Struct 2023;182:110249.
[21] Zhou X, Tan Y, Ke K, Yam MC, Zhang H, Xu J. An experimental and numerical study of brace-type long double C-section steel slit dampers. J Build Eng 2023;64:105555.
[22] Oh SH, Park HY. Experimental study on seismic performance of steel slit damper under additional tensile load. J Build Eng 2022;50:104110.
[23] Naeem A, Kim J. Seismic performance evaluation of a multi-slit damper. Eng Struct 2019;189:332–46.
[24] Moghaddam SH, Shooshtari A. Numerical and experimental investigation on seismic performance of proposed steel slit dampers. J Constr Steel Res 2023;200:107646.

[25] López WA, Sabelli R. Seismic design of buckling-restrained braced frames. Steel tips 2004;78.
[26] Güner T, Topkaya C. Performance comparison of BRBFs designed using different response modification factors. Eng Struct 2020;225:111281.
[27] ASCE 7-22. Minimum Design Loads and Associated Criteria for Buildings and Other Structures. Reston, VA: American Society of Civil Engineers,; 2022.
[28] AISC Committee. (2022). Specification for structural steel buildings (ANSI/AISC 360–22). American Institute of Steel Construction, Chicago-Illinois.
[29] AISC A. AISC 341-22, Seismic Provisions for Structural Steel Buildings. Chicago, IL: American Institute of Steel Construction,; 2022.

Paper VIII:

Kazemi, F., & Jankowski, R. (2023). Machine learning-based prediction of seismic limit-state capacity of steel moment-resisting frames considering soil-structure interaction. Computers & Structures, 274, 106886. doi.org/10.1016/j.compstruc.2022.106886

Computers and Structures 274 (2023) 106886

Contents lists available at ScienceDirect

Computers and Structures

journal homepage: www.elsevier.com/locate/compstruc

Machine learning-based prediction of seismic limit-state capacity of steel moment-resisting frames considering soil-structure interaction

F. Kazemi *, R. Jankowski

Faculty of Civil and Environmental Engineering, Gdańsk University of Technology, ul. Narutowicza 11/12, 80-233 Gdansk, Poland

ARTICLE INFO

Article history:
Received 3 June 2022
Accepted 21 August 2022
Available online 17 October 2022

Keywords:
Machine learning algorithm
Data-driven decision techniques
Supervised learning
Soil-structure interaction
Seismic vulnerability assessment
Seismic limit-state capacity

ABSTRACT

Regarding the unpredictable and complex nature of seismic excitations, there is a need for vulnerability assessment of newly constructed or existing structures. Predicting the seismic limit-state capacity of steel Moment-Resisting Frames (MRFs) can help designers to have a preliminary estimation and improve their views about the seismic performance of the designed structure. This study improved data-driven decision techniques in Python software, known as supervised Machine Learning (ML) algorithms, to find median IDA curves (M-IDAs) for predicting the seismic limit-state capacities of steel MRFs considering Soil-Structure Interaction (SSI) effects. For this purpose, Incremental Dynamic Analyses (IDAs) were performed on the steel MRFs from two to nine-story elevations modeled in Opensees subjected to three ground motion subsets of Far Fault (FF), near-fault Pulse-Like (PL) and No-Pulse (NP) suggested by FEMA-P695. The result of the analysis confirmed that there is no specific model for predicting the M-IDA curve of steel structures; therefore, the best developed ML algorithms to reduce a complex modeling process with high computational cost using 128,000 data points were proposed. To provide convenient access to prediction results, Graphical User Interface (GUI) was developed to predict $S_a(T_1)$ of seismic limit-state performance levels with a large database based on prediction models.

© 2022 Elsevier Ltd. All rights reserved.

1. Introduction

The seismic collapse of the buildings is the most important cause of the loss of lives, property damages, and imposing repair costs that can happen during or after a severe earthquake [1–3]. Therefore, a performance-based earthquake engineering framework aims to quantify the seismic collapse potential of the structures [4]. The most widely used method for estimation of the seismic collapse capacity of a structure is known as Incremental Dynamic Analysis (IDA). Although there are many improvements in the technology and seismic devices, there is a lack of knowledge about forthcoming earthquakes. Therefore, it is necessary to use a relatively large set of ground motion records for determining the IDA curve of a structure. Kazemi et al. [5–7] proposed modification factors to approximately predict the seismic collapse capacities of adjacent steel Moment Resisting Frames (MRFs) and Reinforced Concrete (RC) MRFs due to the pounding phenomenon. In addition, they used seismic limit-state capacities of steel MRFs for retrofitting purposes [8]. It is agreed that the seismic collapse capacity assessment is a time-consuming and complex analysis. Hence, proposing a methodology for reliable prediction of the seismic collapse capacity of structures is needed to avoid prohibitive computational costs.

Nowadays, Machine Learning (ML) methods are widely applied in earthquake engineering to estimate the seismic responses of a structure. ML methodology is to train a model from a previous dataset, known as a training dataset, to predict a set of data as the target, known as a testing dataset. Two main groups of ML are known as supervised learning and unsupervised learning, which was presented in Fig. 1.

According to the definition, the prediction of the seismic collapse capacity can be classified as supervised learning, which uses a mathematical model for the prediction of a set of data with an *n*-sample in the inputs and outputs. The accuracy of a model can be determined by comparing the predictions and the outputs for the testing dataset [9–11]. Burton et al. [12] proposed a procedure using kernel ridge regression to estimate the collapse vulnerability. Mangalathu and Jeon [13] developed ML algorithms for estimating the shear strength of RC beam-column joints and the classification of failure modes. Worden and Green [14] used the ML algorithm to demonstrate a data-based approach for nonlinear modal analysis. Luo and Paal [15] proposed the ML-based backbone curve for the force–deformation behavior of concrete columns. Wang et al.

* Corresponding author at: Faculty of Civil and Environmental Engineering, Gdańsk University of Technology, ul. Narutowicza 11/12, 80-233 Gdansk, Poland.
E-mail addresses: farzin.kazemi@pg.edu.pl (F. Kazemi), jankowr@pg.edu.pl (R. Jankowski).

https://doi.org/10.1016/j.compstruc.2022.106886
0045-7949/© 2022 Elsevier Ltd. All rights reserved.

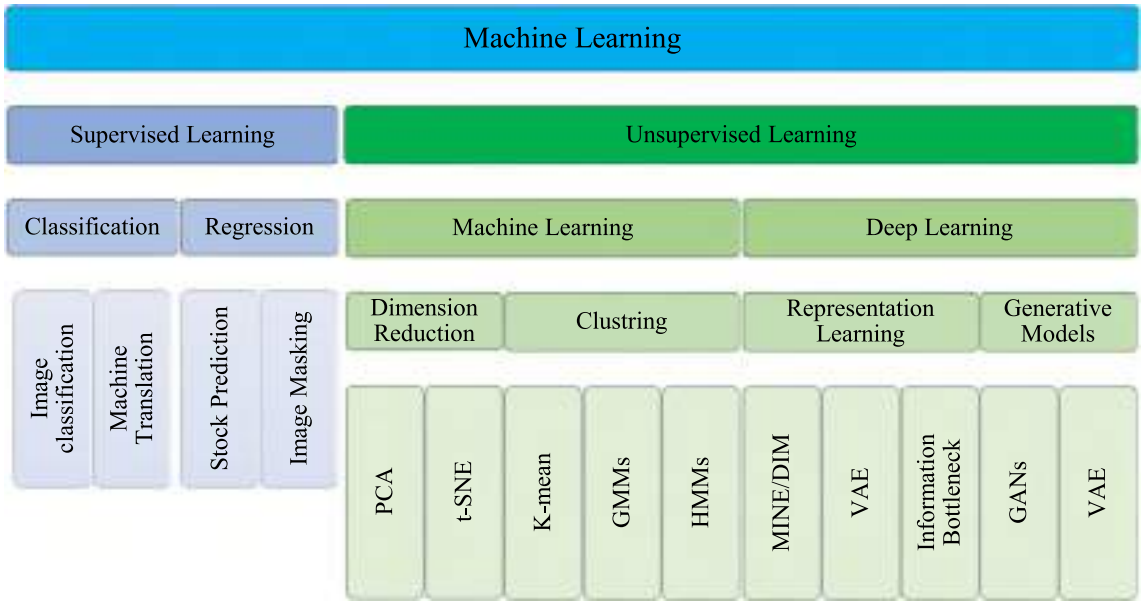

Fig. 1. Classification of unsupervised learning and supervised learning.

[16] used the ANN for predicting seismic fragility curves from the results of IDAs. Zhang et al. [17] used ML models of Random Forest (RF) and regression trees to show the high estimation accuracy of identifying the structural safety status of a four-story RC frame. A method for estimating the residual capacity of damaged buildings was proposed by Zhang and Burton [18]. Kiani et al. [19] developed the RF algorithm for estimating structural responses for determining the seismic fragility curves of the structures. Nguyen et al. [20] used the RF, Artificial Neural Networks (ANNs), and Extreme Gradient Boosting (XGBoost) algorithms to predict the punching shear resistance of slabs. In addition, they developed ML algorithms to predict maximum displacements of pendulum isolation systems [21]. Noureldin et al [22] investigated seismic qualitative and design assessment of structures based on the serviceability using ML algorithms.

Computational cost and analytical efforts to obtain damage states that cover all ranges of damages to structures can prevent to have a reliable estimation of structural behavior. To overcome this issue, ML algorithms can be one possible solution that learns to predict a wider range of damage states using a group of datasets. Therefore, it is a need for designers to have a quick yet reliable and powerful tool for seismic vulnerability assessment of structures that have less computational cost and complexity analysis. Although nonlinear time history analysis is a time-consuming process, the results of the analysis can be used for seismic vulnerability assessments [23,24]. This study aims to explore ML algorithms to efficiently predict the seismic limit state capacity of steel MRFs founded on different soil types assuming nonlinear Soil-Structure Interaction (SSI) effects. Therefore, it would be possible to have an ML-based tool for primary prediction of the seismic limit state capacity of new and already existing structures.

2. Machine learning algorithms

2.1. Random forest

During the implementation of ML algorithms, the most important issue that can affect the results of prediction is overfitting the data. Random Forest (RF) technique, which can be used for both classification and regression problems, showed higher values of variance with lower values of bias for the overfitting problem. Therefore, using them with higher numbers of trees can help to achieve a well-optimized prediction [25]. Fig. 2 presents a visual representation of the RF classifier. In each procedure, n decision trees are used that the n should be found by trial and error. In this study, 400 trees in the forest were assumed, while minimum samples equal to 5 for each leaf, minimum sample split equal to 10, and maximum depth equal to 50 were considered. In addition, different types of RF algorithms can be considered to achieve higher values of prediction and control the overfitting problem. An Extra-Trees Regressor (ETReg) can be used to fit several randomized decision trees on the input dataset. An Extremely Randomized Tree Regressor (ERTReg) can choose trees randomly for the input dataset to improve the speed of calculations while reducing both bias and variance [26]. Moreover, Bagging Regressor (BReg) can be employed to aggregate individual predictions made by fitting the base regressor on the random subsets of the input dataset [27,28].

2.2. Gradient boosting machine

Gradient Boosting Machine (GBM) is an improved RF technique with the ability to use new trees with a learning rate to improve the precision of predictions. In other words, the GBM has the ability to use multiple algorithms on a problem instead of using each of them, and the performance of prediction can be increased [11]. Fig. 3 presents a visual representation of the GBM. In addition, the Histogram-based Gradient Boosting Regression (HistGBR) tree splits the continuous features to predict the values using quantization methods.

It was agreed that HistGBR performs faster than the GBM; therefore, for this study, the performance of HistGBR to predict the seismic limit-state capacity of steel MRFs was achieved. Moreover, fine-tune approach was developed to improve the performance of the HistGBR algorithm. To determine better performance for both algorithms, trial and error strategies were employed to assume 2000 trees in the forest with a learning rate of 0.01, minimum sample split of 100, minimum samples of 30 for each leaf, and maximum depth for each tree equal to 10. By assuming an initial probability of 0.5 for every observation, for each leaf of the trees, the output values in the GBM can be determined as follows:

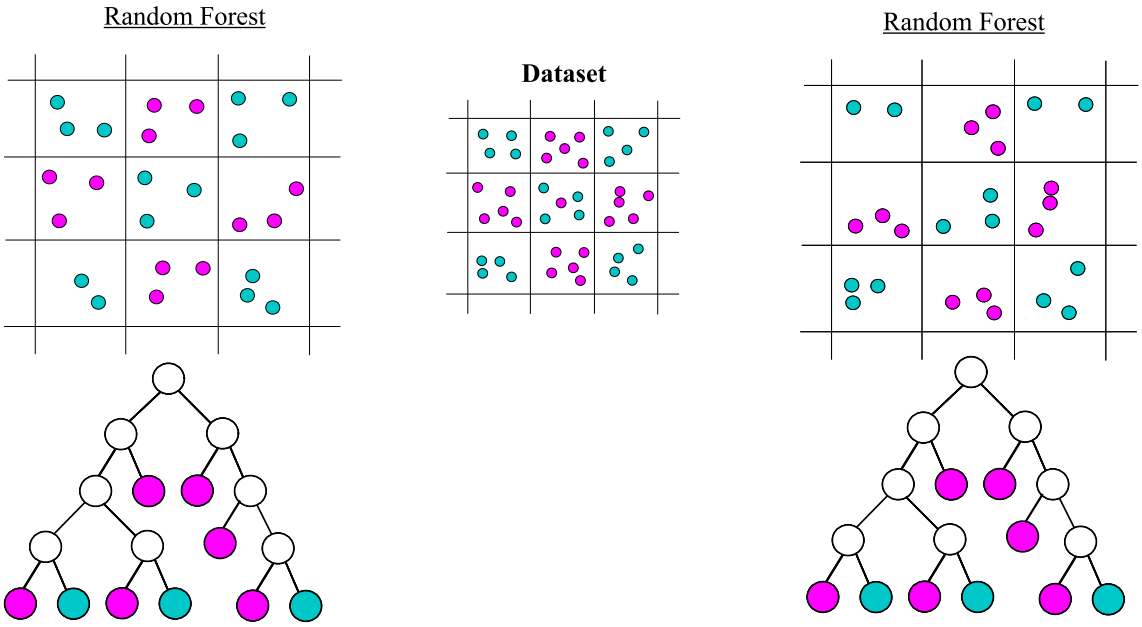

Fig. 2. Visual representation of RF classifier.

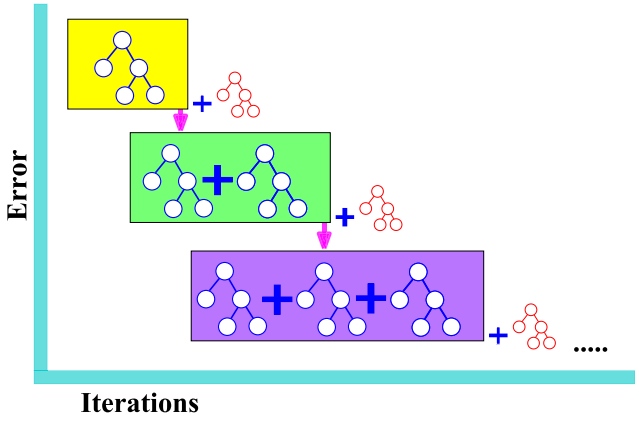

Fig. 3. Visual representation of the GBM.

$$\text{Value} = \frac{\sum_{i=1}^{n} \text{Residual}_i}{\sum_{i=1}^{n} (\text{Previous Probability}_i \times (1 - \text{Previous Probability}_i))} \quad (1)$$

$$\text{Residual}_i = (\text{Observed Value}_i - \text{Predicted Value}_i) \quad (2)$$

2.3. Extreme gradient boosting

The improved algorithm of the GBM is known as Extreme Gradient Boosting (XGBoost), which is a decision tree-based algorithm using the following formula. It can be seen that the main difference between the GBM and XGBoost is the regularization parameter, λ, which has the ability to reduce the small leaves effects [29,30]. Fig. 4 presents the visual representation of the XGBoost, in which the best result of a decision tree was selected for the next decision tree. Fine-tune XGBoost model was developed in Python software to assess the incremental performance by increasing the number of trees.

$$\text{Value} = \frac{\sum_{i=1}^{n} \text{Residual}_i}{\sum_{i=1}^{n} (\text{Previous Probability}_i \times (1 - \text{Previous Probability}_i)) + \lambda} \quad (3)$$

2.4. Artificial neural network

Artificial Neural Networks (ANNs) are a well-known ML algorithm in earthquake engineering due to handle various types of problems. ANNs inspired by the brain neural network and consist of three layers of input data, hidden layers for calculations, and output layers. ANNs used by many researchers for a different types of issues such as positioning temporary facilities on a construction site [31], nonlinear seismic response prediction [32], and seismic limit-state identification of bridge piers [33]. The main feature of ANNs is the ability to learn through examples and change during situations. Since the computations for each node are generally independent of all other nodes, it can be said that they are computing in parallel. In this study, the ANNs were used for predicting the M-IDR of SMRFs as target in the output layer. Moreover, finding suitable weight for each neuron was conducted by an error back

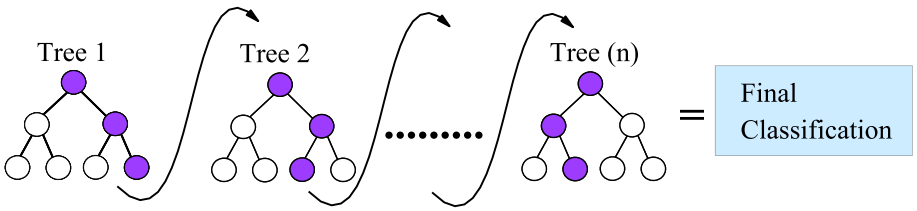

Fig. 4. Visual representation of the XGBoost.

propagation algorithm. There are some activation functions, such as Rectified Linear Unit (Relu), Purelin, Tansing, Tangent hyperbolic, Sigmoid, and Radial basis function, which have different time of computing and can be applied in a variety of engineering problems. It should be noted that the transfer function prevents outputs to reach large values that can decrease the accuracy of ANNs. Therefore, for hidden layers, the activation functions of Relu and Sigmoid were applied in the present study. The hidden layers are between the input and output layers (see Fig. 5), and there is no unique method for selecting the numbers of hidden layers. In this study, the forward propagation was implemented, then, the loss was achieved and backward propagation was used to obtain the parameters for adjusting the weights. To reduce the error, the parameters were updated, and again the forward propagation was implemented. To implement this algorithm, a trial and error procedure was employed to change the number of hidden layers, while other parameters were kept unchanged. This was done for different types of training and testing datasets due the selecting a steel MRF as target of prediction. For example, the results of trial and error showed that having 10 hidden layers achieved the accuracy of 96%, while decreasing or increasing the number of hidden layers led to the reduction in prediction accuracy. In addition, Multi-layer Perceptron Regressor (MLPReg) was considered to map inputs to outputs using a linear function to solve a complex problem. Fig. 6 presents the general architecture of ANN.

2.5. Support vector machine

Support Vector Machine (SVM) is a powerful tool for classifying datasets with high accuracy in both hyperplanes of 2D and 3D spaces. It should be noted that the hyperplane is a decision boundary for classifying the dataset, and the optimum hyperplane should have the maximum margin between datasets (Fig. 6) [34].

Another type of SVM that uses a parameter, v, to control the number of support vectors is known as Nu-Support Vector Regression (NuSVR) and Linear Support Vector Regression (LSVR), which can be used concerning the total samples of the dataset [35] and employing penalties and loss functions for samples [36], respectively.

2.6. Adaptive Boosting

Freund and Schapire [37] proposed a statistical classification to teach subsequent weak learners to find a combination of them for the boosted classifier, known as the Adaptive Boosting (AdaBoost) algorithm. In this study, instead of using weak learners, strong base learners such as decision trees were used to improve the computational accuracy of the model. The k-fold cross-validation can be used to avoid the risk of losing important data points during training the model. Therefore, the strategy of dividing total data into two main parts of approximately 70%-80% for training and 30%-

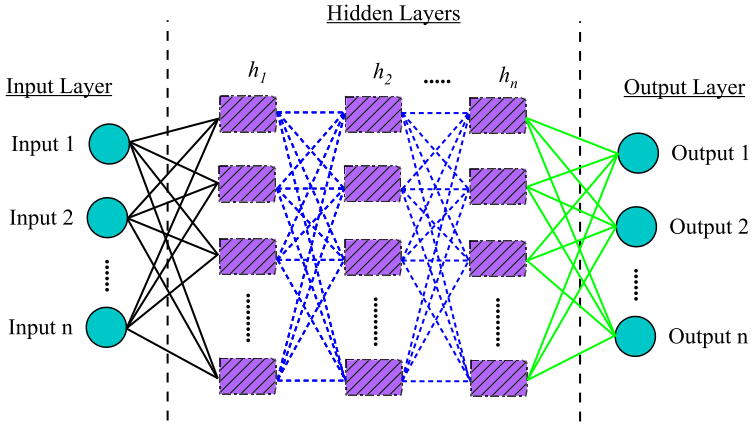

Fig. 5. Architecture of artificial neural network (ANN).

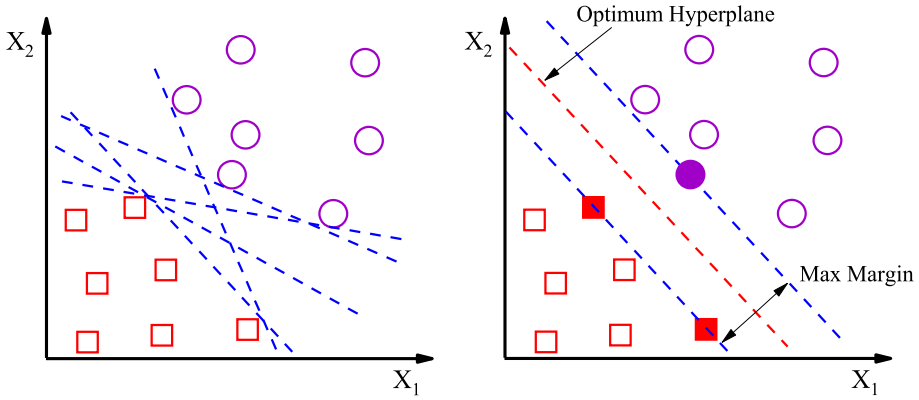

Fig. 6. Support vector machine in the linear dataset.

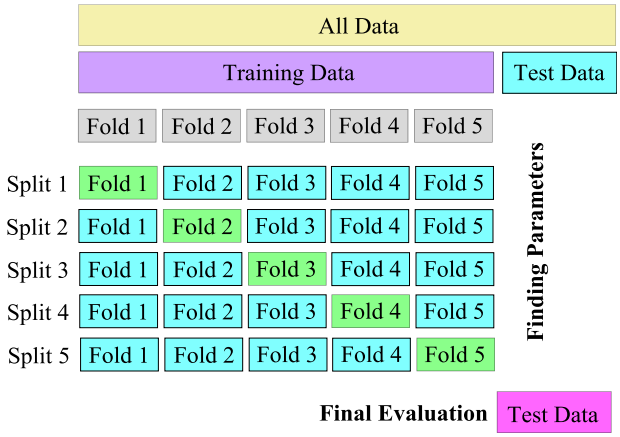

Fig. 7. 5-fold cross-validation methodology.

20% for testing can be used with lower bias and variance [38]. Fig. 7 presents the 5-fold cross-validation methodology, in which one fold was selected as testing data and fourfold was used for training and final evaluation was made by test dataset.

2.7. Regressors models

In this section, the important regressor ML algorithms are described based on their higher accuracy in the prediction of a response variable. Voting Regressor (VReg) has the ability to achieve the final prediction based on the average of the individual data points. Linear Regression (LReg) is a linear approximation model based on minimizing the residual sum of squares of predicted and observed datasets. K-Nearest neighbors Regressor (KNR) can be used for linear prediction based on the local interpolation on the mean of the samples of the training dataset. Gaussian Process Regression (GPReg) aims to renormalize the dataset to achieve a mean of zero with maximum log marginal of samples. Partial Least Squares Regression (PLSReg) uses maximum multidimensional direction in the samples to find the fundamental relations between two matrices in the target dataset [39]. Gamma Regressor (GReg) extends linear models to combine input datasets via an inverse link function with their logarithmic unit deviance [40]. The strategy of the Stacking Regressor (SReg) is to solve problems considering the strength of each estimator to use their output as input of a final estimator [41]. It should be noted that these regressors can be used in supervised learning which is the case in this study.

3. Structural models

In this study, to better investigate the ML algorithms and their ability in the prediction of seismic limit-state capacity, the 2-Story, 3-Story, 4-Story, 5-Story, 6-Story, 7-Story, 8-Story, and 9-Story buildings were modeled assuming four steel MRFs in outer frames presented in the regular plan by blue color in Fig. 8, according to procedures used by Kazemi et al. [6–8]. The height of each story level was assumed to be equal to 4 m. The buildings were located in California with a latitude of 34.039° and longitude of −118.324° assuming four soil types of B, C, D, and E, considering S_{DS} and S_{D1} of 1.306 and 0.463, 1.567 and 0.648, 1.567 and 0.653, and 1.623 and 0.659, respectively [42]. It should be noted that all buildings were modeled in ETABS 2016 software according to seismic codes of ASCE 7–16 [43], AISC 360–16 [44], and AISC 341–10 [45], assuming the floor live load of 1.68 kN/m^2 and dead load of 3.35 kN/m^2. Tables 1 and 2 present the structural elements of the aforementioned steel MRFs.

Some studies (for more detail see [6–8,46]) used a procedure to model three-dimensional buildings with two-dimensional steel MRF in Opensees [47]. To verify the modeling approach, the four-story structure used by Lignos et al. [48] and Del Carpio Ramos et al. [49] was used. The P-Delta effect which can play a crucial role in the seismic limit-state capacity (see [50–52]) can be assumed in steel MRFs using the leaning column. The leaning column, presented in Fig. 8, consists of all gravity loads except those in the steel MRF to consider the gravity column effects in the analysis [53–55]. The main purpose of this study is to consider the real condition of steel MRFs with the possibility of seismic collapse. Therefore, the panel zones were modeled and nonlinear hinges of beams and columns were considered assuming the Modified Ibarra–Krawinkler bilinear hysteretic model (IMK Hinge) [6–8,50–55] in both ends of structural elements (see Fig. 8).

3.1. Numerical modeling of SSI

To improve the accuracy of models with the real condition of buildings, nonlinear SSI effects were considered using a Beam on Nonlinear Winkler Foundation (BNWF) model presented in Fig. 9. The BNWF model has the ability to use a series of nonlinear springs

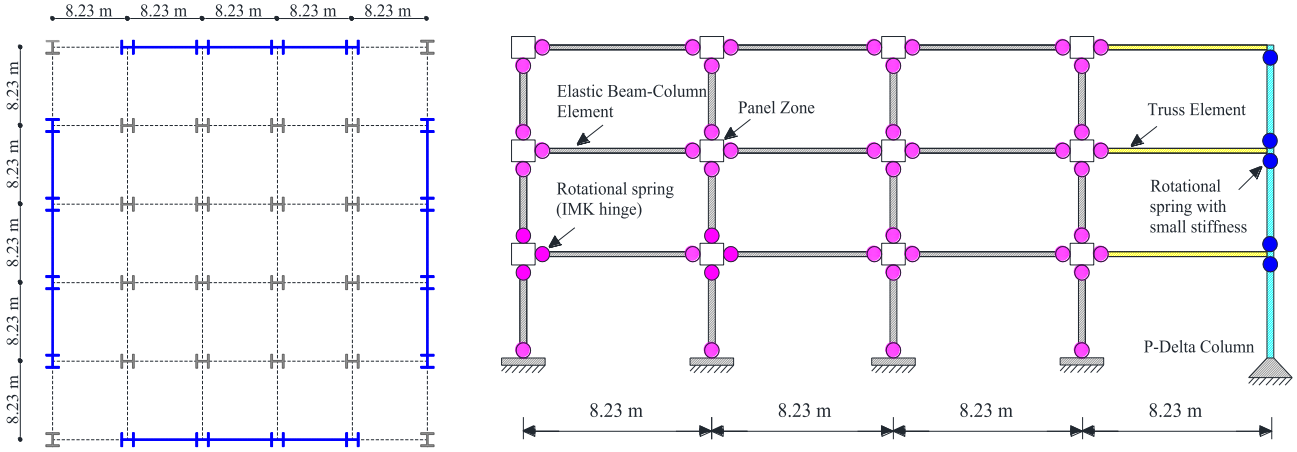

Fig. 8. Structural plan used for modeling of steel MRFs.

Table 1
Structural elements of the 2-Story, 4-Story, 6-Story, and 8-Story steel MRFs.

Model	Story floor	Soil type B		Soil type C		Soil type D		Soil type E	
		Column	Beam	Column	Beam	Column	Beam	Column	Beam
2-story	1st	W14X132	W24X68	W14X159	W24X94	W14X159	W24X94	W14X159	W24X94
	2nd	W14X120	W18X46	W14X120	W18X50	W14X120	W18X50	W14X120	W18X55
4-story	1st	W14X145	W24X76	W14X159	W24X94	W14X159	W27X102	W14X159	W27X102
	2nd	W14X120	W24X76	W14X132	W24X94	W14X132	W27X102	W14X159	W27X102
	3rd	W14X120	W24X76	W14X120	W24X84	W14X120	W24X84	W14X120	W24X84
	4th	W14X120	W24X55	W14X120	W24X55	W14X120	W24X55	W14X120	W24X55
6-story	1st	W14X145	W24X84	W14X176	W27X102	W14X176	W27X102	W14X176	W27X102
	2nd	W14X145	W24X84	W14X159	W27X102	W14X159	W27X102	W14X159	W27X102
	3rd	W14X145	W24X84	W14X145	W27X94	W14X145	W27X102	W14X145	W27X102
	4th	W14X120	W24X84	W14X120	W27X94	W14X120	W27X94	W14X145	W24X84
	5th	W14X120	W24X68	W14X120	W24X84	W14X120	W24X84	W14X120	W24X84
	6th	W14X120	W21X50	W14X120	W21X50	W14X120	W21X50	W14X120	W21X50
8-story	1st	W14X233	W27X94	W14X233	W27X114	W14X233	W27X114	W14X233	W27X114
	2nd	W14X233	W27X94	W14X233	W27X114	W14X233	W27X114	W14X233	W27X114
	3rd	W14X176	W27X94	W14X176	W27X114	W14X176	W27X114	W14X233	W27X114
	4th	W14X176	W24X94	W14X176	W27X102	W14X176	W27X102	W14X176	W27X114
	5th	W14X176	W24X94	W14X176	W27X102	W14X176	W27X102	W14X176	W27X114
	6th	W14X120	W24X84	W14X120	W24X84	W14X159	W27X94	W14X120	W27X94
	7th	W14X120	W24X84	W14X120	W24X84	W14X120	W24X84	W14X120	W24X84
	8th	W14X120	W21X50	W14X120	W21X50	W14X120	W21X50	W14X120	W21X50

Table 2
Structural elements of the 3-Story, 5-Story, 7-Story, and 9-Story steel MRFs.

Model	Story floor	Soil type B		Soil type C		Soil type D		Soil type E	
		Column	Beam	Column	Beam	Column	Beam	Column	Beam
3-story	1st	W14X132	W24X68	W14X159	W24X94	W14X159	W24X94	W14X159	W24X94
	2nd	W14X120	W21X68	W14X120	W24X84	W14X120	W24X94	W14X120	W24X94
	3rd	W14X120	W18X46	W14X120	W18X50	W14X120	W18X50	W14X120	W18X55
5-story	1st	W14X145	W24X76	W14X159	W24X94	W14X159	W27X102	W14X159	W27X102
	2nd	W14X120	W24X76	W14X132	W24X94	W14X132	W27X102	W14X159	W27X102
	3rd	W14X120	W24X76	W14X120	W24X84	W14X120	W24X84	W14X120	W24X84
	4th	W14X120	W24X55	W14X120	W24X84	W14X120	W24X84	W14X120	W24X84
	5th	W14X120	W24X55	W14X120	W24X55	W14X120	W24X55	W14X120	W24X55
7-story	1st	W14X145	W24X84	W14X176	W27X102	W14X176	W27X102	W14X176	W27X102
	2nd	W14X145	W24X84	W14X159	W27X102	W14X159	W27X102	W14X159	W27X102
	3rd	W14X145	W24X84	W14X145	W27X94	W14X145	W27X102	W14X145	W27X102
	4th	W14X120	W24X84	W14X120	W27X94	W14X120	W27X94	W14X145	W24X84
	5th	W14X120	W24X68	W14X120	W24X84	W14X120	W24X84	W14X120	W24X84
	6th	W14X120	W21X50	W14X120	W21X68	W14X120	W21X68	W14X120	W21X68
	7th	W14X120	W21X50	W14X120	W21X50	W14X120	W21X50	W14X120	W21X50
9-story	1st	W14X233	W27X94	W14X233	W27X114	W14X233	W27X114	W14X233	W27X114
	2nd	W14X233	W27X94	W14X233	W27X114	W14X233	W27X114	W14X233	W27X114
	3rd	W14X176	W27X94	W14X176	W27X114	W14X176	W27X114	W14X233	W27X114
	4th	W14X176	W24X94	W14X176	W27X102	W14X176	W27X102	W14X176	W27X114
	5th	W14X176	W24X94	W14X176	W27X102	W14X176	W27X102	W14X176	W27X114
	6th	W14X120	W24X84	W14X120	W24X84	W14X159	W27X94	W14X120	W27X94
	7th	W14X120	W24X84	W14X120	W24X84	W14X120	W24X84	W14X120	W24X84
	8th	W14X120	W21X50	W14X120	W21X68	W14X120	W21X68	W14X120	W24X84
	9th	W14X120	W21X50	W14X120	W21X50	W14X120	W21X50	W14X120	W21X50

and dashpots to capture the nonlinear behavior of foundations. According to Fig. 9, to determine the vertical and rotational resistance, the q-z spring with material behavior of *QzSimple* implemented in Opensees [47] was used. In addition, for passive resistance and sliding resistance of the foundation, *t*-x spring and p-x spring with material behavior *TxSimple* and *PxSimple* were used, respectively (Fig. 10).

To implement the nonlinear behavior of the foundation, the material behavior of *QzSimple*, *TxSimple*, and *PxSimple* implemented in nonlinear zero-length elements were used [56–59]. To calculate the foundation of the steel MRFs, the soil parameters illustrated in Table 3 were used. All foundations were designed according to the designed buildings in ETABS software using SAFE 2016 software. Tables 4 and 5 present the foundations achieved from the design process.

The foundation dimension can be used to calculate the parameters and to define the material behavior of vertical and rotational resistance, sliding resistance, and passive resistance used in the BNWF model. Boulanger et al. [60] proposed equations to calculate the *QzSimple* material model assuming linear behavior of elastic load, q_e, in the elastic region with the displacement, z, and the initial elastic stiffness, k_{ini}. Therefore, the following relationship can be assumed for elastic load:

$$q_e = k_{ini} z \tag{4}$$

To calculate the maximum load, q_0, in the elastic region, the experimentally achieved C_r factor can be multiplied by the ultimate load, q_{ult}, and the equation can be rewritten to determine the nonlinear part as follows:

$$q_0 = C_r q_{ult} \tag{5}$$

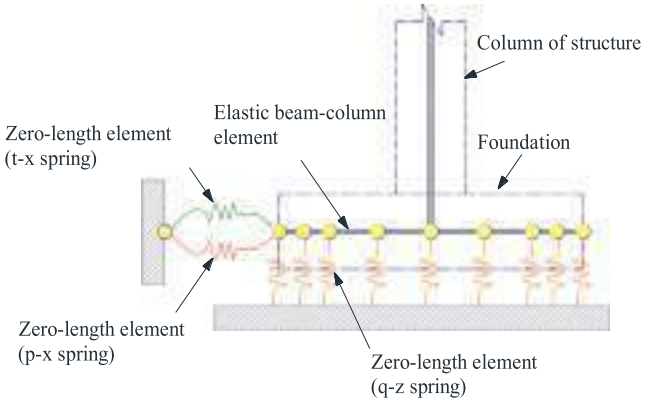

Fig. 9. Implementation of the springs and dashpots in the BNWF model.

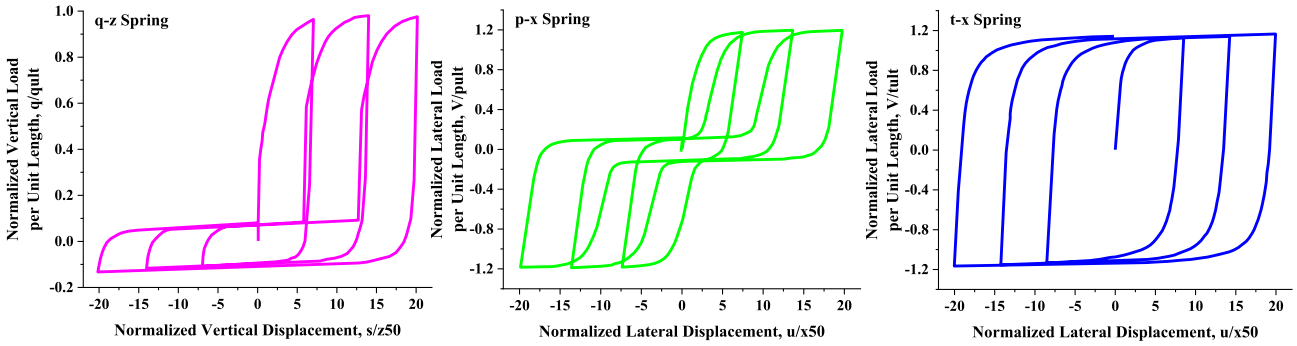

Fig. 10. Normalized load-normalized displacement curves of the q-z spring, p-x spring, and *t*-x spring.

$$q = q_{ult} - (q_{ult} - q_0)\left[\frac{Cz_{50}}{Cz_{50} + |z - z_0|}\right]^n \tag{6}$$

where displacement in the yield point and the 50% of the ultimate load were shown by z_0 and cz_{50}, respectively, and C and n can be used for controlling the post-yield portion and shape of the curve, respectively. It should be noted that Equation (6) can be used for calculating the *TxSimple* and *PxSimple* material models considering various values of C_r, n, and C. To determine the stiffness of vertical and horizontal springs, k_v and k_h, the following equation can be used [61]:

$$\begin{aligned} k_v &= \frac{GL}{1-\upsilon}\left[0.73 + 1.54\left(\frac{B}{L}\right)^{0.75}\right] \\ k_h &= \frac{GL}{2-\upsilon}\left[2 + 2.5\left(\frac{B}{L}\right)^{0.85}\right] \end{aligned} \tag{7}$$

where shear modulus and Poisson's ratio of the soil types, G and υ, can be achieved in Table 3, and the width and length of the assumed foundation can be achieved in Tables 4 and 5.

4. Analytical procedure

This paper aims to explore the best ML algorithm for predicting the seismic limit-state capacities of steel MRFs. For this purpose, the analytical procedure was used to achieve the dataset for training and testing the ML algorithms. Fig. 11. Presents analytical procedures were done in this study to achieve high accuracy ML model.

According to Fig. 11, Incremental Dynamic Analyses (IDAs) were used to assess the seismic performance of steel MRFs assuming $S_a(T_1)$, the spectral acceleration in T_1, as Intensity Measure (IM), and Maximum Interstory Drift Ratio (M-IDR) as demand parameter. Therefore, the IDA curves can be achieved in terms of $S_a(T_1)$ versus M-IDR. It should be noted that the M-IDR of steel MRFs was controlled during analysis until reaching the Total Collapse (TC) performance level that can be defined as the flat part of the IDA curve. In this study, the flat part of IDA curves was achieved in M-IDR of 0.1, then, M-IDR can be in the range of 0.0 to 0.1. More-

Table 3
Seismic design and values of the soil parameters.

Soil type	B	C	D	E
G_o (MPa)	6000	280	60	30
Φ (Degree)	45	42	38	35
c (kPa)	0	0	5	5
γ (kN/m^3)	24	21	19	18
υ	0.25	0.35	0.4	0.45
v_s (m/s)	1565	360	175	120

Table 4
Foundation dimensions of the 2-Story, 4-Story, 6-Story, and 8-Story SMRFs for different soil types.

Steel MRF	Soil type	Width (m)	Length (m)	Height (m)
2-story	B	0.8	26	0.6
	C	0.8	26	0.6
	D	0.8	27	0.6
	E	0.8	27	0.6
4-story	B	1.0	26	0.7
	C	1.0	26	0.7
	D	1.1	27	0.7
	E	1.1	27	0.7
6-story	B	1.3	27	0.8
	C	1.3	27	0.8
	D	1.6	27	0.8
	E	1.6	27	0.8
8-story	B	2.0	27	1.0
	C	2.0	27	1.1
	D	2.5	27	1.1
	E	2.5	27	1.1

Table 5
Foundation dimensions of the 3-Story, 5-Story, 7-Story, and 9-Story SMRFs for different soil types.

Steel MRF	Soil type	Width (m)	Length (m)	Height (m)
3-story	B	1.0	26	0.6
	C	1.0	26	0.6
	D	1.1	27	0.7
	E	1.1	27	0.7
5-story	B	1.3	26	0.7
	C	1.3	26	0.7
	D	1.3	27	0.7
	E	1.3	27	0.7
7-story	B	1.5	27	0.8
	C	1.5	27	0.8
	D	2.0	27	0.8
	E	2.0	27	0.8
9-story	B	2.5	27	1.0
	C	2.5	27	1.0
	D	3.0	27	1.1
	E	3.0	27	1.1

over, Immediate Occupancy (IO), Life Safety (LS), and Collapse Prevention (CP) performance levels were considered corresponding to the M-IDR of 0.7% (0.007), 2.5% (0.025), and 5.0% (0.05), respectively, in accordance with FEMA 356 [62]. Therefore, the selected M-IDR range can contain all performance levels.

The features of the fundamental period (T_1), weight and the total height of structures, the RSN number and the direction of records, soil types, and SSI effects were selected as important sample features of the dataset for prediction. On the other side, $S_a(T_1)$ was assumed for the target of prediction in the selected range of M-IDR. Therefore, the ML algorithms were trained to be able to predict the $S_a(T_1)$ of the selected steel MRF regarding the sample features in the input dataset subjected to assumed records. It should be noted that the real time of simulation for each steel MRF depends on the structural parameters, while the time of analysis for one set of NP or PL records is approximately 96 h. To improve the time of analysis, a hunt & fill algorithm, with the possibility of increasing the IM by a factor of 0.2 and sub-steps of 0.05 and 0.02, was implemented in Opensees [47] software, which can increase the speed of analysis for IDA curve assessment and reduce the time of analysis to approximately 74 h. Moreover, three record subsets of Far Fault (FF), near-fault Pulse-like (PL), and No-Pulse (NP) suggested by FEMA-P695 [63] were selected to perform IDAs. Fig. 12 shows IDA curves and median IDAs (M-IDAs) of steel MRFs founded on soil type E including NP records.

5. Sensitivity analysis

In this section, a sensitivity analysis was performed to find out the capability of ML models for predicting $S_a(T_1)$ based on the dataset features. In order to compare the ML models, coefficient of determination (R^2), Mean Squared Error (MSE), Root Mean Squared Error (RMSE), Root Mean Square Relative Error (RMSRE) and Mean Average Error (MAE) were calculated. According to statistical definition, the coefficient of determination, R^2, can be defined as the accuracy of predicted data by representing the spread of data points from the x = y line; therefore, it is a suitable metric for comparing the results of prediction. Distance metrics can be considered a powerful tool for determining the convergence results of the ML models. MAE determines the absolute distance between observations and predictions and takes the average of all observations into account by the following formula:

$$MAE = \frac{1}{n}\sum_{i=1}^{n}|\text{Observed}_i - \text{Predicted}_i| \tag{8}$$

On the other side, MSE uses a power function to increase the importance of errors or distances regarding the following formula:

$$MSE = \frac{1}{n}\sum_{i=1}^{n}(\text{Observed}_i - \text{Predicted}_i)^2 \tag{9}$$

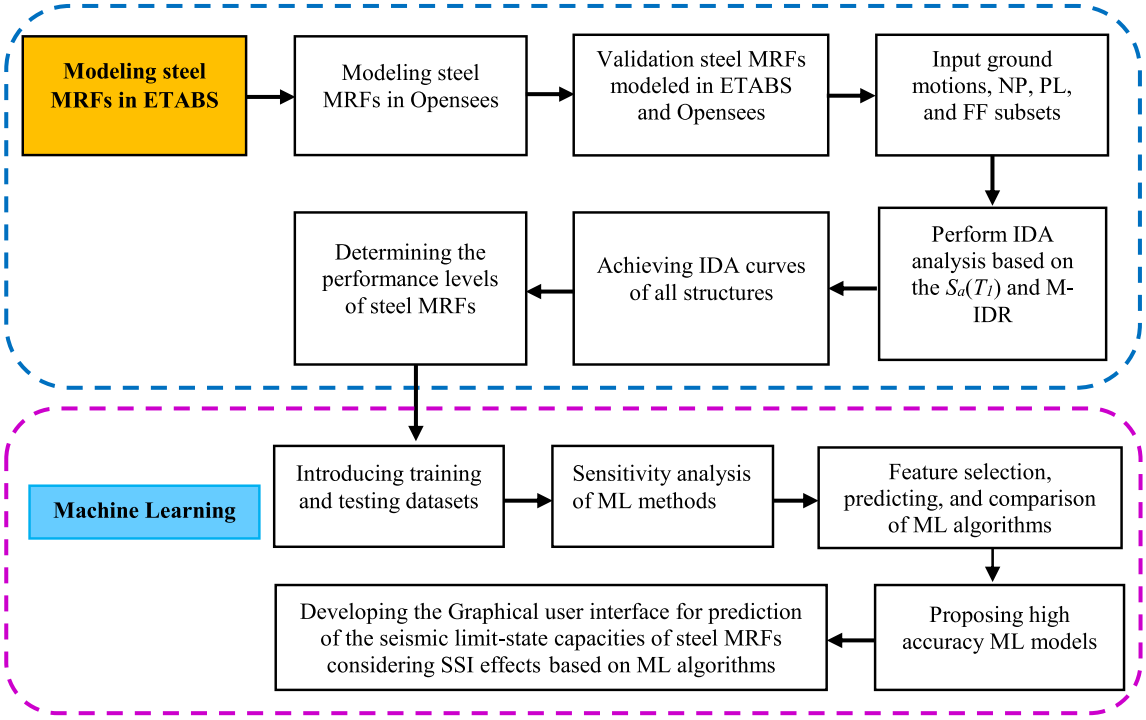

Fig. 11. Analytical procedures to achieve high accuracy model.

In addition, RMSE can be a good metric for comparison due to its ability for changing MSE to its original form considering the penalties for higher errors as shown in the following formula:

$$RMSE = \sqrt{MSE} = \sqrt{\frac{1}{n}\sum_{i=1}^{n}(\text{Observed}_i - \text{Predicted}_i)^2} \quad (10)$$

A performance indicator of RMSRE can be calculated as follows [64]:

$$RMSRE = \sqrt{\frac{1}{n}\sum_{i=1}^{n}\left|\frac{\text{Predicted}_i - \text{Observed}_i}{\text{Observed}_i}\right|^2} \quad (11)$$

Using these metrics helps to compare twenty ML algorithms assumed in this study to find the most accurate models for the rest of the research. In order to provide the reproducibility of methods, details of hyperparameters used for implementing all ML models are presented in Table 6.

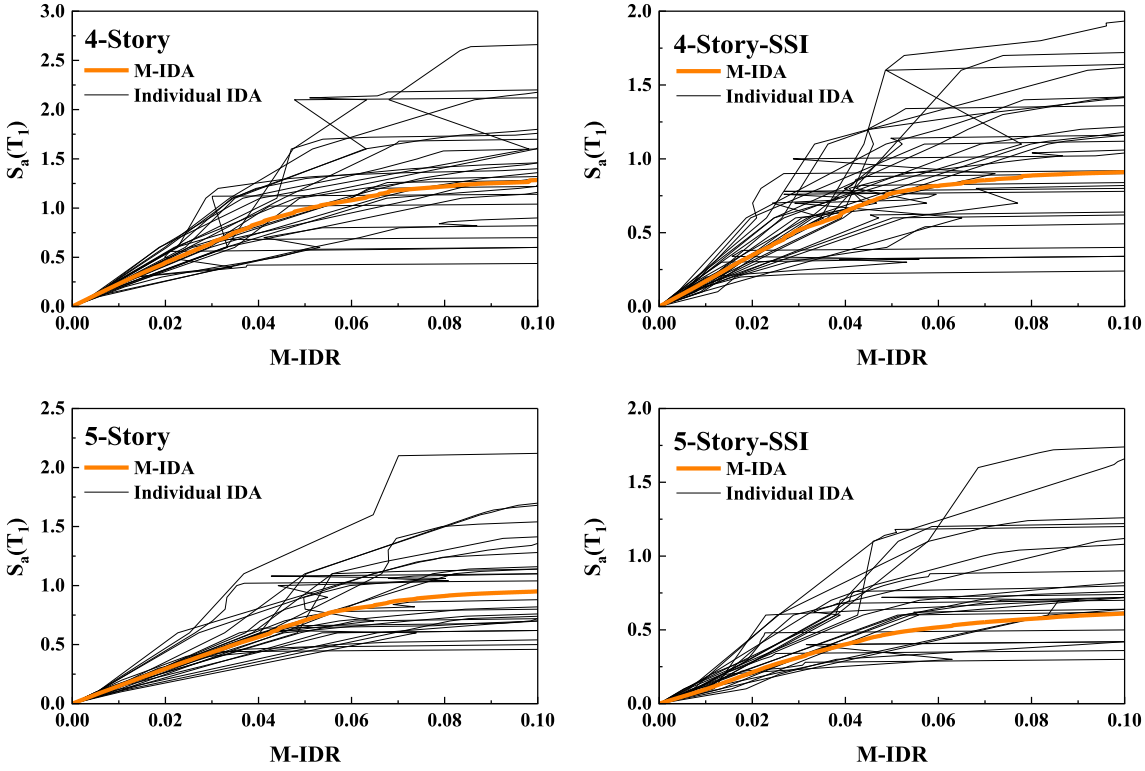

Fig. 12. IDA curves of steel MRFs founded on soil type E including NP records.

Table 6
Hyperparameters used for implementing ML algorithms.

Model	Parameter	Value	Model	Parameter	Value	Model	Parameter	Value
XGBoost	No. of estimators	2000	AdaBoost	No. of estimators	2000	SVM	Random state	3
	Learning rate	0.001		Learning rate	0.01		Loss	Epsilon insensitive
	Min sample leaf	15		Min sample leaf	2		Tolerance	1e-04
	Min sample split	20		Min sample split	2		Max iterations	1000
	Max depth	4		Max depth	20		kernel	rbf
RF	Min sample leaf	10	KNR	No. of neighbors	5	NuSVR	Nu	0.1
	Min sample split	4		weights	distance		Kernel	rbf
	Max depth	20		Leaf size	30		Gamma	0.01
BReg	No. of estimators	200		P value	2		Penalty parameter	1
	Random state	0	PLSReg	No. of components	2		Max iterations	2000
ETReg	No. of estimators	250		Max iterations	500	LSVR	Random state	0
	Random state	0		Tolerance	1e-06		Tolerance	1e-05
	Min sample leaf	4	SReg VReg LReg	No. of estimators	1000		Loss	Epsilon insensitive
	Min sample split	8		Weight	uniform	ERTReg	No. of estimators	2000
GBM	No. of estimators	3000		Verbose	False		Min sample leaf	10
	Learning rate	0.001	GReg	Alpha	1		Min sample split	2
	Min sample leaf	20		Max iterations	200		Random state	3000
	Min sample split	20		Tolerance	1e-04	ANNs	Loss	MSE
	Max depth	10	MLPReg	Hidden layer 1	5		Hidden layer 1	10 (*Relu*)
HistGBR(FN)	No. of estimators	2000		Hidden layer 2	5		Hidden layer 2	10 (*Relu*)
	Learning rate	0.001		Hidden layer 3	2		Hidden layer 3	5 (*Sigmoid*)
	Min sample leaf	10		Activation	Relu		Learning rate	Invscaling
	Min sample split	10		Optimizer	Adam		Optimizer	Adam
	Max depth	5		Max iterations	5000		Max iterations	5000

Tables 7 and 8 illustrate the sensitivity analysis of twenty ML algorithms used for the prediction of the $S_a(T_1)$ based on the input features for the 2-Story steel MRF assuming soil type C including the PL record for training and testing datasets, respectively. For having comparative results with respect to the computing time of all ML algorithms, the score markers were added to Tables 7 and 8. In each ML algorithm, the best algorithm has the score of one, and this shows the ranking of the algorithm among other algorithms. The final column of each table illustrates the total scores between five statistical metrics, and the lowest score shows the best algorithm. In addition, the computing time of analysis for each algorithm was achieved by implementing programming code in Python software, while the percentage of CPU usage was 98%.

According to the total scores of training dataset, the ETReg, GBM, BReg, AdaBoost, and RF algorithms with total scores of 14, 14, 17, 21, and 25 are the five top of the list for having good results of prediction. On the other side, the ANNs, NuSVR, XGBoost, VReg, and SVM algorithms with total scores of 11, 16, 25, 26, and 30 are the five top of the list for having good results of prediction in testing dataset. It worth mentioning that three algorithms of ANNs, NuSVR, and XGBoost have higher computing time comparing to other algorithms.

According to Tables 7 and 8, it can be seen that five ML algorithms of PLSReg, SReg, LReg, GReg, and LSVR have R^2 of 0.697, 0.652, 0.723, 0.595, and 0.648 for the training dataset, respectively, and for the testing dataset, they have R^2 of 0.421, 0.216, 0.578, 0.134, and 0.118, respectively, that are lower than other ML algorithms. In addition, according to the determined total scores, five ML algorithms of PLSReg, SReg, LReg, GReg, and LSVR have the highest scores in both datasets. According to the results, it can be concluded that these ML algorithms have the weakest performance in both training and testing datasets and were removed from the rest of comparison.

6. Performance of ML algorithms

In this section, the performance of fifteen ML algorithms is evaluated by comparing the metric's results for predicting the seismic limit-state capacities of steel MRFs. The unpredictable nature of seismic excitations leads to having no single ML model for predict-

Table 7
Sensitivity results to compare the performance of ML algorithms in the training dataset.

ML algorithms	2-Story steel MRF founded on soil type C including PL records											
	Time (*sec*)	R^2	Score	MSE	Score	RMSE	Score	MAE	Score	RMSRE	Score	Total
XGBoost	925	0.998	2	5.3E-05	9	7.3E-03	9	5.5E-03	9	0.047	8	37
RF	**469**	**0.999**	**1**	**2.3E-05**	**6**	**4.8E-03**	**6**	**3.1E-03**	**6**	**0.014**	**6**	**25**
BReg	**196**	**0.998**	**3**	**8.1E-06**	**4**	**2.8E-03**	**3**	**1.9E-03**	**3**	**0.010**	**4**	**17**
ETReg	**193**	**0.997**	**9**	**1.5E-30**	**1**	**1.2E-15**	**1**	**8.3E-16**	**1**	**1.38E-09**	**2**	**14**
GBM	**675**	**0.998**	**4**	**6.8E-06**	**3**	**2.6E-03**	**2**	**1.6E-03**	**2**	**0.008**	**3**	**14**
HistGBR	289	0.998	5	4.3E-05	7	6.6E-03	7	4.8E-03	7	0.032	7	33
HistGBR(FN)	312	0.996	11	6.9E-05	10	8.3E-03	10	5.8E-03	10	0.067	10	51
AdaBoost	**325**	**0.997**	**10**	**4.4E-06**	**2**	**2.8E-03**	**4**	**2.1E-03**	**4**	**1.25E-12**	**1**	**21**
KNR	290	0.998	6	5.1E-05	8	7.2E-03	8	5.3E-03	8	0.064	9	39
PLSReg	195	0.697	17	9.9E-02	17	3.1E-01	17	2.3E-01	20	2.844	18	89
SReg	190	0.652	18	1.1E-01	18	3.4E-01	18	2.0E-01	17	2.109	17	88
VReg	189	0.961	15	2.3E-02	15	1.5E-01	15	1.1E-01	15	1.460	15	75
LReg	210	0.723	16	9.0E-02	16	3.0E-01	16	2.1E-01	19	2.922	20	87
GReg	236	0.595	20	1.1E-01	19	3.4E-01	19	2.0E-01	18	2.909	19	95
MLPReg	416	0.995	13	1.5E-03	13	3.8E-02	13	2.6E-02	12	0.373	13	64
SVM	870	0.965	14	1.1E-02	14	1.1E-01	14	7.3E-02	14	0.934	14	70
NuSVR	1016	0.998	7	4.0E-04	11	2.0E-02	11	1.7E-02	11	0.199	11	51
LSVR	465	0.648	19	1.1E-01	20	3.4E-01	20	1.9E-01	16	1.926	16	91
ERTReg	579	0.998	8	1.5E-05	5	3.9E-03	5	2.3E-03	5	0.014	5	28
ANNs	1046	0.996	12	1.2E-03	12	3.4E-02	12	2.8E-02	13	0.327	12	61

Table 8
Sensitivity results to compare the performance of ML algorithms in the testing dataset.

ML algorithms	2-Story steel MRF founded on soil type C including PL records											
	Time (*sec*)	R^2	Score	MSE	Score	RMSE	Score	MAE	Score	RMSRE	Score	Total
XGBoost	**828**	**0.890**	**6**	**5.5E-02**	**6**	**2.3E-01**	**6**	**2.1E-01**	**6**	**0.134**	**1**	**25**
RF	395	0.768	9	1.2E-01	9	3.4E-01	8	2.8E-01	8	0.159	4	38
BReg	174	0.765	10	1.2E-01	10	3.4E-01	9	2.8E-01	9	0.160	5	43
ETReg	170	0.761	11	1.2E-01	11	3.4E-01	10	2.8E-01	10	0.162	7	49
GBM	603	0.759	14	1.2E-01	12	3.5E-01	14	2.8E-01	11	0.163	10	61
HistGBR	262	0.772	8	1.1E-01	8	3.4E-01	11	2.8E-01	12	0.162	8	47
HistGBR(FN)	288	0.809	7	9.5E-02	7	3.1E-01	7	2.6E-01	7	0.154	3	31
AdaBoost	304	0.761	12	1.2E-01	13	3.4E-01	12	2.8E-01	13	0.162	6	56
KNR	256	0.659	15	2.7E-01	16	5.2E-01	16	4.8E-01	16	0.299	11	74
PLSReg	177	0.421	17	2.9E-01	17	5.4E-01	17	5.0E-01	17	1.843	18	86
SReg	146	0.216	18	3.9E-01	18	6.2E-01	18	5.7E-01	18	1.416	16	88
VReg	**158**	**0.964**	**3**	**1.8E-02**	**3**	**1.3E-01**	**3**	**8.2E-02**	**2**	**1.119**	**15**	**26**
LReg	189	0.578	16	2.1E-01	15	4.6E-01	15	4.2E-01	15	2.244	20	81
GReg	211	0.134	19	4.6E-01	20	6.8E-01	20	6.3E-01	20	1.729	17	96
MLPReg	386	0.951	5	2.4E-02	5	1.6E-01	5	1.4E-01	5	0.868	13	33
SVM	**766**	**0.956**	**4**	**2.2E-02**	**4**	**1.5E-01**	**4**	**1.2E-01**	**4**	**1.060**	**14**	**30**
NuSVR	**975**	**0.992**	**1**	**4.0E-03**	**1**	**6.3E-02**	**1**	**4.8E-02**	**1**	**0.405**	**12**	**16**
LSVR	386	0.118	20	4.4E-01	19	6.6E-01	19	6.1E-01	19	1.887	19	96
ERTReg	455	0.761	13	1.2E-01	14	3.4E-01	13	2.8E-01	14	0.162	9	63
ANNs	**996**	**0.982**	**2**	**9.1E-03**	**2**	**9.5E-02**	**2**	**8.2E-02**	**3**	**0.147**	**2**	**11**

ing the seismic limit-state capacity. Python software was applied to develop all ML algorithms with the capability of predicting for the training and testing datasets to achieve the best ML model with the highest accuracy of prediction. In addition, a PC with information of Cori3-8100, CPU 3.60 GHz with 16 GB internal RAM was used. All steel MRFs were modeled in Opensees [47] software and the dataset contained 128,000 data points regarding important features of seismic records, record direction, the height and length of the structures, fundamental period, soil types, SSI effects, and steps of IDA analysis. It is worth mentioning that the capability of predicting the seismic limit-state capacity is defined based on predicting the M-IDA curve of steel MRFs. Therefore, in each prediction model, the M-IDA curve of the selected steel MRF, which is defined by 100 data points, is the target of prediction model in the testing dataset, and these data points should be removed from the training dataset, which includes 128,000 data points. In addition, the accuracy of prediction models have been validated by selecting different steel MRFs as target of prediction.

Figs. 13-20 present the prediction results of training and testing datasets for the steel MRFs using ML algorithms including PL records. In each figure, the pie chart shows the R^2 of the ML algorithm for predicting the M-IDA curve of the selected steel MRF. It can be seen that the R^2 for the training dataset presented by pie charts is higher than 0.95, which illustrates the accuracy of more than 95% for the prediction of the training dataset. Therefore, the ML algorithms are well-trained regarding the dataset. For the 2-Story steel MRF, the NuSVR and ANNs had the highest R^2 in all soil types with the accuracy of 98%. In the 3-Story steel MRF founded on soil types B and C, all ML algorithms had more than 97% accuracy for prediction except three ML algorithms of KNR, VReg, and XGBoost, while for soil types D and E, the NuSVR, MLPReg, and ANNs had 98% accuracy of prediction.

In the 4-Story steel MRF for all soil types, the KNR and VReg had the lowest R^2 compared to other ML techniques. In the 5-Story steel MRF founded on soil type B, the NuSVR, SVM, XGBoost, and ANNs had 98% accuracy of prediction, while in the soil types C and D, the VReg had the lowest values of R^2. In addition, the MLPReg, KNR, SVM, XGBoost, and VReg had the lowest R^2 for prediction in soil type E.

The results of prediction for the 6-Story steel MRF show that the MLPReg, KNR, SVM, AdaBoost, HistGBR(FN), and VReg had the lowest R^2 for prediction in soil type B, and the ML algorithms of MLPReg, SVM, and VReg achieved lower values of prediction accuracy in soil type C. Two algorithms of KNR and VReg had R^2 of

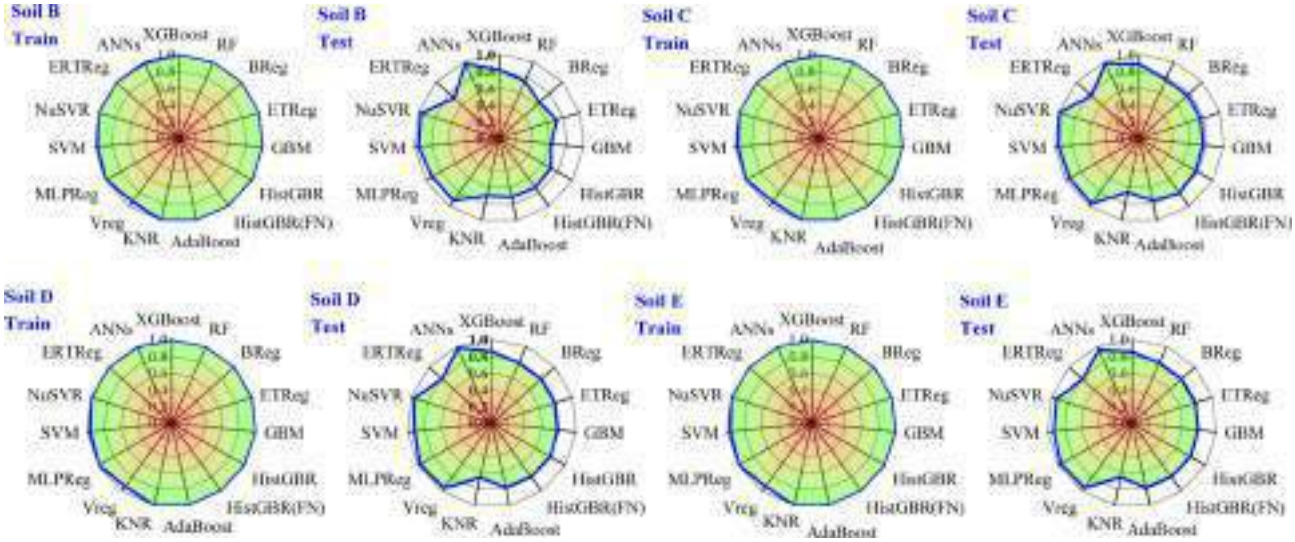

Fig. 13. Prediction results of train and test datasets for the 2-Story steel MRF using all ML algorithms including PL records.

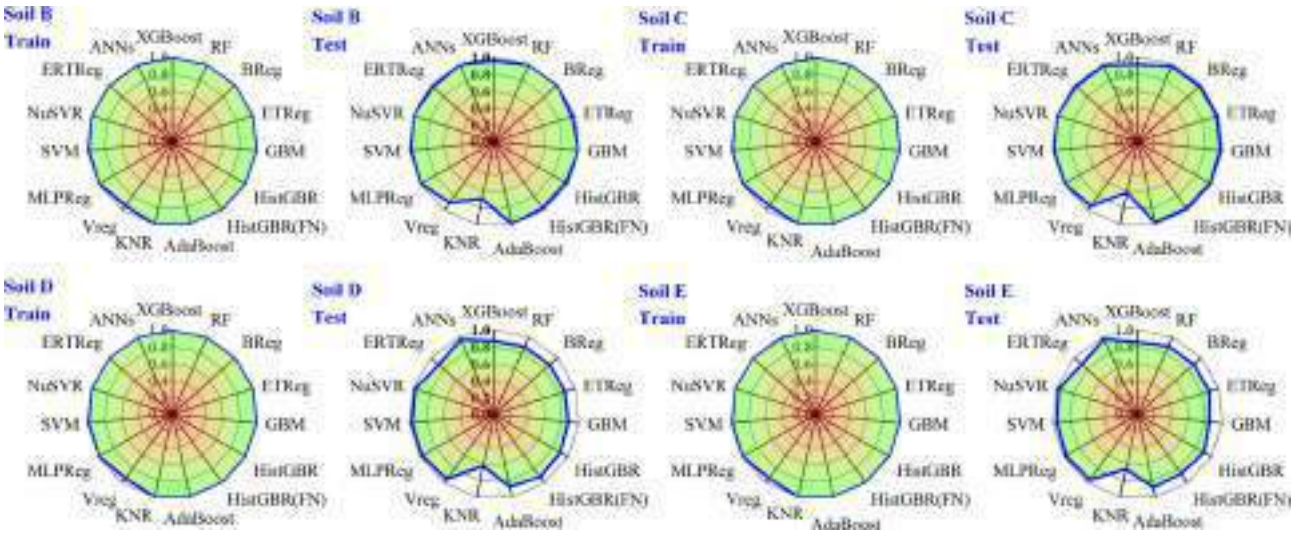

Fig. 14. Prediction results of train and test datasets for the 3-Story steel MRF using all ML algorithms including PL records.

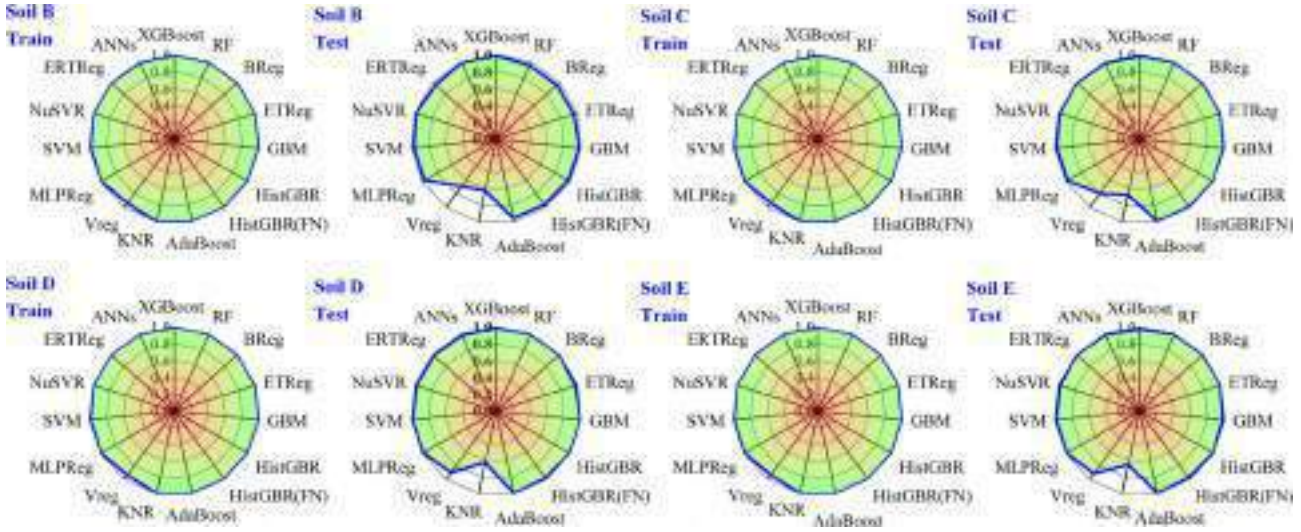

Fig. 15. Prediction results of train and test datasets for the 4-Story steel MRF using all ML algorithms including PL records.

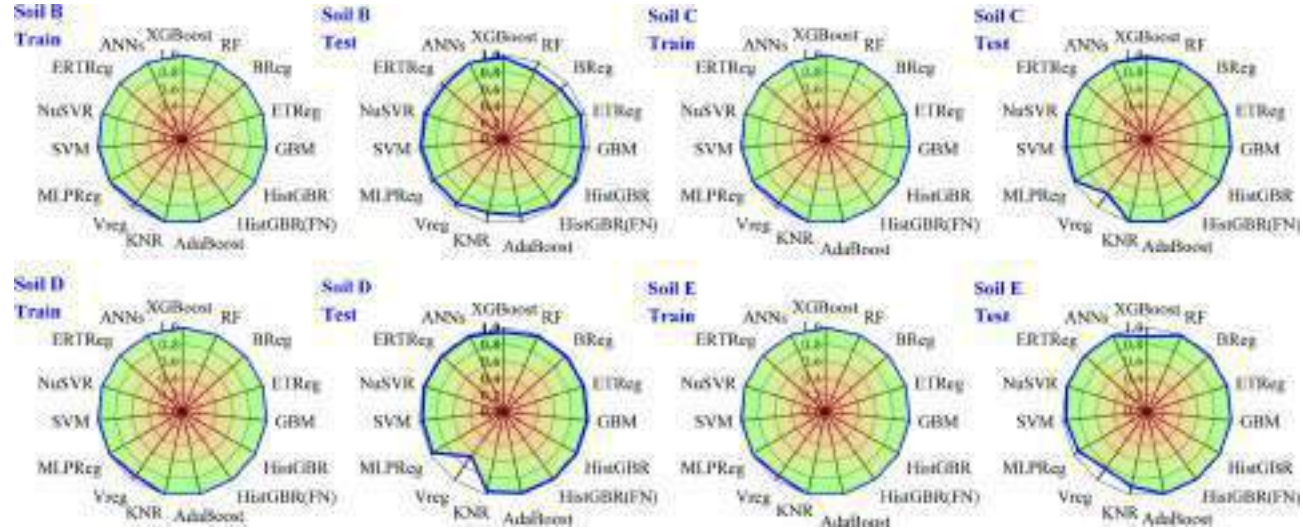

Fig. 16. Prediction results of train and test datasets for the 5-Story steel MRF using all ML algorithms including PL records.

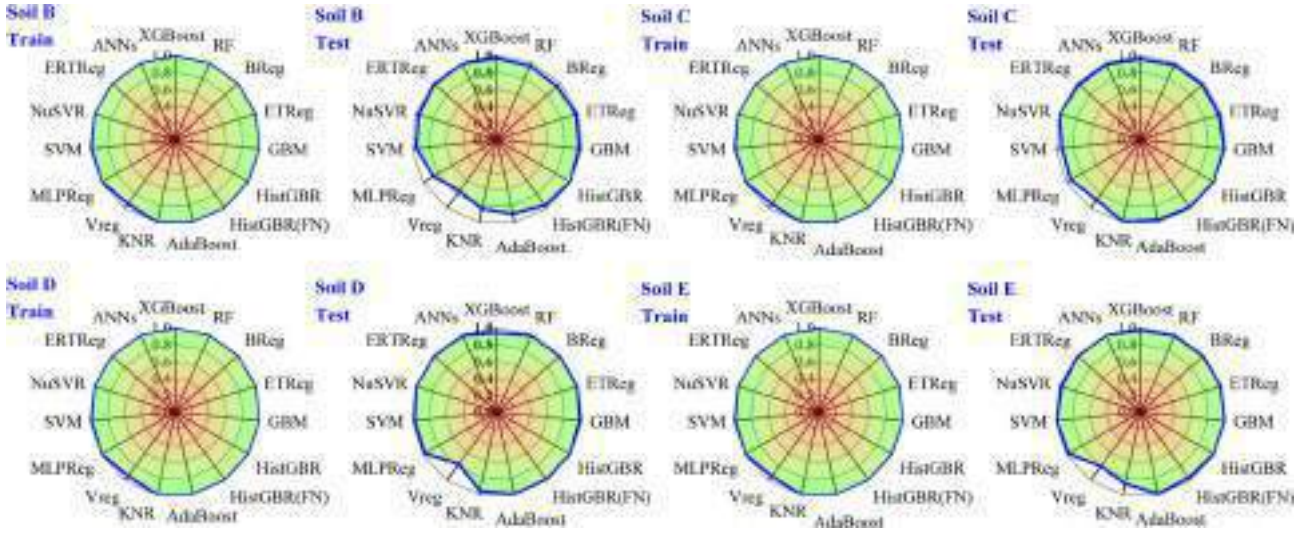

Fig. 17. Prediction results of train and test datasets for the 6-Story steel MRF using all ML algorithms including PL records.

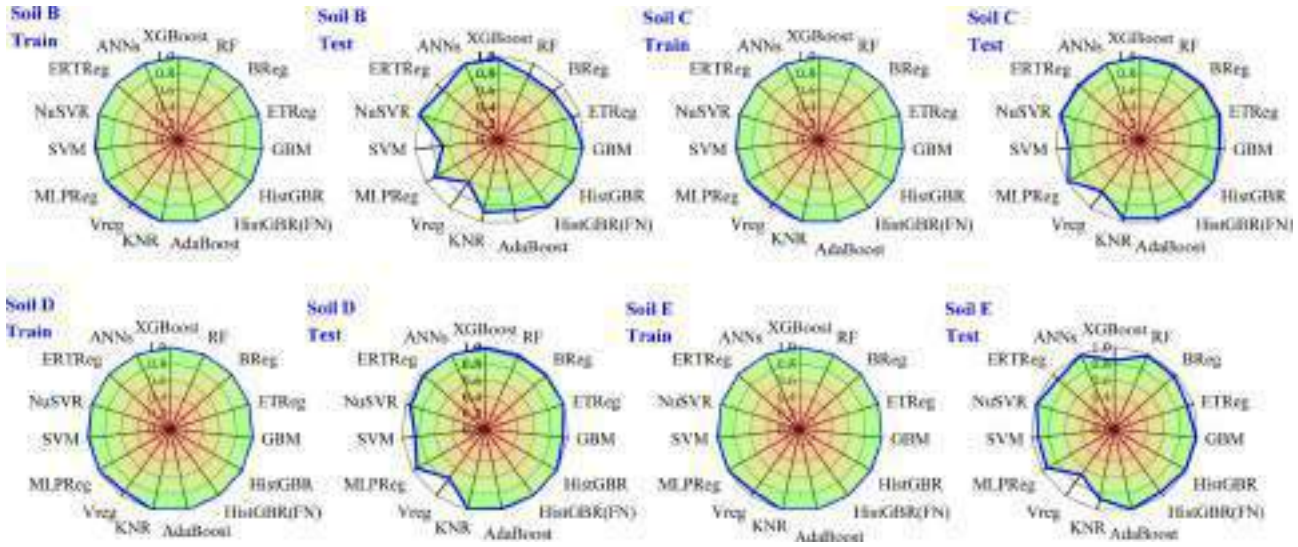

Fig. 18. Prediction results of train and test datasets for the 7-Story steel MRF using all ML algorithms including PL records.

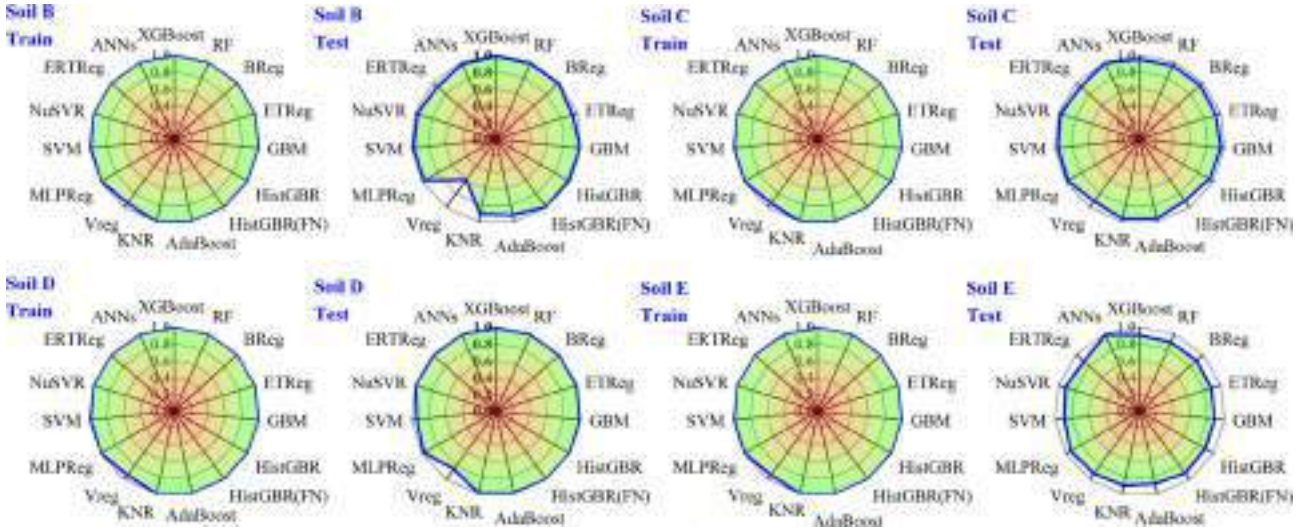

Fig. 19. Prediction results of train and test datasets for the 8-Story steel MRF using all ML algorithms including PL records.

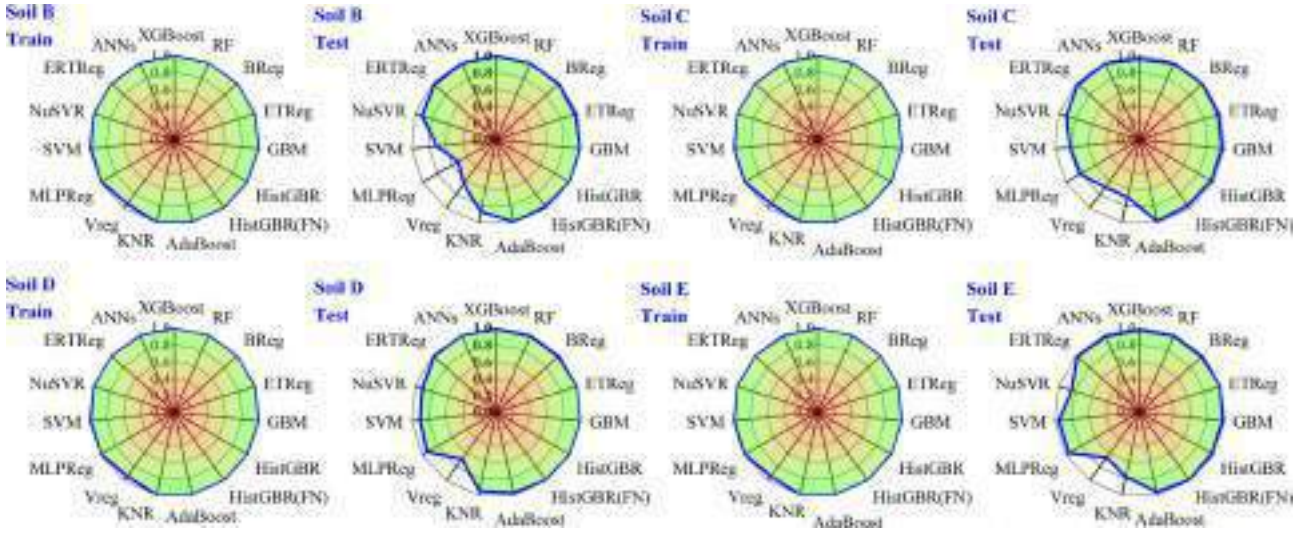

Fig. 20. Prediction results of train and test datasets for the 9-Story steel MRF using all ML algorithms including PL records.

lower than 0.95 for the prediction in soil types of D and E. The NuSVR, GBM, HistGBR, and ANNs had more than 98% accuracy of prediction in the 7-Story steel MRF for soil types B and E, while the VReg and SVM had the lowest values of R^2 for soil types C and D. It can be seen that the ERTReg, ETReg, KNR, AdaBoost and VReg had the accuracy of prediction lower than 95% for the 8-Story steel MRF in soil type B, while four algorithms of the MLPReg, NuSVR, ANNs, and SVM had 99% accuracy of prediction in soil type C. Although the SVM and VReg had the lowest values of R^2 for soil type C, the ANNs algorithm achieved the highest accuracy of prediction among others in soil type E. The results of comparison for the 9-Story steel MRF in soil types B, C, D, and E show that five algorithms of MLPReg, NuSVR, VReg, KNR, and SVM had the lowest values of R^2 and cannot be used for prediction. The

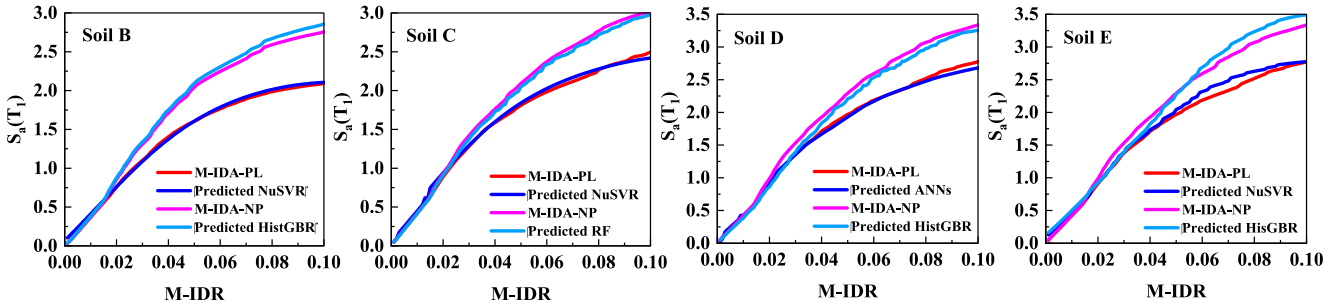

Fig. 21. Predicted M-IDA curves of the 2-Story steel MRF including PL and NP records.

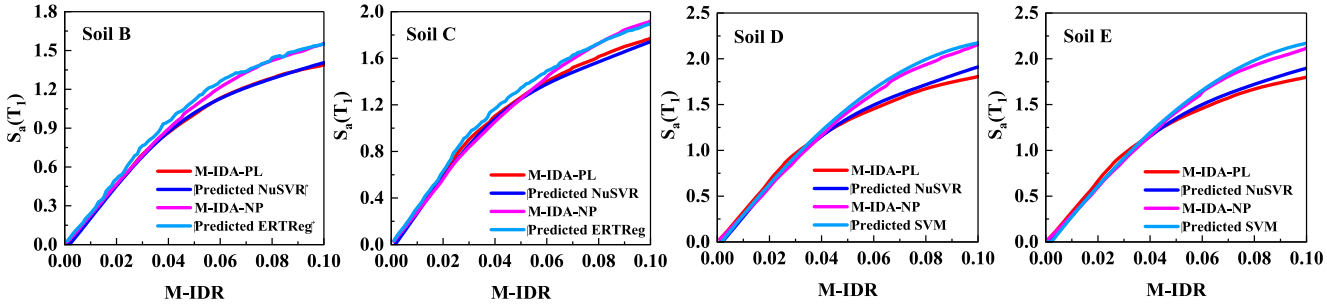

Fig. 22. Predicted M-IDA curves of the 3-Story steel MRF including PL and NP records.

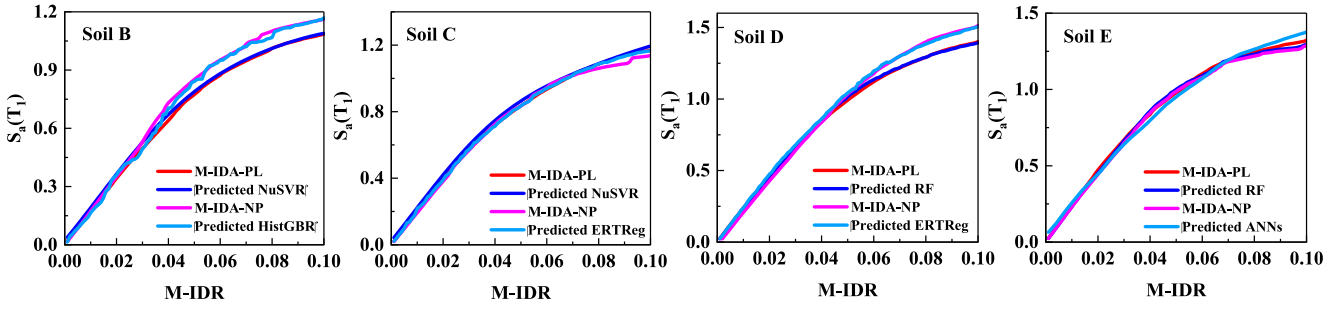

Fig. 23. Predicted M-IDA curves of the 4-Story steel MRF including PL and NP records.

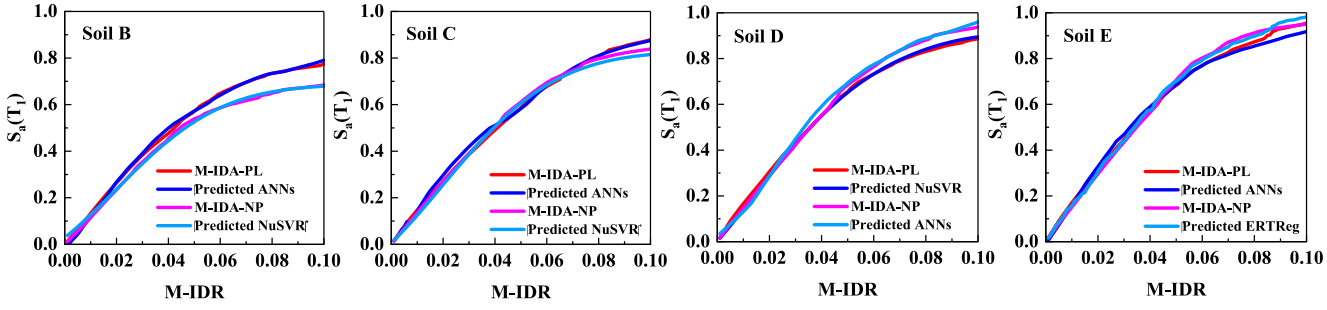

Fig. 24. Predicted M-IDA curves of the 5-Story steel MRF including PL and NP records.

results indicated the important ML algorithms with higher accuracy of prediction that can be used for seismic limit-state capacity assessment as a preliminary vulnerability assessment of steel MRFs.

Many studies were carried out to improve data-driven decision techniques known as ML algorithms to find a specific model for predicting the seismic limit-state capacities of steel structures. It should be noted that due to the complexity and unpredictability nature of seismic excitation, there is no unique model that can be used for estimation; therefore, this paper aims to explore the ML algorithms developed in Python software to find a solution to overcome this issue. According to the algorithms with high accuracy of prediction introduced in Figs. 13-20, the M-IDA curves were extracted from testing results and presented in Figs. 21-28 to show the ML-based M-IDA curves achieved by algorithms.

According to the ML-based M-IDA curves presented in Figs. 21-28, there is no unique model for all structures; hence, the best predicted M-IDA curve model was introduced regarding

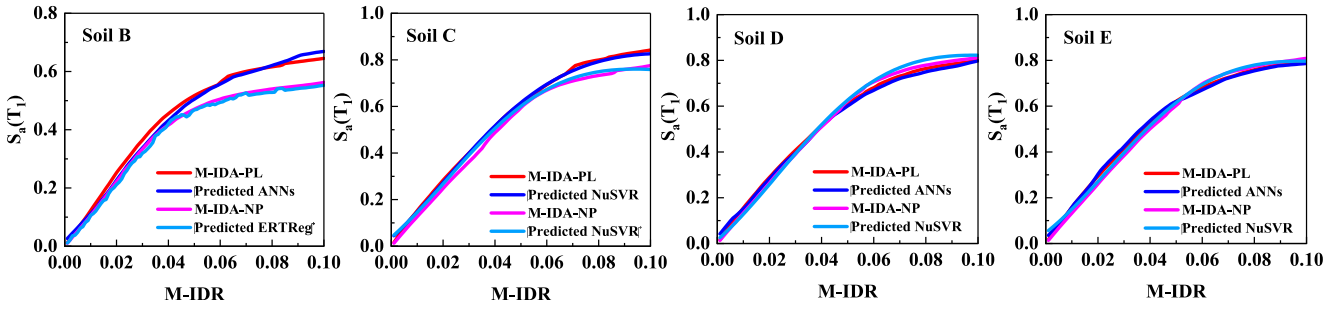

Fig. 25. Predicted M-IDA curves of the 6-Story steel MRF including PL and NP records.

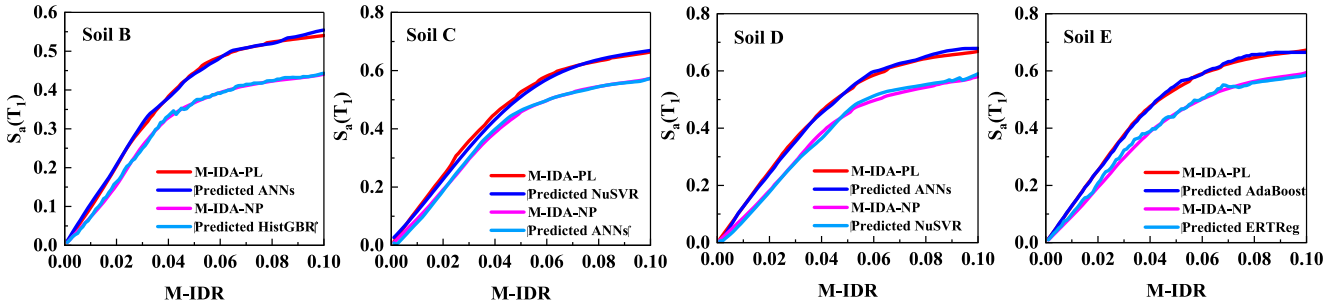

Fig. 26. Predicted M-IDA curves of the 7-Story steel MRF including PL and NP records.

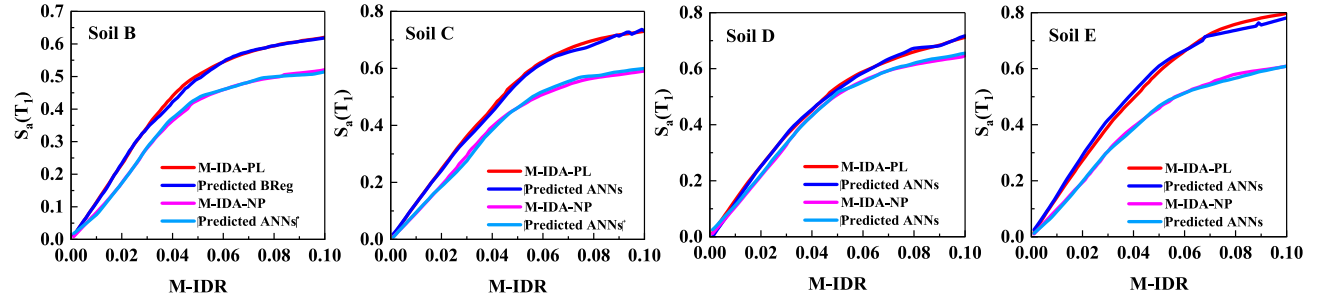

Fig. 27. Predicted M-IDA curves of the 8-Story steel MRF including PL and NP records.

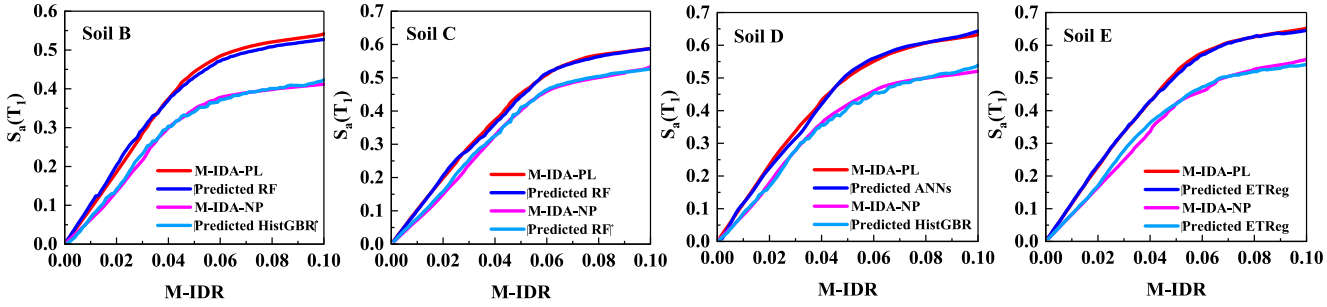

Fig. 28. Predicted M-IDA curves of the 9-Story steel MRF including PL and NP records.

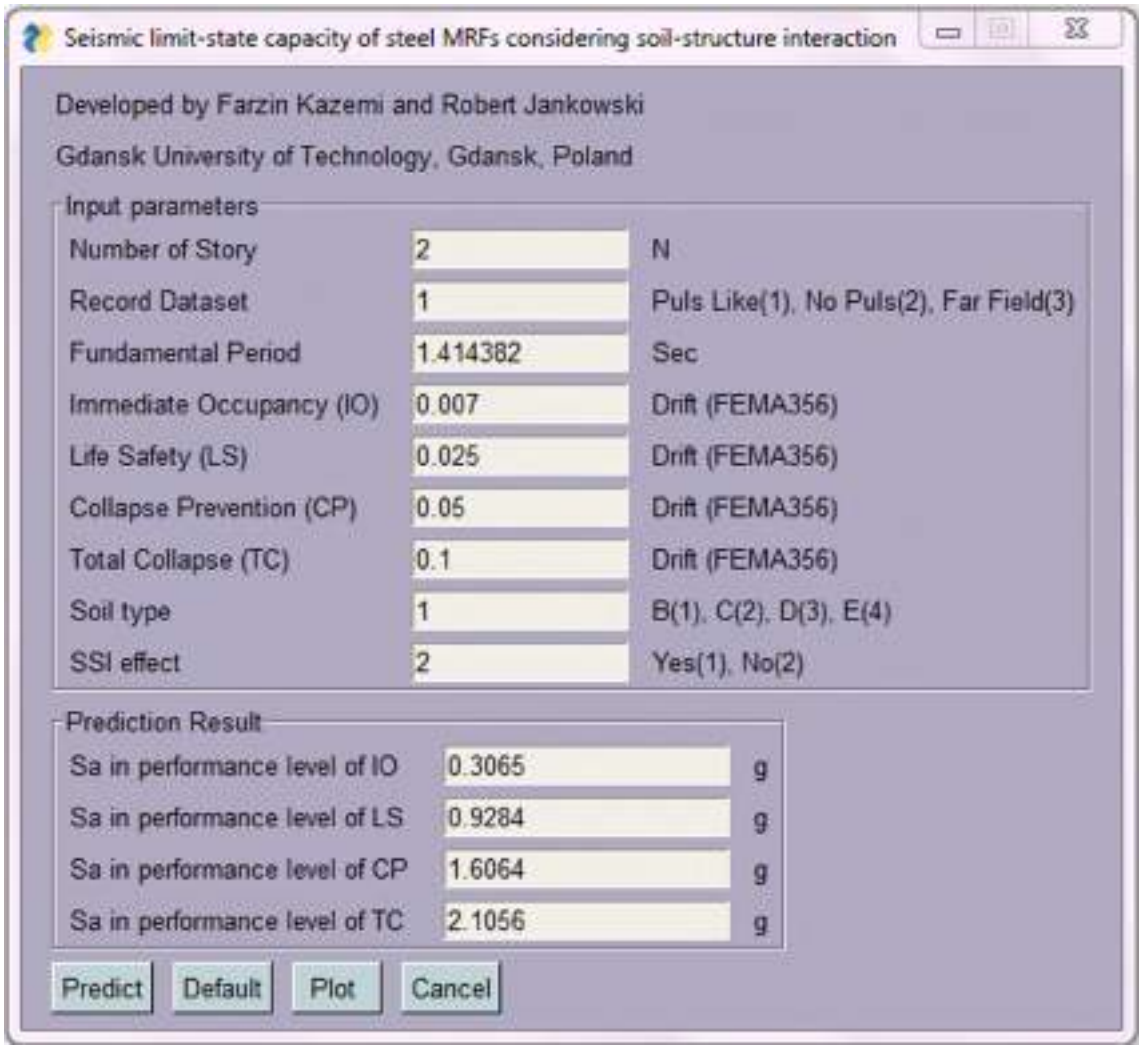

Fig. 29. Predicted M-IDA curves of the 9-Story steel MRF including PL and NP records.

Table 9
The best ML algorithms for predicting the seismic limit-state capacities of steel MRFs without SSI effects.

Steel MRF	**Soil type B**			**Soil type C**		
	PL	**NP**	**FF**	**PL**	**NP**	**FF**
2-Story	NuSVR	HistGBR	NuSVR	NuSVR	RF	RF
3-Story	NuSVR	ERTReg	ANNs	NuSVR	ERTReg	ERTReg
4-Story	NuSVR	HistGBR	ERTReg	NuSVR	ERTReg	HistGBR
5-Story	ANNs	NuSVR	HistGBR	ANNs	NuSVR	NuSVR
6-Story	ANNs	ERTReg	ANNs	NuSVR	NuSVR	NuSVR
7-Story	ANNs	HistGBR	RF	NuSVR	ANNs	ANNs
8-Story	BReg	ANNs	ANNs	ANNs	ANNs	ANNs
9-Story	RF	HistGBR	ANNs	RF	RF	RF
Steel MRF	**Soil type D**			**Soil type E**		
	PL	**NP**	**FF**	**PL**	**NP**	**FF**
2-Story	ANNs	HistGBR	ANNs	NuSVR	HistGBR	ERTReg
3-Story	NuSVR	SVM	NuSVR	NuSVR	SVM	ANNs
4-Story	RF	ERTReg	NuSVR	RF	ANNs	ANNs
5-Story	NuSVR	ANNs	ANNs	ANNs	ERTReg	ERTReg
6-Story	ANNs	NuSVR	ERTReg	ANNs	NuSVR	ANNs
7-Story	ANNs	NuSVR	ANNs	AdaBoost	ERTReg	RF
8-Story	ANNs	ANNs	NuSVR	ANNs	ANNs	ERTReg
9-Story	ANNs	HistGBR	ANNs	ETReg	ETReg	ETReg

Table 10
The best ML algorithms for predicting the seismic limit-state capacities of steel MRFs with SSI effects.

Steel MRF	Soil type B			Soil type C		
	PL	NP	FF	PL	NP	FF
2-Story	SVM	HistGBR	NuSVR	RF	SVM	NuSVR
3-Story	NuSVR	NuSVR	ERTReg	ANNs	ERTReg	ANNs
4-Story	NuSVR	RF	AdaBoost	NuSVR	ERTReg	RF
5-Story	ANNs	ANNs	NuSVR	ERTReg	NuSVR	ANNs
6-Story	ANNs	ANNs	ERTReg	NuSVR	ANNs	NuSVR
7-Story	ANNs	HistGBR(FN)	ANNs	RF	ANNs	BReg
8-Story	BReg	ANNs	NuSVR	ANNs	ANNs	XGBoost
9-Story	RF	HistGBR(FN)	AdaBoost	XGBoost	RF	NuSVR
Steel MRF	**Soil type D**			**Soil type E**		
	PL	**NP**	**FF**	**PL**	**NP**	**FF**
2-Story	SVM	ANNs	ERTReg	NuSVR	HistGBR	HistGBR
3-Story	NuSVR	NuSVR	NuSVR	NuSVR	SVM	NuSVR
4-Story	ETReg	ERTReg	RF	RF	ANNs	ANNs
5-Story	NuSVR	ANNs	NuSVR	ANNs	AdaBoost	HistGBR(FN)
6-Story	ANNs	ANNs	NuSVR	ANNs	NuSVR	XGBoost
7-Story	ANNs	ANNs	RF	ETReg	ERTReg	ERTReg
8-Story	ANNs	ANNs	NuSVR	ANNs	ANNs	ANNs
9-Story	ANNs	HistGBR(FN)	NuSVR	XGBoost	ETReg	HistGBR

the soil types, steel MRFs, and type of records. The results show that the ML-based M-IDA curve has fitted the real M-IDA curve with a higher accuracy including PL and NP records, and can be used for preliminary estimation of seismic limit-state capacity assessment.

7. Graphical user interface

To improve the results of this study for being used by designers and provide convenient access to the prediction results of this study with the capability of considering the wide range of input parameters, Graphical User Interface (GUI) was developed (see Fig. 29). The GUI can help to predict $S_a(T_1)$ for the seismic limit-state performance levels of steel MRFs introduced by FEMA356 [57] considering four soil types, three record subsets, and SSI effects. The designed GUI is based on the highest predicted model introduced in Section 6 for each type of structure. It should be noted that a developed GUI can plot the real M-IDA curve and the ML-based M-IDA curve to better access the figures. In addition, the GUI will be improved and new updates will be added.

8. Conclusion

There is no practical method available for predicting the M-IDA curve of steel structures; therefore, a complex modeling process with high computational cost should be done to achieve the seismic limit-state capacities of structures. The main purpose of this study is to propose the ML-based M-IDA curve of steel structures that can be used as a preliminary estimation with high accuracy of prediction. In addition, the results of the analysis showed that using only one ML algorithm for predicting the M-IDA curve is not possibly efficient for all steel structures, thus, it is suggested to try some of the ML algorithms to find the best fitting curve. For this purpose, numerical analyses were done to prepare datasets for training and testing the ML algorithms. Due to the unpredictable nature of seismic excitations, all algorithms were compared to find the best one with the highest accuracy of prediction by comparing the results of metrics such as R^2, MSE, RMSE, RMSRE and MAE, and computing time. To better show the comparison, score markers were used for prediction of training and testing datasets. The results of comparison showed that the ETReg, GBM, BReg, AdaBoost, and RF algorithms had highest prediction accuracy in training dataset, while the ANNs, NuSVR, XGBoost, VReg, and SVM algorithms were the best prediction models in testing dataset. In addition, the ANNs, NuSVR, and XGBoost algorithms had higher computing time among other algorithms. Tables 9 and 10 illustrate the best ML algorithms for predicting the seismic limit-state capacities of steel MRFs regarding three record subsets excluding and including SSI effects, respectively. In addition, Graphical User Interface (GUI) was developed to predict $S_a(T_1)$ for the seismic limit-state performance levels of steel MRFs contains all results of the analysis were done in this study to help designers for estimation of seismic limit-state performance levels based on the ML methodology. It is worth mentioning that using the developed GUI mitigates the need for computationally expensive, time-consuming, and complex analysis, and further improvements will be added to the updated GUI.

Declaration of Competing Interest

The authors declare that they have no known competing financial interests or personal relationships that could have appeared to influence the work reported in this paper.

Acknowledgments

Numerical calculations were carried out at the Tri-City Academic Supercomputer and Network (*CI TASK*) in Gdańsk, Poland.

References

[1] Elwardany H, Seleemah A, Jankowski R, El-Khoriby S. Influence of soil-structure interaction on seismic pounding between steel frame buildings considering the effect of infill panels. Bull Earthq Eng 2019;17(11):6165–202.
[2] Naderpour H., Danaeifard P. Burkacki D., Jankowski R. Earthquake-induced pounding of medium-to-high-rise base-isolated buildings. Applied Sciences. 9(21), 2019, 4681, 2019.
[3] Rezaei H, Moayyedi SA, Jankowski R. Probabilistic seismic assessment of RC box-girder highway bridges with unequal-height piers subjected to earthquake-induced pounding. Bull Earthq Eng 2020;18(4):1547–78.
[4] Yazdanpanah O, Mohebi B, Kazemi F, Mansouri I, Jankowski R. Development of fragility curves in adjacent steel moment-resisting frames considering pounding effects through improved wavelet-based refined damage-sensitive feature. Mech Syst Sig Process 2022;173:109038.
[5] Kazemi F, Mohebi B, Yakhchalian M. Predicting the seismic collapse capacity of adjacent structures prone to pounding. Can J Civ Eng 2020;47(6):663–77.
[6] Kazemi F, Mohebi B, Jankowski R. Predicting the seismic collapse capacity of adjacent SMRFs retrofitted with fluid viscous dampers in pounding conditions. Mech Syst Sig Process 2021;161:107939.
[7] Kazemi F, Miari M, Jankowski R. Investigating the effects of structural pounding on the seismic performance of adjacent RC and steel MRFs. Bull Earthq Eng 2021;19(1):317–43.
[8] Kazemi F, Asgarkhani N, Manguri A, Jankowski R. Investigating an optimal computational strategy to retrofit buildings with implementing viscous

dampers. International Conference on Computational Science, (ICCS proceeding), Lecture Notes in Computer Science, 2022;13351:184–91. https://doi.org/10.1007/978-3-031-08754-7_25.
[9] Hastie T, Tibshirani R, Friedman J. Overview of supervised learning. In The elements of statistical learning 2009:9–41.
[10] Dollar, P., Tu, Z., Belongie, S. Supervised learning of edges and object boundaries. In 2006 IEEE Computer Society Conference on Computer Vision and Pattern Recognition (CVPR'06), IEEE, 2006, Vol. 2, pp. 1964-1971.
[11] Bagherzadeh F, Mehrani MJ, Basirifard M, Roostaei J. Comparative study on total nitrogen prediction in wastewater treatment plant and effect of various feature selection methods on machine learning algorithms performance. J Water Process Eng 2021;41:102033.
[12] Burton HV, Sreekumar S, Sharma M, Sun H. Estimating aftershock collapse vulnerability using mainshock intensity, structural response and physical damage indicators. Struct Saf 2017;68:85–96.
[13] Mangalathu S, Jeon JS. Classification of failure mode and prediction of shear strength for reinforced concrete beam-column joints using machine learning techniques. Eng Struct 2018;160:85–94.
[14] Worden K, Green PL. A machine learning approach to nonlinear modal analysis. Mech Syst Sig Process 2017;84:34–53.
[15] Luo H, Paal SG. Machine learning–based backbone curve model of reinforced concrete columns subjected to cyclic loading reversals. J Comput Civil Eng 2018;32(5):04018042.
[16] Wang Z, Pedroni N, Zentner I, Zio E. Seismic fragility analysis with artificial neural networks: Application to nuclear power plant equipment. Eng Struct 2018;162:213–25.
[17] Zhang Y, Burton HV, Sun H, Shokrabadi M. A machine learning framework for assessing post-earthquake structural safety. Struct Saf 2018;72:1–16.
[18] Zhang Y, Burton HV. Pattern recognition approach to assess the residual structural capacity of damaged tall buildings. Struct Saf 2019;78:12–22.
[19] Kiani J, Camp C, Pezeshk S. On the application of machine learning techniques to derive seismic fragility curves. Comput Struct 2019;218:108–22.
[20] Nguyen HD, Truong GT, Shin M. Development of extreme gradient boosting model for prediction of punching shear resistance of r/c interior slabs. Eng Struct 2021;235:112067.
[21] Nguyen NV, Nguyen HD, Dao ND. Machine learning models for predicting maximum displacement of triple pendulum isolation systems. Structures 2022;36:404–15.
[22] Noureldin M, Ali A, Sim S, Kim J. A machine learning procedure for seismic qualitative assessment and design of structures considering safety and serviceability. Journal of Building Engineering 2022;50:104190.
[23] Harirchian E, Kumari V, Jadhav K, Raj Das R, Rasulzade S, Lahmer T. A machine learning framework for assessing seismic hazard safety of reinforced concrete buildings. Applied Sciences 2020;10(20):7153.
[24] Li C, Li H, Chen X. A framework for fast estimation of structural seismic responses using ensemble machine learning model. Smart Structures and Systems 2021;28(3):425–41.
[25] Pal M. Random forest classifier for remote sensing classification. Int J Remote Sens 2005;26(1):217–22.
[26] Geurts P, Ernst D, Wehenkel L. Extremely randomized trees Machine learning 2006;63(1):3–42.
[27] Breiman L. Bagging predictors Machine learning 1996;24(2):123–40.
[28] Louppe G, Geurts P. Ensembles on random patches. In: Joint European Conference on Machine Learning and Knowledge Discovery in Databases. Berlin, Heidelberg: Springer; 2012. p. 346–61.
[29] Friedman J, Hastie T, Tibshirani R. Additive logistic regression: a statistical view of boosting (with discussion and a rejoinder by the authors). The annals of statistics 2000;28(2):337–407.
[30] Friedman JH. Greedy function approximation: a gradient boosting machine. Ann Stat 2001:1189–232.
[31] Gholizadeh R, Amiri GG, Mohebi B. An alternative approach to a harmony search algorithm for a construction site layout problem. Can J Civ Eng 2010;37 (12):1560–71.
[32] Li T, Pan Y, Tong K, Ventura CE, de Silva CW. A multi-scale attention neural network for sensor location selection and nonlinear structural seismic response prediction. Comput Struct 2021;248:106507.
[33] Todorov B, Billah AM. Machine learning driven seismic performance limit state identification for performance-based seismic design of bridge piers. Eng Struct 2022;255:113919.
[34] Cortes C, Vapnik V. Support vector machine Machine learning 1995;20 (3):273–97.
[35] Chang CC, Lin CJ. Training v-support vector regression: theory and algorithms. Neural Comput 2002;14(8):1959–77.
[36] Drucker H, Burges CJ, Kaufman L, Smola A, Vapnik V. Support vector regression machines. Advances in neural information processing systems 1996;9.
[37] Freund Y, Schapire RE. A decision-theoretic generalization of on-line learning and an application to boosting. J Comput Syst Sci 1997;55(1):119–39.
[38] Kohavi R. A study of cross-validation and bootstrap for accuracy estimation and model selection. In Ijcai 1995;14–2:1137–45.
[39] Höskuldsson A. PLS regression methods Journal of chemometrics 1988;2 (3):211–28.
[40] McCullagh P, Nelder JA. Generalized linear models. UK: Chapman and Hall. London; 1989.
[41] Wolpert DH. Stacked generalization Neural networks 1992;5(2):241–59.
[42] USGS. US Geological Survey. Accessed November 6, 2012. http://usgs.gov.
[43] Asce. 7–16. Minimum design loads and associated criteria for buildings and other structures. Reston, VA: American Society of Civil Engineers; 2017.
[44] Committee AISC. Specification for structural steel buildings (ANSI/AISC 360–10). Chicago-Illinois: American Institute of Steel Construction; 2016.
[45] AISC, A. AISC 341-10, seismic provisions for structural steel buildings. Chicago, IL: American Institute of Steel Construction, 2016.
[46] Mohebi B, Yazdanpanah O, Kazemi F, Formisano A. Seismic damage diagnosis in adjacent steel and RC MRFs considering pounding effects through improved wavelet-based damage-sensitive feature. Journal of Building Engineering 2021;33:101847.
[47] McKenna F, Fenves GL, Filippou FC, Scott MH. Open system for earthquake engineering simulation (OpenSees). Berkeley: Pacific Earthquake Engineering Research Center, University of California; 2016. berkeley.edu.
[48] Lignos DG, Krawinkler H, Whittaker AS. Prediction and validation of sidesway collapse of two scale models of a 4-story steel moment frame. Earthquake Eng Struct Dyn 2011;40(7):807–25.
[49] Del Carpio Ramos M, Mosqueda G, Hashemi MJ. Large-scale hybrid simulation of a steel moment frame building structure through collapse. J Struct Eng 2016;142(1):04015086.
[50] Kazemi, F., Mohebi, B., Yakhchalian, M. Enhancing the seismic performance of adjacent pounding structures using viscous dampers. In The 16th European Conference on Earthquake Engineering (16ECEE), 18-21, June, Thessaloniki, Greece, 2018.
[51] Kazemi F, Mohebi B, Yakhchalian M. Evaluation the P-delta effect on collapse capacity of adjacent structures subjected to far-field ground motions. Civil Engineering Journal 2018;4(5):1066. https://doi.org/10.28991/cej-0309156.
[52] Mohebi, B., Kazemi, F., Yakhchalian, M. Investigating the P-Delta effects on the seismic collapse capacity of adjacent structures, 16th European Conference on Earthquake Engineering (16ECEE), 18-21, June, Thessaloniki, Greece, 2018.
[53] Asgarkhani N, Yakhchalian M, Mohebi B. Evaluation of approximate methods for estimating residual drift demands in BRBFs. Eng Struct 2020;224:110849.
[54] Yakhchalian M, Asgarkhani N, Yakhchalian M. Evaluation of deflection amplification factor for steel buckling restrained braced frames. Journal of Building Engineering 2020;30:101228.
[55] Yakhchalian M, Yakhchalian M, Asgarkhani N. An advanced intensity measure for residual drift assessment of steel BRB frames. Bull Earthq Eng 2021;19 (4):1931–55.
[56] Elwardany H, Seleemah A, Jankowski R, El-Khoriby S. Influence of soil–structure interaction on seismic pounding between steel frame buildings considering the effect of infill panels. Bull Earthq Eng 2019;17(11):6165–202.
[57] Allotey N, El Naggar MH. Generalized dynamic Winkler model for nonlinear soil–structure interaction analysis. Can Geotech J 2008;45(4):560–73.
[58] Forcellini D. Analytical fragility curves of shallow-founded structures subjected to Soil-Structure Interaction (SSI) effects. Soil Dyn Earthquake Eng 2021;141:106487.
[59] Raychowdhury P, Hutchinson TC. Performance evaluation of a nonlinear Winkler-based shallow foundation model using centrifuge test results. Earthquake Eng Struct Dyn 2009;38(5):679–98.
[60] Boulanger RW, Curras CJ, Kutter BL, Wilson DW, Abghari A. Seismic soil-pile-structure interaction experiments and analyses. J Geotech Geoenviron Eng 1999;125(9):750–9.
[61] Gazetas G. Formulas and charts for impedances of surface and embedded foundations. Journal of geotechnical engineering 1991;117(9):1363–81.
[62] FEMA-356. Prestandard and commentary for the seismic rehabilitation of buildings. Washington, DC: Federal Emergency Management Agency, 2000.
[63] Applied Technology Council, United States. Federal Emergency Management Agency. Quantification of building seismic performance factors. US Department of Homeland Security, FEMA, 2009.
[64] Göçken M, Özçalıcı M, Boru A, Dosdoğru AT. Integrating metaheuristics and artificial neural networks for improved stock price prediction. Expert Syst Appl 2016;44:320–31.

Paper IX:

Kazemi, F., Asgarkhani, N., & Jankowski, R. (2023). Machine learning-based seismic response and performance assessment of reinforced concrete buildings. Archives of Civil and Mechanical Engineering, 23(2), 94. doi.org/10.1007/s43452-023-00631-9

Archives of Civil and Mechanical Engineering (2023) 23:94
https://doi.org/10.1007/s43452-023-00631-9

ORIGINAL ARTICLE

Machine learning-based seismic response and performance assessment of reinforced concrete buildings

F. Kazemi[1] · N. Asgarkhani[1] · R. Jankowski[1]

Received: 19 November 2022 / Revised: 2 February 2023 / Accepted: 26 February 2023 / Published online: 14 March 2023
© The Author(s) 2023

Abstract
Complexity and unpredictability nature of earthquakes makes them unique external loads that there is no unique formula used for the prediction of seismic responses. Hence, this research aims to implement the most well-known Machine Learning (ML) methods in Python software to propose a prediction model for seismic response and performance assessment of Reinforced Concrete Moment-Resisting Frames (RC MRFs). To prepare 92,400 data points of training dataset for developing data-driven techniques, Incremental Dynamic Analyses (IDAs) were performed considering 165 RC MRFs with two-, to twelve-Story elevations having the bay lengths of 5.0 m, 6.1 m, and 7.6 m assuming near-fault seismic excitations. Then, important structural features were considered in datasets to train and test the ML-based prediction models, which were improved with innovative techniques. The results show that improved algorithms have higher R^2 values for estimating the Maximum Interstory Drift Ratio (IDR_{max}), and two improved algorithms of artificial neural networks and extreme gradient boosting can estimate the Median of IDA curves (M-IDAs) of RC MRFs, which can be used to estimate the seismic limit-state capacity and performance assessment of existing or newly constructed RC buildings. To validate the generality and accuracy of the proposed ML-based prediction model, a five-Story RC building with different input features was used, and the results are promising. Therefore, graphical user interface is introduced as user-friendly tool to help researchers in estimating the seismic limit-state capacity of RC buildings, while reducing the computational cost and analytical efforts.

Keywords Machine learning method · Maximum interstory drift ratio · Seismic limit-state capacity · Predicting seismic performance · Seismic probabilistic assessment

1 Introduction

The vulnerability of a building can be evaluated either by in-situ technique of data analysis with non-constructive methods, known as structural health monitoring, or numerical analysis of structural models. The main idea of using such methods is to evaluate the building performance in the operating condition. Although in-situ technique can provide a wide range of data, some practical limitations such as implementing the sensors or actuators and mechanical problems during the time can prevent the performance assessment of structures [1–3]. Therefore, this method can be improved by response prediction methods for buildings subjected to seismic excitations.

Nowadays, the seismic probabilistic assessment of a building needs to perform complicate analysis using precise finite element model, which may need a time-consuming process for evaluating different limit states (e.g., see [4, 5]). Due to the unpredictable nature of ground motions, it is essential to predict the nonlinear structural response during seismic loads to take precautions for reducing the probability of collapse risk. There are some approaches that can be employed to perform nonlinear analysis. The nonlinear static analysis, known also as pushover analysis, can provide information about the base shear versus top floor displacement. While the nonlinear time history analysis uses the pre-recorded earthquakes and performs analysis considering the scale factors defined based on the

✉ F. Kazemi
farzin.kazemi@pg.edu.pl

N. Asgarkhani
neda.asgarkhani@pg.edu.pl

R. Jankowski
jankowr@pg.edu.pl

[1] Faculty of Civil and Environmental Engineering, Gdańsk University of Technology, Ul. Narutowicza 11/12, 80-233 Gdansk, Poland

acceleration spectrum prescribed by design code. Hence, the most accurate approaches of estimating seismic response are conducted by the nonlinear time history analysis and Incremental Dynamic Analysis (IDA) using prior seismic events and finite element methods [6–8]. The prediction of seismic response using these approaches need to prepare complex models and perform time-consuming analysis, while using simplified models (e.g., single-degree of freedom model) are computationally efficient with low performance and behavior compared to the real structures. Therefore, there is a need to introduce a novel Machine Learning (ML)-based method to efficiently and accurately predict the seismic response of RC frames.

Finding the seismic capacity of buildings can help engineers to find a preliminary prediction for the performance levels of the designed building. Kazemi et al. [9, 10] proposed factors for modifying and estimating the collapse capacity of colliding steel Moment-Resisting Frames (MRFs) and colliding Reinforced Concrete (RC) and steel frames [11]. It should be noted that the proposed factors were achieved from complex modeling and analysis; therefore, there is a need to propose a prediction model to avoid such prohibitively complex analysis. Recently, ML algorithms are applied in many civil engineering areas such as failure mode of steel base-plate connection [12], damage identification of bridge [13], damage state of steel frames [14], and RC beams [15]. ML methods are divided into two main parts of supervised and unsupervised algorithms, which the seismic response prediction can be considered as supervised learning using training and testing datasets with the possibility of assuming n-features for n-samples. Therefore, in this method, it is possible to take the important features into account [16–18]. Huang et al. [19] proposed a backpropagation neural network to predict the seismic response of structures. Yinfeng et al. [20] used the Support Vector Machine (SVM) algorithm for predicting the nonlinear time history response of structures. Then, Lagaros and Papadrakakis [21] improved neural networks for predicting the nonlinear time history response of a three-dimensional building using six seismic excitations. De Lautour and Omenzetter [22] developed a methodology for estimating the structural responses using pattern recognition of damages. ML algorithms are in the interest of some researchers to use for nonlinear modal analysis [23], predicting seismic responses for achieving fragility curves [24], and predicting maximum displacements of isolated pendulum system [25]. Oh et al. [26] developed a neural network model for predicting the seismic response of buildings based on the correlation of records using 2700 artificial records. Luo and Paal [27] proposed a novel artificial methodology for seismic response prediction of RC structures using 272 RC columns datasets.

It is confirmed that there is no unique formula for the prediction of Maximum Interstory Drift Ratio (IDR_{max}) and Median of IDA curves (M-IDAs) for any type of RC buildings. The purpose of this research is to develop a powerful ML-based tool with employing the innovative data sampling and hyperparameter optimization methods such as fine-tune method, halving search strategy, grid search method, and *k*-fold cross-validation. For this purpose, a wide range of data points containing 165 RC MRFs with different length and number of bays were numerically determined to prepare training dataset. Then, the ML-based prediction model can be used for estimating the seismic response and seismic limit-state capacities of RC buildings that can be further applied for a preliminary estimation of IDR_{max} and M-IDAs of existing and newly constructed buildings. The seismic response prediction results would help designers to find out the behavior of the designed building, and regarding the behavior, it is possible to control the performance of structural elements for postponing the seismic damages. In other words, estimating the IDR_{max} can be used for predicting the maximum deformation of buildings, and predicting the $Sa(T_1)$ of M-IDAs can be applied for seismic performance levels assessment. Finally, the results of research were used for introducing an estimation tool based on the developed ML algorithms.

2 Structural response prediction model

2.1 Artificial neural network

Due to the high ability of Artificial Neural Networks (ANNs) for prediction, they can be trained for different problems, such as positioning site facilities [28], the seismic limit-state performance of bridge piers [29], estimating the fracture toughness of rocks [30], optimizing the consumption of energy [31], estimating the compressive strength of steel fiber-reinforced concrete [32], seismic vulnerability assessment of RC frames [33], and seismic response prediction of structures [34]. ANNs contain three main parts of the input layer, hidden layers, and output layer, which are connected by some nonlinear function with the adjusted weight. The weight of each neuron can increase or decrease the strength of connection for purpose of minimizing the loss function or error (i.e., the difference between the predicted and actual values). Backward and forward propagation methods can be used for recalculating the weights of each neuron in the previous iteration to minimize the error; then, the process can be repeated with new adjusted weights to achieve a reliable model. The backward propagation method is presented in Fig. 1. In this study, IDR_{max} and $Sa(T_1)$ were defined as targets for backward and forward propagation ANNs. Moreover, Multi-layer Perceptron Regressor (MLPReg)

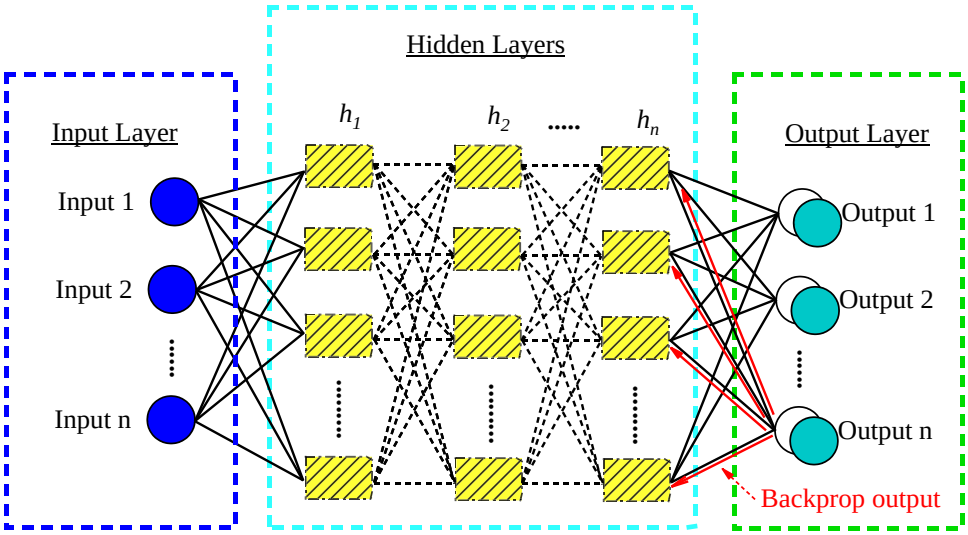

Fig. 1 Functioning of the back-propagation method in ANNs

considers the linear function to predict seismic responses of RC structures.

2.2 Random decision forest

Random decision Forest (RF) can be employed for both regression and classification problems. RF algorithm uses an ensemble multiple bagging models parallel to a different train subset from train data, and achieves the final result based on the majority voting. Figure 2 presents the RF algorithm with the bagging principle.

Although the RF algorithm can be classified as a decision tree, the RF method considers subsets of data to solve the overfitting problem while selecting random observations instead of a set of formulas [35]. It should be noted that different parameters were selected by trial and error to find the lower bias and higher variance values to overcome the overfitting problem and achieve an optimized prediction model. Moreover, different types of RF algorithms known as An Extra-Trees Regressor (ETReg), which randomly selects decision tree to fit input data, and An Extremely Randomized Tree Regressor (ERTReg), which uses the random tree selection to improve the calculations

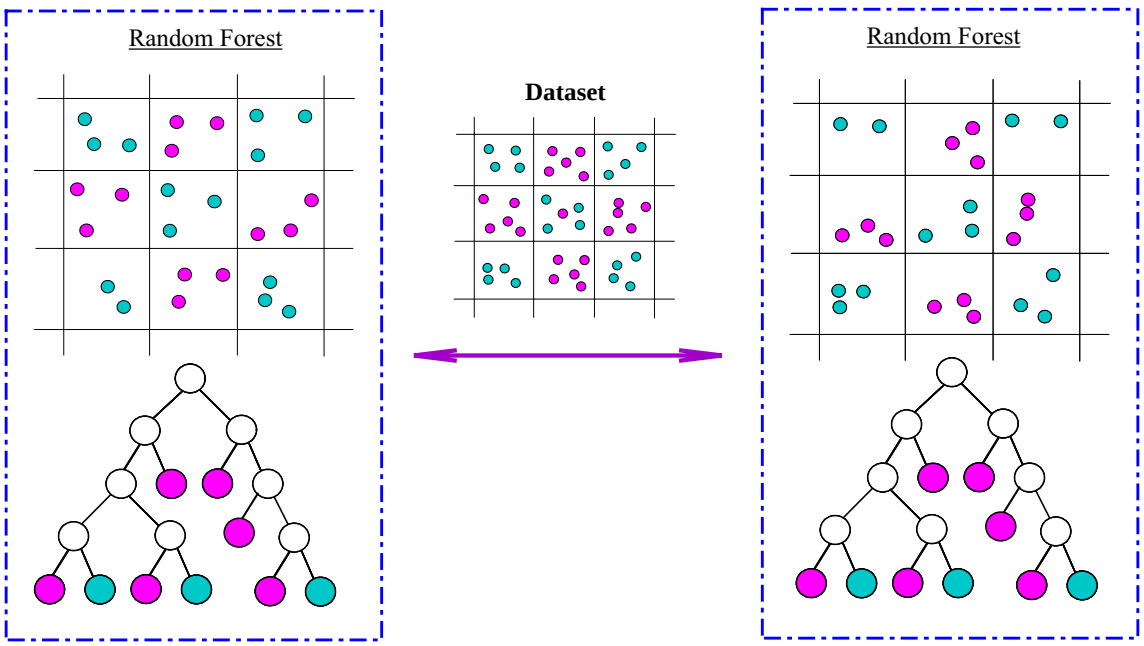

Fig. 2 RF algorithm with the bagging principle

speed [36], and Bagging Regressor (BReg), which aggregate individual predictions were used to find the best prediction model [37].

2.3 Boosting algorithms

Boosting principle is another way of using RF methods. In this principle, weak learners combine in sequential order to create a strong model with higher accuracy of prediction. Adaptive Boosting (AdaBoost) algorithm combines strong base learners such as decision trees with a single split to weight the data points for improving the accuracy of estimation [38]. Gradient Boosting Machine (GBM) comes from the idea of improving the weak learners to enhance their final results by minimizing the loss function. Moreover, Histogram-based Gradient Boosting Regression (HistGBR) considers the quantization method for splitting the features for prediction with a higher speed compared to GBM. To control the accuracy of the results, the following formula can be used considering the initial probability equal to 0.5, and in each step, the value can be compared with the previous step to find an optimized model.

$$\text{Value} = \frac{\sum_{i=1}^{n} \text{Residual}_i}{\sum_{i=1}^{n} (\text{Previous Probability}_i \times (1 - \text{Previous Probability}_i))}, \quad (1)$$

$$\text{Residual}_i = (\text{Actual } (\text{IDR}_{\max i}) - \text{Predicted } (\text{IDR}_{\max i})), \quad (2)$$

Extreme Gradient Boosting (XGBoost) is an improved algorithm of GBM with a regularize factor, λ, to reduce the effectiveness of small leaves [39, 40]. In this study, a fine-tune XGBoost model was used to change the trees number and parameters to find the best target based on the following formula:

$$\text{Value} = \frac{\sum_{i=1}^{n} \text{Residual}_i}{\sum_{i=1}^{n} (\text{Previous Probability}_i \times (1 - \text{Previous Probability}_i)) + \lambda}. \quad (3)$$

2.4 Support vector machine

Support Vector Machine (SVM) is selected as a decision boundary method with the capability of using hyperplane based on the marginal distances for two-dimensional and three-dimensional spaces [41]. In addition, Nu-Support Vector Regression (NuSVR), which considers the ν parameter as the controlling number of vectors [42], and Linear Support Vector Regression (LSVR), which considers functions for loss and penalties [43], were assumed to find a suitable model for estimating $\text{IDR}_{\max}$ and $\text{Sa}(T_1)$. To enhance the performance of ML methods during the training, and reduce the risk of losing the important datasets, the *k*-fold cross-validation was employed. Figure 3 presents the *k*-fold cross-validation methodology, in which, training and testing datasets are 70–80% and 30–20% of total data points, respectively [44]. It is worth mentioning that the *k*-fold cross-validation with different *k* was employed for assumed ML algorithms to find the suitable *k* with higher performance.

2.5 Regressors models

Some important regression algorithms can be used for $\text{IDR}_{\max}$ prediction, which is a supervised regression model while not included in the abovementioned category. For example, these models are not using the hidden layers ability (i.e., ANNs) or boosting methods (i.e., XGBoost); therefore, this subsection is defined to include the ML algorithms used in this research with different ability of predictions.

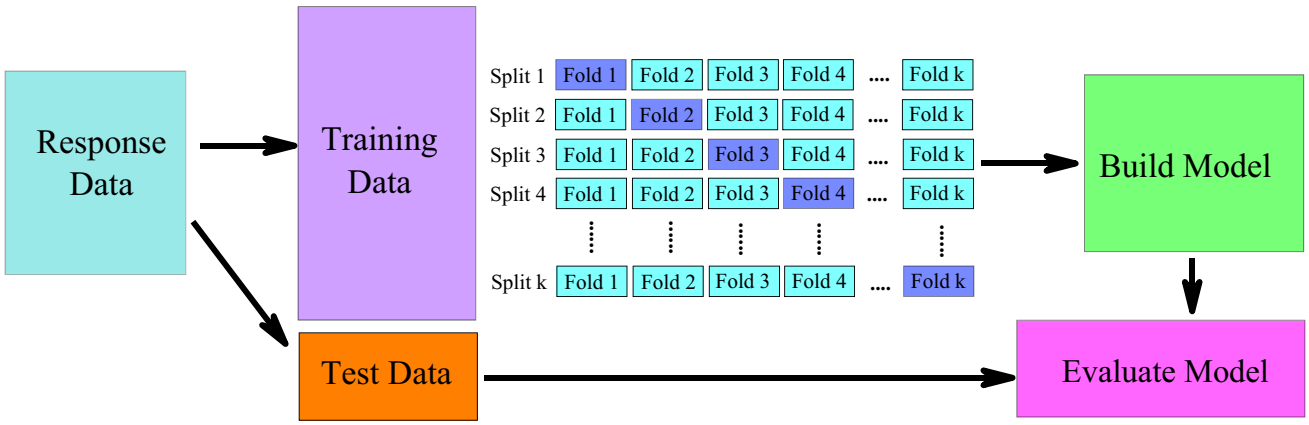

Fig. 3 Architecture of *k*-fold cross-validation

Response Prediction in Voting Regressor (VReg) is based on the average of the individual results, while K-Nearest neighbor Regression (KNR) assume linear estimation on the mean of data points. On the other hand, Gaussian Process Regression (GPReg) renormalizes the targets to find a zero mean for the maximum log marginal of data points. Linear Regression (LReg) considers a linear estimation model to minimize a target of residual sum defined as squares of predicted and actual values. In addition, Gamma Regressor (GReg) uses the strategy of combining data points with an inverse function and their logarithmic unit deviance [45]. The algorithm that uses the strength of estimators for finding the final estimator to solve the prediction model is known as Stacking Regressor (SReg) (see more detail [46]). Partial Least Squares Regression (PLSReg) is another regression model that has the ability to assume maximum multidimensional direction for data points to achieve fundamental relations between inputs and outputs [47]. Since Python libraries provide a great possibility for developing the ML algorithms as well as the free access of this software, the Python software as a general-purpose programming language is selected for implementing ML methods. Therefore, all assumed ML algorithms were developed in Python software and different resampling strategies, such as fine-tune method, halving search strategy, grid search method, and *k*-fold cross-validation were used to improve them as a prediction model.

3 Modeling process

To train the ML algorithms, eleven types of RC buildings including two to twelve-floor elevations (i.e., 2-, to 12-Story buildings) having three bay length types (i.e., 5 m, 6.1 m, and 7.6 m) with the plan presented in Fig. 4 were assumed. All buildings modeled in ETABS software based on the assumption of soil type D, acceleration parameters of $SD_1 = 0.6$ g and SDs = 1.0 g for the construction site of high seismic, and design parameters of $R = 8$, Cd = 5.5, and $\Omega = 3$ in accordance with ASCE 7-16 [48]. It is noteworthy that the acceleration parameters of the construction site were achieved based on the USGS website [49]. In addition, a floor dead load of 8.4 kN/m^2 and a floor live load of 2.4 kN/m^2 were applied to all floor levels of buildings. To design structural elements, the concrete compressive strength of 34.5 MPa (i.e., 5 ksi, see Table 6–2 in reference [50]) was used [51]. Details of structural elements of RC frames assuming the bay length of 6.1 m were presented in Figs. 5, 6 and 7. To perform collapse analysis, all buildings were modeled as two-dimensional RC frames in Opensees [52] assuming the leaning column for those gravity columns not included in models to consider the P-delta effects [53–56]. In addition, the two-dimensional frames were modeled and verified with their corresponding buildings considering modeling procedures used by Haselton and Deierlein [50] and Kazemi et al. [9–11, 57, 58]. According to these procedures, plastic hinge models for simulating seismic collapse presented in Fig. 4 were developed by Ibarra et al. [59] and Altoontash [60]. It should be noted that for considering the real condition of RC buildings, all panel zones were modeled, and concentrate plastic hinge models were used in the ends of structural elements with possibility of achieving seismic collapse (for more detail on modeling see [50]).

To train the ML algorithms, 165 RC MRFs were assumed to have one-, two-, three-, four-, and five-bays, and 2-, to 12-Story elevations having the bay lengths of 5 m, 6.1 m, and 7.6 m. To assess IDR_{max} in different intensity measures and seismic limit-state curves of all 165 RC MRFs, IDAs were performed based on the spectral acceleration in the period of the structure, $Sa(T_1)$, as intensity measure, and IDR_{max} as engineering demand parameter, considering near-fault Pulse-like (PL), and No-Pulse (NP) records introduced by FEMA-P695 [61]. To perform IDAs, an algorithm was developed to implement the hunt and fill methodology using both Opensees [52] and MATLAB [62] software to reduce the time of analysis. It is worth mentioning that the programming code was developed in MATLAB [62] to control the

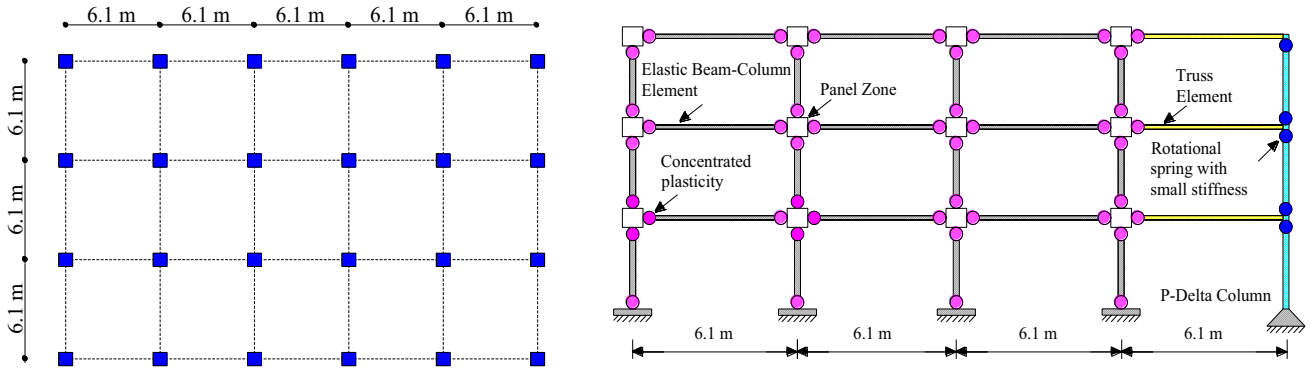

Fig. 4 RC MRFs plan and concentrated plasticity approach employed to model buildings

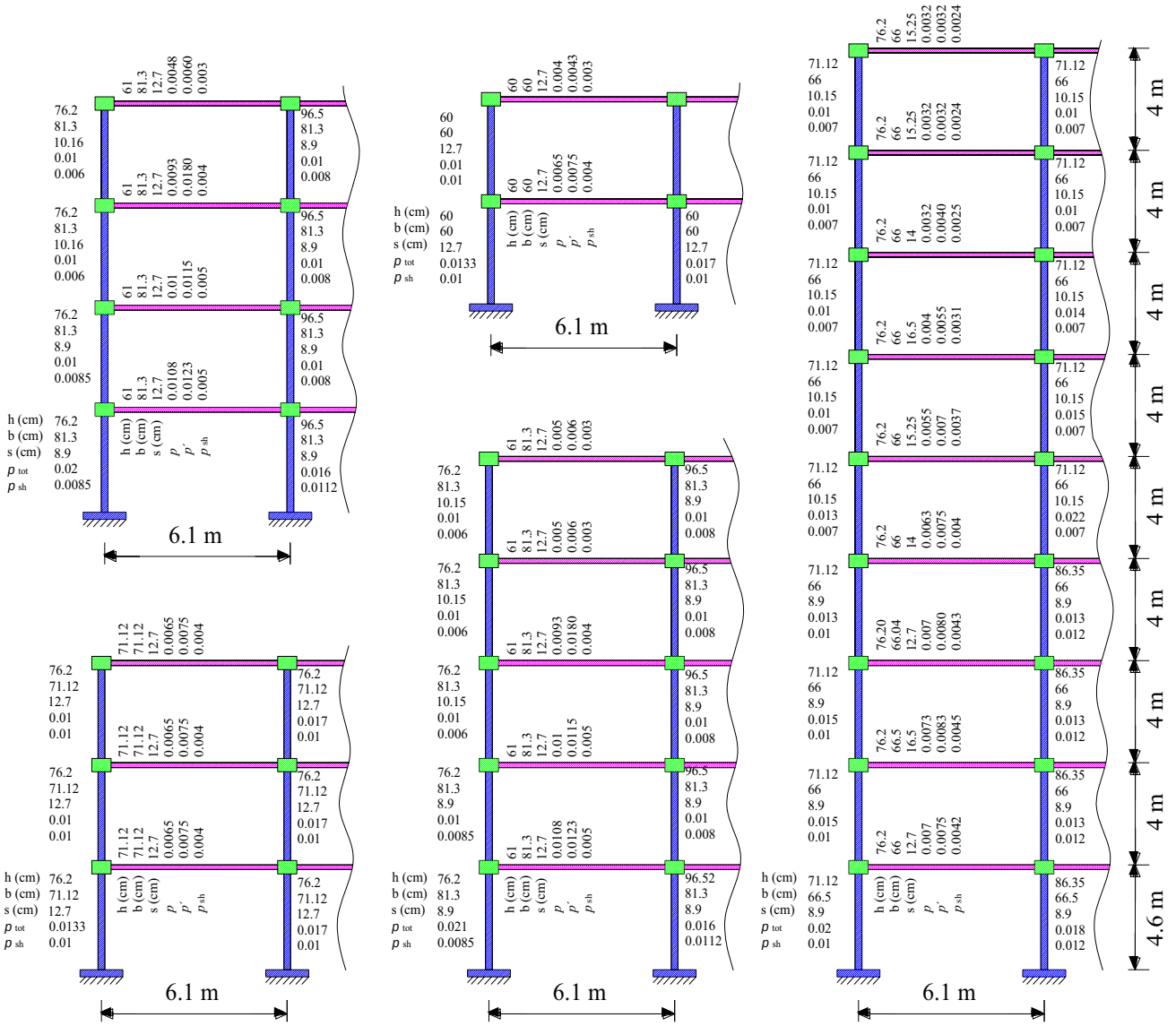

Fig. 5 Structural documentation of the 2-Story, 3-Story, 4-Story, 5-Story, and 9-Story RC MRFs

entire analysis procedure; and in addition, to post-process the results of the analysis. Figure 8 presents the IDA curves of the 2-Story, 4-Story, 8-Story, and 12-Story RC frames having three bays with 6.1 m length including NP records. It should be noted that there is no restriction on the increasing steps of the intensity measure selection in this study; therefore, the results are distributed with different ranges of the Sa(T_1).

The training datasets were prepared with important features of weight, aspect ratio, reinforcement ratio for beams and columns, story number, bay length and the total height of RC frames, Sa(T_1), the direction and RSN number of record, fundamental period (T_1), and IDR_{max} in each step of the analysis, which achieved based on the trial and error. In addition, for seismic response prediction models, the IDR_{max} of selected RC frames was considered as a target in the test dataset, and for seismic limit-state capacity prediction models, the $Sa(T_1)$ of M-IDAs of selected RC frames were considered as a target of prediction in the testing dataset. Therefore, two main training datasets were considered to train and test the prediction models. In addition, 92,400 data points were considered in the training dataset that were achieved by performing IDAs.

4 Analytical procedure

The main purpose of this study is to train ML algorithms for accurate prediction of the IDR_{max} and the seismic limit-state capacity of RC frames using M-IDAs (e.g., presented

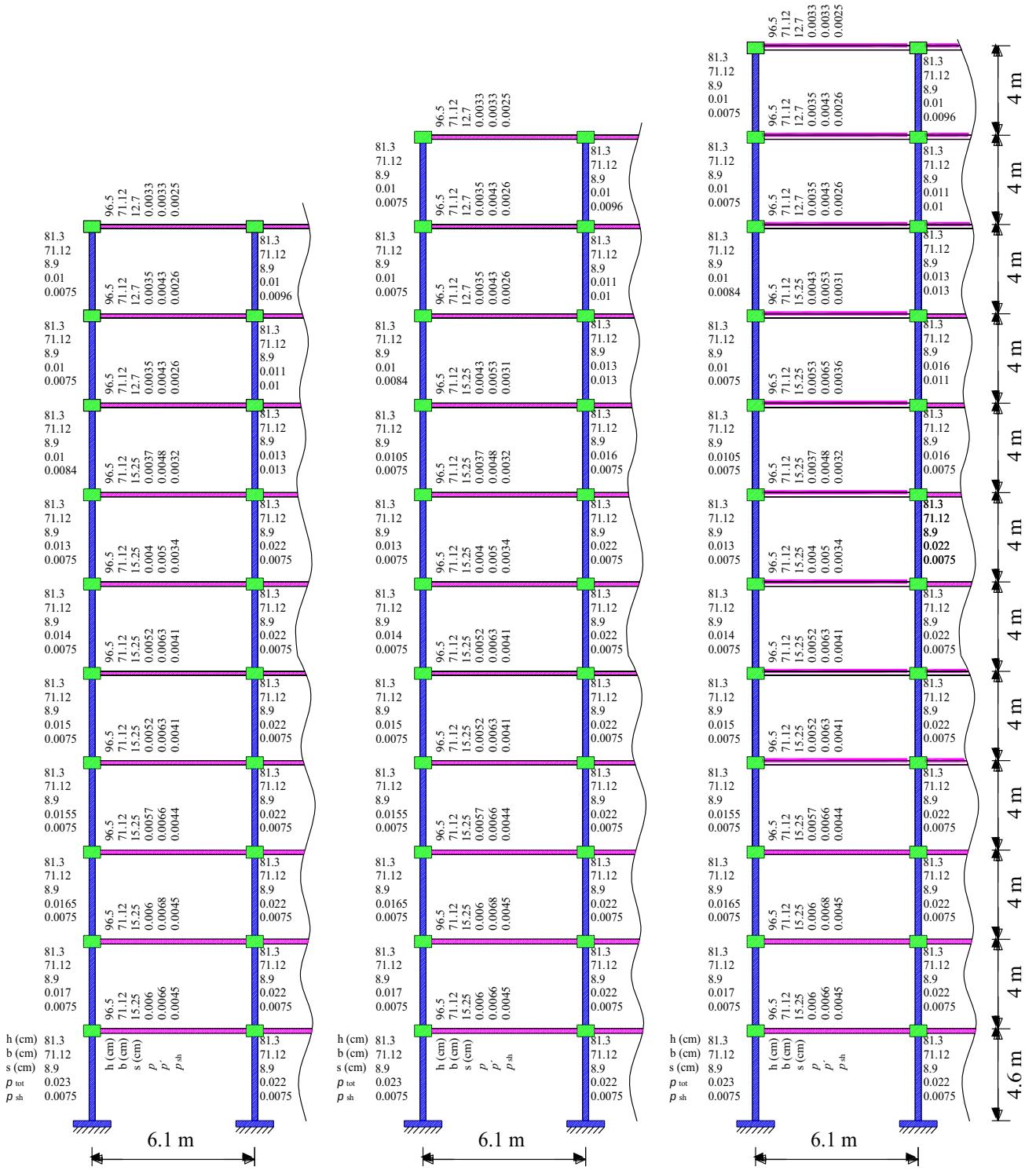

Fig. 6 Structural documentation of the 10-Story, 11-Story, and 12-Story RC MRFs

in pink color in Fig. 8). M-IDAs can be used to estimate the seismic performance levels of the structures assuming a different threshold of IDR_{max} introduced by seismic provisions. Therefore, the analytical procedure presented in Fig. 9 depicts four main parts used for preparing prediction models. The first part in the blue color is the modeling and validation of RC MRFs using ETABS and Opensees [52] softwares (see Sect. 3). The green part, explains the preparation of training and testing datasets based on the IDR_{max} and M-IDAs as targets of prediction. In the red section,

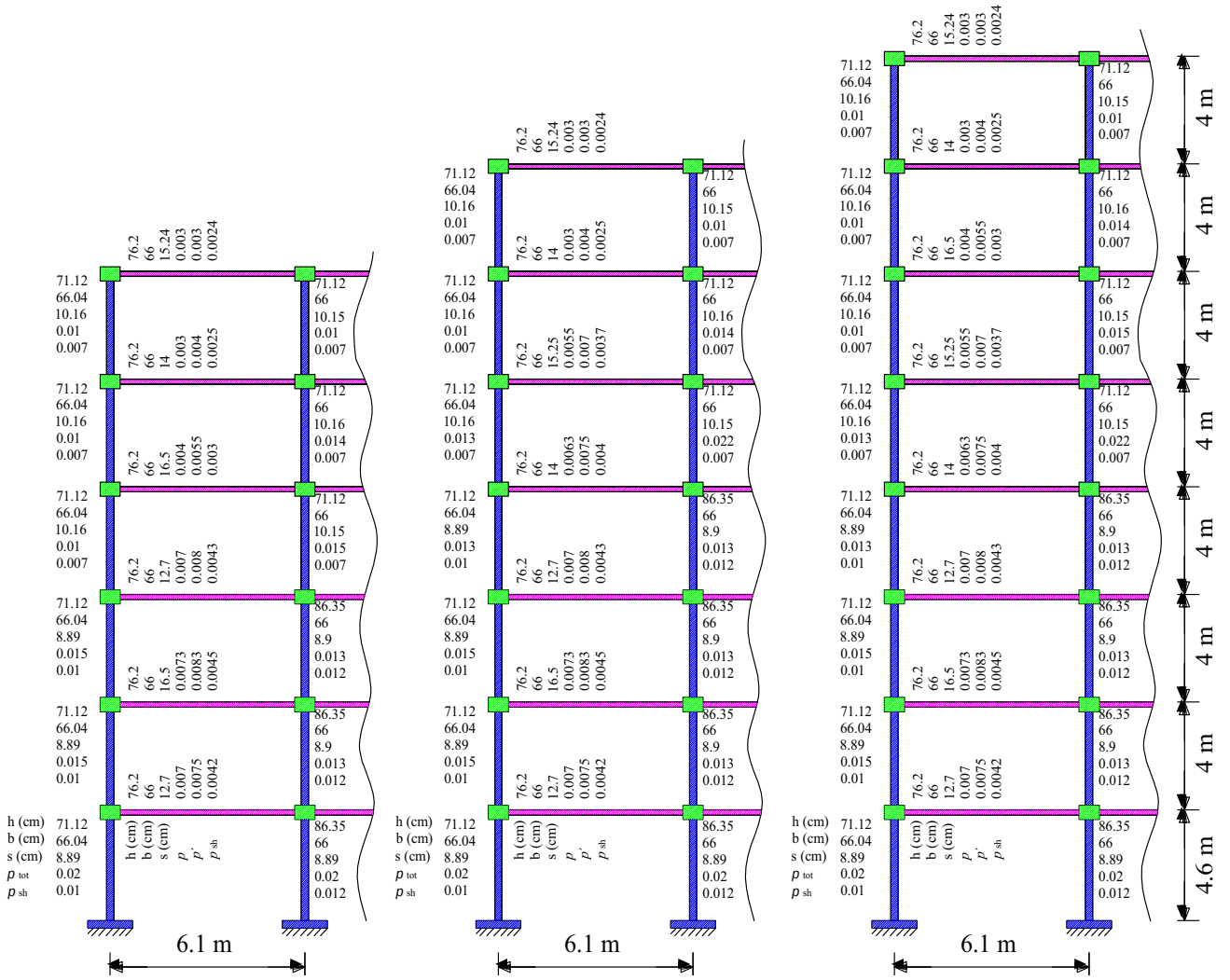

Fig. 7 Structural documentation of the 6-Story, 7-Story, and 8-Story RC MRFs

ML algorithms were implemented in Python software and improved based on some innovative methodologies for the prediction of the two aforementioned targets. After validation of predicting models, some important ML algorithms were selected for the violet part, which shows the second validation of prediction models for a new RC building to show the capability of the proposed ML-based model.

4.1 Data selection method

Although many features can influence the response prediction of structures, introducing all these features can reduce the speed of calculations while increase the overfitting possibility in the algorithms. Therefore, it is necessary to provide the important features while the prediction accuracy remains unchanged during the validations. To do this, different feature selection methods such as filter and wrapper methods, which contains the more suitable methods of forward feature selection, backward feature elimination, and exhaustive feature selection, were used to achieve the importance of input features. Figure 10 presents the relative importance of seven features with higher scores achieved by trial and error using the aforementioned methods. Other features were remove since their relative importance were less than these feature. For estimating the M-IDA curve, three main features of the number of bays, fundamental period of the frame, and IDR_{max} have more scores compared to other features. On the other side, for predicting IDR_{max} as a target, five features of number of stories, weight, fundamental period of the frame, number of bays, and $Sa(T_1)$ have scored more than 10%. According to Fig. 10, these seven features were selected in the training and testing datasets for prediction models.

It is noteworthy that to enhance the ability of the methods, the feature selection approaches were used simultaneously with embedded method to reduce the effects of those data points with low effects on the predictions of selected target.

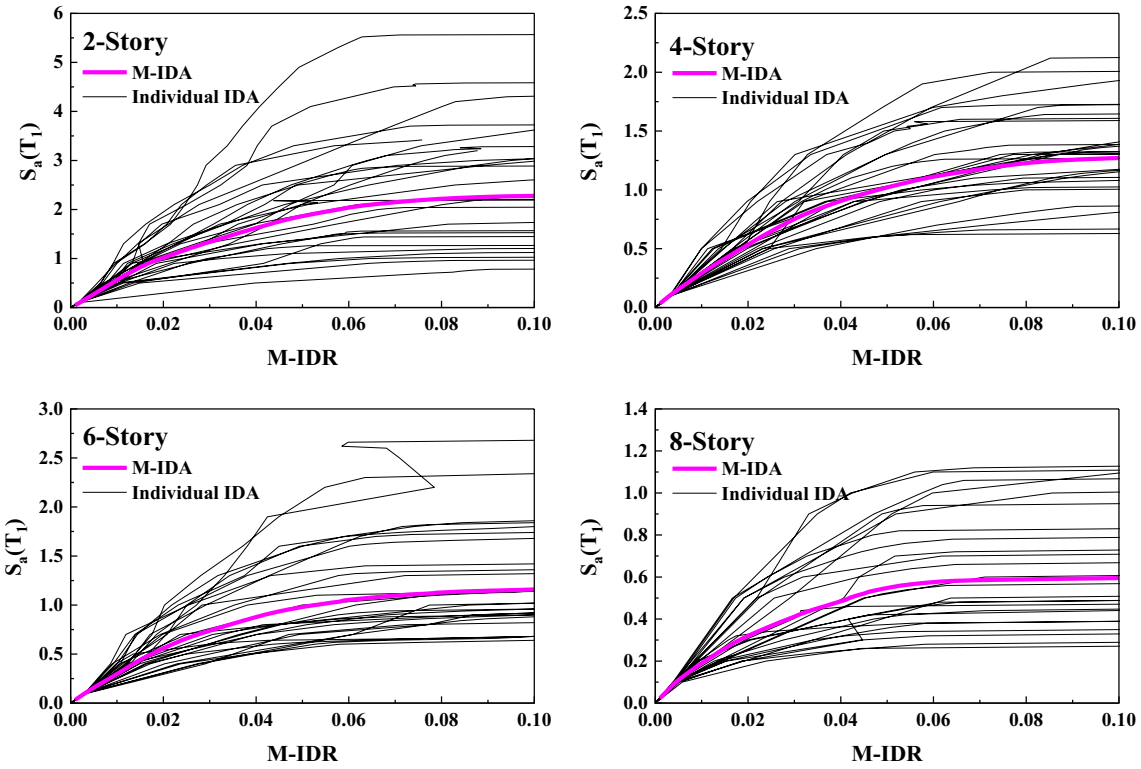

Fig. 8 IDA curves of the RC frames having three bays with 6.1 m including NP records

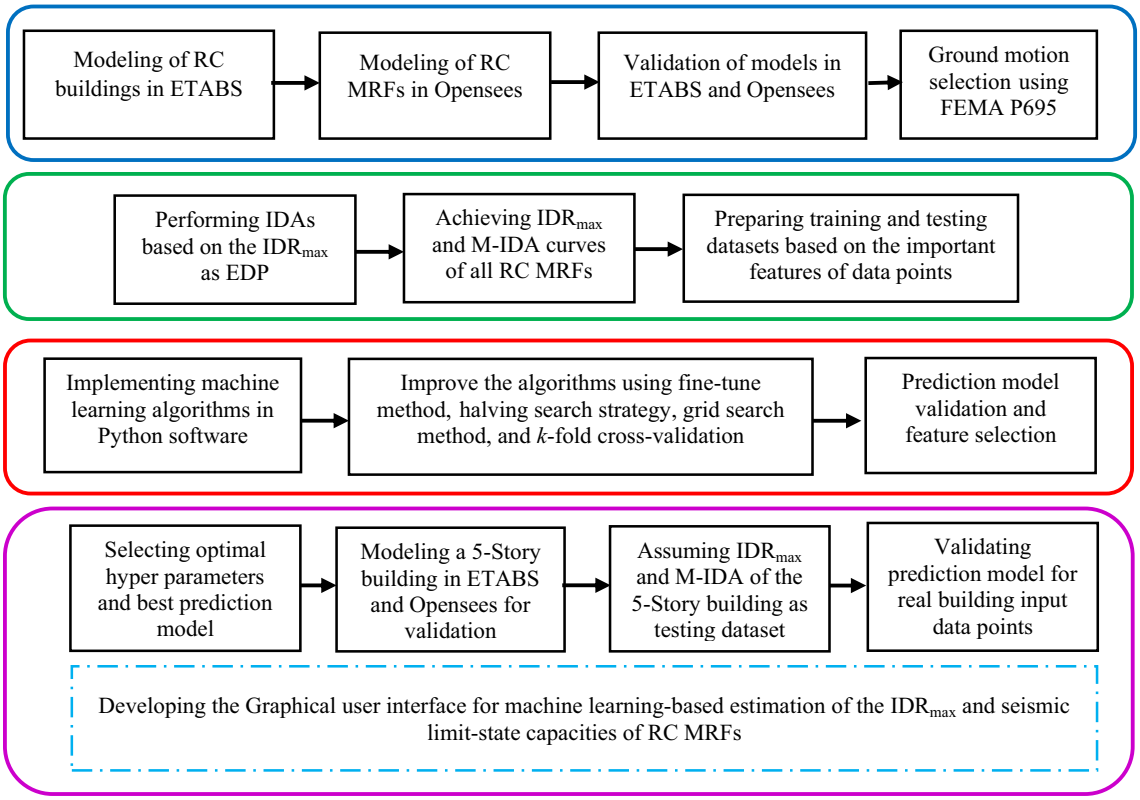

Fig. 9 Analytical procedures are used to achieve a high accuracy model

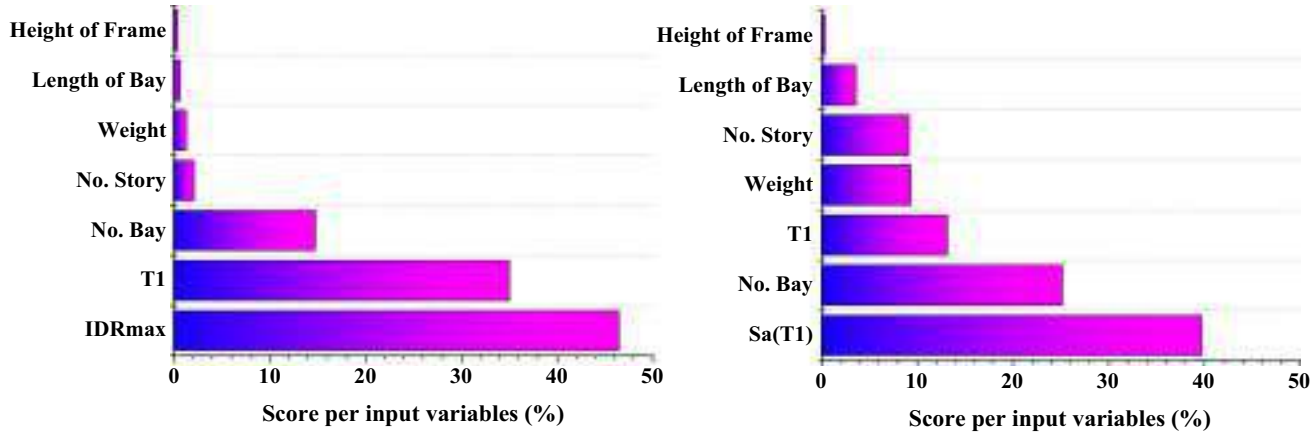

Fig. 10 Relative importance achieved by trial and error for predicting M-IDA curve (left) and IDR_{max} (right) as targets of models

In other words, the developed embedded method reduces the number of data points for reasonable computational cost while increases the capability of ML algorithms and prevents the overfitting problem, which is the most important issue in the performance of models. Therefore, all ML methods improved based on the developed embedded method in purpose of increasing their ability.

To compare the reliability and capability of the aforementioned ML algorithms, the statistical metrics presented in Table 1 were used. The coefficient of determination, R^2, is widely used for presenting the accuracy of prediction and

Table 1 Statistical metrics used for evaluating the ML models

Abbreviation	Formula	Description
R^2	$R^2 = 1 - \frac{\sum_{i=1}^{n} (\text{Actual}_i - \text{Predicted}_i)^2}{\sum_{i=1}^{n} (\text{Actual}_i - \text{Actual}_{avg})^2}$	*R* squared
MSE	$\text{MSE} = \frac{1}{n} \sum_{i=1}^{n} (\text{Actual}_i - \text{Predicted}_i)^2$	Mean squared error
RMSE	$\text{RMSE} = \sqrt{\frac{1}{n} \sum_{i=1}^{n} (\text{Actual}_i - \text{Predicted}_i)^2}$	Root mean squared error
MAE	$\text{MAE} = \frac{1}{n} \sum_{i=1}^{n} \lvert \text{Actual}_i - \text{Predicted}_i \rvert$	Mean absolute error
MARE	$\text{MARE} = \frac{1}{n} \sum_{i=1}^{n} \left\lvert \frac{\text{Actual}_i - \text{Predicted}_i}{\text{Actual}_i} \right\rvert$	Mean absolute relative error
MSRE	$\text{MSRE} = \frac{1}{n} \sum_{i=1}^{n} \left(\frac{\text{Actual}_i - \text{Predicted}_i}{\text{Actual}_i} \right)^2$	Mean square relative error
RMSRE	$\text{RMSRE} = \sqrt{\frac{1}{n} \sum_{i=1}^{n} \left(\frac{\text{Actual}_i - \text{Predicted}_i}{\text{Actual}_i} \right)^2}$	Root mean squared relative error
RRMSE	$\text{RRMSE} = \frac{\sqrt{\frac{1}{n} \sum_{i=1}^{n} (\text{Actual}_i - \text{Predicted}_i)^2}}{\sum_{i=1}^{n} \text{Actual}_i} \times 100$	Relative root mean square error
MBE	$\text{MBE} = \frac{1}{n} \sum_{i=1}^{n} (\text{Actual}_i - \text{Predicted}_i)$	Mean bias error
erMAX	$\text{erMAX} = \max \left(\left\lvert \frac{\text{Actual}_i - \text{Predicted}_i}{\text{Actual}_i} \right\rvert \right)$	Maximum absolute relative error
SD	$\text{SD} = \sqrt{\frac{\sum (X_i - \text{Arithmetic mean})^2}{\text{total number}}}$	Standard deviation of the difference between actual and predicted values
t-stat	$t\text{ - stat} = \sqrt{\frac{(n-1)\text{MBE}^2}{\text{RMSE}^2 - \text{MBE}^2}}$	*t*-Statistic
U_{95}	$U_{95} = \sqrt{1.96(\text{SD}^2 + \text{RMSE}^2)}$	Uncertainty at 95%

can take values between 0.0 and 1.0 (or 0.0% and 100%) to show the spreads of predicted and actual data points from the $x = y$ line. Other metrics compare the actual and predicted values to show the capability of models for minimizing the error, which is the difference between the actual and predicted values.

Twenty ML algorithms were implemented in Python software and used as a prediction model. A sensitivity analysis was performed using the 3-Story RC frame with three bays having bay lengths of 5.0 m subjected to PL records for both models of prediction based on the IDR_{max} and $Sa(T_1)$ as a target. Table 2 shows the comparison of statistical metrics for the performance evaluation of ML algorithms for predicting IDR_{max}. It can be seen that most ML algorithms achieved higher values of R^2, which shows the accuracy of these algorithms. In the IDR_{max} as target of testing dataset, eight methods of PLSReg, SReg, VReg, LReg, GReg, MLPReg, SVM, and LSVR had R^2 values of 0.384, 0.386, 0.585, 0.350, 0.160, 0.205, 0.259, and 0.232, respectively. Although their accuracy of prediction in the training dataset was higher than approximately 90%, their performance in the testing dataset is lower than other algorithms and cannot be considered as reliable models. In addition, In the $Sa(T_1)$ as target of testing dataset, five algorithms of LReg, PLSReg, LSVR, SReg, and GReg had R^2 values of 0.775, 0.774, 0.743, 0.614, and 0.313, respectively. Therefore, these algorithms can be considered as not reliable models that cannot achieve R^2 values higher than 0.77. Comparing the metrics can provide a good information about the capability of the models and their power for estimating the targets. These tables also can be used for selecting the best ML methods. To better compare the metrics, the score marker were used, which provides the number from 1 to 20 for ranking the ML methods for each of the metrics. Then, in each ML methods, the scores of each metrics were determined to compare the capability of them. According to results of Table 2, the BReg, HistGBR, ETReg, RF, ERTReg, GBM, and XGBoost methods achieved scores of 49, 49, 80, 82, 83, 86, and 98, respectively, which are introduced as best methods. Moreover, the methods of PLSReg, LReg, NuSVR, LSVR, MLPReg, GReg, and SVM had the scores of 175, 176, 190, 199, 212, 219, and 243, respectively, in the end of ranking list.

According to results of Table 3, the ANNs, HistGBR, XGBoost, RF, NuSVR, BReg, and ETReg methods achieved scores of 49, 49, 66, 73, 81, 86, and 93, respectively, which are introduced as best models, while the methods of VReg, PLSReg, LReg, LSVR, SReg, and GReg with scores of 190, 215, 222, 236, 244, and 250, respectively, are introduced as weak prediction models. The statistical indicators used for calculating the error of methods depend on the actual and predicted values; therefore, the higher value of the error shows the dispersion of the predicted values. Although the SVM method had

Table 2 Comparison of statistical metrics assuming the 3-Story RC frame with three bays having bay lengths of 5.0 m as test data for predicting IDR_{max}

Model	R^2	MSE	RMSE	MAE	MARE	MSRE	RMSRE	RRMSE	MBE	erMAX	SD	*t*-stat	U_{95}
XGBoost	0.818	2.58	1.61	1.24	0.52	0.86	0.93	0.23	0.20	2.72	0.01	0.41	0.04
RF	0.901	3.42	1.85	1.35	0.21	0.08	0.28	0.26	− 0.12	0.73	0.01	0.21	0.04
BReg	0.898	2.06	1.44	1.04	0.16	0.04	0.21	0.23	0.50	0.52	0.01	1.24	0.03
ETReg	0.890	2.25	1.50	1.10	0.18	0.05	0.23	0.26	0.58	0.60	0.01	1.38	0.04
GBM	0.818	3.03	1.74	1.34	0.28	0.28	0.52	0.21	0.08	2.28	0.01	0.14	0.04
HistGBR	0.888	2.28	1.51	1.07	0.15	0.04	0.20	0.20	0.27	0.48	0.01	0.60	0.03
HistGBR(FN)	0.830	2.76	1.66	1.24	0.48	0.63	0.79	0.36	1.34	3.43	0.01	4.47	0.04
AdaBoost	0.864	5.0	2.24	1.74	0.47	0.39	0.62	0.38	0.05	1.51	0.02	0.07	0.06
KNR	0.795	3.17	1.78	1.17	0.16	0.05	0.21	0.24	0.68	0.57	0.01	1.37	0.04
PLSReg	0.384	6.61	2.57	2.07	1.11	5.09	2.26	0.35	0.07	6.72	0.02	0.09	0.06
SReg	0.386	6.60	2.57	1.89	0.33	0.23	0.48	0.38	0.10	1.47	0.02	0.13	0.06
VReg	0.585	3.14	1.77	1.38	0.52	0.86	0.93	0.23	0.20	2.72	0.01	0.37	0.04
LReg	0.350	6.75	2.60	2.05	0.93	3.32	1.82	0.32	0.08	5.42	0.02	0.10	0.06
GReg	0.160	7.67	2.77	2.36	1.98	19.36	4.40	0.50	− 0.21	13.19	0.02	0.25	0.07
MLPReg	0.205	8.00	2.83	2.22	0.73	4.70	2.17	0.37	− 0.78	10.49	0.01	0.96	0.06
SVM	0.259	11.38	3.37	2.90	3.43	61.48	7.84	0.58	0.58	23.54	0.03	0.58	0.09
NuSVR	0.800	5.37	2.32	1.90	0.78	2.21	1.49	0.32	0.64	5.95	0.02	0.96	0.06
LSVR	0.232	9.12	3.02	2.20	0.56	0.80	0.89	0.39	0.30	2.93	0.02	0.33	0.07
ERTReg	0.894	2.54	1.59	1.18	0.15	0.04	0.21	0.23	0.53	0.53	0.01	1.16	0.04
ANNs	0.863	3.22	1.79	1.35	0.36	0.37	0.61	0.26	0.99	2.18	0.01	2.21	0.04

Table 3 Comparison of statistical metrics assuming the 3-Story RC frame with three bays having bay lengths of 5.0 m as test data for predicting $Sa(T_1)$

Model	R^2	MSE	RMSE	MAE	MARE	MSRE	RMSRE	RRMSE	MBE	erMAX	SD	*t*-stat	U_{95}
XGBoost	0.984	1.37	3.70	3.29	0.04	0.005	0.07	0.02	− 1.06	0.32	0.02	0.99	0.08
RF	0.953	4.01	6.33	5.59	0.05	0.003	0.05	0.03	− 2.36	0.06	0.01	1.33	0.13
BReg	0.952	4.13	6.42	5.68	0.05	0.003	0.05	0.03	− 2.42	0.06	0.01	1.35	0.13
ETReg	0.966	2.92	5.41	5.09	0.06	0.004	0.06	0.04	− 3.00	0.08	0.02	2.21	0.11
GBM	0.951	4.16	6.45	5.92	0.07	0.011	0.10	0.04	− 1.33	0.44	0.03	0.70	0.14
HistGBR	0.984	1.33	3.64	3.32	0.03	0.001	0.04	0.02	− 1.31	0.08	0.01	1.28	0.07
HistGBR(FN)	0.986	1.20	3.46	2.99	0.11	0.018	0.13	0.06	− 4.35	0.44	0.02	–	0.08
AdaBoost	0.919	6.94	8.33	7.40	0.06	0.003	0.06	0.04	− 2.50	0.09	0.02	1.04	0.17
KNR	0.879	10.32	10.16	9.53	0.12	0.023	0.15	0.07	− 3.95	0.54	0.03	1.40	0.21
PLSReg	0.774	19.27	13.88	11.36	0.99	4.876	2.21	0.25	13.47	9.49	0.15	13.24	0.40
SReg	0.614	32.97	18.16	16.19	1.06	5.385	2.32	0.27	15.50	10.01	0.15	5.44	0.46
VReg	0.907	7.90	8.89	8.09	0.49	1.225	1.11	0.12	5.67	4.77	0.08	2.74	0.24
LReg	0.775	19.22	13.86	11.30	1.00	4.927	2.22	0.25	13.66	9.54	0.15	19.26	0.40
GReg	0.313	50.71	22.52	20.82	1.09	5.880	2.42	0.30	13.60	10.43	0.17	2.51	0.56
MLPReg	0.982	1.50	3.88	3.19	0.13	0.022	0.15	0.06	− 4.08	0.22	0.03	–	0.09
SVM	0.987	1.14	3.38	2.93	0.22	0.266	0.52	0.05	− 0.70	2.34	0.05	0.70	0.11
NuSVR	0.993	0.57	2.39	2.19	0.07	0.007	0.08	0.04	− 2.68	0.18	0.01	–	0.05
LSVR	0.743	21.94	14.81	12.40	1.05	5.348	2.31	0.26	14.82	9.92	0.15		0.42
ERTReg	0.947	4.51	6.72	6.22	0.06	0.004	0.07	0.04	− 2.92	0.10	0.02	1.60	0.14
ANNs	0.999	0.09	0.94	0.85	0.04	0.014	0.12	0.01	0.10	0.57	0.01	0.36	0.03

lower performance for predicting IDR_{max} of the 3-Story RC frame, the SVM method achieved the R^2 value of 0.987 for predicting $Sa(T_1)$ that proves the acceptable performance of this method.

5 Performance of prediction models

The most important part of the prediction models is to prepare the datasets according to the important features. The seven important features related to each type of prediction (i.e., $Sa(T_1)$ or IDR_{max}) was plotted in Fig. 10. According to these targets, the training dataset contained 92,400 data points achieved by performing IDAs. In other words, 92,400 nonlinear time history analyses were done based on increasing the intensity measures (i.e., IDA) to prepare the large database for prediction. After preparing suitable datasets, the selected ML algorithms with higher accuracy of prediction (see Tables 2 and 3) were used for seismic response prediction models. Figures 11 and 12 present prediction results of IDR_{max} for the 6-Story and 8-Story RC MRFs assuming five types of bays including PL records. It should be noted that the selected RC MRFs were removed from training datasets during the prediction. For the 6-Story RC MRFs with one-, two-, three-, four-, and five-bays, the ML algorithms of HistGBR, ANNs, and BReg had higher accuracy of prediction values of 90.2%, 93.5%, 94%, 95.4%, and 96.3%, respectively. For the 8-Story RC MRFs with one-, two-, three-, four-, and five-bays, the ML algorithms of ETReg, BReg, and ANNs had higher accuracy of prediction values of 93.8%, 94.3%, 93.4%, 95%, and 95.3%, respectively. It can be seen that in all results, the algorithms had the most precise prediction for IDR_{max} of lower than 4.0% due to the points near the blue lines. Therefore, the mentioned algorithms can be used as a precise prediction model for IDR_{max} lower than 4.0% in all types of RC MRFs.

To present the estimation accuracy of M-IDA curve models, only having higher values of R^2 is not enough due to the relations between the values of before and after data points. Therefore, the best way to present the power of the algorithm is to plot both actual and predicted curves. Figures 13 and 14 show the predicted M-IDAs versus the actual M-IDA curve of the 3-Story and 7-Story RC MRFs having five types of bays subjected to PL records. The two most precise predicted M-IDAs were plotted that show the accuracy of the prediction models used in this study and can be used as a preliminary prediction of M-IDA curves of RC MRFs.

6 Generality of prediction models

In Sect. 5, the capability of ML algorithms for predicting the IDR_{max} and $Sa(T_1)$ of the aforementioned RC frames was presented. To present the overall accuracy of the proposed

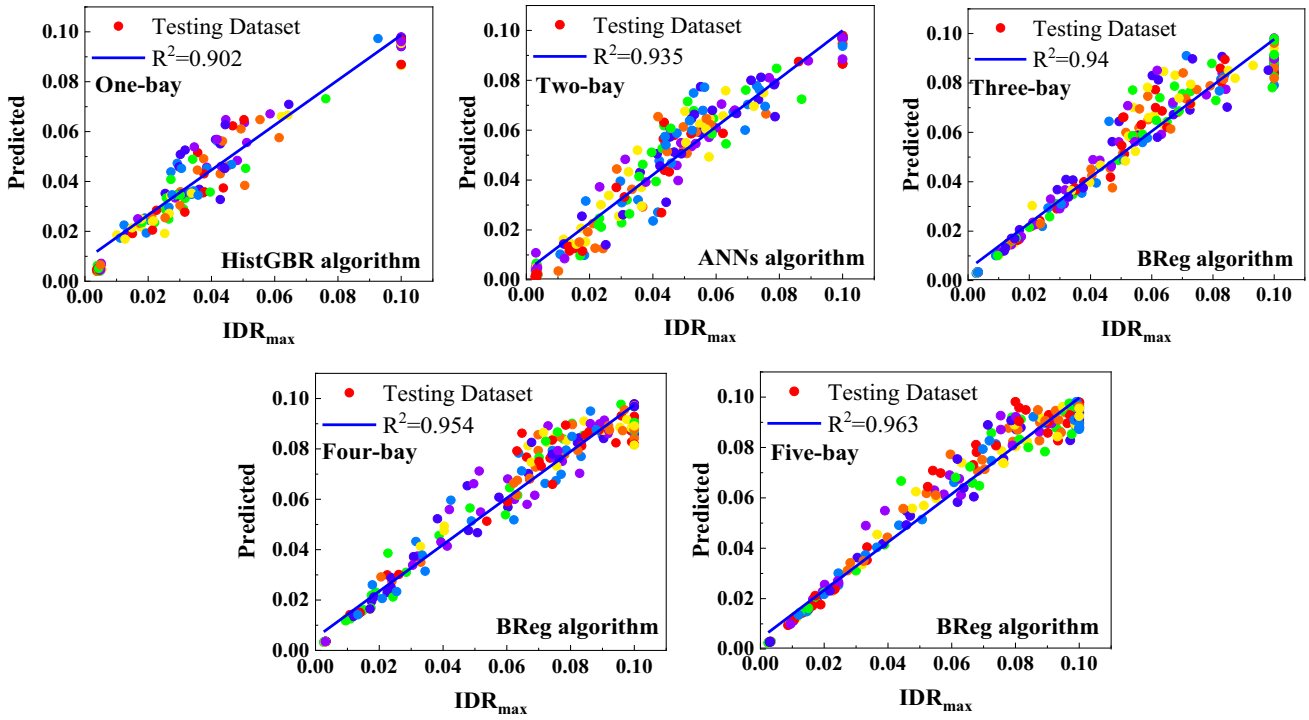

Fig. 11 IDR_{max} prediction results for the 6-Story RC MRFs as testing datasets including PL records

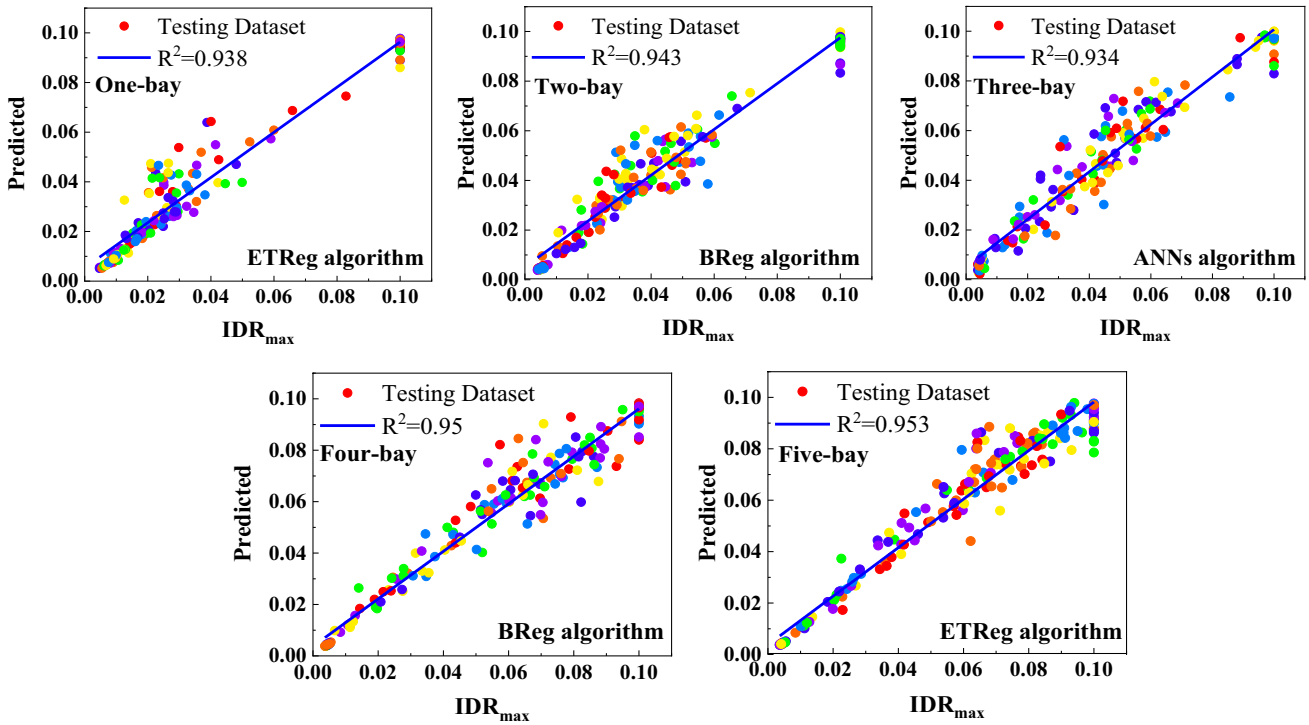

Fig. 12 IDR_{max} prediction results for the 8-Story RC MRFs as testing datasets including PL records

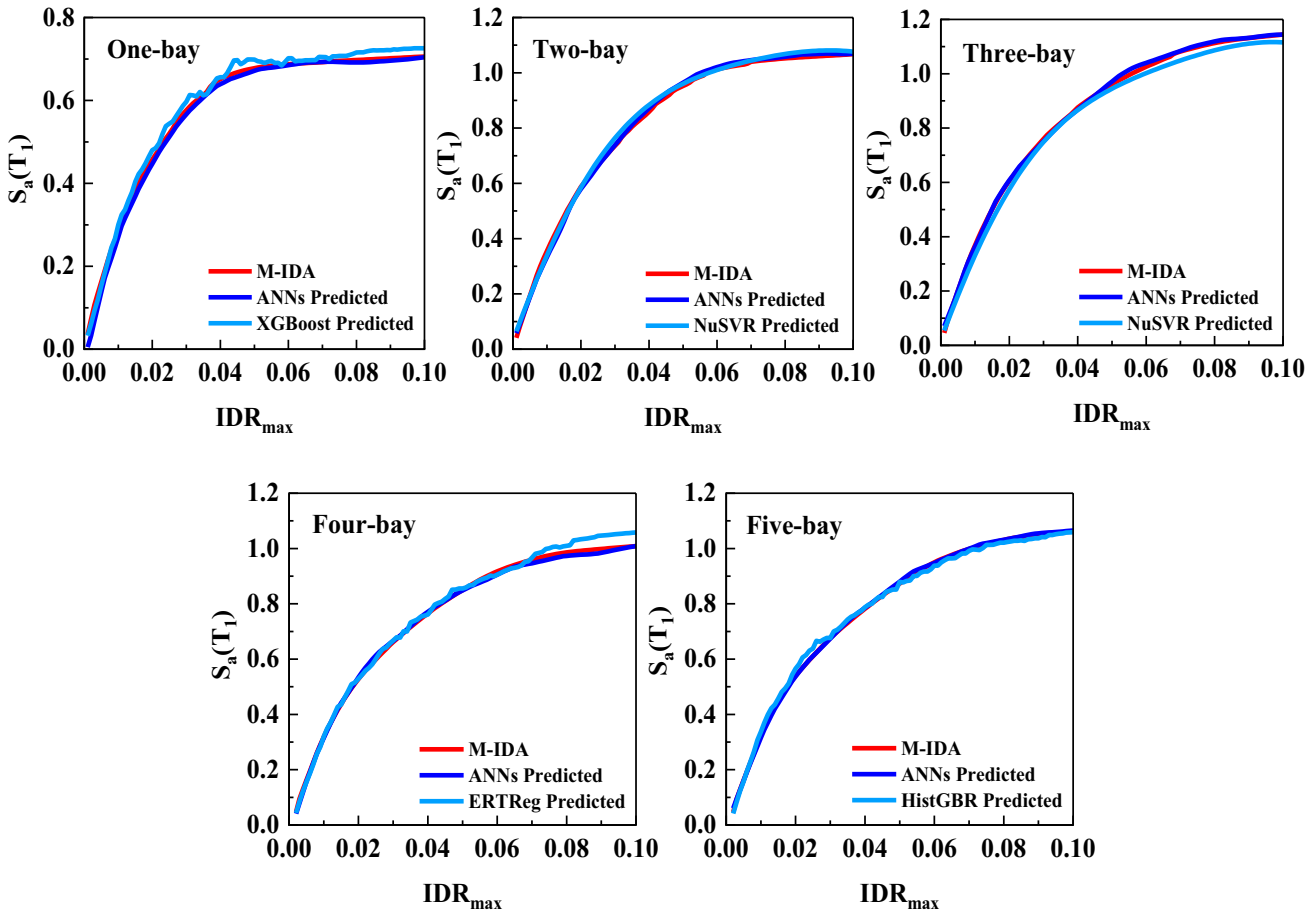

Fig. 13 Predicted M-IDAs of the 3-Story RC MRFs as testing datasets including records

ML-based prediction of IDR_{max} and $Sa(T_1)$ as a target for the M-IDA curve, four case study RC buildings with different structural parameters were assumed to show the reliability and applicability of prediction models. Figure 15 presents the structural plan and documentation of beams and columns of a five-Story RC frame that was used for the performance evaluation of prediction models. It should be added that the testing dataset prepared for this RC frame should have same important features as the training dataset for prediction models (see Fig. 10). Therefore, the selected RC frame was modeled in ETABS and Opensees [52] softwares, and IDAs were performed based on the targets of $Sa(T_1)$ and IDR_{max} including assumed seismic records. The results of the analysis were prepared as a testing dataset; then, trained prediction models were used to estimate IDR_{max} and $Sa(T_1)$ as a target.

Given that it is not possible to have an experimental sample to validate prediction models, to challenge the ability of proposed ML-based models, four cases of selected RC buildings assuming different input features were assumed. In Case A, the bay length of the five-Story RC frame was selected as equal to 6.5 m. In Case B, the bay length and story elevation of the five-Story RC frame were selected equal to 6.5 m and 3.8 m, respectively. For Case C and D, the weight of the five-Story RC frame was reduced by 10% and 20%, respectively, compared to the aforementioned loads assumed in Sect. 3, while the bay length and story elevation were selected equal to 6.5 m and 3.8 m, respectively. These four cases have different input features to challenge the possibility of using proposed ML-based models for any type of RC frame including two record subsets. The fundamental periods of Case A, Case B, Case C, and Case D were equal to 1.351, 1.291, 1.225, and 1.156, respectively. Therefore, all input features of the assumed cases are different from the training models. Figure 16 presents the comparison of R^2 for ML algorithms to predict IDR_{max} of the five-Story RC frames assuming PL records. Four algorithms of BReg, ETReg, ERTReg, and ANNs had higher values of prediction accuracy equal to 95.7%, 93.19%, 90.27%, and 90%, respectively, for the prediction of IDR_{max} in Case A, and had higher values of prediction accuracy equal to 92.78%, 90.31%, 87.85%, and 90.1%, respectively, for prediction of IDR_{max} in Case B. Moreover, in Case C, the ANNs and BReg algorithms achieved a prediction accuracy of 92.9%

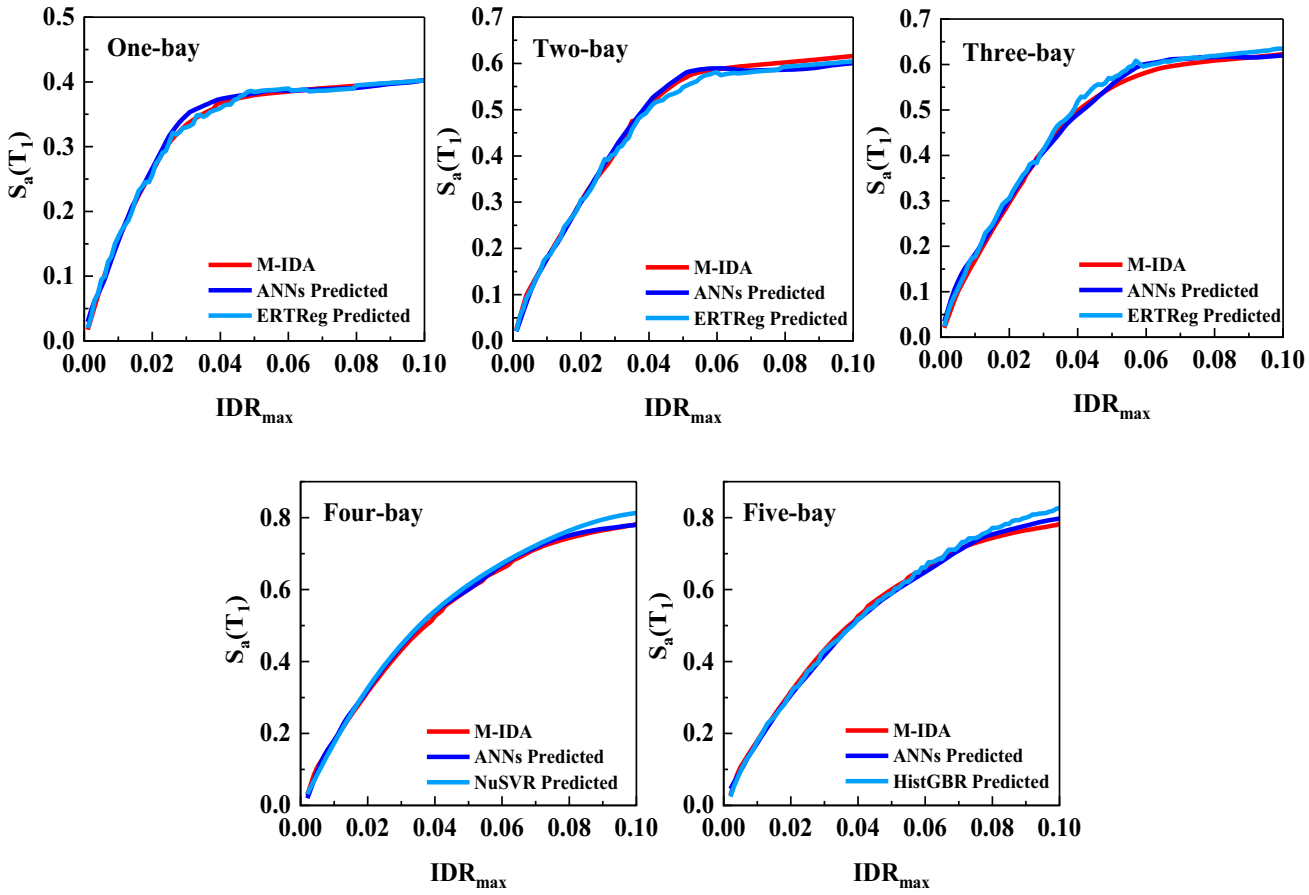

Fig. 14 Predicted M-IDAs of the 7-Story RC MRFs as testing datasets including PL records

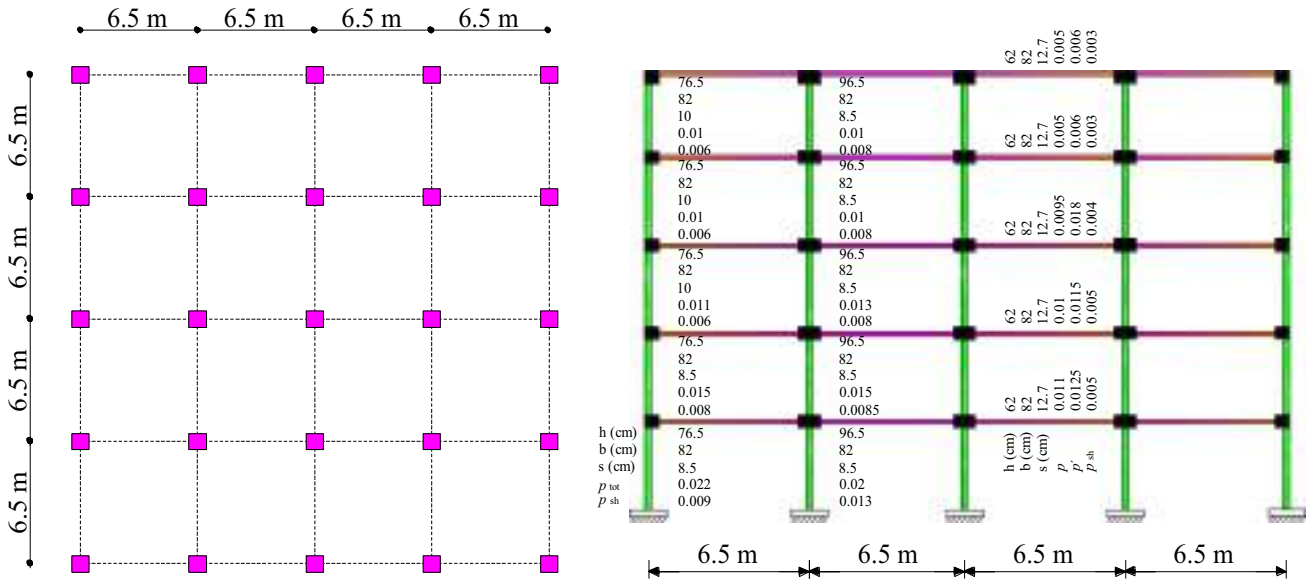

Fig. 15 A five-Story RC frame is used for the performance evaluation of trained prediction models

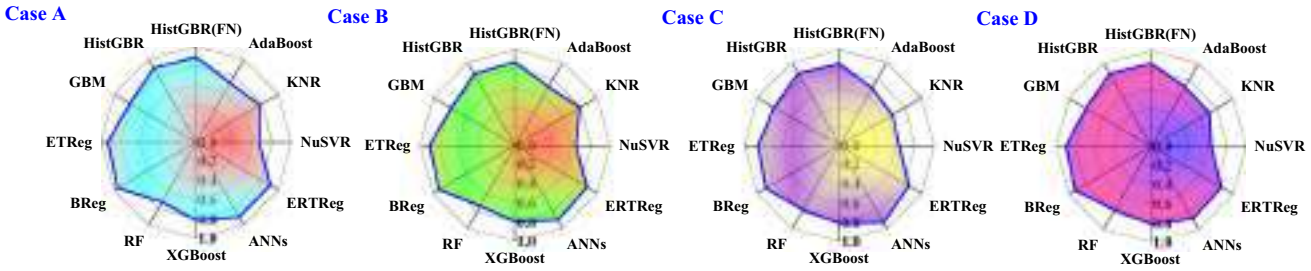

Fig. 16 Pie charts of ML algorithms for predicting IDR_{max} of the five-Story RC frames assuming PL records

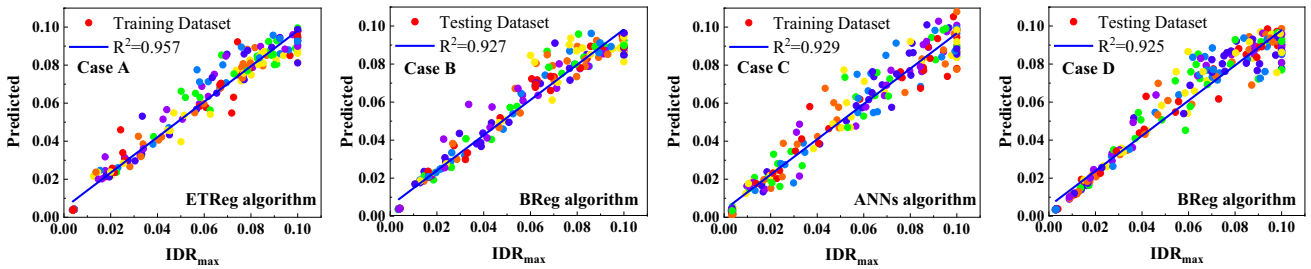

Fig. 17 Predicted IDR_{max} of the five-Story RC frames in the best ML algorithm including PL records

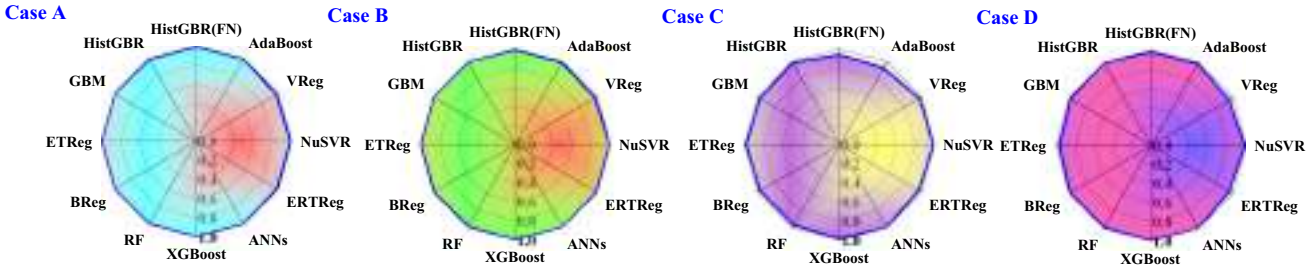

Fig. 18 Pie charts of ML methods for estimating the M-IDA curve of the five-Story RC frames assuming PL records

and 89.76%, respectively, while in Case D, the BReg, ETReg, and ANNs algorithms had a prediction accuracy of 92.5%, 89.93%, and 87.32%, respectively. Figure 17 depicts the scatter plots of predicted IDR_{max} of four cases of the five-Story RC frames in the best ML algorithm including PL records. It should be noted that similar results were observed for NP records, while results regarding PL records were presented for brevity.

Figure 18 presents the pie charts of ML-based models for estimating the M-IDA curve of the five-Story RC frames assuming PL records. ML methods achieved R^2 values higher than 0.97 for predicting testing datasets of four cases. Although the pie charts show the highest values of the predicted M-IDA curve with R^2 of more than 0.97, some of the ML algorithms cannot fit the actual M-IDA curve of RC frames. Therefore, ML algorithms were improved to achieve the best fitting curves. Figure 19 presents the fitted predicted M-IDAs by improved ML algorithms. The ANNs and XGBoost algorithms had the best fitting curves and can be considered the most reliable prediction models.

To determine the seismic performance levels of the five-Story RC frames, the structural performance levels that were defined based on the allowable IDR_{max} values of 1.0%, 2.0%, and 4.0% corresponding to Immediate Occupancy (IO), Life Safety (LS), and Collapse Prevention (CP) performance levels, respectively, were assumed. It is noteworthy that the limit states were described according to the Table C1–3 in FEMA 356 [63] for limiting the damages states of primary structural elements of the lateral force-resisting system. According to allowable performance levels, Table 4 presents the actual values achieved by M-IDAs of the RC frames and those were predicted by improved ML algorithms. According to Table 4, the

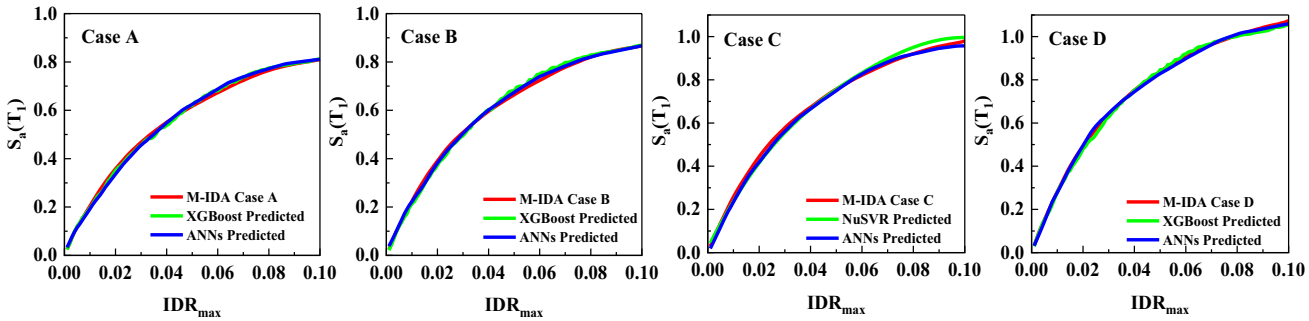

Fig. 19 Predicted M-IDA curves of the five-Story RC frames in the best ML methods including PL records

Table 4 Predicted seismic performance levels of the five-Story RC frames based on the M-IDA curves including PL records

M-IDA curve	Case A			Case B		
	IO	LS	CP	IO	LS	CP
Actual value	0.205	0.357	0.550	0.224	0.390	0.595
XGBoost predicted	0.197	0.351	0.537	0.213	0.378	0.603
ANNs predicted	0.193	0.346	0.548	0.222	0.383	0.601
M-IDA curve	Case C			Case D		
	IO	LS	CP	IO	LS	CP
Actual value	0.257	0.444	0.673	0.281	0.492	0.751
XGBoost predicted	–	–	–	0.278	0.479	0.753
NuSVR predicted	0.237	0.415	0.665	–	–	–
ANNs predicted	0.244	0.429	0.669	0.279	0.495	0.748

predicted values in all performance levels are very close to the actual values; thus, the prediction models have the ability of reliable prediction and can be used by researchers for predicting RC frames.

7 Graphical user interface

The preliminary estimation of the performance levels can widely help designers to know about the weakness of the designed buildings, therefore, they can use the results for vulnerability assessments of structures. To prepare for better accessibility of the results of this research, Graphical User Interface (GUI) was introduced to receive input parameters related to the RC frame and seismic limitation of performance levels and provide the predicted Sa(T_1) regarding the seismic limit-state performance levels of RC MRFs prescribed by FEMA356 [63]. It should be noted that the reliability of prediction models was discussed in Sect. 6, and the introduced GUI can plot the predicted ML-based M-IDA curve while mitigating the need for complex modeling and analyses. It is noteworthy that the input parameters can be easily achieved for the assumed structure, and in addition, for calculating the period of the structure, the formulas that have been provided by the seismic provisions (e.g., ASCE 07-16 [48]) can be used.

8 Conclusions

Recent studies confirm that complex modeling and analysis should be performed to determine seismic responses and seismic performance levels of RC structures, while the most of analyses are time-consuming and need to be done by high-speed computer systems. In addition, the unpredictable nature of seismic events is another factor that affects seismic performance achievement. To overcome this issue, this research proposed ML-based prediction models to estimate the IDR_{max} and Sa(T_1) for the M-IDA curve of the RC frames. The analysis results can be summarized as follows:

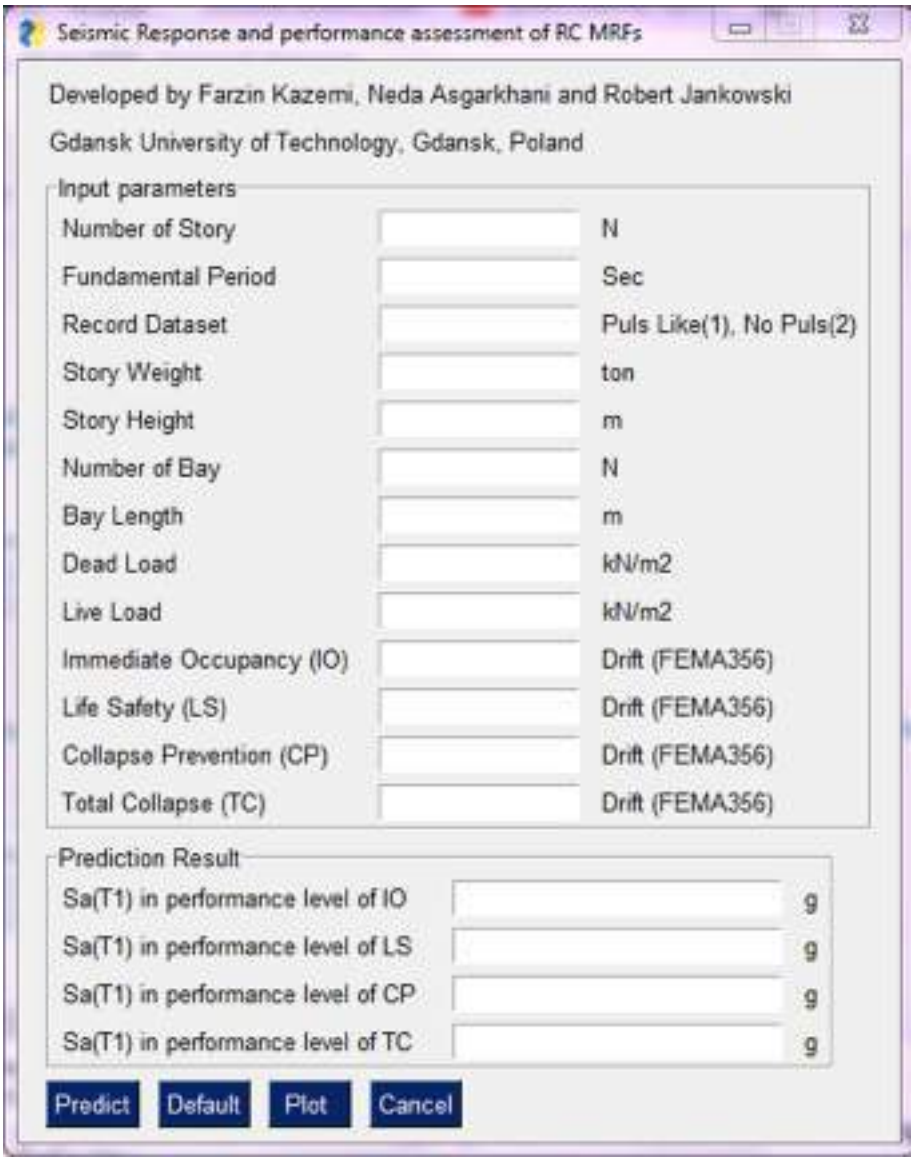

Fig. 20 GUI introduced for predicting the seismic limit-state capacity of RC MRFs

- Assuming IDR_{max} as the target of prediction, eight algorithms of PLSReg, SReg, VReg, LReg, GReg, MLPReg, SVM, and LSVR had lower R^2 values (i.e., less than 65%) and cannot be used as prediction models. On the other hand, eight algorithms of KNR, PLSReg, SReg, LReg, GReg, MLPReg, SVM, and LSVR had lower R^2 values (i.e., less than 77%) for predicting $Sa(T_1)$ as a target. In addition, ML algorithms had the precise prediction values located exactly in the $x = y$ line, assuming allowable IDR_{max} of lower than 4.0%, that shows the ability of the proposed methods for estimating IDR_{max} in all RC MRFs.
- Considering the curve plotting ability that improved in ML methods based on the allowable performance levels (i.e., IDR_{max} values of 1.0%, 2.0%, and 4.0%), three algorithms of the XGBoost, ANNs, and NuSVR can predict the seismic performance levels of the five-Story RC frame using the predicted M-IDA curves. Therefore, they can be considered as proposed prediction models for any type of RC frame.
- Four case study RC buildings were assumed to check the reliability of prediction models. In Case A, the BReg, ETReg, ERTReg, and ANNs algorithms predicted the IDR_{max} with the accuracy of 95.7%, 93.19%, 90.27%, and 90%, respectively, and in Case B, the accuracy of 92.78%, 90.31%, 87.85%, and 90.1%, respectively, were achieved by prediction models. In Case C, the ANNs and BReg algorithms with the accuracy of 92.9% and 89.76%, respectively, in Case D, the BReg, ETReg, and ANNs algorithms with the accuracy of 92.5%, 89.93%, and 87.32%, respectively, can be considered as best models of prediction.

- Graphical User Interface (GUI) was proposed for preliminary estimation of the seismic performance levels of RC frames based on the main important features that can be introduced as input parameters. In addition, the GUI can be able to plot the predicted M-IDA curve regarding both seismic events and facilitate the seismic vulnerability assessment of RC buildings. Moreover, there is no limit for introducing the thresholds of the allowable IDR_{max}, and the users can find the prediction results for the selected IDR_{max}.
- For operating the GUI, (a) receives the main important structural features that affects the seismic response and seismic limit-state capacities, (b) receives the selected IDR_{max} defined by user (e.g., four main IDR_{max} were showed in Fig. 20), (c) predicts the M-IDA curve of introduced RC frames, and (d) presents the $Sa(T_1)$ corresponding to the selected IDR_{max}.

Author contributions All authors contributed to the study conception and design. Material preparation, data collection, and analysis were performed by FK, NA, and RJ. The first draft of the manuscript was written by FK and NA, and all authors commented on previous versions of the manuscript. All authors read and approved the final manuscript. FK: writing—original draft preparation, conceptualization, software, analysis, methodology, modeling. NA: writing—original draft preparation, modeling, software, analysis, and investigation. RJ: writing—review and editing, supervision.

Funding The authors did not receive support from any organization for the submitted work. The authors have no relevant financial or non-financial interests to disclose.

Data availability Data will be made available on request.

Declarations

Conflict of interest The authors declare that there is no conflict of interest with relation to the paper Machine learning-based seismic probabilistic prediction of reinforced concrete buildings submitted for publication in *Archives of Civil and Mechanical Engineering*.

Open Access This article is licensed under a Creative Commons Attribution 4.0 International License, which permits use, sharing, adaptation, distribution and reproduction in any medium or format, as long as you give appropriate credit to the original author(s) and the source, provide a link to the Creative Commons licence, and indicate if changes were made. The images or other third party material in this article are included in the article's Creative Commons licence, unless indicated otherwise in a credit line to the material. If material is not included in the article's Creative Commons licence and your intended use is not permitted by statutory regulation or exceeds the permitted use, you will need to obtain permission directly from the copyright holder. To view a copy of this licence, visit http://creativecommons.org/licenses/by/4.0/.

References

1. Kaya Y, Safak E. Real-time analysis and interpretation of continuous data from structural health monitoring (SHM) systems. Bull Earthq Eng. 2015;13(3):917–34.
2. Ngeljaratan L, Moustafa MA. Structural health monitoring and seismic response assessment of bridge structures using target-tracking digital image correlation. Eng Struct. 2020;213: 110551.
3. Manguri A, Saeed N, Kazemi F, Szczepanski M, Jankowski R. Optimum number of actuators to minimize the cross-sectional area of prestressable cable and truss structures. Structures. 2023;47:2501–14.
4. Kazemi F, Jankowski R. Enhancing seismic performance of rigid and semi-rigid connections equipped with SMA bolts incorporating nonlinear soil-structure interaction. Eng Struct. 2023;274: 114896.
5. Kazemi F, Asgarkhani N, Jankowski R. Probabilistic assessment of SMRFs with infill masonry walls incorporating nonlinear soil-structure interaction. Bull Earthq Eng. 2023;21:1–32.
6. Kazemi F, Mohebi B, Yakhchalian M. Evaluation the P-delta effect on collapse capacity of adjacent structures subjected to far-field ground motions. Civil Eng J. 2018;4(5):1066. https://doi.org/10.28991/cej-0309156.
7. Mohebi B, Kazemi F, Yakhchalian M. Investigating the P-Delta effects on the seismic collapse capacity of adjacent structures. In: 16th European conference on earthquake engineering (16ECEE), 18–21, June, Thessaloniki, Greece. 2018.
8. Kazemi F, Mohebi B, Yakhchalian M. Enhancing the seismic performance of adjacent pounding structures using viscous dampers. In: The 16th European conference on earthquake engineering (16ECEE), 18–21, June, Thessaloniki, Greece. 2018.
9. Kazemi F, Mohebi B, Yakhchalian M. Predicting the seismic collapse capacity of adjacent structures prone to pounding. Can J Civ Eng. 2020;47(6):663–77.
10. Kazemi F, Mohebi B, Jankowski R. Predicting the seismic collapse capacity of adjacent SMRFs retrofitted with fluid viscous dampers in pounding condition. Mech Syst Signal Process. 2021;161: 107939.
11. Asgarkhani N, Kazemi F, Jankowski R. Optimal retrofit strategy using viscous dampers between adjacent RC and SMRFs prone to earthquake-induced pounding. Arch Civ Mech Eng. 2023;23(1):1–26.
12. Kabir MAB, Hasan AS, Billah AM. Failure mode identification of column base plate connection using data-driven machine learning techniques. Eng Struct. 2021;240: 112389.
13. Mangalathu S, Jeon JS. Stripe-based fragility analysis of multi-span concrete bridge classes using machine learning techniques. Earthq Eng Struct Dynam. 2019;48(11):1238–55.
14. Nguyen HD, LaFave JM, Lee YJ, Shin M. Rapid seismic damage-state assessment of steel moment frames using machine learning. Eng Struct. 2022;252: 113737.
15. Wu ZN, Han XL, He A, Cai YF, Ji J. Machine learning-based adaptive degradation model for RC beams. Eng Struct. 2022;253: 113817.
16. Hastie T, Tibshirani R, Friedman J. Overview of supervised learning. In: The elements of statistical learning. New York: Springer; 2009. p. 9–41.
17. Yazdanpanah O, Dolatshahi KM, Moammer O. Rapid seismic fragility curves assessment of eccentrically braced frames through an output-only nonmodel-based procedure and machine learning techniques. Eng Struct. 2023;278: 115290.
18. Kazemi F, Asgarkhani N, Jankowski R. Predicting seismic response of SMRFs founded on different soil types using machine learning techniques. Eng Struct. 2023;274: 114953.

19. Huang CS, Hung SL, Wen CM, Tu TT. A neural network approach for structural identification and diagnosis of a building from seismic response data. Earthq Eng Struct Dynam. 2003;32(2):187–206.
20. Yinfeng D, Yingmin L, Ming L, Mingkui X. Nonlinear structural response prediction based on support vector machines. J Sound Vib. 2008;311(3–5):886–97.
21. Lagaros ND, Papadrakakis M. Neural network based prediction schemes of the non-linear seismic response of 3D buildings. Adv Eng Softw. 2012;44(1):92–115.
22. De Lautour OR, Omenzetter P. Damage classification and estimation in experimental structures using time series analysis and pattern recognition. Mech Syst Signal Process. 2010;24(5):1556–69.
23. Worden K, Green PL. A machine learning approach to nonlinear modal analysis. Mech Syst Signal Process. 2017;84:34–53.
24. Kiani J, Camp C, Pezeshk S. On the application of machine learning techniques to derive seismic fragility curves. Comput Struct. 2019;218:108–22.
25. Nguyen NV, Nguyen HD, Dao ND. Machine learning models for predicting maximum displacement of triple pendulum isolation systems. Structures. 2022;36:404–15.
26. Oh BK, Glisic B, Park SW, Park HS. Neural network-based seismic response prediction model for building structures using artificial earthquakes. J Sound Vib. 2020;468: 115109.
27. Luo H, Paal SG. Artificial intelligence-enhanced seismic response prediction of reinforced concrete frames. Adv Eng Inform. 2022;52: 101568.
28. Gholizadeh R, Amiri GG, Mohebi B. An alternative approach to a harmony search algorithm for a construction site layout problem. Can J Civ Eng. 2010;37(12):1560–71.
29. Todorov B, Billah AM. Machine learning driven seismic performance limit state identification for performance-based seismic design of bridge piers. Eng Struct. 2022;255: 113919.
30. Dehestani A, Kazemi F, Abdi R, Nitka M. Prediction of fracture toughness in fibre-reinforced concrete, mortar, and rocks using various machine learning techniques. Eng Fract Mech. 2022;276: 108914.
31. Adibimanesh B, Polesek-Karczewska S, Bagherzadeh F, Szczuko P, Shafighfard T. Energy consumption optimization in wastewater treatment plants: machine learning for monitoring incineration of sewage sludge. Sustain Energy Technol Assess. 2023;56: 103040.
32. Shafighfard T, Bagherzadeh F, Rizi RA, Yoo DY. Data-driven compressive strength prediction of steel fiber reinforced concrete (SFRC) subjected to elevated temperatures using stacked machine learning algorithms. J Market Res. 2022;21:3777–94.
33. Kazemi F, Asgarkhani N, Jankowski R. Machine learning-based seismic fragility and seismic vulnerability assessment of reinforced concrete structures. Soil Dyn Earthq Eng. 2023;166: 107761.
34. Kazemi F, Jankowski R. Machine learning-based prediction of seismic limit-state capacity of steel moment-resisting frames considering soil-structure interaction. Comput Struct. 2023;274: 106886.
35. Pal M. Random forest classifier for remote sensing classification. Int J Remote Sens. 2005;26(1):217–22.
36. Geurts P, Ernst D, Wehenkel L. Extremely randomized trees. Mach Learn. 2006;63(1):3–42.
37. Louppe G, Geurts P. Ensembles on random patches. In: Joint European conference on machine learning and knowledge discovery in databases. Berlin: Springer; 2012. p. 346–61.
38. Freund Y, Schapire RE. A decision-theoretic generalization of on-line learning and an application to boosting. J Comput Syst Sci. 1997;55(1):119–39.
39. Friedman J, Hastie T, Tibshirani R. Additive logistic regression: a statistical view of boosting (with discussion and a rejoinder by the authors). Ann Stat. 2000;28(2):337–407.
40. Friedman JH. Greedy function approximation: a gradient boosting machine. Ann Stat. 2001;29:1189–232.
41. Cortes C, Vapnik V. Support vector machine. Mach Learn. 1995;20(3):273–97.
42. Chang CC, Lin CJ. Training v-support vector regression: theory and algorithms. Neural Comput. 2002;14(8):1959–77.
43. Drucker H, Burges CJ, Kaufman L, Smola A, Vapnik V. Support vector regression machines. Adv Neural Inf Process Syst. 1996;9.
44. Kohavi R. A study of cross-validation and bootstrap for accuracy estimation and model selection. In Ijcai. 1995;14(2):1137–45.
45. McCullagh P, Nelder JA. Generalized linear models. London: Chapman and Hall; 1989.
46. Wolpert DH. Stacked generalization. Neural Netw. 1992;5(2):241–59.
47. Höskuldsson A. PLS regression methods. J Chemometr. 1988;2(3):211–28.
48. ASCE 7–16. Minimum design loads and associated criteria for buildings and other structures. American Society of Civil Engineers; 2017.
49. United States Geological Survey. https://www.usgs.gov/programs/earthquake-hazards/hazards. Accessed 03 Mar 2022.
50. Haselton CB, Deierlein GG. Assessing seismic collapse safety of modern reinforced concrete frame buildings. PEER Report. 2007;8.
51. Mohebi B, Yazdanpanah O, Kazemi F, Formisano A. Seismic damage diagnosis in adjacent steel and RC MRFs considering pounding effects through improved wavelet-based damage-sensitive feature. J Build Eng. 2021;33: 101847.
52. McKenna F, Fenves GL, Filippou FC, Scott MH. Open system for earthquake engineering simulation (OpenSees). Berkeley, Pacific Earthquake Engineering Research Center, University of California. 2016. http://OpenSees.berkeley.edu. Accessed 21 Oct 2022.
53. Asgarkhani N, Yakhchalian M, Mohebi B. Evaluation of approximate methods for estimating residual drift demands in BRBFs. Eng Struct. 2020;224: 110849.
54. Yakhchalian M, Asgarkhani N, Yakhchalian M. Evaluation of deflection amplification factor for steel buckling restrained braced frames. J Build Eng. 2020;30: 101228.
55. Yakhchalian M, Yakhchalian M, Asgarkhani N. An advanced intensity measure for residual drift assessment of steel BRB frames. Bull Earthq Eng. 2021;19(4):1931–55.
56. Yazdanpanah O, Mohebi B, Kazemi F, Mansouri I, Jankowski R. Development of fragility curves in adjacent steel moment-resisting frames considering pounding effects through improved wavelet-based refined damage-sensitive feature. Mech Syst Signal Process. 2022;173: 109038.
57. Kazemi F, Asgarkhani N, Manguri A, Jankowski R. Investigating an optimal computational strategy to retrofit buildings with implementing viscous dampers. Int Conf Comput Sci ICCS Proc. 2022. https://doi.org/10.1007/978-3-031-08754-7_25.
58. Kazemi F, Jankowski R. Seismic performance evaluation of steel buckling-restrained braced frames including SMA materials. J Constr Steel Res. 2023;201: 107750.
59. Ibarra LF, Medina RA, Krawinkler H. Hysteretic models that incorporate strength and stiffness deterioration. Earthq Eng Struct Dynam. 2005;34(12):1489–511.
60. Altoontash A. Simulation and damage models for performance assessment of reinforced concrete beam-column joints. Dissertation, Department of Civil and Environmental Engineering, Stanford University. 2004.
61. Federal Emergency Management Agency (FEMA P695). Quantification of building seismic performance factors. US Department of Homeland Security, FEMA. 2009.

62. MATLAB/Simulink as a Technical Computing Language. Engineering computations and modeling in MATLAB. 2018.
63. FEMA-356. Prestandard and commentary for the seismic rehabilitation of buildings. Washington, DC: Federal Emergency Management Agency. 2000.

Publisher's Note Springer Nature remains neutral with regard to jurisdictional claims in published maps and institutional affiliations.

Paper X:

Kazemi, F., Asgarkhani, N., & Jankowski, R. (2024). Optimization-based stacked machine-learning method for seismic probability and risk assessment of reinforced concrete shear walls. Expert Systems with Applications, 255, 124897.

doi.org/10.1016/j.eswa.2024.124897

Expert Systems With Applications 255 (2024) 124897

Contents lists available at ScienceDirect

Expert Systems With Applications

journal homepage: www.elsevier.com/locate/eswa

Optimization-based stacked machine-learning method for seismic probability and risk assessment of reinforced concrete shear walls

Farzin Kazemi [a,b,1,*], Neda Asgarkhani [a,b,2,*], Robert Jankowski [a,3]

[a] Faculty of Civil and Environmental Engineering, Gdańsk University of Technology, ul. Narutowicza 11/12, 80-233 Gdańsk, Poland
[b] Department of Structures for Engineering and Architecture, School of Polytechnic and Basic Sciences, University of Naples "Federico II", Naples, Italy

ARTICLE INFO

Keywords:
Reinforced concrete shear wall
Machine learning algorithm
Seismic failure probability
Optimization algorithm
Seismic performance curve
Seismic retrofit

ABSTRACT

Efficient seismic risk assessment aids decision-makers in formulating citywide risk mitigation plans, providing insights into building performance and retrofitting costs. The complexity of modeling, analysis, and post-processing of the results makes it hard to fast-track the seismic probabilities, and there is a need to optimize the computational time. This research addresses seismic probability and risk assessment of reinforced concrete shear walls (RCSWs) by introducing stacked machine learning (Stacked ML) models based on Bayesian optimization (BO), genetic algorithm (GA), particle swarm optimization (PSO), and gradient-based optimization (GBO) algorithms. The study investigates 4-, to 15-Story RCSWs assuming different bay lengths and soil types to build a comprehensive database based on the incremental dynamic analysis (IDA) subjected to 56 near-field pulse-like and no-pulse records. Having 227,200 and 63,384 data points for a median of IDA curve (M_{IDA}) and seismic probability curve, respectively, the proposed Stacked ML models have shown good performance on curve fitting ability by accuracy of 99.1% and 99.4% for M_{IDA} and seismic fragility curves, respectively. In addition, the proposed models can estimate the mean annual frequency, λ, which is a key parameter in seismic risk assessment of buildings. To provide the results of the study for general buildings, a user-friendly GUI is proposed that facilitates result utilization, offering insights into seismic performance levels, providing the estimated M_{IDA} and seismic failure probability curves, and mean annual frequency calculations for specific performance levels and seismic hazard curves.

1. Introduction

A reinforced concrete shear wall (RCSW) is a structural system extensively used in the construction of buildings to provide lateral resistance against various forces, especially horizontal forces like those generated by seismic activities or wind. The RCSW consists of a reinforced concrete wall that is designed to withstand shear forces, mainly due to seismic forces as a result of earthquakes. It is a key component in the lateral load-resisting system of a building since it can reduce the section size of other structural elements such as beams and columns, while it can control the torsional rotation by optimized positioning. The behavior of an RCSW system under extreme conditions, leading to potential collapse and damage, is a critical aspect of structural engineering. Therefore, it is vital to consider different failure mechanisms of the RCSW such as bending/flexural failure, shear failure, out-of-plane failure, and a combination of shear and flexural failure (Lee and Mosalam, 2005; Abraik and Youssef, 2018). Grammatikou et al. (2015) showed that the RCSW failure modes are classified as flexure, diagonal tension, diagonal compression, or sliding shear.

Recent research affirms that modeling procedure, designing, and analysis of RCSW can incur additional costs. However, predicting seismic responses like maximum interstory drift ratio (IDR) and seismic probability curves can assist civil engineers in assessing the current performance of RCSW and seismic risk assessment of buildings, thereby, reducing modeling time and offering a preliminary estimation. Some studies have been performed to take the effects of structural features into account for estimating the seismic behavior and seismic performance of steel structures (Kazemi et al., 2023a; 2024a), and reinforced concrete

* Corresponding authors at: Faculty of Civil and Environmental Engineering, Gdańsk University of Technology, ul. Narutowicza 11/12, 80-233 Gdańsk, Poland.
E-mail addresses: farzin.kazemi@pg.edu.pl (F. Kazemi), neda.asgarkhani@pg.edu.pl (N. Asgarkhani), jankowr@pg.edu.pl (R. Jankowski).
[1] 0000-0002-2448-1465.
[2] 0000-0002-0756-8438.
[3] 0000-0002-6741-115X.

https://doi.org/10.1016/j.eswa.2024.124897
Received 15 December 2023; Received in revised form 25 June 2024; Accepted 25 July 2024
Available online 27 July 2024
0957-4174/© 2024 Elsevier Ltd. All rights are reserved, including those for text and data mining, AI training, and similar technologies.

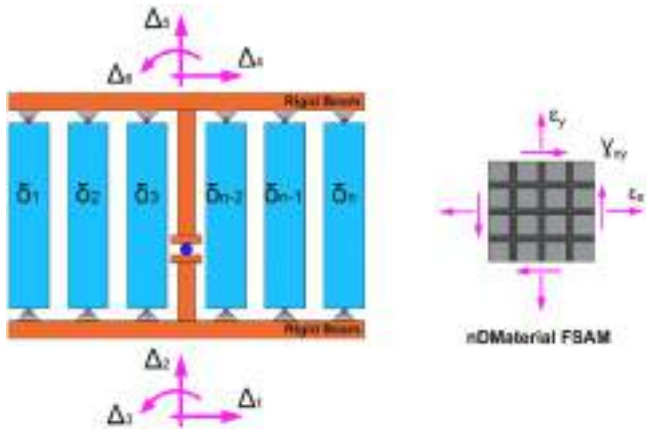

Fig. 1. SFI-MVLEM element used for modeling of RCSW in OpenSees (McKenna et al., 2015).

buildings (Kazemi et al., 2023b), seismic fragility and risk assessment of buildings (Moaf et al., 2023; Kazemi et al., 2023c) using machine learning (ML) methods. Ma et al. (2023) introduced a genetic programming-based symbolic regression model to propose a backbone curve model for RCSWs considering 388 existing RCSWs for training and comparative analysis. However, Deger and Taskin (2022) used the Gaussian process method to estimate the backbone curve of RCSW. Mangalathu et al. (2020) ascertained the failure mode of RCSWs considering geometric layouts, material attributes, and reinforcement specifics. To achieve this, an extensive database with 393 experimental outcomes of diverse geometric configurations was compiled. The study evaluated eight ML models of Naïve Bayes, K-nearest neighbors (KNN), decision tree, random forest (RF), AdaBoost, extreme gradient boosting (XGBoost), LightGBM, and CatBoost to identify the most effective prediction model. Asjodi et al. (2023) introduced a new image-based model for identifying damaged features and plotting the fragility surface of RCSW. Mansourdehghan et al. (2022) presented a damage assessment tool utilizing visual characteristics of a damaged RCSW for recognizing performance of damaged RCSW and estimating the RID and ID_{max} of the walls. These estimations are derived from a database consisting of 236 pictures corresponding to 72 walls. Zhang et al. (2022) utilized a database comprising experimental data from 429 RCSWs sourced from existing literature. The findings demonstrated a high accuracy of 97 % for estimating failure modes of RCSW, with the XGBoost and GBM algorithms proving particularly effective. Notably, factors such as longitudinal reinforcement, shear-to-span aspect, and distributed reinforcement significantly affected the lateral strength of RCSWs. Chou et al. (2022) introduced optimized ML methods to improve the accuracy of the formula for estimating the shear capacity of RCSWs and found out that the XGBoost algorithm with an accuracy of 97.8 % had the best prediction value. Recently, RCSWs have been explored by many researchers for the targets of structural design (Liao et al., 2022), optimization of cost (Atabay and Gulay, 2009; Atabay, 2009), and evaluation of performance (Modirzadeh et al., 2012). Finding the lateral stiffness of RCSWs was in the interest of Le Nguyen et al. (2023), while they only used one method for optimizing the hyperparameters.

Uncertainties represent inherent randomness in the input parameters or boundary conditions of a structural system, such as variations in ground motion characteristics or material properties due to natural variability. On the other hand, model uncertainties stem from simplifications, assumptions, or limitations within the numerical model itself, including idealizations of structural behavior, numerical discretization methods, or the neglect of certain physical phenomena. These uncertainties can manifest in various ways, affecting the accuracy and reliability of numerical predictions. For instance, uncertainties can lead to variability in structural responses under repeated analyses, making it challenging to precisely predict the performance of a structure under different loading conditions. Similarly, model uncertainties can introduce biases or errors in the numerical predictions, potentially resulting in inaccuracies in failure mode predictions or the estimation of structural capacities (Miceli and Castaldo, 2024). The capability of a numerical model to capture the failure mode of a structure is particularly sensitive to these uncertainties. By quantifying and accounting for these uncertainties, engineers can improve the reliability of numerical predictions and make informed decisions regarding the design, assessment, and retrofitting of structures to enhance their resilience against extreme events.

Some formulas have been proposed for estimating the residual drift and IDR of steel buckling-restrained braced frames (Asgarkhani et al., 2020) and steel moment-resisting frames (Erochko et al., 2011). However, due to the complex nature and different input factors, there is a need to prepare a surrogate model for predicting seismic response and probability of RCSWs that remain unsolved problems. In addition, the literature review showed that a small number of datasets (i.e., less than 500 data) have been used for the ML methods, which reduces the capability and generality of the models. However, some well-known ML models have been used for estimating the response of RCSWs, while there is room for a comprehensive investigation of conventional ML algorithms and Stacked ML models for the problem.

To fulfill the shortcomings of previous studies, this research investigates the optimization-based Stacked ML models to estimate the median of incremental dynamic analysis (M_{IDA}) curves that can provide the performance levels of the 4-, to 15-story RCSWs having different input features founded on soil types of B, C, D, and E. Furthermore, the proposed ML models can be used to predict the seismic probability curves (i.e., fragility curves) that is beneficial for seismic risk assessment, while they are automated in hyperparameter selection by optimization methods. To train the ML models, a dataset including 227,200 data points for M_{IDA} curves and 63,384 data points for the seismic probability has been prepared during the analysis of the RCSWs. Therefore, the research includes a wide range of RCSWs having different span lengths, floor levels, and soil types that can be used for estimating a general RCSW. Furthermore, to find out the ability of the proposed ML models, a general RCSW has been selected as a test model and the predictions have been compared. After validation of ML models on the general RCSW, a user-friendly tool has been developed to use the results of this research for a prediction model based on the provided database, hence, the database can be updated in the future by increasing the number of RCSWs.

2. Modeling and analysis methodology

2.1. Modelling of RCSW

The *nDMaterial FSAM* (Fixed-Strut-Angle-Model) is a constitutive model developed by Kolozvari et al. (2015b) to simulate RC panel element's behavior under cyclic load. The model assumes that strain in both reinforcement bars and concrete are the same, implying a strong bond between them. While reinforcing steel bars experience uniaxial stresses along their length, concrete behavior is described using stress–strain relationships in multiple directions, determined by concrete cracking. Despite primarily representing uniaxial behavior, the *FSAM* model also includes effects like biaxial damage and compression softening. To transfer shear stress alongside crack, it employs a friction-based elasto-plastic shear-aggregate interlock model and a linear elastic model for dowel action on the reinforcing steel bars. Although designed for use with the shear-flexure interaction (SFI) model for RCSWa, the *FSAM* model can be applied in various contexts. Therefore, in this study, the *nDMaterial FSAM* has been utilized assuming a friction coefficient of 1.0, and dowel action stiffness of 0.005. The parameters that define the cyclic degradation behavior of the reinforcing bars were adjusted to $R_0 = 20$, $a_1 = 18.5$, and $a_2 = 0.15$ (see Table 3 in Kolozvari et al., 2015a).

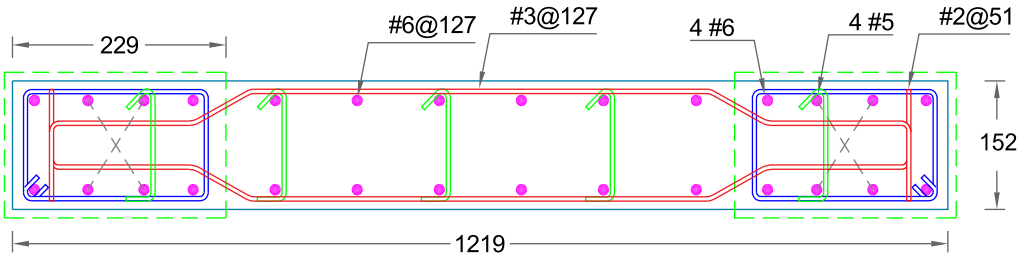

Fig. 2. Cross-section view of the RW-A15-P10-S78 specimen used for verifying modelling of RCSW.

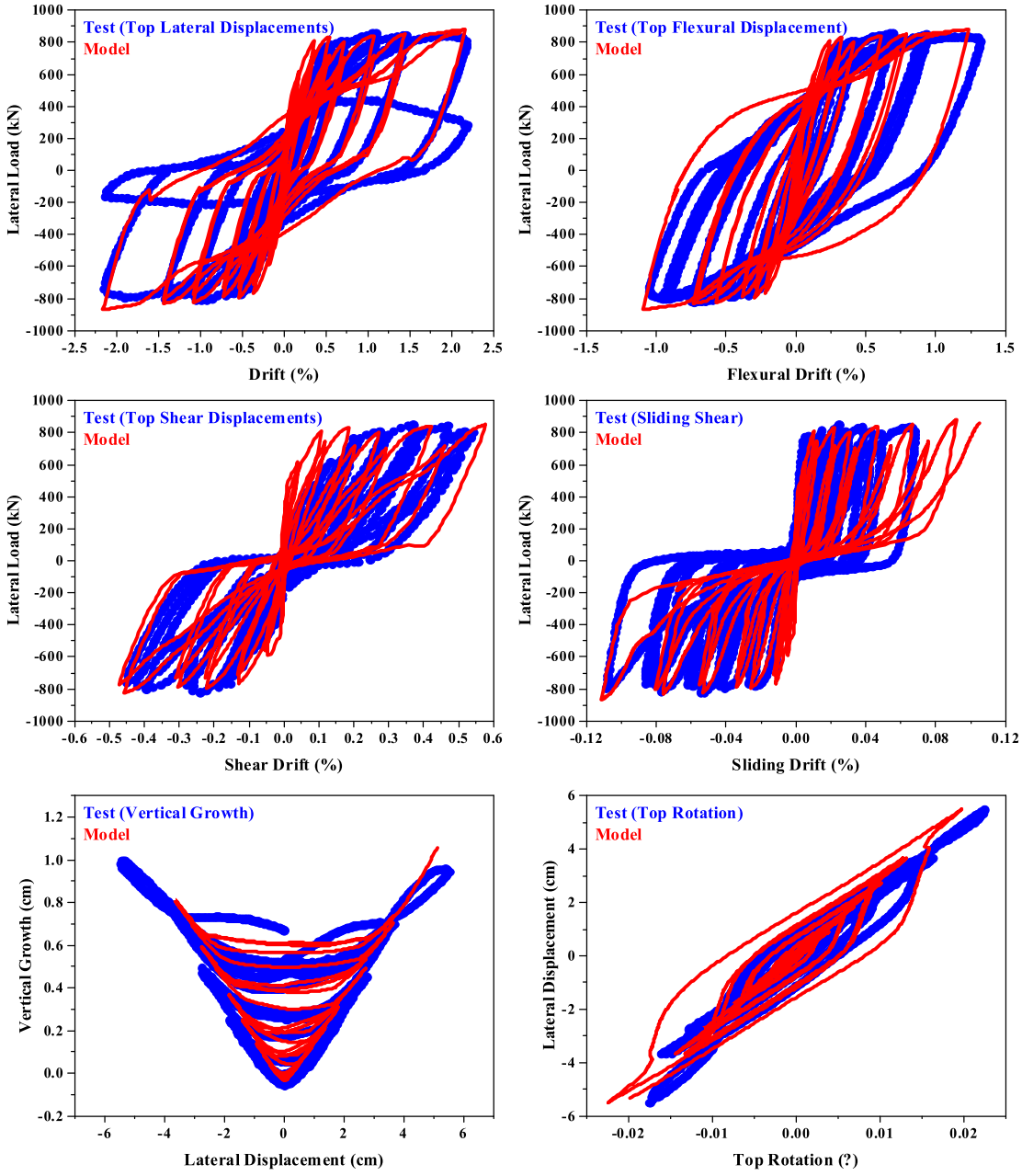

Fig. 3. Comparing the results of the test (RW-A15-P10-S78) and the numerical model of RCSW.

SFI has been observed in numerous experimental investigations (e.g., see Lowes et al., 2012; Dazio et al., 2009) having an aspect ratio greater than 2.0. Therefore, some studies have employed fiber models and multiple-vertical-line-element model (MVLEM) (e.g., see Orakcal et al., 2004) in OpenSees (McKenna et al., 2015) to perfectly model the behavior of RCSW, while the results of models do not incorporate with experimental observations. The strut and tie model, known as the truss approach, is introduced to capture SFI, while some studies used a fiber-based model for RCSW (Jiang et al., 2010). The investigations showed that these models could not perfectly comply with the results of

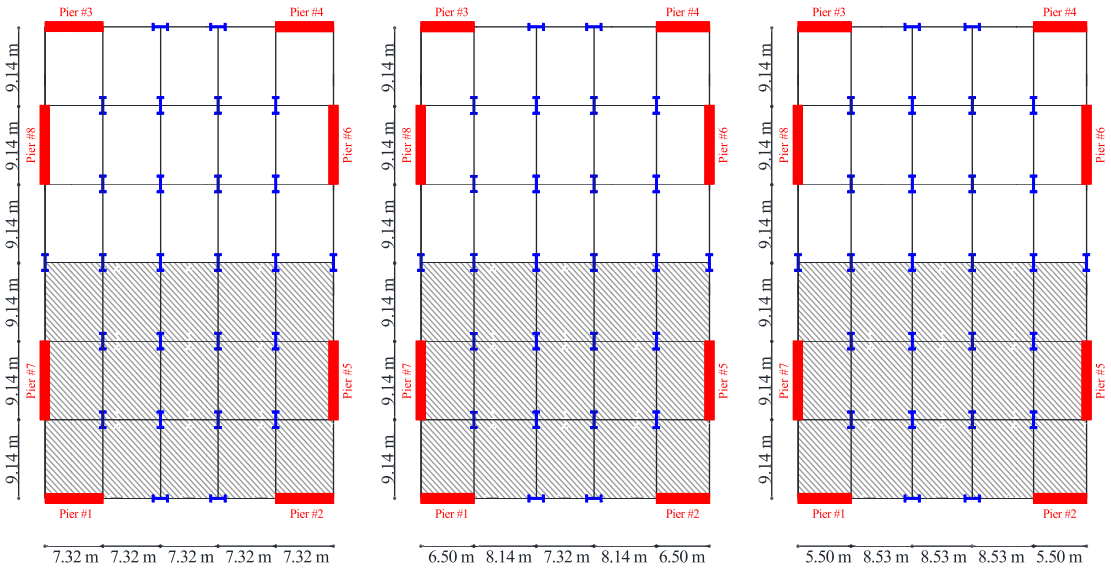

Fig. 4. Three structural plans of buildings used for modeling of RCSW.

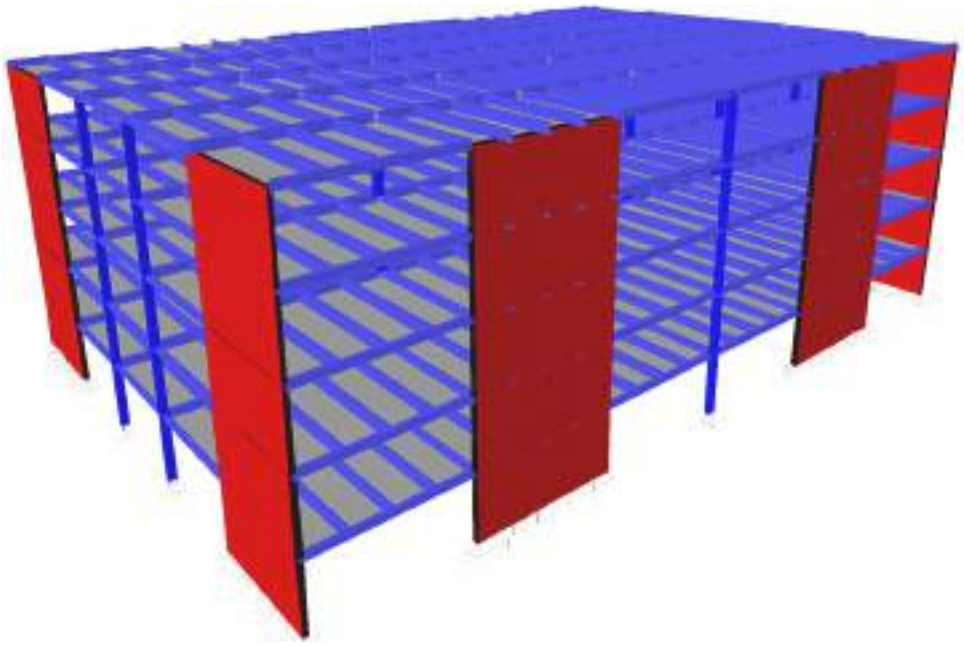

Fig. 5. 3D presentation of the 6-story model in ETABS 2020 software.

experimental evaluation. Therefore, the shear-flexure interaction multiple-vertical-line-element model (SFI-MVLEM) can be used to capture the axial/flexural and shear interaction of the RC shear wall. To use this mode, Kolozvari et al. (2015a and 2015b) developed the *SFI_MVLEM* command in OpenSees (McKenna et al., 2015) to incorporate the 2D RC panels modeled with *nDMaterial FSAM*. Fig. 1 illustrates the *SFI-MVLEM* element used for modeling of RC shear wall in OpenSees (McKenna et al., 2015).

2.2. Verification of RCSW model

To verify the RCSW, the RW-A15-P10-S78 specimen investigated by Kolozvari et al. (2015b) has been selected. Details of reinforcing and dimensions of the specimen RW-A15-P10-S78 are illustrated in Fig. 2. The specimen has two boundaries at the corners shown by the green dashed line, and the web boundary between them. Therefore, the compressive strength for confined and unconfined concrete have been assumed as 72.2 MPa and 55.8 MPa, following the initial tangent modulus of 41051 MPa and 37252 MPa, respectively. In addition, the tensile strength of 2.31 MPa and the initial tangent modulus of 37252 MPa have been considered. The consideration of confinement effects in the modeling approach has been addressed, as outlined by Kolozvari et al. (2015b). Distinct concrete strengths are observed between confined and unconfined sections, necessitating different modeling approaches in OpenSees. Furthermore, Kolozvari et al. (2015b) conducted experimental tests to ascertain the concrete strength in various sections of shear walls, including the middle and corners. This methodology of incorporating different concrete strengths aligns with the rationale of accounting for confinement effects. Moreover, the concrete strength must meet the demands of high-rise buildings. Five RC panels have been modeled, in which, two outer RC panels represent the confined boundary. In addition, six *SFI-MVLEM* have been considered along the RCSW

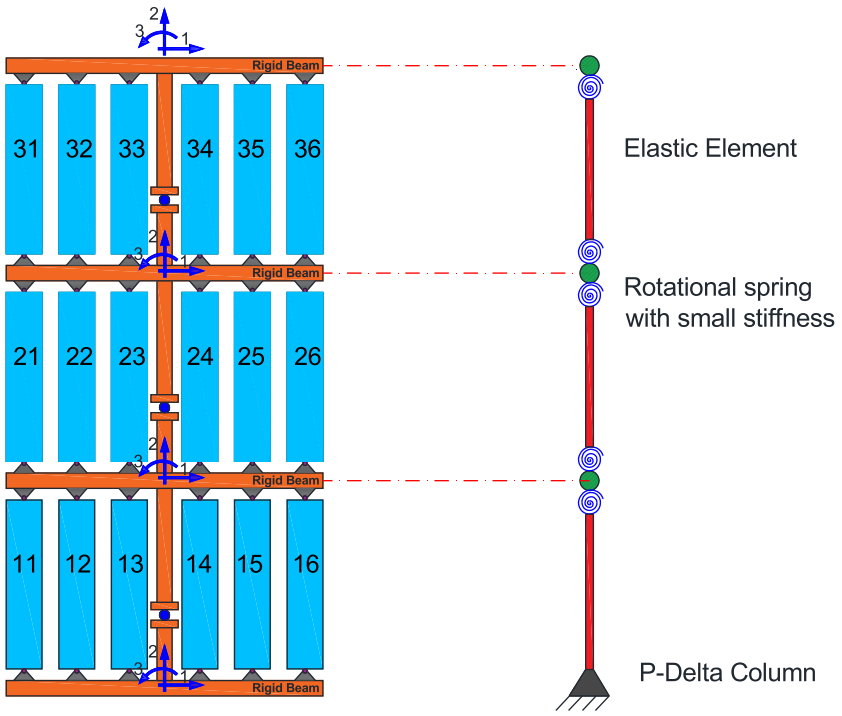

Fig. 6. Modeling of RCSW in OpenSees (McKenna et al., 2015).

model, which has a height of 182.9 cm and an aspect ratio of 1.5. C=0.4 has been used to consider the center of relative rotation. The reinforcement ratio of 6.06 and 0.73 has been used for the boundary and web of RCSW. The RCSW model has been prepared in OpenSees software and displacement-controlled cyclic analysis has been done assuming the loading protocol having drift ratios of 0.5, 0.75, 1.0, 1.5, and 2.0 % (Kolozvari, 2013). Different results of specimen RW-A15-P10-S78 have been compared with the numerical model of RCSW in OpenSees (McKenna et al., 2015), and are plotted in Fig. 3. The results of verification showed that the numerical model has acceptable accuracy to capture the different responses of RCSW and can be used for modeling of buildings investigated in this research.

2.3. Modeling of buildings

In this research, three cases of buildings having 4-, to 15-story levels with floor height of 4.0 m have been modeled, in which, buildings have bay lengths of 5.5 m, 6.5 m, and 7.32 m, as presented in Fig. 4. Eight RCSWs have been considered in symmetric location for each plan to prevent rotational movement. Fig. 5 shows a 3D presentation of a 6-story model in ETABS 2020 software. All columns other than those considered in RCSWs have been modeled as gravity columns. The shaded area allocated half of the plan to the RCSWs in X direction. All structures were located in California assuming latitude and longitude of 37.88° N and 122.08° W, respectively, which four soils of B, C, D, and E are selected according to ASCE 7-22 (2023).

The values of SD_S and SD_1 for the construction site have been assumed according to Asgarkhani et al. (2023). The dead and live loads of 3.35 kN/m^2 and 1.68 kN/m^2 have been considered for floor levels, and the dead and live loads of 1.68 kN/m^2 and 0.96 kN/m^2 have been considered for roof levels assuming the cladding load of 1.20 1.68 kN/m^2 (Kazemi and Jankowski, 2023a; 2023b). In addition, the values of R=6.0, Ω = 2.5, C_d = 5.0, and I=1.0 have been selected according to ASCE 7–22 (2023), and the inherent damping ratio of a 5 % has been assumed. To model buildings, the compressive strength of concrete equal to 34.5 MPa and reinforcement bars with yield strength of 414 MPa have been assumed. Owing to the fact that the building has a regular plan, half of the building has been modeled in OpenSees (McKenna et al., 2015) for performing nonlinear dynamic analysis. The structural details of the RCSWs have been presented in Fig. A-1, and Tables A-1 to A-3 in *Appendix*. For modeling the RCSWs, the procedure that has been verified in Section 2.2 was used. For each RCSW, six RC panels have been modeled, in which, two outer RC panels represent the confined boundary and four RC panels have been used for the web boundary. It is assumed that the confined and unconfined concrete has a compressive strength of 72.2 MPa and 55.8 MPa, respectively (Kolozvari et al., 2018). However, to control the behavior of the reinforcement bar, the parameters of R_0 = 20, a_1 = 18.5, and a_2 = 0.15 have been adjusted for *Steel02* material. It is confirmed that considering the gravity columns can affect the results of nonlinear analysis, therefore, all gravity columns have been modelled as leaning columns as presented in Fig. 6 to include the *P-Δ* effects (Kazemi et al., 2023d).

2.4. IDA analysis

Seismic ground motions can indeed be classified as frequent or non-frequent records based on their recurrence interval or probability of occurrence. Frequent records typically represent seismic events with a higher likelihood of occurrence, such as those associated with lower-magnitude earthquakes or events originating from nearby faults. These ground motions are characterized by shorter return periods and are more commonly observed in seismic hazard analyses for regions with active tectonic activity. On the other hand, non-frequent records correspond to seismic events that have lower probabilities of occurrence but may have larger magnitudes or originate from more distant seismic sources. These events are associated with longer return periods and are often considered in seismic hazard assessments for assessing the potential impact of rare but significant earthquakes (Castaldo and Miceli, 2024). The classification of seismic ground motions into frequent or non-frequent categories is essential for conducting comprehensive seismic risk assessments and designing structures to withstand the effects of earthquakes. To perform IDAs, the near-fault pulse-like (NPL) and near-fault no-pulse (NNP) including 56 non-frequent records extracted from FEMA P695 (FEMA P695) have been used.

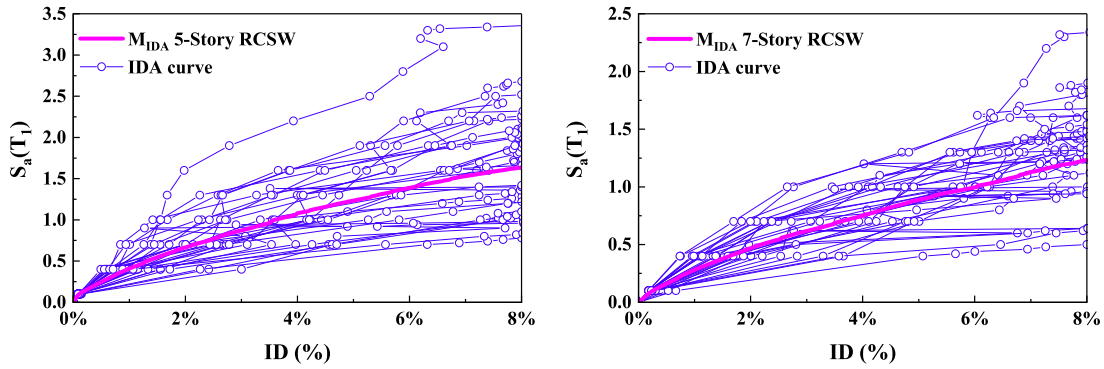

Fig. 7. IDA curves of 5-Story and 7-Story RCSWs with the bay length of 6.5 m.

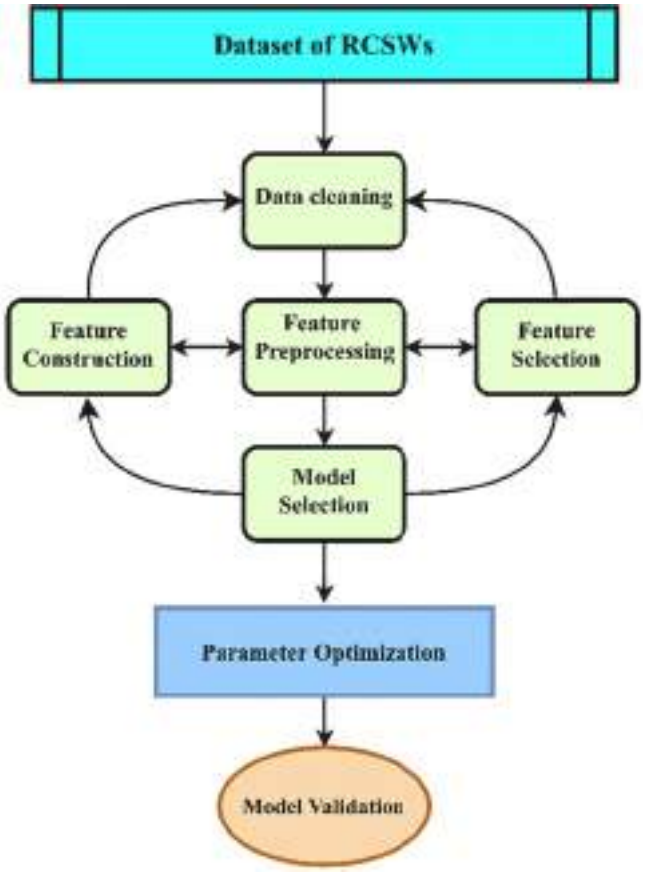

Fig. 8. Illustration of automated TPOT.

The selection of an appropriate parameter to characterize structural damage constitutes a crucial initial phase in the development of any methodology aimed at assessing structural reliability in the face of multiple seismic events. Numerous damage indicators have been put forth in scholarly works, typically falling into two primary categories: those related to deformation and those related to energy (Turchetti et al., 2023). Deformation-based indices encompass metrics such as the maximum drift demand investigated by Gentile and Galasso (2020). During IDA, the structural response (i.e., IDR) is evaluated for a range of ground motion intensity levels (i.e., $Sa(T_1)$), and in each intensity level, the structural response is compared to a predefined threshold of IDR. As the intensity measure increases incrementally, the structural response is assessed at each step, and damage states are assigned based on the calculated values of the demands. Collapse cases occur when the structural response exceeds critical thresholds associated with failure. By capturing seismic responses of RCSWs at floor levels, IDA curves can be plotted, and using the median of IDA (M_{IDA}) curve, the seismic performance levels of RCSWs can be determined. It should be noted that the hunt & fill method has been employed to reduce the computational effort and improve the accuracy of capturing the collapsed capacity. Fig. 7 illustrates IDA curves and M_{IDA} curves of 5-Story and 7-Story RCSWs with the bay length of 6.5 m, respectively. The results of IDAs have been collected for all considered RCSWs and have been prepared for training ML algorithms.

3. Machine learning methods

3.1. Stacked ML model

Some studies have been carried out to find the best prediction model to estimate the seismic response and performance levels, while they used the conventional ML algorithms (Shafighfard et al., 2024; Kazemi et al., 2024a–d). Since the conventional ML algorithms suffer from shortcomings of the dataset that can affect their accuracy, in this research, automated Stacked ML models have been proposed that use some procedures for avoiding the decrease in accuracy due to changing the number of data points. It should be noted that the complex nature of ground motions leads to unpredictable seismic responses; therefore, as much as data points have a wide range of structures, the results of prediction meet the actual values. In this study, the primary objective is to develop a prediction model using ML methods. The aim is to achieve accurate estimations of seismic responses while utilizing a minimal set of training data. Employing a combination of multiple ML methods, such as ensemble or Stacked ML algorithms, elongates prediction times. Consequently, the suggested Stacked ML algorithm needs to be meticulously designed, to ensure efficient utilization of diverse features within the training dataset. The Stacked ML algorithm proposed in this study incorporates feature selection methodologies, namely filter, wrapper, and embedded, to remove extra input features in dataset since constant values can significantly affect the results of the analysis. Furthermore, hyperparameters are fine-tuned using optimization method integrated within the tree-based pipeline optimization tool (TPOT), a Python-based automated machine learning (AutoML) framework, specifically from Auto-sklearn presented in Fig. 8. The utilization of TPOT enhances the efficacy in optimizing ML pipelines within proposed Stacked ML model.

A stacked ML model is a sophisticated ensemble learning method designed to improve predictive accuracy by combining multiple ML algorithms. The procedure begins with the selection of a diverse array of base learners, including artificial neural networks (ANNs), RF, extra-trees regressor (ETR), bagging regressor (BR), GBM, XGBoost, LightGBM, and CatBoost (Dehestani et al., 2022; Asgarkhani et al., 2023), to ensure comprehensive data analysis. Each base learner is individually trained on the training dataset to generate initial predictions. To prevent overfitting, out-of-fold predictions are employed by

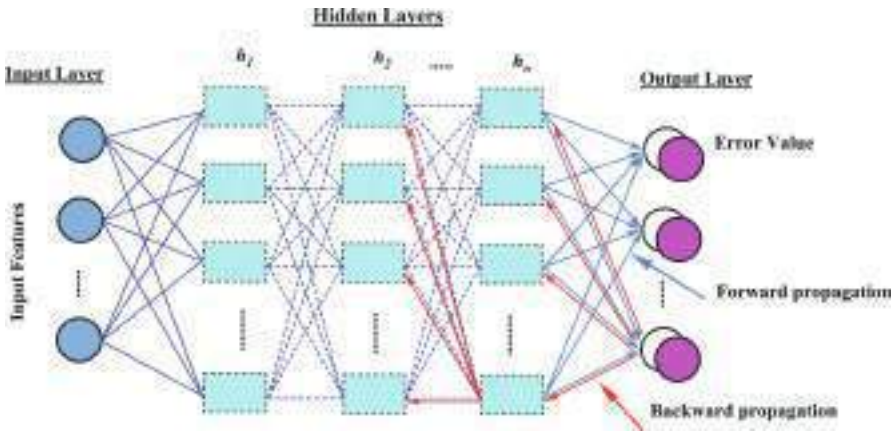

Fig. 9. Architecture of ANNs with backward and forward propagation methodology.

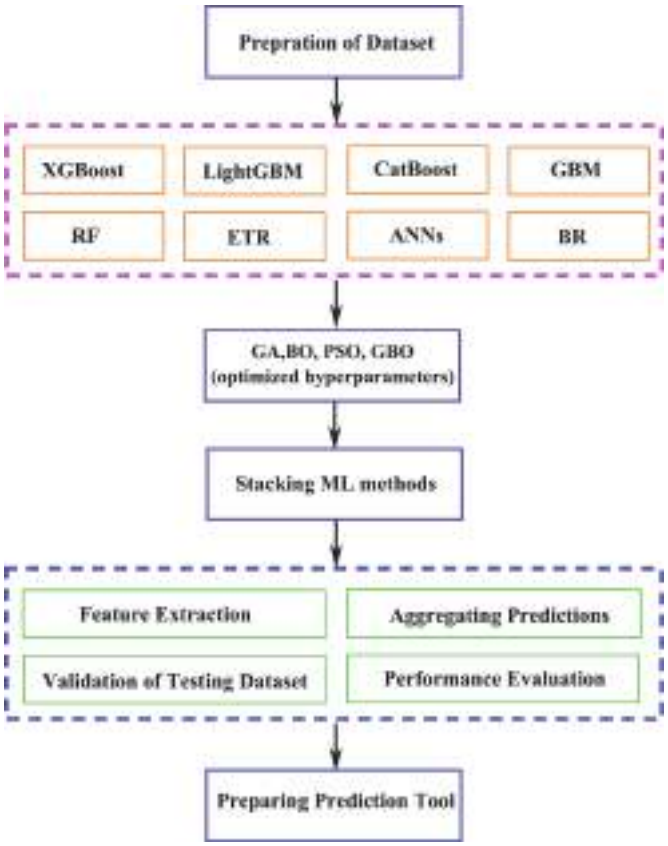

Fig. 10. Architecture of Stacked ML model and the optimal selection of the sub-models.

partitioning the training data into *k* folds, training each model on *k-1* folds, and making predictions on the remaining fold. These out-of-fold predictions, combined with those on the validation set, create *meta*-features. A *meta*-learner, usually a simpler model like linear regression, is then trained on these *meta*-features to determine the optimal combination of the base learners' predictions. This *meta*-learner synthesizes the results, producing a final prediction that integrates the strengths of all individual models while minimizing their weaknesses. Through this meticulous process of combining and weighting the outputs of various algorithms, the stacked ML model achieves superior accuracy and robustness compared to any single model.

In this study, an ANNs algorithm with the methodology of backward and forward propagation has been employed having 3 hidden layers and Relu activation function, which is presented in Fig. 9. Therefore, sub-

Table 2
Statistical metrics to evaluate proposed Stacked ML methods (Asgarkhani et al., 2024a).

Indicator	Formula
Coefficient of determination	$R^2 = 1 - \frac{\sum_{i=1}^{n}(\text{Actual}_i - \text{Predicted}_i)^2}{\sum_{i=1}^{n}(\text{Actual}_i - \text{Actual}_{avg})^2}$
Mean squared error	$MSE = \frac{1}{n}\sum_{i=1}^{n}(\text{Actual}_i - \text{Predicted}_i)^2$
Mean absolute error	$MAE = \frac{1}{n}\sum_{i=1}^{n}\lvert\text{Actual}_i - \text{Predicted}_i\rvert$
Mean absolute relative error	$MARE = \frac{1}{n}\sum_{i=1}^{n}\left\lvert\frac{\text{Actual}_i - \text{Predicted}_i}{\text{Actual}_i}\right\rvert$
Mean square relative error	$MSRE = \frac{1}{n}\sum_{i=1}^{n}\left\lvert\frac{\text{Actual}_i - \text{Predicted}_i}{\text{Actual}_i}\right\rvert^2$
Root mean squared relative error	$RMSRE = \sqrt{\frac{1}{n}\sum_{i=1}^{n}(\frac{\text{Actual}_i - \text{Predicted}_i}{\text{Actual}_i})^2}$
Mean bias error	$MBE = \frac{1}{n}\sum_{i=1}^{n}(\text{Actual}_i - \text{Predicted}_i)$
Maximum absolute relative error	$\text{erMAX} = \max(\left\lvert\frac{\text{Actual}_i - \text{Predicted}_i}{\text{Actual}_i}\right\rvert)$
Standard deviation	$SD = \sqrt{\frac{\sum(X_i - \text{Arithmetic mean})^2}{\text{total number}}}$

Table 1
Hyperparameters of optimal submodels of Stacked ML.

SubModel	n_estimators	learning_rate	min_sample_leaf	min_sample_split	max_depth	random_state
XGBoost	2200	0.01	8	10	6	–
GBM	3000	0.01	8	6	8	–
LightGBM	3200	0.001	–	–	10	–
CatBoost	1800	0.03	–	–	16	–
ETR	2000	–	6	8	–	0
BR	2000	–	–	–	–	0
RF	3400	–	–	–	8	0

Table 3
Pre-processing results considering different kinds of ML algorithms and Stacked ML models.

ML method	R^2	MSE	MAE	MARE	MSRE	RMSRE	MBE	erMAX	SD
XGBoost	0.910	2.7	1.68	0.22	0.037	0.22	0.33	0.73	0.03
RF	0.912	2.35	1.55	0.18	0.052	0.17	0.4	0.45	0.04
BR	0.942	2.19	1.14	0.16	0.015	0.11	0.25	0.22	0.03
ETR	0.963	2.12	1.16	0.12	0.026	0.06	0.15	0.1	0.03
GBM	0.872	3.14	1.88	0.3	0.281	0.77	0.45	1.36	0.06
LightGBM	0.936	2.10	1.14	0.10	0.026	0.15	0.13	1.36	0.04
CatBoost	0.938	2.07	1.13	0.15	0.025	0.13	0.13	1.34	0.04
ANNs	0.942	2.17	1.18	0.14	0.033	0.13	0.26	0.27	0.03
Stacked ML-1	0.964	2	1.03	0.14	0.013	0.1	0.13	0.21	0.01
Stacked ML-2	0.936	2.1	1.14	0.1	0.026	0.14	0.24	0.36	0.02
Stacked ML-3	0.975	2.17	1.16	0.16	0.015	0.11	0.19	0.24	0.01
Stacked ML-4	0.951	2.16	1.19	0.17	0.023	0.1	0.26	0.37	0.01
Stacked ML-5	0.987	2.03	1.06	0.11	0.013	0.05	0.12	0.17	0.01

models integrated into Stacked ML model undergo optimization to enhance results and reduce computation time. Fig. 10 illustrates the Stacked MLs used and the optimal selection of the sub-models. Recognizing that utilizing all sub-models in a singular model does not meet the objective of reducing computation time, a systematic procedure is implemented to select the optimal combination of sub-models within Stacked ML model. To assess effectiveness models, an initial step involved the selection of optimal hyperparameters for ML model predictions presented in Table 1. Subsequently, these ML models were integrated into ensemble model using respective best hyperparameters to evaluate their performance within the combined model.

Since the optimized hyperparameters can improve the performance of ML models, optimization methods of Bayesian optimization (BO), genetic algorithm (GA), particle swarm optimization (PSO), and gradient-based optimization (GBO) have been used to find the best hyperparameters of ML models. For this purpose, those ML methods that can be regulated by hyperparameters have been selected and the value of each hyperparameter has been assumed as the target of optimization. This procedure is time-consuming, therefore, a small part of the dataset has been randomly selected to reduce the time of analysis and improve the efficiency of the algorithms. This can lead to finding the best hyperparameters in a small part of the dataset and doing the main analysis on the all dataset only by the optimized hyperparameters, which can decrease the total time of executions compared to conventional methods of fine-tuning. By using a multi-agent system, where each agent represents an optimization method (i.e., BO, GA, PSO, and GBO), they can communicate and share information, such as best-performing hyperparameters or exploration results. The results confirm that using optimization methods can considerably affect the accuracy of conventional ML models, hence, the Stacked ML models. For instance, for estimating M_{IDA} of the 9-Story RCSW assuming the bay length of 6.5 m and soil D, the results show that the prediction accuracy of XGBoost, RF, BR, ETR, GBM, LightGBM, CatBoost, and ANNs have been increased by 18.1 %, 17.3 %, 4.5 %, 4.1 %, 14.8 %, 10.3 %, 9.8 %, and 15.7 %, respectively. Moreover, due to the significant effects of optimized hyperparameters, the prediction accuracy of Stacked ML-1, Stacked ML-2, Stacked ML-3, Stacked ML-4, and Stacked ML-5 has been increased by 13.6 %, 12.7 %, 14.4 %, 16.2 %, and 15.6 %, respectively. Therefore, using the optimization methods can improve the ML models and they can collaborate to share promising regions in the hyperparameter space.

BO does not have a straightforward mathematical equation; however; its main principles involve using a surrogate model of the Gaussian process and an acquisition function to determine the next point to evaluate. PSO is based on the formula that represents the velocity of particle i, v_i^{t+1} as follows:

$$v_i^{t+1} = w \cdot v_i^t + c_1 \cdot r_1 \cdot (pbest_i - x_i) + c_2 \cdot r_2 \cdot (gbest - x_i) \quad (1)$$

where w is inertia weight, c_1, and c_2 are cognitive and social parameters, r_1 and r_2 are random values between 0.0 and 1.0, and $pbest_i$ and $gbest$ represent personal best position of particle i and global best position found by the swarm. The position of the swarm is updated by:

$$x_i^{t+1} = x_i^t + v_i^{t+1} \quad (2)$$

A mechanism has been developed to aggregate the decisions made by individual optimization agents incorporating the performance criteria (i.e., statistical indicators). However, a hybrid strategy has been used to update the collective performance among the agents. Therefore, each iteration could involve interactions between the optimization methods, adjustments in strategies, and refinement of the hyperparameter search. Finally, the final set of hyperparameters that are the best-optimized hyperparameters of the model have been selected based on the collective performance of the ensemble. It is noteworthy that using this procedure in the automated algorithm reduces the time of hyperparameters optimization for each model, while it can automatically obtain the optimal value in any dataset. The proposed procedure eliminates the need to adjust the ML algorithm, which can significantly increase the speed and accuracy of the model.

3.2. Pre-processing of models

Statistical error indicators, often referred to as performance metrics or evaluation measures, play a crucial role in the assessment and fine-tuning of ML models. These indicators provide quantitative insights into how well a model is performing and help data scientists and researchers make informed decisions about model selection, optimization, and overall effectiveness. Some of the most used statistical indicators are illustrated in Table 2. By quantifying performance, data scientists can assess which model performs better in terms of accuracy, precision, recall, or other relevant metrics. Statistical error indicators offer a systematic and numerical evaluation of a model's performance. They provide a clear, objective measure of how well the model is making predictions or classifications based on the input data. Error indicators help identify overfitting (i.e., where a model is complex and fits train data but performs poorly on new dataset) and underfitting (i.e., where a model is simple and fails to capture underlying patterns).

The process of pre-processing and combining one to six sub-models for an ensemble ML (i.e., Stacked ML) model using error indicators involves several steps to improve the predictive power and robustness of the ensemble. Initially, individual base models or sub-models are trained using the available dataset. Each sub-model can represent a different algorithm, a variation in hyperparameters, or a different subset of the data, depending on the specific ensemble strategy being employed. Then, for regression tasks, error correction techniques such as bias correction or calibration can be applied to minimize prediction biases and improve the overall prediction accuracy. Pre-processing and a combination of sub-models may involve an iterative process. It is common to experiment with different combinations of sub-models, error weighting schemes, and combination methods to find the optimal

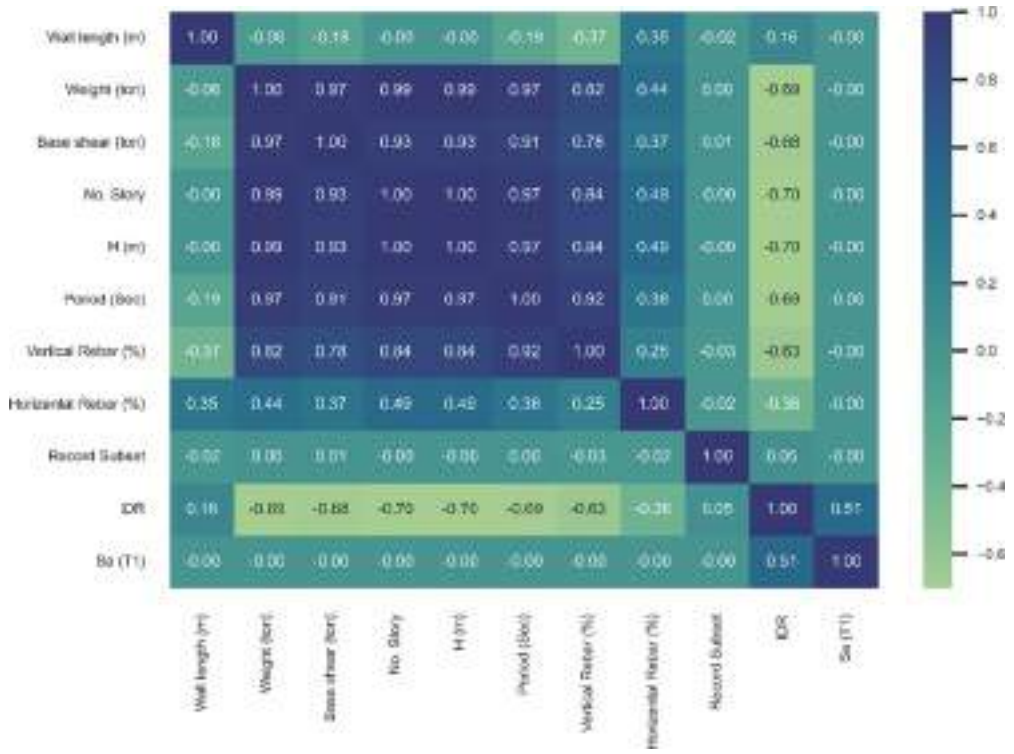

Fig. 11. Heatmap presentation of the M_{IDA} dataset.

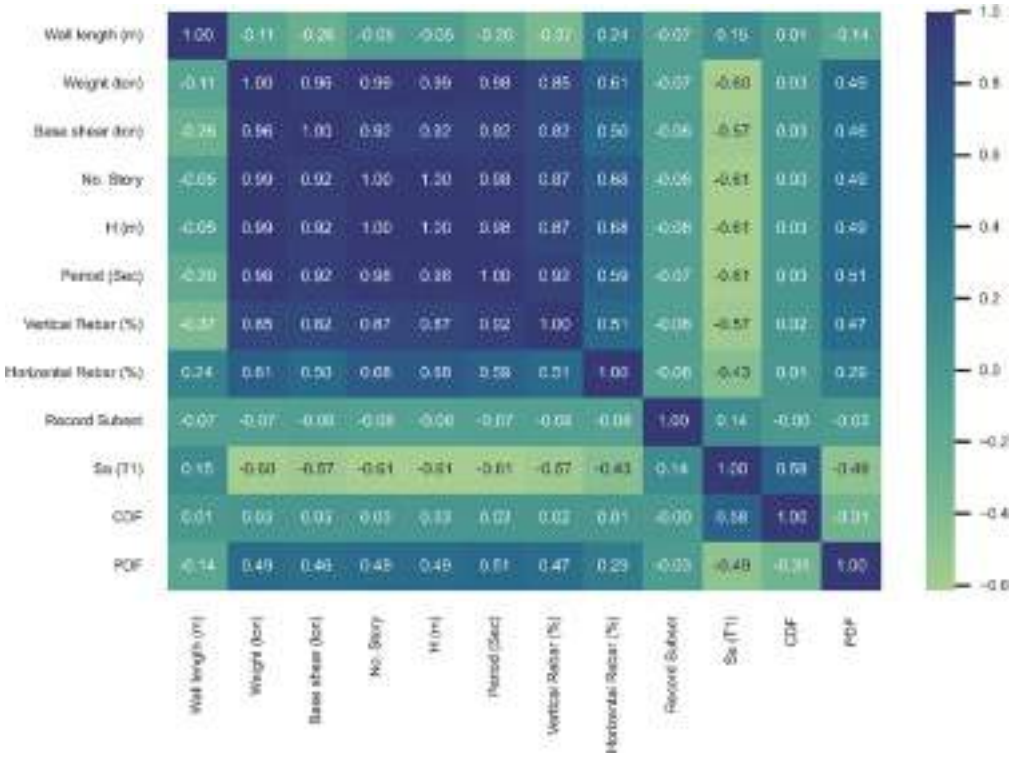

Fig. 12. Heatmap presentation of the seismic probability dataset.

ensemble configuration (Kazemi et al., 2024d). By employing this pre-processing and combination strategy, error indicators with a crucial influence can guide the selection of sub-models resulting in a robust and reliable Stacked ML model. Table 3 presents the results of the pre-processing of ML algorithms and five selected Stacked ML models. It should be noted that the Stacked-ML-1 includes submodels of BR, XGBoost, and GBM, and Stacked-ML-2 includes submodels of ETR, RF, and BR. Stacked-ML-3 includes submodels of ETR, RF, CatBoost, XGBoost, and GBM. Stacked-ML-4 includes submodels of LightGBM, XGBoost, and GBM, and Stacked-ML-5 includes submodels of RF,

Table 4
Statistical details of the dataset used for ML models.

	Wall length (cm)	Weight (ton)	Base shear (ton)	No. Story	H (cm)	Period (Sec)	Vertical Rebar	Horizontal Rebar	IDR	Sa(T_1)
Mean	642.2	2480.4	231.5	9.5	37.6	1.542	0.112	0.036	0.64	0.04
std	74.6	1141.5	47.0	3.5	13.8	0.797	0.057	0.008	0.57	0.02
Min	548.6	785.9	159.4	4	15.8	0.357	0.028	0.005	0.00	0.00
25 %	548.6	1503.6	190.0	6	23.8	0.811	0.062	0.030	0.23	0.02
50 %	650.2	2205.8	232.4	9	35.7	1.520	0.104	0.035	0.45	0.04
75 %	731.5	3644.3	278.1	13	51.5	2.231	0.144	0.040	0.90	0.06
Max	731.5	4306.5	295.2	15	59.4	3.296	0.267	0.050	3.12	0.08

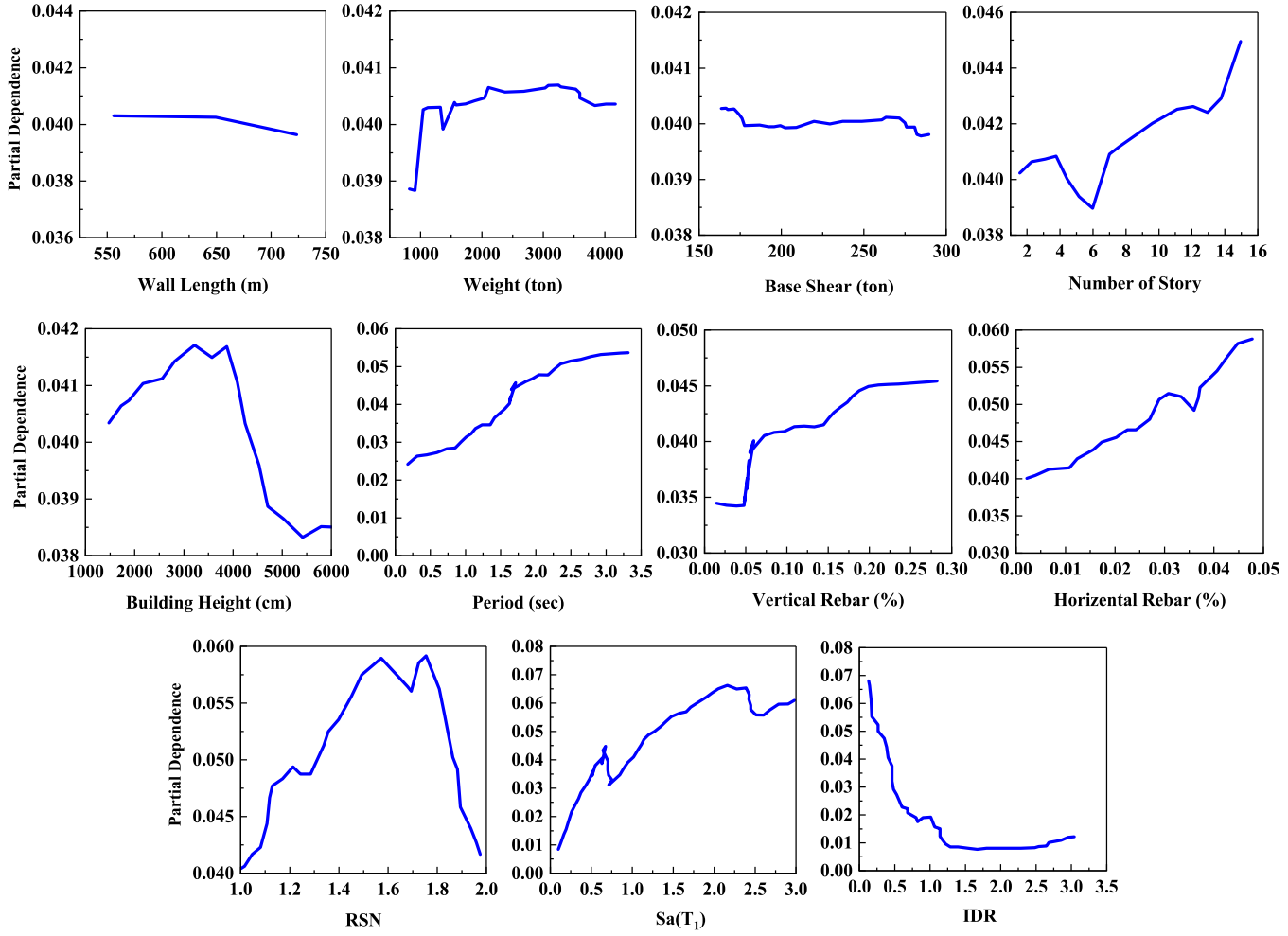

Fig. 13. PDP presentation of input features of M_{IDA} dataset.

XGBoost, and GBM. It is noteworthy that these models have been chosen from different combinations of models according to the results of pre-processing. In addition, the alone ML models have been assumed to compare their performance with Stacked ML models.

3.3. Preparation of datasets

In this paper, the aim is to provide ML-based algorithm to estimate M_{IDA} that are presented in Fig. 7 and estimating the seismic probability curves known as probability density function (PDF) and cumulative distribution function (CDF). For this purpose, two types of datasets have been provided from numerical analysis and the Heatmap of the datasets have been illustrated in Figs. 11 and 12. The M_{IDA} dataset has 227,200 data points, and the seismic probability dataset has 63,384 data points. Table 4 presents the statistical details of the dataset used for ML models. A Heatmap of a dataset is a visual representation that uses colors to display the values of the data in a matrix format and presents the relationship between variables in a dataset to identify patterns, trends, and correlations. Regarding the correlations presented in the Heatmap, a positive correlation means that when one variable increases, the other tends to increase as well, while a negative correlation means that when one variable increases, the other tends to decrease. However, the Heatmap can be a key feature selection tool for reducing the less important features from the dataset due to lower correlation values. The intensity of the color in the Heatmap cell indicates the strength of the relationship between variables. Darker colors represent stronger correlations, while lighter colors represent weaker or no correlations. When dealing with ML and feature selection, Heatmap can assist in identifying the most relevant features. Features that have a strong correlation with the target variable can be prioritized for model training. It can be seen that the input features have a positive correlation with each other and the target of prediction, thus, they should be considered in the analysis.

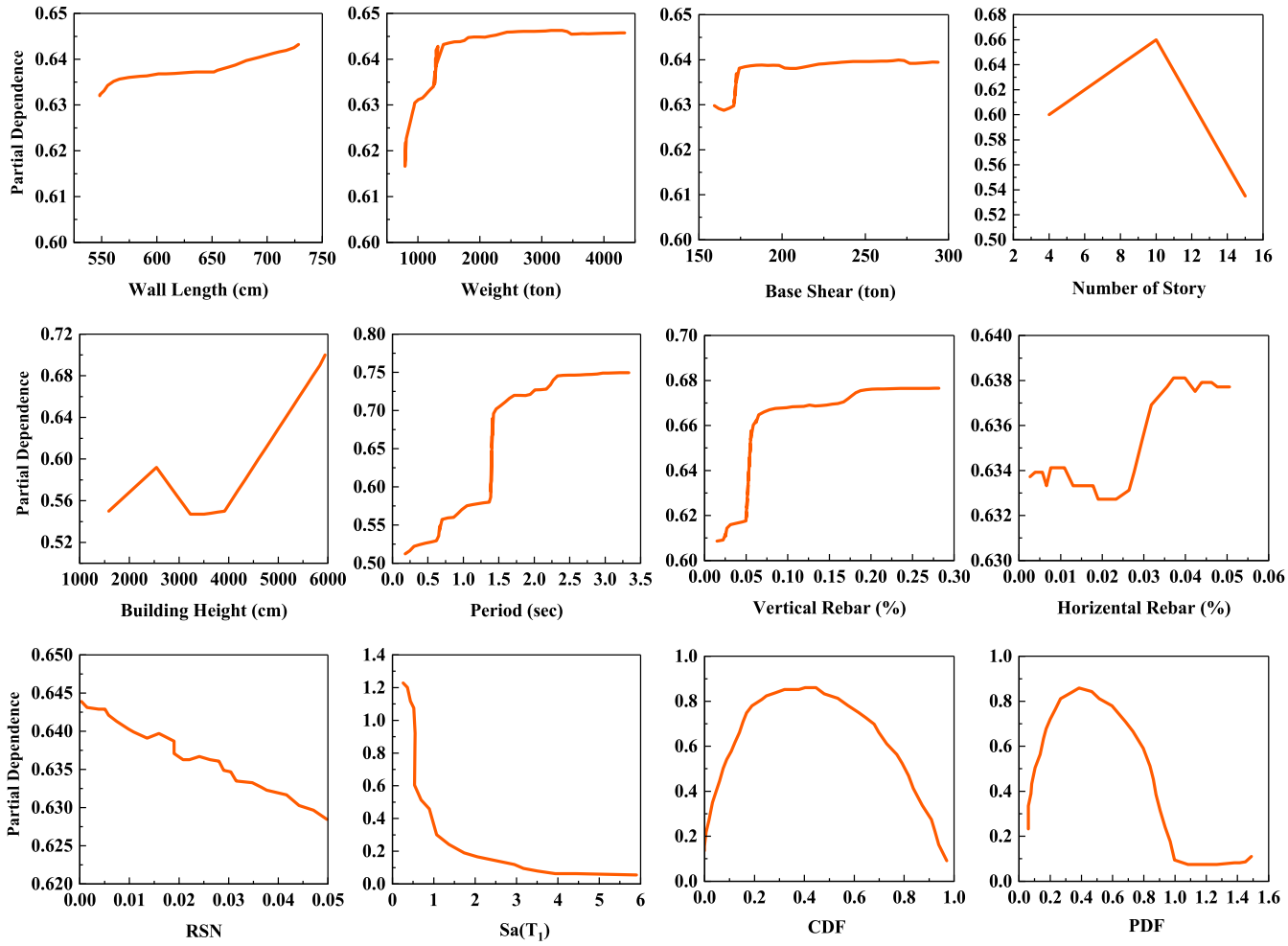

Fig. 14. PDP presentation of input features of seismic probability dataset.

Notably, Heatmap also serves to illustrate correlations between input features and predictive targets, such as $S_a(T_1)$ in Fig. 11 and CDF and PDF in Fig. 12. It is essential to highlight that all input features relevant to the design and analysis of the structures such as seismic characteristics have been accounted for the pre-processing stage of ML algorithms. However, feature selection approaches play a crucial role in model training and the performance of prediction models. Therefore, different types of feature selection approaches such as filter, wrapper, and embedded methods have been employed to assess the datasets. The scope of this research limits the thorough discussion of data sampling outcomes. Nevertheless, the results obtained through Heatmap analysis and partial dependence plots (PDP) demonstrate the selection of the most significant input features for predictive modeling and neglecting those less important features.

3.4. Partial dependence plot

The PDP is an analytical tool used to assess and illustrate the effects of individual features on the prediction target within an ML model. It aids in discerning whether these effects are positive or negative concerning the model's predictive performance. PDPs are instrumental for isolating the influence of a single feature while keeping other variables constant, allowing for a comprehensive examination of how changes in the feature affect the model's predictions. When exploring the PDP of a feature, it becomes evident whether increasing or decreasing values of that feature positively or negatively affect the prediction target. By visualizing the PDP, data analysts, and ML practitioners can better understand the relationships between individual features and the predictive outcome (Asgarkhani et al., 2024a). For this purpose, the PDP of two datasets has been illustrated in Figs. 13 and 14, which provide a formal and structured means to uncover the directional effects of features on prediction targets. It can be seen that all the features have fluctuated alongside of vertical axis and show the complicated relationship between the targets of prediction. Therefore, the input features have a direct influence on the results and cannot be neglected during analysis. It is essential to emphasize that, given constant effects of other features; they were excluded from the comparison and were not taken into account when assessing ML models.

3.5. Estimating the median of IDA curves

In this section, the estimated M_{IDA} curves have been compared with those of actual curves to find out the curve-fitting ability of the proposed methods. Fig. 15 illustrates predicted M_{IDA} curves of the 7-story RCSW located on soil B given a bay length of 5.5 m that has been used as a test for ML models including NNP records. It can be seen that conventional ML algorithms presented in Fig. 16(a) and (b), have less capability of fitting to the actual M_{IDA} curve, and they should be improved with novel resampling and pipeline methods. Stacked ML models have acceptable accuracy (see Stacked ML-1 to Stacked ML-3) and they are the best-fitted models among others (see Stacked ML-4 and Stacked ML-5).

Pipeline methods, in the context of ML and data analysis, refer to a structured approach to building and deploying ML models. An ML-based pipeline is a sequence of data processing components and ML algorithms arranged in a specific order to automate the flow of data from preprocessing to model training and evaluation. These components can

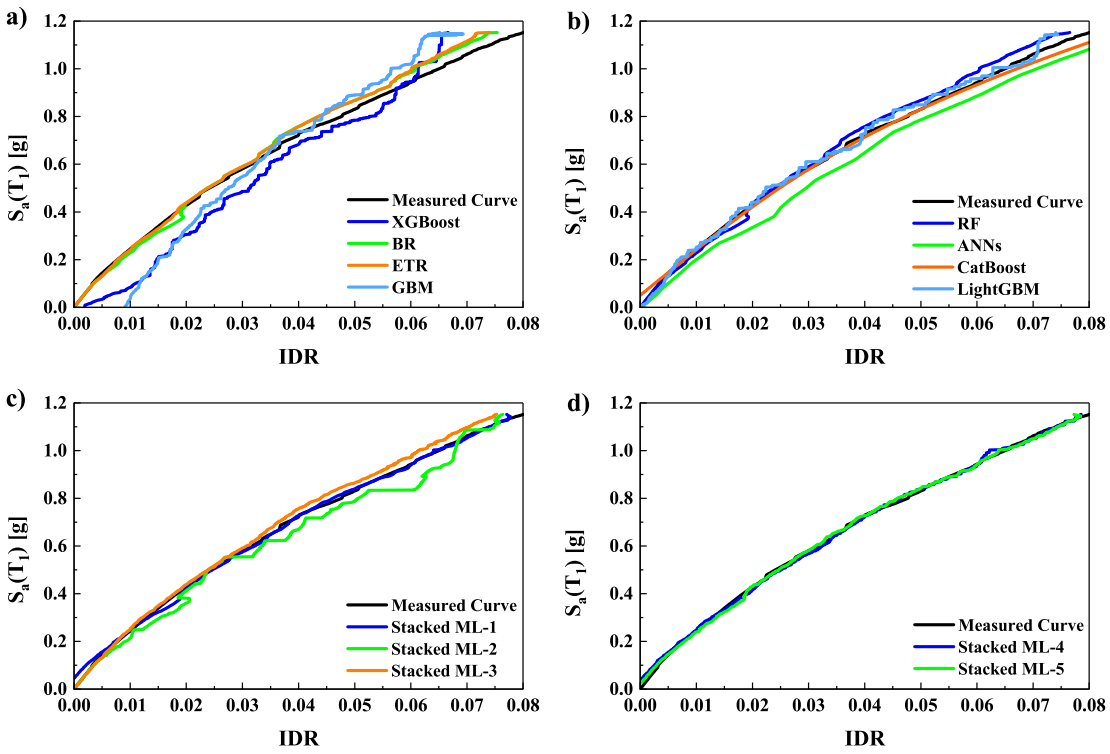

Fig. 15. Estimated M_{IDA} curves of the 7-story RCSW located on soil B given bay length of 5.5 m used as a test for ML models including NNP records.

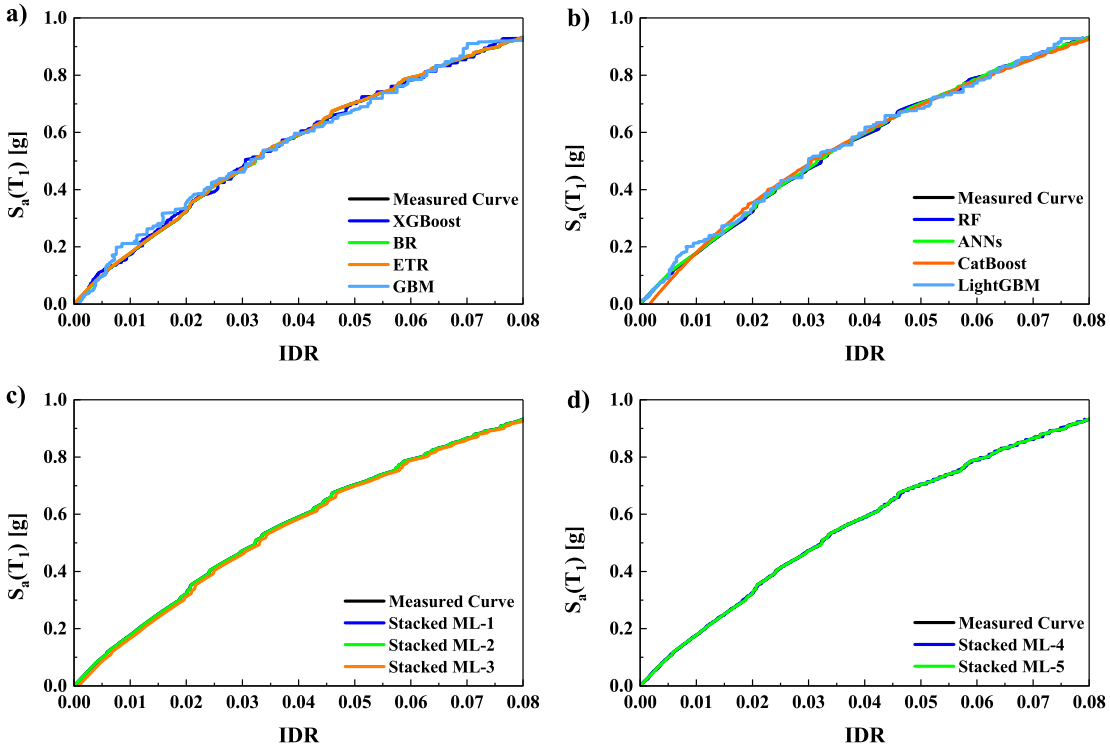

Fig. 16. Estimated M_{IDA} curves of the 9-story RCSW located on soil D given a bay length of 6.5 m used as a test for ML models including NPL records.

include data pre-processing steps like feature scaling, feature selection, and data cleaning, as well as model selection and hyperparameter tuning. The use of pipeline methods streamlines the process of developing, testing, and deploying ML models. It ensures consistency and reproducibility by encapsulating the entire workflow in a single structure. This approach is particularly valuable in complex ML projects where multiple pre-processing steps and models need to be evaluated. Pipelines allow for efficient experimentation, model selection, and optimization, making them a fundamental part of machine-learning workflows in both research and production settings.

By resampling methods that aim to enhance the quality of imbalanced datasets and pipeline methods that provide an organized and

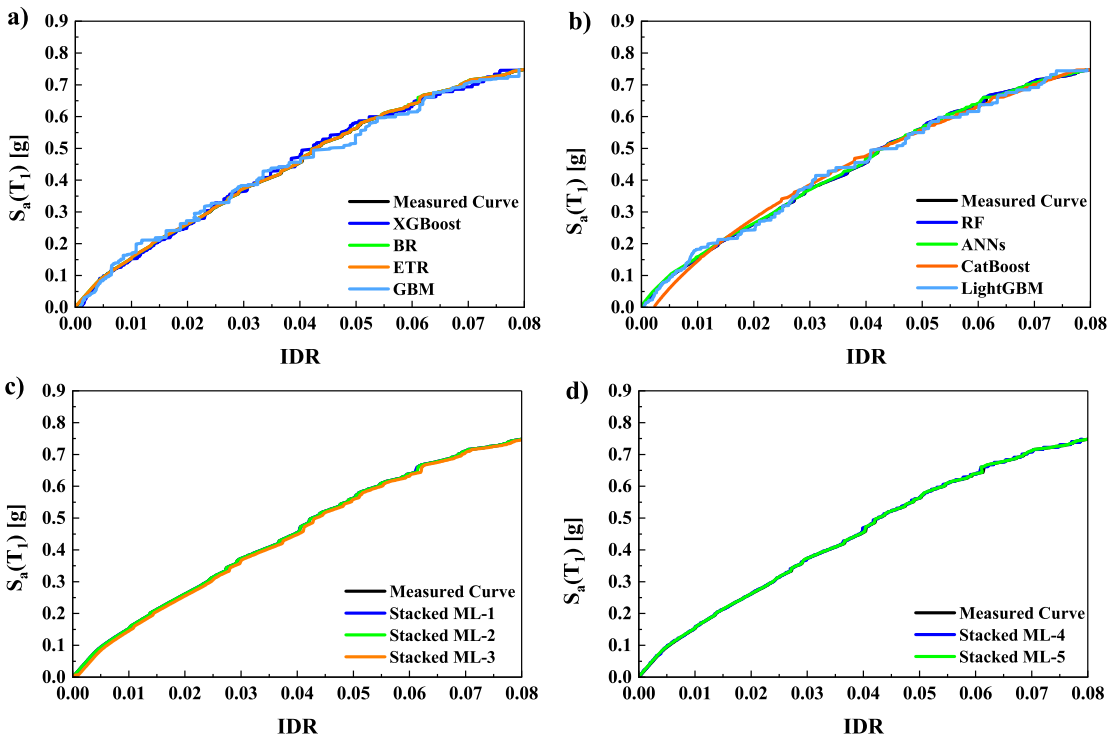

Fig. 17. Estimated M_{IDA} curves of the 11-story RCSW located on soil C given a bay length of 7.5 m used as a test for ML models including NPL records.

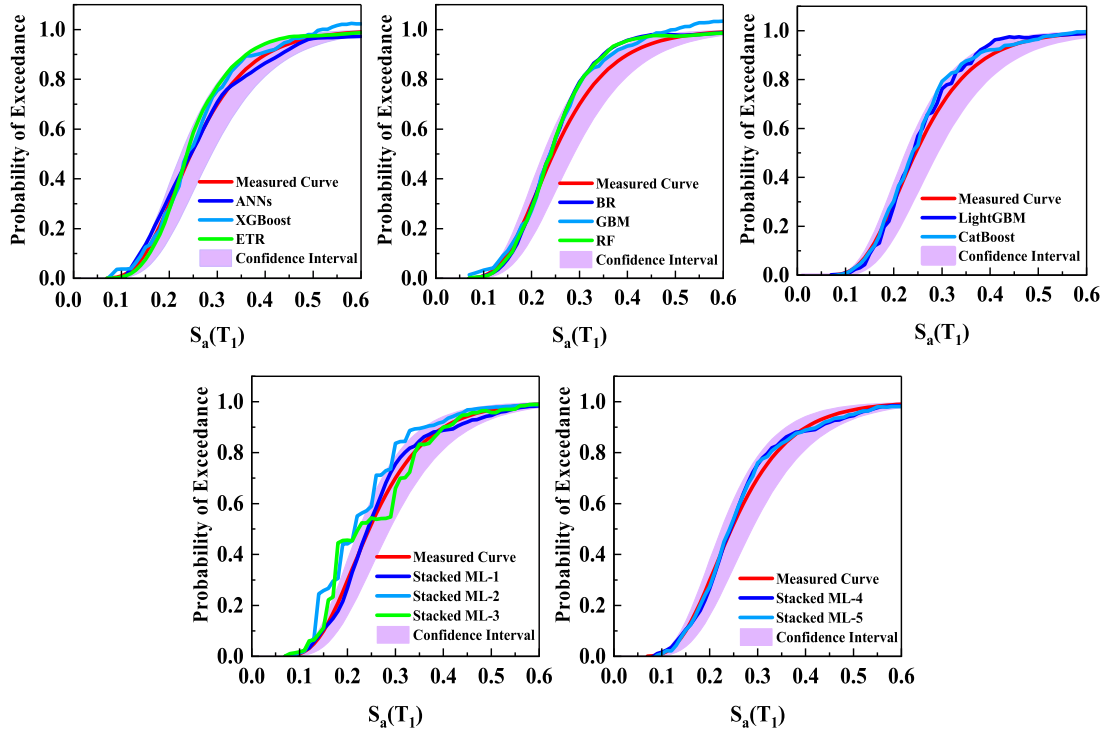

Fig. 18. Estimated fragility curves in life-safety performance level for the 7-Story RCSW located on soil B given bay length of 5.5 m including NNP records.

automated framework for designing and deploying ML models, it is possible to enhance the curve-fitting ability. In this research, the conventional ML algorithms have been improved to have better curve-fitting ability. Fig. 16 illustrates the predicted M_{IDA} curves of the 9-story RCSW located on soil D given a bay length of 6.5 m, and Fig. 17 illustrates the predicted M_{IDA} curves of the 11-story RCSW located on soil C given a bay length of 7.5 m, which have been used as a test for ML models including NPL records. Compared to Fig. 15, the results have been significantly improved and the models have better accuracy. In addition, the results confirmed that the proposed ML models have a prediction accuracy of more than 99.1 % and can be used as surrogate models for estimating M_{IDA} curves of RCSWs founded on different soil types.

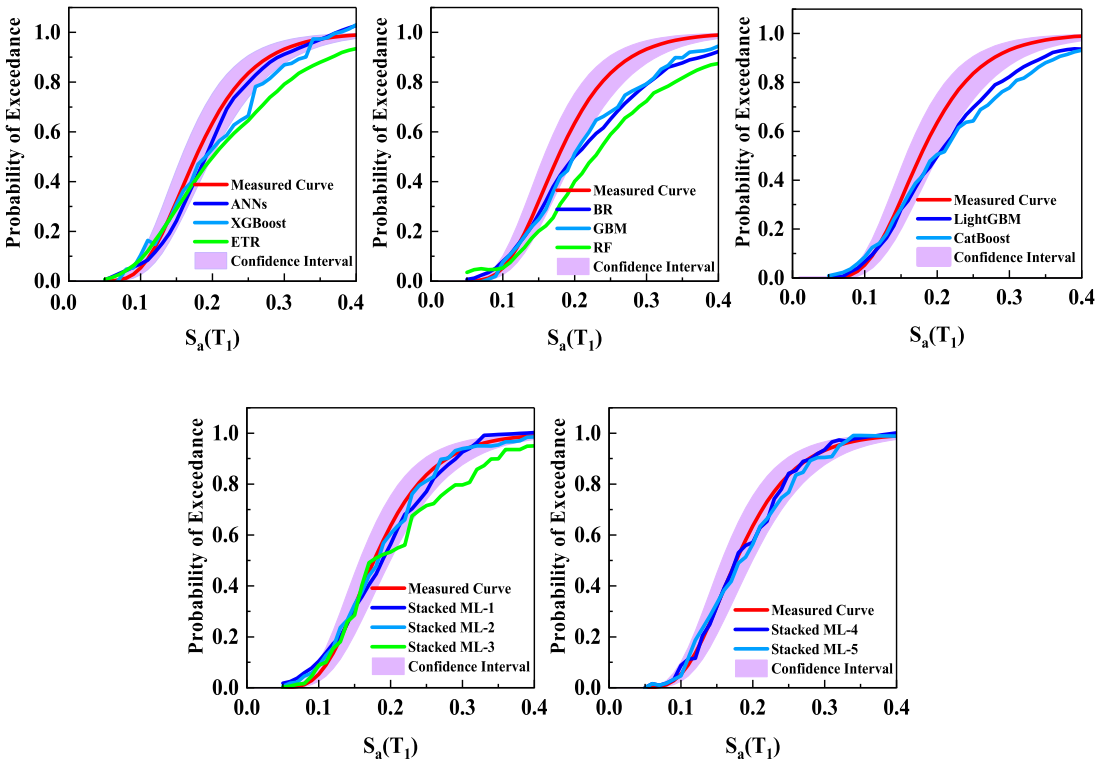

Fig. 19. Estimated fragility curves in life-safety performance level for the 9-Story RCSW located on soil D given bay length of 6.5 m including NPL records.

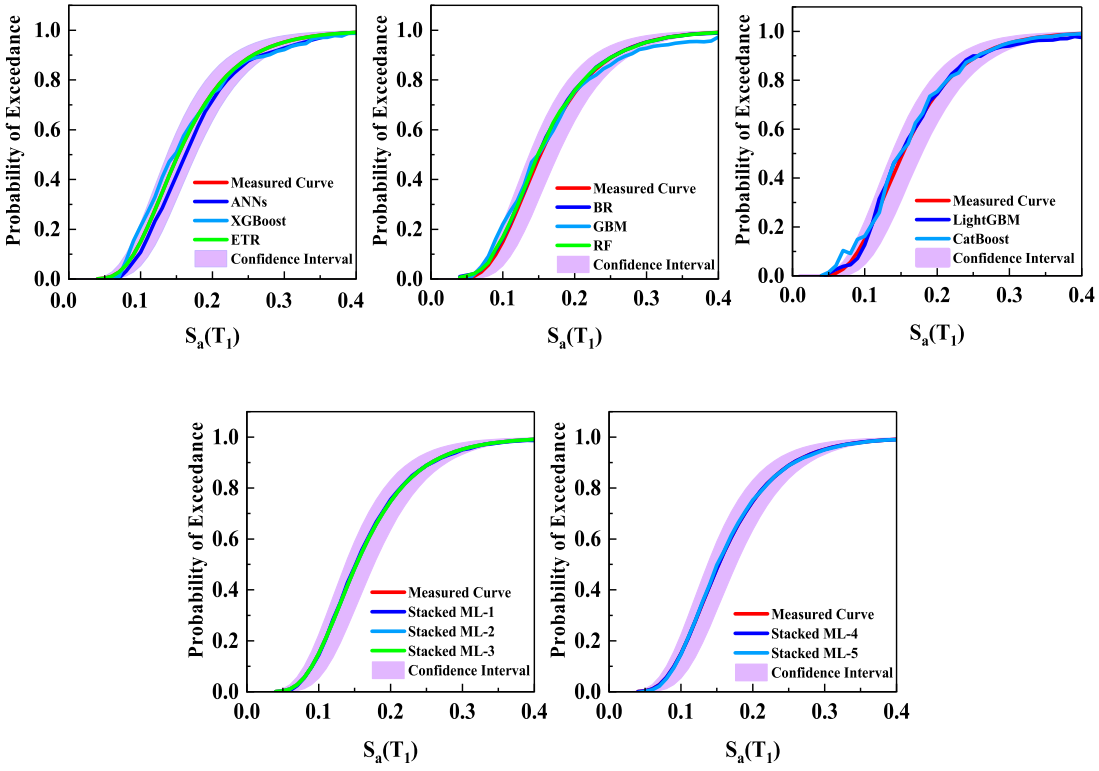

Fig. 20. Estimated fragility curves in life-safety performance level for the 11-story RCSW located on soil C given bay length of 7.5 m including NPL records.

3.6. Estimating seismic probability curves

This section is devoted to discussing capability of proposed ML models to estimate seismic probability curves that play a crucial role in seismic risk assessment. The modeling and analysis of such complicated buildings aim to provide seismic probability curve to be considered in seismic risk assessment. However, this study aims to facilitate seismic risk assessments by providing a surrogate model based on the proposed ML algorithms to ease the way and reduce computational cost and time. This procedure can provide a fast-track seismic risk assessment and it

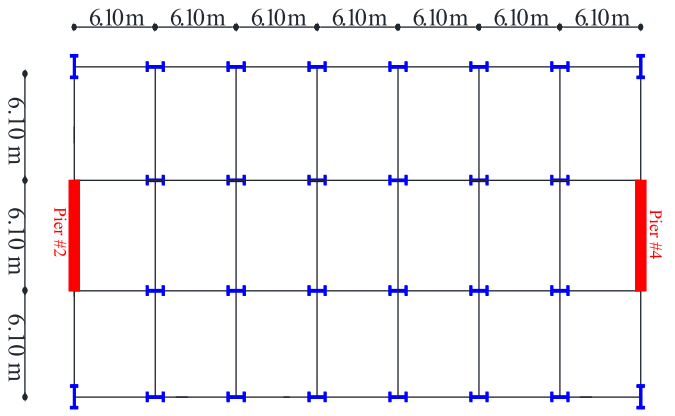

Fig. 21. Structural plan of a 5-story building having RCSW as lateral-force resisting system located on soil D given bay length of 6.1 m (20 *ft*).

can be widely used by structural designers for design, retrofit, and preliminary evaluation of existing buildings. In the context of fragility curves, confidence interval boundaries represent the upper and lower limits of a range within which the true value of a fragility parameter (e.g., probability of exceeding a damage state) is likely to fall with a specific level of confidence (e.g., 95 %). These boundaries are estimated based on statistical analysis of the data used to develop the fragility curve, typically assuming a normal distribution. Confidence interval boundaries provide valuable information for interpreting fragility curves and understanding the inherent uncertainty associated with the estimated probabilities. By considering this, risk assessments can account for the potential variability in fragility estimates, leading to more robust and realistic risk evaluations. Moreover, confidence interval boundaries can help decision-makers understand the level of confidence they can place in fragility-based risk estimates. Therefore, confidence interval boundaries have been plotted to compare the fragility curves of actual curve and predictions made by proposed ML models.

Fig. 18 shows the estimated fragility curves in the life-safety performance level for the 7-Story RCSW located on soil B given a bay length of 5.5 m including NNP records, and Fig. 19 illustrates the estimated fragility curves in the life-safety performance level for the 9-Story RCSW located on soil D given bay length of 6.5 m including NPL records. It can be seen that before applying the resampling and pipeline methods, only Stacked ML-4 and Stacked ML-5 have acceptable accuracy in predicting the seismic fragility curves. However, other ML models have less accuracy in estimation. Therefore, the resampling and pipeline methods play a crucial role in enhancing the ability of ML models. To support this result, the improved ML models have been used for predicting fragility curves in life-safety performance level for the 11-Story RCSW located on soil C given 7.5 m bay length having NPL presented in Fig. 20. It is shown that improving the ML models significantly increased curve fitting accuracy of conventional ML algorithms by approximately 43.8 %. Moreover, Stacked ML models are the best-fitted curves with an accuracy of 99.4 % that are an outstanding result. The higher accuracy of proposed ML models can guarantee the results of seismic risk assessment. More results of the estimated fragility curves in total collapse performance level for the 7-, 9-, and 11-Story RCSWs using ML models are presented in Figs. A-2 to A-4 in *Appendix*.

4. Using ML models for seismic risk assessment

4.1. Estimating seismic curves of a general building

In this section, the authors tried to explain the way of using the proposed ML models for seismic risk assessment of buildings having RCSWs as lateral resisting systems. For this purpose, a 5-story building that occupies a ground area of approximately 42.67 m by 18.29 m (140 *ft* × 60 *ft*) with feature spans of about 6.1 m has been considered. The lateral force resistance of the building is achieved through two identical RCSWs having 30.48 cm (12 *in*) depth and 6.1 m (240 *in*) length located in the middle of the building as presented in Fig. 21. This building's structural design is tailored for residential use in California and adheres to a design category following ASCE 7–22 (2023) given soil D, a uniform dead load of 7.21 kN/m^2, and a live load of 1.93 kN/m^2 (ASCE 7–22, Table 4-1). Detailed cross-sections of RCSW, inclusive of the reinforcement specifications, are visually documented in Fig. 22 (Kolozvari et al., 2015c).

After designing the building, the model was prepared in OpenSees (McKenna et al., 2015) to perform IDAs and to determine the M_{IDA} curves including NPL and NNP sets. Fig. 23 illustrates the IDA curves of 5-story RCSW given 6.1 m bay including NPL and NNP sets. As it is expected, the M_{IDA} curve of NPL records has higher values of $Sa(T_1)$ compared to the M_{IDA} curve of NNP records. The results of IDAs have been used to determine seismic fragility curves at different performances of life-safety and total collapse.

4.2. Using proposed ML models to estimate seismic curves

As presented in Section 3, the ML models are improved based on the new methods and the results showed that they have a good ability to learn the curves and can be implemented for curve fitting purposes. To use their ability for a general problem, a 5-Story RCSW has been modeled and analyzed to be used as a test dataset for the proposed ML models. Fig. 24 illustrates the results of estimating M_{IDA} curves of the 5-Story RCSW located on soil D given a bay length of 6.1 m subjected to NPL and NNP records using proposed ML models. Except for Stacked ML-2, other methods have a better fitting on the actual curve that confirms the capability of the proposed methods.

To better compare the results, Table 5 has been prepared that shows the results of the indicators for estimating M_{IDA} curves of the 5-Story RCSW considering different ML models. It is shown that Stacked ML-4 with 99.9 % accuracy and the lowest error values is the best ML model among other methods in both NPL and NNP records. While the Stacked ML-1 has the lowest accuracy among other methods, the results

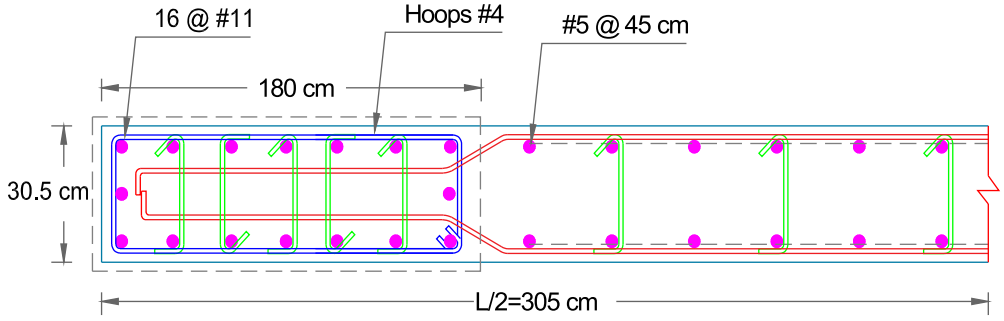

Fig. 22. Cross-section view of the RCSW of the 5-story building (Kolozvari et al., 2015c).

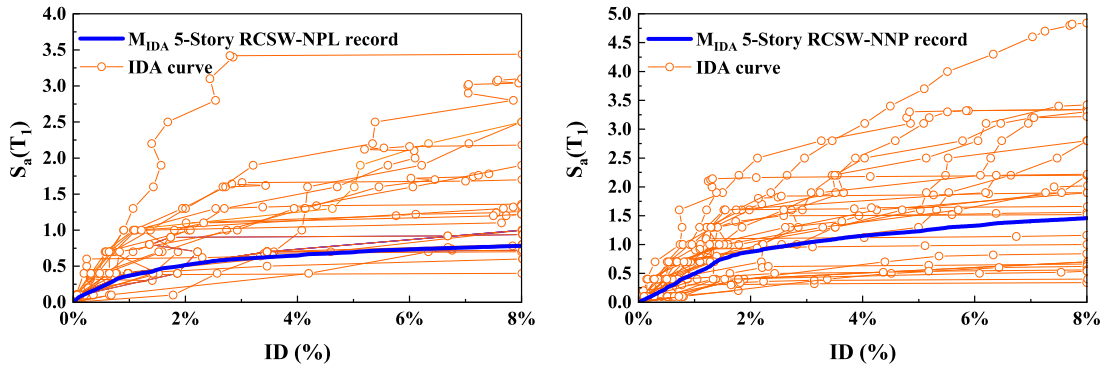

Fig. 23. IDA curves of the 5-Story RCSW given 6.1 m bay including NPL and NNP sets.

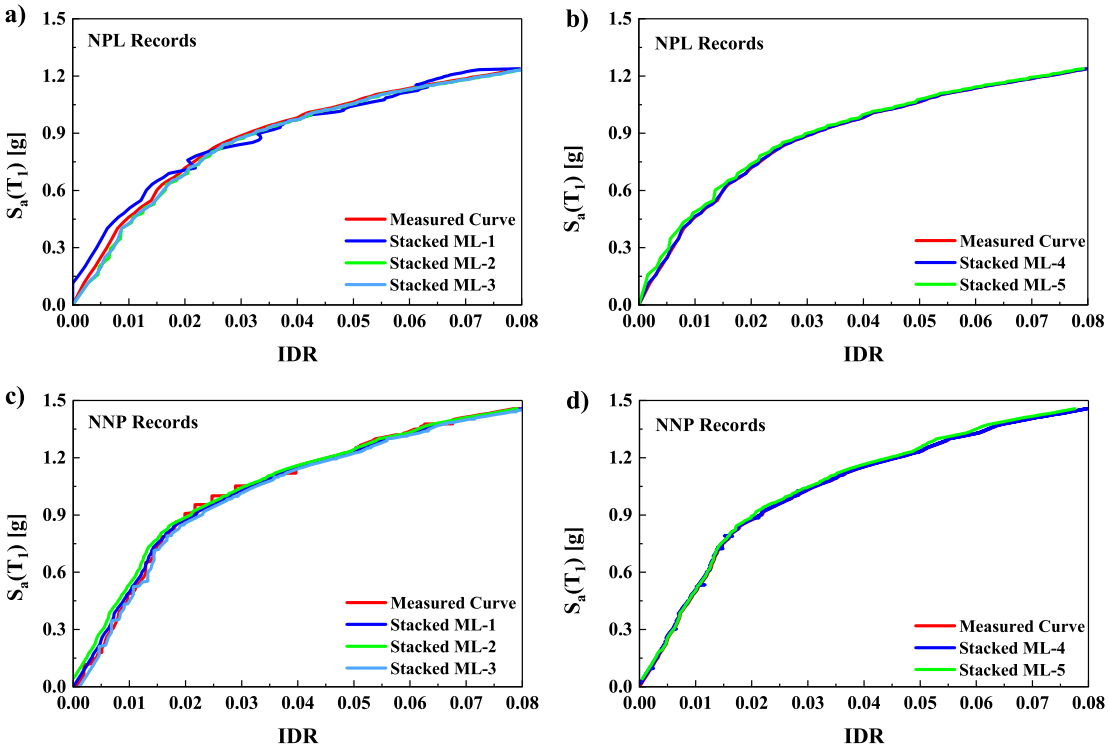

Fig. 24. Estimated M_{IDA} curves of the 5-Story RCSW located on soil D given bay length of 6.1 m used as a general test dataset for ML models.

Table 5
Indicators results for estimating M_{IDA} curves of the 5-Story RCSW considering different ML models.

Record	ML algorithm	R^2	MSE (e-8)	MAE (e-4)	MARE (e-1)	MSRE (e-1)	RMSRE	MBE (e-3)	erMAX	SD (e-2)
NPL	Stacked ML-1	0.978	1154.09	29.41	1.242	0.442	0.210	−0.113	1.0	0.344
	Stacked ML-2	0.997	134.83	10.85	0.654	0.214	0.146	1.060	1.0	0.046
	Stacked ML-3	0.998	103.30	9.88	0.608	0.196	0.140	0.963	1.0	0.031
	Stacked ML-4	0.999	6.13	2.08	0.228	0.130	0.114	−0.110	1.0	0.022
	Stacked ML-5	0.998	106.63	9.90	0.618	0.205	0.143	−0.990	1.0	0.028
NNP	Stacked ML-1	0.995	278.29	11.15	0.701	0.789	0.281	−0.681	5.0	0.152
	Stacked ML-2	0.998	80.14	8.92	0.575	0.166	0.129	−0.892	0.9	0.007
	Stacked ML-3	0.998	120.67	10.77	1.084	3.722	0.610	1.076	11.0	0.022
	Stacked ML-4	0.999	5.47	1.58	0.125	0.028	0.053	−0.146	0.8	0.018
	Stacked ML-5	0.998	24.44	4.83	0.751	0.875	0.296	−1.209	2.0	0.026

of predictions made by other Stacked ML models can be still a good estimation of seismic curves.

The proposed methods also have been used to estimate the seismic probability curves at different performance levels. For instance, Fig. 25 illustrates the results of estimating fragility curves in life-safety performance level for the 5-Story RCSW located on soil D given bay length of 6.1 m subjected to NPL and NNP records using proposed ML models. Although the results previously showed acceptable accuracy of proposed

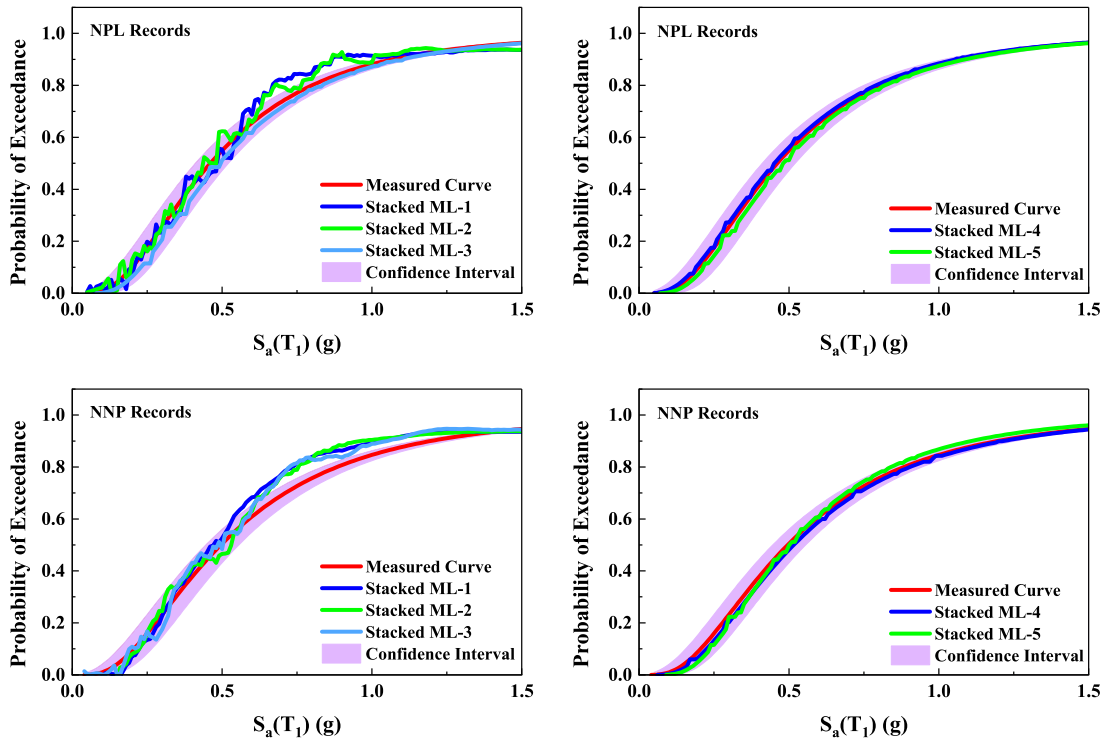

Fig. 25. ML-based fragility curves in life-safety performance level for the 5-Story RCSW located on soil D given bay length of 6.1 m used as a general test dataset for ML models.

Table 6
Indicators results for estimating fragility curves in life-safety performance level for the 5-Story RCSW considering different ML models.

Record	ML algorithm	R^2	MSE (e-3)	MAE (e-2)	MARE (e-1)	MSRE (e-1)	RMSRE	MBE (e-3)	erMAX	SD (e-2)
NPL	Stacked ML-1	0.934	1.44	3.14	3.273	53.414	2.311	−10.444	29.0	3.811
	Stacked ML-2	0.940	0.98	2.40	2.012	8.974	0.947	7.150	9.9	2.948
	Stacked ML-3	0.985	0.47	1.39	0.747	0.342	0.185	−1.915	0.9	1.653
	Stacked ML-4	0.999	0.05	0.45	0.449	0.303	0.174	4.457	1.7	0.550
	Stacked ML-5	0.992	0.20	0.92	0.600	0.281	0.168	−4.195	1.0	1.073
NNP	Stacked ML-1	0.940	2.33	4.59	28.888	8535.486	29.216	0.250	415.6	4.532
	Stacked ML-2	0.943	1.96	4.15	12.984	1423.824	11.932	0.222	166.8	4.157
	Stacked ML-3	0.935	1.71	3.86	6.331	566.517	7.527	1.845	110.4	3.880
	Stacked ML-4	0.997	0.38	1.35	0.838	0.444	0.211	−1.520	1.0	1.386
	Stacked ML-5	0.988	0.35	1.63	0.891	0.563	0.237	1.333	1.8	1.697

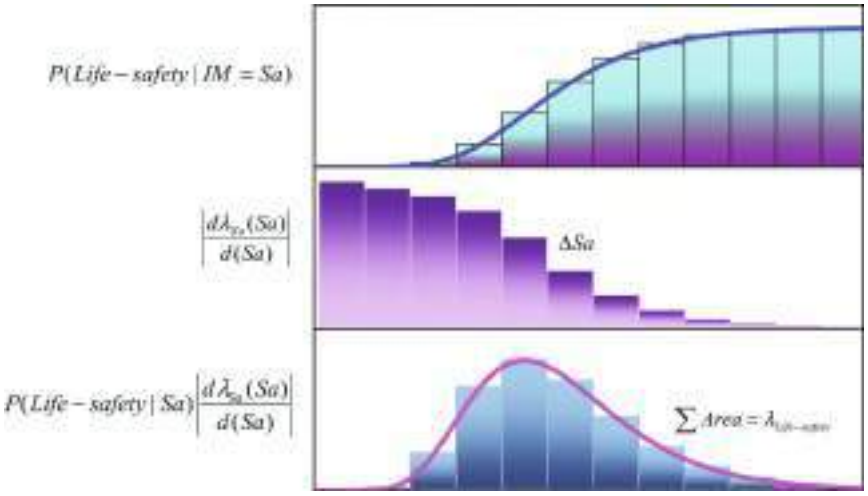

Fig. 26. The graphical expression determining $\lambda_{Life\text{-}safety}$ deaggregation curve.

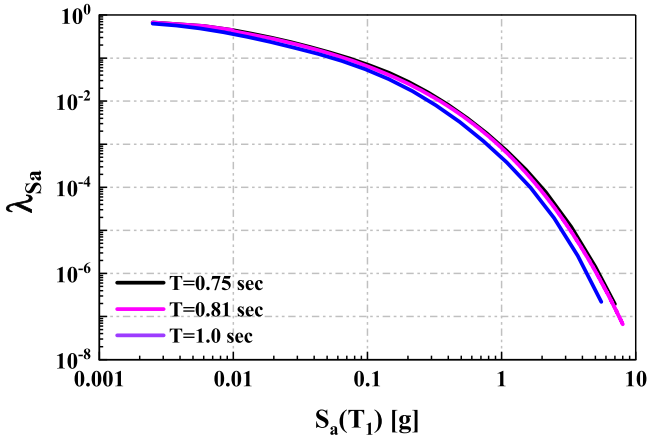

Fig. 27. Seismic hazard curves considering the construction site of the 5-Story RCSW.

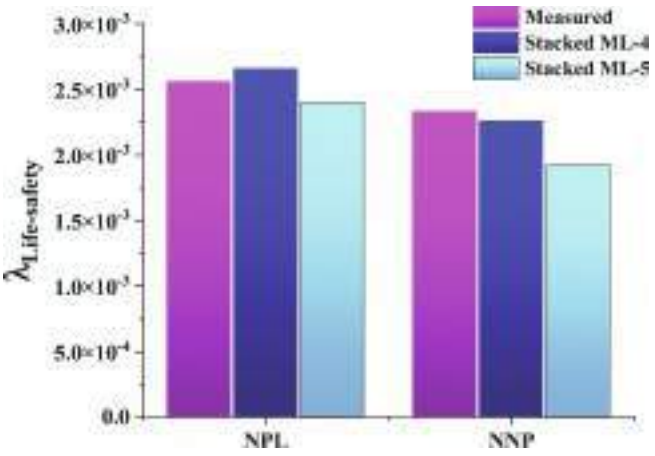

Fig. 28. Comparing values of $\lambda_{Life\text{-}safety}$ for the actual and predicted fragility curves of the 5-Story RCSW.

Stacked ML models, only Stacked ML-4 and Stacked ML-5 have better curve fitting results for estimating seismic failure probability curves. To support the results, Table 6 has been calculated that illustrates the results of the indicators for estimating fragility curves in life-safety performance level for the 5-Story RCSW considering different ML models. According to Table 6, for NPL records, the Stacked ML-4, Stacked ML-5, and Stacked ML-3 with accuracies of 99.9 %, 99.2 %, and 98.5 % are the best prediction methods, respectively, and for NNP records, the Stacked ML-4 and Stacked ML-5 with accuracies of 99.7 % and 98.8 % are the best prediction methods of this research, respectively. Furthermore, the proposed Stacked ML models have lower values of error indicators that confirm their ability to estimate fragility curves with higher reliability. Although the result of the life-safety performance level is presented, similar results have been seen for other performance levels.

4.3. Using ML-based seismic probability curve for seismic risk assessment

In this section, the procedures employed for seismic risk assessment of buildings are explained using the seismic fragility curves estimated by ML methods in the previous section. In other words, the seismic risk assessment of the 5-story building can be determined by two types of actual seismic fragility curves and predicted ones, and the comparison between them can illustrate the capability of the proposed Stacked ML models. A fragility curve is mostly known as a graphical representation of the probability of a structural (or non-structural component) in a building (or infrastructure system) exceeding a specific damage or performance level (i.e., life-safety) when subjected to a particular loading event, typically an earthquake. Since fragility curves are important tools in seismic risk assessment and risk management for buildings, they are widely used to determine the vulnerability of structures to seismic hazards and inform risk mitigation strategies (Asgarkhani et al., 2023). Moreover, they are a key component of vulnerability assessments, which help evaluate the expected damage and loss for a portfolio of buildings subjected to seismic events. This information is valuable for prioritizing retrofit or risk reduction measures and optimizing resource allocation for disaster preparedness. Therefore, the reason behind the use of proposed ML models is to avoid computational modeling and reduce the time of decision makers. This information can be used to assess the cost-effectiveness of retrofitting or strengthening measures and developing emergency response plans (Kazemi et al., 2023c). One way to use the fragility for seismic risk assessment is to determine mean annual frequency, $\lambda_{Life\text{-}safety}$, using formula:

$$\lambda_{Life-safety} = \int_0^{\infty} P(Life - safetyperformance|Sa) \times |d\lambda_{Sa}(Sa)| \quad (3)$$

$$\lambda_{Life-safety} = \int_0^{\infty} P(Life - safetyperformance|Sa) \times \left|\frac{d\lambda_{Sa}(Sa)}{d(Sa)}\right| \times d(Sa) \quad (4)$$

where the $\left|\frac{d\lambda_{Sa}(Sa)}{d(Sa)}\right|$ illustrates hazard curve slope and can be changed to discrete formula:

$$\lambda_{Life-safety} = \sum_{i=1}^{n} P(Life - safetyperformance|Sa_i) \times \left|\frac{d\lambda_{Sa}(Sa_i)}{d(Sa)}\right| \times \Delta(Sa) \quad (5)$$

The expression of Equation (3) is to multiply the fragility curve by hazard curve slope of the site of the building, and then, calculate the area of the under curve to determine the $\lambda_{Life\text{-}safety}$. Therefore, the process has been presented in Fig. 26 and has been done for the predicted and actual fragility curves that have been presented in the previous section.

There are some approaches to calculating the seismic hazard curve, while the easiest way is to use the online USGS hazard application to extract the seismic hazard curves. Fig. 27 illustrates seismic hazard curves considering construction site of 5-story RCSW with a period of 0.81 sec. Seismic hazard curve has been calculated based on the two other seismic hazards of $T_1 = 0.75$ sec and $T_2 = 1.0$ sec. By calculating the hazard curve and seismic fragility curve, it is possible to determine the $\lambda_{Life\text{-}safety}$ deaggregation curve, and then, calculate the area under the curve that represents the $\lambda_{Life\text{-}safety}$.

The values have been calculated for the two ML models of Stacked ML-4 and Stacked ML-5 and are presented in Fig. 28. Proposed Stacked ML models have a good estimation of $\lambda_{Life\text{-}safety}$ and can be used by decision-makers. Furthermore, the $\lambda_{Life\text{-}safety}$ for the actual curve of NPL and NNP records were determined equal to 0.256 % and 0.233 %, respectively. However, the values of 0.268 % and 0.215 % have been achieved by the proposed Stacked ML-4 for the NPL and NNP records, respectively. In addition, Stacked ML-5 has predicted values of 0.23 % and 0.192 % for the NPL and NNP records, respectively. Considering the reducing the modeling time, analysis complexity, and fast-tracking of the proposed ML models, the differences between the values can be acceptable. Moreover, it is possible to have the results for a wide range of buildings since different numbers of floor levels are constructed in city areas.

5. GUI–based seismic risk assessment

In this section, the aim is to reduce the complexity of using optimization-based Stacked ML models, since changing the parameters and hyperparameters requires a good understanding of Pythons software. Therefore, the authors provided a graphical user interface (GUI) presented in Fig. 29 that can be easily filled by the user in order to

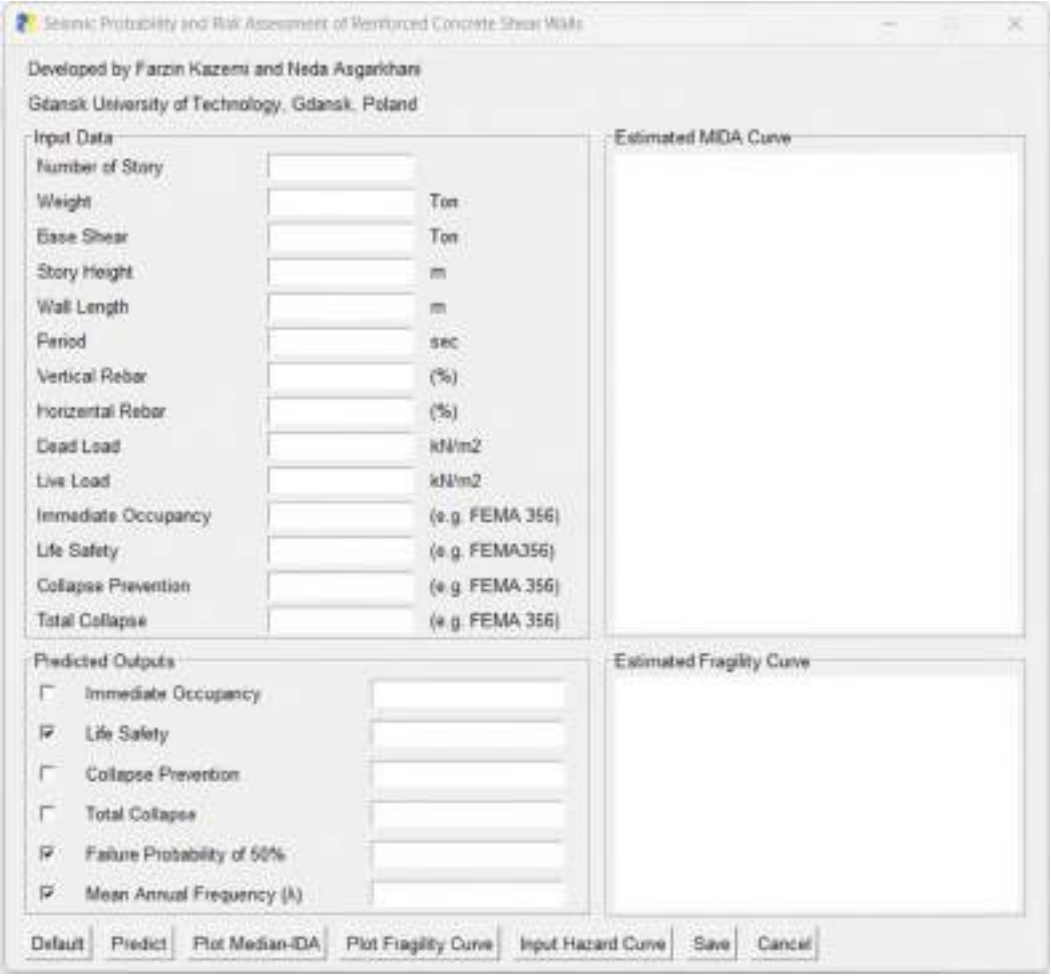

Fig. 29. GUI-based seismic risk assessment tool for RCSWs (. available at https://github.com/FarzinKazemi)

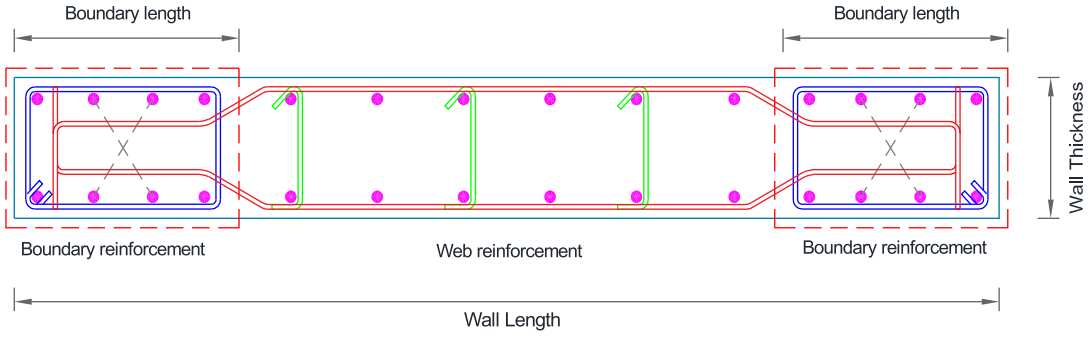

Fig. A-1. Details of RC shear walls used in this research.

seismic risk assessment of RCSWs. Moreover, the results of this study have been added to the database of the GUI and can be updated in the future. The GUI can provide a wide range of information for structural designers such as seismic performance levels of RCSWs in different predefined performance thresholds, predicted M_{IDA} curve and seismic failure probability curve in different predefined performance thresholds, and finally, calculating the mean annual frequency for the selected performance level (e.g., $\lambda_{Life\text{-}safety}$) and defined seismic hazard curve. This ability makes this tool more useful since all calculations are done in one platform and it is possible to have results for different types of RCSWs with no limitations on use. To work with the tool for the seismic risk assessment, there is a need to upload hazard curve in two columns of a text file, and then, tick the box of performance level (e.g., life-safety), the failure probability, and the mean annual frequency. Then, by pushing the "predict" bottom, the curves will be plotted and values will be presented in the predefined boxes. It is noteworthy that optimization algorithms have been implemented in the GUI to improve the proposed ML models by opting for hyperparameters for different datasets.

6. Conclusions

This research comes into the main problem of seismic risk assessment

Table A-1
Structural details of RCSWs having a bay length of 5.5 m.

RCSWs	Floor	Wall thickness (cm)	$\rho_{Boundary,Y}$(%)	$\rho_{Boundary,X}$(%)	$\rho_{Web,Y}$(%)	$\rho_{Web,X}$(%)
4-Story	1st -2nd	30	0.516	2.093	0.516	2.093
	3rd 4th	20	0.774	0.967	0.774	0.967
5-Story	1st -2nd	40	0.387	1.861	0.387	1.861
	3rd 4th	30	0.516	0.951	0.516	0.951
	5th	25	0.619	0.542	0.619	0.542
6-Story	1st -2nd	50	0.31	1.922	0.31	1.922
	3rd 4th	40	0.387	1.106	0.387	1.106
	5th -6th	25	0.619	0.542	0.619	0.542
7-Story	1st -2nd	55	0.282	2.371	0.282	2.371
	3rd 4th	45	0.344	1.519	0.344	1.519
	5th -6th	30	0.516	0.951	0.516	0.951
	7th	25	0.619	0.712	0.619	0.712
8-Story	1st -2nd	60	0.258	2.502	0.258	2.502
	3rd 4th	55	0.282	1.684	0.282	1.684
	5th -6th	45	0.344	0.949	0.344	0.949
	7th -8th	25	0.619	0.712	0.619	0.712
9-Story	1st -2nd	80	0.29	2.209	0.29	2.209
	3rd 4th	60	0.258	1.887	0.258	1.887
	5th -6th	45	0.344	1.519	0.344	1.519
	7th -8th	30	0.516	0.951	0.516	0.951
	9th	25	0.619	0.712	0.619	0.712
10-Story	1st -2nd	90	0.344	2.246	0.344	2.246
	3rd 4th	70	0.332	2.158	0.332	2.158
	5th -6th	60	0.258	1.353	0.258	1.353
	7th -8th	45	0.344	0.877	0.344	0.877
	9th-10th	25	0.619	0.712	0.619	0.712
11-Story	1st -2nd-3th	110	0.282	2.191	0.282	2.191
	4th-5th	100	0.31	1.46	0.31	1.46
	6th -7th	90	0.344	0.939	0.344	0.939
	8th -9th	60	0.258	0.627	0.258	0.627
	10th	45	0.344	0.464	0.344	0.464
	11th	30	0.516	0.527	0.516	0.527
12-Story	1st -2nd-3th	120	0.252	2.33	0.252	2.33
	4th-5th-6th	100	0.31	1.715	0.31	1.715
	7th -8th	80	0.29	0.984	0.29	0.984
	9th-10th	60	0.282	0.627	0.282	0.627
	11th	45	0.344	0.464	0.344	0.464
	12th	30	0.516	0.527	0.516	0.527
13-Story	1st -2nd-3th	130	0.238	2.324	0.238	2.324
	4th-5th-6th	110	0.282	1.928	0.282	1.928
	7th -8th	90	0.344	1.128	0.344	1.128
	9th-10th	70	0.332	0.84	0.332	0.84
	11th-12th	45	0.344	0.464	0.344	0.464
	13th	35	0.443	0.452	0.443	0.452
14-Story	1st -2nd-3th	130	0.238	2.719	0.238	2.719
	4th-5th-6th	110	0.282	2.279	0.282	2.279
	7th -8th	90	0.344	1.52	0.344	1.52
	9th-10th	80	0.29	0.953	0.29	0.953
	11th-12th	60	0.258	0.565	0.258	0.565
	13th -14th	35	0.443	0.452	0.443	0.452
15-Story	1st -2nd-3th	130	0.238	3.016	0.238	3.016
	4th-5th-6th	110	0.282	2.6	0.282	2.6
	7th -8th	90	0.344	1.988	0.344	1.988
	9th-10th	80	0.29	1.261	0.29	1.261
	11th-12th	60	0.258	0.9	0.258	0.9
	13th -14th	45	0.344	0.517	0.344	0.517
	15th	30	0.516	0.5274	0.516	0.5274

Table A-2
Structural details of RCSWs having a bay length of 6.5 m.

RCSWs	Floor	Wall thickness (cm)	$\rho_{Boundary,Y}$(%)	$\rho_{Boundary,X}$(%)	$\rho_{Web,Y}$(%)	$\rho_{Web,X}$(%)
4-Story	1st -2nd	25	0.619	1.237	0.619	1.237
	3rd 4th	20	0.774	0.678	0.774	0.678
5-Story	1st -2nd	30	0.516	1.252	0.516	1.252
	3rd 4th	30	0.619	0.636	0.619	0.636
	5th	25	0.774	0.336	0.774	0.336
6-Story	1st -2nd	35	0.443	1.419	0.443	1.419
	3rd 4th	30	0.516	0.868	0.516	0.868
	5th -6th	25	0.619	0.459	0.619	0.459
7-Story	1st -2nd	40	0.387	1.698	0.387	1.698
	3rd 4th	35	0.443	1.0169	0.443	1.0169
	5th -6th	30	0.516	0.467	0.516	0.467
	7th	25	0.619	0.459	0.619	0.459
8-Story	1st -2nd	40	0.387	2.13	0.387	2.13
	3rd 4th	35	0.443	1.491	0.443	1.491
	5th -6th	30	0.516	0.736	0.516	0.736
	7th -8th	25	0.619	0.459	0.619	0.459
9-Story	1st -2nd	45	0.344	2.116	0.344	2.116
	3rd 4th	40	0.387	1.609	0.387	1.609
	5th -6th	35	0.443	1.006	0.443	1.006
	7th -8th	30	0.516	0.67	0.516	0.67
	9th	25	0.619	0.459	0.619	0.459
10-Story	1st -2nd	45	0.344	2.604	0.344	2.604
	3rd 4th	40	0.387	2.024	0.387	2.024
	5th -6th	35	0.443	1.257	0.443	1.257
	7th -8th	30	0.516	0.84	0.516	0.84
	9th-10th	25	0.619	0.459	0.619	0.459
11-Story	1st -2nd-3th	80	0.344	1.62	0.344	1.62
	4th-5th	80	0.29	1.314	0.29	1.314
	6th -7th	70	0.332	0.936	0.332	0.936
	8th -9th	55	0.282	0.685	0.282	0.685
	10th	45	0.282	0.288	0.282	0.288
	11th	30	0.344	0.265	0.344	0.265
12-Story	1st -2nd-3th	90	0.344	2.062	0.344	2.062
	4th-5th-6th	80	0.29	1.538	0.29	1.538
	7th -8th	70	0.332	1.179	0.332	1.179
	9th-10th	60	0.282	0.837	0.282	0.837
	11th	50	0.282	0.657	0.282	0.657
	12th	35	0.443	0.25	0.443	0.25
13-Story	1st -2nd-3th	90	0.344	2.0098	0.344	2.0098
	4th-5th-6th	80	0.29	1.503	0.29	1.503
	7th -8th	70	0.332	0.9059	0.332	0.9059
	9th-10th	55	0.282	0.597	0.282	0.597
	11th-12th	45	0.344	0.288	0.344	0.288
	13th	30	0.516	0.265	0.516	0.265
14-Story	1st -2nd-3th	100	0.31	2.128	0.31	2.128
	4th-5th-6th	90	0.344	1.62	0.344	1.62
	7th -8th	80	0.29	1.1	0.29	1.1
	9th-10th	70	0.332	0.711	0.332	0.711
	11th-12th	55	0.282	0.544	0.282	0.544
	13th -14th	45	0.344	0.288	0.344	0.288
15-Story	1st -2nd-3th	100	0.31	2.409	0.31	2.409
	4th-5th-6th	90	0.344	1.894	0.344	1.894
	7th -8th	80	0.29	1.29	0.29	1.29
	9th-10th	70	0.332	0.949	0.332	0.949
	11th-12th	55	0.282	0.597	0.282	0.597
	13th -14th	45	0.344	0.288	0.344	0.288
	15th	30	0.516	0.265	0.516	0.265

Table A-3
Structural details of RCSWs having a bay length of 7.5 m.

RCSWs	Floor	Wall thickness (cm)	$\rho_{Boundary,Y}$(%)	$\rho_{Boundary,X}$(%)	$\rho_{Web,Y}$(%)	$\rho_{Web,X}$(%)
4-Story	1st -2nd	25	0.619	0.92	0.619	0.92
	3rd 4th	20	0.774	0.476	0.774	0.476
5-Story	1st -2nd	30	0.516	0.929	0.516	0.929
	3rd 4th	30	0.619	0.476	0.619	0.476
	5th	25	0.774	0.381	0.774	0.381
6-Story	1st -2nd	35	0.443	1.082	0.443	1.082
	3rd 4th	30	0.516	0.63	0.516	0.63
	5th -6th	25	0.619	0.381	0.619	0.381
7-Story	1st -2nd	40	0.387	1.257	0.387	1.257
	3rd 4th	35	0.443	0.796	0.443	0.796
	5th -6th	30	0.516	0.406	0.516	0.406
	7th	25	0.619	0.381	0.619	0.381
8-Story	1st -2nd	40	0.387	1.543	0.387	1.543
	3rd 4th	35	0.443	1.055	0.443	1.055
	5th -6th	30	0.516	0.602	0.516	0.602
	7th -8th	25	0.619	0.441	0.619	0.441
9-Story	1st -2nd	45	0.344	1.659	0.344	1.659
	3rd 4th	40	0.387	1.204	0.387	1.204
	5th -6th	35	0.443	0.796	0.443	0.796
	7th -8th	30	0.516	0.478	0.516	0.478
	9th	25	0.619	0.441	0.619	0.441
10-Story	1st -2nd	45	0.344	1.8171	0.344	1.8171
	3rd 4th	40	0.387	1.595	0.387	1.595
	5th -6th	35	0.443	1.055	0.443	1.055
	7th -8th	30	0.516	6.084	0.516	6.084
	9th-10th	25	0.619	0.574	0.619	0.574
11-Story	1st -2nd-3th	80	0.344	1.1152	0.344	1.1152
	4th-5th	80	0.29	0.94	0.29	0.94
	6th -7th	70	0.332	0.712	0.332	0.712
	8th -9th	55	0.282	0.543	0.282	0.543
	10th	45	0.282	0.284	0.282	0.284
	11th	30	0.344	0.264	0.344	0.264
12-Story	1st -2nd-3th	90	0.344	1.431	0.344	1.431
	4th-5th-6th	80	0.29	1.219	0.29	1.219
	7th -8th	70	0.332	0.939	0.332	0.939
	9th-10th	60	0.282	0.675	0.282	0.675
	11th	50	0.282	0.527	0.282	0.527
	12th	35	0.344	0.19	0.344	0.19
13-Story	1st -2nd-3th	90	0.344	1.711	0.344	1.711
	4th-5th-6th	80	0.29	1.219	0.29	1.219
	7th -8th	70	0.332	0.997	0.332	0.997
	9th-10th	55	0.282	0.48	0.282	0.48
	11th-12th	45	0.344	0.288	0.344	0.288
	13th	30	0.516	0.264	0.516	0.264
14-Story	1st -2nd-3th	100	0.31	1.747	0.31	1.747
	4th-5th-6th	90	0.344	1.281	0.344	1.281
	7th -8th	80	0.29	0.828	0.29	0.828
	9th-10th	70	0.332	0.594	0.332	0.594
	11th-12th	55	0.282	0.48	0.282	0.48
	13th -14th	45	0.344	0.171	0.344	0.171
15-Story	1st -2nd-3th	100	0.31	1.862	0.31	1.862
	4th-5th-6th	90	0.344	1.386	0.344	1.386
	7th -8th	80	0.29	1.043	0.29	1.043
	9th-10th	70	0.332	0.664	0.332	0.664
	11th-12th	55	0.282	0.492	0.282	0.492
	13th -14th	45	0.344	0.277	0.344	0.277
	15th	30	0.516	0.367	0.516	0.367

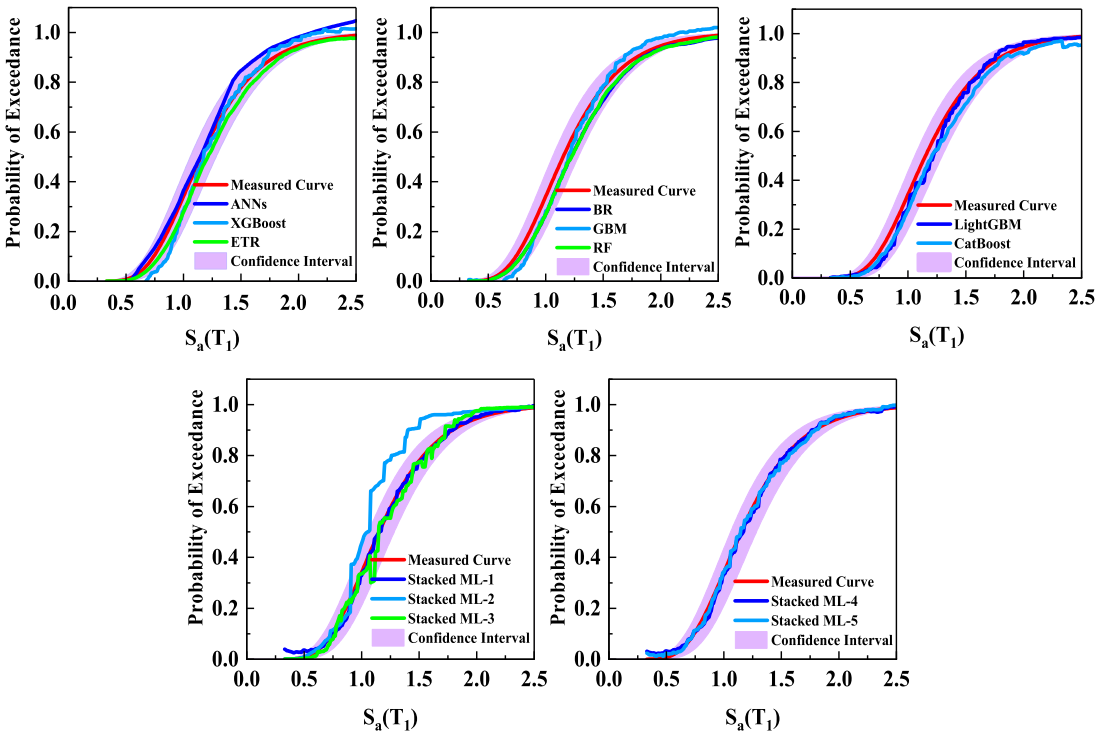

Fig. A-2. Estimated fragility curves in total collapse performance level for the 7-Story RCSW located on soil B given bay length of 5.5 m including NNP records.

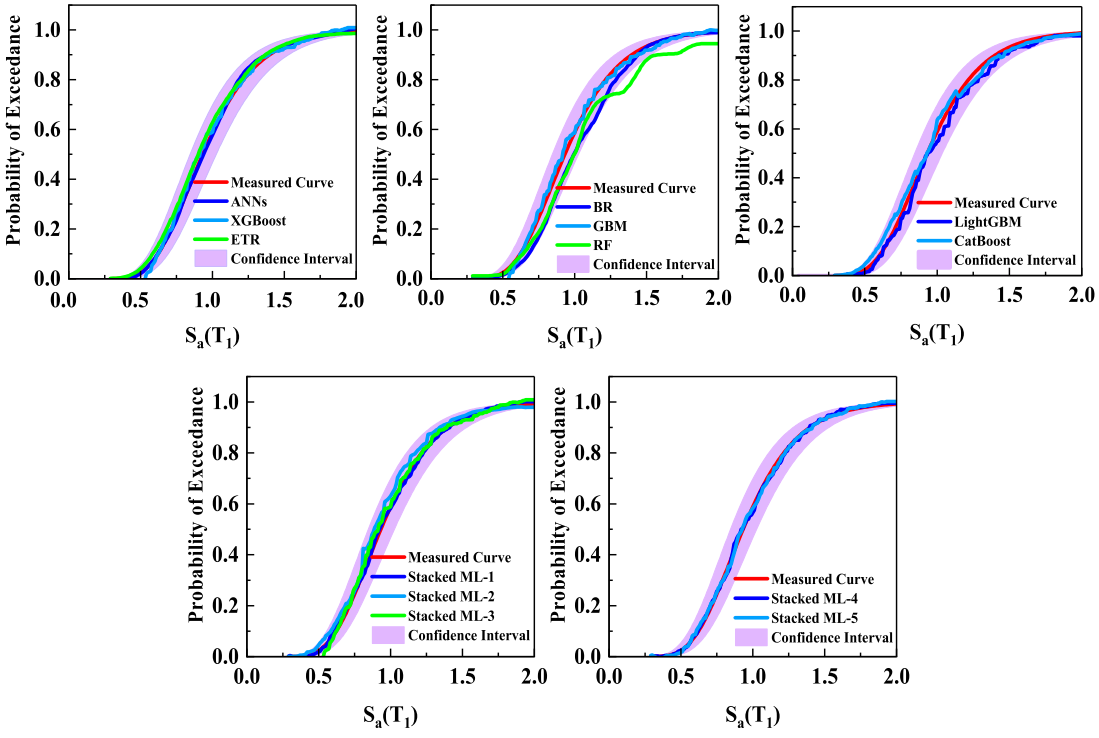

Fig. A-3. Estimated fragility curves in total collapse performance level for the 9-Story RCSW located on soil D given bay length of 6.5 m including NPL records.

of RCSWs and provides an optimization-based ML prediction tool for seismic probability and risk assessment of RCSWs. The fast track of seismic risk assessment of RCSWs can help decision-makers provide a risk plan for a city and provide information on the current performance levels of buildings and the retrofitting cost. Therefore, to provide a wide range of databases, the 4-, to 15-story RCSWs having different bay lengths and four constructional soil types have been investigated. The results of the study showed that:

- Improved ML models with resampling and pipeline methods showed significant improvements (by approximately 43.8 %) in the curve-fitting ability. For instance, the accuracy of estimating M_{IDA} curves of RCSWs improved up to 99.1 %. In addition, optimization-based Stacked ML models are the best-fitted curves with an accuracy of

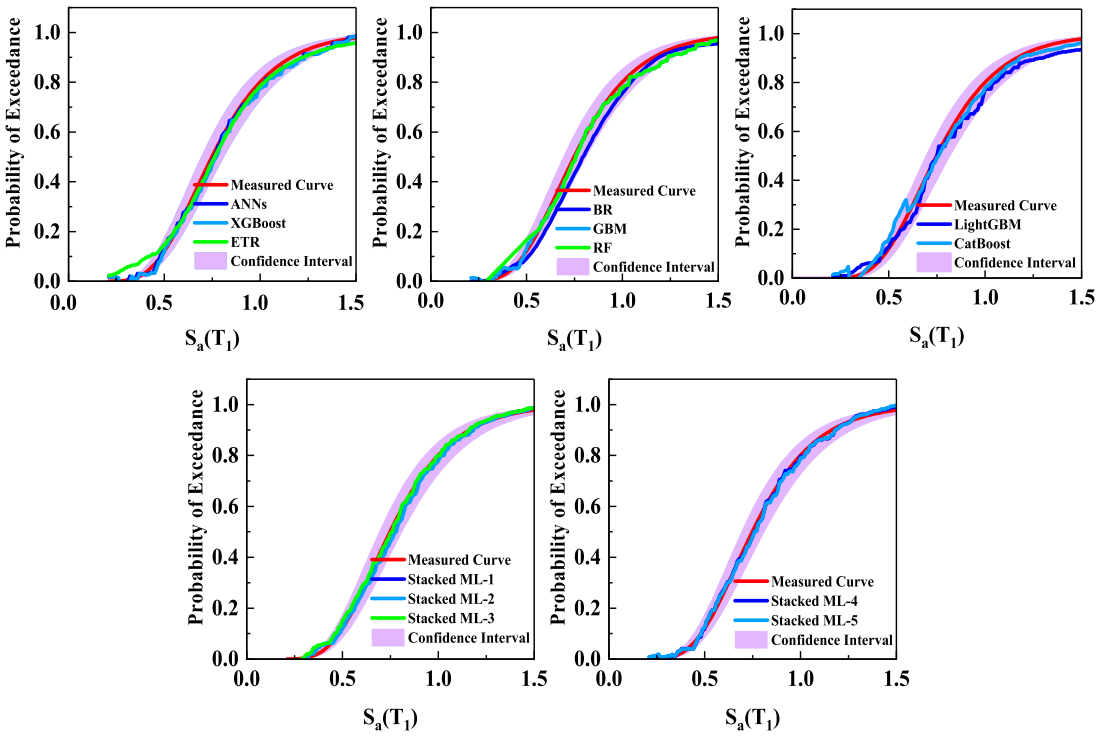

Fig. A-4. Estimated fragility curves in total collapse performance level for the 11-story RCSW located on soil C given bay length of 7.5 m including NPL records.

99.4 % for estimating the fragility curve in life-safety performance level. The higher accuracy of proposed optimization-based Stacked ML models can guarantee result of seismic risk assessment.

- To validate the proposed optimization-based Stacked ML models, a 5-story RCSW has been modeled and analyzed to be used as a test dataset for the proposed ML models. Results confirm that Stacked ML models have curve fitting ability and could estimate M_{IDA} and seismic probability curves of a general building. According to results, for NPL records, the Stacked ML-4, Stacked ML-5, and Stacked ML-3 with accuracies of 99.9 %, 99.2 %, and 98.5 % are the best prediction methods, respectively, and for NNP records, the Stacked ML-4 and Stacked ML-5 with accuracies of 99.7 % and 98.8 % are the best prediction models. Furthermore, the proposed Stacked ML models have lower values of error indicators that confirm their ability to estimate fragility curves with higher reliability.
- Proposed optimization-based Stacked ML models have a good estimation of $\lambda_{Life\text{-}safety}$ that can be used by decision-makers. The $\lambda_{Life\text{-}safety}$ for the actual curve of NPL and NNP records were determined equal to 0.256 % and 0.233 %, respectively. However, the values of 0.268 % and 0.215 % have been achieved by the proposed Stacked ML-4 for the NPL and NNP records, respectively. Moreover, Stacked ML-5 has predicted values of 0.23 % and 0.192 % for the NPL and NNP records, respectively. The differences between the values are in the acceptable range since the ML models can reduce the modeling time and analysis complexity while the seismic risk assessment can be done in a couple of seconds for a wide range of buildings.
- Considering the minimum knowledge of Python programming language, it will be hard to use the results and proposed ML models. Therefore, the authors provided a GUI that can be easily filled by the user in order to seismic risk assessment of RCSWs. The GUI can provide information for structural designers ranging from seismic performance levels of RCSWs, predicted M_{IDA} and seismic failure probability curves in different predefined performance thresholds, and finally, calculating mean annual frequency for assumed performance level and defined seismic hazard curve.

CRediT authorship contribution statement

Farzin Kazemi: Writing – original draft, Conceptualization, Methodology, Formal analysis, Software, Resources, Validation. **Neda Asgarkhani:** Writing – original draft, Investigation, Data curation, Resources, Methodology, Formal analysis, Software, Validation. **Robert Jankowski:** Supervision, Writing – review & editing.

Declaration of competing interest

The authors declare that they have no known competing financial interests or personal relationships that could have appeared to influence the work reported in this paper.

Data availability

Data will be made available on request.

Acknowledgments

The authors express their gratitude to Professor (Associate) Benyamin Mohebi for his valuable contributions and assistance throughout the modeling process.

Appendix

Fig. A-1 presents the reinforcement detail of RCSW and Tables A-1 to A-3 illustrate the details of RCSWs having bay lengths of 5.5 m, 6.5 m, and 7.5 m, respectively.

Figs. A-2–A-4 presents the estimated fragility curves in total collapse performance level for the 7-, 9-, and 11-Story RCSWs using ML models.

References

Abraik, E., & Youssef, M. A. (2018). Seismic fragility assessment of superelastic shape memory alloy reinforced concrete shear walls. *Journal of Building Engineering, 19*, 142–153.

Applied Technology Council, & United States. Federal Emergency Management Agency (FEMA P695). (2009). Quantification of building seismic performance factors. US Department of Homeland Security, FEMA.

ASCE/SEI 7-22. (2023). Minimum design loads for buildings and other structures. Reston, VA: American Society of Civil Engineers.

Asgarkhani, N., Kazemi, F., Jakubczyk-Gałczyńska, A., Mohebi, B., & Jankowski, R. (2024a). Seismic response and performance prediction of steel buckling-restrained braced frames using machine-learning methods. *Engineering Applications of Artificial Intelligence, 128*, Article 107388.

Asgarkhani, N., Kazemi, F., & Jankowski, R. (2023). Machine learning-based prediction of residual drift and seismic risk assessment of steel moment-resisting frames considering soil-structure interaction. *Computers & Structures, 289*, Article 107181.

Asgarkhani, N., Yakhchalian, M., & Mohebi, B. (2020). Evaluation of approximate methods for estimating residual drift demands in BRBFs. *Engineering Structures, 224*, Article 110849.

Asjodi, A. H., Dolatshahi, K. M., & Burton, H. V. (2023). Three-dimensional fragility surface for reinforced concrete shear walls using image-based damage features. *Earthquake Engineering & Structural Dynamics*.

Atabay, Ş. (2009). Cost optimization of three-dimensional beamless reinforced concrete shear-wall systems via genetic algorithm. *Expert Systems with Applications, 36*(2), 3555–3561.

Atabay, S., & Gulay, F. G. (2009). The study of the effect of changes in cost of the materials used in 3-D shear-wall reinforced concrete structures on the optimum dimensions. *Expert Systems with Applications, 36*(3), 4331–4337.

Chou, J. S., Liu, C. Y., Prayogo, H., Khasani, R. R., Gho, D., & Lalitan, G. G. (2022). Predicting nominal shear capacity of reinforced concrete wall in building by metaheuristics-optimized machine learning. *Journal of Building Engineering, 61*, Article 105046.

Dazio, A., Beyer, K., & Bachmann, H. (2009). Quasi-static cyclic tests and plastic hinge analysis of RC structural walls. *Engineering Structures, 31*(7), 1556–1571.

Deger, Z. T., & Taskin, G. (2022). A novel GPR-based prediction model for cyclic backbone curves of reinforced concrete shear walls. *Engineering Structures, 255*, Article 113874.

Dehestani, A., Kazemi, F., Abdi, R., & Nitka, M. (2022). Prediction of fracture toughness in fibre-reinforced concrete, mortar, and rocks using various machine learning techniques. *Engineering Fracture Mechanics, 276*, Article 108914.

Erochko, J., Christopoulos, C., Tremblay, R., & Choi, H. (2011). Residual drift response of SMRFs and BRB frames in steel buildings designed according to ASCE 7–05. *Journal of Structural Engineering, 137*(5), 589–599.

Gentile, R., & Galasso, C. (2020). Gaussian process regression for seismic fragility assessment of building portfolios. *Structural Safety, 87*, Article 101980.

Grammatikou, S., Biskinis, D., & Fardis, M. N. (2015). Strength, deformation capacity and failure modes of RC walls under cyclic loading. *Bulletin of Earthquake Engineering, 13*, 3277–3300.

Jiang, H., & Kurama, Y. C. (2010). Analytical Modeling of Medium-Rise Reinforced Concrete Shear Walls. *ACI Structural Journal, 107*(4).

Kazemi, F., & Jankowski, R. (2023a). Seismic performance evaluation of steel buckling-restrained braced frames including SMA materials. *Journal of Constructional Steel Research, 201*, Article 107750.

Kazemi, F., & Jankowski, R. (2023b). Machine learning-based prediction of seismic limit-state capacity of steel moment-resisting frames considering soil-structure interaction. *Computers & Structures, 274*, Article 106886.

Kazemi, F., Asgarkhani, N., & Jankowski, R. (2023a). Predicting seismic response of SMRFs founded on different soil types using machine learning techniques. *Engineering Structures, 274*, Article 114953.

Kazemi, F., Asgarkhani, N., & Jankowski, R. (2023b). Machine learning-based seismic response and performance assessment of reinforced concrete buildings. *Archives of Civil and Mechanical Engineering, 23*(2), 94.

Kazemi, F., Asgarkhani, N., & Jankowski, R. (2023c). Machine learning-based seismic fragility and seismic vulnerability assessment of reinforced concrete structures. *Soil Dynamics and Earthquake Engineering, 166*, Article 107761.

Kazemi, F., Asgarkhani, N., & Jankowski, R. (2024). Enhancing seismic performance of steel buildings having semi-rigid connection with infill masonry walls considering soil type effects. *Soil Dynamics and Earthquake Engineering, 177*, Article 108396.

Asgarkhani, N., Kazemi, F., & Jankowski, R. (2024b). Active Learning on Ensemble Machine-Learning Model to Retrofit Buildings Under Seismic Mainshock-Aftershock Sequence. In *In International Conference on Computational Science* (pp. 470–478).

Kazemi, F., Shafighfard, T., & Yoo, D. Y. (2024c). Data-driven modeling of mechanical properties of fiber-reinforced concrete: A critical review. *Archives of Computational Methods in Engineering*, 1–30.

Kazemi, F., Asgarkhani, N., Shafighfard, T., Jankowski, R., & Yoo, D. Y. (2024d). Machine-Learning Methods for Estimating Performance of Structural Concrete Members Reinforced with Fiber-Reinforced Polymers. *Archives of Computational Methods in Engineering*, 1–33.

Kolozvari, K., Orakcal, K., & Wallace, J. W. (2015a). Modeling of cyclic shear-flexure interaction in reinforced concrete structural walls. i: theory. ASCE. *J. Struct. Eng., 141*(5), 04014135.

Kolozvari, K., Tran, T., Orakcal, K., & Wallace, J. W. (2015b). Modeling of cyclic shear-flexure interaction in reinforced concrete structural walls. ii: Experimental validation, ASCE. *Journal of Structural Engineering, 141*(5), 04014136.

Kolozvari, K., Orakcal, K., & Wallace, J. W. (2015c). Shear-flexure interaction modeling for reinforced concrete structural walls and columns under reversed cyclic loading. *Pacific Earthquake Engineering Research Center, University of California, Berkeley, PEER Report*, (2015/12).

Kolozvari, K. I. (2013). *Analytical modeling of cyclic shear-flexure interaction in reinforced concrete structural walls*. Los Angeles: University of California.

Kolozvari, K., Orakcal, K., & Wallace, J. W. (2018). New opensees models for simulating nonlinear flexural and coupled shear-flexural behavior of RC walls and columns. *Computers & Structures, 196*, 246–262.

Le Nguyen, K., Trinh, H. T., Banihashemi, S., & Pham, T. M. (2023). Machine learning approaches for lateral strength estimation in squat shear walls: A comparative study and practical implications. *Expert Systems with Applications, 239*, 1–19.

Lee, T. H., & Mosalam, K. M. (2005). Seismic demand sensitivity of reinforced concrete shear-wall building using FOSM method. *Earthquake Engineering & Structural Dynamics, 34*(14), 1719–1736.

Liao, W., Huang, Y., Zheng, Z., & Lu, X. (2022). Intelligent generative structural design method for shear wall building based on "fused-text-image-to-image" generative adversarial networks. *Expert Systems with Applications, 210*, Article 118530.

Lowes, L. N., Lehman, D. E., Birely, A. C., Kuchma, D. A., Marley, K. P., & Hart, C. R. (2012). Earthquake response of slender planar concrete walls with modern detailing. *Engineering Structures, 43*, 31–47.

Ma, G., Wang, Y., & Hwang, H. J. (2023). Genetic programming-based backbone curve model of reinforced concrete walls. *Engineering Structures, 283*, Article 115824.

Mangalathu, S., Jang, H., Hwang, S. H., & Jeon, J. S. (2020). Data-driven machine-learning-based seismic failure mode identification of reinforced concrete shear walls. *Engineering Structures, 208*, Article 110331.

Mansourdehghan, S., Dolatshahi, K. M., & Asjodi, A. H. (2022). Data-driven damage assessment of reinforced concrete shear walls using visual features of damage. *Journal of Building Engineering, 53*, Article 104509.

McKenna, F., Fenves, G. L., & Scott, M. H. (2015). *Open system for earthquake engineering simulation*. Berkeley, CA: Pacific Earthquake Engineering Research Center.

Miceli, E., & Castaldo, P. (2024). Robustness improvements for 2D reinforced concrete moment resisting frames: Parametric study by means of NLFE analyses. *Structural Concrete, 25*(1), 9–31.

Moaf, F. O., Kazemi, F., Abdelgader, H. S., & Kurpińska, M. (2023). Machine learning-based prediction of preplaced aggregate concrete characteristics. *Engineering Applications of Artificial Intelligence, 123*, Article 106387.

Modirzadeh, M., Tesfamariam, S., & Milani, A. S. (2012). Performance based earthquake evaluation of reinforced concrete buildings using design of experiments. *Expert Systems with Applications, 39*(3), 2919–2926.

Orakcal, K., Wallace, J. W., & Conte, J. P. (2004). Flexural modeling of reinforced concrete walls-model attributes. *Structural Journal, 101*(5), 688–698.

Shafighfard, T., Kazemi, F., Bagherzadeh, F., Mieloszyk, M., & Yoo, D. Y. (2024). Chained machine learning model for predicting load capacity and ductility of steel fiber–reinforced concrete beams. *Computer-Aided Civil and Infrastructure Engineering*.

Turchetti, F., Tubaldi, E., Patelli, E., Castaldo, P., & Málaga-Chuquitaype, C. (2023). Damage modelling of a bridge pier subjected to multiple earthquakes: A comparative study. *Bulletin of Earthquake Engineering, 21*(9), 4541–4564.

Zhang, H., Cheng, X., Li, Y., & Du, X. (2022). Prediction of failure modes, strength, and deformation capacity of RC shear walls through machine learning. *Journal of Building Engineering, 50*, Article 104145.

Castaldo, P., & Miceli, E. (2023). Optimal single concave sliding device properties for isolated multi-span continuous deck bridges depending on the ground motion characteristics. *Soil Dynamics and Earthquake Engineering, 173*, Article 108128.